Transactions of the ASME®

Transactions of the ASME, Journal of Heat Transfer (ISSN 0022-1481) is published bi-monthly (Feb., Apr., June, Aug., Oct., Dec.) by The American Society of Mechanical Engineers, Three Park Avenue, New York, NY 10016. Periodicals postage paid at New York, NY and additional mailing offices. POSTMASTER: Send address changes to Transactions of the ASME, Journal of Heat Transfer, c/o THE AMERICAN SOCIETY OF MECHANICAL ENGINEERS, 22 Law Drive, Box 2300, Fairfield, NJ 07007-2300. **CHANGES OF ADDRESS** must be received at Society headquarters seven weeks before they are to be effective. Please send old label and new address. **STATEMENT from By-Laws.** The Society shall not be responsible for statements or opinions advanced in papers or ... printed in its publications (B7.1, Para. 3), **COPYRIGHT** © **2001** by The American Society of Mechanical Engineers. For authorization to photocopy material for internal or personal use under those circumstances not falling within the fair use provisions of the Copyright Act, contact the Copyright Clearance Center (CCC), 222 Rosewood Drive, Danvers, MA 01923, tel: 978-750-8400, *www.copyright.com.* Request for special permission or bulk copying should be addressed to Reprints/Permission Department. **INDEXED** by Applied Mechanics Reviews and Engineering Information, Inc. Canadian Goods & Services Tax Registration #126148048.

Journal of Heat Transfer

Published Bimonthly by The American Society of Mechanical Engineers

VOLUME 123 • NUMBER 2 • APRIL 2001

TECHNICAL PAPERS

(Contents continued on inside back cover)

This journal is printed on acid-free paper, which exceeds the ANSI Z39.48-1992 specification for permanence of paper and library materials. ♾™
♻ 85% recycled content, including 10% post-consumer fibers.

Journal of Heat Transfer Volume 123, Number 2 APRIL 2001

Heat Exchangers

TECHNICAL NOTES

ANNOUNCEMENTS

Gap Formation and Interfacial Heat Transfer Between Thermoelastic Bodies in Imperfect Contact

S. L. Lee
Professor
Mem. ASME

C. R. Ou
Department of Power Mechanical Engineering,
National Tsing-Hua University,
Hsinchu 30043, Taiwan

In this paper, the integration scheme is employed to solve a coupling problem of transient heat conduction and displacement due to thermal deformation. Based on the resulting displacement, gap or contact pressure on the interface of two thermoelastic bodies in imperfect contact is estimated. Such information is then used to determine the interfacial heat transfer between the two thermoelastic bodies. This again affects the temperature distribution and thus the thermal deformation. In the course of heat transfer and thermal deformation, effect of thermal rectification also is taken into account. Numerical solutions of transient and steady-state quantities including gap formation, normal stress, and temperature are demonstrated for a pair of stainless steel and aluminum with conforming shapes. Such an analysis of conduction-deformation interaction based on a finite-difference-like scheme has not been studied in the past. [DOI: 10.1115/1.1338133]

Keywords: Contact Resistance, Finite Difference, Heat Transfer, Stress, Transient

Introduction

Gap formation or a great decrease in the contact pressure due to thermal deformation of conforming bodies in contact is encountered in many industrial cases. Duplex heat exchanger tubes [1,2] and casting systems [3–5] are some of the examples. Thermal deformation does not significantly affect the thermal conductivity of the solid bodies. However, it could cause gap formation or a great decrease in the contact pressure that would lead to a large thermal resistance across the interface. Such a thermal resistance might even dominate the entire heat transfer process when both contact bodies are good thermal conductors and/or the interstitial gaseous (or vacuum) medium has a very low thermal conductivity.

In conventional studies (e.g., Barry and Goodling [6], Tzong and Lee [7]), the interface thermal resistance is usually assigned as a constant due to the lack of reliable information. Some investigators estimated the interface thermal resistance with the method of inverse heat conduction [5] or an assumption of free thermal expansion [8]. To resolve the problem, some efforts were made by measuring the gap formation directly [4,5] and indirectly [3]. Unfortunately, it does not seem possible to develop an empirical correlation for estimation of gap distribution from the very limited measured data.

The thermophysical phenomena between two contact/separate bodies are very complex. For separate surfaces with a very small gap or contact surfaces with surface roughness, the Smolukhovskii effect on the thermal conductivity of the interstitial gaseous medium could be considerable [9–14]. Such an effect arises from the influence of the solid ''wall'' on the mean free path of the gas molecules. In addition, experimental studies evidence the thermal hysteresis and rectification phenomena in thermal contact resistance for bodies in imperfect contact.

For a joint subjected to a cyclic loading, Clausing and Chao [15] and Thomas and Probert [10] observed the thermal hysteresis that the thermal contact resistance during unloading is usually lower than the corresponding values during the first loading. As remarked by Madhusudana and Fletcher [17], during first loading, the actual contact area is formed by the elastoplastic deformation of asperities on the contact surfaces coupled with the elastic deformation of the large-scale irregularities and the underlying materials. During the unloading, the reduction of the actual contact area is due only to the elastic recovery of both the asperities and the bulk sublayers. This seems to be a good explanation for the thermal hysteresis.

The so-called thermal rectification refers to a particular physical phenomenon that the thermal contact resistance between bodies A and B might depend on the heat transfer direction, from A to B or from B to A. The thermal rectification was first noted by Starr [18]. Subsequent experimental observations [16,19,20] and theoretical analysis [20–22] confirmed its existence for dissimilar materials in contact. For similar materials, lower thermal contact resistance was observed with heat flux from a rough surface to a smooth surface [16,20]. Although the reasoning has not yet been completely understood, the thermal rectification is generally recognized to arise from thermal distortion of contact surfaces [13,17,20,23].

The experimental results of Padgett and Fletcher [19] suggest that the interfacial heat transfer is dominated by the contact pressure for surfaces in imperfect contact. Similarly, the gap width would become the dominator when the surfaces are separate. To handle such a coupling problem of thermal deformation and heat transfer, Song et al. [24] developed a coupled finite element model to simulate a metal casting process. Gap formation in the mold-casting interface was formulated by using an interface element without considering the thermal rectification effect. Huang et al. [8] estimated the gap width on the mold-casting interface for a casting system with the assumption of free thermal expansion. The stress in the entire mold-casting system was assumed zero such that no stress analysis was performed. The purpose of the present work is to demonstrate a simple numerical procedure for study of gap formation and interfacial heat transfer on the interface of two thermoelastic bodies in contact. The integration scheme for displacement-stress analysis [25] is employed to solve the gap formation and contact pressure. The interfacial thermal resistance across the conforming surfaces is then determined from the computed gap width and contact pressure through the use of the experimental results of thermal rectification from Padgett and

Contributed by the Heat Transfer Division for publication in the JOURNAL OF HEAT TRANSFER. Manuscript received by the Heat Transfer Division January 20, 2000; revision received, July 12, 2000. Associate Editor: B. Peterson.

Fletcher [19]. The temperature distribution is solved with an integration scheme for energy equation [7]. Such an analysis of temperature/deformation interaction based on a finite-difference-like scheme has not been studied in the past.

Theoretical Analysis

Consider a pair of two-dimensional metals with conforming surface as shown in Fig. 1. The outer metal is a square stainless steel 304 of dimension $L\times L$, while inside is coupled with an aluminum 2024-T4. Both metals are initially at stress-free state and in contact at a zero contact pressure when they have the same uniform temperature T_{in}. Let the outer surface temperature of the stainless steel be suddenly changed to T_1 at $x=0$ and T_2 at $x=L$, while the other two sides ($y=0$ and $y=L$) are insulated. The outer surface of the stainless steel is maintained motionless during the entire heat transfer process, while the thermal deformation assumes plain stress. If a plain strain situation is assumed, the Young's modulus E and the Poisson ratio ν in the following plain stress formulation should be replaced by $E/(1-\nu^2)$ and $\nu/(1-\nu)$, respectively.

After imposing the above assumptions and introducing the dimensionless quantities

$$E^*=\frac{E}{E_{\rm ref}},\quad \xi=\frac{x}{L},\quad \eta=\frac{y}{L},\quad u=\frac{U}{L},\quad v=\frac{V}{L},$$

$$\alpha^*=\alpha(T_1-T_2),\quad \theta=\frac{T-T_2}{T_1-T_2},\quad \kappa=\frac{k}{k_{\rm ref}},\quad \tau=\left(\frac{k}{\rho c_p}\right)_{\rm ref}\frac{t}{L^2},$$

$$\gamma=\frac{\rho c_p}{(\rho c_p)_{\rm ref}},\quad \rho^*=\frac{\rho}{\rho_{\rm ref}},\quad \beta=\left(\frac{k/\rho c_p}{L\sqrt{E/\rho}}\right)_{\rm ref} \tag{1}$$

the governing equations can be written as [7,25]

$$\frac{\partial}{\partial\xi}\left(\frac{E^*}{1+\nu}\frac{\partial u}{\partial\xi}\right)+\frac{\partial}{\partial\eta}\left(\frac{E^*}{1+\nu}\frac{\partial u}{\partial\eta}\right)=\frac{\partial(E^*\phi)}{\partial\xi}-\frac{\partial(E^*\psi)}{\partial\eta}+\rho^*\beta^2\frac{\partial^2 u}{\partial\tau^2} \tag{2}$$

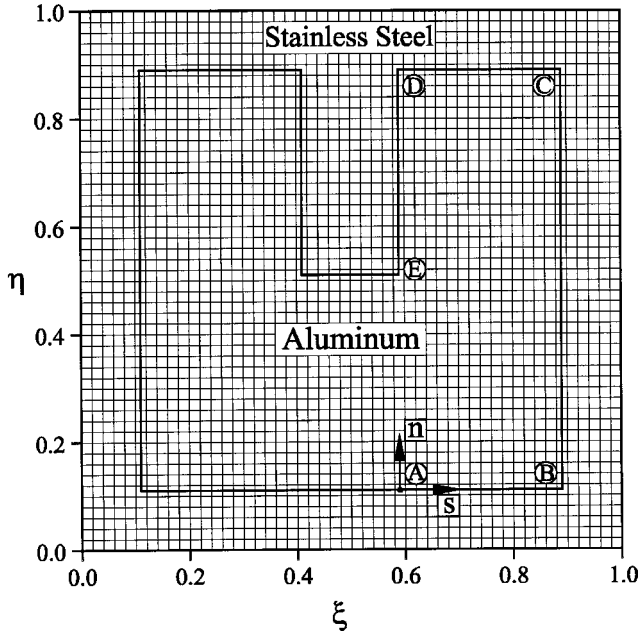

Fig. 1 System description and grids for the two-dimensional problem

$$\frac{\partial}{\partial\xi}\left(\frac{E^*}{1+\nu}\frac{\partial v}{\partial\xi}\right)+\frac{\partial}{\partial\eta}\left(\frac{E^*}{1+\nu}\frac{\partial v}{\partial\eta}\right)=\frac{\partial(E^*\psi)}{\partial\xi}+\frac{\partial(E^*\phi)}{\partial\eta}+\rho^*\beta^2\frac{\partial^2 v}{\partial\tau^2} \tag{3}$$

$$\gamma\frac{\partial\theta}{\partial\tau}=\frac{\partial}{\partial\xi}\left(\kappa\frac{\partial\theta}{\partial\xi}\right)+\frac{\partial}{\partial\eta}\left(\kappa\frac{\partial\theta}{\partial\eta}\right) \tag{4}$$

$$\phi=\frac{1}{1-\nu}\alpha^*(\theta-\theta_{\rm in})-\frac{\nu}{1-\nu^2}I,\quad \psi=\frac{\omega}{2(1+\nu)}, \tag{5}$$

$$I=\frac{\partial u}{\partial\xi}+\frac{\partial v}{\partial\eta},\quad \omega=\frac{\partial v}{\partial\xi}-\frac{\partial u}{\partial\eta}. \tag{6}$$

The associated boundary conditions are

$$u(0,\eta,\tau)=0,\quad v(0,\eta,\tau)=0,\quad u(1,\eta,\tau)=0,\quad v(1,\eta,\tau)=0$$
$$u(\xi,0,\tau)=0,\quad v(\xi,0,\tau)=0,\quad u(\xi,1,\tau)=0,\quad v(\xi,1,\tau)=0$$
$$\theta(0,\eta,\tau)=1,\quad \theta(1,\eta,\tau)=0,$$
$$\partial\theta(\xi,0,\tau)/\partial\eta=0,\quad \partial\theta(\xi,1,\tau)/\partial\eta=0. \tag{7}$$

The initial condition is

$$\theta(\xi,\eta,0)=\theta_{\rm in}. \tag{8}$$

Note that the dimensionless material properties $(E^*,\nu,\gamma,\kappa,\alpha^*)$ are discontinuous functions across the stainless steel-aluminum interface. Their values are

$$(E^*,\nu,\gamma,\kappa,\alpha^*)=(E_s/E_{\rm ref},\nu_s,(\rho c_p)_s/(\rho c_p)_{\rm ref},k_s/k_{\rm ref},(\alpha^*)_s)\quad \text{in stainless steel} \tag{9a}$$

$$(E^*,\nu,\gamma,\kappa,\alpha^*)=(E_a/E_{\rm ref},\nu_a,(\rho c_p)_a/(\rho c_p)_{\rm ref},k_a/k_{\rm ref},(\alpha^*)_a)\quad \text{in aluminum}, \tag{9b}$$

where the subscripts s and a denote quantities of stainless steel and aluminum, respectively.

In the course of heat transfer, the stainless steel-aluminum interface could be either separate or in contact with each other at a contact pressure due to thermal deformation of both metals. Figure 2 illustrates a pair of schematic conforming surfaces when they are in contact at a normal pressure $-\sigma_{nn}$ or when they are separate with a small gap δ. In case they are in contact (Fig. 2(a)), the interfacial thermal resistance is expressible as

$$R_{\rm inf}=(R_m^{-1}+R_g^{-1})^{-1}, \tag{10}$$

where R_m is the thermal contact resistance of the conforming surfaces in vacuum, while R_g stands for the thermal resistance through the interstitial gaseous medium. The two thermal resistance modes should be modeled in parallel [10].

Experimental data of thermal contact resistance R_m are available for some particular metals and surface roughness [16,19]. There is also a theory dealing with the thermal resistance through the interstitial gaseous medium R_g [9,10], i.e.

$$R_g=\frac{\overline{\varepsilon}}{k_g},\quad \overline{\varepsilon}=S_n\Big/\int_0^{S_n}\frac{dS_n}{\varepsilon+l_1+l_2}, \tag{11}$$

where k_g is the thermal conductivity of the interstitial gaseous medium. S_n and $\varepsilon(S_n)$ denote, respectively, the apparent contact area of the surfaces and the surface roughness, while l_1 and l_2 are known as ''temperature jump distances'' due to the Smolukhovskii effect at both surfaces. Note that the equivalent thickness of the interstitial gas $\overline{\varepsilon}$ defined in Eq. (11) is the volumetric reciprocal mean reciprocal ($vrmr$) value of the surface roughness. If there is an additional small gap δ in the interface as illustrated in Fig. 2(b), it is reasonable to add a thermal resistance R_δ into Eq. (10) in series for simplicity. This yields

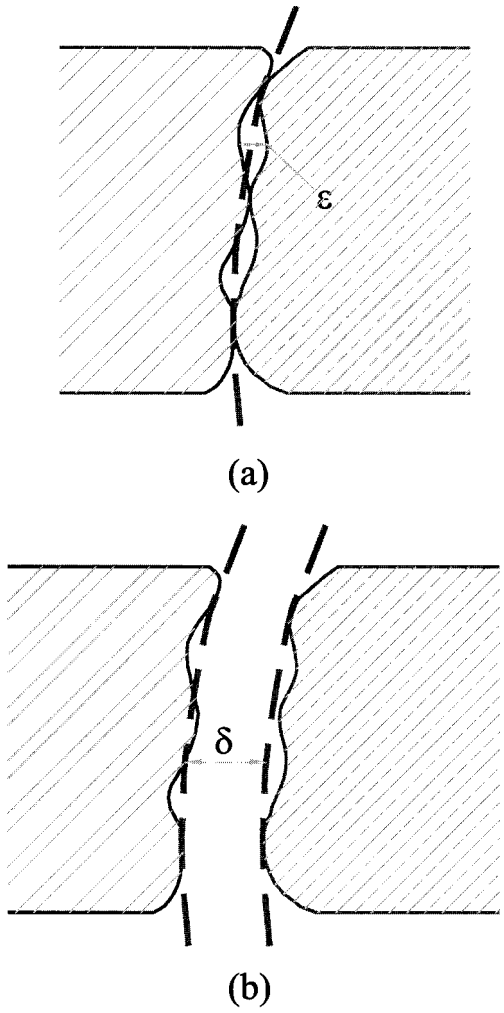

Fig. 2 A pair of schematic rough surfaces (*a*) in contact, or (*b*) when separated

$$R_{\inf}=(R_m^{-1}+R_g^{-1})^{-1}+R_\delta \tag{12}$$

$$R_\delta=\delta/k_g\,. \tag{13}$$

The first term on the right-hand-side of Eq. (12) should be evaluated at zero contact pressure such that Eq. (12) continuously reduces to Eq. (10) when the gap δ diminishes to zero. The use of Eqs. (12) and (13) will preclude the possibility of resulting an unphysical solution remarked by Barber [26], Comninou and Dundurs [27], and Comninou et al. [28].

As reported by Madhusudana [29], the thermal resistance of interstitial gas R_g does not depend on the gas pressure as long as the gas pressure is not below 100 torr (133 kPa). It seems to depend mainly on the topography of the interstitial gas (11). However, knowledge of both topography of surface roughness (ε) and temperature jump distance ($l=l_1+l_2$) is required in the use of the theory (11). The former depends on the deformation of the asperities, while the latter is a function of $\varepsilon+\delta$. Both are very difficult to determine. Fortunately, the effect of gas resistance R_g on the overall resistance $R_{\inf}$ is generally small, especially when the surfaces are metallic and/or there is a large gap δ. Therefore, Eq. (12) can be practically simplified as

$$R_{\inf}=R_m+R_\delta\,. \tag{14}$$

Such a simplification has been widely adopted by the previous investigators (e.g., [1,2,24,30–32]).

Note also that in evaluating the interfacial thermal resistance $R_{\inf}$, contribution of thermal radiation is negligible up to about 600°C [29,33]. In their experimental study on air gap formation in solidification processes of a pure aluminum and an Al-13.2 % Si alloy, Nishida et al. [4] found that heat conduction was the dominant mode of the interfacial heat transfer across the air gap. Heat transfer by thermal radiation was negligibly small. Thus, contribution of thermal radiation is neglected in the present study as suggested by Madhusudana and Fletcher [17]. Nevertheless, validation of this assumption will be examined later.

Solution Method

In the present study, the displacement Eqs. (2) and (3) are solved on a Cartesian grid system (ξ_i,η_j) as shown in Fig. 1 by using an integration scheme for displacement-stress analysis [25]. The grid system is arranged such that the stainless steel-aluminum interface intersects the grid line between two adjacent grid points. At the locations where gap forms ($\delta>0$), the stainless steel-aluminum interface is treated as a boundary with free surface condition (zero traction). Otherwise, the interface will be assumed perfectly bonded. As demonstrated in Lee and Ou [25], the displacements on both sides of a separate interface can be accurately computed from the resulting displacements at the nearest grid points. This allows the gap on the interface to be evaluated. The interface will be shifted to the type of contact interface for next iteration if the gap width becomes negative. Similarly, the normal stress at a contact interface can be simply estimated with a linear interpolation from the computed stresses at the nearest grid points on both sides of the interface. Separate interface will be assumed for next iteration if the normal stress becomes tensile. For a given temperature field θ, the numerical procedure should be iterated until the solution converges and satisfies the particular requirement along the stainless steel-aluminum interface:

$$\begin{aligned}&\sigma_{nn}\leqslant 0 \ \text{ and } \ \delta=0 \quad \text{for contact interface}\\ &\delta>0 \ \text{ and } \ \sigma_{nn}=0 \quad \text{for separate interface.}\end{aligned} \tag{15}$$

The integration scheme has been proven to produce very accurate solutions for both displacement and stresses [25].

With a similar manner, the energy Eq. (4) is discretized with the integration scheme for heat transfer analysis [7]. The resulting algebraic equation at point $P(\xi_i,\eta_j)$ can be written in the form

$$\begin{aligned}&(a_W)_{i,j}\theta_{i-1,j}+(a_E)_{i,j}\theta_{i+1,j}+(a_S)_{i,j}\theta_{i,j-1}+(a_N)_{i,j}\theta_{i,j+1}\\&\quad+(a_P)_{i,j}\theta_{i,j}=(a_R)_{i,j}\end{aligned} \tag{16}$$

$$(a_W)_{i,j}=\left(\overline{\Delta\xi}_i\int_{\xi_{i-1}}^{\xi_i}\frac{1}{\kappa}d\xi\right)^{-1},\quad (a_E)_{i,j}=\left(\overline{\Delta\xi}_i\int_{\xi_i}^{\xi_{i+1}}\frac{1}{\kappa}d\xi\right)^{-1} \tag{17}$$

$$(a_S)_{i,j}=\left(\overline{\Delta\eta}_j\int_{\eta_{j-1}}^{\eta_j}\frac{1}{\kappa}d\eta\right)^{-1},\quad (a_N)_{i,j}=\left(\overline{\Delta\eta}_j\int_{\eta_j}^{\eta_{j+1}}\frac{1}{\kappa}d\eta\right)^{-1}$$

$$(a_P)_{i,j}=-(a_W)_{i,j}-(a_E)_{i,j}-(a_S)_{i,j}-(a_N)_{i,j}-(\gamma/\Delta\tau) \tag{18}$$

$$(a_R)_{i,j}=-(\gamma/\Delta\tau)\,\theta_0\,, \tag{19}$$

where

$$\begin{aligned}&\Delta\xi_i=\xi_{i+1}-\xi_i\,,\quad \Delta\eta_j=\eta_{j+1}-\eta_j\\&\overline{\Delta\xi}_i=(\Delta\xi_{i-1}+\Delta\xi_i)/2,\quad \overline{\Delta\eta}_j=(\Delta\eta_{j-1}+\Delta\eta_j)/2.\end{aligned} \tag{20}$$

The unsteady term $\partial\theta/\partial\tau$ has been discretized with a fully implicit scheme on the time step $\Delta\tau$, while the subscript ''0'' denotes quantity at the previous time level $\tau_0=\tau-\Delta\tau$.

Note that the integration in the weighting factors (17) represents the thermal resistance between two adjacent grid points. Hence, the weighting factor $(a_E)_{i,j}$ is expressible as

$$(a_E)_{i,j}=(\overline{\Delta\xi}_i)^{-1}\left(\int_{\xi_i}^{\xi_{i+1}}\frac{1}{\kappa}d\xi+\Re_{\inf}\right)^{-1} \tag{21a}$$

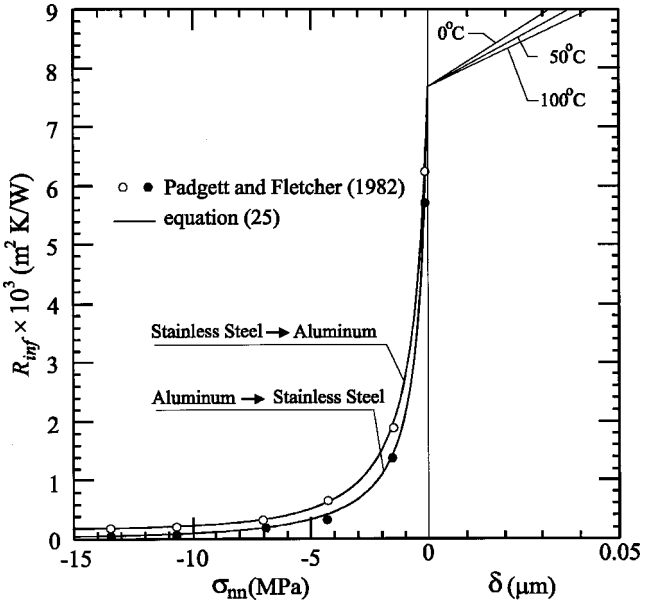

Fig. 3 Interfacial thermal resistance between stainless steel 304 and aluminum 2024-T4

$$\Re_{\text{inf}} = R_{\text{inf}}(k_{\text{ref}}/L) \tag{21b}$$

if a stainless steel-aluminum interface with the interfacial thermal resistance R_{inf} occurs in the interval $[\xi_i, \xi_{i+1}]$. For convenience, the numerical procedure is described as follows:

1 Let the displacement (u_0, v_0), the gap δ_0 and the normal stress $(\sigma_{nn})_0$ at the stainless steel-aluminum interface are all zero, and $\theta_0 = \theta_{\text{in}}$ at the initial time level $\tau_0 = \tau - \Delta\tau = 0$.
2 Estimate the interfacial thermal resistance R_{inf} based on δ_0 and $(\sigma_{nn})_0$.
3 Solve the energy equation (4) to yield the temperature θ for the present time level τ.
4 From Eqs. (2) and (3), determine the displacement (u, v), the gap δ and the normal stress σ_{nn} corresponding to the temperature θ for the present time level τ.
5 If the present time level τ has reached the prescribed time limit, then stop the computation. Otherwise, set $\delta_0 = \delta$ and $(\sigma_{nn})_0 = \sigma_{nn}$, and return to step 2.

It should be pointed out here that the interfacial thermal resistance R_{inf} would keep changing when the temperature varies from θ_0 to θ as time elapses from τ_0 to τ. Unfortunately, the detailed temperature variation is not known during the time step $\Delta\tau$ when the problem is solved numerically. To achieve a good numerical stability, the interfacial thermal resistance R_{inf} is assumed unchanged within each time step as described in step 2 of the numerical procedure. Hence, the time step should be sufficiently small.

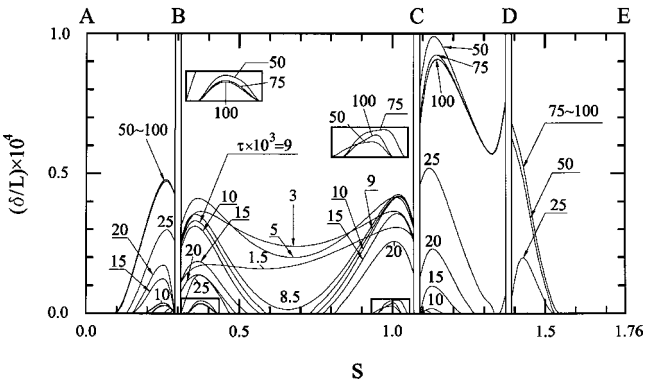

Fig. 4 Result of Gap formation along the interface (note: the two subfigures are for gaps near the corners B and C at τ = 0.050, 0.075, and 0.100)

Results and Discussion

Numerical solutions including the displacement (u, v), the gap δ, the normal stress σ_{nn}, and the temperature θ, are obtained for the parameters

$$(L, T_{\text{in}}, T_1, T_2) = (10 \text{ cm}, 50°\text{C}, 100°\text{C}, 0°\text{C}) \tag{22}$$

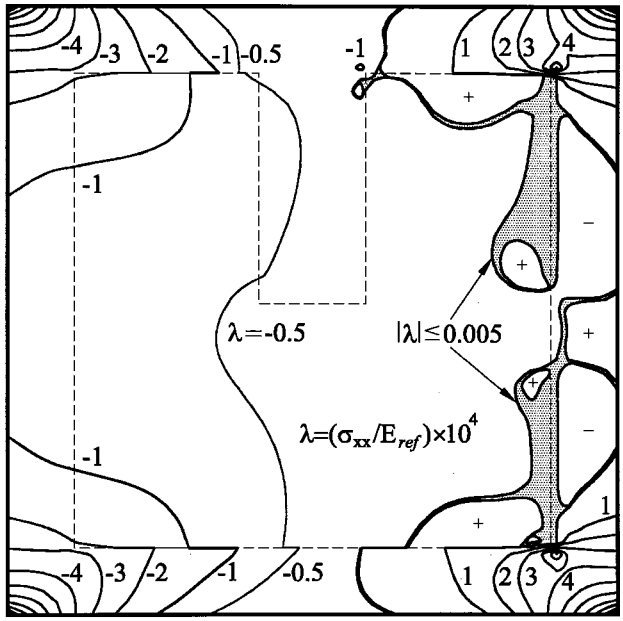

(a)

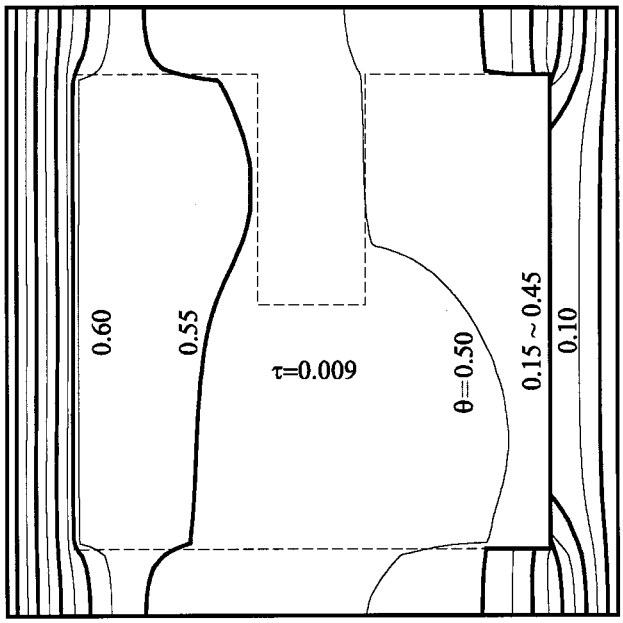

(b)

Fig. 5 (*a*) Result of normal stress σ_{xx} at τ=0.009; (*b*) result of isotherms at τ=0.009

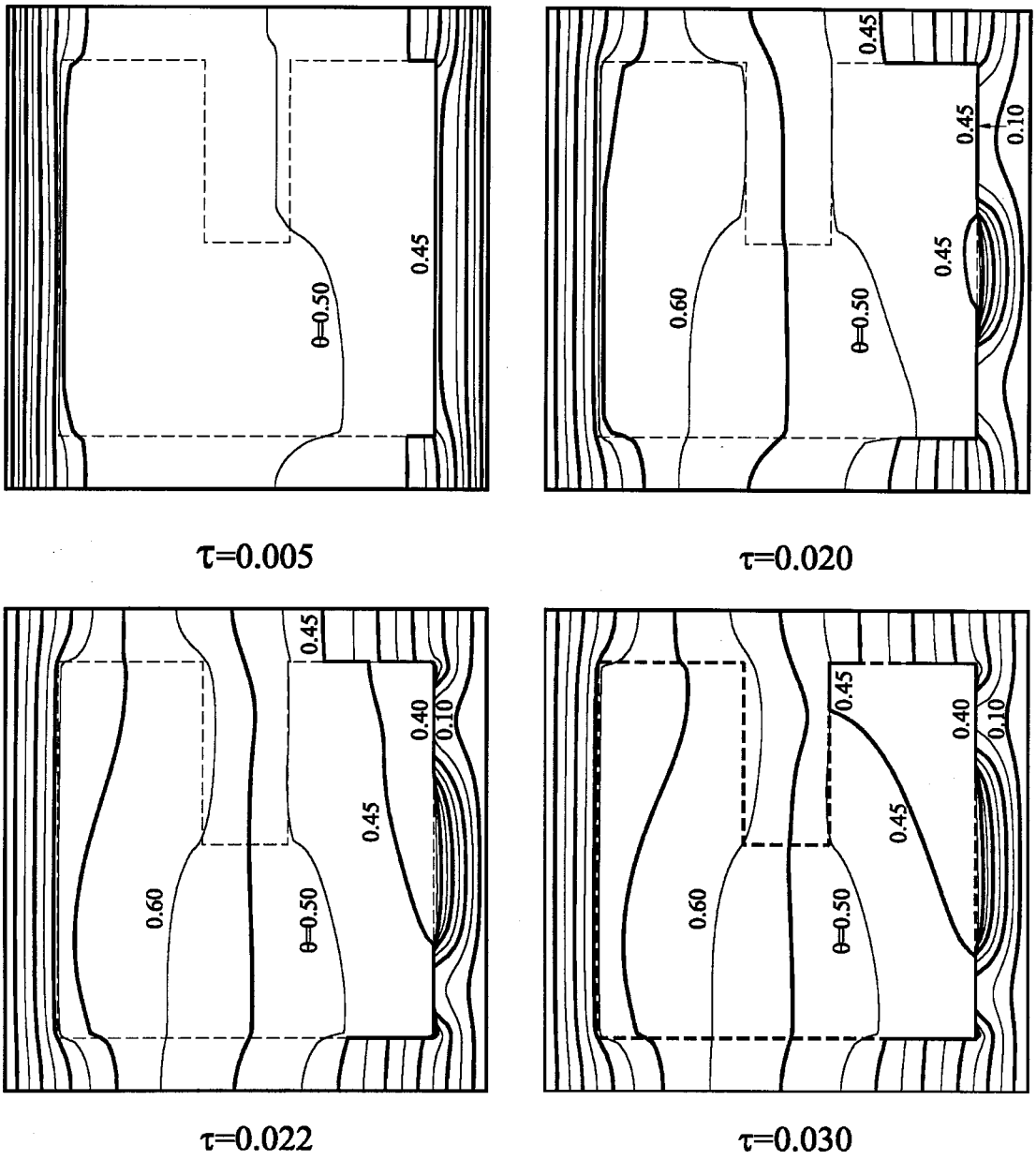

Fig. 6 Result of isotherms at $\tau=0.005$, 0.020, 0.022, and 0.030

as well as the following mechanical and thermophysical properties of stainless steel and aluminum

$$\nu_s=0.3,\quad \nu_a=0.37,\quad \alpha_s=1.25\times10^{-5}\,\mathrm{K}^{-1},$$
$$\alpha_a=2.40\times10^{-5}\,\mathrm{K}^{-1}$$
$$E_s=0.2079\times10^{6}(1-1.905\times10^{-4}T)\mathrm{MPa}$$
$$E_a=0.06739\times10^{6}(1-3.917\times10^{-4}T)\mathrm{MPa}$$
$$k_s=14.06(1+1.422\times10^{-3}T)\,\mathrm{W\,m^{-1}\,K^{-1}}$$
$$k_a=171.4(1+0.671\times10^{-3}T)\,\mathrm{W\,m^{-1}\,K^{-1}} \tag{23}$$
$$(\rho c_p)_s=3.502\times10^{6}(1+1.275\times10^{-3}T)\,\mathrm{J\,m^{-3}\,K^{-1}}$$
$$(\rho c_p)_a=2.320\times10^{6}(1+0.824\times10^{-3}T)\,\mathrm{J\,m^{-3}\,K^{-1}},$$

where the temperature T is in °C. The referenced quantities used in the dimensionless transformation (1) are the properties of stainless steel 304 at $T=0$°C, i.e.,

$$E_{\mathrm{ref}}=0.2079\times10^{6}\ \mathrm{MPa},\quad k_{\mathrm{ref}}=14.06\,\mathrm{W\,m^{-1}\,K^{-1}},$$
$$\rho_{\mathrm{ref}}=8{,}000\,\mathrm{kg\,m^{-3}} \tag{24}$$
$$(\rho c_p)_{\mathrm{ref}}=3.502\times10^{6}\,\mathrm{J\,m^{-3}\,K^{-1}},\quad \beta=7.876\times10^{-9}.$$

It is interesting to note that the diffusivity ratio β is essentially zero. This implies that propagation of stresses is extremely fast as compared to heat transfer. Hence, the inertia term of the displacement equations (2) and (3) are negligible.

In the present study, Eq. (14) is employed to estimate the interfacial thermal resistance R_{inf} as required in step 2 of the numerical procedure. The surface roughness of the stainless steel and the aluminum are assumed 0.256 μm and 0.513 μm, respectively, such that the experimental results of thermal rectification from Padgett and Fletcher [19] are valid for the thermal contact resistance R_m in the present case. For convenience, their experimental data are correlated with

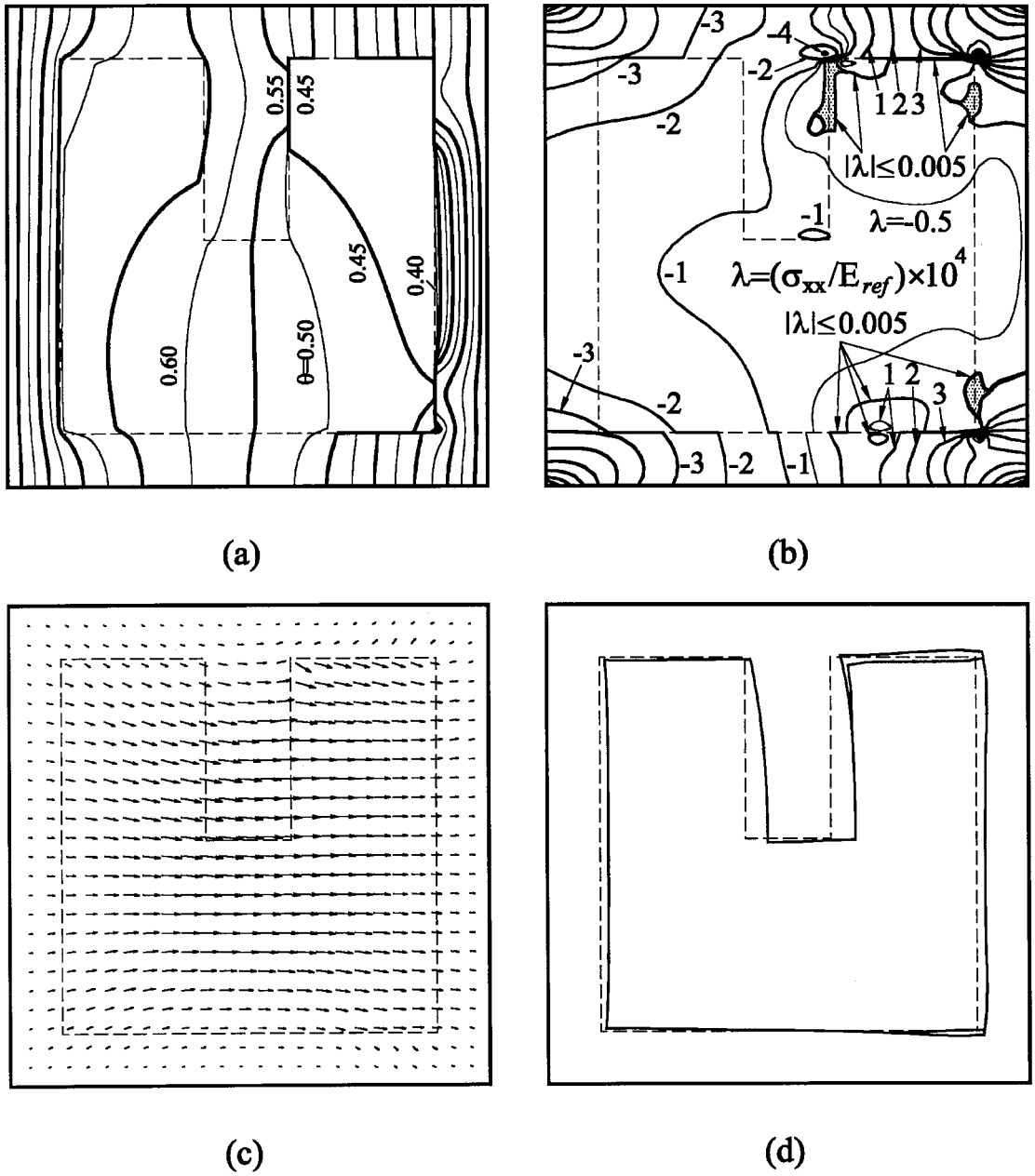

Fig. 7 Isotherms, normal stress σ_{xx}, displacement (×250), and gap (×250) in steady state

$$R_m=(Ad+f)^{-1},\quad A=\frac{\exp(-a\sigma_{nn})-\exp(ab)}{\exp(-a\sigma_{nn})+\exp(ac)}$$

$$(a,b,c,d,f)=(0.2590,11.24,11.03,11.36,10.86)$$

from aluminum to stainless steel

$$(a,b,c,d,f)=(0.3328,4.317,6.001,3.827,1.601) \tag{25}$$

from stainless steel to aluminum.

The hysteresis effect, however, is neglected for simplicity. The gaseous medium in the gap is assumed to be air that has a thermal conductivity of

$$k_g=0.0241(1+3.17\times10^{-3}T)\,\mathrm{W\,m^{-1}\,K^{-1}}. \tag{26}$$

This achieves an interfacial thermal resistance $R_{\inf}$ in terms of σ_{nn} and δ as plotted in Fig. 3. Note that R_m and σ_{nn} in Eq. (25) are measured in $m^2\,\mathrm{K\,W^{-1}}$ and MPa, respectively.

To validate the accuracy of the numerical result, five time steps ($\Delta\tau=0.0100, 0.0050, 0.0020, 0.0010, 0.0005$) were employed for grid tests on three grid systems ($\Delta\xi=\Delta\eta=0.03333, 0.025, 0.02$). The solution procedure was iterated until the resulting dimensionless displacement and temperature converged within an absolute error of 2×10^{-9}. The numerical solution was found to strongly depend on the time step. By contrast, the solution was not so sensitive to the spatial grid mesh. The discrepancy between the resulting temperatures $\theta(\xi,\eta,\tau)$ based on the time steps $\Delta\tau=0.0010$ and 0.0005 on the grid mesh $\Delta\xi=\Delta\eta=0.02$ (as illustrated in Fig. 1) was less than 0.0005. Hence, the numerical result based on the finest grids $\Delta\xi=\Delta\eta=0.02$ and $\Delta\tau=0.0005$ will be discussed in this section. The time step corresponds to 1.245 *seconds* in real time.

Figure 4 reveals the history of the resulting gap formation $\delta(s,\tau)$ on the interface of the two conforming bodies. For convenience of presentation, a normal-tangent coordinates system (n, s)

is employed. The points *A, B, C, D, E* shown on the upper abscissa of Fig. 4 are the corners of the interface (see Fig. 1). The number for each curve in Fig. 4 denotes the time $\tau \times 10^3$. In the present heat transfer process, the initial temperature of the entire system is $\theta_{in}=0.5$. After the boundary conditions $\theta(0,\eta,\tau)=1$ and $\theta(1,\eta,\tau)=0$ are imposed, the stainless steel in the region $0.89<\xi\leqslant 1$ and $0.11<\eta<0.89$ is cooled with a stationary boundary at $\xi=1$. This leads to a gap formation on $\overline{BC}$ due to the shrinkage of the stainless steel at very beginning of the heat transfer process ($\tau\leqslant 0.003$). In a later stage of the heat transfer process ($\tau>0.003$), a thermal expansion arising from the heating surface at $\xi=0$ forces the aluminum block to move rightward. As a result, the gap width on $\overline{BC}$ increases at first and decreases later as observable from Fig. 4. The aluminum block was found to touch the stainless steel eventually at $\tau=0.009$ in a region near $s=0.65$ (or $\eta=0.5$). This situation seems to cause subsequent gap formation on the other interfaces $\overline{AB}$ and $\overline{CD}$.

To investigate the thermoelastic phenomena at this particular time $\tau=0.009$, the resulting normal stress σ_{xx} and temperature θ for $\tau=0.009$ are plotted in Fig. 5(*a*) and 5(*b*), respectively. The number labeled on each iso-stress curve in Fig. 5(*a*) stands for the value of

$$\lambda=(\sigma_{xx}/E_{\text{ref}})\times 10^4. \tag{27}$$

The gray region denotes the area where σ_{xx} is essentially zero ($|\lambda|\leqslant 0.005$). Figure 5(*a*) indicates that the stainless steel in the region $0\leqslant\eta\leqslant 0.11$ is compressed in $0\leqslant\xi<0.6$, while tensed in $0.6\leqslant\xi<1$. Similar situation exists in the region $0.89\leqslant\eta\leqslant 1$. This can be attributed to heating and cooling (expansion and shrinkage) of the stainless steel as shown in Fig. 5(*b*). Due to gap formation, the normal stress σ_{xx} vanishes on the interface $\overline{BC}$ except for a region near $\eta=0.5$ where the expanded aluminum block touches the stainless steel (see Figs. 4 and 5(*a*)). Note also that it takes time to transport energy across an interface after contact of two separate surfaces. This might account for the fact that the temperature jump (from $\theta=0.15$ to $\theta=0.45$) on the interface $\overline{BC}$ still prevails at $\tau=0.009$ even in the contact region near $\eta=0.5$ (see Fig. 5(*b*)).

In the present study, the initial temperature of the entire system is $\theta=0.5$. As time elapses, isotherms with $\theta>0.5$ move rightward from the boundary $\xi=0$ while that with $\theta<0.5$ move leftward from $\xi=1$. Figure 6 presents the isotherms at $\tau=0.005$, 0.020, 0.022, and 0.030. As depicted in Fig. 4, gap forms on the interface $\overline{BC}$ at very beginning of the heat transfer process. Consequently, there is a temperature jump from $\theta=0.30$ to $\theta=0.45$ across the interface $\overline{BC}$ at the time $\tau=0.005$. It is interesting to see from Fig. 6 that the isotherm $\theta=0.45$ enters the aluminum block at a region near $(\xi,\eta)=(0.89,0.5)$ after the aluminum touches the stainless steel. Note also that the gap reaches the maximum value 10 μm near corner *C* at $\tau=0.050$ as observable from Fig. 4, while the average temperature inside the gap is about $\bar{T}=30°\text{C}$. This suggests that the thermal radiation is far smaller than the heat conduction, i.e., $4\sigma(\bar{T}+273)^3=6.31$ versus $k_g/\delta=2790\ \text{W m}^{-2}\text{K}^{-1}$.

Figure 7 shows the temperature θ, the normal stress σ_{xx}, the displacement (u,v), and the gap δ of the system in steady state. Again, the parameter λ is defined by Eq. (27). For convenience, both displacement and gap have been amplified by a factor of 250. It is noted that the thermal conductivity ratio of aluminum and stainless steel is as large as 12. Hence, the steady state temperature gradient inside the stainless steel should be larger than that inside the aluminum. Such a characteristic is clearly reflected in the present results. Due to the particular boundary condition of zero displacement (7), the maximum displacement occurs in a region near the center of the system. In this connection, the rectangular protrusion of the stainless steel is seen to move rightward. Gaps thus appear on the interfaces $\overline{AB}$ and $\overline{CD}$ as observable from Figs. 4 and 7(*d*). The corresponding von Mises stress,

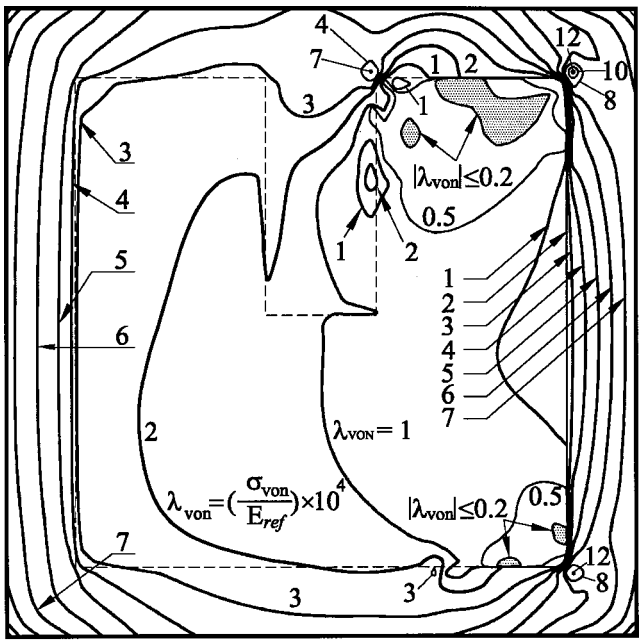

Fig. 8 Result of von Mises stress in steady state

$$\sigma_{\text{von}}=\sqrt{\sigma_{xx}^2+\sigma_{yy}^2+3\sigma_{xy}^2-\sigma_{xx}\sigma_{yy}} \tag{28a}$$

$$\lambda_{\text{von}}=(\sigma_{\text{von}}/E_{\text{ref}})\times 10^4. \tag{28b}$$

a good barometer for failure theory of isotropic ductile material, is provided in Fig. 8. From Fig. 8, large von Mises stresses ($\sigma_{\text{von}}=0.0012\ E_{\text{ref}}=249.5$ MPa) are seen to exist in the stainless steel at the corners *B, C, D*. This implies a high possibility of material failure at these spots. The result reveals also a stress discontinuity jumping from $\lambda_{\text{von}}=0.2$ to $\lambda_{\text{von}}=2$ across the interface $\overline{CD}$ due to gap formation. Similar situation exists in $\overline{AB}$, $\overline{BC}$, and $\overline{DE}$.

Conclusion

Gap formation and interfacial heat transfer between two thermoelastic bodies in imperfect contact have been studied in this paper. The coupling problem of transient heat conduction and displacement due to thermal deformation is solved with an integration scheme. Gap or contact pressure on the interface of the solid bodies is computed from the resulting displacement. The interfacial thermal resistance is then estimated from the numerical results of gap and contact pressure. Effect of thermal rectification is also taken into account. For the particular physical system under study, gap is found to form on the interface of two thermoelastic bodies near the cooling side. A temperature jump thus exists across the interface, while the stress normal to the interface vanishes. These findings consist with physical reasoning.

Accuracy of the integration scheme has been demonstrated in previous studies. Due to its simplicity and great accuracy as compared to finite element methods, the integration scheme is believed to be an efficient method for heat transfer in contact problems. It would provide accurate gap distribution or contact pressure results as long as the interfacial heat transfer coefficient can be efficiently determined. This requires simple and reliable models for thermal contact resistance corresponding to the computed gap or contact pressure. More experimental studies are needed especially for various combinations of surface roughness on both sides. In this connection, Smolukhovskii effect and thermal hysteresis could be considerable under some particular circumstances. As a final note, it is mentioned that the present numerical method applies to three-dimensional problems as well.

However, further improvement of this method is required for problems with curvilinear interface. This would be possible through a coordinate transformation.

Acknowledgment

The authors wish to express their appreciation to the National Science Council of Taiwan for the financial support of this work through the project NSC 83-0401-E007-008.

Nomenclature

c_p = specific heat [$J\,kg^{-1}\,K^{-1}$]
E, E^* = elastic modulus [M Pa], $E^* = E/E_{ref}$
I = dilation, $\partial u/\partial \xi + \partial v/\partial \eta$
k = thermal conductivity [$W\,m^{-1}\,K^{-1}$]
L = length [m]
(n, s) = normal and tangent coordinates along the interface
R_g = thermal resistance through interstitial gaseous medium, Eq. (11)
R_δ = gaseous thermal resistance due to gap formation, δ/k_g
R_{inf}, $\Re_{inf}$ = interfacial resistance [$m^2\,K\,W^{-1}$], $\Re_{inf} = R_{inf}(k_{ref}/L)$
R_m = thermal contact resistance in vacuum, [$m^2\,K\,W^{-1}$]
T = temperature [°C]
t = time [s]
(U, V) = displacement [m]
(u, v) = dimensionless displacement, $(U/L, V/L)$
(x, y) = coordinates [m]

Greek Letters

α, α^* = thermal expansion [K^{-1}], $\alpha^* = \alpha(T_1 - T_2)$
β = diffusivity ratio, $(k/\rho c_p)/(L\sqrt{E/\rho})$
γ = $\rho c_p/(\rho c_p)_{ref}$
δ = gap [m]
$\Delta\tau$ = time step
ε = surface roughness [m], see Fig. 2(*a*)
θ = dimensionless temperature, $(T - T_2)/(T_1 - T_2)$
κ = thermal conductivity, k/k_{ref}
λ = $(\sigma/E_{ref}) \times 10^4$
ν = Poisson ratio
(ξ, η) = dimensionless coordinates, $(x/L, y/L)$
ρ = density [$kg\,m^{-3}$]
σ = stress [MPa]
τ = dimensionless time, $(k/\rho c_p)_{ref}(t/L^2)$
ϕ = defined in Eq. (5)
ψ = defined in Eq. (5)
ω = angular displacement, $\partial v/\partial \xi - \partial u/\partial \eta$

Subscripts

0 = time level $\tau_O = \tau - \Delta\tau$
a = aluminum
g = gaseous
in = initial
inf = interfacial
ref = reference
s = stainless steel

References

[1] Srinivasan, M. G., and France, D. M., 1985, ''Nonuniqueness in Steady-State Heat Transfer in Prestressed Duplex Tubes—Analysis and Case History,'' ASME J. Appl. Mech., **52**, pp. 257–262.
[2] Barber, J. R., 1986, ''Nonuniqueness and Stability for Heat Conduction Through a Duplex Heat Exchanger Tube,'' J. Therm. Stresses, **9**, pp. 69–78.
[3] Majumdar, J., Raychaudhuri, B. C., and Dasgupta, S., 1981, ''An Instrumentation Scheme for Multipoint Measurement of Mold-Metal Gap in an Ingot Casting System,'' Int. J. Heat Mass Transf., **24**, pp. 1089–1095.
[4] Nishida, Y., Droste, W., and Engler, S., 1986, ''The Air-Gap Formation Process at the Casting-Mold Interface and the Heat Transfer Mechanism through the Gap,'' Metall. Trans. B, **17B**, pp. 833–844.
[5] Hwang, J. C., Chuang, H. T., Jong, S. H., and Hwang, W. S., 1994, ''Measurement of Heat Transfer Coefficient at Metal/Mold Interface During Casting,'' Transactions of the American Foundrymen's Society, **104**, pp. 877–883.
[6] Barry, G. W., and Goodling, J. S., 1987, ''A Stefan Problem With Contact Resistance,'' ASME Journal of Heat Transfer, **109**, pp. 820–825.
[7] Tzong, R. Y., and Lee, S. L., 1992, ''Solidification of Arbitrarily Shaped Casting in Mold-Casting System,'' Int. J. Heat Mass Transf., **35**, pp. 2795–2803.
[8] Huang, H., Suri, V. K., Hill, J. L., and Berry, J. T., 1993, ''Issues in Thermal Contact and Phase Change in Porosity Prediction,'' ASME J. Eng. Mater. Technol., **115**, pp. 2–7.
[9] Rapier, A. C., Jones, T. M., and McIntosh, J. E., 1963, ''The Thermal Conductance of Uranium Dioxide/Stainless Steel Interfaces,'' Int. J. Heat Mass Transf., **6**, pp. 397–416.
[10] Popov, V. H., and Krasnoborod'ko, A. I., 1975, ''Thermal Contact Resistance in a Gaseous Medium,'' J. Eng. Phys., **28**, pp. 633–638.
[11] Madhusudana, C. V., and Fletcher, L. S., 1981, ''Gas Conductance Contribution to Contact Heat Transfer,'' AIAA Paper 81-1163.
[12] Wesley, D. A., and Yovanovich, M. M., 1986, ''A New Gaseous Gap Conductance Relationship,'' Nucl. Technol., **72**, pp. 70–74.
[13] Fletcher, L. S., 1988, ''Recent Developments in Contact Conductance Heat Transfer,'' ASME J. Heat Transfer, **110**, pp. 1059–1070.
[14] Song, S., Yovanovich, M. M., and Goodman, F. O., 1993, ''Thermal Gap Conductance of Conforming Surfaces in Contact,'' ASME J. Heat Transfer, **115**, pp. 533–540.
[15] Clausing, A. M., and Chao, B. T., 1965, ''Thermal Contact Resistance in a Vacuum Environment,'' ASME Journal of Heat Transfer, **87**, pp. 243–251.
[16] Thomas, T. R., and Probert, S. D., 1970, ''Thermal Contact Resistance: The Directional Effect and Other Problems,'' Int. J. Heat Mass Transf., **13**, pp. 789–807.
[17] Madhusudana, C. V., and Fletcher, L. S., 1986, ''Contact Heat Transfer—The Last Decade,'' AIAA J., **24**, pp. 510–523.
[18] Starr, C., 1936, ''The Copper Oxide Rectifier,'' J. Appl. Phys., **7**, pp. 15–19.
[19] Padgett, D. L., and Fletcher, L. S., 1982, ''The Thermal Contact Conductance of Dissimilar Metals,'' AIAA Paper 82–0885.
[20] Stevenson, P. F., Peterson, G. P., and Fletcher, L. S., 1991, ''Thermal Rectification in Similar and Dissimilar Metal Contacts,'' ASME Journal of Heat Transfer, **113**, pp. 30–36.
[21] Dundurs, J., and Panek, C., 1976, ''Heat Conduction Between Bodies With Wavy Surfaces,'' Int. J. Heat Mass Transf., **19**, pp. 731–736.
[22] Somers II, R. R., Fletcher, L. S., and Flack, R. D., 1987, ''Explanation of Thermal Rectification,'' AIAA J., **25**, pp. 620–621.
[23] Williams, A., 1976, ''Directional Effects of Heat Flow Across Metallic Joints,'' *Mechanical Engineering Transactions*, *Australian Institute of Engineers*, Paper No. 3448.
[24] Song, R., Dhatt, G., and Ben Cheikh, A., 1990, ''Thermo-Mechanical Finite Element Model of Casting System,'' Int. J. Numer. Methods Eng., **30**, pp. 579–599.
[25] Lee, S. L., and Ou, C. R., 1999, ''Integration Scheme for Elastic Deformation and Stresses,'' ASME J. Appl. Mech., **66**, pp. 978–985.
[26] Barber, J. R., 1978, ''Contact Problems Involving a Cooled Punch,'' J. Elast., **8**, pp. 409–423.
[27] Comninou, M., and Dundurs, J., 1979, ''On the Barber Boundary Conditions for Thermoelastic Contact,'' ASME J. Appl. Mech., **46**, pp. 849–853.
[28] Comninou, M., Dundurs, J., and Barber, J. R., 1981, ''Planar Hertz Contact With Heat Conduction,'' ASME J. Appl. Mech., **48**, pp. 549–554.
[29] Madhusudana, C. V., 1975, ''The Effect of Interface Fluid on Thermal Contact Conductance,'' Int. J. Heat Mass Transf., **18**, pp. 989–991.
[30] Barber, J. R., and Zhang, R., 1988, ''Transient Behaviour and Stability for the Thermoelastic Contact of Two Rods of Dissimilar Materials,'' Int. J. Mech. Sci. **30**, pp. 691–704.
[31] Olesiak, Z. S., and Pyryev, Yu. A., 1996, ''Transient Response in a One-Dimensional Model of Thermoelastic Contact,'' ASME J. Appl. Mech., **63**, pp. 575–581.
[32] Olesiak, Z. S., and Pyryev, Yu. A., 1996, ''On Nonuniqueness and Stability in Barber's Model of Thermoelastic Contact,'' ASME J. Appl. Mech., **63**, pp. 582–586.
[33] Fenech, H., and Rohsenow, W. M., 1959, ''Thermal Conductance of Metallic Surfaces in Contact,'' USAEC Report No. NYO-2136, Massachusetts Institute of Technology, Cambridge, MA.

Effect of Constant Heat Flux Boundary Condition on Wall Temperature Fluctuations

A. Mosyak

E. Pogrebnyak

G. Hetsroni
Fellow ASME
e-mail: hetsroni@tx.technion.ac.il

Department of Mechanical Engineering,
Technion-IIT, Haifa, 32000 Israel

An experimental study of the wall temperature fluctuations under different thermal-wall boundary conditions was carried out. Statistics obtained from the experiments are compared with existing experimental and numerical data. The wall temperature fields are also examined in terms of the coherent thermal structures. In addition the effect of the thermal entrance region on the wall temperature distribution is also studied. For water flow in a flume and in a rectangular channel, the mean spacing of the thermal streaks does not depend on the thermal entrance length and on the type of thermal-wall boundary conditions. The wall temperature fluctuations depend strongly on the type of wall thermal boundary conditions. Overall, the picture that emerges from this investigation confirms the hypothesis that moderate-Prandtl-number heat transfer at a solid wall is governed by the large-scale coherent flow structures. [DOI: 10.1115/1.1345886]

Keywords: Boundary Layer, Channel Flow, Forced Convection, Heat Transfer, Temperature, Turbulence

1 Introduction

Heat transfer from solid walls to flowing fluids is a topic of extreme scientific interest as well as of immense practical importance. Experimental methods aimed at enhancing it may be costly and time-consuming, hence Direct Numerical Simulation (DNS) of fluid mechanics and heat transfer can be very attractive. DNS can be regarded as a numerical experiment, which may replace its laboratory counterpart, but its numerical and physical accuracy must first be confirmed.

DNS studies of turbulent heat transfer in channel flow were carried out by Kim and Moin [1], Lyons and Hanratty [2], Kasagi et al. [3], and Lu and Hetsroni [4]. Current DNS calculations assume that the wall-temperature fluctuations are zero, and thus cannot account for the existence of a thermal pattern on the solid wall. Such a pattern, often referred to as thermal streaks, was observed and studied in experiments carried out by Iritani et al. [5], Hetsroni and Rozenblit [6], and Hetsroni et al. [7]. These studies showed that the fluctuations are not zero under constant wall heat-flux boundary conditions and that the unsteady heat conduction inside the wall, associated with the turbulent flow, should be allowed for.

Heat transfer calculations, assuming both zero and nonzero fluctuations of the wall temperature, were performed by Kasagi et al. [8] and by Sommer et al. [9]. It was demonstrated that the fluctuations are strongly influenced by the thermal properties and thickness of the wall. Two types of wall boundary conditions were investigated: (1) constant wall heat flux axially, and constant temperature peripherally, and (2) constant wall heat flux both axially and peripherally. In practical applications and in experimental studies, however, these ideal conditions are not likely to occur and the calculations should be verified experimentally.

The object of the present study is, accordingly, experimental investigation of the thermal pattern on the heated wall. Two cases of axially constant heat flux at the wall are studied; whereby the thermal wall boundary condition along the periphery is close to isothermal and to isoflux, respectively.

The first case is realized if the heating element is made of, say, a thick copper plate, the second one—when it is made of, say, very thin electrical conductive material with low thermal conductivity. It should be noted that in neither case was it possible to realize ideal thermal wall boundary conditions. We will refer to the case of constant heat flux axially and quasi-isothermal peripherally as H1, and to that of constant heat flux axially and quasi-isoflux peripherally as H2.

Experimental Facilities

The experiments were performed in two recirculation test rigs: in a flume and in a rectangular channel. The two-dimensional flume or channel flow offers several advantages for studies of near-wall coherent structures, as flow visualization is then relatively easy. It was shown by Donohue et al. [10] that the flow is fully developed when the channel is over 100 channel depths long. The turbulent structure of Newtonian two-dimensional flume or, channel flows has been thoroughly studied. The principal disadvantages compared with pipe-flow facilities are that long high aspect-ratio channels are more difficult to build and the Reynolds number range with a given pump is narrower. As a result, experiments in the present study were conducted up to $\mathrm{Re}=20{,}000$.

The flume flow system is the one described by Hetsroni and Rozenblit [6] and only the main hydraulic parameters are covered here. It comprised of a stainless steel open flume 4.3 m long, 0.32 m wide, 0.1 m deep, and water at constant inlet temperature was recirculated in it. The flow depth was 0.037 m; fully developed flow was established in the region beyond 2.5 m downstream from the flume inlet, as was confirmed through the water velocity profile and the distribution of the root-mean-square values of the streamwise velocity fluctuations measured at the center line of the flume, i.e., at $z=0$ (z is the spanwise direction, x the streamwise direction, and y normal to the bottom). The heated test section was located at a distance of 2.5 m from the inlet.

For the H1 conditions we used a section made of a copper plate 0.30 m long, 0.15 m wide, and 0.02 m thick. The temperature distribution over the heated surface was measured from the outer side by 18 thermocouples, and from the liquid side by a Liquid Crystal Sheet (LCS). In the present study, Teflon coated T-type thermocouples (diameter 0.3 mm) were used. Thermocouples were peened into small holes drilled in the test section. The local outer-wall temperature was obtained from the temperature from the temperatures measured by thermocouples using equation for a plane wall. Since the temperature drop through the wall was

Contributed by the Heat Transfer Division for publication in the JOURNAL OF HEAT TRANSFER. Manuscript received by the Heat Transfer Division January 11, 2000; revision received September 29, 2000. Associate Editor: A. Bejan.

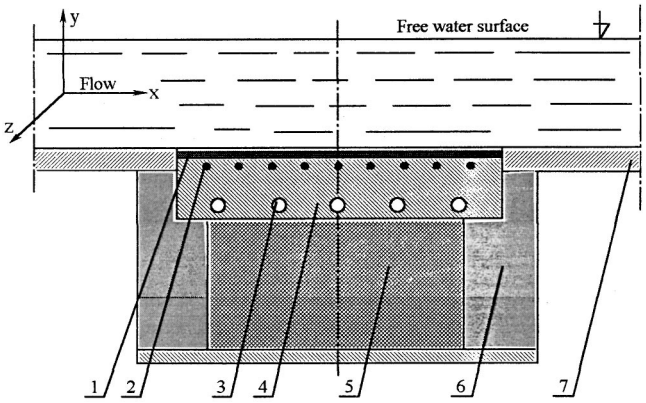

Fig. 1 Test section made of thick copper plate. (H1 thermal wall boundary condition.) [1-liquid crystal sheet, 2-thermocouple, 3-electrical heater, 4-copper plate, 5-insulation, 6-pertinax frame, 7-bottom of flume].

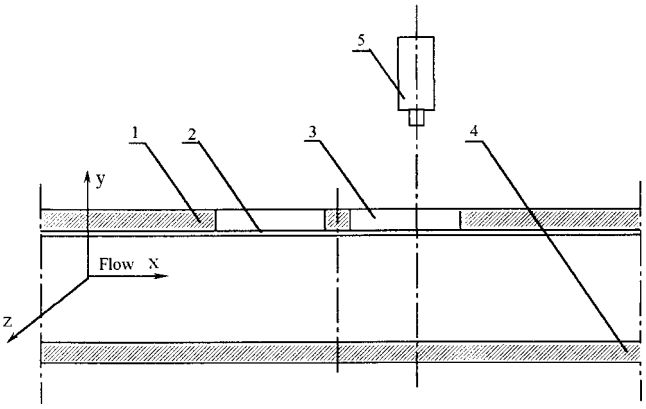

Fig. 3 Test section made of thin stainless steel strip. (H2 thermal wall boundary condition.) [1-top of channel, 2-stainless steel strip, 3-window, 4-bottom of channel, 5-IR camera].

small, the thermal conductivity of the wall was assumed independent of the normal direction and was evaluated at the local measured temperature. The operational procedure for the water tests without heating showed that the wall temperatures always agreed with ± 0.1 K. Heating was effected by means of cartridge electrical elements. The details of the test section are shown in Fig. 1.

The channel flow system is shown in Fig. 2. The 7.2 m long, 0.2 m wide, and 0.02 m deep rectangular channel comprised, twelve Plexiglas sections 0.6 m each carefully joined to ensure a hydraulic smooth surface throughout. Water from a tank with a heat exchanger was delivered by a pump, passed through a control valve, flow meter and flow straightener to a development section, provided for hydrodynamical and thermal development of the boundary layer. The temperature measurements were carried out in the test section. The heating strips 0.6×0.2 m each were installed at the top inside the channel from the front end of the development section to a distance of 0.6 m beyond the test section. These strips were made of 0.05 mm thick stainless steel and arranged so that the boundary layer could be heated along different distances from the inlet to the test section. The latter was provided with two 0.2×0.16 m windows to which the strips were bonded with contact adhesive and coated on the air side with black mat paint about 0.02 mm thick.

For the H2 condition DC current up to 300A was applied to the heating strips, and measurements were taken at different lengths of the heated stretch. The test section is shown in Fig. 3.

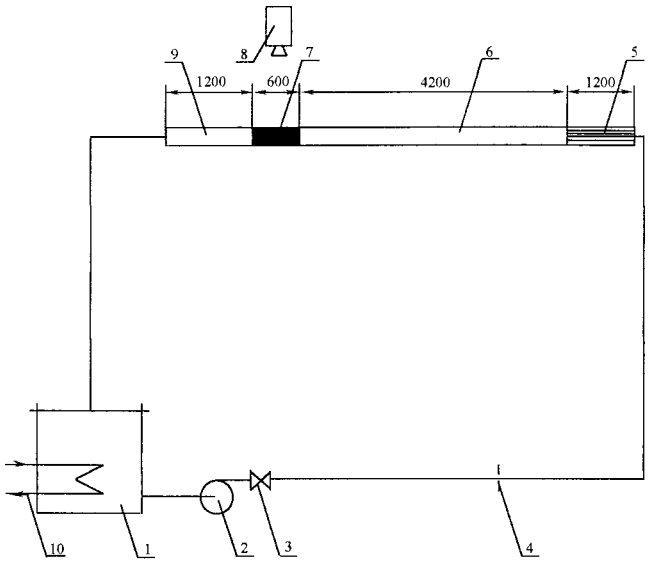

Fig. 2 Loop of rectangular channel [1-tank, 2-pump, 3-control valve, 4-flow meter, 5-straightener, 6-development section, 7-test section, 8-IR camera, 9-outlet section, 10-heat exchanger]

Measurement Techniques

For measuring the temperature field from the water side under the conditions H1, light from a halogen lamp was directed onto the liquid crystal layer. Depending on the temperature the liquid crystal displays different colors. Before experimental runs the color was calibrated versus the temperature, with the same illumination as for the experimental runs. The color play was recorded by a 3CCD video camera and analyzed by means of a specially devised software package. The 35C1W liquid crystal sheet used in the present yields the color play at the 35–36 C level with a minimum detectable temperature difference of 0.1 K.

For the H2 conditions a Thermal Imaging Radiometer was used with a typical horizontal and vertical resolution of 256 pixels per line. Since the heating strip was very thin (0.05 mm), the temperature difference between its surfaces did not exceed 0.1 K, Hetsroni and Rozenblit [6]. A computer program made it possible to store the information and to compute the statistics of the thermal field.

The response times were 0.4 s, 0.05 s, and 0.04 s for the measurements by thermocouples, liquid crystal sheet and infrared radiometer, respectively. The different system (liquid crystal sheet and infrared radiometer) used for the measurements of surface temperature fluctuations had about the same frequency response.

The water temperature was measured by a precision mercury thermometer with accuracy 0.1 K, the pressure drop was measured by a Motorola pressure transducer with accuracy ± 1.5 percent, the mean flow velocity was measured with accuracy ± 1 percent, the electric power was determined with accuracy ± 0.5 percent.

Data Reduction and Experimental Conditions

The local heat transfer coefficient α_x is defined as

$$\alpha_x = \frac{q}{t_{wx} - t_{fx}}, \tag{1}$$

where q is the heat flux, t_{wx} the local inner wall temperature, t_{fx} the mean fluid temperature at the longitudinal position. The calculated Reynolds number is $\mathrm{Re}=UH/v$ and $\mathrm{Re}=UD_h/v$ for the flume and the channel, respectively, U being the bulk velocity at a cross section of the flume or channel, H the flow depth in the flume, D_h the channel hydraulic diameter, ν the kinematic viscosity. The dimensionless thermal entrance length was calculated as

Table 1 Experimental conditions

Quantity	Parameter	Unit	Flume	Channel
Reynolds number	Re		8000 - 10000	10000 - 20000
Prandtl number	Pr_f		5.9	5.5
Prandtl number	Pr_w		4.9	4.0
Dimensionless entrance length	$\bar{x}$		2.2 - 4.9	2.7 - 39
Thermal activity ratio	K		0.044	0.12
Dimensionless wall thickness	δ^{++}		7.1	0.08
Heat flux	q	$\frac{kW}{m^2}$	10 - 12	14 - 16

$\bar{x}=x/H$ or $\bar{x}=x/D_h$ for the flume and the channel, respectively. The fluid properties were evaluated at the average of the mean fluid and wall temperature.

In experiments, when the dimensionless thermal entrance length did not exceed $\bar{x}=5$ the bulk fluid local temperature was assumed independent of axial position, x, since only a small length of the test section was heated. At $\bar{x}>10$ it is assumed that bulk fluid temperature increases linearly along the test section. The test measurements indicated that in this case the wall temperature also increased linearly in the streamwise direction.

Throughout this study the distances are also normalized using the ''inner variables'', υ/u^*, where u^* is the shear velocity $u^*=(\tau_w/\rho)^{0.5}$, τ the shear stress, ρ density. The method for the evolution of the shear velocity in the flume involved fitting the velocity profile, in the logarithmic portion of the profile, to the ''universal'' velocity profile. For channel flow shear velocities were calculated from the pressure drop measurements. The root mean square of the wall temperature variance $\theta^+=\overline{(\theta^2)}^{0.5}$ is normalized by the friction temperature $\theta^*=q/\rho c_p u^*$, (where c_p is specific heat at constant pressure), so that the dimensionless temperature fluctuation is $\overline{(\theta^2)}^{0.5}/\theta^*$, where θ is the fluctuating wall temperature. The heat transfer interaction between the fluid and a solid may be characterized by the thermal activity ratio $K=[(\rho c_p k)_f/(\rho c_p k)_w]^{0.5}$, the dimensionless wall thickness $\delta^{++}=\delta^+\cdot(a_f/a_w)^{0.5}$ Kasagi et al. [8], and the Prandtl numbers Pr_f and Pr_w. Here, k is the thermal conductivity, $\delta^+=(\delta u^*)/\upsilon$, δ the wall thickness, a the thermal diffusity, the subscripts ''f'' and ''w'' denote properties at the fluid and wall temperature, respectively. The experimental conditions are listed in Table 1.

Test Procedure

Heat Losses. The axial heat conduction for the heated test sections was calculated from the wall temperature distribution in the streamwise direction. The heat transfer in the axial direction was less than 0.5 percent of that in the wall normal direction for the thin stainless steel heater, and less than 1 percent for the thick copper heater. The heat balance for the variation of the outside ambient temperature was also verified by direct measurements. The total heat losses were about 1 percent for the stainless steel heater and 2–3 percent for the copper heater, depending on the heat flux.

Experiments in the Flume. It was shown earlier by Hetsroni et al. [11], that the distribution of the dimensionless streamwise velocity versus the dimensionless wall-normal distance in the flume is in good agreement with the measurements presented by Antonia et al. [12], and the distribution of the turbulence intensity agrees well with the data by Nishino and Kasagi [13]. The experimentally obtained heat-transfer coefficients are in accord with the predictions of Kays [14]. In the present study we determined the

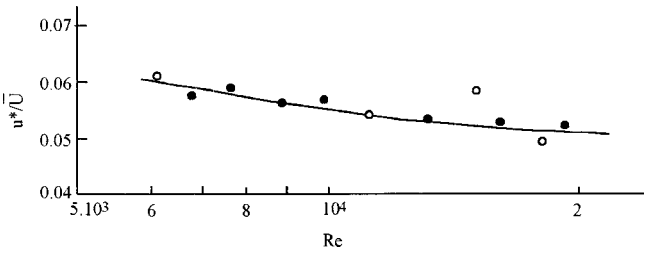

Fig. 4 Wall-shear velocities in channel water flow [●-present study; ○-data of Donohue [10]]

temperature distribution on the heated surface from the water side with an LCS and from the solid side with thermocouples. In both cases the standard deviation of the local wall temperature from the space and time averaged surface temperature did not exceed 0.2 K in the heat flux range $q=10-12\,kW/m^2$. The thickness and high thermal conductivity of the copper plate used in the present study allow to assume that the wall temperature is nearly constant. For experiments without liquid crystal sheet, at Re=5200 and $q=10^4\,W/m^2$ the mean wall temperature was 28.7 °C, the mean water temperature was 20.0 °C. In this case the maximum increase of the wall temperature in the streamwise direction does not exceed 0.3 K and the estimated conduction heat rate in the axial direction was about 1.2 W, while heat rate in the wall normal direction was 450 W.

It should be noted, in the present study the ''isothermal boundary condition (H1)'' means that the wall temperature does not change in the streamwise direction. Expression ''isoflux boundary condition (H2)'' means that the wall temperature fluctuations are not zero. It will be shown that the copper heating plate provides very small wall temperature fluctuations. It was believed that the H1 thermal wall boundary condition existed.

Experiments in the Channel. A number of verification runs were undertaken prior to data logging. Figure 4 shows the Reynolds number dependence of the wall-shear velocity normalized by the bulk (mass average) velocity. The data obtained in the present study are in good agreement with the results reported by Donohue [10].

Figure 5 shows the dependence of the dimensionless local heat transfer coefficient α_x/α_o on the dimensionless distance, $\bar{x}$, from the start of heating at Re=17000. Here α_o is the experimental asymptotic heat transfer coefficient. The data of Hartnett [15] for water heat transfer at Re=16,900 are also shown for comparison. The good agreement between these experimental results is established.

The distinct feature of these experiments is that the rms of the wall temperature fluctuations in the H2 case is about an order higher than in the H1 case.

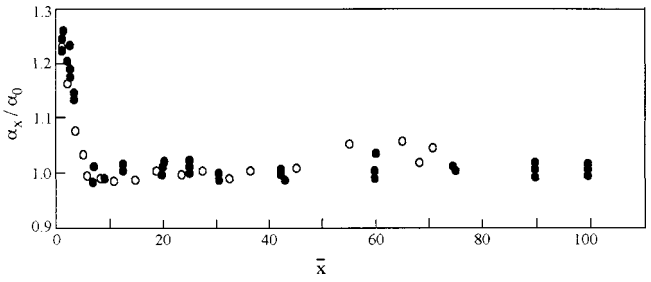

Fig. 5 Dependence of dimensionless local heat transfer coefficient on dimensional thermal entry length [●-present study; ○-data by Hartnett [15]]

Results

Macro-Scale Thermal Structure. As pointed out, appearance of the macro-scale thermal structures on the wall in a turbulent flow was observed previously. These structures (so-called thermal streaks) are oriented mainly in the streamwise direction, moving slowly downstream and meandering about in the lateral direction, with some twisting and merging with the neighboring coherent flow structures. No experimental study seems, however, to be available on their behavior with allowance for the unsteady heat conduction in the solid wall and the thermal entrance region.

The temperature distribution on the heated wall can be considered as a trace of the flow structure there. The streak spacings were obtained by infrared or liquid crystal sheet visualization technique. The mean spanwise spacings were determined by examining the two-point correlations of the temperature fluctuations in the spanwise direction as in the case of the low-speed streaks [1].

Thermal Streaks Spacing Under Isothermal (H1) Wall Boundary Condition. The dimensionless spacing of the thermal streaks λ^+ versus the dimensionless thermal entrance length is shown in Fig. 6, where $\lambda^+ = \lambda u^*/v$ (λ being the average streak spacing at a given value of $\bar{x}$). One can conclude that the value of λ^+ does not change within the measurement uncertainty of $\Delta\lambda^+ = \pm 5$.

Thermal Streaks Spacing Under Isoflux (H2) Wall Boundary Condition. Figures 7 and 8 show the behavior of λ^+ in the thermal entrance and developed regions, respectively. In the present case two-point correlations indicate $\lambda^+ = 95$ (Fig. 7) and $\lambda^+ = 97$ (Fig. 8). From Figs. 6, 7, and 8 one can conclude that in both H1 and H2 thermal wall boundary conditions λ^+ is about 100. This value is in close agreement with the results presented by Iritani et al. [5] and Hetsroni et al. [7]. The well-known experiments established that the mean streak spacing between near-wall coherent flow structures is also about 100 wall units, a result confirmed by the high-resolution DNS of Kim and Moin [1]. They showed that at Prandtl number Pr=0.71, the temperature in the near-wall region is highly correlated with the streamwise velocity. The present experiments were carried out at Prandtl number Pr =5.5–5.9 and in this case the spacing is also about 100 wall units. This result is consistent with the experimental observation of Iritani et al. [5], who performed simultaneous visualizations of the velocity and temperature fields in a turbulent boundary layer of water flow, using hydrogen bubbles for the velocity field and a surface-mounted liquid-crystal sheet, sensitive to the wall temperature, for the scalar field. Kim and Moin [1] showed that although the sublayer of the thermal boundary layer is a strong function of the Prandtl number, it appears that thermal streaks in the wall region are almost independent of the molecular Prandtl number.

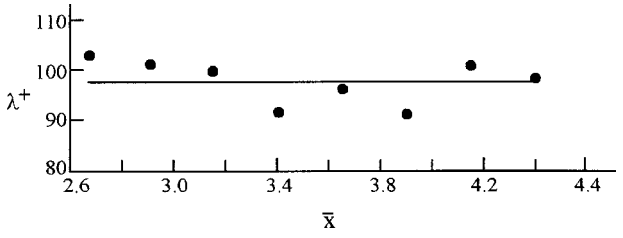

Fig. 6 Behavior of thermal streak spacing in streamwise direction. Thermal entrance region (H1 case).

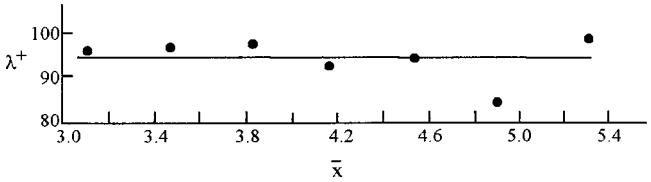

Fig. 7 Thermal streaks in thermal entrance region. Channel flow (H2 case).

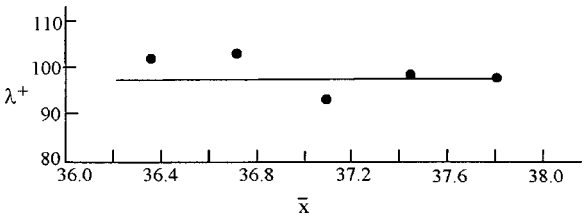

Fig. 8 Thermal streaks in the developed region (H2 case)

Wall Temperature Fluctuation

Figures 9 and 10 show the wall temperature variation in the spanwise direction for H1 and H2 case respectively. One can see that in the case of H2 the temperature fluctuations are higher. We will discuss this issue below.

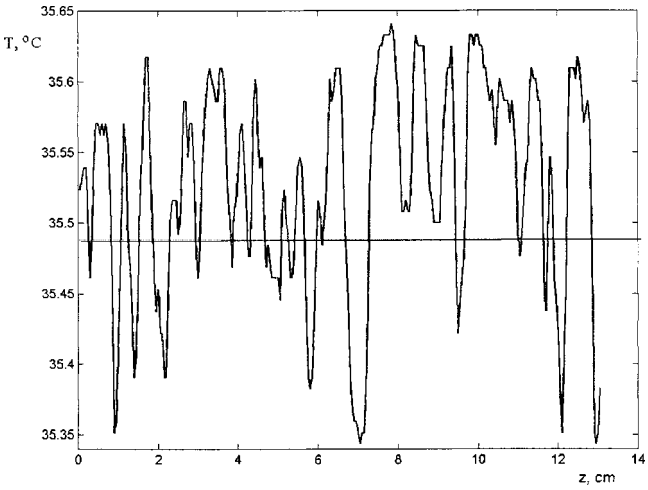

Fig. 9 Wall temperature variation in the spanwise direction (H1 case)

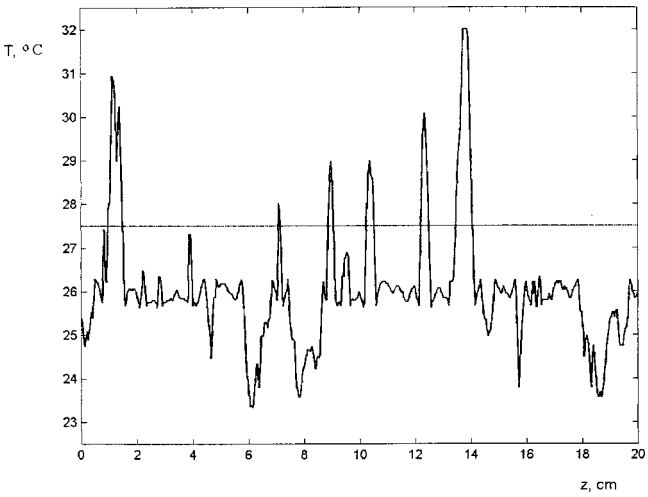

Fig. 10 Wall temperature variation in the spanwise direction (H2 case)

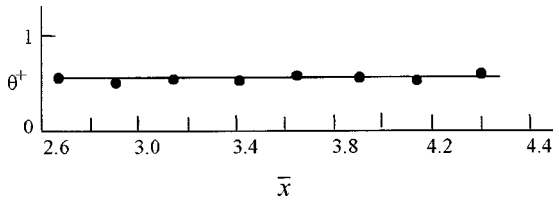

Fig. 11 Dependence of wall temperature fluctuation on thermal entrance length (H1 case)

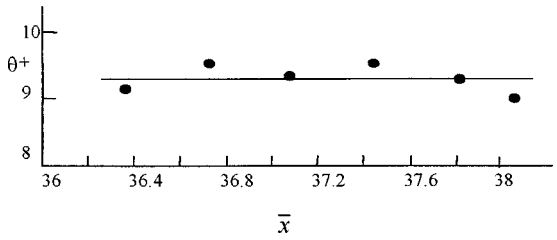

Fig. 13 Wall temperature fluctuation in developed thermal boundary layer

H1 Wall Temperature Boundary Condition. The plot of the dimensionless wall temperature fluctuation on the heated wall, θ^+, versus the dimensionless thermal entrance length, $\bar{x}$, is given in Fig. 11. As mentioned above, wall temperatures were determined both by liquid-crystal sheet and by thermocouples, with good agreement between these two methods. Figure 11 shows that the behavior of the wall temperature is independent of the thermal entrance length.

Before closing this section, let us add a remark on the behavior of θ^+ versus the thermal entrance length. Under fully developed thermal and hydrodynamic conditions, temperature fluctuations are a consequence of turbulent velocity fluctuations of the flow and are closely correlated with its structure, depending on the Prandtl number and the distance from the wall. However, due to the thermal interaction of the flow with the wall, there also arise temperature fluctuations. Therefore, the problem concerning the temperature fluctuation of the liquid near the wall should be considered in a related manner. To-date, scant attention has been paid to the effect of the thermal entrance length in this context. The results of the present study indicate that the wall temperature fluctuation in the thermal entrance region in the H1 case is similar to isothermal wall. This conclusion agrees quite well with the experimental results of Hishida and Nagano [16], where the test section was heated by saturated steam under atmospheric pressure, thereby ensuring a uniform wall temperature. It was established that in the inner part of the boundary layer the overall characteristics of the temperature fluctuations and the correlations between it and the flow velocity are almost identical throughout the thermal entrance region.

H2 Wall Temperature Boundary Condition. The wall temperature fluctuations for the thermal entrance region and for the developed thermal boundary layer are shown in Figs. 12 and 13 respectively. The θ^+ versus $\bar{x}$ pattern in the first figure indicates that wall temperature fluctuation lessens in the streamwise direction, while the second figure shows that in the developed thermal boundary layer the wall temperature fluctuation is uniform, but at a much higher level than in the H1 case. This means that the effect of the thermal wall boundary conditions on the wall temperature fluctuation is very strong. The present experimental results have been compared with the numerical calculations of Kasagi et al. [8], showing reasonable agreement with numerical calculation.

Unlike with the H1 case, no experimental study seems to be available on wall temperature fluctuations in the H2 case. In the experiments of Subramanian and Antonia [17] an electrically heated stainless-steel foil served as the wall surface in the turbulent boundary layer. As was shown by Kasagi et al. [8] in air flow (in particular, under the conditions of the above experiments) the wall temperature fluctuation should be negligibly small, so that the wall can be regarded as ideally isothermal. The experiments of Slanciauskas et al. [18] were made in a two-dimensional water channel flow with 0.8 mm thick stainless steel foil attached to a 5 mm thick Plexiglas board and heated directly by an electric current. Here again the heated surface cannot be regarded as an ideal isoflux wall, since the heat transfer took place through a thick board by thermal conduction. At the same time, the H2 case of thermal wall boundary condition is very important in validating new methods of numerical calculation of a passive scalar distribution in a turbulent velocity field. For every location of $\bar{x}$, the intensity of the velocity fluctuation decreases as the wall is approached, so that in the H2 case the temperature field becomes less correlated with its velocity counterpart in the immediate vicinity of the wall.

In the present study we did not observe any difference between the heat transfer coefficients obtained in the H1 and H2 thermal wall boundary conditions. In other words, the H2 condition tend to increase θ^+ only, while the normal turbulent heat flux is essentially independent of the wall temperature fluctuation. This was also verified by the calculations of Sommer et al. [9]. The influence of the isothermal and isoflux temperature boundary condition is important for the analytical approximation and heat transfer calculations. These two types set the limits for the conjugate heat transfer calculations. Effect of the thermal boundary condition is very important in the near-wall region, i.e., at high Prandtl numbers. As was pointed out by Kasagi et al. [8], the thermal activity ratios for air flow is very small for all practical wall materials. On the other hand, thermal activity ratios for water flow are large enough, and in the combination with the varying wall thickness and heat conductivity almost isothermal and isoflux wall temperature conditions can be achieved in experiments and in engineering devices. Value of wall temperature fluctuations is the crucial parameters for the resolution requirements for DNS at high Prandtl numbers.

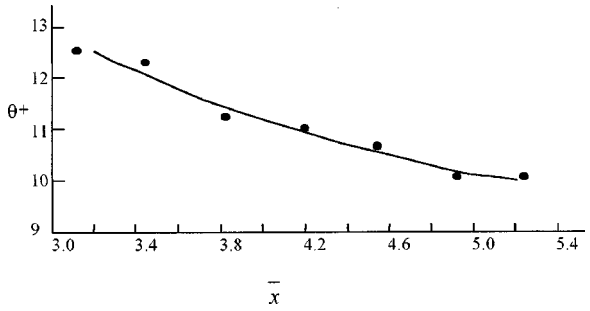

Fig. 12 Dependence of wall temperature fluctuation on thermal entrance length (H2 case)

Conclusions

- The spacing of the thermal streaks on the wall is independent of the thermal entrance length.
- The wall temperature fluctuations at a constant wall heat flux axially and a constant temperature peripherally (H1) is also independent of the thermal entrance length.
- The wall temperature fluctuations at a constant wall heat flux axially and peripherally (H2) lessens in the streamwise direction in the thermal entrance region.

• The wall temperature fluctuation depends strongly on the type of wall temperature boundary condition: its rms under the H2 wall boundary conditions is about an order of magnitude higher than that under the H1.

• For heat transfer from the solid wall in water flow almost isothermal or isoflux boundary condition can be achieved, depending on wall thickness and its thermal conductivity. At high values of heat flux for the wall temperature oscillations may be, in fact, more damaging, than high absolute wall temperatures. Knowledge of the value of wall temperature fluctuations is very important for designing and operation of engineering devices.

Acknowledgments

This research was supported by the Basic Research Foundation administered by the Israel Academy of Science and Humanities and by the Israel Ministry of Science. It was also supported by the Fund for the Promotion of Research at the Technion. E. Pogrebnyak was supported by the Center for Absorption in Science, Israel Ministry of Immigrant Absorption.

Nomenclature

a = thermal diffusivity
c_p = specific heat of the fluid at constant pressure
D_h = channel hydraulic diameter
H = flow depth
K = thermal activity ratio
k = thermal conductivity
Pr = Prandtl number
q = heat flux
Re = Reynolds number
T = temperature
t_{fx} = mean fluid temperature at the longitudinal position
t_{wx} = local inner wall temperature
U = bulk velocity
$u^*=(\tau_w/\rho)^{0.5}$ = friction velocity
x = streamwise distance
y = distance from the wall
z = spanwise distance
$\overline{x}=x/H,\ x/D_h$ = dimensionless thermal entrance length
α_x = local heat transfer coefficient
δ = wall thickness
$\delta^+=\delta u^*/v$ = dimensionless wall thickness normalized by the boundary layer parameters, u^* and v
$\delta^{++}=\delta^+(a_f/a_w)^{0.5}$ = dimensionless wall thickness normalized by ratio of thermal diffusities
λ = thermal streaks spacing
$\lambda^+=\lambda u^*/v$ = dimensionless thermal streaks spacing
ρ = density
ν = kinematic viscosity
θ = wall temperature fluctuations
$\theta^*=q/\rho c_p u^*$ = friction temperature
$\theta^+=\overline{(\theta^2)}^{0.5}/\theta^*$ = dimensional RMS of the wall temperature fluctuations
τ_w = shear stress

Subscripts

w = wall
f = fluid

References

[1] Kim, J., and Moin, P., 1989, ''Transport of Passive Scalars in a Turbulent Channel Flow,'' *Turbulent Shear Flows, VI*, J. C. Andre, et al., eds., Springer-Verlag, Berlin, pp. 85–96.
[2] Lyons, S. L., and Hanratty, T. J., 1991, ''Direct Numerical Simulation of Passive Heat Transfer in a Turbulent Channel Flow,'' Int. J. Heat Mass Transf., **34**, pp. 1149–1161.
[3] Kasagi, N., Tomita, Y., and Kuroda, A., 1992, ''Direct Numerical Simulation of Passive Scalar Field in a Turbulent Channel Flow,'' ASME J. Heat Transfer, **114**, pp. 598–606.
[4] Lu, D. M., and Hetsroni, G., 1995, ''Direct Numerical Simulation of a Turbulent Open Channel Flow with Passive Heat Transfer,'' Int. J. Heat Mass Transfer, **38**, pp. 3241–3251.
[5] Iritani, Y., Kasagi, N., and Hirata, M., 1984, ''Heat Transfer Mechanism and Associated Turbulence Structure in a Near-Wall Region of a Turbulent Boundary Layer,'' *Proc. Turbulent Shear Flows, IV*, L. J. S. Bradbury, et al., eds., Springer-Verlag, Berlin, pp. 223–234.
[6] Hetsroni, G., and Rozenblit, R., 1994, ''Heat Transfer to a Liquid-Solid Mixture in a Flume,'' Int. J. Multiphase Flow, **20**, pp. 671–689.
[7] Hetsroni, G., Zakin, J. L., and Mosyak, A., 1997, ''Low-Speed Streaks in Drag-Reduced Turbulent Flow,'' Phys. Fluids, **9**, pp. 2397–2404.
[8] Kasagi, N., Kuroda, A., and Hirata, M., 1989, ''Numerical Investigation of Near-Wall Turbulent Heat Transfer Taking Into Account the Unsteady Heat Conduction in the Solid Wall,'' ASME J. Heat Transfer, **111**, pp. 385–392.
[9] Sommer, T. P., So, R. M. C., and Zhang, H. S., 1994, ''Heat Transfer Modeling and the Assumption of Zero Wall Temperature Fluctuations,'' ASME J. Heat Transfer, **116**, pp. 855–863.
[10] Donohue, G. L., Tiederman, W. G., and Reischman, M. M., 1972, ''Flow Visualization of the Near-Wall Region in a Drag-Reducing Channel Flow,'' J. Fluid Mech., **56**, pp. 559–575.
[11] Hetsroni, G., Mosyak, A., Rozenblit, R., and Yarin, L. P., 1999. ''Thermal Patterns on the Smooth and Rough Walls in Turbulent Flows,'' Int. J. Heat Mass Transf., **42**, pp. 3815–3829.
[12] Antonia, R. A., Teitel, M., Kim, J., and Browne, L. W. B., 1992, ''Low Reynolds Number Effects Fully Developed Turbulent Flow,'' J. Fluid Mech., **236**, pp. 579–605.
[13] Nishino, K., and Kasagi, N., 1989, ''Turbulence Statistics Measurements in a Two-Dimensional Channel Flow Using a Three-Dimensional Particle Tracking Velocimeter,'' *Proc. of the 7th Symposium on Turbulent Shear Flows*, Stanford, pp. 22.1.1–22.1.6.
[14] Kays, W. M., *Convective Heat and Mass Transfer*, McGraw-Hill, NY.
[15] Hartnett, J. P., 1955, ''Experimental Determination of the Thermal Entrance Length for the Flow of Water and Oil in Circular Pipes,'' ASME J. Heat Transfer, **77**, pp. 1211–1220.
[16] Hishida, M., and Nagano, Y., 1978, ''Structure of Turbulent Temperature and Velocity Fluctuations in the Thermal Entrance Region of a Pipe,'' *Proc. 6th International Heat Transfer Conference*, Toronto, Canada, **2**, pp. 531–536.
[17] Subramanian, C. S., and Antonia, R. A., 1981, ''Effect of Reynolds Number on a Slightly Heated Turbulent Boundary Layer,'' Int. J. Heat Mass Transf., **24**, pp. 1833–1846.
[18] Slanciauskas, A., Drizius, M. R., and Zukauskas, A., 1973, ''Temperature Fluctuations in the Wall Region During Turbulent Flow of a Viscous Liquid Along a Plate,'' Heat Transfer-Sov. Res., **5**, pp. 74–83.

Y.-L. Lin
Research Associate

T. I.-P. Shih
Professor
Fellow ASME
e-mail: tomshih@egr.msu.edu

Department of Mechanical Engineering,
Michigan State University,
East Lansing, MI 48824-1226

M. A. Stephens[1]
Department of Mechanical Engineering,
Carnegie Mellon University,
Pittsburgh, PA 15213-3890

M. K. Chyu
Leighton Orr Chair Professor and Chairman
Fellow ASME
Department of Mechanical Engineering,
University of Pittsburgh,
Pittsburgh, PA 15261

A Numerical Study of Flow and Heat Transfer in a Smooth and Ribbed U-Duct With and Without Rotation

Computations were performed to study the three-dimensional flow and heat transfer in a U-shaped duct of square cross section under rotating and non-rotating conditions. The parameters investigated were two rotation numbers (0, 0.24) and smooth versus ribbed walls at a Reynolds number of 25,000, a density ratio of 0.13, and an inlet Mach number of 0.05. Results are presented for streamlines, velocity vector fields, and contours of Mach number, pressure, temperature, and Nusselt numbers. These results show how fluid flow in a U-duct evolves from a unidirectional one to one with convoluted secondary flows because of Coriolis force, centrifugal buoyancy, staggered inclined ribs, and a 180 deg bend. These results also show how the nature of the fluid flow affects surface heat transfer. The computations are based on the ensemble-averaged conservation equations of mass, momentum (compressible Navier-Stokes), and energy closed by the low Reynolds number SST turbulence model. Solutions were generated by a cell-centered finite-volume method that uses second-order flux-difference splitting and a diagonalized alternating-direction implicit scheme with local time stepping and V-cycle multigrid.
[DOI: 10.1115/1.1345888]

Keywords: Computational; Forced Convection; Heat Transfer; Mixed Convection; Turbines

1 Introduction

To improve thermal efficiency, gas-turbine stages are being designed to operate at increasingly higher inlet temperatures. This increase is enabled by advances in two areas, cooling technology and materials. With cooling, inlet temperatures can far exceed allowable material temperatures.

A widely used method for cooling vanes and blades is to bleed lower-temperature air from the compressor and circulate it within and around each airfoil. This air, referred to as the coolant, generally enters each airfoil from its root and exits from its tip and/or trailing edge. It also could exit from strategically placed holes for film cooling. While inside each airfoil, the coolant typically flows through a series of straight ducts connected by 180 deg bends with the walls roughened with ribs or pin fins to enhance heat transfer. For efficiency, effective cooling must be accomplished with minimal cooling flow and pressure loss. This need for efficiency is even more urgent for gas turbines with low NO_x combustors, which compete for the same cooling air.

The importance of efficient and effective cooling has led many investigators to study the flow and heat transfer in internal coolant passages and to develop and evaluate design concepts. Most experimental studies on internal coolant passages have focused on non-rotating ducts, which are relevant to vanes. See, for example, Han et al. [1], Chyu et al. [2], Liou et al. [3], Iacovides et al. [4], and the references cited there. Experimental studies on rotating ducts, which are relevant to blades, have been less numerous. Wagner et al. [5,6], Morris and Salemi [7], Han et al. [8], and Cheah et al. [9] investigated rotating ducts with smooth walls. Taslim et al. [10], Wagner et al. [11], Zhang et al. [12], Johnson et al. [13], Zhang et al. [14], Tse [15], and Kuo and Hwang [16] reported studies on rotating ducts with ribbed walls.

Most of the earlier computational studies on internal coolant passages have been two-dimensional. In recent years, a number of three-dimensional studies have been reported. Three-dimensional studies are needed if there are ribs, 180 deg bends, and/or rotation. Besserman and Tanrikut [17], Wang and Chyu [18], and Rigby et al. [19] studied non-rotating smooth ducts with 180 deg bends. Iacovides et al. [20,21], Medwell et al. [22], Tekriwal [23], Dutta et al. [24], Tolpaldi [25], Stephens et al. [26], Hwang et al. [27], Stephens and Shih [28], and Chen et al. [29] studied rotating smooth ducts. Prakash and Zerkle [30,31], Abuaf and Kercher [32], Stephens et al. [33], Rigby et al. [34], Rigby [35], and Bohn et al. [36] studied ducts with normal ribs.

Very few investigators performed computational studies on ducts with inclined ribs, which are used in advanced designs. Stephens et al. [37,38] studied inclined ribs in a straight duct under non-rotating conditions. Bonhoff et al. [39] studied inclined ribs in a non-rotating U-duct (i.e., a duct with two straight sections and a 180 deg bend). More recently, Stephens and Shih [40], Bonhoff et al. [41], and Shih et al. [42,43] studied inclined ribs in U-ducts under rotating conditions. In the study by Bonhoff et al. [39,41], a Reynolds stress equations model (RSM) with wall functions was used. In the studies by Stephens et al. [38], Stephens and Shih [40], and Shih et al. [42,43], a low-Reynolds-number SST turbulence model was used (i.e., integration is to the wall so that wall functions are not needed).

When computing U-ducts with ribs, it is important for the geometry of the ribs to be captured correctly. This is because they exert considerable influence on the flow and heat transfer. When wall functions are used, the rib geometry is compromised. This is because boundary conditions are applied at one grid point or cell away from the boundary, and the location of that grid point or cell boundary is typically at a y^+ of 30 to 200. Also, existing wall functions cannot account for flow physics occurring in the low-Reynolds-number region next to ribs such as density variations from temperature gradients, strong pressure gradients, impingement flows, and flow separation.

[1]Currently Project Engineer, Pratt & Whitney, Middletown, Connecticut.

Contributed by the Heat Transfer Division for publication in the JOURNAL OF HEAT TRANSFER. Manuscript received by the Heat Transfer Division April 28, 1999; revision received September 25, 2000. Associate Editor: J. Han.

The objective of this study is to use a low-Reynolds number two-equation turbulence model that can account for the near-wall effects to investigate the flow and heat transfer in a rotating and a non-rotating U-duct with smooth and ribbed walls. Wall functions will not be used. The focus is to examine the nature of the flow induced by inclined ribs, a 180 deg bend, and rotation and how that flow affects surface heat transfer, especially in the region around the bend. The bend region is of interest because it is generally smooth though there are ribs upstream and downstream of it. Also, the turning of the bend is typically very tight (i.e., the radius of curvature for the convex wall is much less than the duct hydraulic diameter) so that there is a large separated region, which further complicates the flow.

Description of Problem

A schematic diagram of the U-duct investigated is shown in Figs. 1 and 2. It has a square cross section and is made up of two straight ducts and a 180 deg bend. The geometry of the straight ducts is the same as that reported by Wagner et al. [5,6]. The geometry of the bend is somewhat different, and is taken from the current experimental setup at United Technologies Research Center (Wagner and Steuber [44]). The dimensions of this U-duct are as follows (see Fig. 1): the duct hydraulic diameter is $D_h = 1.27$ cm (0.5 in). The radial position relative to the axis of rotation is $R_r/D_h = 41.85$ and $R_t/D_h = 56.15$. The length of the straight ducts is $L/D_h = 14.3$. The inner and outer radii of the 180 deg bend are $R_i/D_h = 0.22$ and $R_o/D_h = 1.44$.

Two variations of the U-duct were investigated, one with smooth walls and another with ribs. When ribbed, there are ten ribs in each straight duct, five on the leading wall and five on the trailing wall, all with the same pitch. The ribs on those two walls are staggered relative to each other with the ribs on the leading wall offset from those on the trailing wall by a half pitch (p). The ribs are located just upstream or downstream of the 180 deg bend. All ribs are inclined with respect to the flow at an angle (α) of 45 deg. The cross section of the rounded ribs (Fig. 2) is made up of three circular arcs of radius R, where R equals 0.0635 cm (0.025 in) so that the rib height (e) is 0.127 cm (0.05 in) and the rib-height to hydraulic-diameter (e/D_h) is 0.1. The pitch-to-height ratio (p/e) is five (same as the UTRC experiments).

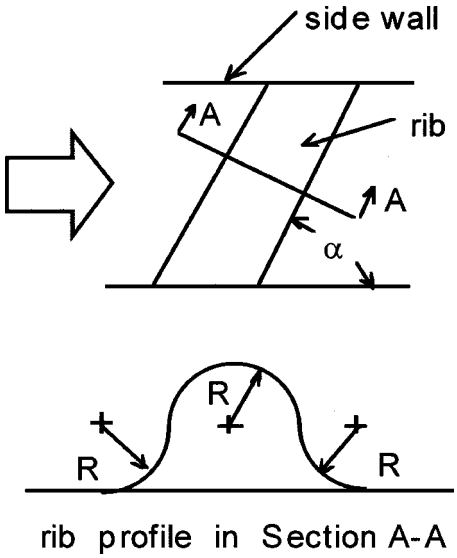

Fig. 2 Schematic of rib geometry

Table 1 Summary of cases studied*

Case No.	Rotation No.	Smooth/Ribbed
C1	0	smooth
C2	0.24	smooth
C3	0	ribbed
C4	0.24	ribbed

* For all cases, Re = 25,000, $\Delta\rho/\rho = 0.13$, and $M_i = 0.05$.

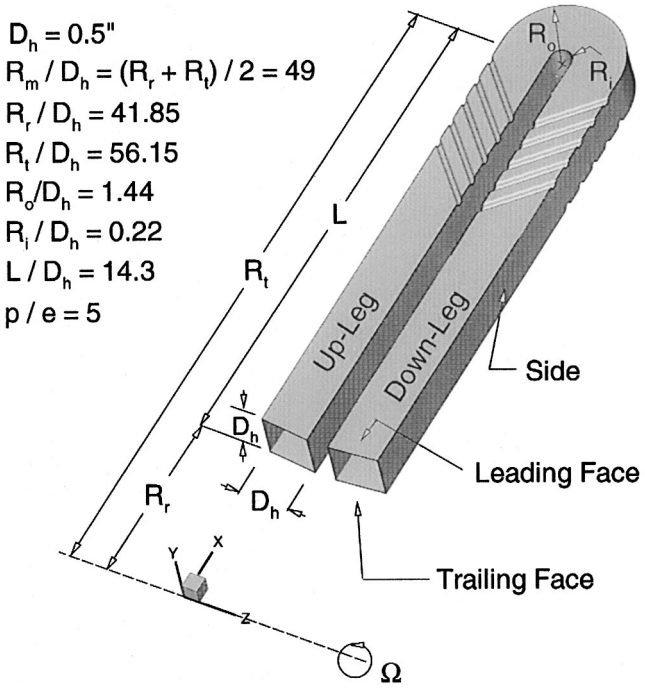

Fig. 1 Schematic of problem studied

All four walls of the U-duct including rib surfaces are maintained at a constant temperature of $T_w = 344.83$ K. At the duct inlet, the coolant air has a uniform temperature of $T_i = 300$ K at the inlet, which gives an inlet coolant-to-wall temperature ratio of 0.87 and an inlet density ratio of $\Delta\rho/\rho = 0.13$. Unlike the temperature profile, the velocity profile at the inlet should not be uniform because of the extensive flow passages upstream of it. Since fully developed velocity profiles do not exist for compressible flows, the velocity profile used is the one at the exit of a non-rotating straight duct of length $150\,D_h$ with adiabatic walls and the same cross section and flow conditions as the U-duct studied here. The Reynolds and rotation numbers at the duct inlet are Re=25,000 and Ro=0.24, respectively. To completely define this problem, either the inlet pressure or the inlet Mach number must be specified. Here, the inlet Mach number is specified at $M_i = 0.05$, which gives rise to a rotational speed of 3132 rpm for Ro=0.24. A summary of the cases studied is given in Table 1.

Problem Formulation

The flow and heat transfer in the U-duct are modeled by the ensemble-averaged conservation equations of mass (continuity), momentum (compressible Navier-Stokes), and total energy for a thermally and calorically perfect gas with Sutherland's model for thermal conductivity. These equations are written in a coordinate system that rotates with the duct so that steady-state solutions with

respect to the duct can be computed (Steinthorsson et al. [45]) and Prakash and Zerkle [31]). The continuity equation is

$$\frac{\partial \rho}{\partial t}+\frac{\partial \rho u}{\partial x}+\frac{\partial \rho v}{\partial y}+\frac{\partial \rho w}{\partial z}=0, \tag{1}$$

where u, v, and w are the x, y, and z-components of the velocity relative to the duct. The momentum equations are

$$\frac{\partial}{\partial t}\begin{bmatrix}\rho u\\ \rho v\\ \rho w\end{bmatrix}+\frac{\partial}{\partial x}\begin{bmatrix}\rho uu\\ \rho vu\\ \rho wu\end{bmatrix}+\frac{\partial}{\partial y}\begin{bmatrix}\rho uv\\ \rho vv\\ \rho wv\end{bmatrix}+\frac{\partial}{\partial z}\begin{bmatrix}\rho uw\\ \rho vw\\ \rho ww\end{bmatrix}$$
$$=\frac{\partial}{\partial x}\begin{bmatrix}P^*+\tau_{xx}\\ \tau_{yx}\\ \tau_{zx}\end{bmatrix}+\frac{\partial}{\partial y}\begin{bmatrix}\tau_{xy}\\ P^*+\tau_{yy}\\ \tau_{zy}\end{bmatrix}+\frac{\partial}{\partial z}\begin{bmatrix}\tau_{xz}\\ \tau_{yz}\\ P^*+\tau_{zz}\end{bmatrix}+\phi, \tag{2a}$$

where

$$P^*=P+\frac{2}{3}\rho k \tag{2b}$$

$$\phi=\begin{bmatrix}\phi_x\\ \phi_y\\ \phi_z\end{bmatrix}=\begin{bmatrix}\rho\Omega^2 x\\ \rho\Omega^2 y\\ 0\end{bmatrix}+\begin{bmatrix}2\rho v\Omega\\ -2\rho u\Omega\\ 0\end{bmatrix}. \tag{2c}$$

The first and second terms on the right-hand-side of Eq. (2c) represent the centripetal and the Coriolis force, respectively. In Eq. (2c), the rotation is about the z-axis (see Fig. 1). The energy equation is given by

$$\frac{\partial \hat{e}}{\partial t}+\frac{\partial}{\partial x}(\hat{e}+P^*)u+\frac{\partial}{\partial y}(\hat{e}+P^*)v+\frac{\partial}{\partial z}(\hat{e}+P^*)w$$
$$=\frac{\partial}{\partial x}(\tau_{xx}u+\tau_{xy}v+\tau_{xz}w-q_x)$$
$$+\frac{\partial}{\partial y}(\tau_{yx}u+\tau_{yy}v+\tau_{yz}w-q_y)$$
$$+\frac{\partial}{\partial z}(\tau_{zx}u+\tau_{zy}v+\tau_{zz}w-q_z)+\phi_e, \tag{3a}$$

where $\hat{e}$ is mechanical plus thermal energy per unit volume; q_i is Fourier conduction in the i^{th} direction; τ_{ij} is the effective stress; and

$$\phi_e=\phi_x u+\phi_y v+\phi_z w. \tag{3b}$$

The ensemble-averaged conservation equations given by Eqs. (1) to (3) were closed by the SST turbulence model (Menter [46] and Menter and Rumsey [47]), which can account for near wall low-Reynolds number effects. The SST model was selected because it eliminates dependence on freestream k and has a limiter to control overshoot in k with adverse pressure gradients so that separation is predicted more accurately.

The k and ω transport equations in the SST model are as follows:

$$\frac{\partial k}{\partial t}+u\frac{\partial k}{\partial x}+v\frac{\partial k}{\partial y}+w\frac{\partial k}{\partial z}=\frac{P_k}{\rho}-\beta_k k\omega+\frac{1}{\rho}\left[\frac{\partial}{\partial x}\left(\mu+\frac{\mu_t}{\sigma_k}\right)\frac{\partial k}{\partial x}+\frac{\partial}{\partial y}\left(\mu+\frac{\mu_t}{\sigma_k}\right)\frac{\partial k}{\partial y}+\frac{\partial}{\partial z}\left(\mu+\frac{\mu_t}{\sigma_k}\right)\frac{\partial k}{\partial z}\right] \tag{4a}$$

$$\frac{\partial \omega}{\partial t}+u\frac{\partial \omega}{\partial x}+v\frac{\partial \omega}{\partial y}+w\frac{\partial \omega}{\partial z}=\frac{P_\omega}{\rho}-\beta_\omega\omega^2+2(1-F)\frac{\sigma_2}{\omega}\left(\frac{\partial k}{\partial x}\frac{\partial \omega}{\partial x}+\frac{\partial k}{\partial y}\frac{\partial \omega}{\partial y}+\frac{\partial k}{\partial z}\frac{\partial \omega}{\partial z}\right)$$
$$+\frac{1}{\rho}\left[\frac{\partial}{\partial x}\left(\mu+\frac{\mu_t}{\sigma_\omega}\right)\frac{\partial \omega}{\partial x}+\frac{\partial}{\partial y}\left(\mu+\frac{\mu_t}{\sigma_\omega}\right)\frac{\partial \omega}{\partial y}+\frac{\partial}{\partial z}\left(\mu+\frac{\mu_t}{\sigma_\omega}\right)\frac{\partial \omega}{\partial z}\right]. \tag{4b}$$

The first term on the right-hand side (RHS) of the above two equations represent production. The second term on the RHS of Eq. (4a) and the second and third terms in Eq. (4b) represent dissipation. The remaining terms on the RHS represent diffusion. The convective transport terms are all on the left-hand side. In Eqs. (4a) and (4b), the turbulent viscosity, production terms, f, and F are given by

$$\mu_t=\min\left(\frac{\rho k}{\omega},\frac{a_1\rho k}{Wf}\right) \tag{4c}$$

$$P_k=\mu_t W^2 \tag{4d}$$

$$P_\omega=g\rho W^2 \tag{4e}$$

$$f=\tanh(\Pi) \tag{4f}$$

$$\Pi=\max(2\Gamma_3,\Gamma_1) \tag{4g}$$

$$F=\tanh(\Gamma^4) \tag{4h}$$

$$\Gamma=\min[\max(\Gamma_1,\Gamma_3),\Gamma_2] \tag{4i}$$

$$\Gamma_1=\frac{500\mu}{\xi^2\rho W} \tag{4j}$$

$$\Gamma_2=\frac{4\rho\sigma_2 k}{\xi^2 C_\sigma} \tag{4k}$$

$$\Gamma_3=\frac{\sqrt{k}}{\xi C_\mu \omega} \tag{4l}$$

$$C_\sigma=\max\left[\frac{2\rho\sigma_2}{\omega}\left(\frac{\partial k}{\partial x}\frac{\partial \omega}{\partial x}+\frac{\partial k}{\partial y}\frac{\partial \omega}{\partial y}+\frac{\partial k}{\partial z}\frac{\partial \omega}{\partial z}\right),10^{-20}\right], \tag{4m}$$

where W is vorticity, and ξ is the normal distance from the solid wall. The constants in Eqs. (4a) to (4e) are calculated by the following weighted formula:

$$\phi=F\phi_1+(1-F)\phi_2. \tag{4n}$$

In the above equation, ϕ is a constant such as σ_k, σ_ω, β_k, and g that is being sought by a weighted average between ϕ_1 and ϕ_2. The ϕ_1 and ϕ_2 terms corresponding to constant such as σ_k, σ_ω, β_k, g_1, and g_2 are as follows:

$$\sigma_{k1}=0.85 \tag{4o}$$

$$\sigma_{k2}=1.0 \tag{4p}$$

$$\sigma_{\omega 1}=0.5 \tag{4q}$$

$$\sigma_{\omega 2}=0.856 \tag{4r}$$

$$\beta_{k1,}=0.075 \tag{4s}$$

$$\beta_{k2}=0.0828 \tag{4t}$$

$$g_1=\frac{\beta_{k1}}{C\mu}-\frac{\sigma_1\theta^2}{\sqrt{C_\mu}} \tag{4u}$$

$$g_2 = \frac{\beta_{k2}}{C\mu} - \frac{\sigma_2 \theta^2}{\sqrt{C_\mu}}. \quad (4v)$$

Other constants, which do not involve weighted averaging, are $\theta = 0.41$, $\beta_\omega = C_\mu = 0.09$, and $a_1 = 0.31$.

Note that by using a low-Reynolds number turbulence model, integration of the conservation equations as well as the turbulence model is made all the way to the wall. Thus, the boundary conditions (BCs) used on all walls are zero velocity, constant wall temperature (344.83 K) and zero turbulent kinetic energy. The BC for ω on the wall is ω equals to $60v/(\beta \Delta y^2)$ as proposed by Wilcox [48] for hydraulically smooth surfaces. In that BC, β equals to 3/40, and Δy is the normal distance of the first grid point from the wall. The first grid point from the wall must be within a y^+ of unity.

Other BCs needed are as follows. At the duct entrance, a developed profile is specified for velocity, but the temperature profile is taken to be uniform (see previous section for details). Turbulence quantities (k and ω) are specified in a manner that is consistent with the velocity profile (average turbulent intensity was 5 percent). Only pressure is extrapolated. At the duct exit, an average back pressure is imposed but the pressure gradients in the two spanwise directions are extrapolated. This is because secondary flows induced by inclined ribs, the bend, and centripetal/Coriolis forces cause pressure variations in the spanwise directions. Density and velocity are extrapolated.

Though only solutions steady with respect to the duct are of interest, initial conditions were needed because the unsteady form of the conservation equations was used. The initial conditions used are the solutions of the steady, one-dimensional, inviscid equations, namely,

$$\frac{\partial \rho u}{\partial x} = 0, \quad \frac{\partial \rho u^2}{\partial x} = -\frac{\partial P}{\partial x} + \rho \Omega^2 x, \quad \frac{\partial \rho u h}{\partial x} = \rho u \Omega^2 x. \quad (5)$$

Numerical Method of Solution

Solutions to the governing equations just described were obtained by using a research code, called CFL3D (Thomas et al. [49] and Rumsey and Vatsa [50]). In this study, the CFL3D code (Version 4.1) was modified so that it can account for steady-state solutions in a rotating frame of reference by adding source terms that represent centripetal and Coriolis forces in the momentum and energy equations (see Eqs. (2) and (3)). The modified CFL3D code has been validated for flow in a non-rotating duct with square and rounded ribs (Stephens et al. [26,33]) and flow in a rotating duct with smooth walls (Stephens et al. [38] and Stephens and Shih [28]).

This code is based on a cell-centered finite-volume method. All inviscid terms are approximated by the second-order accurate flux-difference splitting of Roe [51]. All diffusion terms are approximated conservatively by differencing derivatives at cell faces. Since only steady-state solutions are of interest, time derivatives are approximated by the Euler implicit formula. The system of nonlinear equations that results from the aforementioned approximations to the space and time-derivatives are analyzed by using a diagonalized alternating-direction scheme (Pulliam and Chaussee [52]) with local time-stepping and three-level V-cycle multigrid (Anderson et al. [53]).

The domains of the smooth and ribbed ducts are replaced by H-H structured grids (Fig. 3). The number of grid points in the streamwise direction from inlet to outlet is 257 for the smooth duct and 761 for the ribbed duct. Whether smooth or ribbed, the number of grid points in the cross-stream plane is 65×65. The number of grid points and their distribution were obtained by satisfying a set of rules such as aligning the grid with the flow direction as much as possible, keeping grid aspect ratio near unity in regions with recirculating flow, and having at least 5 grid points within a y^+ of 5 (see Stephens et al. [38]). As a further test, the aforementioned grid systems were refined by a factor of 25 percent, first in the streamwise and then in the cross-stream directions. This grid independence study showed the predicted surface heat transfer coefficient to vary by less than 2 percent.

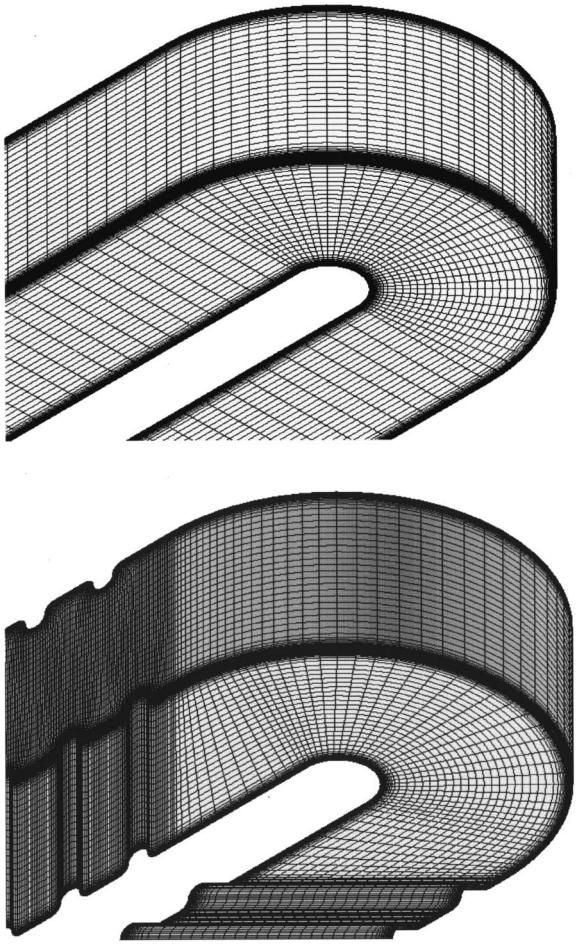

Fig. 3 Grid systems used for smooth and ribbed U-duct

On the Cray C-90 computer, where all solutions were generated, the memory and CPU time requirements for each run are 55 megawords (MWs) and 16 hours for the smooth duct and 155 MWs and 40 hours for the ribbed duct. The CPU time given is for a converged steady-state solution (steady in a frame relative to the duct), which typically involved 3000 iterations.

Results

The results of this study are presented in Figs. 4–14. Note that the scales in Figs. 7–9 are not same from plot to plot in order to highlight key features in each plot. In discussing these results, the four walls of the U-duct are referred to as leading, trailing, outer, and inner, whether there is rotation or not. When there is no rotation, leading and trailing are the same for the smooth case and nearly the same for the ribbed case, so only results for one wall are given. The inner and outer walls refer to the U-shaped ones at R_i and R_o, respectively (Fig. 1).

Nature of Fluid Flow. The nature of the flow in the U-duct is complicated. In the following, the complexity of this flow is examined in a step-by-step manner, adding one complicating feature at a time.

Non-Rotating Smooth Duct. For a smooth non-rotating duct (Case C1 in Table 1), Figs. 4–6 and Fig. 9 show the following. In the up-leg part of the U-duct, the velocity profile has a maximum

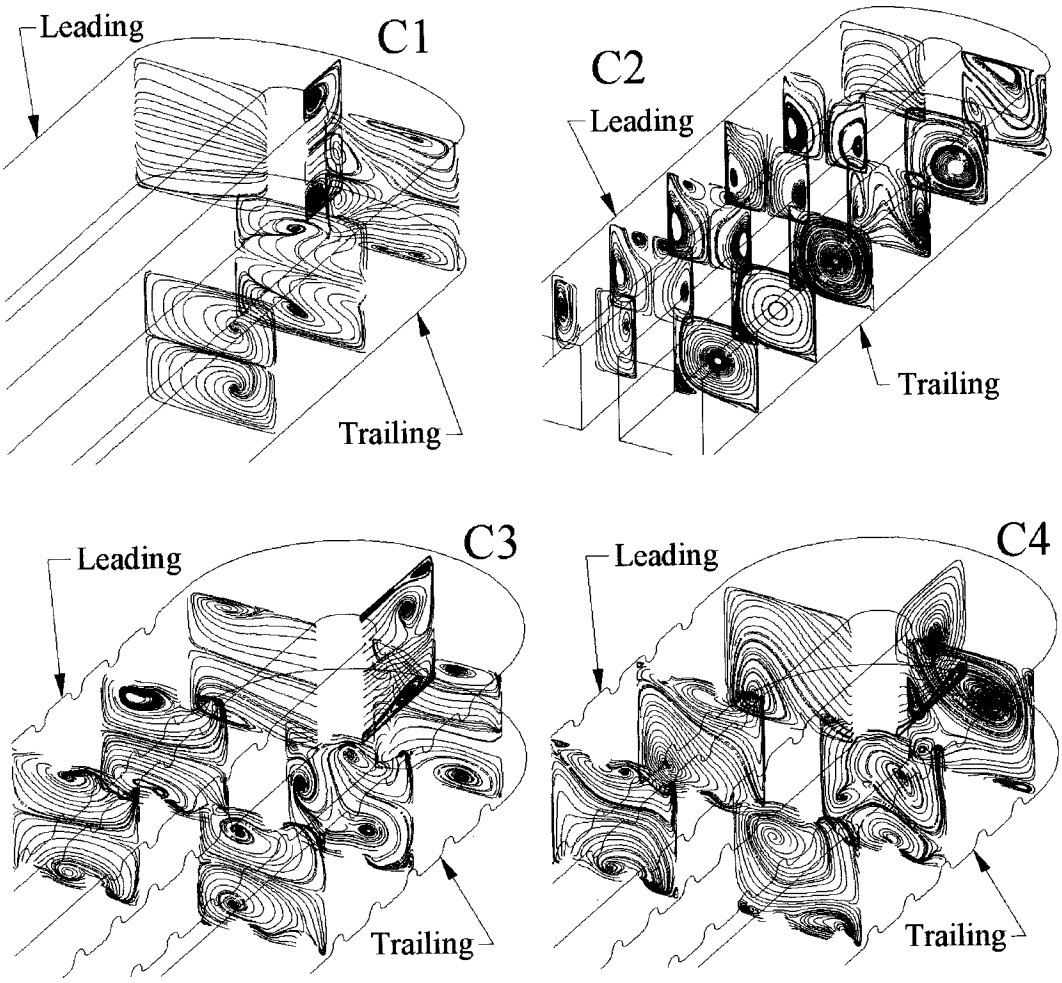

Fig. 4 Streamlines projected on selected *y-z* planes and the mid *x-y* plane

at about the center of the duct cross section. The coolant is coolest near the center of the duct cross section with thermal boundary layers growing along all four walls of the duct along the streamwise direction (Fig. 6). The expected pairs of vortices in each of the four corners of the duct cross section were not predicted because the turbulence model used cannot account for anisotropic effects. Not resolving these vortices is acceptable since their magnitudes are extremely small when compared to secondary flows induced by rotation, bend, and ribs (see Lin et al. [54]).

At about $1.25\,D_h$ to $1\,D_h$ upstream of the bend, the flow becomes affected by the bend (Figs. 4, 5, 6, and 9). As the flow approaches and enters the bend, it accelerates near the inner wall but decelerates and reverses next to the outer wall (Fig. 5). Near the middle of the bend, the flow separates on the inner wall (Fig. 5). This separated region is largest about the mid *x-z* plane and smallest next to the leading/trailing face. With this separated region, which reduces the effective passage cross-section, the speed of flow near the outer wall is increased markedly.

Along the bend, a rather complicated pressure gradient forms with higher pressure next to the outer wall and lower pressure next to the inner wall (Fig. 9). The nature of this gradient depends on the curvature of the streamlines in the core of the duct where flow speed is highest. The curvature in the streamlines, however, depends on the geometry of the bend and whether or not there are separation bubbles in the bend since they effectively change the bend geometry. The Dean-type secondary flows created by this pressure gradient can clearly be seen in Fig. 4 and Fig. 6 (C1–P3). Because of the separation bubble in the bend, the pressure gradient and the Dean-type secondary flows induce another pair of secondary flows within the separation bubble (Fig. 6 C1–P4). The net effect of these secondary flows is to transport cooler fluid near the center of the duct cross section towards the outer wall and parts of the leading/trailing faces (Fig. 6).

Downstream of the bend, only the secondary flows of the Dean type persist until the duct exit. The Dean-type secondary flow coupled with the separation bubble around the bend caused the maximum in the velocity profile in the down-leg part of the duct to be shifted towards the outer wall.

Rotating Smooth Duct. The effects of rotation on a smooth U-duct in which the coolant-to-wall temperature is less than unity (Case C2 in Table 1) can be inferred from Figs. 4–6 and Fig. 9. In the up-leg part of the duct, Fig. 4 shows rotation to induce secondary flows. Two symmetric counter-rotating flows are formed by the Coriolis force as early as D_h into the duct. With radially outward flow, the rotation orientation is from the trailing face to the leading face along the outer and inner walls, transporting cooler air from near the center of the duct cross section to the trailing face first. Since the thermal boundary layer starts on the trailing face, gas temperature near that face is lower than that near the leading face (Fig. 6).

With higher temperature and hence lower density near the leading face, centrifugal buoyancy tends to decelerate the flow on the leading face more so than that on the trailing face (Fig. 5). With lower velocity and hence thicker boundary layer next to the leading face, the Coriolis-induced secondary flows cause the formation of additional pairs of vortices near that face (C2 in Fig. 4). This was also observed by Iacovides and Launder [20], Stephens

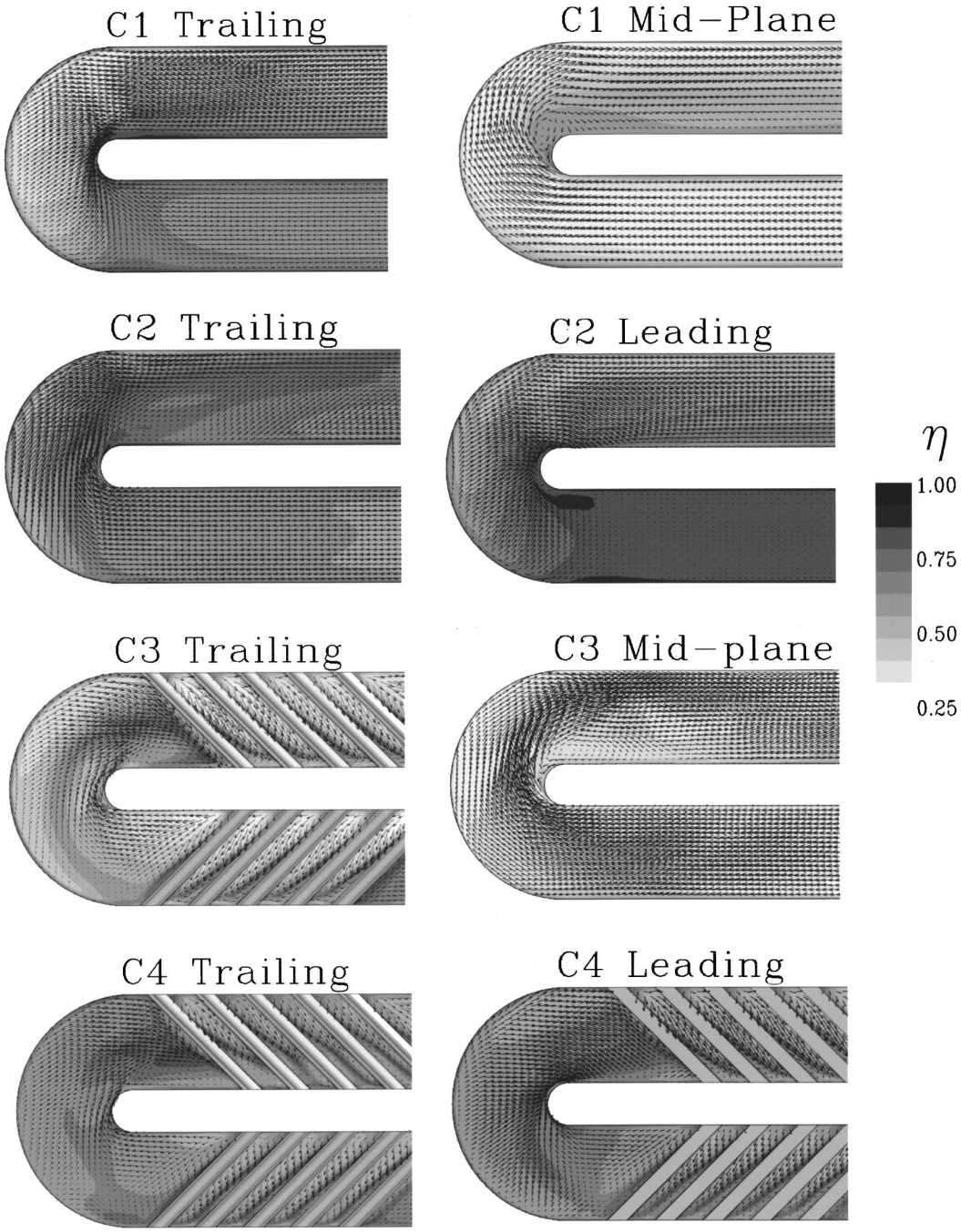

Fig. 5 Normalized temperature (η) and velocity vectors projected at the middle *x-z* plane and at 0.01 D_h away from ribbed surfaces

et al. [26], Bonhoff et al. [39], and Stephens and Shih [28]. Stephens et al. [38] showed that at a rotation number of 0.48 and a density ratio of 0.13, centrifugal buoyancy causes massive flow separation on the leading face.

With rotation, the pressure gradient in the 180 deg bend changed considerably. The pressure gradient induced by rotation in the radial direction is much stronger than the pressure gradient induced by the bend from streamline curvature. Note that when there is rotation, lines of constant pressure are nearly flat in the bend (contrast C1 and C2 in Fig. 9). With such a pressure distribution, the flows next to the inner and outer walls are decelerated similarly as they approach the bend, which is in sharp contrast to the non-rotating smooth duct. On the leading face, where the flow is also being decelerated by centrifugal buoyancy, there is considerable flow reversal upstream of the bend (Fig. 5). As the flow goes around the bend, it separates with the separated region larger near the trailing face than near the mid-plane or leading face, which also differs from the non-rotating case (Fig. 5).

The evolution of the secondary flows through the bend is as follows. In the bend, the pressure gradient enhances secondary flows that flow from the outer wall to the inner wall along either the leading or the trailing face. Thus, the pair of counter-rotating flows formed upstream of the bend by the Coriolis force became asymmetric after going through the bend. Of the two, the secondary flow that flowed from the trailing face to the leading face along the outer wall became dominant (C2–P3 and C2–P4 in Fig. 6). The net effect of the secondary flows is to transport the cooler

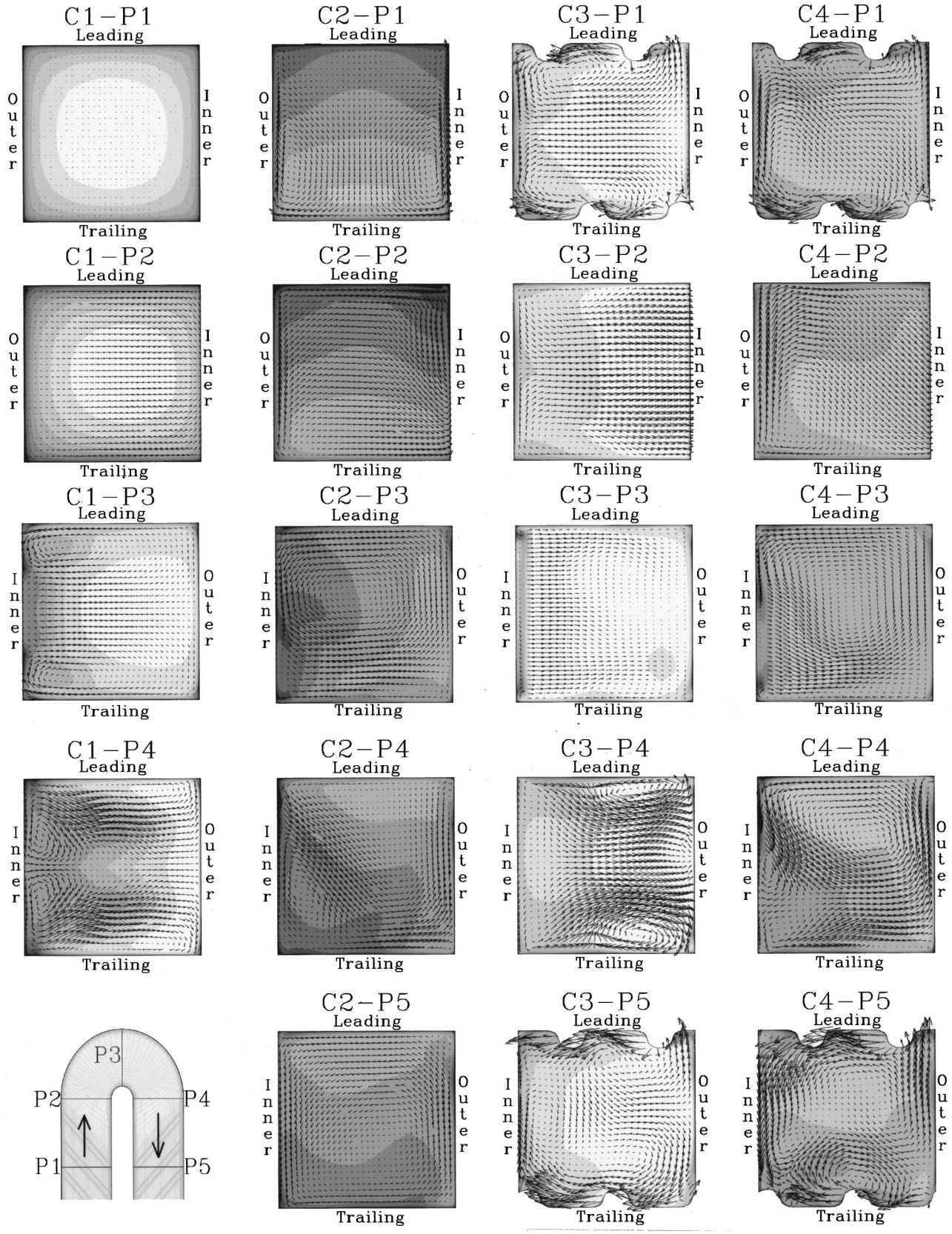

Fig. 6 Normalized temperature (η) and velocity vectors projected at selected planes (P1, . . . ,P5). Scale for η is same as the one in Fig. 5.

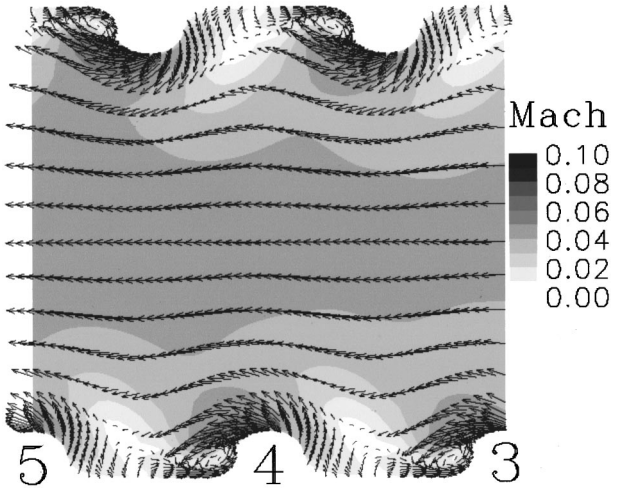

Fig. 7 Mach number and velocity vectors projected on the middle *x-y* plane for case C3 in up-leg part of U-duct. 3, 4, and 5 denote the 3rd, 4th, and 5th ribs.

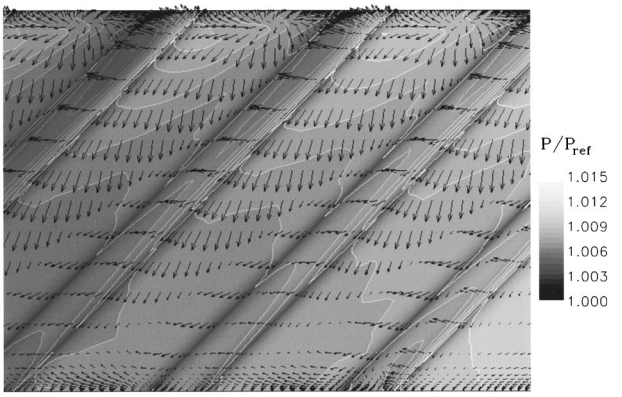

Fig. 8 Pressure contours and velocity vectors projected at 0.01 D_h away from the ribbed surface for case C3. Flow is from right to left over the first four ribs in the up-leg part.

fluid near the trailing face just upstream of the bend in a spiral, first towards the outer wall, then towards the leading face, and so on (Fig. 6).

Downstream of the bend, only the secondary flow that flows from the trailing face to the leading face along the outer wall persists. The effect of centrifugal buoyancy in the down-leg part of the duct is to accelerate instead of decelerate the lower density fluid. See Stephens and Shih [28] for other details.

Finally, note that rotation not only increases pressure radially, it also increases temperature radially because of the compression.

Non-Rotating Ribbed Duct. The effects of staggered inclined ribs on a non-rotating U-duct (Case C3 in Table 1) can be inferred from Figs. 4–9. Figures 4–6 show inclined ribs to induce a pair of secondary flows. In the up-leg part, they flow from the inner wall to the outer-side wall along the leading/trailing faces (Fig. 5). Because of the staggered arrangement of the ribs on the leading and trailing faces, the secondary flows oscillate in size along the streamwise direction (not shown). These secondary flows transport cooler fluid first towards the inner wall and then to the leading and trailing faces.

As the flow approaches the bend from the up-leg part, the pressure gradient induced by the bend causes essentially no flow reversal on the leading and trailing faces (Fig. 5), which differs from the non-rotating smooth duct. Around the bend, Dean-type

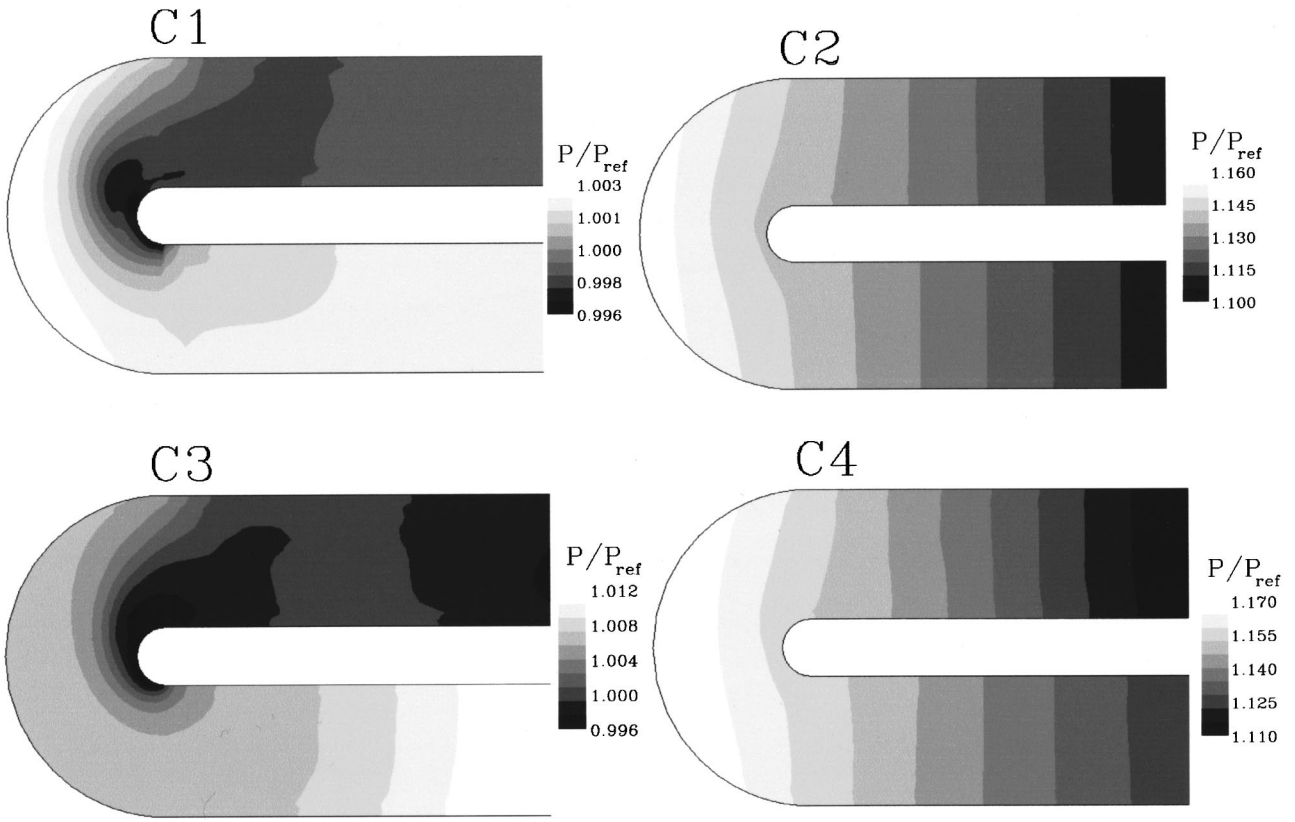

Fig. 9 Normalized pressure in the middle *x-z* plane

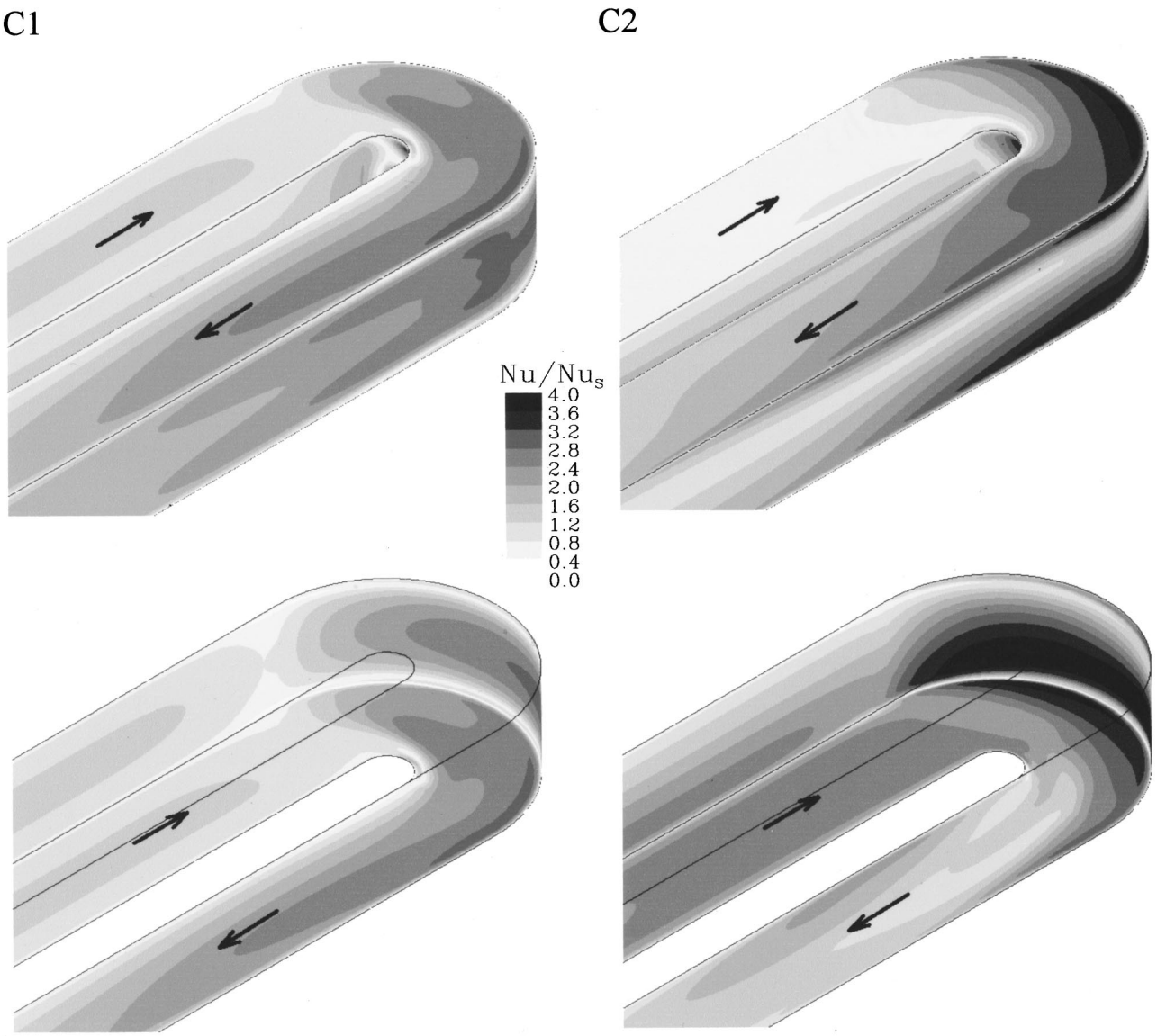

Fig. 10 Nu/Nu$_s$ for cases C1 and C2. Top: leading. Bottom: trailing.

secondary flows form, but is confined near the leading/trailing and outer walls by the rib-induced secondary flows, which rotate in the opposite sense (Fig. 6). If the ribs in the up-leg part were inclined at −45 deg instead of +45 deg, then the rib-induced secondary flows would be rotating in the same sense as the Dean-type ones. For such a case, the bend would just re-enforce the secondary flows formed by the inclined ribs.

Similar to the case without ribs, there is a large separated region around the bend next to the inner wall. However, it differs in that the separation region is larger and the reattachment on the leading/trailing faces is strongly influenced by the location of the first inclined rib downstream of the bend (Fig. 5).

Downstream of the bend, inclined ribs again induce a pair of secondary flows (Fig. 4). This pair flows from the outer wall to the inner wall along the leading and trailing faces (Figs. 5 and 6). The rib inclination is such that the sense of rotation is the same as that of the Dean-type ones. The net effect of these flows is to transport cooler fluid to the leading and trailing faces that start from the outer wall.

From Fig. 5, it can be seen that the flow between ribs just above the ribbed wall has a higher and a lower-speed region. To examine this, a blow-up of this region is shown in Figs. 7 and 8 for the up-leg part of the U-duct. From Fig. 7, it can be seen that there is flow separation downstream of each rib. From Fig. 8, it can be seen that the fluid associated with the higher-speed flow is brought by the secondary flow into the region between the ribs, which for the up-leg part, is from the inner wall to the outer wall. The fluid associated with the lower-speed flow came from the upstream rib without first going through a spiral. Figure 8 also shows that for the up-leg part, the pressure is highest near the inner wall and the upstream side of each rib. This adverse pressure gradient causes the flow near the rib surface to curve backwards (Figs. 5 and 8). The flow and pressure distribution between ribs in the down-leg part are not shown because they are similar to those in the up-leg part. The exception is that the pressure is higher near the outer wall instead of the inner wall due to differences in rib inclination.

Rotating Ribbed Duct. The effects of rotation on a ribbed duct (Case C4 in Table 1) can be inferred from Figs. 4–6 and Fig. 9. When there is rotation, the flow approaching the ribs is characterized by secondary flows induced by Coriolis force, flow deceleration near the leading face by centrifugal buoyancy, and cooler fluid near the trailing face. As a result, the secondary flows induced by the ribs are asymmetric with the one next to the trailing

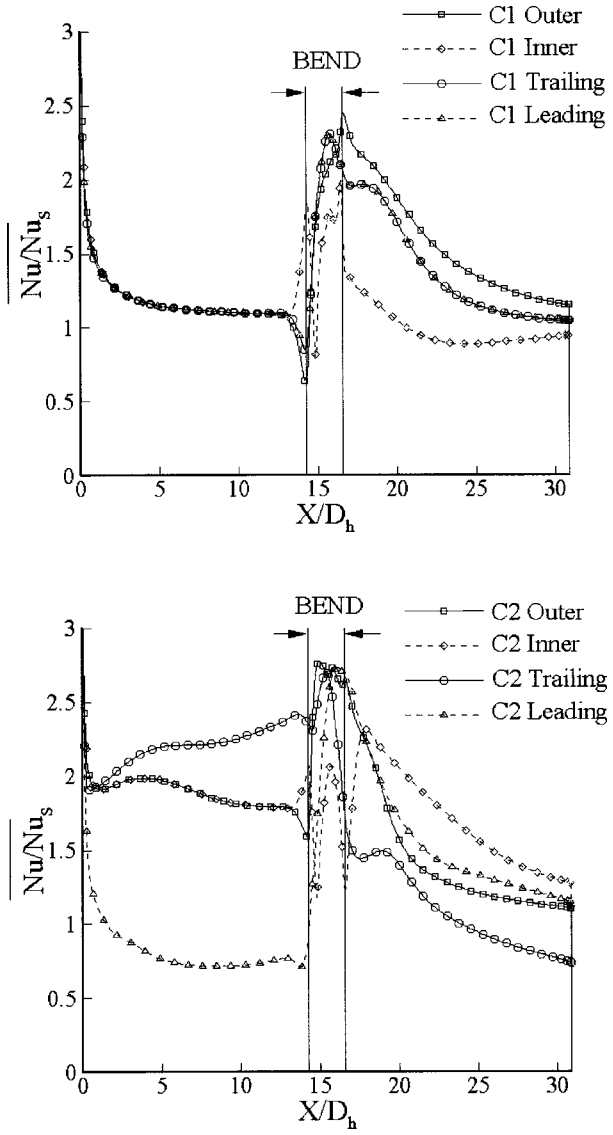

Fig. 11 Spanwise-averaged Nu/Nu_s on leading, trailing, outer, and inner walls as a function of distance along U-duct from inlet to outlet for cases C1 and C2

face much stronger because the streamwise momentum is much higher there. In fact, just upstream of the bend, that secondary flow dominates (Figs. 4 and 6).

Similar to the rotating smooth duct, the pressure gradient in the radial direction induced by rotation is quite strong. The bend curved the otherwise nearly parallel lines of constant pressure only slightly (Fig. 9). With such a pressure gradient, the flow is decelerated as it approaches the bend and accelerated as it leaves with magnitudes that do not differ appreciable from the inner wall to the outer wall. But, very close to the inner wall, there is acceleration as the flow enters the bend followed by flow separation in which the separation bubble on the trailing face is much larger than that on the leading face (Fig. 5). With this pressure gradient, the dominant secondary flow induced by the ribs is re-enforced and pushed towards the leading face. Thus, the Dean-type secondary flow is highly asymmetric with the one next to the trailing face being quite small (Fig. 6).

In the down-leg part, the inclined ribs generate a pair of secondary flows that flow from the outer wall to the inner wall along the leading and trailing faces. They have the same sense of rotation as those generated by the bend (i.e., the Dean-type secondary

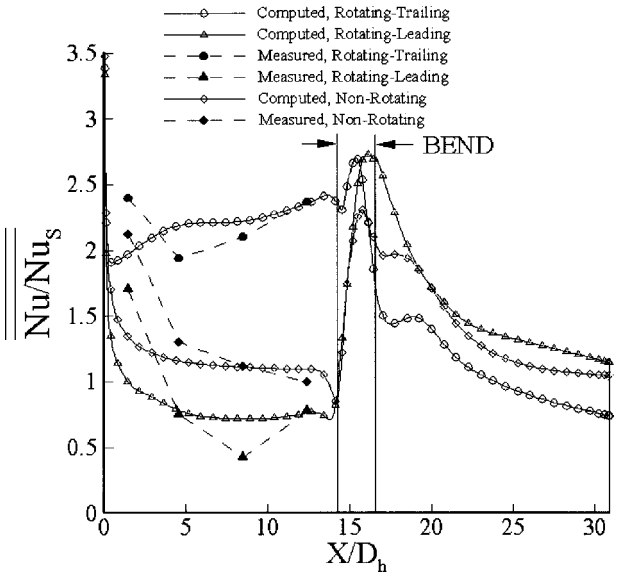

Fig. 12 Peripherally-averaged Nu/Nu_s as a function of distance along U-duct from inlet to outlet. The measured data is from Wagner et al. [5].

flows). Similar to the up-leg part, however, they are asymmetric because the flow upstream was asymmetric. Further downstream in the down-leg part, the duct becomes smooth again. From there, Coriolis and centrifugal buoyancy again begin to exert their influence as secondary flows induced by the ribs decay.

Heat Transfer Characteristics. Results for heat transfer are given in Figs. 10–14 in terms of Nu/Nu_s and its averages in which the averaging is along a spanwise grid line on either one wall (inner, outer, leading, or trailing) or on all four walls. Note that the grid lines are inclined in regions with the inclined ribs. The heat transfer coefficient h in Nu is computed by using a bulk temperature that accounts for temperature rise due to rotation. See Nomenclature for the functional form of T_b, which is the solution of Eq. (5) (Stephens and Shih [28]). Note that $T_b = T_i$ if there is no rotation.

For a non-rotating smooth duct, Fig. 10 (C1) shows that heat transfer reaches a minimum just upstream of the bend because the flow decelerates most there. The heat transfer is greatly increased by the bend because of the secondary flows and the impingement of the flow on the outer wall. Figure 11 shows the average Nu/Nu_s on the inner, outer, and leading/trailing walls along the duct from inlet to outlet. From this figure, it can be seen that the bend increases the heat transfer rate by almost a factor of two just after the bend on the outer and on the leading/trailing faces. This magnitude of increase was also observed experimentally by Iacovides et al. [4] for a smooth U-duct, though with a stronger curvature at the bend ($(R_o + R_i)/D_h = 0.65$ instead of 0.83) and a higher Reynolds number (95,000 instead of 25,000).

With rotation, heat transfer in the up-leg part is higher on the trailing face than the leading face because secondary flows induced by the Coriolis force transported cooler fluid to the trailing face first (Fig. 10 (C2)). Around the bend, the heat transfer on the trailing face becomes lower than that on the leading face (Figs. 10 and 11). This is because the secondary flows transported cooler fluid closer to the leading face (Fig. 6). In the down-leg part, heat transfer is also lower on the trailing face because of the large separated region just downstream of the bend and secondary flows induced by the bend. Figure 12 compares the peripherally averaged Nu/Nu_s along the smooth U-duct under rotating and non-rotating conditions. The measurements by Wagner et al. [5] are also included.

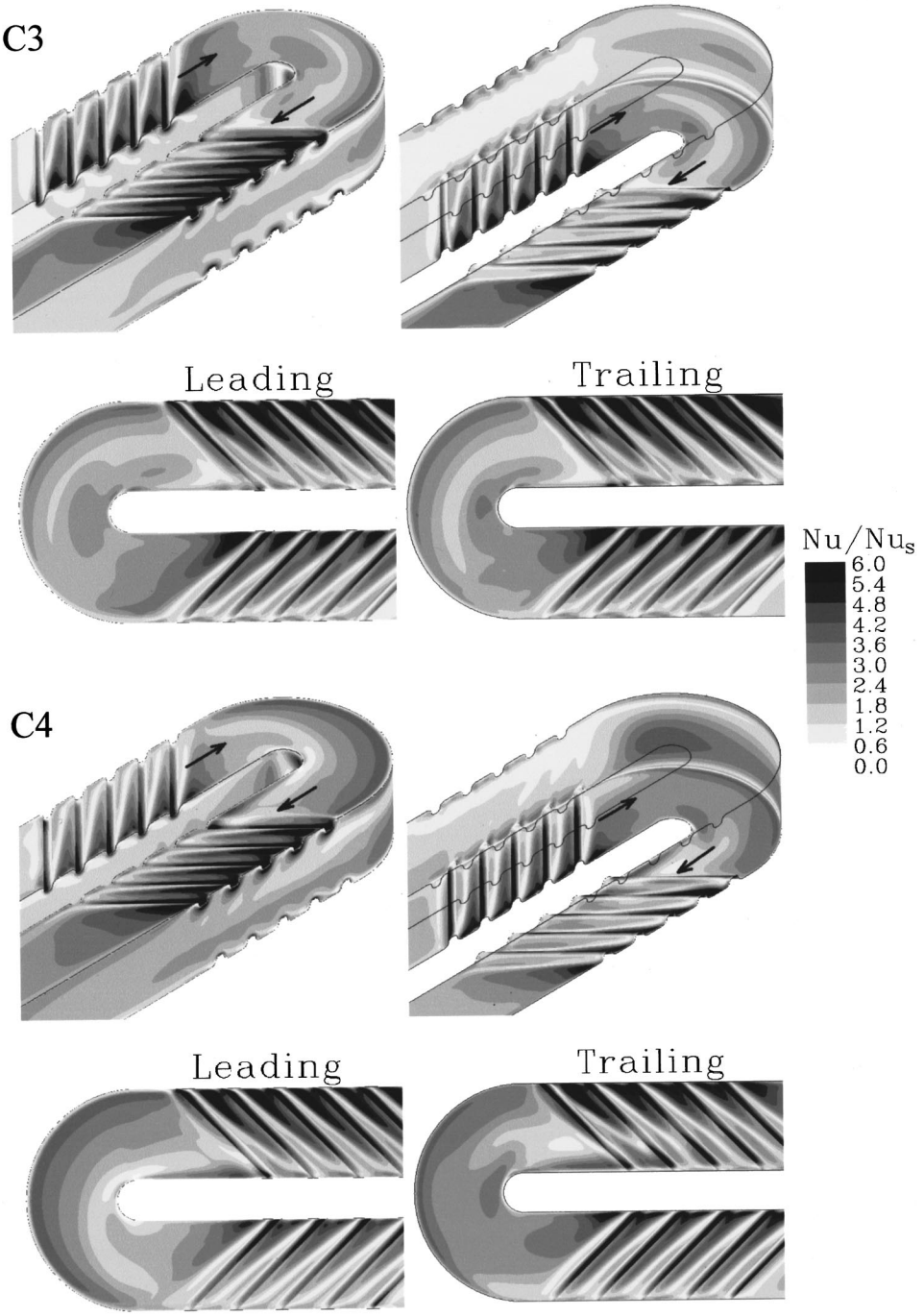

Fig. 13 Nu/Nu$_s$ for cases C3 and C4

When there are inclined ribs in a non-rotating duct, the heat transfer is greatly enhanced in the region with the ribs, both in the up-leg and down-leg parts (Figs. 13 and 14). The increase in heat transfer on the leading and trailing faces are similar despite the offset from staggering. On each rib, the heat transfer is high on the forward side and low on the backward side (Fig. 13). This can be understood in terms of the stagnation and wake flows created by the main flow in the streamwise direction (Figs. 7 and 8). In the region between the ribs, the heat transfer is high from the inner wall if up-leg part and from the outer wall if down-leg part. The heat transfer is high on the leading and trailing faces near either the inner or outer walls because the secondary flows induced by the ribs cause cooler fluid to impinge there first. In the region between ribs, there is a strip of low heat transfer (Fig. 13) because that is where the high-speed and low-speed flows converge (Fig. 8). Since the surface heat transfer varies considerably in the region about the ribs, up to a factor of six or more, it is important to investigate not just the averaged heat transfer rate, but also the local heat transfer characteristics.

When a ribbed duct rotates, the heat transfer on the leading and trailing faces differs in a manner similar to that for a rotating smooth duct. Basically, heat transfer on leading face is less than that on the trailing face in the up-leg part (Figs. 13 and 14). In the down-leg part, heat transfer on the leading face approaches that on the trailing face (Fig. 14). Distributions of Nu/Nu$_s$ about each rib and between ribs are similar in character to the ribbed non-rotating duct (Fig. 13).

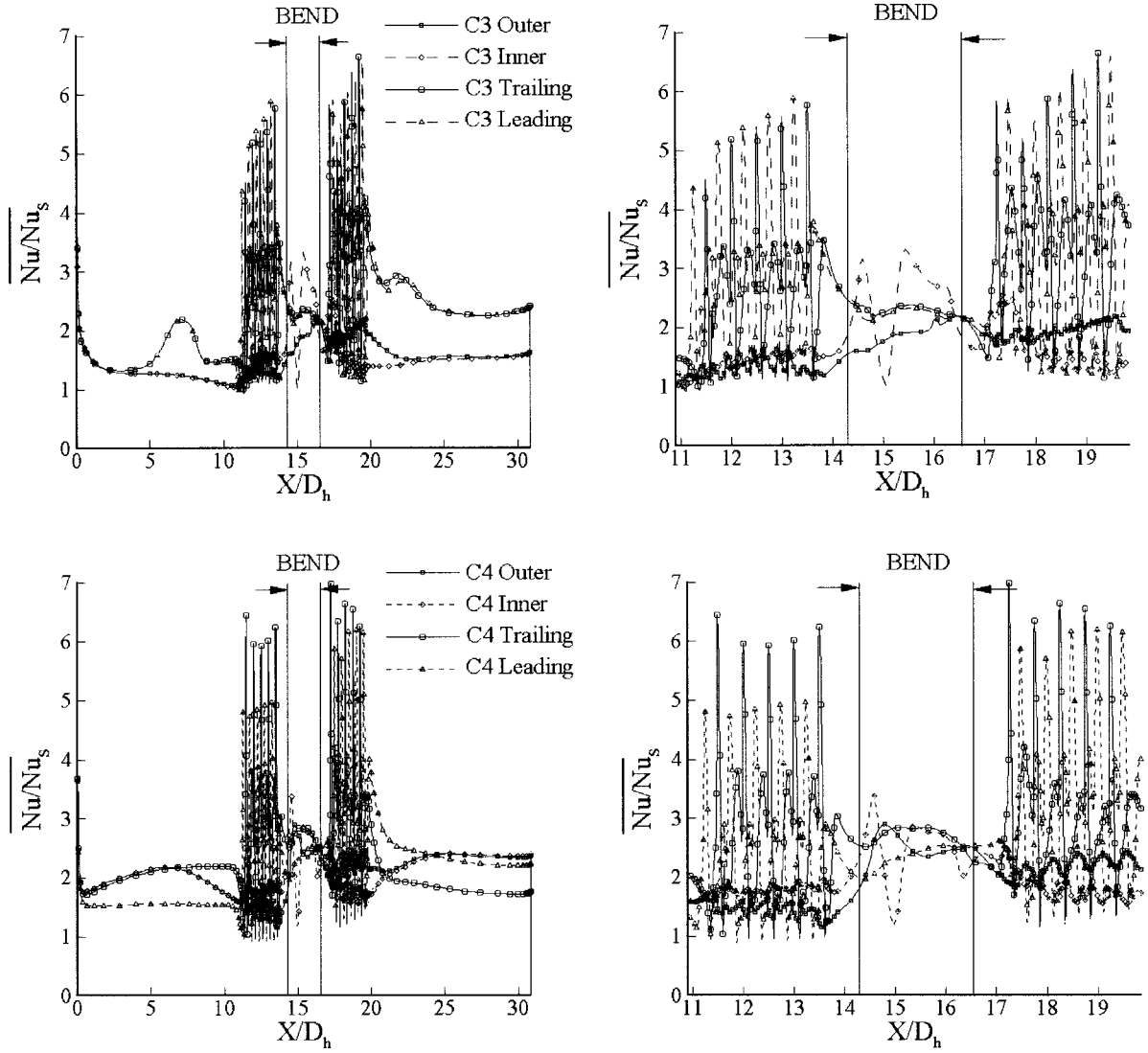

Fig. 14 Spanwise-averaged Nu/Nu_s on leading, trailing, outer, and inner walls as a function of distance along U-duct from inlet to outlet for cases C3 and C4

Summary

Computations were performed to study the fluid flow and heat transfer in a smooth and a ribbed U-shaped duct under rotating and non-rotating conditions. On flow structure, one should not think about the interactions between secondary flows induced by Coriolis, 180 deg bends, and inclined ribs because each of these secondary flows may never form depending upon upstream flow conditions. Instead, one should examine how Coriolis, centrifugal buoyancy, and pressure gradients induced by streamline curvature from bends and inclined ribs affect the local flow structure. On heat transfer, secondary flows were found to have pronounced effects. Basically, heat transfer coefficient is higher when secondary flows impinge on a surface, and lower when they leave a surface.

For the conditions of the present study, the following conclusions can be made on the effects of rotation on a smooth and a ribbed duct:

• For a smooth U-duct without rotation, the flow is dominated by the streamwise separation around the bend and by the Dean-type secondary flows formed by the 180 deg bend. As a result of this flow, surface heat transfer is higher around and downstream of the bend.

• For a smooth U-duct with rotation, Coriolis force and centrifugal buoyancy dominate in the up-leg part. In the bend, the nature of the pressure gradient is dominated by rotation instead of streamline curvature or flow separation around the bend. This pressure gradient favors a secondary flow that flows from the outer wall to the inner wall along the leading face. This secondary flow is then distorted by the Coriolis force and centrifugal buoyancy in the down-leg part. As a result, heat transfer is lower on the leading face and higher on the trailing face in the up-leg part. Around and downstream of bend, heat transfer on the leading face is higher than that on the trailing face.

• For a ribbed duct without rotation, the flow is dominated by inclined ribs and the bend. In the up-leg part, a nearly symmetric pair of secondary flows forms that oscillates slightly in size along the streamwise direction. In the bend, the pressure gradient from streamline curvature re-enforces the rib-induced secondary flow that rotates in the same sense as the Dean-type secondary flows, and weakens the one that rotates in the opposite sense. In the down-leg part, the ribs re-enforce the Dean-type secondary flows. Though ribs greatly enhance heat transfer when compared to the smooth-wall case, there are regions of low heat transfer regions between ribs.

• For a ribbed duct with rotation, secondary flows setup by Coriolis force and centrifugal buoyancy in the up-leg part upstream of the ribs can have a strong effect on the secondary flows induced by the ribs. Basically, it weakens the rib-induced secondary flow next to the leading face. Similar to the rotating smooth duct, the nature of the pressure gradient is dominated by rotation instead of streamline curvature or flow separation around the bend. This pressure gradient favors a secondary flow that flows from the outer wall to the inner wall along the leading face. This secondary flow is then re-enforced by ribs in the down-leg part. As a result, heat transfer is lower on the leading face and higher on the trailing face in the up-leg part. Around and downstream of bend, heat transfer on the leading face approach that on the trailing face.

Acknowledgments

This work was partially supported by grant NAG 3-1727 under the Smart Green Engine Project from the NASA Glenn Research Center with Kestutis C. Civinskas as the technical monitor. The computer time was provided by NASA's National Aeronautics Simulation Facility and by the Pittsburgh Supercomputing Center. The authors are grateful for this support.

Nomenclature

C_p = constant pressure specific heat
D_h = hydraulic diameter of duct
h = heat transfer coefficient ($h=q_w/(T_w-T_b)$)
k = turbulent kinetic energy
L = length of straight portion of duct
M_i = Mach number ($M_i=V_i/\sqrt{\gamma RT_i}$)
Nu = Nusselt number ($\mathrm{Nu}=hD_h/\kappa$)
Nu_s = Nusselt number for smooth duct ($\mathrm{Nu}_s=0.023\,\mathrm{Re}^{0.8}\,\mathrm{Pr}^{0.4}$)
q_w = wall heat transfer rate per unit area
R_i, R_o = inner and outer radius of 180 deg bend (Fig. 1)
R_r, R_t = radius from axis of rotation (Fig. 1)
R = gas constant for air
Re = Reynolds number ($\mathrm{Re}=\rho_i V_i D_h/\mu$)
Ro = rotation number ($\mathrm{Ro}=\Omega D_h/V_i$)
T_b = bulk temperature defined by $T_b=T_i+\Omega^2(x^2-R_r^2)/2C_p$
V_i = average velocity at duct inlet
x, y, z = coordinate system rotating with duct (Fig. 1)
X = coordinate along the axis of the U-duct from inlet to outlet
u, v, w = x, y, z-components of velocity relative to duct

Greek

κ = thermal conductivity of coolant
η = normalized temperature ($\eta=(T-T_i)/(T_w-T_i)$)
ρ = density
$\Delta\rho/\rho$ = $(T_w-T_i)/T_w$
τ_{ij} = shear stress
ω = dissipation rate per unit k
Ω = angular rotation speed of duct

References

[1] Han, J. C., and Zhang, Y. M., 1992, ''High Performance Heat Transfer Ducts with Parallel Broken and V-Shaped Broken Ribs,'' Int. J. Heat Mass Transf., **35**, No. 2, pp. 513–523.
[2] Chyu, M. K., and Natarajan, V., 1995, ''Surface Heat Transfer from a Three-Pass Blade Cooling Passage Simulator,'' ASME J. Turbomach., **117**, No. 4, pp. 650–656.
[3] Liou, T.-M., Tzeng, Y.-Y., and Chen, C.-C., 1998, ''Fluid Flow in a 180 Deg Sharp Turning Duct with Different Divider Thicknesses,'' ASME 98-GT-189.
[4] Iacovides, H., Jackson, D. C., Kelemenis, G., and Launder, B. E., 1999, ''The Measurement of Local Wall Heat Transfer in Stationary U-Ducts of Strong Curvature, with Smooth and Rib-Roughened Walls,'' ASME Paper 99-GT-254.
[5] Wagner, J. H., Johnson, B. V., and Hajek, T. J., 1991, ''Heat Transfer in Rotating Passages with Smooth Walls and Radial Outward Flow,'' ASME J. Turbomach., **113**, No. 1, pp. 42–51.
[6] Wagner, J. H., Johnson, B. V., and Kopper, F. C., 1991, ''Heat Transfer in Rotating Serpentine Passages with Smooth Walls,'' ASME J. Turbomach., **113**, No. 3, pp. 321–330.
[7] Morris, W. D., and Salemi, R., 1992, ''An Attempt to Uncouple the Effects of Coriolis and Buoyancy Forces Experimentally on Heat Transfer in Smooth Circular Tubes That Rotate in the Orthogonal Mode,'' ASME J. Turbomach., **114**, No. 4, pp. 858–864.
[8] Han, J. C., Zhang, Y. M., and Lee, C. P., 1994, ''Influence of Surface Heating Condition on Local Heat Transfer in a Rotating Square Channel With Smooth Walls and Radially Outward Flow,'' ASME J. Turbomach., **116**, No. 1, pp. 149–158.
[9] Cheah, S. C., Iacovides, H., Jackson, D. C., Ji, H., and Launder, B. E., 1996, ''LDA Investigation of the Flow Development through Rotating U-Ducts,'' ASME J. Turbomach., **118**, pp. 590–596.
[10] Taslim, M. E., Rahman, A., and Spring, S. D., 1991, ''An Experimental Investigation of Heat Transfer Coefficients in a Spanwise Rotating Channel with Two Opposite Rib-Roughened Walls,'' ASME J. Turbomach., **113**, No. 1, pp. 75–82.
[11] Wagner, J. H., Johnson, B. V., Graziani, R. A., and Yeh, F. C., 1992, ''Heat Transfer in Rotating Serpentine Passages with Trips Normal to the Flow,'' ASME J. Turbomach., **114**, No. 4, pp. 847–857.
[12] Zhang, N., Chiou, J., Fann, S., and Yang, W.-J., 1993, ''Local Heat Transfer Distribution in a Rotating Serpentine Rib-Roughened Flow Passage,'' ASME J. Heat Transfer, **115**, No. 3, pp. 560–567.
[13] Johnson, B. V., Wagner, J. H., Steuber, G. D., and Yeh, F. C., 1994, ''Heat Transfer in Rotating Serpentine Passages with Selected Model Orientations for Smooth or Skewed Trip Walls,'' ASME J. Turbomach., **116**, pp. 738–744.
[14] Zhang, Y. M., Han, J. C., Parsons, J. A., and Lee, C. P., 1995, ''Surface Heating Effect on Local Heat Transfer in a Rotating Two-Pass Square Channel with 60 deg Angled Rib Turbulators,'' ASME J. Turbomach., **117**, No. 2, pp. 272–280.
[15] Tse, D. G. N., 1995, ''Flow in Rotating Serpentine Coolant Passages with Skewed Trip Strips,'' Report R95-9089F, Scientific Research Associates, Inc., Glastonbury, CN.
[16] Kuo, C. R., and Hwang, G. J., 1996, ''Experimental Studies and Correlations of Radially Outward and Inward Air-Flow Heat Transfer in a Rotating Square Duct,'' ASME J. Heat Transfer, **118**, No. 1, pp. 23–30.
[17] Besserman, D. L., and Tanrikut, S., 1991, ''Comparison of Heat Transfer Measurements With Computations for Turbulent Flow Around a 180 Degree Bend,'' ASME Paper 91-GT-2.
[18] Wang, T.-S., and Chyu, M. K., 1994, ''Heat Convection in a 180-Deg Turning Duct with Different Turn Configurations,'' AIAA J. of Thermophysics and Heat Transfer, **8**, No. 3, pp. 595–601.
[19] Rigby, D. L., Ameri, A. A., and Steinthorsson, E., 1996, ''Internal Passage Heat Transfer Prediction Using Multiblock Grids and a k-ω Turbulence Model,'' ASME Paper 96-GT-188.
[20] Iacovides, H., and Launder, B. E., 1991, ''Parametric and Numerical Study of Fully Developed Flow and Heat Transfer in Rotating Rectangular Ducts,'' ASME J. Turbomach., **113**, No. 3, pp. 331–338.
[21] Iacovides, H., Launder, B. E., and Li, H.-Y., 1996, ''The Computation of Flow Development through Stationary and Rotating U-Ducts of Strong Curvature,'' Int. J. Heat Fluid Flow, **17**, pp. 22–33.
[22] Medwell, J. O., Morris, W. D., Xia, J. Y., and Taylor, C., 1991, ''An Investigation of Convective Heat Transfer in a Rotating Coolant Channel,'' ASME J. Turbomach., **113**, No. 3, pp. 354–359.
[23] Tekriwal, P., 1991, ''Heat Transfer Predictions with Extended k-ε Turbulence Model in Radial Cooling Ducts Rotating in Orthogonal Mode,'' ASME J. Heat Transfer, **116**, No. 2, pp. 369–380.
[24] Dutta, S., Andrews, M. J., and Han, J. C., 1994, ''Simulation of Turbulent Heat Transfer in a Rotating Duct,'' AIAA J. of Thermophysics and Heat Transfer, **9**, No. 2, pp. 381–382.
[25] Tolpadi, A. K., 1994, ''Calculation of Heat Transfer in a Radially Rotating Coolant Passage,'' AIAA Paper 94-0261.
[26] Stephens, M. A., Chyu, M. K., Shih, T. I-P., and Civinskas, K. C., 1996, ''Calculations and Measurements of Heat Transfer in a Square Duct with Inclined Ribs,'' AIAA Paper 96-3163.
[27] Hwang, J.-J., Wang, W.-J., and Lai, D.-Y., 1997, ''Numerical Simulation of Turbulent Heat Transfer and Flow in a Rotating Multiple-Pass Square Channel,'' ASME 97-GT-367.
[28] Stephens, M. A., and Shih, T. I-P., 1999, ''Flow and Heat Transfer in a Smooth U-Duct with and without Rotation,'' AIAA Journal of Propulsion and Power, **15**, No. 2, pp. 272–279.
[29] Chen, H.-C., Jang, Y.-J., and Han, J.-C., 1999, ''Computation of Flow and Heat Transfer in Rotating Two-Pass Square Channels by a Reynolds Stress Model,'' ASME Paper 99-GT-174.
[30] Prakash, C., and Zerkle, R., 1992, ''Prediction of Turbulent Flow and Heat Transfer in a Radially Rotating Square Duct,'' ASME J. Turbomach., **114**, No. 4, pp. 835–846.
[31] Prakash, C., and Zerkle, R., 1995, ''Prediction of Turbulent Flow and Heat Transfer in a Ribbed Rectangular Duct with and without Rotation,'' ASME J. Turbomach., **117**, pp. 255–264.
[32] Abuaf, N., and Kercher, D. M., 1994, ''Heat Transfer and Turbulence in a Turbulated Blade Cooling Circuit,'' ASME J. Turbomach., **116**, pp. 169–177.
[33] Stephens, M. A., Shih, T. I-P., and Civinskas, K. C., 1995, ''Computation of

Flow and Heat Transfer in a Rectangular Channel with Ribs,'' AIAA Paper 95-0180.
[34] Rigby, D. L., Steinthorsson, E., and Ameri, A. A., 1997, ''Numerical Prediction of Heat Transfer in a Channel with Ribs and Bleed,'' ASME Paper 97-GT-431.
[35] Rigby, D. L., 1998, ''Prediction of Heat and Mass Transfer in a Rotating Ribbed Coolant Passage with a 180 Degree Turn,'' ASME Paper 98-GT-329.
[36] Bohn, D. E., Becker, V. J., Kusterer, K. A., Otsuki, Y., Sugimoto, T., and Tanaka, R., 1999, ''3-D Internal Flow and Conjugate Calculations of a Convective Cooled Turbine Blade With Serpentine-Shaped and Ribbed Channels,'' ASME Paper 99-GT-220.
[37] Stephens, M. A., Shih, T. I-P., and Civinskas, K. C., 1995, ''Effects of Inclined Rounded Ribs on Flow and Heat Transfer in a Square Duct,'' AIAA Paper 95-2115.
[38] Stephens, M. A., Shih, T. I-P., and Civinskas, K. C., 1996, ''Computations of Flow and Heat Transfer in a Rotating U-Shaped Square Duct with Smooth Walls,'' AIAA Paper 96-3161.
[39] Bonhoff, B., Tomm, U., and Johnson, B. V., 1996, ''Heat Transfer Predictions for U-Shaped Coolant Channels with Skewed Ribs and With Smooth Walls,'' ASME Paper 96-TA-7.
[40] Stephens, M. A., and Shih, T. I-P., 1997, ''Computations of Compressible Flow and Heat Transfer in a Rotating Duct with Inclined Ribs and a 180-Degree Bend,'' ASME Paper 97-GT-192.
[41] Bonhoff, B., Tomm, U., Johnson, B. V., and Jennions, I., 1997, ''Heat Transfer Predictions for Rotating U-Shaped Coolant Channels with Skewed Ribs and With Smooth Walls,'' ASME 97-GT-162.
[42] Shih, T. I-P., Lin, Y.-L., and Stephens, M. A., 1998, ''Flow and Heat Transfer in an Ribbed U-Duct under Typical Engine Conditions,'' ASME Paper 98-GT-213.
[43] Shih, T. I-P., Lin, Y.-L., and Stephens, M. A., 2000, ''Flow and Heat Transfer in an Internal Coolant Passage,'' Int. J. Rotating Mach., in press.
[44] Wagner, J. H., and Steuber, G. D., 1994, private communication.
[45] Steinthorsson, E., Shih, T. I-P., and Roelke, R. J., 1991, ''Computations of the Three-Dimensional Flow and Heat Transfer within a Coolant Passage of a Radial Turbine Blade,'' AIAA Paper 91-2238.
[46] Menter, F. R., 1993, ''Zonal Two-Equation k-ω Turbulence Models for Aerodynamic Flows,'' AIAA Paper 93-2906.
[47] Menter, F. R., and Rumsey, C. L., 1994, ''Assessment of Two-Equation Turbulence Models for Transonic Flows,'' AIAA Paper 94-2343.
[48] Wilcox, D. C., 1993, *Turbulence Modeling for CFD*, DCW Industries, La Canada, CA.
[49] Thomas, J. L., Krist, S. T., and Anderson, W. K., 1990, ''Navier-Stokes Computations of Vortical Flows over Low-Aspect-Ratio Wings,'' AIAA J., **28**, No. 2, pp. 205–212.
[50] Rumsey, C. L., and Vatsa, V. N., 1993, ''A Comparison of the Predictive Capabilities of Several Turbulence Models Using Upwind and Central-Difference Computer Codes,'' AIAA Paper 93-0192.
[51] Roe, P. L., 1981, ''Approximate Riemann Solvers, Parameter Vector and Difference Schemes,'' J. Comput. Phys., **43**, pp. 357–72.
[52] Pulliam, W. R., and Chaussee, D. S., 1981, ''A Diagonal Form of an Implicit Approximate Factorization Algorithm,'' J. Comput. Phys., **39**, pp. 347–363.
[53] Anderson, W. K., Thomas, J. L., and Whitfield, D. L., 1988, ''Multigrid Acceleration of the Flux-Split Euler Equations,'' AIAA J., **26**, No. 6, pp. 649–654.
[54] Lin, Y.-L., Shih, T. I-P., Civinskas, K. C., Rigby, D. L., and Ameri, A. A., 1998, ''Nonlinear Versus Linear k-ω Model for Predicting Flow and Heat Transfer in a Smooth U-Duct,'' AIAA Paper 98-3560.

Geometric Optimization of Periodic Flow and Heat Transfer in a Volume Cooled by Parallel Tubes

Luiz A. O. Rocha
Research Assistant
e-mail: lar2@duke.edu

Adrian Bejan
J. A. Jones Professor
of Mechanical Engineering,
Fellow ASME
e-mail: abejan@duke.edu

Duke University,
Department of Mechanical Engineering
and Materials Science,
Box 90300,
Durham, NC 27708-0300

This paper addresses the fundamental problem of maximizing the thermal contact between an entire heat-generating volume and a pulsating stream of coolant that bathes the volume. The coolant flows through an array of round and equidistant tubes. Two laminar flow configurations are considered: stop-and-go flow, where the reservoir of coolant is on one side of the volume, and back-and-forth flow, where the volume is sandwiched between two reservoirs of coolant. The total heat transfer rate between the volume and the coolant is determined numerically for many geometric configurations in the pressure drop number range $10^2 \leqslant B \leqslant 10^6$, *and* $Pr \geqslant 1$. *The optimal tube radius and the maximum volumetric heat transfer rate are determined numerically. The numerical optimization results are later predicted based on scale analysis by matching the longitudinal and transversal time scales of the temperature field in each tube, for each pulsation stroke. The predicted scales lead to power-law formulas that correlate the results and summarize the optimal geometry. The optimal tube size is nearly the same in stop-and-go flow and back-and-forth flow, and is independent of the pulsation frequency.* [DOI: 10.1115/1.1337654]

Keywords: Bioengineering, Constructal, Optimization, Periodic, Pulsating

Introduction

The most recent constructal work dedicated to compact heat exchangers and the cooling of electronic packages has focused attention on *geometry*—how shapes and structures can be designed so that a global performance objective is met subject to global constraints [1]. Such work has always been a part of heat transfer, as in the classical example of the fin with parabolic profile [2–4], where the optimal geometry was the question. The interest in this fundamental aspect of heat transfer has grown out of necessity, because of the need to increase heat transfer rates per unit volume in a wide variety of modern applications. The optimization of geometric structure is now a self-standing technique for augmenting heat transfer.

Examples that come closer to the geometric optimization that will be described in this paper are the designs where the internal spacings between heat generating components are optimized so that the given volume is used to its fullest. In volumes cooled by single-phase laminar natural convection through vertical channels between heat-generating boards there is an optimal spacing, or an optimal number of boards [5–7]. The optimal internal spacing scales as the height of the volume times the Rayleigh number (based on height) raised to the power $-1/4$. Internal structure can also be optimized when the volume is filled with heat generating components of other shapes, such as horizontal cylinders and staggered vertical plates [8,9].

In volumes cooled by forced convection there is an analogous geometric optimization opportunity. When the coolant flows through a stack of parallel-plate channels, the optimal channel spacing is proportional to the flow length times the pressure drop number (based on flow length) raised to the power $-1/4$ [4,10–15]. Similar spacings can be optimized for assemblies where the heat generating components are shaped as staggered parallel plates, bundles of cylinders in cross-flow, and arrays of square pin fins with impinging three-dimensional flow [16–18].

The optimization of geometry unites natural convection with forced convection, and highlights an interesting analogy between the two mechanisms. According to Petrescu [19], in forced-convection geometries the pressure drop number plays the same role that the Rayleigh number plays in natural-convection geometries. The electronics cooling literature is rich in additional examples of how the optimization of shape and structure leads to improved performance at the system level [20–25].

The optimized geometries reviewed above are for the *steady-state* cooling of volumes (assemblies) that generate heat. In each case, a steady stream bathes the volume almost uniformly, collects the generated heat current, and discharges it outside the volume. The optimization of the internal structure minimizes the global thermal conductance between the entire volume and the stream of coolant.

In the present paper we propose the companion fundamental problem of optimizing internal geometry when the cooling is provided by *time-dependent* (pulsating) flow. The coolant flows through an array of parallel tubes. Two flow configurations are considered. In ''stop-and-go'' flow the reservoir of cold fluid is on one side of the volume, and the fluid flows intermittently in one direction. In ''back-and-forth'' flow the heat generating volume is sandwiched between two reservoirs of cold fluid, while the flow direction switches periodically. In both configurations the objective is to minimize the overall thermal resistance between the volume and the coolant, i.e., to maximize the *usefulness* of the volume as an assembly of heat-generating components. This objective is met by optimizing the tube size, or the number of tubes installed in the given volume [1].

Model

Consider the round tube of variable internal radius r_0 and length L shown in Fig. 1. The tube connects two fluid reservoirs of temperature T_0. The tube wall temperature is uniform, T_w. The fluid is driven through the tube by the pressure difference between

Contributed by the Heat Transfer Division for publication in the JOURNAL OF HEAT TRANSFER. Manuscript received by the Heat Transfer Division February 3, 2000; revision received, September 27, 2000. Associate Editor: G. P. Peterson.

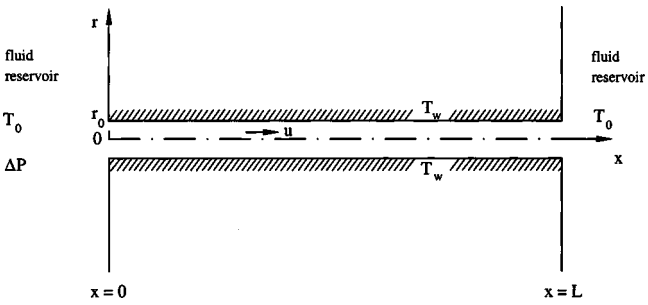

Fig. 1 Round tube (T_w) connecting two reservoirs of fluid at the same temperature (T_0)

the two reservoirs, $\Delta P = P(x=0) - P(x=L)$, which is assumed to be a known function of time (Fig. 2). Our objective is to select the tube geometry and driving force $\Delta P(t)$ such that the time-averaged heat transfer rate between the tube surface and the fluid, per unit of duct volume, is maximal. The duct volume is not fixed.

We begin with the simplifying assumption that the fluid is viscous enough so that the effect of fluid inertia is negligible. This is equivalent to assuming that, in an order of magnitude sense, the fluid has a Prandtl number greater than 1. The extensive body of work on convection in developing flows through ducts shows that this assumption is adequate in the entire half-domain $\mathrm{Pr} \gtrsim 1$ [15,26], more precisely $\mathrm{Pr} \gtrsim 0.5$, according to the classical formulas of convection ([4]). Its merit is that it makes the radial component of velocity negligible, and reduces the momentum equations to a single equation

$$\frac{\partial P}{\partial x} = \mu\left(\frac{\partial^2 u}{\partial r^2} + \frac{1}{r}\frac{\partial u}{\partial r}\right), \tag{1}$$

where $u(r,t)$ is the longitudinal velocity. Integrated from $x=0$ to $x=L$, this equation shows explicitly the role played by the imposed pressure difference,

$$-\frac{\Delta P(t)}{L} = \mu\left(\frac{\partial^2 u}{\partial r^2} + \frac{1}{r}\frac{\partial u}{\partial r}\right). \tag{2}$$

Integrating this equation in the radial direction, and invoking the boundary conditions $u=0$ at $r=r_0$ and $\partial u/\partial r = 0$ at $r=0$, we obtain the time-dependent velocity distribution

$$u(r,t) = \frac{r_0^2 \Delta P(t)}{4\mu L}\left(1 - \frac{r^2}{r_0^2}\right). \tag{3}$$

The time dependence of the fluid velocity is the same as that of the instantaneous pressure difference (Fig. 2).

The temperature field $T(x,r,t)$ inside the tube is governed by the energy equation

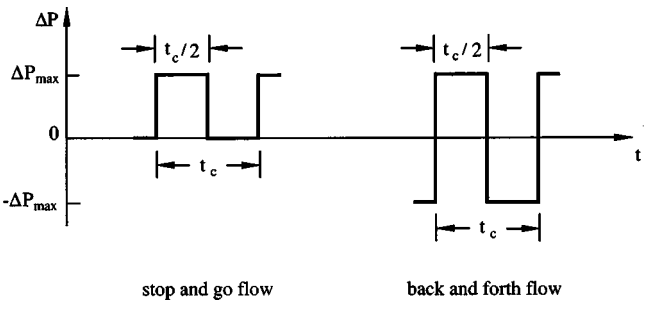

Fig. 2 Two pressure-difference cycles and flows: stop and go, and back and forth

$$\frac{\partial T}{\partial t} + u\frac{\partial T}{\partial x} = \frac{\alpha}{r}\frac{\partial}{\partial r}\left(r\frac{\partial T}{\partial r}\right), \tag{4}$$

where α is the thermal diffusivity of the fluid. There are three boundary conditions: $T = T_w$ at $r = r_0$, $\partial T/\partial r = 0$ at $r=0$, and $T = T_0$ in the cross-section that at the time t serves as entrance for the flow ($x=0$, or $x=L$). The numerical solutions and optimization work described in the next section are based on solving Eq. (4) in conjunction with the u expression (3) in many configurations $[r_0, L, \Delta P(t)]$.

The nondimensionalization of the problem is based on the observation that in this wide class of applications the imposed parameters are usually the period of the cycle executed by the periodic flow (t_c), and the pressure difference scale ($\Delta P_{\max}$). This is true not only in engineering systems with flows driven by reciprocating devices, but also in living systems such as lungs and vascularized tissues.

The time scale t_c also sets the length scale $(\alpha t_c)^{1/2}$. This length is the radial distance to which thermal diffusion travels through the fluid during the time t_c. The velocity scale follows from Eq. (3): $u \sim (\alpha t_c)^{1/2} \Delta P_{\max}/\mu$. The temperature difference scale is also known, $T_w - T_0$. In conclusion, the recommended dimensionless variables are

$$(\tilde{r}, \tilde{x}, \tilde{r}_0, \tilde{L}) = (r, x, r_0, L)/(\alpha t_c)^{1/2} \tag{5}$$

$$\tilde{t} = t/t_c \quad \tilde{u} = u\mu/[(\alpha t_c)^{1/2} \Delta P_{\max}] \tag{6}$$

$$\tilde{P} = \frac{\Delta P}{\Delta P_{\max}} \quad \tilde{T} = \frac{T - T_0}{T_w - T_0}. \tag{7}$$

Equations (3) and (4) become

$$\tilde{u} = \frac{\tilde{r}_0^2 \tilde{P}}{4\tilde{L}}\left(1 - \frac{\tilde{r}^2}{\tilde{r}_0^2}\right) \tag{8}$$

$$\frac{\partial \tilde{T}}{\partial \tilde{t}} + B\tilde{u}\frac{\partial \tilde{T}}{\partial \tilde{x}} = \frac{1}{\tilde{r}}\frac{\partial}{\partial \tilde{r}}\left(\tilde{r}\frac{\partial \tilde{T}}{\partial \tilde{r}}\right), \tag{9}$$

where B is the pressure drop number based on $\Delta P_{\max}$ and the length scale $\lambda = (\alpha t_c)^{1/2}$,

$$B = \frac{\Delta P_{\max} \lambda^2}{\mu\alpha} = \frac{\Delta P_{\max} t_c}{\mu} \tag{10}$$

The boundary conditions for Eq. (9) are

$$\tilde{T} = 1 \ \text{ at } \ \tilde{r} = \tilde{r}_0 \tag{11}$$

$$\partial \tilde{T}/\partial \tilde{r} = 0 \ \text{ at } \ \tilde{r} = 0 \tag{12}$$

$$\tilde{T} = 0 \ \text{ in the inlet plane, } \tilde{x} = 0 \ \text{ or } \ \tilde{x} = \tilde{L}. \tag{13}$$

The imposed pressure difference is periodic, as shown in Fig. 2. The longitudinal fluid velocity is proportional to the instantaneous $\Delta P(t)$, cf. Eq. (3). Two flow regimes are studied. Stop-and-go flow occurs when $\Delta P = \Delta P_{\max}$ during half of the cycle, and $\Delta P = 0$ during the other half. The fluid flows back and forth when ΔP switches between $\Delta P_{\max}$ and $-\Delta P_{\max}$ at the end of each half cycle.

Heat Transfer Rate Per Unit Volume

The quantity of interest is the average heat transfer rate per unit of duct volume used. We calculated this quantity in the following two ways: (i) by integrating the heat flux through the tube wall; and (ii) by calculating the enthalpy imparted to the fluid during one cycle.

The calculation of the time-averaged heat transfer rate proceeds in four steps. First, the local heat flux through the tube surface, into the fluid, is

$$q'' = k\left(\frac{\partial T}{\partial r}\right)_{r=r_0}. \tag{14}$$

This is integrated over the entire surface, and the result is the total instantaneous heat transfer rate

$$q_1 = \int_0^L q'' 2\pi r_0\, dx. \tag{15}$$

The heat transferred during an entire cycle is $\overline{q_1} t_c$, where $\overline{q_1}$ is the cycle-averaged heat transfer rate,

$$\overline{q_1} = \frac{1}{t_c}\int_t^{t+t_c} q_1\, dt. \tag{16}$$

In view of Eqs. (14)–(16) and the notation (5)–(7), the average heat transfer rate per unit of duct volume is given by

$$\frac{\overline{q_1}}{\pi r_0^2 L} = \frac{2k}{\alpha t_c}(T_w - T_0) Q_1, \tag{17}$$

where Q_1 is the dimensionless integral

$$Q_1 = \frac{1}{\tilde{r}_0 \tilde{L}}\int_{\tilde{t}}^{\tilde{t}+1}\left[\int_0^{\tilde{L}}\left(\frac{\partial \tilde{T}}{\partial \tilde{r}}\right)_{\tilde{r}=\tilde{r}_0} d\tilde{x}\right] d\tilde{t}. \tag{18}$$

The effectiveness of the duct space as an architectural feature designed for transferring heat to the fluid is described by the value of Q_1. The corresponding dimensionless total instantaneous heat transfer rate is, cf. Eq. (15),

$$\tilde{q}_1 = \frac{q_1}{2\pi k (T_w - T_0)(\alpha t_c)^{1/2}} = \tilde{r}_0 \int_0^{\tilde{L}}\left(\frac{\partial \tilde{T}}{\partial \tilde{r}}\right)_{\tilde{r}=\tilde{r}_0} d\tilde{x}. \tag{19}$$

The alternative is to calculate the enthalpy carried away by the fluid that leaves the tube. The instantaneous stream of enthalpy that leaves the tube is

$$q_2 = \int_0^{r_0} \rho c_p (T_{\text{out}} - T_{\text{in}}) u_{\text{out}} 2\pi r\, dr, \tag{20}$$

where u_{out} is the Hagen-Poiseuille distribution (3). The integral (20) is performed over the tube cross-section that serves as outlet, for example, $x = L$ for stop-and-go flow. For back and forth flow, the plane of the outlet is $x = 0$ during one half of the cycle, and $x = L$ during the other half. The inlet temperature is always $T_{\text{in}} = T_0$. The dimensionless version of q_2 is

$$\tilde{q}_2 = \frac{q_2}{2\pi k (T_w - T_\infty)(\alpha t_c)^{1/2}} = B\int_0^{\tilde{r}_0} \tilde{T}_{\text{out}} \tilde{u}_{\text{out}} \tilde{r}\, d\tilde{r}. \tag{21}$$

The enthalpy collected by fluid during an entire cycle is $\overline{q_2} t_c$, where

$$\overline{q_2} = \frac{1}{t_c}\int_t^{t+t_c} q_2\, dt. \tag{22}$$

Dividing this quantity by the tube volume we obtain

$$\frac{\overline{q_2}}{\pi r_0^2 L} = \frac{2k}{\alpha t_c}(T_w - T_0) Q_2, \tag{23}$$

where Q_2 is the enthalpy-based alternative to Eq. (18),

$$Q_2 = \frac{B}{\tilde{r}_0^2 \tilde{L}}\int_{\tilde{t}}^{\tilde{t}+1}\left[\int_0^{\tilde{r}_0} \tilde{T}_{\text{out}} \tilde{u}_{\text{out}} \tilde{r}\, d\tilde{r}\right] d\tilde{t}. \tag{24}$$

In the next section, the accuracy of the numerical method is documented by comparing Q_2 and Q_1. This is a global criterion, as Q_1 and Q_2 are integrals over the tube volume and pressure cycle. The instantaneous total heat transfer rate $\tilde{q}_1$ is not equal to the instantaneous enthalpy flow rate $\tilde{q}_2$, because the difference accounts for the thermal inertia effect (sensible heating) of the fluid present inside the tube.

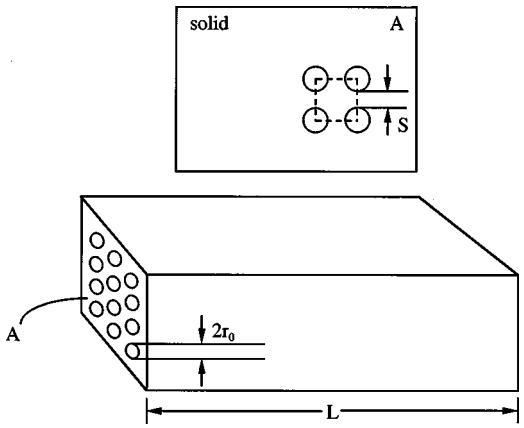

Fig. 3 Bundle of tubes in a fixed volume connecting two reservoirs of fluid at the same temperature

Another way to see the origin of the figure of merit represented by the heat transfer per unit volume used (Q_1, Q_2), is to imagine that a large number of tubes (r_0, L) are machined in parallel through a volume of length L and frontal area A (Fig. 3). The volume AL is fixed, but the number of tubes (n) and the tube size (r_0) are not. For simplicity, assume that the tube centers form squares, such that

$$n = \frac{A}{(2r_0 + S)^2}. \tag{25}$$

Assume further that the spacing between adjacent tubes (S) is a fraction (σ) of the tube diameter,

$$S = \sigma 2r_0. \tag{26}$$

We are interested in the total heat transfer rate between the fluid that flows through the n tubes and the volume AL. The contribution is $\overline{q_1}$ from one tube, and $n\overline{q_1}$ from all the tubes. The total heat transfer rate per unit volume used is $n\overline{q_1}/(AL)$, or in dimensionless form,

$$\frac{n\overline{q_1}}{AL}\frac{\alpha t_c}{k(T_w - T_0)} = \frac{\pi}{2(1+\sigma)^2} Q_1. \tag{27}$$

In summary, to maximize the Q_1 integral (18), which was based on a single tube, is equivalent to maximizing the total heat transfer rate divided by the total volume of the bundle, Eq. (27). In other words, the geometric maximization of Q_1 teaches us how to select the dimensions of the tube bundle so that the entire volume AL is reached most effectively by the fluid when the pressure cycle is specified $(t_c, \Delta P_{\max})$.

Numerical Method

The problem represented by Eq. (9), conditions (11)–(13) and the time-dependent velocity distribution (3) was solved by using a finite differences scheme. First, the time derivative $\partial \tilde{T}/\partial \tilde{t}$ was evaluated using second-order finite centered-difference form of the second spatial derivative, and first order central finite differences for the first derivatives [27]. Next, $\partial \tilde{T}/\partial \tilde{t}$ was integrated in time using the fourth-order Runge-Kutta method with adaptive step size control [28]. Finally, the Q_1 integral (18) was calculated using the trapezoidal rule, and it was monitored over enough time cycles of flow pulsations until its value did not change by more than 0.1 percent from one period to the next.

The cylindrical domain of Fig. 1 was covered by a mesh with uniform interval sizes in the $\tilde{x}$ and $\tilde{r}$ directions. The appropriate

Table 1 Test showing the achievement of grid independence for calculations in stop-and-go flow ($\tilde{L}=10$, $\Delta\tilde{t}=0.001$, $B=10^4$, and $\tilde{r}_0=0.95$)

$\Delta\tilde{r}=\Delta\tilde{x}$	number of nodes ($\tilde{r}\times\tilde{x}$)	Q_1	$\left\|\frac{Q_1^i-Q_1^{i-1}}{Q_1^i}\right\|$
0.1	10×101	1.3951	–
0.05	20×201	1.7915	0.2841
0.025	39×401	1.7809	0.0059
0.0125	77×801	1.7765	0.0025

Table 4 The heat transfer per unit volume in stop-and-go flow ($\tilde{L}=100$, $B=10^4$): comparison between the wall heat flux method [Q_1, Eq. (18)] and the enthalpy method [Q_2, Eq. (24)].

$\tilde{r}_0$	Q_1	Q_2
2	0.117	0.120
2.5	0.152	0.157
3	0.162	0.166
3.5	0.160	0.164
4	0.154	0.158

mesh size for each value of $\tilde{L}$ was determined by successive refinements, until the further grid doubling of the number of grid points in both directions met the criterion $|(Q_1^i-Q_1^{i-1})/Q_1^i|<0.01$. Here Q_1^i represents the heat transfer per unit volume calculated using the current mesh size, and Q_1^{i-1} corresponds to the preceding mesh size. Tables 1 and 2 show how grid independence was achieved in one case of stop-and-go and back-and-forth flows.

The values of $\tilde{r}_{0,\mathrm{opt}}$ and $Q_{\max}$ were calculated by varying the value of $\tilde{r}_0$ in Eq. (18). The grid independence test was repeated for $\tilde{r}_{0,\mathrm{opt}}$. The numerical accuracy of this method was at least of order $[\Delta\tilde{t}^2,\Delta\tilde{x}^2,\Delta\tilde{r}^2]$ for the most refined mesh. The maximum increments used were $\Delta\tilde{t}=0.001$ and $\Delta\tilde{x}=\Delta\tilde{r}=0.1$ for the stop-and-go flow case reported in Table 3.

As an additional check on numerical accuracy, we compared the global heat transfer measures Q_1 and Q_2, cf. Eqs. (18) and (24). Table 4 shows representative values of these integrals for several values of $\tilde{r}_0$. The agreement between Q_1 and Q_2 is consistently within 2.5 percent.

Optimal Tube Size

The flow and temperature field was simulated numerically for many tube geometries $(\tilde{r}_0,\tilde{L})$, in the pressure pulse range $10^2\leqslant B\leqslant 10^6$ for both pulsating regimes, stop and go, and back and forth. The solid-material spacing was set at $\sigma=0.1$, because it does not affect the results of the geometric optimization. In each case we fixed B, $\tilde{L}$ and the pulsating regime, and monitored the variation of the volumetric heat transfer integral Q_1 with respect to the tube size $\tilde{r}_0$. As shown in Fig. 4, we found that Q_1 reaches a distinct maximum ($Q_{\max}$) at an optimal tube size ($\tilde{r}_{0,\mathrm{opt}}$). The optimal tube size is nearly the same for stop-and-go flow and back-and-forth flow.

The procedure documented in Fig. 4 was repeated for a large number of geometries: the resulting values of $\tilde{r}_{0,\mathrm{opt}}$ and $Q_{\max}$ are summarized in Figs. 5–8. The optimal tube size increases with $\tilde{L}$, and decreases with B. These trends are the same in stop-and-go flow and back-and-forth flow (Figs. 5 and 7). The maximized heat transfer has the opposite behavior, as it decreases with $\tilde{L}$ and increases with B. Again, the type of pulsating flow regime does not appear to affect the slopes of the curve that would pass through the data (compare Figs. 6 and 8).

The apparent alignment of the data plotted in Figs. 5–8 suggests the existence of scaling laws that would allow us to correlate the data, and anticipate optimal results that are not covered by this numerical study. We were able to derive these laws from the principle of global objective—the function of the tubes with pulsating flow. That function is to maximize the thermal contact between the entire volume of Fig. 3 and the T_0 fluid from the neighboring reservoirs. It is to maximize the use of volume.

For example, consider the transfer of heat during back-and-forth flow. During the first half of the cycle, the fluid coats the tube wall with boundary layers of temperature comparable to T_w. During the return stroke, another fresh charge of T_0 fluid sweeps

Table 2 Grid refinement test for back-and-forth flow ($\tilde{L}=10$, $\Delta\tilde{t}=0.001$, $B=10^4$, and $\tilde{r}_0=0.75$)

$\Delta\tilde{r}=\Delta\tilde{x}$	number of nodes ($\tilde{r}\times\tilde{x}$)	Q_1	$\left\|\frac{Q_1^i-Q_1^{i-1}}{Q_1^i}\right\|$
0.1	8×101	2.4883	–
0.05	16×201	2.4533	0.0141
0.025	31×401	2.4364	0.0069
0.0125	61×801	2.4296	0.0028

Table 3 Grid refinement test for stop-and-go flow ($\tilde{L}=80$, $\Delta\tilde{t}=0.001$, $B=10^2$, and $\tilde{r}_0=8.95$)

$\Delta\tilde{r}=\Delta\tilde{x}$	number of nodes ($\tilde{r}\times\tilde{x}$)	Q_1	$\left\|\frac{Q_1^i-Q_1^{i-1}}{Q_1^i}\right\|$
0.4	23×201	0.03708	–
0.2	45×401	0.03713	0.0013
0.1	90×801	0.03715	0.0005

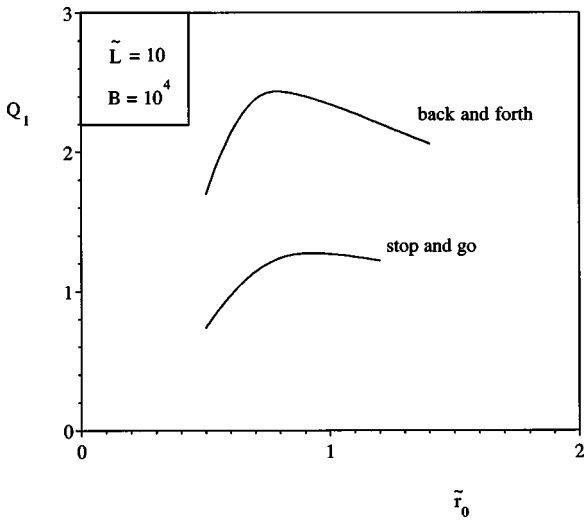

Fig. 4 The geometric maximization of the total heat transfer rate per cycle and per unit volume

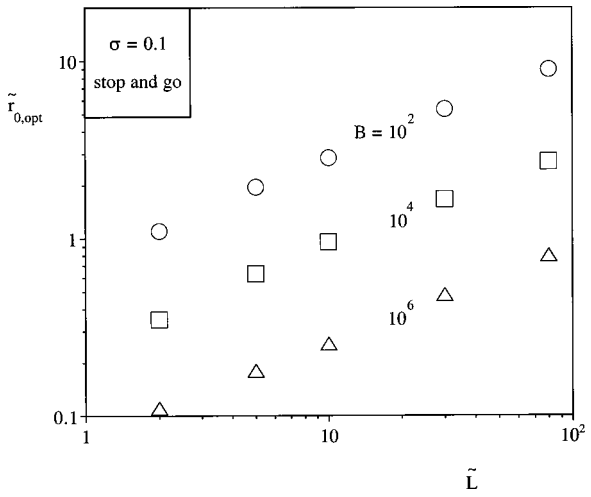

Fig. 5 The optimal tube sizes for stop-and-go flow

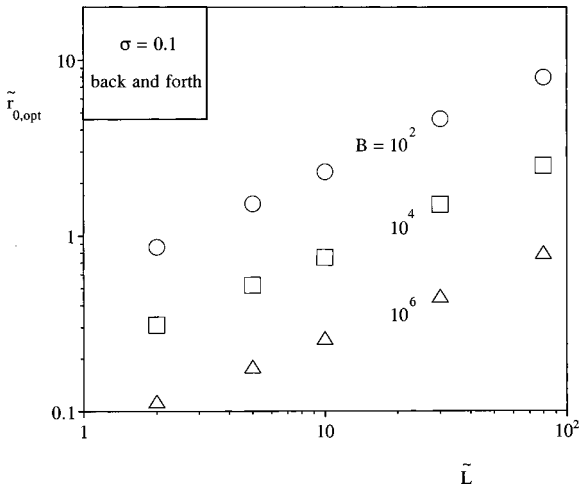

Fig. 7 The optimal tube sizes for back-and-forth flow

the tube volume, and its job is to make the closest thermal contact possible with the heated boundary layers created during the first stroke.

Each fresh fluid column that enters and fills a tube does its best when the time of residence in the tube matches the time of transversal thermal diffusion across the tube. In this special case, each tube is filled ''just right''. There is no fresh fluid (T_0) that passes from reservoir to reservoir, unaffected by the tube wall. There is also no inert (dead) trailing section of the tube choked with isothermal fluid already at the wall temperature T_w.

The residence time is $t \sim L/u$, where the u scale follows from Eq. (3), namely $u \sim r_0^2 \Delta P_{\max}/(\mu L)$. The resulting scale of the residence time, or the time of sweeping the entire length of the tube is

$$t \sim \frac{\mu L^2}{r_0^2 \Delta P_{\max}}. \tag{28}$$

The time of thermal diffusion across the tube is

$$t \sim \frac{r_0^2}{\alpha}. \tag{29}$$

Setting these two time scales equal, i.e., eliminating t between Eqs. (28) and (29), we obtain the special tube size for best use of tube volume,

$$r_{0,\mathrm{opt}} \sim L^{1/2} \left(\frac{\Delta P_{\max}}{\alpha \mu} \right)^{-1/4}. \tag{30}$$

The dimensionless counterpart of this $r_{0,\mathrm{opt}}$ scale,

$$\tilde{r}_{0,\mathrm{opt}} \sim \tilde{L}^{1/2} B^{-1/4} \tag{31}$$

is somewhat deceiving, because the nondimensionalization (Eqs. (5)–(6)) was based on the time scale of the pressure pulse, t_c. The optimal tube size (30) is independent of the time scale of the pressure pulse.

To summarize, the balance between the longitudinal and transversal time scales (28), (29) pinpointed the optimal tube size. This result is new. The existence of this optimal geometry has not been recognized yet in studies where the flow channel geometry is assumed given, and pulsation frequency is optimized in order to maximize the heat transfer between the two fluid reservoirs [29–32].

This theoretical development allowed us to correlate all the $\tilde{r}_{0,opt}$ data of Figs. 5 and 7 by using the power law suggested by Eq. (31),

$$\tilde{r}_{0,\mathrm{opt}} = C_r \tilde{L}^{1/2} B^{-1/4}. \tag{32}$$

The success of this correlation is evident in Fig. 9. The coefficient $C_r = 3.08$ approximates with a standard deviation of 14 percent all

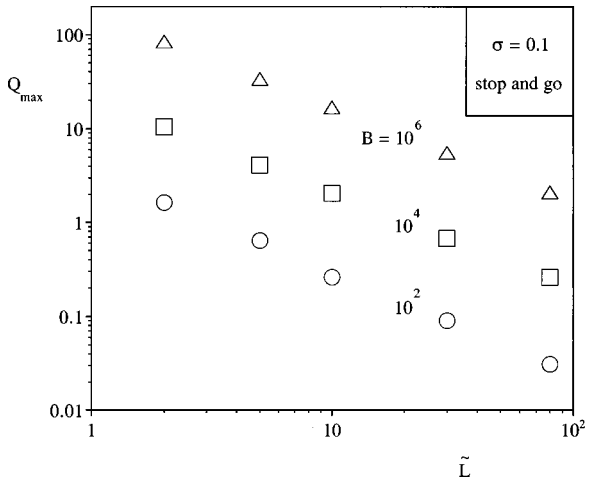

Fig. 6 The maximum heat transfer per flow cycle and unit volume for stop-and-go flow

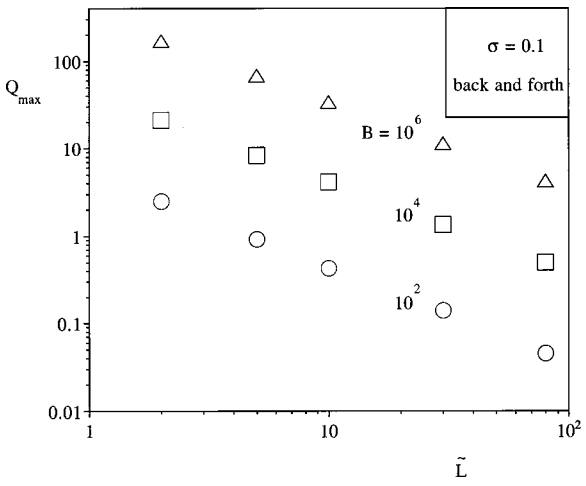

Fig. 8 The maximum heat transfer per flow cycle and unit volume for back-and-forth flow

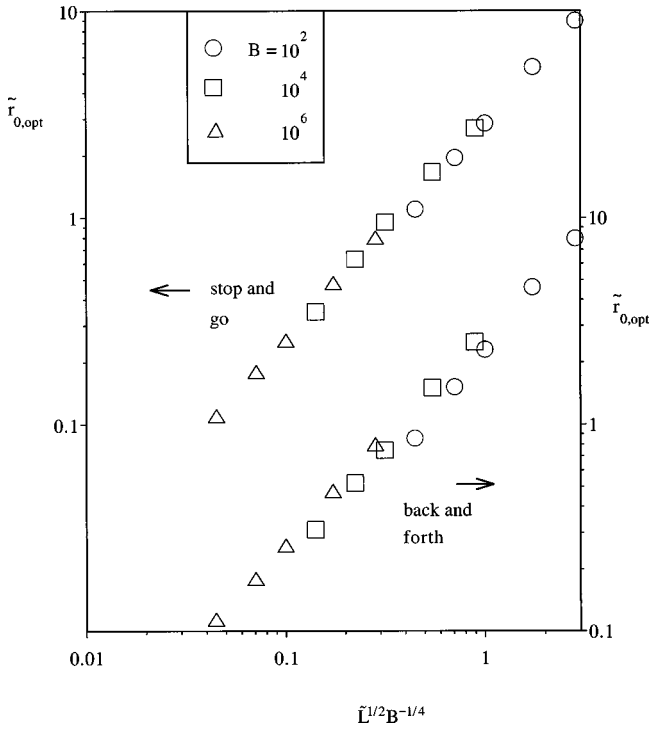

Fig. 9 Correlation of the numerical data for the optimal tube size, cf. Figs. 5 and 7

the data for stop-and-go flow. The corresponding coefficient for back-and-forth flow is $C_r=2.70$, which approximates within 21 percent the data of Fig. 7.

The same method leads us to the correlation for the $Q_{\max}$ values of Figs. 6 and 8. The order of magnitude replacements for Eqs. (14)–(16) are, respectively, $q'' \sim k\Delta T/r_0$, $q_1 \sim k\Delta TL$, and $\overline{q_1} \sim k\Delta TL$. The $\overline{q_1}$ scale allows us to write Eq. (17) approximately as

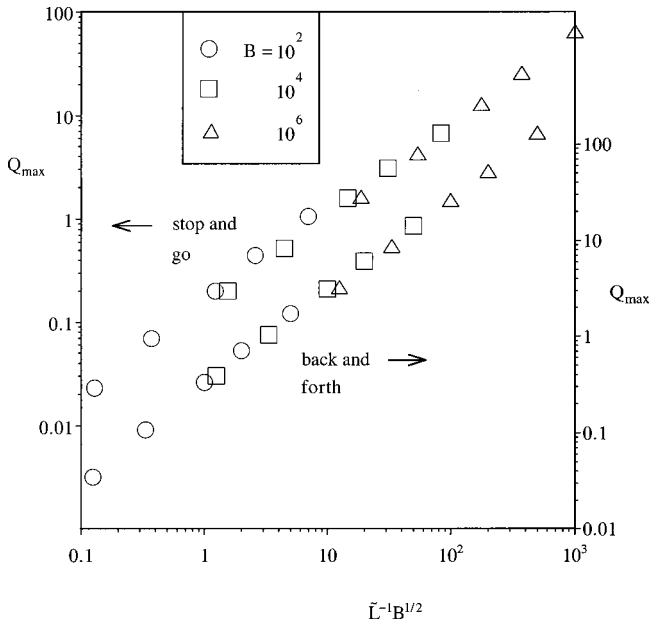

Fig. 10 Correlation of the numerical data for the maximum heat transfer per flow cycle and unit volume, cf. Figs. 6 and 8

$$\frac{k\Delta TL}{r_o^2 L} \sim \frac{k\Delta T}{\alpha t_c} Q_1 . \tag{33}$$

The heat transfer maximum ($Q_1 \sim Q_{\max}$) occurs at $r_0 \sim r_{0,\mathrm{opt}}$, which according to Eq. (33) means

$$Q_{\max} \sim \tilde{r}_{0,\mathrm{opt}}^{-2}. \tag{34}$$

In view of $\tilde{r}_{0,\mathrm{opt}}$ scale (31), we can expect $Q_{\max}$ to vary as

$$Q_{\max} \sim \tilde{L}^{-1} B^{1/2}. \tag{35}$$

The recommended correlation,

$$Q_{\max} = C_Q \tilde{L}^{-1} B^{1/2} \tag{36}$$

is supported strongly by the data plotted in Fig. 10. These data have been developed case by case in Figs. 6 and 8. The leading factor is $C_Q = 0.13 \pm 0.21$ for stop-and-go flow, and $C_Q = 0.26 \pm 0.41$ for back-and-forth flow.

Conclusions

In this paper we showed that the cooling of a heat-generating volume can be maximized via geometric optimization when the coolant flows in pulses through the volume. There is an optimal way to place the passages through the volume. In this study we assumed that the flow passages are parallel round tubes. The optimal arrangement consists of using tubes of a certain radius, which corresponds to a certain spacing between adjacent tube centers [cf., σ = constant in Eq. (26)]. Alternatively, the optimization of tube size is equivalent to optimizing the number of tubes installed in the given volume, cf. Eq. (25).

The optimal tube sizes were correlated successfully by matching the longitudinal and transversal time scales of the time-dependent temperature field inside each tube, Eqs. (28), (29). The equality of these two time scales means that the tube fills itself with ''useful fluid'' during each stroke, or that the tube volume is used to its fullest. The predicted tube size, Eq. (30), and the maximum heat transfer rate per unit volume, Eq. (34), are supported by the large number of results developed numerically. An important feature is that the optimal tube radius does not depend on the time scale of the flow pulsation. The optimal radius increases as $L^{1/2}$ and decreases as $\Delta P_{\max}^{-1/4}$.

The rate of heat removal per unit volume is greater in back-and-forth flow than in stop-and-go flow (Figs. 4 and 10). The optimized tube size, however, is practically the same for both flow regimes. This means that the optimized geometry is robust relative to changes in external parameters such as the flow direction and frequency of pulsations. Robustness was also a feature in all the internal structures optimized for steady-flow cooling, which were reviewed in the Introduction.

The experience with the optimization of geometry for steady-state heat transfer showed that the constructal optimization principle—optimal internal structure for best global performance—works in all the applications in which it has been used [1]. Optimal spacings have been developed for simple geometries (e.g., parallel-plates channels) and complicated geometries. Similarly, the principle that in this paper was demonstrated for a relatively simple design (round, equidistant tubes) can be expected to apply in more complex designs with pulsating cooling flows. These extensions deserve to be considered in follow-up studies, in the wide arena of engineered and natural flow systems [1].

Acknowledgments

Luiz A. O. Rocha's work was supported by CAPES-Brasília, Brazil. Adrian Bejan's research was supported by a grant from the National Science Foundation.

Nomenclature

A = frontal area, m^2
B = pressure drop number, Eq. (10)
$C_{Q,r}$ = coefficients, Eqs. (32), (36)
k = thermal conductivity, W/m K
L = tube length, m
n = number of tubes
P = pressure, Pa
$q_{1,2}$ = total instantaneous heat transfer rate, W, Eqs. (15), (20)
$\tilde{q}_{1,2}$ = dimensionless total instantaneous heat transfer rate, Eqs. (19), (21)
q'' = heat flux, W/m^2K
$Q_{1,2}$ = dimensionless measure of the average heat transfer rate per unit volume, Eqs. (18), (24)
r = radial direction, m
r_0 = tube radius, m
S = spacing between tubes, m
t = time, s
t_c = period of pulsation cycle, s
T = temperature, K
T_w = wall temperature, K
T_0 = coolant inlet temperature, K
u = longitudinal velocity, m/s
x = longitudinal direction, m

Greek Symbols

α = thermal diffusivity, m^2/s
Δ = difference
λ = length scale, m, Eq. (10)
μ = viscosity, kg/sm
σ = geometric ratio, $S/(2r_0)$

Subscripts

max = maximum
opt = optimum

Superscripts

$(\tilde{\ })$ = dimensionless, Eqs. (5)–(7)
$(\bar{\ })$ = time averaged

References

[1] Bejan, A., 2000, *Shape and Structure, from Engineering to Nature*, Cambridge University Press, Cambridge, UK.
[2] Schmidt, E., 1926, ''Die Wärmeübertragung durch Rippen,'' Z. Ver. Dt. Ing., **70**, pp. 885–889, pp. 947–951.
[3] Snider, A. D., and Kraus, A. D., 1986, ''The Quest for the Optimum Longitudinal Fin Profile,'' ASME HTD-Vol. 64, pp. 43–48.
[4] Bejan, A., 1993, *Heat Transfer*, Wiley, New York.
[5] Bejan, A., 1984, *Convection Heat Transfer*, Wiley, New York, chap. 4, Problem 11, p. 157.
[6] Bar-Cohen, A., and Rohsenow, W. M., 1984, ''Thermally Optimum Spacing of Vertical, Natural Convection Cooled, Parallel Plates,'' ASME J. Heat Transfer, **106**, pp. 116–123.
[7] Anand, N. K., Kim, S. H., and Fletcher, L. S., 1992, ''The Effect of Plate Spacing on Free Convection between Heated Parallel Plates,'' ASME J. Heat Transfer, **114**, pp. 515–518.
[8] Bejan, A., Fowler, A. J., and Stanescu, G., 1995, ''The Optimal Spacing Between Horizontal Cylinders in a Fixed Volume Cooled by Natural Convection,'' Int. J. Heat Mass Transf., **38**, pp. 2047–2055.
[9] Ledezma, G. A., and Bejan, A., 1997, ''Optimal Geometric Arrangement of Staggered Vertical Plates in Natural Convection,'' ASME J. Heat Transfer, **119**, pp. 700–708.
[10] Nakayama, W., Matsushima, H., and Goel, P., 1988, ''Forced Convective Heat Transfer from Arrays of Finned Packages,'' in *Cooling Technology for Electronic Equipment*, W. Aung, ed., pp. 195–210, Hemisphere, New York.
[11] Nakayama, W., 1994, ''Information Processing and Heat Transfer Engineering: Some Generic Views on Future Research Needs,'' in *Cooling of Electronic Systems*, S. Kakac, H. Yüncü and K. Hijikata, eds., Kluwer Academic, Dordrecht, The Netherlands, pp. 911–943.
[12] Knight, R. W., Goodling, J. S., and Hall, D. J., 1991, ''Optimal Thermal Design of Forced Convection Heat Sinks—Analytical,'' ASME J. Electron. Packag., **113**, pp. 313–321.
[13] Matsushima, H., Yanagida, T., and Kondo, Y., 1992, ''Algorithm for Predicting the Thermal Resistance of Finned LSI Packages Mounted on a Circuit Board,'' Heat Transfer Jap. Res., **21**, No. 5 pp. 504–517.
[14] Bejan, A., and Sciubba, E., 1992, ''The Optimal Spacing for Parallel Plates Cooled by Forced Convection,'' Int. J. Heat Mass Transf., **35**, pp. 3259–3264.
[15] Bejan, A., 1995, *Convection Heat Transfer*, 2nd Ed., Wiley, New York.
[16] Fowler, A. J., Ledezma, G. A., and Bejan, A., 1997, ''Optimal Geometric Arrangement of Staggered Plates in Forced Convection,'' Int. J. Heat Mass Transf., **40**, pp. 1795–1805.
[17] Bejan, A., 1995, ''The Optimal Spacings for Cylinders in Crossflow Forced Convection,'' ASME J. Heat Transfer, **117**, pp. 767–770.
[18] Stanescu, G., Fowler, A. J., and Bejan, A., 1996, ''The Optimal Spacing of Cylinders in Free-Stream Cross-Flow Forced Convection,'' Int. J. Heat Mass Transf., **39**, pp 311–317.
[19] Petrescu, S., 1994, ''Comments on the Optimal Spacing of Parallel Plates Cooled by Forced Convection,'' Int. J. Heat Mass Transf., **37**, p. 1283.
[20] Aung, W., ed., 1988, *Cooling Technology for Electronic Equipment*, Hemisphere, New York.
[21] Moffat, R. J., and Ortega, A., 1988, ''Direct Air Cooling of Electronic Components,'' in *Advances in Thermal Modeling of Electronic Components and Systems Vol. I*, A. Bar-Cohen and A. D. Kraus, eds., Hemisphere, New York, pp. 129–282.
[22] Peterson, G. P., and Ortega, A., 1990, ''Thermal Control of Electronic Equipment and Devices,'' Adv. Heat Transfer, **20**, pp. 181–314.
[23] Kakac, S., Yüncü, H., and Hijikata, K., eds., 1994, *Cooling of Electronic Systems*, Kluwer, Dordrecht, The Netherlands.
[24] Kraus, A. D., and Bar-Cohen, A., 1995, *Design and Analysis of Heat Sinks*, Wiley, New York.
[25] Kim, S. J., and Lee, S. W., eds., 1996, *Air Cooling Technology for Electronic Equipment*, CRC Press, Boca Raton, FL.
[26] Shah, R. K., and London, A. L., 1978, *Laminar Flow Forced Convection in Ducts*, Supplement 1 to *Advances in Heat Transfer*, Academic Press, New York.
[27] Özisik, M. N., 1994, *Finite Difference Methods in Heat Transfer*, CRC Press, Boca Raton, FL.
[28] Press, W. H., Teukolsky, S. A., Vetterling, W. T., and Flannery, B. P., 1992, *Numerical Recipes in FORTRAN*, Cambridge University Press, Cambridge, New York.
[29] Chatwin, P. C., 1975, ''On the Longitudinal Dispersion of Passive Contaminant in Oscillatory Flows in Tubes,'' J. Fluid Mech., **71**, pp. 513–527.
[30] Watson, E. J., 1983, ''Diffusion in Oscillatory Pipe Flow,'' J. Fluid Mech., **133**, pp. 233–244.
[31] Kurzweg, U. H., and Zhao, L. D., 1984, ''Heat Transfer by High-Frequency Oscillations: a New Hydrodynamic Technique for Achieving Large Effective Thermal Conductivities,'' Phys. Fluids, **27**, pp. 2624–2627.
[32] Kurzweg, U. H., 1985, ''Enhanced Heat Conduction in Oscillating Viscous Flows Within Parallel-Plate Channels,'' J. Fluid Mech., **156**, pp. 291–300.

Directional Spectral Emittance of a Packed Bed: Correlation Between Theoretical Prediction and Experimental Data

Rogério Lopes

Luís M. Moura

Dominique Baillis
E-mail: domino@cethil.insa-lyon.fr

Jean-François Sacadura

Institut National des Sciences Appliquées de Lyon,
Center de Thermique de Lyon (CETHIL),
UPRESA CNRS Q5008,
20, avenue Albert Einstein 69621
Villeurbanne Cedex, France

Directional spectral emittance of an absorbing and scattering isothermal system of packed spheres is predicted by a radiative model based on the discrete ordinates method. Radiative properties for the bed of packed opaque spheres are obtained using geometric optics laws corrected with a scaling factor to take into account the dependent scattering. This model requires the knowledge of several parameters. Particle diameter and porosity can be easily obtained, but particle hemispherical spectral reflectivity is very difficult to obtain a priori. This particle reflectivity is determined by an identification method (Gauss method of linearization) applied to bidirectional spectral reflectance data obtained from an experimental device using a Fourier transform infrared spectrometer. Directional spectral emittance is measured using a direct radiometric technique that has been recently proposed. For a system of packed opaque spheres at high temperature, good agreement is observed between experimental results of directional spectral and computed theoretical data. [DOI: 10.1115/1.1338134]

Keywords: Heat Transfer, Packed Beds, Participating Media, Porous Media, Radiation, Spheres

Introduction

Thermal radiation is the predominant mode of energy transfer in many engineering systems. A wide variety of these systems involves semi-transparent media that are porous materials or media containing particulates that play a key-role in the radiative transfer mechanisms. Some examples of these materials are soot, fibers, foams, reticulated ceramics, and packed sphere system. An extensive review of the radiative transfer in dispersed media was carried out by Viskanta and Mengüc in 1989 [1] and by Baillis-Doermann and Sacadura in 1998 [2] with a specific attention to advances that have been made since the beginning of the 1990s.

Radiative heat transfer through a system of randomly packed spheres has received much attention due to its many industrial applications. Such media are semi-transparent. A number of theoretical and experimental studies have been reported in the literature. These studies have shown that radiative heat transfer involves complex radiative interactions between the individual spheres due to the closely packed system [3,4]. Results of previous studies have led to a better understanding of the radiative heat transfer mechanism in a packed-spheres system.

To this end, Brewster and Tien [5] applied a two flux model to calculate the hemispherical transmittances of a packed bed of spheres; radiative properties were predicted from uncorrelated-scattering theory. Yang et al. [6] used the Monte Carlo method to simulate the energy bundle traveling through the voids of a bed. They showed that the thermal radiative properties depend strongly on the packing structure and the size and emissivity of constituent spheres.

Kamiuto [7] proposed a correlated-scattering theory for a packed bed consisting of relatively large spheres. In this paper, it is found that his transfer calculations based on correlated-scattering theory provide better agreement with the Chen and Churchill [8] experimental results than his previous transfer calculations based on uncorrelated-scattering theory.

Singh and Kaviany [9] presented an approach for modeling dependent radiative heat transfer in beds of large spherical particles (geometric optics theory). They showed that the radiative properties for a bed of opaque spheres can be obtained from the independent properties by scaling the optical thickness while leaving the albedo and the phase function unchanged. The scaling factor was found to depend mainly on the porosity and was almost independent of the reflectivity. These authors also concluded from this study that the results obtained from the correlated-scattering theory of Kamiuto do not generally show good agreement with the results obtained from the Monte Carlo method.

Jones et al. [10] measured the spectral directional distribution of radiation intensity at the exposed boundary of a packed bed of opaque spheres using a direct radiometric technique. The purpose of these measurements was to provide an experimental data base of radiative intensity with which to correlate intensity field solutions of the radiative equation in packed beds. Intensity exiting the bed was numerically simulated using a discrete ordinates solution to the radiative transfer equation, with combined mode radiation-conduction solution of the coupled energy conservation equation. Radiative properties were computed using the large size parameter correlated-scattering theory from Kamiuto [7]. The measured intensity results showed good agreement with computed results in near-normal directions, though agreement in near-grazing directions was poor. With these results, they concluded that either radiative transfer near the boundaries of this medium might not be adequately represented by a continuous form of the radiative transfer equation, or that the properties derived from correlated-scattering theory were insufficient.

The objective of this paper is to present and to compare two methodologies to determine directional spectral emittance of packed beds:

- One is a coupled theoretical-experimental approach; it uses theoretical model and parameter estimation technique.

Contributed by the Heat Transfer Division for publication in the JOURNAL OF HEAT TRANSFER. Manuscript received by the Heat Transfer Division November 23, 1999; revision received, July 7, 2000. Associate Editor: M. P. Menguc.

- The other is experimental, it is based on a new device using a direct radiometric technique.

First, the packed sphere systems studied are described. Then the coupled experimental-theoretical approach is presented. Emittances are calculated by solving the radiative transfer equation by using the discrete ordinates method. Radiative properties are predicted with geometric optics theory combined with correlated scaling factor for large size parameter proposed by Singh and Kaviany [9]. This model requires knowledge of the particle morphological characteristics (particle diameter and porosity) and particle spectral hemispherical reflectivity. Particle dimension and porosity can be obtained from microscopic analysis but the particle spectral hemispherical reflectivity is very difficult to obtain directly. For that reason this parameter is identified with the Gauss linearization method. This approach uses experimental and theoretical results bidirectional spectral reflectance for a bed of randomly packed spheres. The theoretical model calculating spectral bidirectional reflectance is described. Although the solution is also based on the discrete ordinate method, the methodology differs from the emittance model; for the reflectance case, the medium is assumed cold and the boundary conditions are different from the ones considered for emitting medium. The experimental device measuring reflectance data includes a Fourier Transform Infrared Spectrometer. Results of identified hemispherical reflectivity of oxidized bronze particle are presented.

Then the paper describes the new experimental device [11] aimed at measuring the spectral directional emittance of semitransparent media (packed spheres system). The temperature gradient in the sample has been minimized. Thus, measurements of spectral directional emittance at high temperature in the infrared range have been carried out on packed spheres samples.

Finally experimental and theoretical results of directional spectral emittance are compared.

Packed Spheres System

The radiatively participating porous medium considered in this study is a monodispersion of oxide bronze spherical particles. It is assumed that the packing geometry is random. When heated, the bronze oxidizes and a black oxide forms on the particle boundary surface. In order to ensure that oxide growth does not continue during measurements, the samples are heated in a furnace at 923 K for 72 hours. Four different samples are studied. Figure 1 depicts the picture taken from a microscope for particle sample #3. For each medium, spheres are assumed to have a uniform diameter, as specified by the supplier. The dimensional characteristics of the four samples are given in Table 1. The bed thickness L, particle volume fraction f_v and particle diameter d are also outlined in the Table 1. Samples are solid, spheres are linked.

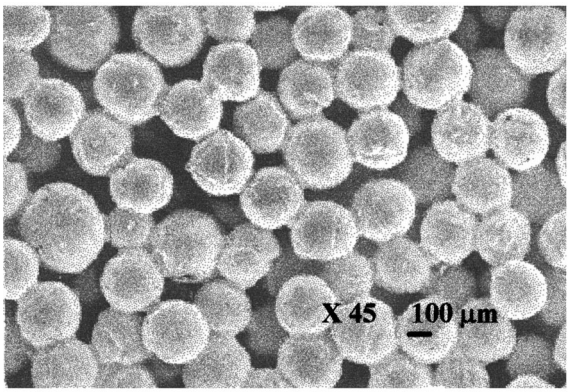

Fig. 1 Picture of packed spheres sample (#3): magnification is 45; scale bar depicts 100 μm.

Table 1 Morphological parameters

Sample reference	Sample Thickness L (mm)	f_v	Sphere diameter d (μm)
1	3.24	0.768	100
2	2.93	0.730	200
3	2.94	0.689	300
4	4.91	0.612	400

Theoretical Emittance Model

Radiative Transfer Equation. The Radiative Transfer Equation (RTE) describes the variation of the spectral radiative intensity for an absorbing-emitting-scattering medium in a given direction as a function of optical depth. For an azimuthally symetric medium, the RTE can be written as

$$\mu \frac{\partial I_\lambda(\tau,\mu)}{\partial \tau} + I_\lambda(\tau,\mu) = S_\lambda(\tau,\mu,T), \tag{1}$$

where the source term is:

$$S_\lambda(\tau,\mu,T) = (1-\omega) I_{\lambda b}(T) + \frac{\omega}{2}\left(\int_{-1}^{1} I_\lambda(\tau,\mu') p(\mu',\mu) d\mu' \right),$$

where $\mu = \cos(\theta)$, θ is the direction of the propagation in the medium as measured from the normal of the sample, $I_\lambda(\tau,\mu)$ is the spectral intensity of the radiation, $I_{\lambda b}(T)$ is the blackbody intensity, τ is the optical coordinate, T is the absolute temperature, ω is the albedo, which is the ratio of the scattering to the extinction coefficients, and $p(\mu,\mu')$ is the scattering phase function.

Boundary conditions for an isothermal semitransparent plane medium, without external incident radiation, is expressed in the following form:

$$\begin{cases} \tau = 0 \quad I_\lambda(0,\mu) = 0 \quad \mu > 0 \\ \tau = \tau_0/2 \quad I_\lambda(\tau_0/2,\mu) = I_\lambda(\tau_0/2,-\mu) \quad \mu < 0. \end{cases} \tag{2}$$

The boundary condition for $\tau = \tau_0/2$ is due to the symmetry of the problem.

The uniformity of temperature within the packed bed can be written as:

$$0 < \tau < \tau_0/2 \quad T(\tau) = T_0 \tag{3}$$

The directional spectral emittance of the medium is defined as:

$$\varepsilon_\lambda(0,\mu,T_0) = \frac{I_\lambda(0,\mu)}{I_{\lambda b}(T_0)} \quad \mu > 0. \tag{4}$$

Solution Method. Spectral directional emittance of absorbing and scattering isothermal packed-spheres system is predicted using a radiative model based on the DOM associated with the control volume method. This model differs from the reflectance model by the fact that for emittance, the emission term of the medium is accounted in the RTE. The boundary conditions are also different. A quadrature with integration limits from 0 to 1 over 120 directions is considered [12]. This quadrature satisfies key-half-moments of the radiative intensity and matches measurements in the normal-direction. A linear scheme (diamond) is employed to evaluate the radiative intensity in the control volume and a variable mesh with a grid concentration near boundaries is used to avoid oscillations or negative values of the radiative intensity.

Radiative Properties. The radiative properties required to solve the radiative transfer equation are the spectral volumetric scattering and absorption coefficients and the spectral phase function. The properties of the packed bed can be obtained from the particle radiative properties by adding up the effects of all the particles [13]. Consequently, the radiative properties of the medium can be determined using the following parameters: particle diameter (d), particle volume fraction (f_v), and particle spectral hemispherical reflectivity (ρ_λ). Assuming spherical shape for particles, absorption, extinction and scattering coefficients as well as scattering phase function can be calculated from the Mie theory. Two independent parameters, complex index of refraction ($\tilde{n}$) and the size parameter ($x=\pi d/\lambda$) are required as input. When the particle size parameter x is much greater than unity and when the refractive index is not too small ($x|\tilde{n}-1|\gg 1$), the series expansions used to evaluate the expression in the Mie theory converge very slowly. For these cases, it is preferable to use geometrical optics theory to predict the radiative properties. The details of the model for independent radiative properties prediction are given by Brewster [13]. If a packed bed consists of large diffuse spheres, then the uncorrelated radiative properties become (the subscript u means uncorrelated):

$$p(\mu)=(8/3\pi)(\sqrt{1-\mu^2}-\mu\cos^{-1}\mu) \tag{5}$$

$$\omega_u=\rho_\lambda \tag{6}$$

$$\beta_u=1.5f_v/d. \tag{7}$$

Singh and Kaviany [9] presented scaling factors so that the independent radiative properties can be scaled to give the dependent properties of the particulate media. The scaling factor, γ proposed by Singh and Kaviany [9], is evaluated by finding the ratio of the slopes calculated by the Monte Carlo method (Singh and Kaviany [9]) and by independent theory. The scaling factor scales the extinction coefficient, leaving the phase function and the albedo unchanged:

$$\beta_c=\gamma\beta_u \tag{8}$$

The values of γ for $\rho_\lambda=0.9$ and $f_v<0.7$ can be obtained from the following polynomial expression:

$$\gamma=1+1.84f_v-3.15f_v^2+7.2f_v^3. \tag{9}$$

Since the effect of particle hemispherical reflectivity on γ is small (Singh and Kaviany [9]), Eq. (8) can be used to obtain the value for other particle hemispherical reflectivities.

The parameter d and f_v can be determined from microscopic analysis. The main difficulty remains to determine ρ_λ. The particle spectral hemispherical reflectivity (ρ_λ) cannot be obtained from direct measurement. Moreover, because of the great discrepancy in the reported data [14] it is not possible to obtain its values from the literature. The problem is not necessarily due the inaccuracy of the methods used for measurements, but from the type of materials themselves. For the same chemical composition, results may be very different due to the thickness and roughness of the layer of the oxide covering the particle. So it has been preferred to determine ρ_λ by using an inverse method.

Estimation of Particle Hemispherical Reflectivity

This method uses experimental results of spectral reflectances ($R_{e\lambda}$) obtained for several measurement directions (i) for a given sample, and theoretical reflectance ($R_{t\lambda}$) obtained for the same measurement directions and for the same samples. The $R_{t\lambda}$ are calculated using different ρ_λ, f_v, and d as parameters. For each wavelength the objective is to estimate the parameter ρ_λ that minimizes the quadratic difference ($\mathbf{F}$) between the measured and calculated reflectances over the N measurement directions:

$$\mathbf{F}(\rho_\lambda)=\sum_{i=1}^{N}[R_{ti}(\rho_\lambda)-R_{ei}]^2. \tag{10}$$

The method used in this work is the Gauss linearization method ([15]) that minimizes $\mathbf{F}$ by setting to zero its derivatives with respect to each of the unknown parameters. This nonlinear parameter estimation problem is solved iteratively. For each iteration, k, the following equation is obtained:

$$\left[\sum_{i=1}^{N}\left(\frac{\partial R_{ti}}{\partial\rho_\lambda}\right)^2\right]^k(\Delta\rho_\lambda)^k=\left[\sum_{i=1}^{N}(R_{ti}-R_{ei})\frac{\partial R_{ti}}{\partial\rho_\lambda}\right]^k. \tag{11}$$

The solution of this equation gives $\Delta\rho_\lambda^k$, that is added to ρ_λ^k for each iteration k. The convergence is obtained when $\Delta\rho_\lambda^k/\rho_\lambda^k<10^{-3}$. More details of this technique are available in the literature [16].

For each wavelength λ, the number of identified parameter is one (ρ_λ), the number of measurement direction is $N=12$. The ratio of the number of measurements to the number of unknown parameter is 12. This ratio being large, the identification is appropriate.

Experimental Setup. The experimental setup used to measure infrared bidirectional reflectances is schematically shown in Fig. 2. It has been already used in the literature [17]. The objective in the experiments is to determine the fraction of the incident beam reflected by the sample in the wavelength range of 1.8 μm–11.0 μm. The spectrometer is a FTS 60 A (Bio-Rad Inc.), of Fourier transform type. The source of radiation, which approximates the blackbody emission spectrum at 1300°C, is a ceramic globar. An entrance stop with a movable hole (4.0 mm diameter) determines the solid angle of the beam. The incident beam, taken normal to the sample surface, is collimated with a small divergence angle of 2.3 degree. The Michelson interferometer principle is used [18], so that the exit beam can be measured by a detector, as a function of path difference between the fixed and movable mirrors (Fig. 2). The detection system, composed of a spherical mirror collecting the beam and concentrating it on a detector HgCdTe (1.8–15 μm range), is mounted on a goniometer arm to allow bidirectional reflection measurements in the plane of incidence. Both the spectrometer and the detection system are purged with dry air and connected to a data acquisition system.

The experimental arrangement allows the measurement of spectral reflectance. The sample holder permits measurement of energy with and without sample. When there is no sample, the energy is measured in the incident direction (reference measurement). When a sample is mounted on the sample holder, the detection system is rotated around the sample in different backward directions to measure the reflected energy. The ratio of the reflected to the incident energies provides the reflectance, $R_e(\theta,\lambda)$, which is defined as:

$$R_e(\theta,\lambda)=\frac{I(\theta,\lambda)}{I_0 d\Omega_0}, \tag{12}$$

where $I(\theta,\lambda)$ is the reflected intensity in the direction θ and I_0 the intensity of the collimated beam normally incident onto the sample within a solid angle $d\Omega_0$. When there is no sample the incident flux detected by the sensor is proportional to $I_0 d\Omega_0$.

Note that in this study the effect polarization on bidirectional reflectance is not considered.

Theoretical Model. Radiative transfer equation is solved numerically. The emission term does not need to be considered in the RTE because of the optical modulation used in the experiments. The azimuthal symmetry is assumed. Spectral radiative properties used in Eq. (1) are determined using geometric optics theory (Eqs. 5–7) combined with the scaling factor (Eq. 9) of Singh and Kaviany [9] that involves the unknown hemispherical reflectivity ρ_λ. The boundary conditions are given based on the experimental device:

1 the medium is unbounded

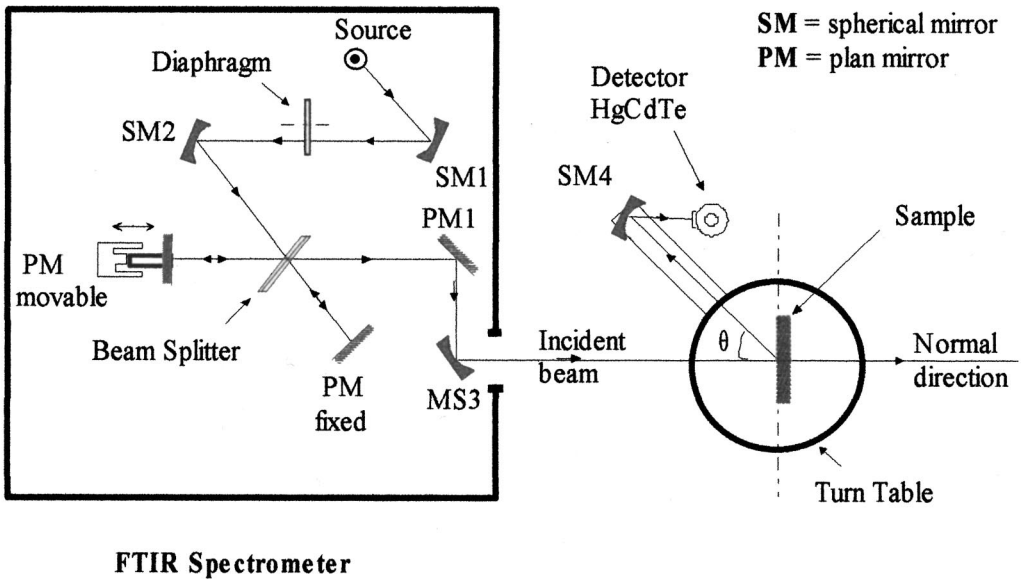

Fig. 2 Experimental device using a FTIR spectrometer to measure spectral bidirectional reflectance for plane of incidence [17]

2 a collimated beam of intensity I_0 with a divergence half-angle θ_0 is incident normally onto one sample face ($\tau=0$). These boundary conditions are expressed as:

$$\begin{cases} \tau=0 \rightarrow \begin{cases} I_\lambda(0,\mu)=I_0 & \mu_0 \leqslant \mu \leqslant 1 \\ I_\lambda(0,\mu)=0 & 0<\mu<\mu_0, \end{cases} \\ \tau=\tau_0 \rightarrow I_\lambda(\tau_0,\mu)=0 \quad \mu<0 \end{cases} \tag{13}$$

where $\mu_0=\cos\theta_0$

The DOM is applied to solve the integro-differential equation (Eq. 1) without the emission term. Details of the solution methodology have been reported by Nicolau [19]. A quadrature over 24 directions is adopted in the DOM. The spherical space is discretized into 12 directions for the positive range of μ and 12 other symmetric directions for the negative μ. This quadrature is a combination of two Gaussian quadratures [19]. This solution, combined with the radiative properties prediction model, allows the determination of theoretical reflectances from the parameters d, f_v, ρ_λ of the sample subjected to a collimated incident flux.

Application to Packed Bed. Experiments were carried out for four different packed beds of oxidized bronze spherical particles. The dimensional characteristics of the packed beds are given in Table 1.

Measurements were performed for all the 12 backward directions of the quadrature. Spectral reflectance data were obtained for 120 wavelengths in the range from 1.8 μm to 11.0 μm. These wavelengths correspond to the points shown in Fig. 3.

The particle spectral hemispherical reflectivities were determined from sample bidirectional reflectances using the parameter estimation method described above. It can be recalled that this method is based on a minimization of the quadratic error between theoretical and experimental data of spectral bidirectional reflectance (theoretical reflectance are obtained using the DOM with a quadrature over 24 directions). The estimated values of the particle hemispherical reflectivity are shown on Fig. 3 for all four samples. These results are then used to calculate radiative properties from Eqs. (5)–(9). Doermann [20] has shown that uncertainty for the estimated hemispherical reflectivity from this parameter

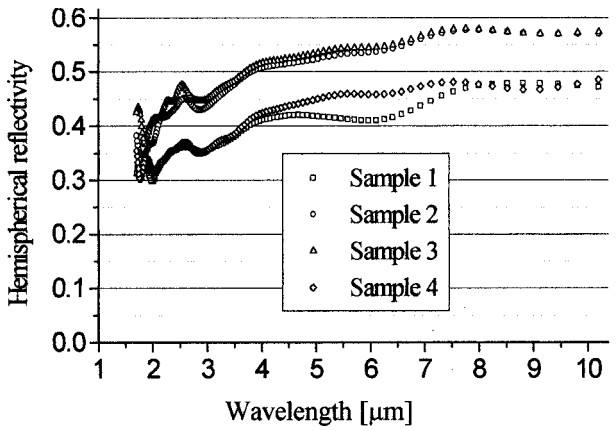

Fig. 3 Particle spectral hemispherical reflectivity: values obtained from the parameter estimation approach.

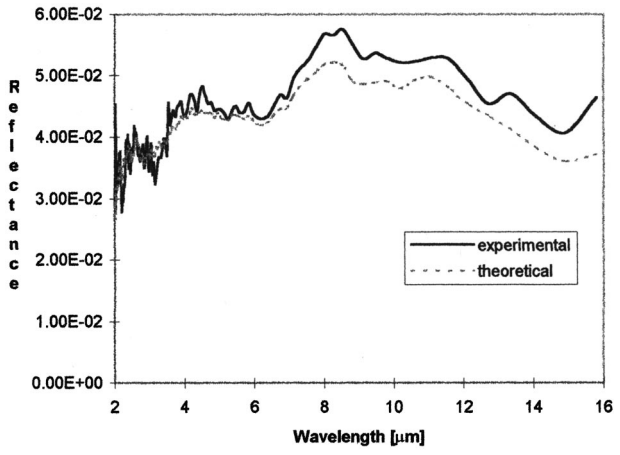

Fig. 4 Experimental and theoretical reflectance for sample 1 for an angle of 170 deg with the incident direction

estimation method are very weak. They are independent of the uncertainties in the porosity and particle diameter.

Experimental and theoretical results of reflectance are compared. There is a good agreement, deviations are less than the experimental uncertainties obtained by measuring reflectance several times for the same sample [20]. Results are shown on Fig. 4 for sample 1 for the backward direction $\theta = 170$ deg. For the other samples and other directions results are similar.

Emittance Measurement

The objective of this section is to describe the experimental assembly used in this work (Fig. 5) for measuring the directional spectral emittance. This experimental set up [11] was developed to minimize the temperature gradient in the medium (by ensuring a nearly isothermal volume) and the radiative flux incoming from any external source. The isothermal condition in the medium is achieved by simultaneously heating both sides of the sample with a high power laser (4 kW, CO_2 10.6 μm) which was split into two identical beams using a beam splitter (50 percent–50 percent $\pm$ 1 percent). The power of both laser beams is measured by a calorimeter; these measurements show that energy coming from each side may be matched to be equal to within 1 percent.

As the energy distribution of a laser beam is not uniform, two kaleidoscopes are used for homogenization of energy distribution [21]. A kaleidoscope is a copper tube with a square opening. The tube faces are buffed as mirror. Preliminary tests on thermal paper show that good homogenization is obtained by using the kaleidoscope with a square opening. Another technique to analyze the energy distribution is based on the temperature data provided by an infrared camera. This technique leads to a temperature map of this surface directly related to the energy distribution of the laser beam. In addition, this method provides information on the surface temperature fluctuations over time. Temperature cartography measurements are carried out when using the laser beam with and without the kaleidoscope and are compared to point out the efficiency of this homogenization technique. The use of a monochromatic source ($\lambda = 10.6\ \mu$m) permits separation of the radiative flux due to the source from that coming from the sample itself as spectral measurements are performed.

Temperature Measurements. Pyrometric determination of the temperature generally requires the preliminary knowledge of the material emittance at the temperature, the wavelength and in the direction of the measurement. The sample temperature is determined by pyrometer measurements in the wavelength range from 1.5 μm to 1.6 μm. It is assumed that emittance is not strongly dependent on temperature. The emittance used in this measurement is obtained from the transmittance and reflectance measurements performed at room temperature obtained with a Perkin-Elmer Lambda 900 spectrometer (Emittance=1-Transmittance-Reflectance). Uncertainty of the pyrometric measurements are studied. Indeed, after to have verify that temperature measured by the pyrometer is the same for the two faces of sample, temperature of one face of the sample is measured with a thermocouple (of type K) and is compared with temperature measured with pyrometer. A relative deviation on temperatures inferior to 3.5 percent is observed for the four samples. This weak deviation seems to confirm the assumption that emittance is not strongly dependent on temperature.

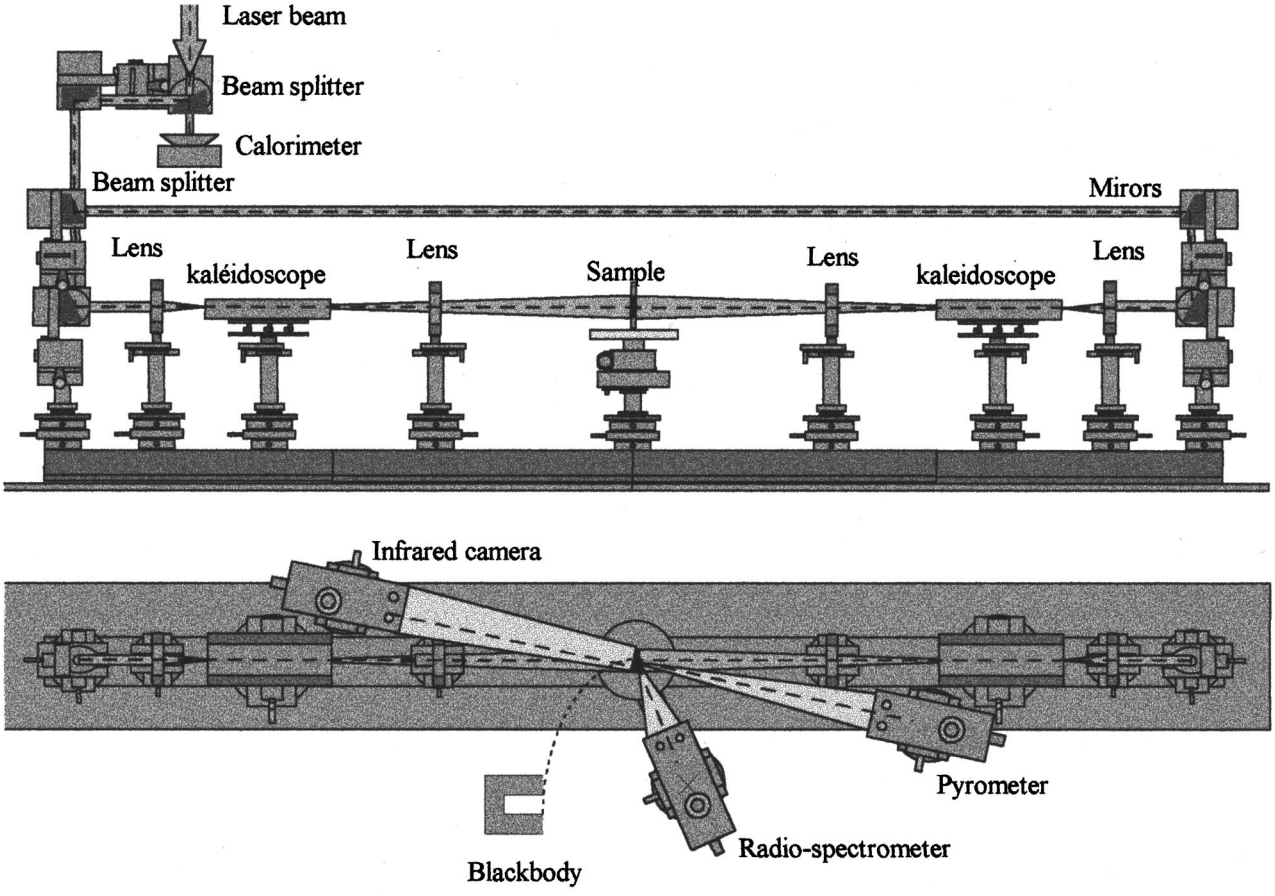

Fig. 5 Experimental device used to measure directional spectral emission. The radio-spectrometer and the pyrometer are rotated to acquire the measurement on the blackbody.

Radiometer Emittance Measurements. The procedure of measurement of directional spectral emission is based on the definition of the directional spectral emittance (Eq. 4). The radiometer collects the heat flux emitted by the sample and by a reference blackbody at the same temperature, through the same spectral range and solid angle (Fig. 5). Under these conditions, the directional spectral emittance can be defined as the ratio of spectral fluxes emitted by the sample and by the reference blackbody. Spectral measurement of the emitted radiation is carried out using an interference filter spectro-radiometer. The radiometer Heimann KT4S is mounted on a rotating arm allowing the measurement of the radiation emitted by the sample at several angles. The sample area viewed by the radiometer during the measurements is a function of the direction of measurement. The surface area of the sample heated by the laser beams is 12×12 mm. For a distance of measurement of 30 cm, the view area of the radiometer is 1.5 mm of diameter.

The radiometer, equipped with a bolometric detector, uses four different narrow band infrared filters with center wavelength (CWL) and half bandwidth (HBW) of: $1.99\pm 0.10\,\mu$m, $2.97\pm 0.12\,\mu$m, $4.00\pm 0.15\,\mu$m and $4.99\pm 0.17\,\mu$m. Center wavelength and half bandwidth tolerance is ± 30 nm.

System Calibration. The experimental device (spectro-radiometer) needs to be calibrated so that millivolt reading (V_λ) taken from the samples can be directly converted to absolute spectral directional intensity (I_λ). Using a blackbody reference, a spectral calibration factor (F_λ) is directly obtained by relating the spectral blackbody intensity evaluated at the known temperature to the millivolt radiometer reading of the blackbody radiation. This factor is used to relate millivolt readings from the sample to absolute spectral intensities. The radiometer calibration factor is defined as:

$$F_\lambda(T_b)=\frac{\delta S\,\delta\Omega}{V_{\lambda b}(T_b)}\int_{\lambda-\Delta\lambda/2}^{\lambda+\Delta\lambda/2} I_{\lambda b}(T_b)\,d\lambda \tag{14}$$

$$I_\lambda(\tau_0,\mu,T)=\frac{V_\lambda(\tau_0,\mu,T)F_\lambda(T)}{\delta\lambda\,\delta S\,\delta\Omega}, \tag{15}$$

where δS is the sample surface projected onto a plane perpendicular to the incident beam, $\delta\Omega$ is the detection solid angle, $\delta\lambda$ is the wavelength interval.

Uncertainty Analysis. The emissivity can be expressed by the following relation:

$$\varepsilon_\lambda(\tau_0,\mu,T)=\frac{V_\lambda(\tau_0,\mu,T)F_\lambda(T)}{\delta S\,\delta\Omega\displaystyle\int_{\lambda-\Delta\lambda/2}^{\lambda+\Delta\lambda/2} I_{\lambda b}(T)\,d\lambda}. \tag{16}$$

As a result, the experimental uncertainty in the spectral emissivity is:

$$U_{\varepsilon\lambda}{}^2=\left(\frac{\partial\varepsilon_\lambda}{\partial V_\lambda}U_{V\lambda}\right)^2+\left(\frac{\partial\varepsilon_\lambda}{\partial T}U_T\right)^2+\left(\frac{\partial\varepsilon_\lambda}{\partial V_{\lambda b}}U_{V\lambda b}\right)^2+\left(\frac{\partial\varepsilon_\lambda}{\partial T_b}U_{T_b}\right)^2, \tag{17}$$

where $\delta\lambda$, δS, and $\delta\Omega$ are considered to be perfectly repeatable. As shown by Jones et al. [22], considering that $T_b\approx T$ and $I_{\lambda b}(T_b)\approx I_{\lambda b}(T)$ the epxerimental uncertainties are:

$$U_{\varepsilon\lambda}{}^2=(1+\varepsilon_\lambda{}^2)\left(\frac{\delta V_S}{V_S}t_{2,90}\right)+\left(\frac{4\varepsilon_\lambda}{T}\right)^2(U_{Tb}{}^2+U_T{}^2). \tag{18}$$

Uncertainties are calculated for $20\text{ deg}\leqslant\theta\leqslant 160$ deg. For samples referenced 1, 2, 3 uncertainties are 7 percent and for sample 4 they are 11 percent.

Discussion of Theoretical and Experimental Results

Figures 6–13 show comparisons between measured and predicted spectral directional emittances for the four different samples considered. For the angular range $20\text{ deg}\leqslant\theta\leqslant 160$ deg, for samples # 2 and 3 the relative difference between measurement and prediction is less than 7 percent, and for samples # 1 and 4 the relative difference is less than 11 percent. For each sample several emittance measurements were performed; overall the results were repeatable.

If the test sample is not sufficiently thin and if the measurements are attempted at high temperatures, the samples may display an internal temperature gradient. This may be a reason of having larger errors in estimated emissivity values for samples #1 and #4 than for samples #2 and #3. Samples #1 and #4 are thicker than #2 and #3.

Within the angular interval of $5\text{ deg}\leqslant\theta\leqslant 20$ deg there is increasing disagreement, the measured emittance decreases while the predicted emittance remains relatively constant. This behavior can be explained, as suggested by Jones [10], by the

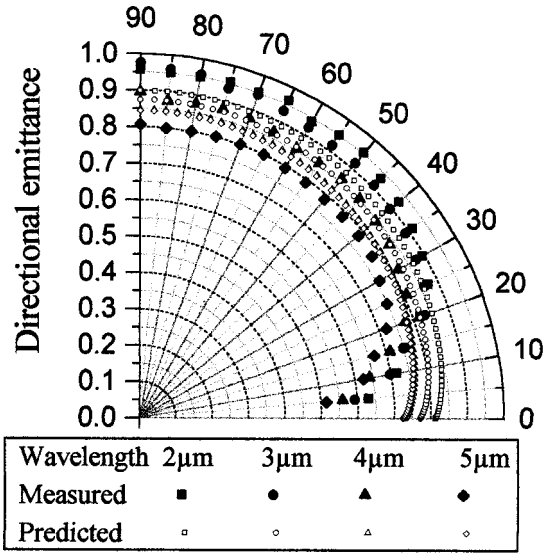

Fig. 6 Comparison of measured and predicted spectral directional emittance of sample 1 ($L=3.24$ mm, $f_v=0.768$, $d=100\,\mu$m, and $T=870$ K)

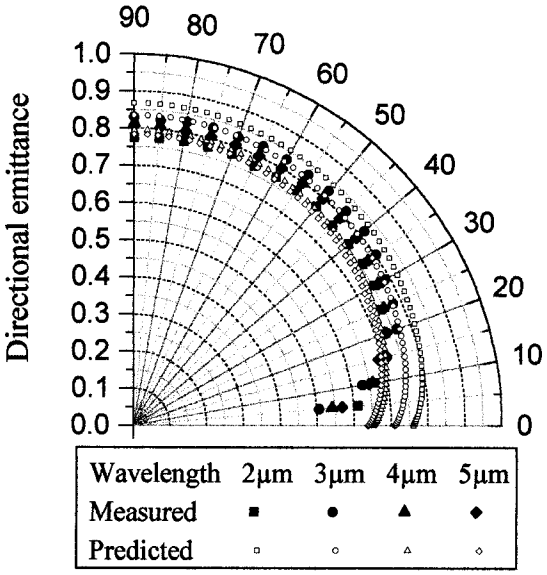

Fig. 7 Comparison of measured and predicted spectral directional emittance of sample 2 ($L=2.93$ mm, $f_v=0.730$, $d=200\,\mu$m, and $T=917$ K)

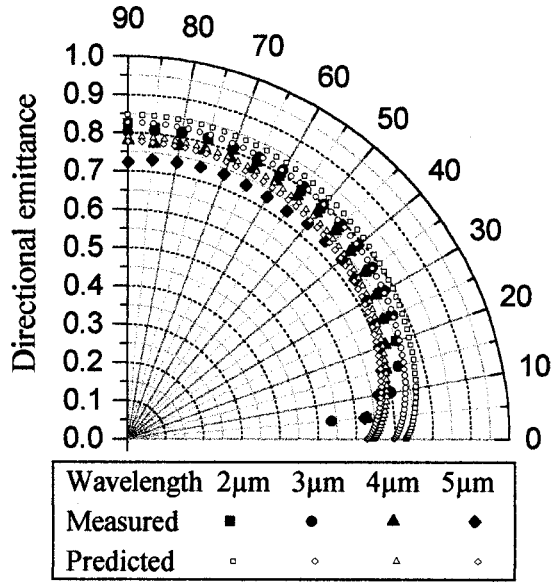

Fig. 8 Comparison of measured and predicted spectral directional emittance of sample 3 ($L=2.94$ mm, $f_v=0.689$, $d=300$ μm, and $T=890$ K)

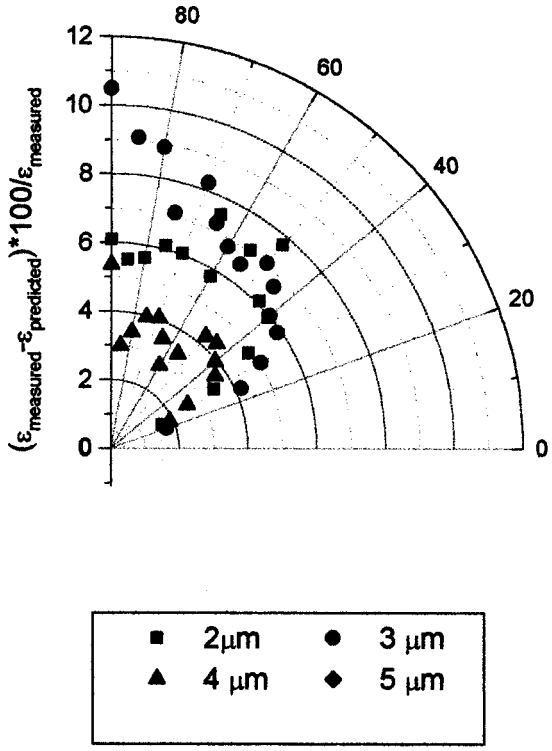

Fig. 10 Relative difference between measured and predicted spectral directional emittance of sample 1 ($L=3.24$ mm, $f_v=0.768$, $d=100$ μm, and $T=870$ K)

fact that radiative transfer near the boundaries of the packed bed might not be adequately represented by a continuous form of the radiative transfer equation.

The good agreement between the predictions and the measured data indicates that the method is reliable. It should be pointed out, however, that such comparisons of emittance are of limited value unless the specimens are prepared from the same material and through the same process. Such factors as grain size and porosity are expected to have a noticeable effect on emittance. Note that, emittance is always considered as a surface property for opaque materials; for non-opaque materials, it should be a volume property. Since the flux emitted by a non-opaque medium carries information about the medium, its internal behavior must also be taken into account in order to predict directional emittance accurately.

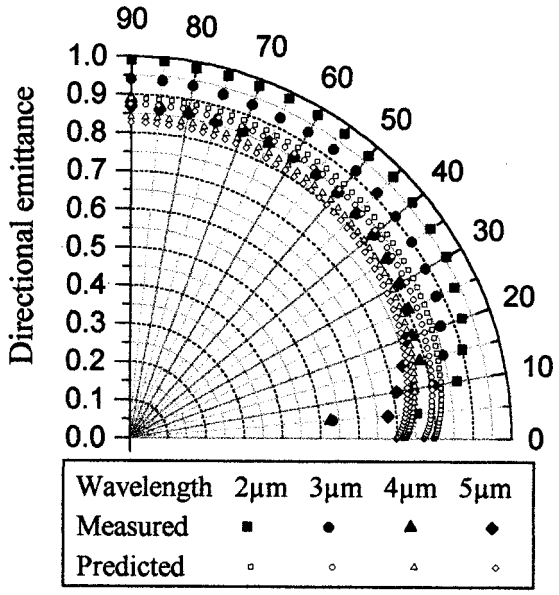

Fig. 9 Comparison of measured and predicted spectral directional emittance of sample 4 ($L=4.91$ mm, $f_v=0.612$, $d=400$ μm, and $T=888$ K)

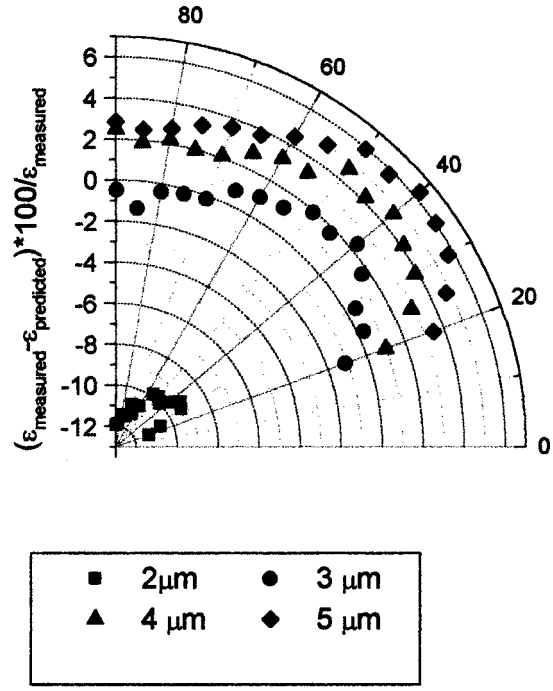

Fig. 11 Relative difference between measured and predicted spectral directional emittance of sample 2 ($L=2.93$ mm, $f_v=0.730$, $d=200$ μm, and $T=917$ K)

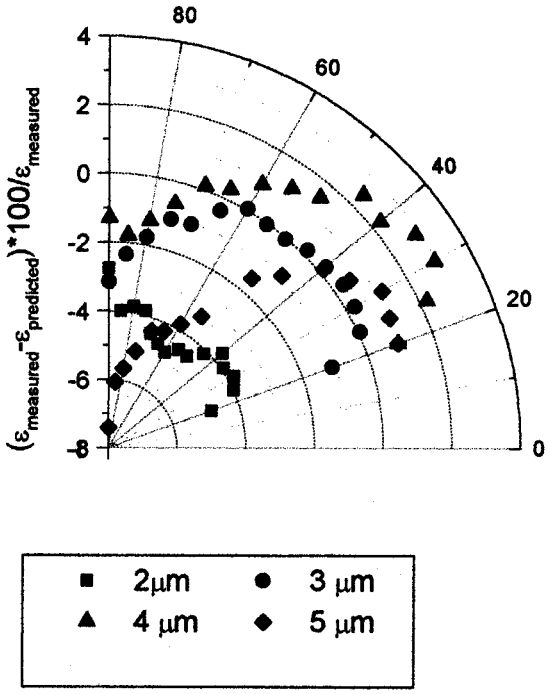

Fig. 12 Relative difference between measured and predicted spectral directional emittance of sample 3 ($L=2.94$ mm, $f_v=0.689$, $d=300$ μm, and $T=890$ K)

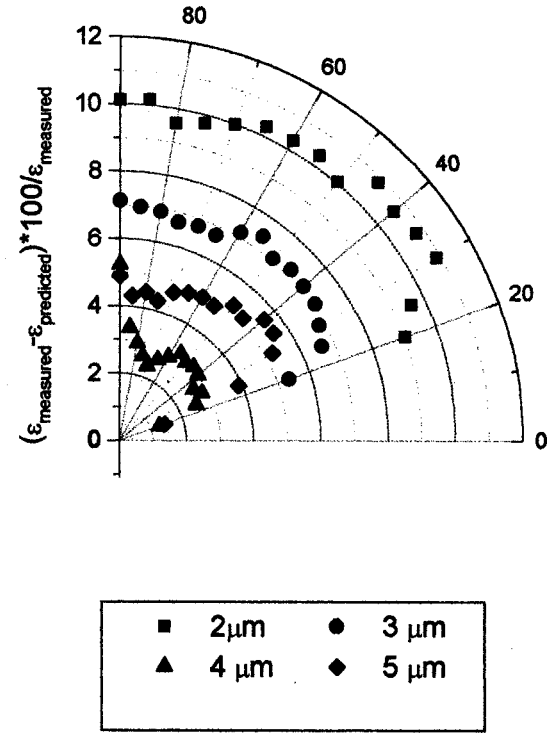

Fig. 13 Relative difference between measured and predicted spectral directional emittance of sample 4 ($L=4.91$ mm, $f_v=0.612$, $d=400$ μm, and $T=888$ K)

Conclusions

In this paper, we described:

- an experimental methodology permitting to measure the directional emittance of packed-spheres system, and
- a theoretical approach to estimate the emittance of a packed bed using fundamental physical parameters f_v, d, ρ_λ.

The spectral directional emittance of an isothermal packed bed of monodisperse, opaque, large spherical particles is measured using a radiometric system. The spectral directional emittance is predicted using a radiative model based on the discrete ordinates method associated with the control volume method to solve the radiative transfer equation. Dependent radiative properties used as inputs to the radiative transfer equation are calculated from the geometrical optics theory combined with a scaling factor. The parameters used to find the uncorrelated radiative properties related to geometrical optics are determined from microscopic analysis and a parameter estimation technique to determine the hemispherical reflectivity of the material (ρ_λ). This estimation approach uses experimental results of spectral bidirectional reflectances obtained for several measurement directions for a given set of samples, and theoretical reflectance obtained for the same measurement directions as the experimental ones and for the same samples.

The comparison of model predictions and experimental data for packed-sphere bed shows good agreement with an error of less than 11 percent; this error is on the same order of experimental uncertainty. If the hemispherical reflectivity is identified and the morphological parameters (porosity and grain size) of the packed spheres are known, the model can be used to compute the directional spectral emittance. However, the compared values diverge near grazing angles. This suggests that development of a more detailed radiation model for packed-sphere system appears warranted.

Acknowledgments

The first two authors (doctoral students) were financially supported by CNPq-Brazil grants, during this work.

Nomenclature

d = $2r$, particle diameter
$\mathbf{F}$ = quadratic difference
f_v = volume fraction
I = intensity
L = thickness of a participating medium
N = number of directions in discrete ordinates method (DOM)
p = phase function
R = reflectance
S = term source
T = absolute temperature
U = uncertainties
x = $2\pi r/\lambda$, size parameter

Greek Symbols

β = extinction coefficient
θ = direction of propagation as measured from the normal of the sample
ε = emittance
λ = wavelength
γ = scaling factor
μ = $\cos\theta$
ρ = particle hemispherical reflectivity
τ = optical coordinate
τ_0 = optical thickness of the sample
Ω = solid angle
ω = albedo

Subscripts

b = blackbody
c = correlated
e = experimental

t = theoretical
u = uncorrelated

Abbreviations

DOM = Discrete Ordinates Method
RTE = Radiative Transfer Equation

References

[1] Viskanta, R., and Mengüç, M. P., 1989, ''Radiative Transfer in Dispersed Media,'' Appl. Mech. Rev., **42**, No. 9, pp. 241–259.
[2] Baillis-Doermann, D., and Sacadura, J. F., 1998, ''Thermal Radiation Properties of Dispersed Media: Theoretical Prediction and Experimental Characterization,'' *2nd ICHMT Int. Symp. On Radiative Transfer*, Kusadasi, Turquie, Radiative Transfer II, P. Mengüç, ed., Begell House Inc, NY, pp. 1–38.
[3] Drolen, B. L., and Tien, C. L., 1987, ''Independent and Dependent Scattering in Packed-Sphere Systems,'' Journal of Thermophysics, **1**, No. 1, pp. 63–68.
[4] Tien, C. L., 1988, ''Thermal Radiation in Packed and Fluidized Beds,'' ASME J. Heat Transfer, **110**, pp. 1230–1242.
[5] Brewster, M. Q., and Tien, C. L., 1982, ''Radiative Transfer in Packed Fluidized Beds: Dependent Versus Independent Scattering,'' ASME J. Heat Transfer, **104**, pp. 573–579.
[6] Yang, Y. S., Howell, J. R., and Klein, D. E., 1983, ''Radiative Heat Transfer Through a Randomly Packed Bed of Spheres by the Monte Carlo Method,'' ASME J. Heat Transfer, **105**, pp. 325–332.
[7] Kamiuto, K., 1990, ''Correlated Radiative Transfer in Packed-Sphere Systems,'' J. Quant. Spectrosc. Radiat. Transf., **43**, No. 1, pp. 39–43.
[8] Chen, J. C., and Churchill, S. W., 1963, ''Radiant Heat Transfer in Packed Beds,'' AIChE J., **9**, pp. 35–41.
[9] Singh, B. P., and Kaviany, M., 1992, ''Modelling Radiative Heat Transfer in Packed Beds,'' Int. J. Heat Mass Transf., **35**, No. 6, pp. 1397–1405.
[10] Jones, P. D., McLeod, D. G., and Dorai-Raj, D. E., 1996, ''Correlation of Measured and Computed Radiation Intensity Exiting a Packed Bed,'' ASME J. Heat Transfer, **118**, pp. 94–102.
[11] Lopes, R., Moura, L. M., Delmas, A., and Sacadura, J.-F., 1998, ''Directional Spectral Emittance of Ceramic Material: Theoretical Prediction Compared to Experimental Data,'' *7th AIAA/ASME Joint Thermophysics and Heat Transfer Conference*, Albuquerque, New Mexico.
[12] Moura, L. M, Baillis, D., and Sacadura, J. F., 1997, ''Analysis of the Discrete Ordinate Method: Angular Discretization,'' 14th Brazilian Congress of Mechanical Engineering, December 8–12, COB1425, Bauru, Brazil (in portuguese).
[13] Brewster, M. Q., 1992, *Thermal Radiative Transfer and Properties*, Wiley, New York, pp. 301–336.
[14] Touloukian, Y. S., and DeWitt, D. P., 1972, *Thermophysical Properties of Matter; Thermal Radiative Properties: Nonmetalic Solids*, IFI/Plenum, New York.
[15] Beck, J. V., and Arnold, K. J., 1977, *Parameter Estimation in Engineering and Science*, Wiley, New York.
[16] Nicolau, V. P., Raynaud, M., and Sacadura, J. F., 1994, ''Spectral Radiative Properties Identification of Fiber Insulating Materials,'' Int. J. Heat Mass Transf., **37**, pp. 321–324.
[17] Baillis, D., Raynaud, M., and Sacadura, J. F., 1999, ''Spectral Radiative Properties of Open-Cell Foam Insulation,'' J. Thermophys. Heat Transfer, **13**, No. 3, pp. 292–298.
[18] Griffiths, P. R., 1975, *Chemical Infrared Fourier Transform Spectroscopy*, Wiley, New York, p. 337.
[19] Nicolau, V. P., 1994, ''Identification des propriétés radiatives des matériaux semi-transparents diffusants,'' Ph.D. thesis n° 94 ISAL. 0001, INSA de Lyon, France.
[20] Doermann, D., 1995, ''Modélisation des transferts thermiques dans des matériaux semi-transparents de type mousse à pores ouverts et prédiction des propriétés radiatives,'' Ph.D. thesis n° 95 ISAL. 0010, INSA de Lyon, France.
[21] Li, J. C., Lopes, R., Vialle, C., and Sacadura, J. F., 1999, ''Study of an Optical Device for Energy Homogenization of a High Power Laser Beam,'' J. Laser Appl., **11**, No. 6.
[22] Jones, P. D., Dorai-Raj, D. E., and McLeod, D. G., 1996, ''Spectral-Directional Emittance of Oxidized Copper,'' J. Thermophys. Heat Transfer, **10**, No. 2, pp. 343–349.

Infinitesimal-Area Radiative Analysis Using Parametric Surface Representation, Through NURBS

K. J. Daun[1]
kyle_daun@mail.utexas.edu

K. G. T. Hollands

University of Waterloo,
Department of Mechanical Engineering,
Waterloo, Ontario,
Canada N2L 3G1

The use of form factors in the treatment of radiant enclosures requires the radiosity be approximated as uniform over finite areas, and so when higher accuracy is required, an infinitesimal-area analysis should be applied. This paper describes a generic infinitesimal-area formulation suited in principle for any enclosure containing a transparent medium. The surfaces are first represented parametrically, through ''non-uniform rational B-spline'' (NURBS) functions, the industry standard in CAD-CAM codes. The kernel of the integral equation is obtained without user intervention, using NURBS algorithms, and then the integral equation is solved numerically. The resulting general-purpose code, which proceeds directly from surface specification to solution, is tested on problems taken from the literature. [DOI: 10.1115/1.1351168]

Keywords: Heat Transfer, Numerical Methods, Radiation

Introduction

As currently practiced, radiant enclosure analyses often involve form factors, even though their use requires the approximation of uniform radiosity over each individual surface of the enclosure. This simplification means that there will be an error in the answer, which can only be reduced by dividing the enclosure into progressively smaller areas. Infinitesimal-area analysis eliminates this drawback.

In this paper, by representing the surfaces parametrically, we arrive at an explicit formulation of the two-variable integral equation associated with infinitesimal-area analysis. The kernel in this explicit form is found to be ''generic'' in the sense that it has the same general form regardless of the enclosure geometry. The kernel can be obtained directly with algebraic steps that involve taking derivatives but not integrals. Such steps can be programmed in terms of computer algebra, and for a given size grid, the whole process can be made to proceed automatically from surface specification to solution.

Before reviewing the relevant literature, it is useful to distinguish between single and two-variable problems in infinitesimal-area analysis. Single-variable problems are those which can be reduced to solving an integral equation in one independent variable, like the one in $y(x)$

$$y(x)=f(x)+\lambda\int_a^b y(t)k(x,t)dt, \tag{1}$$

whereas for two-variable problems, the subject integral equation is in two variables, like the one in $z(x,y)$

$$z(x,y)=f(x,y)+\lambda\int\int_{R_{uv}} z(u,v)K(x,y,u,v)dudv. \tag{2}$$

In these equations (which are Fredholm integral equations of the 2nd kind), $k(x,t)$ and $K(x,y,u,v)$ are the appropriate kernels. Textbooks [1–3] have recognized the basic two-variable character of the integral equations, although the specific solutions that they report are for single-variable problems.

Infinitesimal-area analysis for single-variable problems was first developed by Buckley [4,5], who treated temperature-specified circular-cylinders. Hottel and Keller [6] developed a numerical technique, for treating cylindrical-enclosures of circular and rectangular cross-section with adiabatic side-walls. By neglecting radiosity variation around the rectangular cross-section, they treated these enclosures as single-variable problems, which strictly they are not. In other single-variable treatments, Sparrow and Albers [7] and Sparrow et al. [8] analyzed the cylindrical enclosures first treated by Buckley [4,5], and Usiskin and Siegel [9] treated the circular-cylinder with black, temperature-specified ends and a heat flux-specified lateral surface.

Sparrow and Haji-Sheikh [10] were the first to treat two-variable problems. They analyzed the problem of opposing square plates separated by zero-radiosity side-walls. Later, the same authors treated the two-variable problem of adjoining square plates [11], with again zero-radiosity walls forming the rest of the enclosure. Their method was to solve the integral equation analytically, either using a variational method, or by use of ortho-normal functions and least square minimization. Both of the two-variables cases treated by Sparrow and Haji-Sheikh involved only two radiating surfaces, both being flat.

Several other numerical methods, such as view-factor methods and Monte Carlo methods [12,13] have been developed to treat two-variable enclosure problems. Tan et al. [14] summarized some of the more recent work, especially approaches developed for treating enclosures containing participating media. To our knowledge, however, none of these methods apply the infinitesimal-area analysis method through the parametric representation of the enclosure surfaces. There are some advantages to this technique, as this paper will endeavor to demonstrate.

In this paper, after reviewing the parametric representation of surfaces, we derive the general equations from which the kernel for the two-variable problem can be obtained from the functions defining the parametric representation. We then describe a general method for solving the integral equation by numerical methods. Taken together, these two steps have been implemented into a single general code, and the code has been exercised on several infinitesimal-area enclosure problems taken from the literature.

[1]Present address: The University of Texas at Austin, Department of Mechanical Engineering, Austin, Texas, 78712-1063

Contributed by the Heat Transfer Division for publication in the JOURNAL OF HEAT TRANSFER. Manuscript received by the Heat Transfer Division November 8, 1999; revision received October 3, 2000. Associate Editor M. P. Menguc.

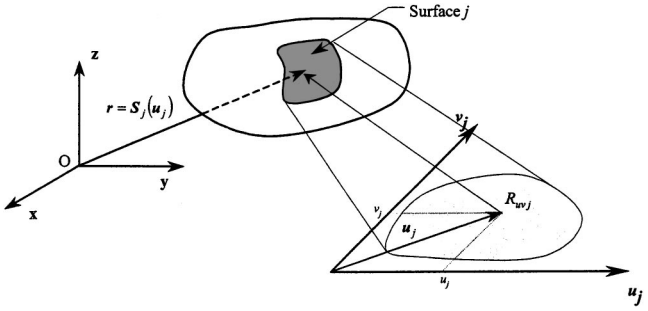

Fig. 1 Parametric representation of an enclosure surface

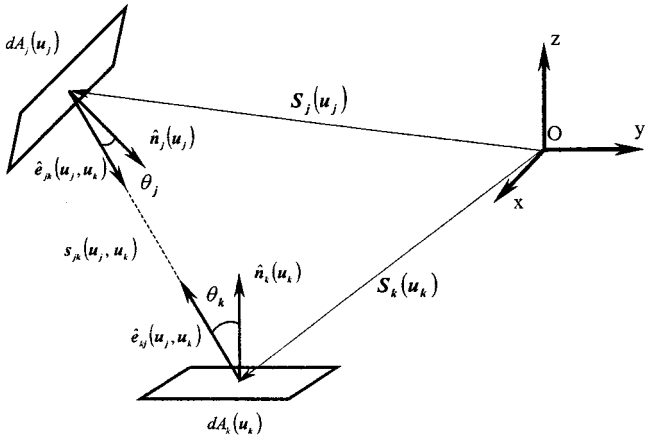

Fig. 2 Geometry between two-infinitesimal areas

For representing surfaces parametrically, the non-uniform rational B-splines, commonly called ''NURBS'' [15,16] was adopted for these test cases. This representation is widely-used in CAD-CAM, and computer graphics, and the versatility of the existing NURBS algorithms and its wide-ranging literature provides one of the main attributes of the present approach. NURBS methods have been devised to represent almost any engineering surface in a compact, standardized formulation.

In the first part of this paper, the method is developed assuming an ''unobstructed'' enclosure—that is an enclosure where the path between any two-points on the enclosure surface is not blocked by another part of the enclosure wall; in other words, every point on the enclosure surface can ''see'' every other point. The exercising of the method on test cases involving unobstructed enclosures is reported next. An extension to obstructed enclosures is discussed in the final section. This extension is, however, not exercised on any test cases in the present paper, which is mainly aimed at introducing the basic ideas of parametric representation, through NURBS.

Infinitesimal-Area Analysis Through Parametric Surface-Representation

Parametric Representation of Surfaces. Consider an enclosure composed of N diffuse-gray surfaces. For simplicity in representation, a uniform emissivity is assumed over each surface, but this is not a necessary requirement for the method. Each surface is represented parametrically. In the case of the j^{th} surface, the parameters will be denoted u_j and v_j, so the representation is expressed by

$$\mathbf{r}=\mathbf{S_j}(u_j,v_j)=\mathbf{S_j}(\mathbf{u_j}), \tag{3a}$$

where $\mathbf{r}=(x,y,z)$ is the position vector, two component vector $\mathbf{u_j}=(u_j,v_j)$, and $\mathbf{S_j}=(P_j,Q_j,R_j)$ is a vector function of u_j and v_j. That is, to define the shape of the j^{th} surface we write

$$x=P_j(\mathbf{u_j}),y=Q_j(\mathbf{u_j}),z=R_j(\mathbf{u_j}). \tag{3b}$$

Parameters u_j and v_j are allowed to range over a restricted region R_{uvj} in the (u_j,v_j) plane, and as they do so, the tip of the position vector (with tail at the origin) carves out the surface in real space, as shown in Fig. 1. Thus the three functions P_j, Q_j, and R_j and the region R_{uvj} completely define the j^{th} surface, both in terms of its shape and its extent. The parametric representation of surfaces is explained in greater detail in certain calculus texts, for example, that of Adams [17].

The boundary conditions can be expressed parametrically. Each surface is assumed to have either a specified temperature distribution or a specified heat flux distribution. Thus, for any surface j, we have either $T_j=T_j(\mathbf{u_j})$ or $q_{sj}=q_{sj}(\mathbf{u_j})$.

Radiosity Equation Under Parametric Representation. In the present formulation, the infinitesimal areas are produced by infinitesimal changes in parameters u_k and v_k. The infinitesimal area dA_k cut out on surface k when u_k goes from u_k to u_k+du_k and v_k goes from v_k to v_k+dv_k is

$$dA_k(\mathbf{u_k})=J_k(\mathbf{u_k})du_kdv_k, \tag{4}$$

where $J_k(\mathbf{u_k})$ is the discriminant, given by

$$J_k(\mathbf{u_k})=\left[\left(\frac{\partial(Q_k,R_k)}{\partial(u_k,v_k)}\right)^2+\left(\frac{\partial(R_k,P_k)}{\partial(u_k,v_k)}\right)^2+\left(\frac{\partial(P_k,Q_k)}{\partial(u_k,v_k)}\right)^2\right]^{1/2}, \tag{5}$$

where

$$\frac{\partial(Q_k,R_k)}{\partial(u_k,v_k)}=\begin{vmatrix}\dfrac{\partial Q_k(\mathbf{u_k})}{\partial u_k} & \dfrac{\partial Q_k(\mathbf{u_k})}{\partial v_k}\\ \dfrac{\partial R_k(\mathbf{u_k})}{\partial u_k} & \dfrac{\partial R_k(\mathbf{u_k})}{\partial v_k}\end{vmatrix} \tag{6}$$

and similar expressions applying for the other Jacobians in Eq. (5).

With such elemental areas, one can now express the radiosity equation as follows:

$$q_{oj}(\mathbf{u_j})=B_j(\mathbf{u_j})+G_j\sum_{k=1}^{N}\int\int_{R_{uv,k}} q_{ok}(\mathbf{u'_k})K(\mathbf{u_j},\mathbf{u'_k})du'_kdv'_k, \tag{7}$$

where for T-specified surfaces,

$$B_j(\mathbf{u_j})=\varepsilon_j\sigma T_j^4(\mathbf{u_j}),\quad G_j=\rho_j \tag{8}$$

and for q-specified surfaces,

$$B_j(\mathbf{u_j})=q_{sj}(\mathbf{u_j}),\quad G_j=1. \tag{9}$$

The kernel, $K(\mathbf{u_j},\mathbf{u_k})$, in integral Eq. (7) is given by

$$K(\mathbf{u_j},\mathbf{u_k})=\frac{\cos\theta_j(\mathbf{u_j},\mathbf{u_k})\cdot\cos\theta_k(\mathbf{u_j},\mathbf{u_k})J_k(\mathbf{u_k})}{\pi|\mathbf{s_{jk}}(\mathbf{u_j},\mathbf{u_k})|^2}, \tag{10}$$

which is equal to the form factor from dA_j to dA_k, divided by du_kdv_k. (If $\mathbf{u_j}=\mathbf{u_k}$, $K(\mathbf{u_j},\mathbf{u_k})$ is set equal to zero.) The kernel can be expressed in terms of $\mathbf{S_j}(\mathbf{u_j})$ and $\mathbf{S_k}(\mathbf{u_k})$, as follows. The vector $\mathbf{s_{jk}}(\mathbf{u_j},\mathbf{u_k})$ in Eq. (10) connects $\mathbf{S_j}(\mathbf{u_j})$ and $\mathbf{S_k}(\mathbf{u_k})$ and is given by

$$\mathbf{s_{jk}}(\mathbf{u_j},\mathbf{u_k})=\mathbf{S_k}(\mathbf{u_k})-\mathbf{S_j}(\mathbf{u_j}). \tag{11}$$

The angles θ_k and θ_j are the angles between vector $\mathbf{s_{jk}}(\mathbf{u_j},\mathbf{u_k})$ and the local unit-normal vectors on surface j and k, respectively, as shown in Fig. 2. Their cosines can, therefore, be found from appropriate dot products. The unit-normal vectors are found from

$$\hat{\mathbf{n}}_\mathbf{k}(\mathbf{u_k}) = \frac{\left[\dfrac{\partial(Q_k,R_k)}{\partial(u_k,v_k)}, \dfrac{\partial(R_k,P_k)}{\partial(u_k,v_k)}, \dfrac{\partial(P_k,Q_k)}{\partial(u_k,v_k)}\right]}{J_k(\mathbf{u_k})} \tag{12}$$

with a similar equation applying for $\hat{\mathbf{n}}_\mathbf{j}(\mathbf{u_j})$. Introducing $\hat{\mathbf{e}}_\mathbf{jk}(\mathbf{u_j},\mathbf{u_k})$ and $\hat{\mathbf{e}}_\mathbf{kj}(\mathbf{u_j},\mathbf{u_k})$ as the unit vectors in the directions $\mathbf{s_{jk}}(\mathbf{u_j},\mathbf{u_k})$ and $\mathbf{s_{kj}}(\mathbf{u_j},\mathbf{u_k})$, respectively, the kernel can be rewritten as

$$K(\mathbf{u_j},\mathbf{u_k}) = \frac{[\hat{n}_j(u_j)\cdot\hat{e}_{jk}(\mathbf{u_j},\mathbf{u_k})]\cdot[\hat{\mathbf{n}}_\mathbf{k}(\mathbf{u_k})\cdot\hat{\mathbf{e}}_\mathbf{kj}(\mathbf{u_j},\mathbf{u_k})]}{\pi|\mathbf{s_{jk}}(\mathbf{u_j},\mathbf{u_k})|^2} J_k(\mathbf{u_k}) \tag{13}$$

the unit vectors being given by

$$\hat{\mathbf{e}}_\mathbf{jk}(\mathbf{u_j},\mathbf{u_k}) = -\hat{\mathbf{e}}_\mathbf{kj}(\mathbf{u_j},\mathbf{u_k}) = \frac{\mathbf{s_{jk}}(\mathbf{u_j},\mathbf{u_k})}{|\mathbf{s_{jk}}(\mathbf{u_j},\mathbf{u_k})|} = \frac{\mathbf{S_k}(\mathbf{u_k})-\mathbf{S_j}(\mathbf{u_j})}{|\mathbf{S_k}(\mathbf{u_k})-\mathbf{S_j}(\mathbf{u_j})|}. \tag{14}$$

Thus, once the enclosure surfaces are represented parametrically, the kernel of the governing integral equations can be evaluated by straightforward calculus operations. These operations can be done automatically by using a computer algebra system, such as MAPLE™ or Mathematica™. They can also be found directly using NURBS algorithms, as will be described later.

Generalized Radiosity Equation. To get a form more convenient for numerical analysis, it is preferable to develop a governing equation containing one integral over the entire enclosure rather than the sum of N integrals over each enclosure surface, as in Eq. (7). This is accomplished by mapping all of the separate R_{uvj} regions onto a single u-v plane by a series of linear transformations. After mapping, these separate regions are combined into a single region R_{uv} in the u-v plane, with R_{uv} encompassing the total enclosure surface. The mapping must be such that none of the R_{uvj} regions overlap after mapping, but by a suitable choice of transformation parameters, this can always be arranged. The entire enclosure is now represented by a single (piece-wise) parametric equation and so Eq. (7) can be simplified to

$$q_o(\mathbf{u}) = B(\mathbf{u}) + G(\mathbf{u}) \int_{R_{uv}} \int q_o(\mathbf{u}')K(\mathbf{u},\mathbf{u}')du'dv', \tag{15}$$

where $B(\mathbf{u}) = B_j(\mathbf{u_j})$ and $G(\mathbf{u}) = G_j$ when $\mathbf{u}$ lies on the j^{th} part R_{uv}. The procedure for finding the generalized kernel $K(\mathbf{u},\mathbf{u}')$ is to first determine the two regions on the u-v plane on which $\mathbf{u}$ and $\mathbf{u}'$ lie (say they are the jth and kth, respectively). One then reverse maps $\mathbf{u}$ into $\mathbf{u_j}$ and $\mathbf{u}'$ into $\mathbf{u}'_\mathbf{k}$, and then equates $K(\mathbf{u},\mathbf{u}')$ to $K(\mathbf{u_j},\mathbf{u}'_\mathbf{k})$. A similar reverse mapping applies for getting $B(\mathbf{u})$ and $G(\mathbf{u})$.

Single-Variable Enclosure Problems. As was mentioned in the Introduction, most previous applications of infinitesimal-area analysis has involved single-variable problems, and it is useful at this stage to express that formulation in terms of the present formulation. For single-variable problems, there will be a known way of parameterizing the surface (surface parameterization is not unique) such that the radiosity distribution is a function of only one of the parameters, say u, rather than two-parameters, u and v. If the temperature, specified heat-flux and emissivity are constant with respect to v, then q_o, G and B are dependent only on u. Equation (15) can be simplified by splitting the double integral into two separate integrals over u and v, and extracting $q_o(u')$ from the inner integral, to give

$$q_o(u) = B(u) + G(u) \int_a^b q_o(u')\left[\int_{g(u')}^{h(u')} K(\mathbf{u},\mathbf{u}')dv'\right]du', \tag{16}$$

where $g(u)$ and $h(u)$ are the bounding functions of R_{uv}. The inner integration is carried out to yield a new kernel $k(u,u')$, appropriate for single-variable enclosures:

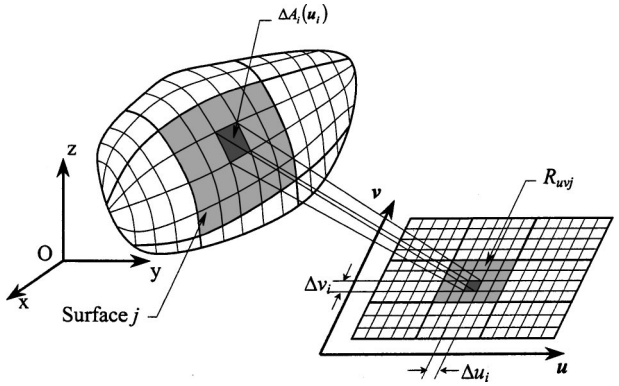

Fig. 3 Discretization of R_{uv}

$$k(u,u') = \int_{g(u')}^{h(u')} K(u,v,u',v')dv'. \tag{17}$$

It is to be noted that according to the right hand side of Eq. (17), we might expect $k(u,u')$ to be a function of v as well as u and u', but it is clear from Eq. (16) that this must not be the case. This means that the integral equation can be re-written as

$$q_o(u) = B(u) + G(u) \int_a^b q_o(u')k(u,u')du' \tag{18}$$

which is the single-variable radiosity equation.

Numerical Solution of the Integrated Equation. Analytical solutions to the integral equations are ordinarily not possible, and numerical methods must be employed to find the radiosity distribution. First, the parametric region R_{uv} is discretized into a grid of n elements, each centered at (u_i,v_i) with a length of Δu_i and a width of Δv_i, as illustrated in Fig. 3. (Figure 3 presupposes that the sub-regions are rectangular, which is always possible with the NURBS representation adopted here.) Each discrete element on R_{uv} corresponds to a finite area element of the surface of the enclosure. Equation (15) can now be rewritten by approximating the integral by a summation of the contributions from all the discrete elements on R_{uv}:

$$q_{oi} = b_i + g_i \sum_{k=1}^{n} q_{ok}K_{ik}\Delta u_k \Delta v_k, \tag{19}$$

where $b_i = B(\mathbf{u_i})$, $g_i = G(\mathbf{u_i})$, and K_{ik} is the kernel function between elements i and k, i.e., $K_{ik} = K(\mathbf{u_i},\mathbf{u_k})$. Writing Equation (19) on each element results in n simultaneous equations that can be rearranged into the matrix equation

$$\mathbf{Aq_o} = \mathbf{b}. \tag{20}$$

Equation (20) is solved for increasingly large values of n, and one thereby infers the asymptote as $n \to \infty$.

In general, matrix $\mathbf{A}$ is found to be dense, because radiation transfer occurs between almost all elements of the enclosure. Therefore, it is preferable to use an iterative solver in order to obtain a solution expediently. However, if the enclosure contains at least one q-specified surface, matrix $\mathbf{A}$ is no longer diagonally dominant. For these problems, it is necessary to apply underrelaxation to the iterative solver or to employ a direct solver [18].

Implementation

To validate this method, the algorithm was applied to some problems considered previously in the literature. A personal computer with a Pentium II™ 233 MHz processor and 96 megabytes of RAM was programmed in C++.

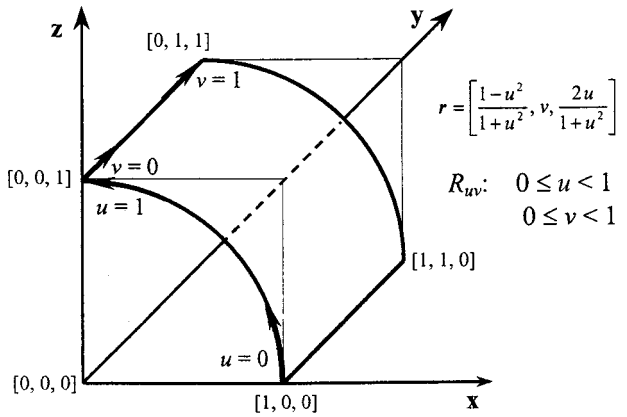

Fig. 4 Quarter cylinder representation in NURBS

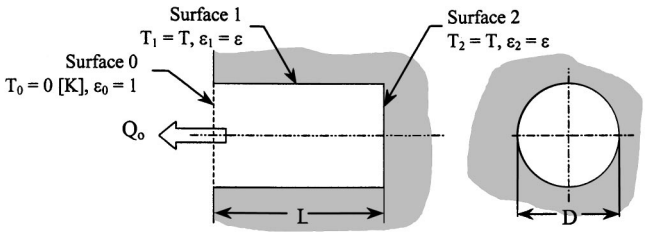

Fig. 5 Isothermal, cylindrical enclosure analyzed by Sparrow et al. [8]

Method. The enclosure surfaces were parameterized using NURBS algorithms. Accordingly, the individual parametric equations were all ratios of polynomial functions of parameters u_j and v_j. For example, the Fig. 4 shows the NURBS representation of a quarter-cylinder. Detailed treatments of NURBS are given by Piegl and Tiller [15] and Farin [16]. Using NURBS algorithms it is possible to readily code analytical representations for the partial derivatives in Eqs. (6) and (12), without the use of a computer algebra program like MAPLE; the derivatives are also ratios of polynomial functions.

In the problems treated in this section, each region of R_{uv} was subdivided into the same number of elements. The division lines were always parallel to the u or v axis and equally spaced, with $\Delta u = \Delta v$. Also, to increase the accuracy of the solution for a given number of elements (grid size), the summation rule for form factors was enforced, as follows. The sum of all the kernels in any row, say the ith, multiplied by their corresponding area elements in R_{uv} is a numerical approximation of the point form factor from point (u_i, v_i) to the rest of the enclosure, and it should therefore equal unity. That is,

$$\sum_{k=1}^{n} K_{ik} \Delta u_k \Delta v_k \approx \int_{R_{uv}} \int K(\mathbf{u_i}, \mathbf{u_k}) du_k dv_k = 1. \tag{21}$$

Due to discretization error, however, the sum in Eq. (21) is not precisely unity. The summation rule can be enforced by introducing a weighting factor, w_i, defined as

$$w_i = \frac{1}{\sum_{k=1}^{n} K_{ik} \Delta u_k \Delta v_k} \tag{22}$$

and then multiplying each off-diagonal element of the ith row with w_i. The diagonal elements of the modified matrix **A** are kept equal to unity.

To further increase the solution accuracy, Richardson extrapolation [19] was implemented whenever possible, as follows. The exact analytical solution, Φ_∞, is composed of the numerical solution, Φ_n, obtained with n elements, plus a discretization error ε_n, so that $\Phi_\infty = \Phi_n + \varepsilon_n$. According to the extrapolation method, the discretization error is assumed to be a power function of the number of elements used to obtain the numerical solution: i.e., $\varepsilon_n \approx \alpha n^p$. If the number of elements is systematically increased in a geometrical way, it is possible to evaluate the discretization error and thus approximate the exact solution. In particular, if three successive grid refinements have $n_1 = ab^c$, $n_2 = ab^{2c}$ and $n_3 = ab^{3c}$ elements (where a, b, and c are constants), p is found from

$$p = \frac{\log\left(\frac{\Phi_{ab^{2c}} - \Phi_{ab^{3c}}}{\Phi_{ab^c} - \Phi_{ab^{2c}}}\right)}{\log(b^c)}, \tag{23}$$

and the exact solution is then approximated by

$$\Phi_\infty \approx \Phi_{ab^c} + \frac{\Phi_{ab^c} - \Phi_{ab^{2c}}}{(b^c)^p - 1}. \tag{24}$$

Richardson extrapolation can only be used when successively larger values of n result in a monotonic series for Φ_n.

Validation and Demonstration of Method. Sparrow et al. [8] determined the total heat transfer Q_o emanating from an isothermal-cylindrical cavity at temperature T, as shown in Fig. 5, expressing their results in terms of the apparent emissivity, defined by $\varepsilon_a = 4Q_o/(\pi D^2 \sigma T^4)$. Using the method described in the previous section, the radiosity distribution for enclosures with a L/D ratio of 0.25, 0.5, 1, 2, and 4, and a wall emissivity of 0.5, 0.75, and 0.9 was obtained, and the corresponding apparent emissivities calculated. Each surface being temperature-specified, a Gauss-Seidel algorithm was used to solve for the radiosity distribution. The solution at a given grid size was considered to have converged when the relative difference between the radiosity values of successive iterations was less than 10^{-6}, at all grid locations.

The most refined grid had $n = 3072$, and these results are compared with the results of Sparrow et al. [8] in Table 1. With the exception of the case of $L/D = 4$ and $\varepsilon = 0.5$, the discretization error diminished monotonically with successive values for n, which permitted Richardson extrapolation to be used to estimate the exact solution. These results are also summarized in Table I. In each case, the solutions obtained at $n = 3072$ were within 0.3 percent of the published solution and the solutions obtained with Richardson extrapolation were all within 0.1 percent of the published results.

In another study, Usiskin and Siegel [9] determined the radiosity distribution along the length of various circular cylinders. The first problem they considered was a heated cylinder with black end-walls set to 0 K, as shown in Fig. 6. The radiosity distribution was expressed non-dimensionally in terms of $\Phi_q^*(x/L)$, where $\Phi_q^*(x/L) = q_o(x/L)/q_s$. The second problem was an adiabatic cylinder with one end-wall set to 0 K, as shown in Fig. 7. For this problem, the radiosity distribution was expressed in terms of $\Phi(x/L)$, where $\Phi(x/L) = q_o(x/L)/\sigma T^4$.

In both cases, cylinders with L/D ratios of 1 and 4 were tested. Because the enclosures contained a surface with a specified heat-flux, LU decomposition was used to invert the coefficient matrix. The distributions of $\Phi_q^*(x/L)$ and $\Phi(x/L)$ found using the present method agreed with the published data. A cubic spline was fit to the data points obtained at the highest level of refinement ($n = 3072$) to approximate a continuous radiosity distribution. Radiosity values corresponding to the locations of the published data points were then obtained by interpolation and extrapolation. The data for the heated cylinder is summarized in Table 2, and the data

Table 1 Comparison of ε_a with results of Sparrow et al. [8]

L/D	ε	$\varepsilon_{a\ (Sparrow\ et\ al)}$	$\varepsilon_{a\ (n=3072)}$	Relative Difference	$\varepsilon_{a\ (R.E.)}$	Relative Difference
0.25	0.90	0.9434	0.9425	-0.10%	0.9435	0.01%
	0.75	0.8491	0.8480	-0.13%	0.8491	0.00%
	0.50	0.6569	0.6557	-0.18%	0.6568	-0.02%
0.5	0.90	0.9618	0.9610	-0.08%	0.9620	0.02%
	0.75	0.8948	0.8938	-0.11%	0.8947	-0.01%
	0.50	0.7424	0.7416	-0.11%	0.7423	-0.01%
1	0.90	0.9720	0.9712	-0.08%	0.9722	0.02%
	0.75	0.9229	0.9219	-0.11%	0.9227	-0.02%
	0.50	0.8084	0.8073	-0.14%	0.8080	-0.05%
2	0.90	0.9746	0.9736	-0.10%	0.9747	0.01%
	0.75	0.9308	0.9293	-0.16%	0.9305	-0.03%
	0.50	0.8331	0.8309	-0.26%	0.8325	-0.07%
4	0.90	0.9749	0.9741	-0.08%	0.9750	0.01%
	0.75	0.9317	0.9309	-0.09%	0.9316	-0.01%
	0.50	0.8367	0.8357	-0.12%	N/A	N/A

for the adiabatic cylinder is summarized in Table 3. In all cases, the radiosity distribution obtained with the two-dimensional algorithm is within 1 percent of the published data.

The problems analyzed by Hottel and Keller [6] included estimating the heat loss Q_{o1} through a cubical hole, as shown in Fig. 8. They expressed the results in terms of the non-dimensional total radiation heat transfer, F_{01}, defined by $F_{01}=Q_{01}/(A\sigma(T_0^4-T_1^4))$, where A is the area of the hole cross section and T_1 and T_2 are the temperatures on each side of the hole. Hottel and Keller treated the problem as one-dimensional by neglecting radiosity

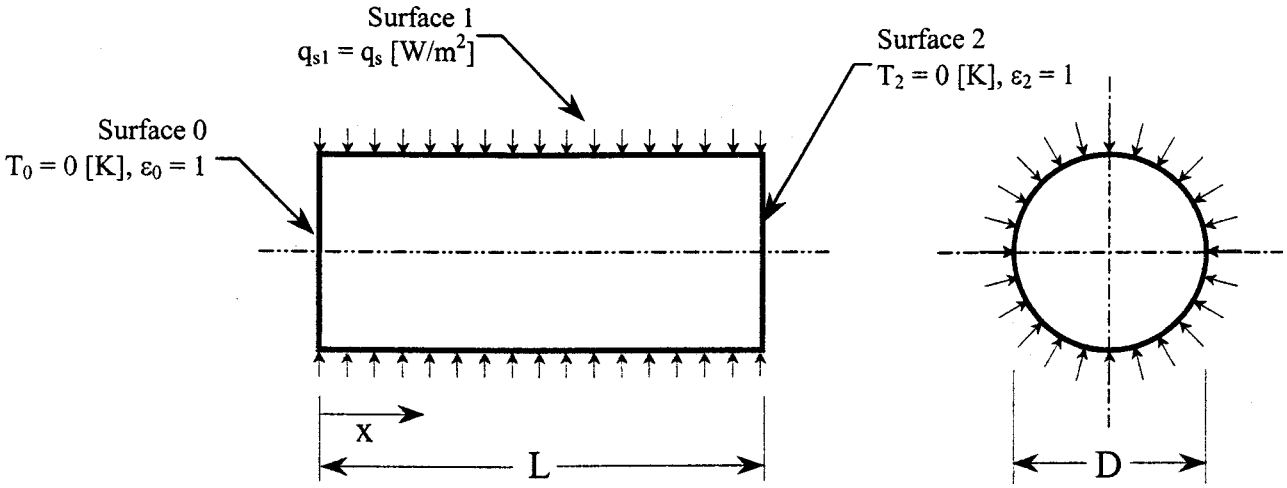

Fig. 6 Heated cylinder with end walls at 0 [K], Usiskin and Siegel [9]

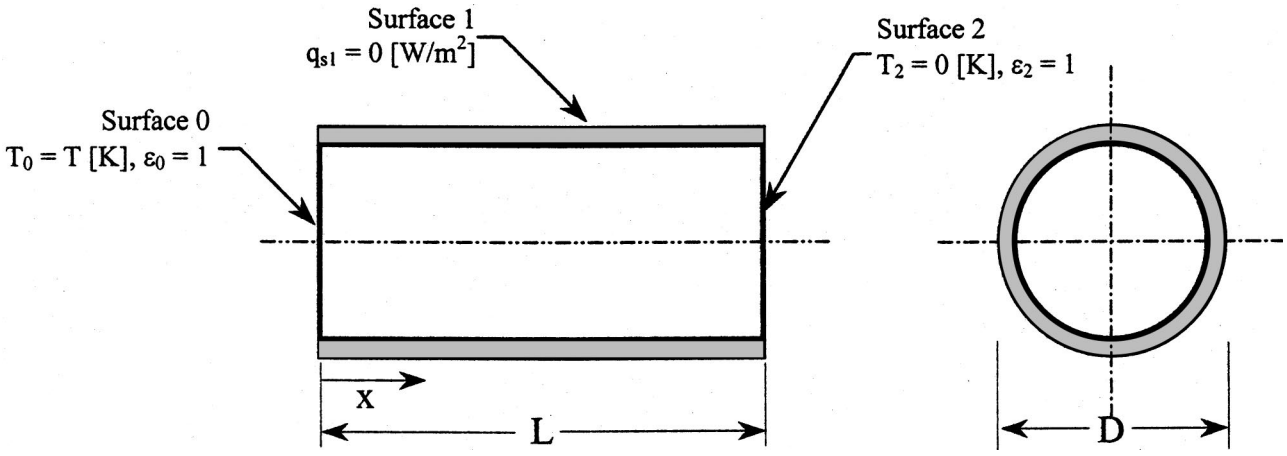

Fig. 7 Adiabatic cylinder with end walls of different temperature, Usiskin and Siegel [9]

Table 2 Comparison of Φ^*_q with Usiskin and Siegel [9]

	L/D = 1			L/D = 4		
x/L	$\Phi^*_{q(n=3072)}$	$\Phi^*_{q(US)}$	Relative Difference	$\Phi^*_{q(n=3072)}$	$\Phi^*_{q(US)}$	Relative Difference
0	2.04	2.06	-0.97%	4.97	4.95	0.40%
0.125	2.30	2.31	-0.43%	8.59	8.61	-0.23%
0.25	2.48	2.49	-0.40%	11.17	11.2	-0.27%
0.375	2.59	2.60	-0.38%	12.71	12.6	0.87%
0.5	2.63	2.64	-0.38%	13.23	13.2	0.23%

variation along the circumference of the hole. In the present solution, the matrix was inverted through LU decomposition, and Richardson extrapolation was implemented to approximate the converged solution. The results are summarized in Fig. 9. The Richardson-extrapolated solution was within 0.6 percent of the solution obtained by Hottel and Keller [6], well within the accuracy of this published value.

Computational Effort. The computational effort required to solve for the radiosity distribution depended on the enclosure geometry and the boundary conditions. Generally, the hardest problems to solve were enclosures that contained *q*-specified surfaces, *T*-specified surfaces with low emissivites, or a large number of surfaces that joined at angles of 90 deg or less. For example, the *T*-specified cylinder treated by Sparrow et al. [8] required only 3072 elements (about one hour of CPU time) to obtain a solution within 0.3 percent of the published solution. The cubical enclosure treated by Hottel and Keller [6] was far more difficult, requiring 6144 elements to obtain a solution within 0.6 percent of the published solution. Whenever applicable, Richardson extrapolation significantly reduced the computational effort. In the problem treated by Sparrow et al. [8], the solutions obtained with Richardson extrapolation were typically an order of magnitude in better agreement with the published solutions, compared with the solutions obtained at the highest level of grid refinement.

The computational effort required to yield the present solutions was very much greater than what would have been required if the problems had been posed and analyzed as single-variable problems, as was done by the previous workers. In this case, a solution obtained using n elements has approximately the same accuracy as a solution obtained with n^2 elements, if the enclosure was treated as a two-variable problem. On the other hand, if the problem statement were altered slightly, say, in the case of the cylinder to make the temperature vary with circumferential as well as axial position, then the single-variable solution could not be used. Also, the parallelepiped enclosures of Hottel and Keller [6] really required the two-variable solution for fully realistic modeling.

Table 3 Comparison of Φ with Usiskin and Siegel [9]

	L/D = 1			L/D = 4		
x/L	$\Phi_{(n=3072)}$	$\Phi_{(US)}$	Relative Difference	$\Phi_{(n=3072)}$	$\Phi_{(US)}$	Relative Difference
0	0.762	0.759	0.40%	0.901	0.900	0.11%
0.125	0.696	0.696	0.00%	0.796	0.797	-0.13%
0.25	0.630	0.631	-0.16%	0.695	0.697	-0.29%
0.375	0.565	0.566	-0.18%	0.597	0.599	-0.33%
0.5	0.500	0.500	0.00%	0.500	0.500	0.00%

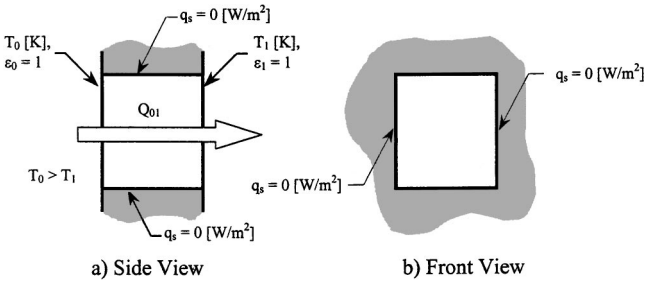

Fig. 8 Enclosure treated by Hottel and Keller [6]

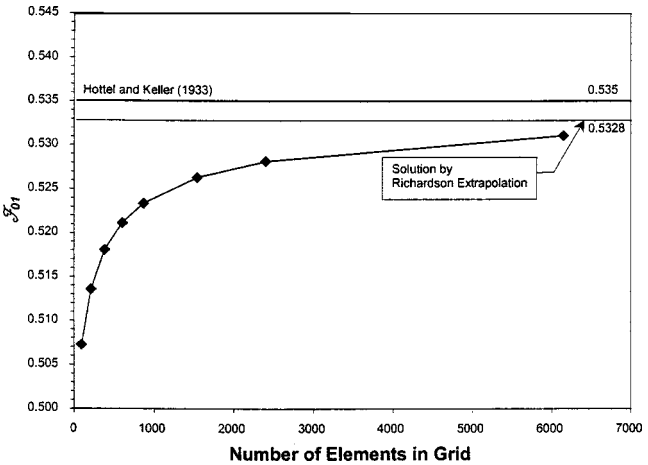

Fig. 9 Grid refinement study for the problem of Fig. 8

Enclosures With Obstructions

Problem Statement. In practice, many enclosures contain obstructions — i.e., the path between some pairs of points is blocked by intervening surfaces, as in Fig. 10(*a*). This possibility has been ignored in earlier sections, and we now discuss its inclusion. We first derive the form that the radiosity equation takes when there are obstructions within the enclosure. The effect of obstructions can be accommodated by introducing a special multiplier, $\beta(\mathbf{u},\mathbf{u}')$, in front of $K(\mathbf{u},\mathbf{u}')$ in Eq. (15), so that the actual kernel of the integral equation is $\beta(\mathbf{u},\mathbf{u}')K(\mathbf{u},\mathbf{u}')$, rather than $K(\mathbf{u},\mathbf{u}')$ itself. The ''blockage factor,'' $\beta(\mathbf{u},\mathbf{u}')$, will either be zero or unity depending on whether another part of the surface blocks the path between the point at $\mathbf{u}$ and $\mathbf{u}'$.

To provide a more precise mathematical statement of this condition, we first let $\mathbf{s}(\mathbf{u},\mathbf{u}')$ represent the vector connecting two arbitrary points on the enclosure surface located at $\mathbf{u}$ and $\mathbf{u}'$, respectively, and let $\hat{\mathbf{e}}(\mathbf{u},\mathbf{u}')$ denote the unit vector in the direction $\mathbf{s}(\mathbf{u},\mathbf{u}')$: $\hat{\mathbf{e}}(\mathbf{u},\mathbf{u}')=\mathbf{s}(\mathbf{u},\mathbf{u}')/|\mathbf{s}(\mathbf{u},\mathbf{u}')|$. We can now express $\beta(\mathbf{u},\mathbf{u}')$ as follows: $\beta(\mathbf{u},\mathbf{u}')=0$ if and only if there exists at least one point, $\mathbf{u}^*$, in R_{uv} that satisfies the following:

$$|\mathbf{r}(\mathbf{u}^*,\mathbf{u})|<|\mathbf{r}(\mathbf{u}',\mathbf{u})| \quad \text{and} \quad \hat{\mathbf{e}}(\mathbf{u}^*,\mathbf{u})\cdot\hat{\mathbf{e}}(\mathbf{u}',\mathbf{u})=1; \qquad (25)$$

if $\mathbf{u}^*$ does not exist, $\beta(\mathbf{u},\mathbf{u}')=1$. It is clear that $\hat{\mathbf{e}}(\mathbf{u},\mathbf{u}^*)\cdot\hat{\mathbf{e}}(\mathbf{u},\mathbf{u}')$ is the cosine of the angle between $\hat{\mathbf{e}}(\mathbf{u},\mathbf{u}^*)$ and $\hat{\mathbf{e}}(\mathbf{u},\mathbf{u}')$, so by equating this dot product to unity (the second condition), we are ensuring that the point at $\mathbf{u}^*$ is aligned with the path connecting $\mathbf{u}$ and $\mathbf{u}'$. Also, the first condition ensures that $\mathbf{u}^*$ is in the foreground, so it does indeed obstruct the path.

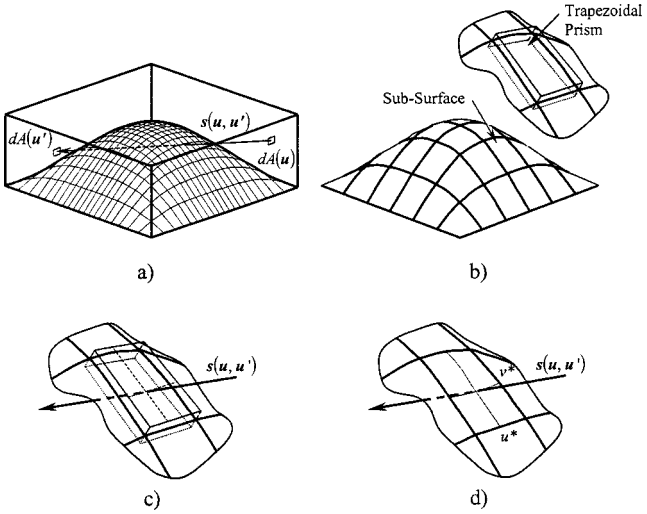

Fig. 10 Treatment of enclosures with obstructions [21]: (*a*) an enclosure with an obstruction; (*b*) surfaces are initially split to form sub-surfaces (a trapezoidal prism is constructed around each subsurface); (*c*) each trapezoidal prism is checked for ray intersection; (*d*) if a ray intersects a trapezoidal prism, the corresponding sub-surface is checked for ray intersection by finding u* through Newton iteration

Finding the Blockage Factor. In the discretized form of the radiosity equation, Eq. (19), there will be a β_{ik} in front of K_{ik}, and we will need to check for the existence of **u*** between only a finite number of pairs of points. (The actual number is $n(n-1)$, or essentially n^2.) There are a number of possible approaches. Most involve ray-tracing; that is, one looks for an intersection of the ray connecting **u** and **u**′ with the enclosure, at **u***. Generally, checking for the intersection of a ray and a higher-order surface, such as a NURBS surface, will be computationally expensive if one does this by substituting the equation for the ray into the equation for the surface and then applies a numerical root-finding procedure in two unknowns, making sure that all the possible roots have been accounted for. Another way is to check for intersection of the ray with each of the n surfaces formed in the numerical solution of the radiosity equation — that is, the n elementary surfaces cut out by the change Δu in u and Δv in v. Each surface of these surfaces can be approximated as a small planar region whose normal is the surface normal at the center of the element. Checking for intersection of a ray with a planar region demands the manipulation of linear equations and is therefore not computationally demanding in itself, but the check would have to be made as many as $n-2$ times per pair, and since there are roughly n^2 pairs, up to about n^3 intersection checks will have to be made in all. If (as was roughly in the case of the case studies reported earlier) the value of n is 3000, there will be up to 27×10^9 checks for the entire enclosure, and so this checking could be very computationally demanding. An advantage of this approach is that when one increases n as part of the grid refinement study, one automatically increases the fidelity by which the planar elemental areas models the real elemental areas, so one grid refinement study will account for both types of deviations from reality.

Methods Based on Computer Graphics. Highly efficient ray-tracing algorithms have been developed in the computer graphics field, to resolve the problems associated with creating life-like images in a time-efficient manner. While much of the early development in computer graphics had been based on dividing the real surfaces (even if curved) into planar elementary surfaces [20], there has been considerable recent work on parametrizing curved surfaces with higher order equations (such as in NURBS), because this approach means that many fewer elementary surfaces are required to follow real surface closely. This approach has stimulated further work on ray-tracing for curved surfaces, especially NURBS representations [21]. The associated ray-tracing algorithms can be adapted directly for analysing thermal radiation problems.

A recent development by Qin et al. [21] has advanced the state-of-the-art of ray-tracing NURBS surfaces. The general method is illustrated in Fig. 10. First, all the NURBS surfaces are repeatedly sub-divided — by a special NURBS process called knot insertion — and a close-fitting trapezoidal prism is then formed around each sub-surface, as in Fig. 10(*b*). This process is repeated until the height of each trapezoidal prism, measured in a local coordinate system fixed to the corresponding sub-surface, is below a pre-set tolerance. For each relevant pair of points **u** and **u**′, the connecting ray is checked for possible intersection with each and every trapezoidal-prism. If an interception occurs, there is a very high probability that the actual surface has also been intercepted in that region. As a further check, the corresponding sub-surface are checked for intersection by solving a system of two non-linear equations with two unknowns, for which Qin et al. provide a highly efficient algorithm based on Newton's Method.

Compared to the method of checking each of the n surface elements arising in the numerical solution to the integral equation, this technique has the advantage of requiring considerably fewer sub-surfaces than the number of area elements n used to solve the integral equation, so checking sub-surfaces is much less time-consuming than checking area elements. Compared to the method of substituting the equation for the ray into the higher-order equation for the surface and then using a numerical root-finder, Qin et al.'s technique has the advantage that on the rare occasion that higher-order root-finding must be used, there will be an excellent first guess (say the center of the trapezoidal prism) for the starting value for the iterative process and since it is highly unlikely that the relatively small and flat sub-surfaces have multiple roots, it will not be necessary to check for multiple roots. Thus, the Qin et al. technique is a combination of the two techniques, that is in general much less computationally-demanding than either taken alone, as is demonstrated in sample problems solved by these workers. It should be noted that if one or more of the enclosure surfaces are flat (a common occurrence in engineering enclosures), there is only one sub-surface to check for that enclosure surface, as the subdivision process would automatically test the surface itself for flatness before subdividing.

In the implementation of the Qin et al. method on a thermal radiation problem, one will have two degrees of freedom on which the time for execution will depend: the number n and the pre-set tolerance δ associated with approximating the sub-surface by a plane (the height of the trapezoidal prism). The computed answer for a given n should not effect the answer, only the execution time. By trial and error, at relatively low settings for n, one should be able to roughly establish the value of δ that minimizes the execution time at that n, and one could keep to that value afterwards as the grid refinement study proceeds.

Conclusions

Parametric surface representation permits a formalism by which the radiosity distribution within enclosures can be determined expediently in a generic infinitesimal-area analysis technique. The first step is to represent each enclosure surfaces parametrically, through non-uniform rational B-splines (NURBS) functions. The kernel of the governing integral equations can then be derived automatically by special NURBS algorithms, and the integral equations so formulated. These equations can then solved by numerical methods to yield the radiosity distribution. Once a suitable method for determining the blockage factor has been incorporated into the kernel of the integral equation, this basic approach would

appear to be applicable to any transparent enclosure geometry — including geometries having obstructions — without modifying the basic algorithm.

Arriving at suitable parametric surface representations should not pose a large problem, provided some preliminary work has been done. Engineers and other radiant analysts are accustomed to using tables of form factors, and it is possible that they could also become equally accustomed to using tables of the NURBS-type parametric surface representations of the common engineering surfaces. Such tables need not be so extensive, because one needs the parametric representations for individual surfaces, not for the *pairs* of surfaces needed for form factors. The tables could also be made part of a computer file, in which case the surface parameterization could be transparent to the user, who would simply select the surface from a menu. NURBS algorithms also permit representation of non-standard surfaces, working, say, from a set of surface co-ordinates. Once the parametric surface representation is set up, the remaining steps in the enclosure solution can be made to proceed directly.

Acknowledgments

We are grateful to Professor S. Bedi, of the Department of Mechanical Engineering, University of Waterloo for suggesting the NURBS approach and for his assistance and guidance regarding the NURBS algorithms. This work was supported by a grant from the Natural Sciences and Engineering Research Council Canada.

Nomenclature

$\mathbf{A}$ = matrix in Eq. (20)

A_{ik} = element of $\mathbf{A}$ matrix $\begin{cases} \text{for } i=k & A_{ik}=1 \\ \text{for } i\neq k & A_{ik}=-g_i K(\mathbf{u_i},\mathbf{u_k})\Delta u_k \Delta v_k \end{cases}$

$B(\mathbf{u})$ = see Eqs. (8) and (9)

$\mathbf{b}$ = column vector containing $b_1, b_2, \ldots b_n$

b_i = $B(\mathbf{u}_i)$

$dA_j(\mathbf{u}_j)$ = infinitesimal area element

$\hat{e}_{jk}(\mathbf{u_j},\mathbf{u_k})$ = unit vector in the direction $\mathbf{r_{jk}}$, Figure 2

F_{01} = dimensionless heat transfer in enclosure of Fig. 8

$G(\mathbf{u})$ = generalized reflectivity term

G_i = see Eqs. (8) and (9)

$\mathbf{g}$ = Column vector containing $g_1, g_2, \ldots g_n$

g_i = $G(\mathbf{u_i})$

$J_j(\mathbf{u_j})$ = surface discriminant, see Eq. (4)

$K(\mathbf{u},\mathbf{u}')$ = kernel function of a two-variable integral equation

$k(u,u')$ = kernel function of a single-variable integral equation

N = number of enclosure surfaces

n = number of discrete elements

$\hat{n}_j(\mathbf{u_j})$ = unit normal vector at $\mathbf{u_j}$

$P_j(\mathbf{u_j})$ = x-component of $\mathbf{S_j}(\mathbf{u_j})$

p = exponent for Richardson extrapolation, Eq. (23)

$T(\mathbf{u})$ = temperature at $\mathbf{u}$, K

Q_j = total heat leaving surface j

$Q_j(\mathbf{u_j})$ = y-component of $\mathbf{S_j}(\mathbf{u_j})$

$q_o(\mathbf{u})$ = radiosity at $\mathbf{u}$, W/m^2

$\mathbf{q_o}$ = column vector containing $q_{o1}, q_{o2}, \ldots q_{on}$

$q_s(\mathbf{u})$ = imposed heat flux at $\mathbf{u}$, W/m^2

$\mathbf{r}$ = position vector

$\mathbf{s_{jk}}(\mathbf{u_j},\mathbf{u_k})$ = vector from $\mathbf{S_j}(\mathbf{u_j})$ to $\mathbf{S_k}(\mathbf{u_k})$, Fig. 2

$R_j(\mathbf{u_j})$ = z-component of $\mathbf{S_j}(\mathbf{u_j})$

R_{uv} = parametric region on u-v plane

$\mathbf{S_j}(\mathbf{u_j})$ = parametric vector function defining a surface in three-dimensional space

u,v = parameters for surface representation

$\mathbf{u}$ = two-component vector equivalent to (u,v)

w_i = weights used to enforce summation rule, Eq. (22)

ε = emissivity

ε_a = apparent emissivity

ρ = reflectivity

Φ = non-dimensional radiosity distribution within a heated cylinder

Φ_q^* = non-dimensional radiosity distribution within an adiabatic cylinder

θ_{jk} = angle between $\hat{e}_{jk}$ and $\hat{n}_j$, Fig. 2

Subscripts and Superscripts

i, k = discrete element indices

j, k = surface indices

N = number of elements

References

[1] Siegel, R., and Howell, J. R., 1992, *Thermal Radiation Heat Transfer*, 3rd Ed., Taylor and Francis, Washington D.C., p. 288.

[2] Modest, M. F., 1993, *Radiative Heat Transfer*, McGraw-Hill, New York, p. 213.

[3] Eckert, E. R. G., and Drake, R. M., 1987, *Analysis of Heat and Mass Transfer*, 2nd Ed., Hemisphere, Washington, D.C., p. 640.

[4] Buckley, H., 1927, ''On the Radiation From the Inside of a Circular Cylinder,'' Philos. Mag., **4**, pp. 753–762.

[5] Buckley, H., 1928, ''On the Radiation from the Inside of a Circular Cylinder—Part II,'' Philos. Mag., **6**, pp. 447–457.

[6] Hottel, H. C., and Keller, J. D., 1933, ''Effect of Reradiation on Heat Transmission in Furnaces and Through Openings,'' Trans. ASME, **53**, pp. 39–49.

[7] Sparrow, E. M., and Albers, L. U., 1960, ''Apparent Emissivity and Heat Transfer in a Long Cylindrical Hole,'' J. Heat Transfer , **82**, pp. 253–255.

[8] Sparrow, E. M., Albers, L. U., and Eckert, E. R. G., 1962, ''Thermal Radiation Characteristics of Cylindrical Enclosures,'' J. Heat Transfer , **84**, pp. 73–80.

[9] Usiskin, C. M., and Siegel, R., 1960, ''Thermal Radiation from a Cylindrical Enclosure with Specified Wall Heat Flux,'' J. Heat Transfer , **82**, pp. 369–374.

[10] Sparrow, E. M., and Haji-Sheikh, A., 1965, ''A Generalized Variational Method for Calculating Radiant Interchange Between Surfaces,'' J. Heat Transfer, **87**, pp. 103–109.

[11] Sparrow, E. M., and Haji-Sheikh, A., 1970, ''The Solution of Radiative Exchange Problems by Least Squares Techniques,'' Int. J. Heat Mass Transf., **13**, pp. 647–650.

[12] Haji-Seikh, A., 1988, ''Monte Carlo Methods'' in *Handbook of Numerical Heat Transfer*, W. J. Minkowycz et al., eds. Wiley, New York, pp. 673–717.

[13] Siegel, R., and Howell, J. R., 1992, *Thermal Radiation Heat Transfer*, 3rd Ed., Taylor and Francis, Washington D.C., p. 480.

[14] Tan, Z., Wang, D., Srinivasan, K., and Prezekwas, A. J., 1998, ''Numerical Simulation of Coupled Radiation and Convection for Complex Geometries,'' *Proceedings, 7th AIAA/ASME Joint Thermophysics and Heat Transfer Conference*, Albuquerque, New Mexico, July 15–18, 1998, AIAA.

[15] Piegl, L., and Tiller, W., 1997, *The NURBS Book*, 2nd Ed., Springer-Verlag, Berlin.

[16] Farin, G., 1997, *Curves and Surfaces for CAGD: A Practical Guide*, 4th Ed., Academic Press, New York.

[17] Adams, R. A., 1987, *Calculus of Several Variables*, Addison-Wesley, Don Mills, pp. 214–216.

[18] Chapara, S. C., and Canale, R. P., 1988, *Numerical Methods for Engineers*, 2nd Ed., McGraw-Hill, New York, p. 266.

[19] Ferziger, J. H., and Peric, M., 1996, *Computational Methods for Fluid Dynamics*, Springer-Verlag, Berlin, p. 59.

[20] Glassner, A. S., *An Introduction to Ray-Tracing*, London Academic.

[21] Qin, K., Gong, M., Guan, Y., and Wang, W., 1997, ''A New Method for Speeding Up Ray Tracing NURBS Surfaces,'' Comput. Graph., **21** No. 5, pp. 577–586.

Nucleate Pool Boiling From Coated and Spirally Wrapped Tubes in Saturated R-134a and R-600a at Low and Moderate Heat Flux

Shou-Shing Hsieh
Sun-Yat Sen Professor
of Mechanical Engineering,
Dean of Engineering
Fellow ASME

Tsung-Ying Yang
Graduate Student

Department of Mechanical Engineering,
National Sun-Yat Sen University,
Kaohsiung, Taiwan,
Republic of China

Pool nucleate boiling heat transfer experiments from coated surfaces with porous copper (Cu) and molybdenum (Mo) and spirally wrapped with helical wire on copper surfaces with micro-roughness immersed in saturated R-134a and R-600a were conducted. The influence of coating thickness, porosity, wrapped helical angle, and wire pitch on heat transfer and boiling characteristics including bubble parameters were studied. The enhanced surface heat transfer coefficients with R-600a as refrigerant found are 2.4 times higher than those of the smooth surfaces. Photographs indicate that the average number of bubbles and bubble departure diameters has been found to increase linearly with heat flux, while the bubble diameters exhibit opposite trend in both refrigerants. Furthermore, the heat transfer of the boiling process for the present enhanced geometry (coated and wrapped) was modeled and analyzed. The experimental data for plasma coating and spirally wrapped surfaces were correlated in terms of relevant parameters, respectively to provide a thermal design basis for engineering applications. [DOI: 10.1115/1.1351818]

1 Introduction

Many water chillers of the centrifugal type have evaporators utilizing a flood type of operation whereby the water is circulated through the tube and refrigerant evaporated on the shellside of the tubes which is an area of nucleate boiling. While designing the evaporator of such a system, one must be able to accurately predict the boiling heat transfer coefficients of the refrigerants used. However, the prediction of the heat transfer coefficient is difficult because the boiling phenomenon is rather complex and is influenced by many variables, such as surface conditions, heater size, geometry, material, and refrigerants, etc. In addition, most refrigeration systems are expected to perform at a high coefficient of performance and energy efficiency. One method of achieving this goal is to enhance the boiling heat transfer coefficient between the refrigerant and the heat source in the evaporator.

Various methods of enhancing nucleate boiling heat transfer have been described by Thome [1] which provided a comprehensive survey, and discussed the fundamental phenomena of boiling on enhanced surfaces. These surfaces can take a number of forms from simple low integral fins with varying fin profile to more complicated re-entrant cavity type surfaces such as structured and porous coated surfaces. Moreover, various materials have been attached to the surfaces of plates and wound on tubes in an attempt to augment nucleate pool boiling heat transfer such as wires for both wetting (metallic) and non-wetting (nylon) conditions (see Thome [1]). Although a considerable amount of published data exists in the literature on nucleate boiling enhancement, little study has been done on the effects of plasma coating techniques as well as wire spirally wrapped on these surfaces. Recently, Hsieh and Weng [2] reported a study of nucleate pool boiling from plasma coated surfaces in saturated R-134a and R-407c.

In recent years, environmental concerns over the use of CFCs as working fluids in refrigeration and air-conditioning plants have led to the development of alternative fluids. Among these alternatives, R-134a and R-600a are used as a replacement for the commonly used CFC-12. Moreover, considerable effort has recently been made to find ways to design more compact and efficient evaporators for the process and refrigeration industries based on CFCs/non-CFCs. Industries are currently undergoing a massive conversion process from CFC to HFC (like R-134a) or HC (like R-600a). The conversion establishes a need for refrigerant data on the replacement refrigerants such as R-134a and R-600a used in this study. The objective of this paper is to develop a surface treatment with coating and/or wrapped process that will provide high heat transfer rates in nucleate pool boiling and to enlarge the pool boiling data for alternative refrigerants of R-134a and R-600a. Moreover, the entire heat transfer of boiling process for the present enhanced tubes was also modeled.

2 Analysis

One of the objectives of the present study is to model the heat transfer of the boiling process for the present enhanced geometry. Following Hsieh et al. [3], the present boiling phenomena can be analyzed as follows: The heat transfer model proposed for this study involves the thermal layer forming at the nucleation sites between periods of bubble nucleation and thin film evaporation, a turbulent natural convection mechanism taking place in the regions uninvolved in bubble nucleation. Model verification was performed through nucleate pool boiling experimental data for the present enhanced geometries for two different working fluids of R-600a and R-134a.

To accomplish these aforementioned tasks, the following work was conducted (1) modeling for heat transfer mechanism was developed using the model in which there are natural convection, transient conduction, and microlayer evaporation on boiling heat transfer, and (2) verification of boiling heat transfer model using both R-600a and R-134a was conducted. Detailed model description can be found in Hsieh et al. [3].

3 Experimental Setup and Procedure

3.1 Test Facility and Test Section. The experimental apparatus for the study is shown in Fig. 1. It consists rectangular container with the dimensions of 300×370×200 mm made from

Contributed by the Heat Transfer Division for publication in the JOURNAL OF HEAT TRANSFER. Manuscript received by the Heat Transfer Division August 3, 2000; revision received December 4, 2000. Associate Editor: F.-B. Cheung.

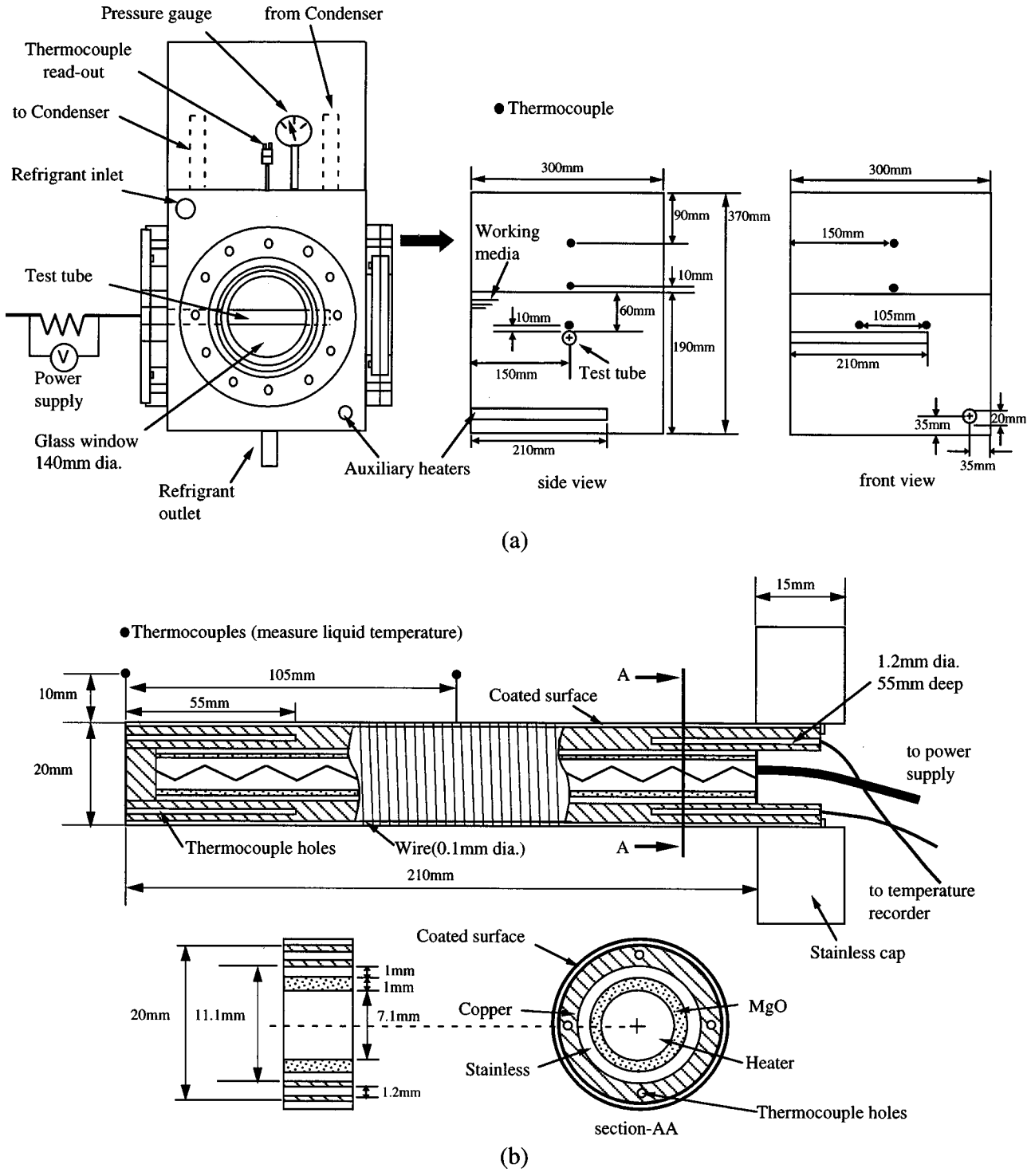

Fig. 1 Pool boiling apparatus setup: (*a*) test section; (*b*) thermocouple positions and test specimen

stainless steel, a stainless steel side panel provided with ports for electric wires, a pressure gauge and thermocouples, a vacuum pump, a reflux condenser, auxiliary heaters, and a test section support. Insulation was peripherally provided on the outside of the tank. The evaporator tube was designed to simulate a portion of a typical rod in refrigerant-flooded evaporator. It was fabricated from a copper tube. The test specimen is soldered to a flange at one end of the tank. The copper tubes were 20 mm in outer diameter, with an inner diameter of 12 mm. Each cartridge heater was 220 mm long with an actual heated length of 210 mm and 11.95 mm in diameter with a maximum power output 378W and was inserted into the copper tube. Thermal contact between the heater and the tube is enhanced by applying a two walled structure (Mgo+stainless steel) of heat sink compound on the heater before installing it in the tube. The test section included both smooth and treated surfaces. The dimensional specifics of the surfaces treated and given in Table 1.

The eight test specimens studied had the general characteristics shown in Fig. 1. Four holes of 1.2 mm diameter and 55 mm deep were drilled at each end of the tubes at 90 deg intervals with the

Table 1 The specifications and dimensions of treated surfaces

Tube No. (designated symbol)	surface(coating material)	helical wire (angle)	thickness of porous layer $\delta(\mu m)$	surface roughness Ra(μm)	porosity ε	mean pore diameter $\eta(\mu m)$
Tube1(S)	smooth	——	——	0.05	——	——
Tube2(S2)	smooth	2°	——	0.03	——	——
Tube3(S1.5)	smooth	1.5°	——	0.06	——	——
Tube4(S1)	smooth	1°	——	0.07	——	——
Tube5(CM)	Mo	——	300	6.63	0.053	3
Tube6(CM1)	Mo	1°	300	6.67	0.055	3
Tube7(CU)	Cu	——	100	7.84	0.057	4
Tube8(CU1)	Cu	1°	100	7.69	0.058	4

axis within about 1.2 mm of the smooth surface for insertion of wall temperature thermocouples. The tubes with coating surfaces were provided by Metal Industrial Research and Development Center (MIRDC) of Taiwan.

The porosity (ε), thickness of porous layer (δ) and mean pore diameter (η) of the coated surfaces were calculated according to photographs of the polished samples using an image analysis software like OPTIMAS provided by Industrial Technology Research Institute (ITRI) of Taiwan, and the surface roughness (Ra) was measured by a profile measuring device and a readout by a Surfer order SE-3000 developed by Lusaka Laboratory Ltd. The detailed characteristics of the coated surfaces and the dimensions of the tubes tested are also listed in Table 1. Note that even smooth surfaces have a micro-roughness.

The bubble development process was viewed through a gated, intensified, high-resolution CCD video camera (JVC Model CCD Gr-DVM70) in a direction normal to the test tubes. Video imaging system was used to record and capture the images of vapor bubble above (about one bubble diameter to warrant the bubble departure completely) the heated surface. This system is capable of shutter speeds up to 1/500th of a second and can provide images at a speed of 30 frames per second with an aperture of F8 and a time delay between two frames smaller than 50 nanoseconds.

This indicates that the camera provides capability to ''freeze'' the growing and departure bubbles on the heating surfaces every 1/30 s. Successive frames are individually viewed to determine the number of bubbles, the bubble departure diameters, and the bubble departure frequencies. The video image was magnified by a factor of 5 using a focal length of 16 cm. The lighting provided by one LPL-BROM CINE 500W floodlight was filtered through a diffuser for the video photography. Video images were synchronized and transferred to an IBM 586 PC, where they were digitized by a frame grabber board and analyzed by image processing software. This commercially available (MGI Video Wave III, Canada) with custom-modified software can rapidly obtain the vapor characteristics above the heated surfaces for the number, sizes, frequencies of bubbles, and the motion analysis of the selected sites for a sequence of images.

Calibrated copper-constantan (T-type) sheath thermocouples of diameter 1.1 mm were employed to measure the wall temperature. To minimize longitudinal heat conduction, silicon rubber and Devon five minute epoxy glue mixed with polystyrene foam were applied at the ends for the use with R-600a and R-134a. The liquid temperature in the container was measured by two thermocouples placed 20 mm below the free surface of the liquid and were positioned midway and the end along the tube. The temperature difference between these two points was between ± 0.1 °C at the maximum power input. Another two thermocouples were used to measure the vapor temperature and was positioned midway along the tube about 10 mm and 105 mm, respectively above the liquid surface.

Table 2 Properties of R-134a at 18 °C, 537.06 kPa (data from ICI), R-600a at 18 °C, 283.91 kPa (data from ASHRAE)

Properties	R-134a	R-600a
composition(formula)	CH_2F-CF_3	C_4H_8
substitute for	R-12	R-12
ODP[R-11=1.0]	0	0
GWP[R-11=1.0]	0.26	0
Flammability	No	Yes
toxicity [AEL(TLV)][ppm]	1000	1000
boiling temperature at 1 atm [° C]	-26	-11.6
critical pressure [MPa]	4.05	3.64
reduced pressure	0.132	0.078
critical temperature [° C]	101	134.7
lubricant (compressor)	(Polyol-)Easter	-
ρ_l [kg/m^3]	1232.1	559.3
ρ_v [kg/m^3]	26.089	7.450
C_{pl} [kJ/kgK]	1.396	2.411
C_{pv} [kJ/kgK]	0.971	1.763
h_{fg} [kJ/kg]	184.19	337.39
k_l [W/mK]	0.0851	0.0987
μ_l [μPa.s]	231.2	163.0
σ [N/m]	0.00919	0.01091
molecular weight	102.030	58.125
boiling point [bar]	3.421(at 4.4 ° C)	1.927(at 6 ° C)
Prandtl number(liquid at 18 ° C)	3.793	3.982

Note: ODP: Ozone Depletion Potential GWP: Global Warming Potential
AEL: Allowable Exposure Limit TLV: Threshold Limit Value

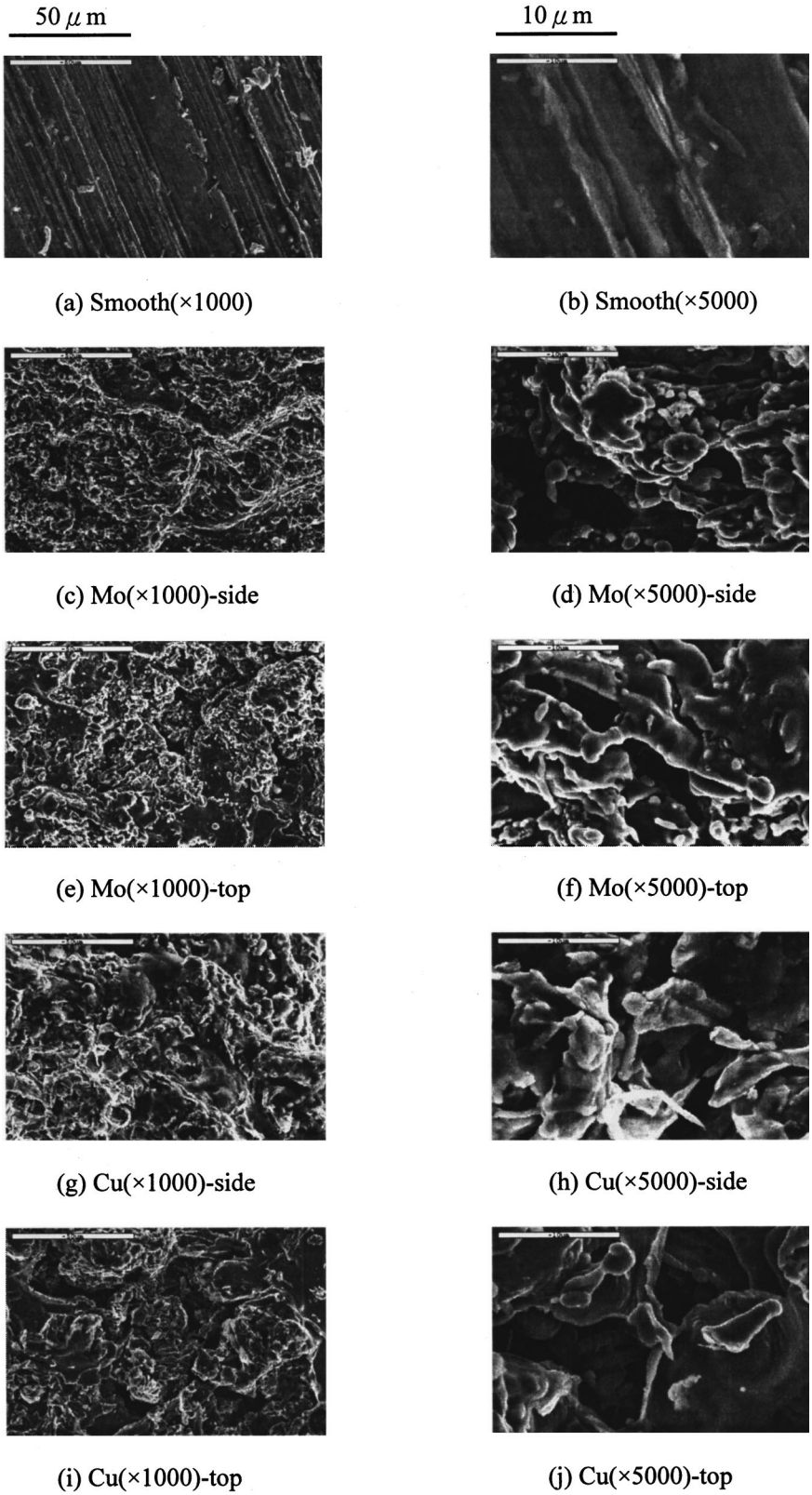

Fig. 2 SEM photographs (×1000 and ×5000) of enhanced tube microstructure

3.2 Working Fluid Used. The working fluid enhancement technique and its preparation used in the present experiments were R-600a and R-134a. The properties of R-600a or R-134a supplied by ICI (Imperial Chemical Industries) Chemicals and Polymers Limited and ASHRAE (American Society of Heating, Refrigeration and Air Conditioning Engineers) are given in Table 2. During all the tests, the saturation temperature was kept near 18 °C. It is found that there is a higher latent heat value for R-600a as compared to that of R-134a. So is the surface tension. Using R-600a to replace R-134a seems promising in the near future if the flammability problem of the R-600a can be solved.

3.3 Enhanced Surface Preparation. Two types of enhancement techniques were used; one is plasma coating and one is wire spirally wrapping. For plasma coating, a scanning electron microscope (SEM) image of several typical treated surfaces including smooth surfaces with micro-roughness is depicted in Fig. 2.

The substrate material used in the present study is copper. The surfaces of the test copper tubes were first polished by an emery paper (No. 500). Plasma spraying of Cu ($k=401$ W/mK) and Mo ($k=138$ W/mK) was carried out using PT-F4 plasma gun at 28 to 52.5 kW power for the purpose of observing any effect that may be produced by differences in thermal conductivity of the substrate material. The plasma jet is about 5 to 10 cm long and the nozzle-substrate distance is about 14 cm. The carrier gas is Ar+ H_2 flowing typically at 41 min^{-1}. Helium was added to increase gas flow and Cu and Mo powders with grain sizes 45 to 135 μm were used. The plasma condition was: a 750 A current, a 310 g h^{-1} powder feed rate, a substrate temperature of 200 °C and a 14 cm spraying distance. Two tubes were wrapped with 0.1 mm diameter copper helical wire with/without coating. The wires were carefully wrapped so as to be in tight contact with the heating surface. Before starting each experiment, the heating surface was again polished with No. 1000 emery paper to obtain the same surface condition for all runs. Table 1 gives more detailed data regarding the three types of surface treatments in the present study. Three smooth tubes and two coated tubes were also wrapped with 0.1 mm diam. copper wire. The helical angle was defined as $\theta=\tan^{-1}p/\pi d_o$, where d_o is the smooth tube outside diameter and p is the pitch of wire ($\theta=2$ deg, $p=1.97$ mm; $\theta=1.5$ deg, $p=1.48$ mm; and $\theta=1$ deg, $p=0.99$ mm).

3.4 Experimental Procedure. Prepared test sections were cleaned with chlorinol and water and finally, with acetone. The tank was cleaned with acetone before each run. Once the evaporator tube was installed, the system was evacuated to a pressure of about 30 Pa. If no leaks were detected over a 24 h interval, the evaporator was charged with the washing fluid from a reservoir to a level of 60 mm above the top of the tube. This resulted in a vapor pressure of 537.06 kPa (R-134a) and 283.91 kPa (R-600a), respectively.

The power was given to the pool to degas the test fluids, R-134a and R-600a, at heat flux of 30 kW/m^2 for 1.5 h and 1 h, respectively. The saturation temperature at the measured pressure was compared to the pool temperature measured by the thermocouple. The power supplied to the test section was gradually, and slowly, reduced to zero. The test pool was maintained close to the saturation temperature with an auxiliary heater for about 40 min; then it was switched off to minimize convective effects. The heating power supplied to the test section was slowly and gradually increased to nearly 30 kW/m^2. Both increasing and decreasing heat flux data were taken in order to obtain more accurate data and to observe boiling hysteresis. For the decreasing data, the heat flux was reduced from 30 kW/m^2 in pre-determined steps by means of a variac. It generally took about 30 min to achieve steady conditions after the power level was changed.

During all the tests, the saturation temperature was kept near 18 °C for both R-134a and R-600a supplied by ICI and ASHRAE, respectively. More detailed relevant properties of the refrigerants in this study are given in Table 2. The liquid level was kept approximately 60 mm above the test tube. All the data were obtained and reduced with a computer-controlled data acquisition system.

3.5 Precautions Taken During Experiments. In measuring boiling heat transfer coefficients, great care must be exercised to ensure good accuracy. The following lists are those precautions:

1 The pool temperature was compared to the saturation temperature corresponding to the measured saturation pressure for refrigerants. This ensures that there are no noncondensibles in the container. It also verifies that there is no subcooling in the liquid pool within ±0.2 °C.

2 To ensure that the correct wall temperature was measured, a tightly pressed thermocouple was put onto the wall of a sleeve insert with thermal jointing compound applied to the tube. In addition, a three-dimensional heat transfer model was employed to correct the wall temperature measured (i.e., to minimize the conductance and capacitance effect) to obtain a more accurate (or nearly true) wall temperature. Consequently, 0.1 °C accuracy was expected.

3 The heater was tested for circumferential uniformity of heat flux. Nonuniformities in the heat flux were smoothed out followed the methodology described in Hsieh and Weng [2].

4 Precautions were taken against aliasing and overlapping images by repeating the experiments several times and keeping track the bubble path very accurately at low heat flux levels (≤900 kW/m^2).

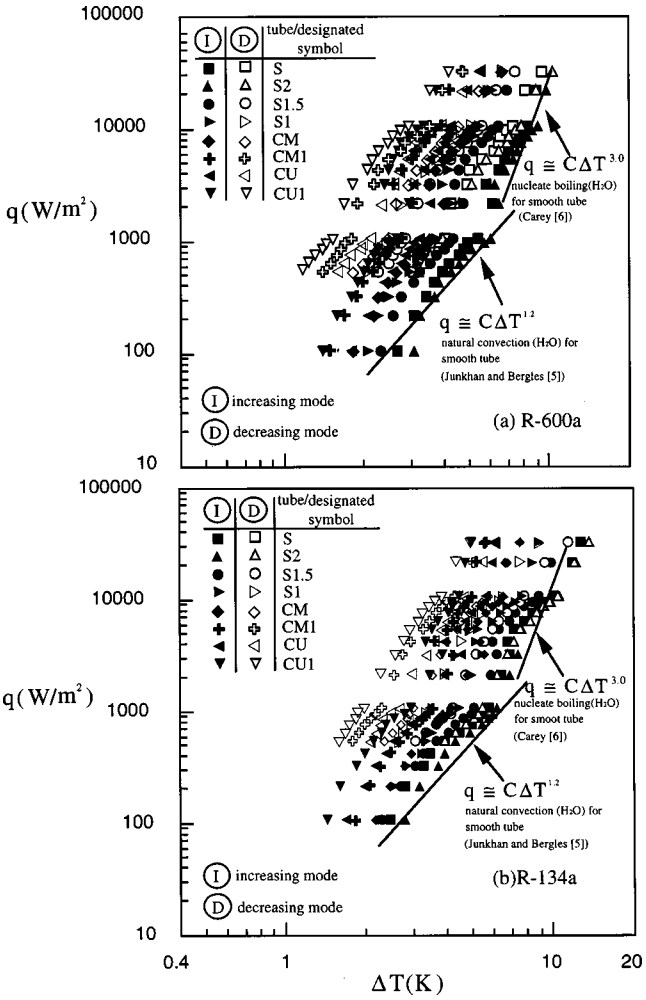

Fig. 3 Boiling curves of enhanced tubes for R-600a and R-134a

4 Data Reduction and Uncertainty Analysis

For each power input, the heat transfer coefficient was calculated on the basis of bulk fluid saturation temperature (T_{sat}), tube heat flux, and the average (T_{avg}) of the four tube wall temperatures. The heat transfer coefficient at each power input was then calculated, following $h=Q/[A(T_{avg}-T_{sat})]$ when A is the heated area of the tube.

Table 3 Degree of superheat and departure diameter in the present study

Refrigerant	Designated symbol	Tube	Degree of superheat ΔT[K]	r_b[μm]*	$2r_b$	d_b[mm] (experiment)	d_b[mm] (Zuber [10])
R-600a	S	Smooth	6.2	0.35	0.70	1.30	1.32
	S2	Smooth ($\theta = 2^\circ$)	6.5	0.33	1.06	1.51	1.34
	S1.5	Smooth ($\theta = 1.5^\circ$)	4.8	0.47	0.94	1.11	1.21
	S1	Smooth ($\theta = 1^\circ$)	4.3	0.53	0.66	0.98	1.17
	CM	Coated surface (Mo)	4.1	0.57	1.14	0.84	1.15
	CM1	Coated surface (Mo) ($\theta = 1^\circ$)	3.1	0.76	1.52	0.73	1.05
	CU	Coated surface (Cu)	3.6	0.64	1.28	0.77	1.10
	CU1	Coated surface (Cu) ($\theta = 1^\circ$)	3.0	0.77	1.54	0.67	1.04
R-134a	S	Smooth	7.0	0.13	0.26	0.82	0.95
	S2	Smooth ($\theta = 2^\circ$)	7.5	0.12	0.24	0.85	0.97
	S1.5	Smooth ($\theta = 1.5^\circ$)	6.3	0.15	0.30	0.66	0.92
	S1	Smooth ($\theta = 1^\circ$)	5.5	0.16	0.32	0.62	0.88
	CM	Coated surface (Mo)	6.0	0.15	0.30	0.53	0.85
	CM1	Coated surface (Mo) ($\theta = 1^\circ$)	4.3	0.23	0.46	0.49	0.81
	CU	Coated surface (Cu)	4.6	0.21	0.42	0.50	0.83
	CU1	Coated surface (Cu) ($\theta = 1^\circ$)	3.9	0.24	0.48	0.47	0.78

* : upon boiling incipience
r_b : embryonic bubble radius
d_b: bubble departure diameter

Using the method of Kline and McClintock [4], uncertainty estimates were made considering the errors of the instruments, the measurement variance, geometry uncertainty and calibration errors for the heat flux, temperature, and bubble dynamic parameter measurements. The uncertainty in the wall superheat was dominated by the uncertainty in the wall temperature measurements. The value of the four wall temperatures were recorded and compared for examining the variations caused either by nonuniformities in the cartridge heater or by the test tube soldering and assembly procedure. Wall superheat uncertainty can be attributed primarily to thermocouple calibration (± 0.1 °C) and temperature correction from the thermocouple reading to the reference surface. The maximum variation of the four measured wall temperatures was ± 0.3 °C at the maximum heat flux ($\cong 30$ kW/m^2). The uncertainty in the saturation temperature was estimated to be less than ± 0.1 °C.

Substrate conduction heat losses were quantified at different heat flux conditions by solving three-dimensional conduction problems with a finite-difference solver. This loss varied between 10.2 percent and 0.2 percent for heat flux conditions between 0.8 kW/m^2 to 30 kW/m^2, respectively. The other primary contributor to heat flux uncertainty was heated surface area. Combining these effects lead to overall uncertainty estimates in heat flux of 11.2 percent at the lowest heat input. Based on these uncertainties, it indicates the uncertainty of the wall heat transfer coefficient to be about ± 15 percent at $q = 0.8$ kW/m^2.

Accuracy of the diameter measurements is estimated within ± 1.9 percent/ or ± 0.6 percent at the minimum/or maximum diameter with an extreme high space resolution (~ 9.5 nm) of CCD camera. The uncertainty in the number of bubbles was found within ± 7.1 percent for the minimum and ± 4.9 percent for the maximum number of bubbles. Uncertainty estimates for time is ± 1.7 percent. The frequencies reported are average values and the observed fluctuations in frequency are less than ± 8 percent. The data presented refer to individual and isolated bubbles.

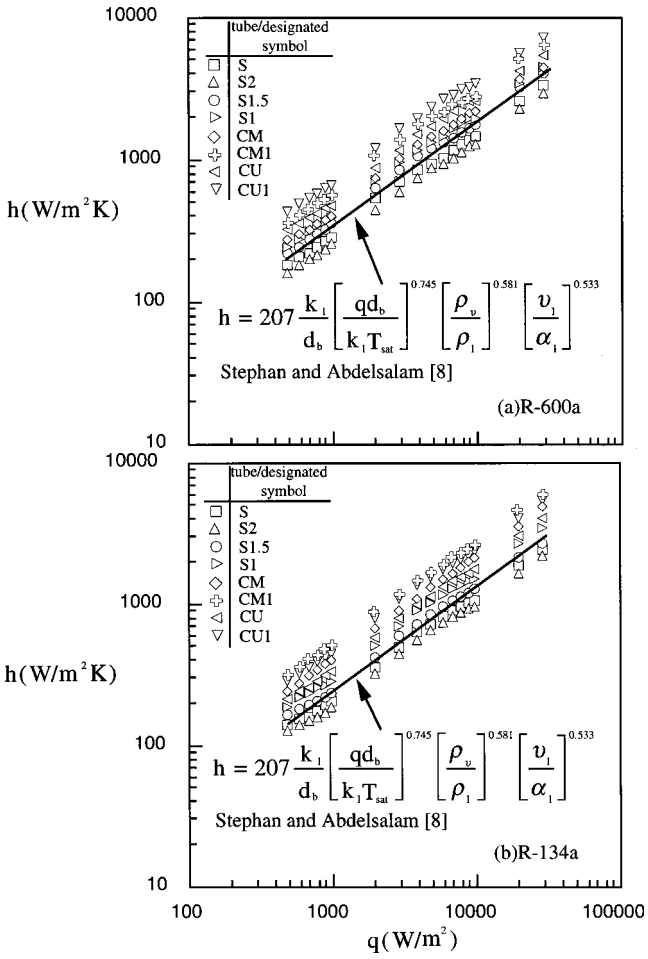

Fig. 4 Heat transfer comparison for R-600a and R-134a

Table 4 Enhancement of present coated/wrapped tubes

Relevant studies	Refrigent	Coating material	Surface roughness (μm)	Helical angle (°)	h/h_s Heat flux (kW/m^2) 5	10	20
present study	R-600a	smooth	0.05	—	1.00	1.00	1.00
		smooth	0.03	2	0.88	0.91	0.90
		smooth	0.06	1.5	1.20	1.21	1.24
		smooth	0.07	1	1.39	1.42	1.44
		Mo	6.63	—	1.57	1.62	1.63
		Mo	6.67	1	2.12	2.16	2.15
		Cu	7.84	—	1.82	2.01	1.93
		Cu	7.69	1	2.29	2.37	2.20
present study	R-134a	smooth	0.05	—	1.00	1.00	1.00
		smooth	0.03	2	0.87	0.89	0.88
		smooth	0.06	1.5	1.16	1.19	1.17
		smooth	0.07	1	1.40	1.42	1.43
		Mo	6.63	—	1.57	1.54	1.53
		Mo	6.67	1	2.00	2.14	1.97
		Cu	7.84	—	1.79	1.77	1.76
		Cu	7.69	1	2.05	1.95	2.02
Hsieh and Weng [2]	R-134a	Mo	11.30	—	1.92	1.94	1.80
		Cu	6.79	—	1.70	1.79	1.68
		Al	13.58	—	1.91	1.95	1.81
		Zn	8.90	—	1.68	2.07	2.34

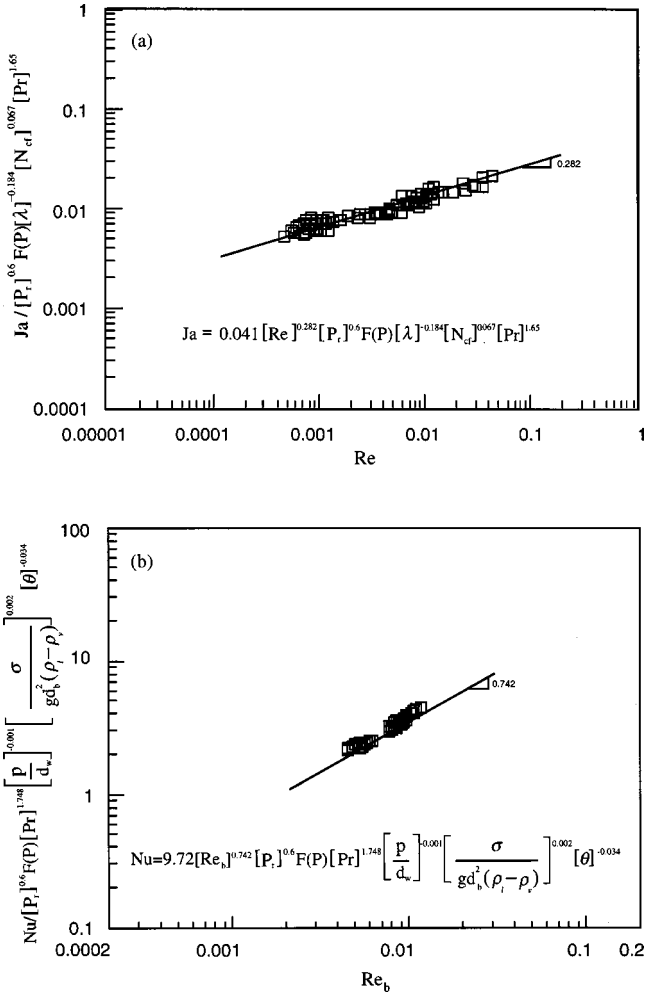

Fig. 5 The present correlation with experimental data

5 Results and Discussions

More than 80 tests runs were performed on smooth and coated and wrapped tubes in saturated R-134a and R-600a. Some of these tests were repeated after several months to verify the reproducibility. The repeated data agreed well and were within the previously mentioned experimental accuracy.

A typical result of JSM-6400 SEM examination for the surface images (×1000 and ×5000) of smooth and coated tubes is illustrated in Fig. 2(*a*)–(*j*), respectively. The references surface (smooth) has a sparse number of small cavities (<0.5 μm) for both image (×1000 and ×5000). Figures 2(*c*)–(*f*) illustrate the SEM image (×1000 and ×5000) with Mo coated tubes from top and side view. The distribution appears rather random in these micrographs (×5000). The microstructures are laid with a total thickness ≅300 μm and results in a cavity size of about 3 μm. Again, surface orientation is random, some lying vertically and some horizontally, which produces a porous microstructure with a mean pore diameter of 3 μm and a porosity of 0.053 with Cu coated. Figures 2(*g*)–(*j*) indicate a higher mean pore diameter (4 μm) and a higher porosity of 0.057 but a lower value of thickness of porous layer (≅100 μm). The multi-layered porous structures result in increased nucleate sites above the substrate (base) material as shown in Figs. 2(*c*)–(*i*) which are believed to provide reentrant cavities and to have a large variation in pore size and shape. This structure appears beneficial for the entrapment of vapor and generation of nucleation sites as well as function as a vapor escape passage.

5.1 Boiling Characteristics. The present heat transfer characteristics were governed by porous layer thickness, the pore diameter, the surface porosity, the contact angle and their complex effect for the tubes with plasma coating; while for spirally wrapped tubes, the helical angle and pitches of the wire and their combined effect would have some influences on heat transfer behavior. Figure 3 compares pool boiling data for the smooth and coated surface as well as helical wire wrapped tubes at identical bulk liquid conditions for R-600a and R-134a, respectively, as shown in Figs. 3(*a*) and (*b*). Also included in Fig. 3(*a*) are the results for water in natural convection (Junkhan and Bergles [5]) and nucleate boiling (Carey [6]) regimes, respectively for comparisons. Like Hsieh and Weng [2], for coated tubes, the effects due to the contact angle and surface porosity seem the same. Therefore, it appears that the parameters with the most influence are the porous layer thickness and the pore diameter of the treated surface which determines the probability of flooding the reentrant cavities and the degrees of superheat required for bubble growth.

The mechanism which described the boiling process from porous structures of the present plasma coating surfaces can be explained as follows; it appears that the heat is conducted to a liquid vapor at the upper surface of the porous structure. This conduction supposedly occurs through the matrix (see Fig. 2 for details) formed by the solid portion of these wick and liquid in the porous spaces. It is recognized that the vapor bubbles exist within the pores formed by the void space between two solid portions. Heat is transferred by conduction through the solid matrix and then by conduction across the liquid portion. The pores within the matrix are interconnected so that liquid can be supplied to the pores and

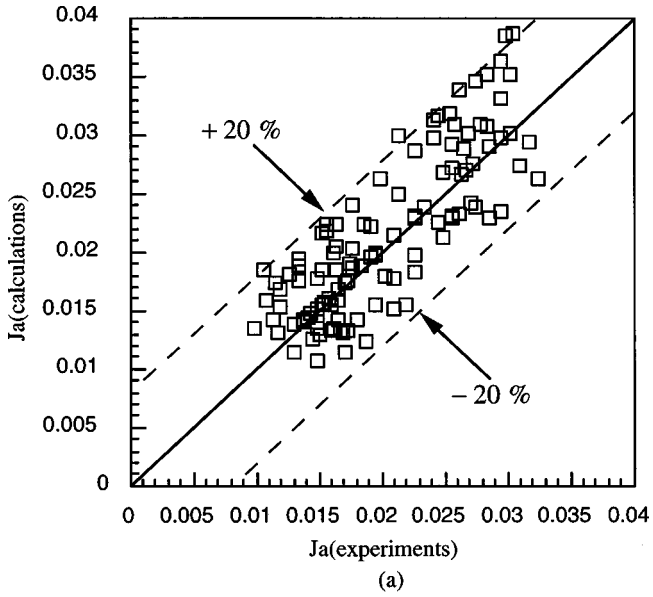

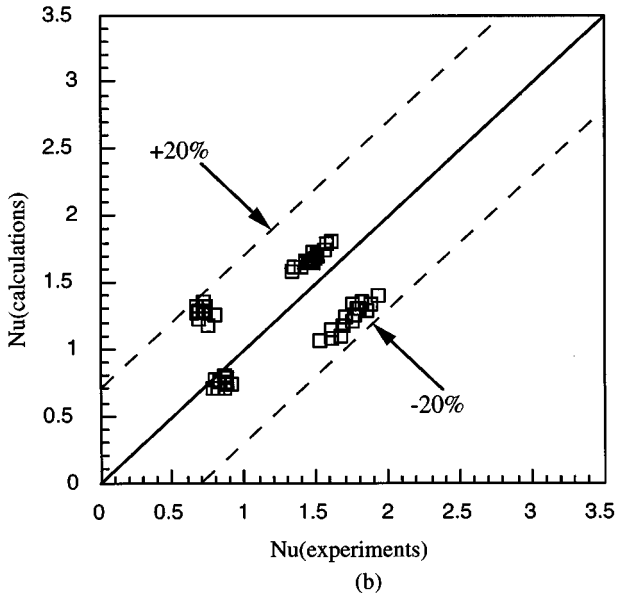

Fig. 6 The deviation with experimental data

vapor can pass through the matrix to the free liquid surface. As vapor is generated within a pore, the pressure in the vapor bubble increases [1]. When the pressure is sufficiently high, it overcomes the surface tension retention force and the vapor if forced through the interconnected channels (pores) to the liquid surfaces. On the other hand, for wrapped tubes, since the additional nucleation sites were created and the cross sectional area in the microstructure channel of the coated and smooth surface was reduced, the resulting boiling performances would be substantially improved. This is similar to the results found by Marto et al. [7]. The observed difference in the boiling curves are indications of variations in the surface microstructures between the smooth and enhanced surfaces. Again, like Hsieh and Weng [2], the data (see Fig. 3 for increasing heat flux) show that the hysteresis phenomenon can be observed for both smooth and enhanced surfaces. However, the hysteresis effect of the coated surfaces seems stronger (~1 K temperature overshoot for Cu coated but in R-600a) than that of smooth surface. This is because the porous matrix existed on coated surfaces was flooded with liquid so that only small sites are available for nucleation. In addition, due to almost the same contact angle for both R-134a and R-600a, the difference in hysteresis effect cannot be clearly seen in Figs. 3(*a*) and (*b*).

Moreover, the boiling curves in Fig. 3(*a*) show that the best heat transfer performance of the enhanced tubes one may obtain. This is because the coated (Cu and Mo) tubes with copper wire wrapped and helical angle $\theta=1$ deg, have more additional nucleation sites and, consequently, result in more vapor bubbles rising on the helical wire sides. Followed by the coated tubes (Cu and Mo) without wrapped wires and then, smooth tubes with wire wrapped. However, little difference in performance is discernible between Cu and Mo. For smooth tubes with helical wire wrapped, the heat transfer performance becomes lower as helical angle increases. Basically, there are three competing mechanisms which affect heat transfer performance for tubes with wrapped wires; namely, (*a*) as stated earlier, the cross sectional area was reduced resulting in heat transfer increase; (*b*) the boiling would be enhanced by refrigerant wetting capability; and (*c*) that the wire on the boiling surface would prevent the bubble from freeing itself from the surface, which would inhibit the boiling, and this effect would become bigger with decreasing wire pitch. Helical angle also seems to have some influence on heat transfer performance as evidenced by a bad heat transfer performance for helical angle $\theta=2$ deg as compared to those of $\theta=1$ deg and 1.5°. Similarly, Fig. 3(*b*) indicates the same trend as Fig. 3(*a*) does except R-134a as the refrigerant.

Generally, the heat transfer performance in R-600a is better than that in R-134a due to a relative higher latent heat value (almost two times) and surface tension force (19 percent higher) for R-600a. Furthermore, the enhanced tube as compared to the smooth surface demonstrate lower temperature differentials for initiation of vaporization and lower ΔT's for equal heat fluxes. The slope of the boiling curves as shown in Fig. 3 are usually steeper than the smooth surface slope indicating a situation where the enhanced surfaces are more effective in thermal transport than the smooth surfaces. In summary, the order of degree of superheat for total eight tubes using each designated symbol listed in Table 1 are the following: For R-600a, $\Delta T_{s2}>\Delta T_s>\Delta T_{s1}>\Delta T_{CM}>\Delta T_{cu}>\Delta T_{CM1}>\Delta T_{cu1}$; while, for R-134a, $\Delta T_{s2}>\Delta T_s>\Delta T_{s1.5}>\Delta T_{CM}>\Delta T_{s1}>\Delta T_{cu}>\Delta T_{CM1}>\Delta T_{cu1}$. Such corresponding values are listed in Table 3. Moreover, the values (heat transfer enhancement) of h/h_s are listed in Table 4 at $q=5$, 10, 20 kW/m^2, respectively. It is found that heat transfer enhancement was ranged from 1.16 to 2.37 for R-600a and R-134a refrigerant. Also listed in Table 4 are the data from Hsieh and Weng [2] in R-134a for comparison. Except that Fig. 3 shows, all boiling experiments were run with decreasing heat flux.

5.2 Heat Transfer Performance and Correlations. Generally speaking, as shown in Fig. 4(*a*) for R-600a the best heat transfer performance was found for Cu1 tube followed by CM1 tube, Cu tube, Mo tube, S1 tube, S1.5 tube, S tube, and the least value was found for S2 tube. The same trend was found for R-134a as also shown in Fig. 4(*b*). However, for Cu and Mo coated tubes with wrapped wire, the thermal performance again seems no big difference. Also included in Figs. 4(*a*) and (*b*) are the results from the correlation of Stephan and Abdelsalam [8] for smooth tube. The present smooth tube results agree well with those of [8]. Moreover, the trend appears the same as q increases for coated tubes.

Following Rudemiller and Lindsay [9] with dimensional analysis for the present study, a correlation for plasma coated tubes (without wrapped) of the present boiling data for both R-600a and R-134a was developed. In addition, the data for smooth tubes with wrapped wire were also correlated using relevant parameters.

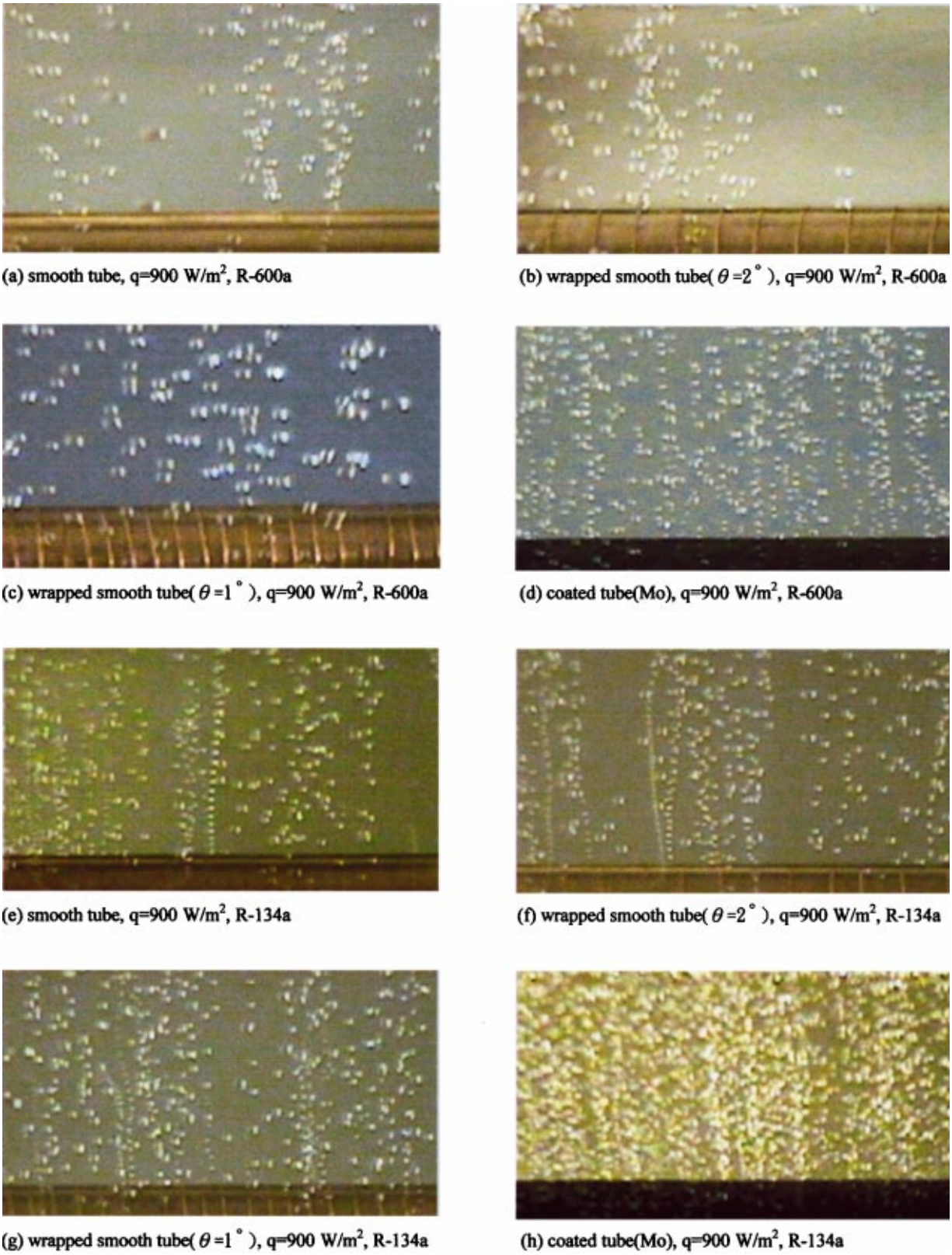

Fig. 7 Illustraiton of boiling visualizations

Both correlations are shown in Fig. 5. The pressure effect was also included in terms of reduced pressure ratio P_r through the present tests at only one reduced pressure for R-1334a and R-600a, respectively, and a pressure function *F(P)* (Carey [6]) for completeness. For plasma coating heating surfaces, the conventional Jacob number (Ja) defined as $C_{pl}\Delta T/h_{fg}$ was correlated in form of $\mathrm{Re}=q\eta/h_{fg}\mu_l\varepsilon$, where η is average pore diameter and ε is the porosity, geometric scale factor $\lambda=\eta/\delta$; δ is porous layer thickness and the constant heat flux number $N_{cf}=\mu_l^2/\eta\rho_l\sigma$. The correlation as shown in Fig. 5 has the following form

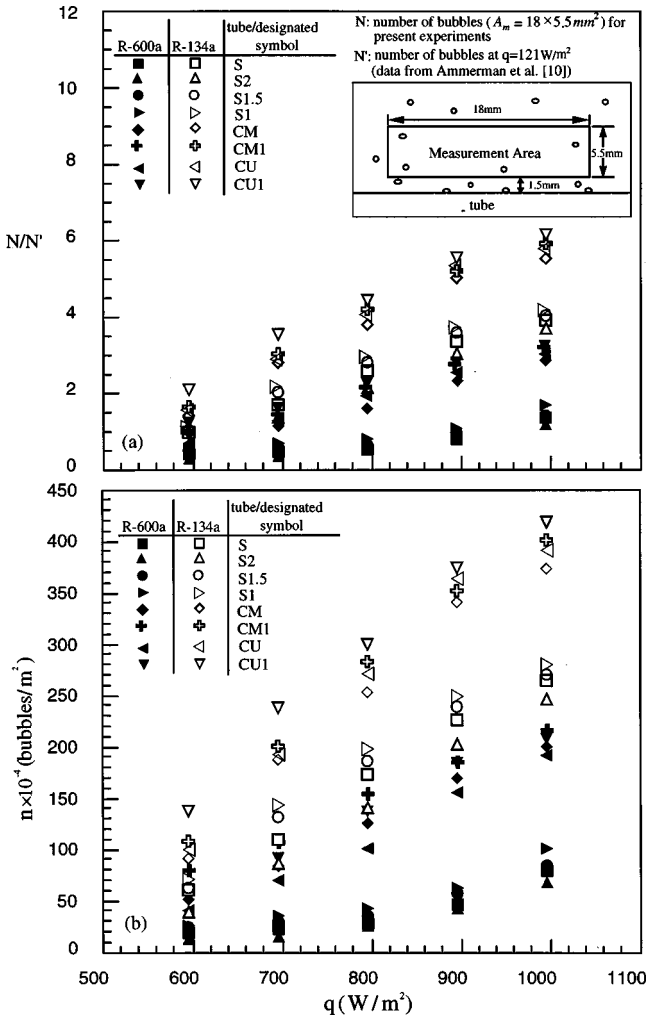

Fig. 8 Ratio of number of bubbles (N/N') and n in measurement area versus q

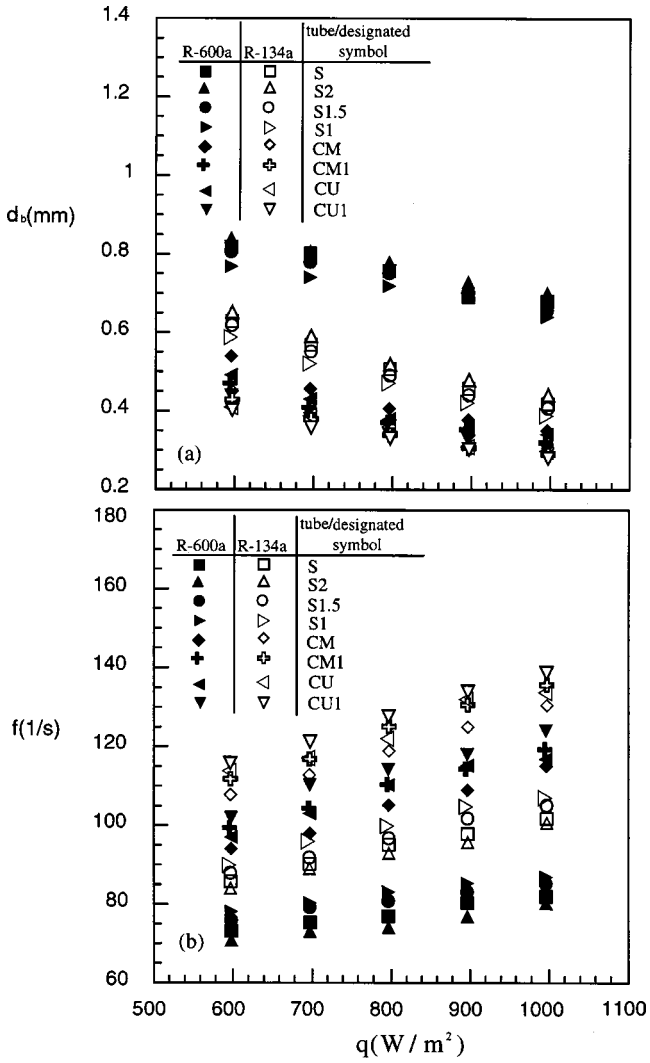

Fig. 9 Bubble departure diameter and frequency as function of heat flux

$$\mathrm{Ja}=0.041[\mathrm{Re}]^{0.282}[P_r]^{0.6}F(P)[\lambda]^{-0.184}[N_{cf}]^{0.067}[\mathrm{Pr}]^{1.65}$$

$$4.960\times10^{-4}\leqslant\mathrm{Re}\leqslant4.943\times10^{-2}$$

$$3.793\leqslant\mathrm{Pr}\leqslant3.982 \qquad (13)$$

$$1\times10^{-2}\leqslant\lambda\leqslant4\times10^{-2}$$

$$1.089\times10^{-3}\leqslant N_{cf}\leqslant1.574\times10^{-3}$$

$$F(P)=1.8P_r^{0.17}+4P_r^{1.2}+10P_r^{10},$$

which is applicable to the plasma coating without wire wrapped heating surfaces used in R-134a and R-600a. This correlation has the same form as Rudemiller and Lindsay [9] except the power dependence of each individual term.

For the smooth tubes with wire wrapped, the heat transfer coefficient $\mathrm{Nu}=hd_b/k$ can be represented as also shown in Fig. 5 in terms of Prandtl number (Pr), Reynolds number $\mathrm{Re}_b=qd_b/\mu_l h_{fg}$, dimensionless pitch of wire $=p/d_w$; p is pitch and d_w is the wire diameter, inverse buoyancy number $=\sigma/gd_b^2(\rho_l-\rho_v)$, d_b is the measured bubble departure diameter, and helical angle θ (in radians) which has the following form

$$\mathrm{Nu}=9.72[\mathrm{Re}_b]^{0.742}[P_r]^{0.6}[\mathrm{Pr}]^{1.748}[p/d_w]^{-0.001}$$
$$\times[\sigma/gd_b^2(\rho_l-\rho_v)]^{0.002}[\theta]^{-0.034}$$

$$4.691\times10^{-3}\leqslant\mathrm{Re}_b\leqslant1.225\times10^{-2}$$

$$9.9\leqslant p/d_w\leqslant19.7 \qquad (14)$$

$$1.848\leqslant\sigma/gd_b^2(\rho_l-\rho_v)\leqslant1.944$$

$$1.745\times10^{-2}\leqslant\theta\leqslant3.491\times10^{-2}$$

$$3.793\leqslant\mathrm{Pr}\leqslant3.982$$

and, again, measured d_b were used in Eq. (14). Furthermore, in Fig. 6, it is found that both correlations can predict 95 percent of the data within ±20 percent.

5.3 Boiling Visualization and Bubble Parameters. Visual tests with the transparent sight-glass window of the test section showed a particular liquid-vapor exchange occurring during nucleate boiling. Overall, the thermal performance and boiling phenomena are strongly influenced by the type of refrigerant and enhanced surface condition. Although the bubble departure diameter and frequency are considerably varied around the circumfer-

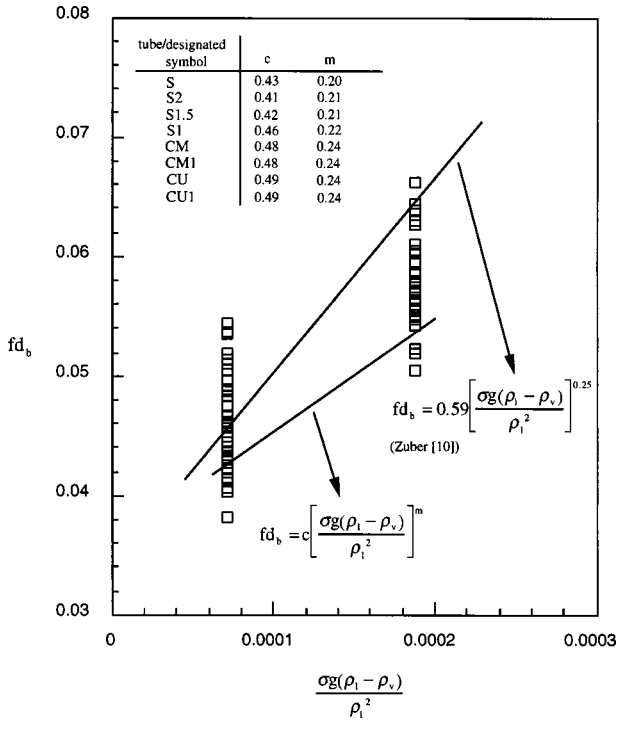

Fig. 10 fd_b **versus** $\sigma g(\rho_1-\rho_v)/\rho_1^2$

ence of tubes, careful attention was made to the location where the bubble are released and counted. Figure 7 is a photograph taken at 900 W/m^2 for S, S1, S2, and CM tubes in R-134a and R-600a refrigerants. It shows, qualitatively, the tube in the fully developed nucleate boiling regime except Figs. 7(*e*) and (*f*) where the nucleate boiling is still developing. At this stage (900 W/m^2), no bubble agglomeration was observed to occur and overlapping images were carefully avoided. The bubble size seems in R-600a bigger than that in R-134a as compared to Figs. 7(*a*)–(*d*) and the corresponding photographs for R-134a. For quantitative analysis, a simple optical method was used to measure bubble parameters at $600 \leqslant q \leqslant 1000$ W/m^2; namely, departure diameter and frequency. The bubbles with a measured area on the video-screen are counted easily. To compare with the data reported by Ammerman et al. [10], the same measurement area, 5.5 mm high by 18 mm wide, centered above the tube, was defined within each digitized photo using the image processor.

Figure 8(*a*) shows the ratio of number of bubbles (N/N'). N' was calculated (at $q=121$ W/m^2) from Ammerman et al. [10]. Even though the different working fluids and heating surfaces they have, the comparison was still made. The number of bubbles reported (N) are averaged values. The data have been taken at a heat flux $q=600$, 700, 800, 900, and 1000 W/m^2, respectively, and refer to individual, isolated bubbles, not influenced by their neighbors. Naturally, bubble growth after departure and bubble agglomeration were considered as possible sources of error. Figure 8(*b*) clearly indicates the number of bubbles per unit area used in a particular measured area to assist the illustration of Fig. 8(*a*).

In general, the number of bubbles increases as q increases. Different symbols (e.g., Cu indicates copper coated surface, see Table 1, for details) are used to characterize different heating surfaces. The trend for all enhanced surfaces seems the same. However, for the magnitude, there appears two groups; tube Cu1, Cu, CM1, and CM is one group and tubes S, S1, S1.5, and S2 is another group for both R-600a and R-134a. The values of R-134a are higher than those of R-600a. Furthermore, the trend for bubble development is also in agreement with those of Ammerman et al. [10]. Taking a closeup examination of Fig. 8, it is found, for example, that the present value of N/N' ratio can be up to 6 at $q \cong 1000$ W/m^2 for Cu1 tube and the rate of increase with heat flux for all the tubes considered herein seems the same.

The data in Fig. 9(*a*) indicate that for all tubes considered, the bubble diameter slightly decreases as the heat flux increases. While, the corresponding frequency slightly increases. The frequency fluctuations were found at a given site over a population of bubbles and becoming larger at higher heat fluxes. The departure diameters were generally found to be somewhat higher in R-600a and thus the frequencies to be somewhat lower. The measured and calculated departure diameters based on Zuber [11] are also listed in Table 3. Also listed in Table 3 are data for embryonic bubble radius calculated from $P_s(T_w)-P_s(T_s)=2\sigma(T_w)/r_b$ for comparison and reference. Again, as stated before, it is found that the corresponding departure diameters and embryonic bubble radius in R-600a are bigger than those in R-134a because R-600a has a little higher ($\approx$19 percent higher) surface tension. As a result, a higher bubble frequency R-134a is due to a lower required bubble pressure for growth and departure. Moreover, enhanced surfaces, like coated and wrapped surfaces, have smaller bubble diameters. Among those bubble diameters measured, Cu1 tube has the smallest bubble diameters and thus the highest frequency in both R-600a and R-134a as one would expect. Frequency increases gradually versus heat flux at heat flux $\leqslant 900$ W/m^2 can also be seen. However, the frequency then begins to flatten out at $q \geqslant 900$ W/m^2 in the fully developed region. Frequency values are shown versus heat flux in Fig. 9(*b*). Finally, the relationship among frequency f, bubble diameters d_b, and $\sigma g(\rho_l-\rho_v)/\rho_l^2$ was found and it is shown in Fig. 10. The traditional $fd_b \cong$ constant is found in the present study. Actually, the present results were correlated as a function of $\sigma g(\rho_l-\rho_v)/\rho_l^2$ within ± 15 percent of the original data which is shown in Fig. 10. The average value (value of m indicating the slope of the curve in Fig. 11) of power for above-stated term was found to be about 0.23 which is very similar to that of Zuber [11] ($=0.25$).

5.4 Model Validity Assessment/Heat Transfer Prediction. As previously stated, following Hsieh et al. [3], a prediction of heat flux for the present enhanced tubes can also be divided into the microlayer evaporation component (q_{ME}), nucleate boiling component (q_{NB}) and natural convection component (q_{NC}) which can be individually calculated from the relevant equations (Hsieh et al. [3]) through a known active nucleation density (n') and degree of superheat (ΔT_{sat}) obtained from the measurements for each case. Figure 11 depicts the total predicted heat flux q_p and each component of q with measured heat flux q_M on enhanced heating surfaces for R-600a. It appears that the predicted heat flux is almost exactly the same as q measured. It can be seen that $q_{cycle}=(q_{ME}\cdot t_g+q_{NB}t_w)/(t_g+t_w)$ where t_g is the time of bubble growth and t_w is the waiting time for reformation of the thermal boundary layer; namely, latent heat dominates the heat transfer contribution among the predicted heat flux especially for plasma coated tubes (e.g., CM, CM1, Cu, and Cu1 tubes). For all the tubes considered, the contribution of latent heat transfer increases sharply with the increases in wall superheat. This finding coincides with that of Hsieh et al. [3]. Similarly, the data shown in Fig. 12 indicates the comparison of the present model with experimental data for R-134a. Again, the similar behavior was found as that for R-600a and, again, it clearly shows the good agreement between the prediction and the experimental data. The trend and magnitude seem similar compared to Fig. 11. However, the latent heat portion, q_{cycle} takes a less part of heat transfer contribution this time compared to the q_{cycle} in Fig. 11. Consequently, natural convection component plays a relative major role in this heat transfer process especially for smooth/wrapped tubes (e.g., S, S1, S2, and S1.5). This is perhaps because R-134a has a lower latent heat value (nearly one half) than that of R-600a but has nearly the same wetting ability and, in turn, the bubble departure diameter (frequency) in R-134a is lower (higher) than that in R-600a. Tak-

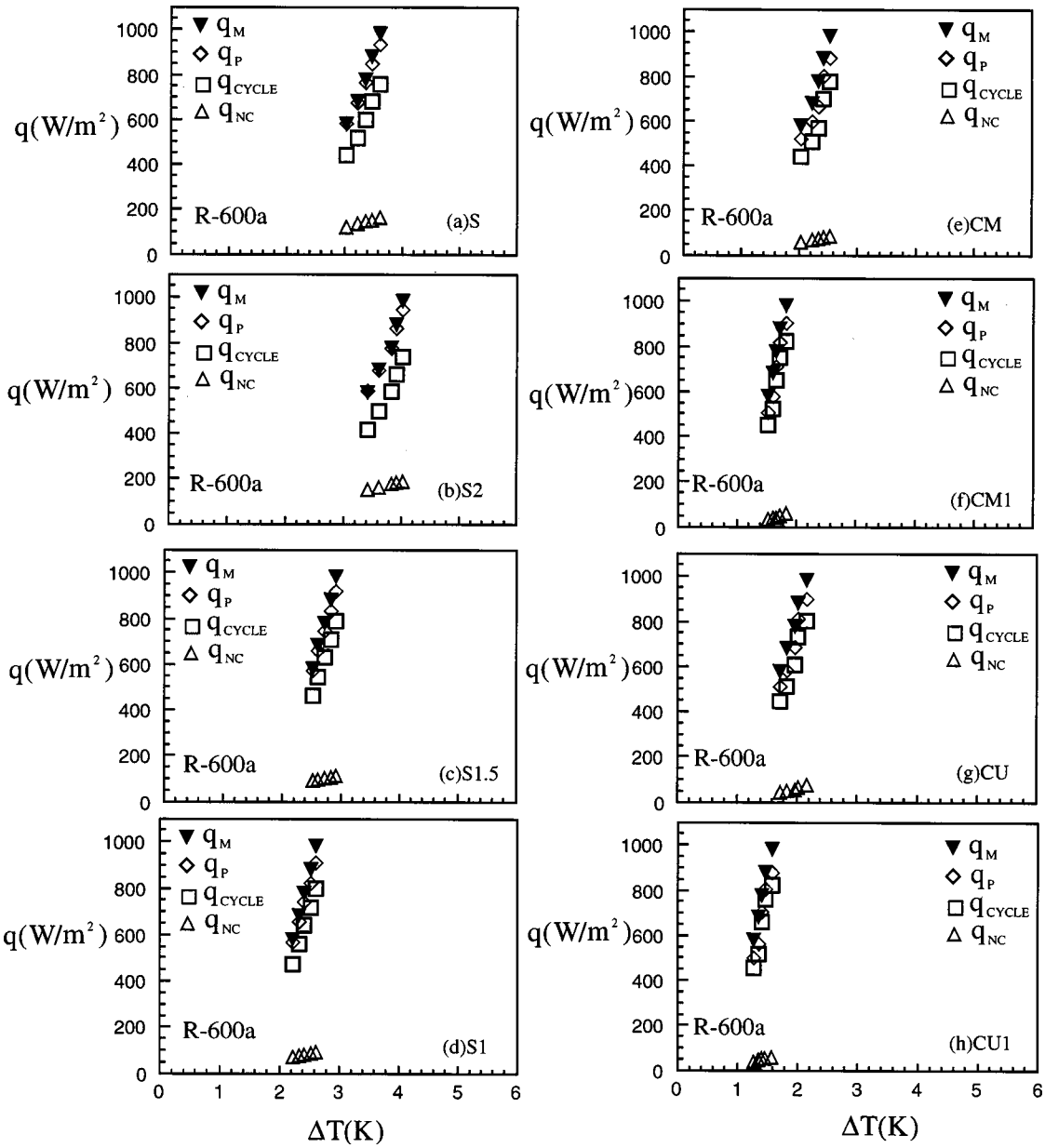

Fig. 11 Comparison of the model with the experimental data for R-600a

ing a further look of Figs. 11 and 12, it can also be seen that the boiling curve is much more steep for R-600a than that of R-134a.

6 Conclusions

Pool boiling plasma coating and wire wrapped tubes for two different refrigerants (R-134a and R-600a) at low and moderate heat flux was extensively studied. The results lead to the following conclusions.

1 Boiling heat transfer is enhanced by both thin layer porous matrix coated and wire wrapped on the heating surface, with an enhancement of up to 1.2~2.3 times for most cases under study. The geometric factor such as surface roughness of coated surface and helical angle of the wrapped tube should be properly chosen to warrant a heat transfer enhancement.

2 Correlations for thermal performance were made for coated and wrapped surface each, respectively.

3 Through boiling visualization (at $600 \leqslant q \leqslant 1000$ W/m^2), the photographs qualitatively as well as quantitatively indicate that the presence of enhanced surface generates more active and stable nucleation sites in the vicinity of the porous matrix and wrapped wire. Bubble departure diameter in R-134a is smaller than that in R-600a. While for R-600a, the bubble frequency is much less than that in R-134a. Generally, a small increase of number of bubbles and departure frequency has been observed with linearly increasing heat flux.

4 The results have generally again confirmed the previous speculated mechanism [2,6,12] of boiling with porous metallic matrix surface coating. Namely, nucleation takes place within the matrix and in steady boiling, vaporization occurs within the matrix. Also, the enhanced mechanisms for wrapped tubes were further examined and confirmed.

5 Following Hsieh et al. [3], model validity assessment for the present enhanced surface, was made and good agreement was found.

6 The natural convection contribution in R-134a is much bigger than that in R-600a which indicates bubble vaporization dominant in R-600a due to a higher latent heat value.

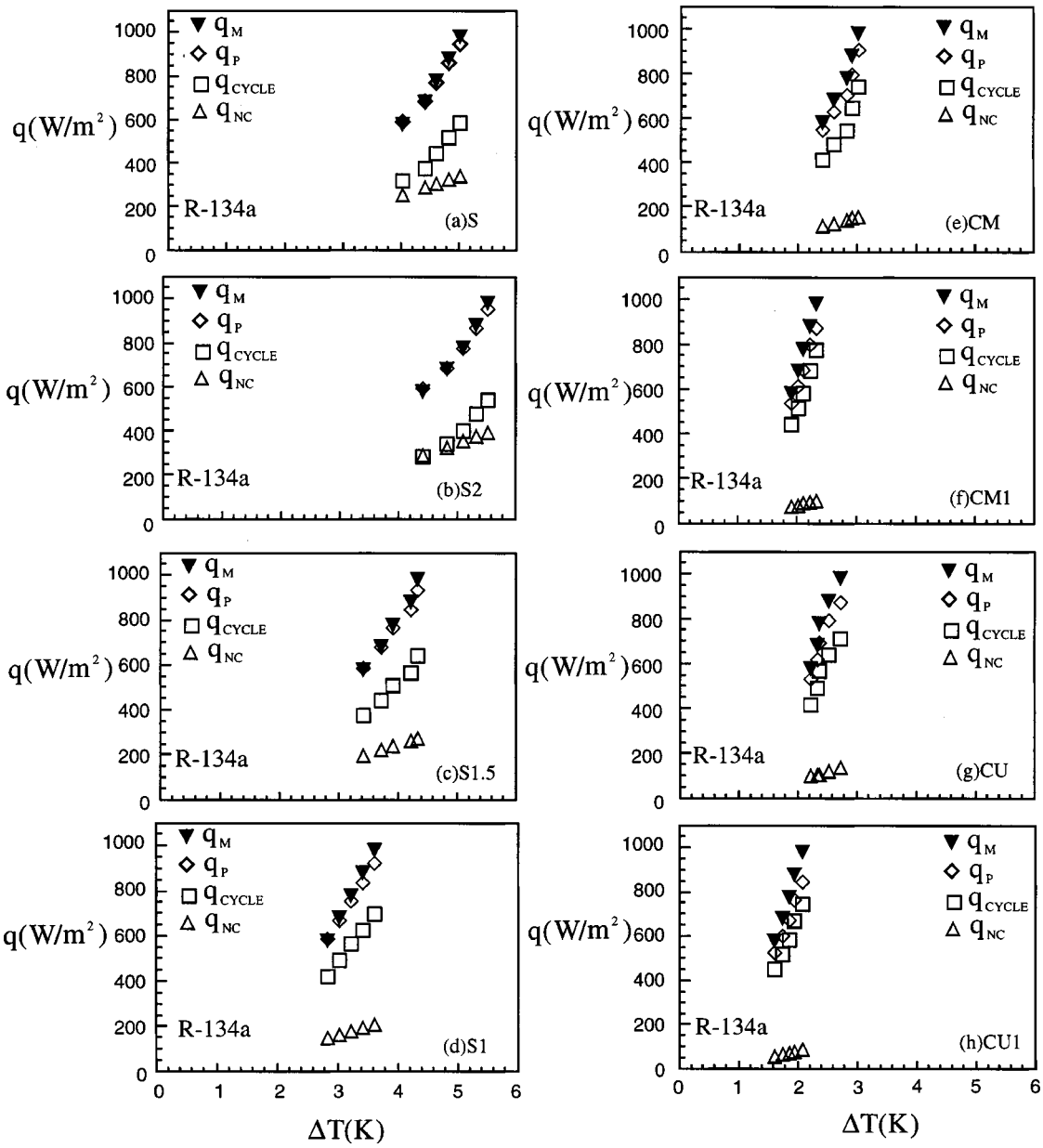

Fig. 12 Comparison of the model with the experimental data for R-134a

Acknowledgment

This work was supported by a research grant NSC 89-2212-E-110-026) from the National Science Council, Taiwan, R.O.C.

Nomenclature

C_p = specific heat at constant pressure, kJ/kg·K
d_b = bubble departure diameter, mm
d_o = outside diameter of test tube, mm
d_w = helical wire diameter, mm
$F(p)$ = pressure function, $1.8\,Pr^{0.17}+4Pr^{1.2}+10Pr^{10}$
f = bubble departure frequency, s^{-1}
h_{fg} = latent heat, kJ/kg
Ja = Jacob number, $C_{pl}\Delta T/h_{fg}$
L = length of test tube, mm
N = number of bubble generated
N' = total number of bubble generated, data from Ammerman et al. [10]
Nu = Nusselt number, hd_b/k
N_{cf} = constnat heat flux number, $N_{cf}=\mu_l^2/\eta\rho_l\sigma$
n = number of bubble generated per unit area, bubbles/m^2
n' = active nucleation site density, sites/m^2
P = pressure, kPa
P_c = critical pressure, kPa
P_r = reduced pressure P/P_c
p = pitch of the wire, mm
Q = heat transfer rate, W
q = heat flux (Q/A), W/m^2
Ra = roughness, μm
Re = Reynolds number for plasma coated tube, $q\eta/h_{fg}\mu_l\varepsilon$

Re_b = Reynolds number for wire wrapped tube based on bubble departure diameter, $qd_b/\mu_l h_{fg}$
r_b = embryonic bubble radius, μm
ΔT = temperature difference, K
ΔT_{sat} = degree of superheat, K
t_b = bubble growth time
t_w = waiting period$=3t_g$

Greek Symbols

δ = porous layer thickness, μm
ε = porosity (%)
η = average pore diameter, μm
θ = helical angle, degree or radian
λ = geometric scale factor, η/δ

Subscripts

avg = average
b = bubble
c = critical
l = liquid
M = measured
ME = microlayer evaporation
NC = natural convection
p = predict
r = reduced
s = smooth tube
sat = saturation
v = vapor

References

[1] Thome, J. R., 1990, *Enhanced Boiling Heat Transfer*, Hemisphere, New York, pp. 28–63.
[2] Hsieh, S.-S. and Weng, C.-J., 1997, ''Nucleate Pool Boiling from Coated Surfaces in Saturated R-134a and R-407c,'' Int. J. Heat Mass Transf. **40**, 519–532.
[3] Hsieh, S.-S., Weng, C.-J., and Chiou, J.-J., 1999 ''Nucelate Pool Boiling on Ribbed Surfaces with Micro-Roughness at Low and Moderate Heat Flux,'' ASME J. Heat Transfer **121**, 376–385.
[4] Kline, S. J. and McClintock, F. A., 1953, ''Describing Uncertainties in Single Sample Experiments,'' Mech. Eng. (Am. Soc. Mech. Eng.) **75**, 3–8.
[5] Junkhan, C. H. and Bergles, A. E., 1976, ''Heat Transfer Laborating Data Acquisition System,'' Heat Transfer Laboratory Report HTL-12, ISU-ERI-Ames-77178, Iowa State University, Ames, IA.
[6] Carey, V. P. 1992, *Liquid-Vapor Phase Change Phenomena*, Hemisphere, Washington D.C., p. 233.
[7] Marto, P. J., Monlson, J. A., and Maynard, M. D., 1966, ''Nucleate Pool Boiling of Nitrogen with Different Surface Conditions,'' ASME J. Heat Transfer **90**, 437–444.
[8] Stephan, K. and Abdelsalam, M., 1980, ''Heat Transfer Correlation for Natural Convection Boiling,'' Int. J. Heat Mass Transf. **23**, 73–87.
[9] Rudemiller, G. R., and Lindsay, J. D., 1990, ''An Investigation of Boiling Heat Transfer in Fibrous Porous Media,'' *Proceedings of the Ninth International Heat Transfer Conference*, **5**, pp. 159–164.
[10] Ammerman, C. N., You, S. M., and Hong, Y. S., 1996, ''Identifciation of Pool Boiling Heat Transfer Mechanisms from a Wire Immersed in Saturated FC-72 Using a Single-Photo/LDA Method,'' ASME J. Heat Transfer **118**, 117–123.
[11] Zuber, N., 1963, ''Nucleate Boiling: The Region of Isolated Bubble and the Similarity With Natural Convection,'' Int. J. Heat Mass Transf. **6**, 53–78.
[12] Bergles, A. E. and Chyu, M. C., 1982, ''Characeristic of Nucleate Pool Boiling From Porous Metallic Coatings,'' ASME J. Heat Transfer **104**, 279–285.

Study of Subcooled Film Boiling on a Horizontal Disc: Part I—Analysis[1]

D. Banerjee

V. K. Dhir

Mechanical and Aerospace Engineering Department, University of California, Los Angeles, Los Angeles, CA 90095

In this work subcooled film boiling on a horizontal disc was studied analytically/numerically. Linearized stability analysis of a vapor film underlying a pool of heavier liquid was performed in three-dimensional, cylindrical coordinates. From the analysis the dominant wavelength and configuration of vapor releasing nodes was identified. Complete numerical simulation of the nonlinearly evolving interface have been carried out in axisymmetric coordinates. Finite difference method was used to simultaneously solve the equations governing conservation of mass, momentum, and energy in the vapor and liquid phases. The equations for the two phases were coupled through the matching of normal and tangential stresses and continuity of mass and energy at the interface. Second order projection method was employed for decoupling velocities from pressure. Numerical grid generation method was utilized to construct a grid system which was aligned with the interface. From the simulations the shape of the nonlinearly evolving interface, the growth rate of the interface, the flow and temperature fields in the vapor and liquid, and rate of heat transfer from the wall and into the subcooled liquid have been determined.
[DOI: 10.1115/1.1345889]

Keywords: Boiling; Film; Heat Transfer; Phase Change; Two-Phase

1 Introduction

The study of subcooled film boiling has significant applications in space vehicle and other systems operating in micro-gravity, thermal issues in high speed civil transport, heat treatment of metals, nuclear reactor design, cryogenic cooling for superconducting applications, and thermal storage systems among others.

Although film boiling has been studied extensively in the past, only a limited number of investigations have been performed for saturated and subcooled film boiling on horizontal surfaces. Berenson [1] used two-dimensional Taylor instability to obtain an expression for the saturated film boiling heat transfer coefficient on a horizontal surface. Berenson [1] proposed a static bubble model where he assumed that the vapor bubbles were arranged on a square grid with spacing equal to the ''most dangerous wavelength'' (λ_{d2}) obtained from two-dimensional analysis of Taylor instability.

Hosler and Westwater [2] experimentally investigated saturated film boiling of water and Freon-11 on a horizontal surface and found the heat transfer data to show a large variability. However, the mean data tended to show a good agreement with predictions from Berenson's model. More recently Ramilison and Lienhard [3] reproduced Berenson's experiments and obtained film and transition boiling data by controlling the temperature of the horizontal disc. They found that transition film boiling data for Freon-113, acetone, benzene and *n*-pentane deviated from the prediction from Berenson's semi-empirical model and the magnitude of deviations depended on the surface condition. Klimenko and Shelepen [4] have developed a generalized correlation for saturated film boiling on a horizontal surface.

Very recently Son and Dhir [5] performed a complete numerical simulation of saturated film boiling on a horizontal surface. They carried out an axisymmetric analysis of the region surrounding the bubble releasing nodes. From the analysis it was shown that heat transfer coefficients vary strongly both spatially and temporally. The predicted bubble diameter at departure and height were found to be in agreement with the reported data but area and time averaged heat transfer coefficients were about 34 percent lower than those obtained from Berenson's model. The discrepency was attributed to the presence of three dimensional effects which were not considered in the numerical simulations.

Hamill and Baumeister [6] performed a theoretical analysis of subcooled film boiling on a horizontal plate. Based on the maximum entropy generation rate postulate and by assuming a static and empirical configuration for the vapor bubbles, they arrived at an estimate for the film boiling heat transfer coefficients in subcooled film boiling. The authors superimposed the contribution of radiation heat transfer and convection in the subcooled liquid on the film boiling heat transfer coefficient for saturated liquid as

$$\overline{h} = \overline{h}_o + 0.88\overline{h}_r + 0.12\overline{h}_{nc}\frac{\Delta T_{\text{sub}}}{\Delta T_W}, \tag{1}$$

where, $\overline{h}_o$ is the saturation film boiling heat transfer coefficient, and $\overline{h}_r$ and $\overline{h}_{nc}$ are the radiation and convection heat transfer coefficients, respectively. However, no experimental data were provided in support of the analysis.

Linearized analysis of two dimensional Taylor instability has been performed by several investigators. Dhir and Lienhard [7] extended Bellman and Pennington's [8] analysis to include the combined effect of fluid viscosity and radial curvature of a cylinderical interface to obtain the ''most dangerous'' wave length and the corresponding growth rate. Sernas et al. [9] were the first to suggest for film boiling a three-dimensional Taylor wave pattern in cartesian coordinates. This wave pattern eliminated the conceptual difficulties that existed in wave patterns based on two-dimensional analysis. Jacobs [10] studied Taylor instability in a circular geometry in which a liquid column formed in a circular pipe was accelerated downward in air. Jacobs also performed weakly nonlinear analysis of the three-dimensional Taylor instability. The analysis involved small perturbation expansions about the critical wavenumber (corresponding to zero growth rate). Predictions of shapes of the non-linear instabilities from this method were found to match the experimentally observed shapes during the initial part of the growth of the instability. The growth rates predicted from linear theory were found to be valid much later in time than the weakly non-linear analysis. The analyses also

[1]This work received support from the National Science Foundation.

Contributed by the Heat Transfer Division for publication in the JOURNAL OF HEAT TRANSFER. Manuscript received by the Heat Transfer Division January 20, 2000; revision received October 31, 2000. Associate Editor: V. Carey.

showed that the axisymmetric instabilities (e.g., circular and hexagonal) grow much faster compared to other geometries (e.g., square, rectangular, etc.). However, the axisymmetric solutions did not converge to the Cartesian coordinate solutions, for radial wave numbers approaching infinity, because of the nature of the coefficients of the governing equations.

In this study linear three-dimensional analysis of Taylor instability has been performed in cylindrical coordinates with the objective of predicting the configuration of wave crests on a circular disc. The motivation for such a study is to evaluate the pattern of vapor bubbles under pool boiling conditions for film boiling on a horizontal flat disk. The vapor bubble pattern identified from the linear analysis of three-dimensional Taylor instability is utilized for numerical simulation of non-linear evolution of the interface in subcooled film boiling.

2 Analysis

2.1 Linear Three-Dimensional Taylor Instability Analysis. The instability at the interface of a lighter fluid underlying a heavier fluid has been modeled in this study, where the acceleration due to gravity is directed from the heavier to the lighter fluid. Under the assumptions that the fluids are inviscid and incompressible, the fluid layers are of infinite depth, and the nonlinear terms are small, the linearized governing equations for both fluids, expressed in cylindrical coordinates are as follows:

Continuity Equation

$$\frac{1}{r}\frac{\partial(ru)}{\partial r}+\frac{1}{r}\frac{\partial w}{\partial \theta}+\frac{\partial v}{\partial y}=0 \tag{2}$$

Momentum Equation

$$\rho\frac{\partial u}{\partial t}=-\frac{\partial p}{\partial r} \tag{3}$$

$$\rho\frac{\partial w}{\partial t}=-\frac{1}{r}\frac{\partial p}{\partial \theta} \tag{4}$$

$$\rho\frac{\partial v}{\partial t}=-\frac{\partial p}{\partial y}-\rho g, \tag{5}$$

where u, w, and v are the radial, polar and vertical components of the velocity vector $\vec{\mathbf{u}}$. In terms of the potential function ϕ, the velocity can be written as

$$\vec{\mathbf{u}}=\nabla\phi=u\hat{\mathbf{r}}+w\hat{\theta}+v\hat{\mathbf{y}}, \tag{6}$$

where $\hat{\mathbf{r}}$, $\hat{\theta}$, $\hat{\mathbf{y}}$ are the unit vectors in the radial, angular and vertical direction in cylindrical polar coordinates and ∇ is the gradient operator. Substituting Eq. (6) in the continuity equation (Eq. (2)) we obtain,

$$\nabla^2\phi=\frac{1}{r}\frac{\partial}{\partial r}\left(r\frac{\partial\phi}{\partial r}\right)+\frac{1}{r^2}\frac{\partial^2\phi}{\partial\theta^2}+\frac{\partial^2\phi}{\partial y^2}=0. \tag{7}$$

The solution of the above equation is given by

$$\phi(r,\theta,y,t)=C_{mn}J_m(k_nr)\cos(m\theta)e^{(-k_ny)}e^{(-i\omega_nt)}, \tag{8}$$

where J_m is the Bessel function of the first kind of order m. Here m and n denote the eigenvalues of Eq. (7), while k_n denotes the wavenumber corresponding to mode number n. The shape of the perturbed interface is assumed to be

$$\overline{\eta}(r,\theta,t)=\overline{\eta}_oJ_m(k_nr)\cos(m\theta)e^{(-i\omega_nt)}, \tag{9}$$

where $\overline{\eta}_o$ is the initial amplitude of the interfacial disturbance and ω_n denotes the growth rate (It should be noted that $m=0$ corresponds to the two-dimensional case).

The kinematic condition at the interface yields

$$v|_{\overline{\eta}}=\frac{\partial\overline{\eta}}{\partial t}+(\vec{u}\cdot\nabla)v. \tag{10}$$

Substituting Eqs. (6), (8), and (9) in the above equation after neglecting the nonlinear terms (the last term on the right in the above equation), the following relation is obtained:

$$C_{mn}=\frac{i\overline{\eta}_o\omega_n}{k_n}. \tag{11}$$

Since the Taylor instability during film boiling results in a standing wave, above a wave crest at $r=r_n$ we can impose $u|_{\overline{\eta}}=0$. Hence from Eqs. (6) and (8) we also get the relation:

$$\frac{\partial}{\partial r}J_m(k_nr)|_{r=r_n}=0 \tag{12}$$

$$k_n=\alpha_{mn}/r_n, \tag{13}$$

where α_{mn} is the n^{th} root of Eq. (12) and r_n is the radius of the concentric ring number n of the wave crests. The values of α_{mn} can be obtained from a standard handbook of mathematical functions. The same relationship was used by Daly [11] for numerical simulation of two-dimensional Taylor instability in cylindrical coordinates. However, this would suggest that the values of wavenumber approach zero for an infinite size heater, which is conceptually erroneous. This paradox will be resolved as we solve the dispersion relation.

Dispersion Relation. Substituting Eq. (6) in Eq. (5) and integrating in the y direction from 0 to $\overline{\eta}$ the solution for the pressure $p|_{\overline{\eta}}$ at $y=\overline{\eta}$ is obtained as

$$p|_{\overline{\eta}}=p_o-\rho g\,\eta+\rho\frac{\partial\phi}{\partial t}, \tag{14}$$

where p_o is the mean pressure at the interface in the unperturbed condition.

Using the relation

$$p_v-p_l=\gamma/R_s \tag{15}$$

and Eqs. (8), (11), and (14) for liquid and vapor we get

$$(\rho_l+\rho_v)\frac{\omega_n^2\overline{\eta}}{k_n}=\frac{\gamma}{R_s}-(\rho_l-\rho_v)g\overline{\eta}, \tag{16}$$

where R_s is the radius of curvature of the interface. An expression for R_s is obtained as (see Daly [11]):

$$\frac{1}{R_s}=\frac{1}{R_1}+\frac{1}{R_2};\quad \frac{1}{R_1}=\left|\frac{\partial^2\overline{\eta}}{\partial r^2}\right|;\quad \frac{1}{R_2}=\left|\frac{1}{r}\frac{\partial\overline{\eta}}{\partial r}\right|. \tag{17}$$

Substituting Eq. (9) in the Eq. (16), the dispersion relation is obtained as

$$\omega_{n_i}^2=\frac{-\gamma k_n^3\left|-1+\dfrac{m^2}{4k_n^2r^2}\right|+(\rho_l-\rho_v)gk_n}{(\rho_l+\rho_v)}, \tag{18}$$

where ω_{n_i} is the imaginary component of ω_n. Using the characteristic length l_o and characteristic growth rate ω_o defined as

$$l_o=\left[\frac{\gamma}{(\rho_l-\rho_v)g}\right]^{1/2};\quad \omega_o=\left[\left(\frac{\rho_l-\rho_v}{\rho_l+\rho_v}\right)\left(\frac{g}{l_o}\right)\right]^{1/2} \tag{19}$$

the dispersion relation Eq. (18) is obtained in dimensionless form as

$$\left(\frac{\omega_{n_i}^2}{\omega_o^2}\right)=(k_nl_o)\left[-(k_nl_o)^2\left|-1+\frac{m^2}{4k_n^2r^2}\right|+1\right]. \tag{20}$$

The characteristic length, l_o is obtained by balancing surface tension and buoyancy forces, whereas the chacteristic frequency, w_o,

is representative of the growth rate of Taylor instability of the interface between two inviscid fluid layers of infinite extent.

Three cases are possible from terms within the absolute-value sign:

Case 1: $m^2 > 4k_n^2 r^2$

$$\left(\frac{\omega_{n_i}^2}{\omega_o^2}\right) = (k_n l_o)\left[(k_n l_o)^2 - \left\{\left(\frac{m}{2r/l_o}\right)^2 - 1\right\}\right] \tag{21}$$

Case 2: $m^2 = 4k_n^2 r^2$

$$\left(\frac{\omega_{n_i}^2}{\omega_o^2}\right) = k_n l_o \tag{22}$$

Case 3: $m^2 < 4k_n^2 r^2$

$$\left(\frac{\omega_{n_i}^2}{\omega_o^2}\right) = (k_n l_o)\left[-(k_n l_o)^2 + \left\{\left(\frac{m}{2r/l_o}\right)^2 + 1\right\}\right] \tag{23}$$

Critical Wavelength. For each of the three possible dispersion relationships, the critical wavelength corresponding to zero growth rate can be obtained by setting $\omega_{n_i} = 0$ in Eqs. (21), (22), and (23). For purposes of clarity a characteristic radius is obtained as $r_o = m/2k_{n_c}$ where k_{n_c} is obtained from the dispersion relations as follows:

Case 1: $m^2 > 4k_n^2 r^2$ (or $r < r_o$):

$$k_{n_c} = \frac{1}{l_o}\left[\left(\frac{m}{2r/l_o}\right)^2 - 1\right]^{1/2} \tag{24}$$

Case 2: $m^2 = 4k_n^2 r^2$ (or $r = r_o$):

$$k_{n_c} = 0 \tag{25}$$

Case 3: $m^2 < 4k_n^2 r^2$ (or $r > r_o$):

$$k_{n_c} = \frac{1}{l_o}\left[\left(\frac{m}{2r/l_o}\right)^2 + 1\right]^{1/2} \tag{26}$$

It should be noted that for Case 1 and Case 3 the relationship between ''most dangerous wavenumber'' or k_{n_d} (corresponding to maximum growth rate) and the critical wavenumber, k_{n_c} is given by

$$k_{n_d} = k_{n_c}/\sqrt{3}, \tag{27}$$

which is the same as in two-dimensional analyses in Cartesian coordinates (Bellman and Pennington [8]) and is also the same in three-dimensional analyses in Cartesian coordinates (Sernas et al., [9]). For Case 2, since $k_{n_c} = 0$ this is valid only for $m = 0$. Thus this is same as two-dimensional configuration and hence we obtain the same relation as Eq. (27), though here we arrive at the solution $k_{n_d} = k_{n_c}/\sqrt{(3)} = 0$.

Case 2 yields a trivial solution, which is not relevant to the present case. Also, from Case 1 the values of k_n obtained are not of significance in the situation analyzed here since these values of k_n occur before the first ring of crests. Hence, Cases 1 and 2 are not of interest.

Case 3 yields the only viable solution to k_n. Equation (26) implies that as the radius of the heater approaches infinity, the critical wavenumber approaches the value obtained from analyses performed in Cartesian coordinates. Hence, this resolves the paradox mentioned earlier.

2.2 Numerical Analysis Of Nonlinear Growth of the Interface. Numerical simulations of the evolution of the vapor liquid interface during subcooled film were carried out by assuming that the process could be considered to be axisymmetric. In carrying out the analysis the wall temperature was specified and was assumed to remain constant during the evolution of the interface. The thermophysical properties of the vapor were evaluated at the mean of the wall and interface temperatures. Similarly the liquid properties were calculated at the mean temperature between interface and the pool. Radiation contribution was neglected under the assumption that wall temperatures were not high enough for heat loss by radiation to be significant. In dimensionless form the equations governing the conservation of mass, momentum, and energy are written for vapor and liquid, respectively, as follows:

$$\frac{\partial(ru_v)}{\partial r} + \frac{\partial(rv_v)}{\partial y} = 0 \tag{28}$$

$$\frac{Du_v}{Dt} = -\frac{\partial p_v}{\partial r} + \frac{1}{\mathrm{Re}_v}\left(\nabla^2 u_v - \frac{u_v}{r^2}\right) \tag{29}$$

$$\frac{Dv_v}{Dt} = -\frac{\partial p_v}{\partial y} + \frac{1}{\mathrm{Re}_v}\nabla^2 v_v \tag{30}$$

$$\frac{D\theta_v}{Dt} = \frac{1}{\mathrm{Pr}_v\,\mathrm{Re}_v}\nabla^2\theta_v \tag{31}$$

$$\frac{\partial(ru_l)}{\partial r} + \frac{\partial(rv_l)}{\partial y} = 0 \tag{32}$$

$$\frac{Du_l}{Dt} = -\frac{\partial p_l}{\partial r} + \frac{\hat{\rho}}{\hat{\mu}}\frac{1}{\mathrm{Re}_v}\left(\nabla^2 u_l - \frac{u_l}{r^2}\right) \tag{33}$$

$$\frac{Dv_l}{Dt} = -\frac{\partial p_l}{\partial y} + \frac{\hat{\rho}}{\hat{\mu}}\frac{1}{\mathrm{Re}_v}\nabla^2 v_l + \frac{\hat{\rho}}{\hat{\alpha}\hat{\mu}}\frac{\mathrm{Ra}_l}{\mathrm{Pr}_v\,\mathrm{Re}_v^2}\theta_l \tag{34}$$

$$\frac{D\theta_l}{Dt} = \frac{1}{\hat{\alpha}}\frac{1}{\mathrm{Pr}_v\,\mathrm{Re}_v}\nabla^2\theta_l, \tag{35}$$

where for general dependent variable, ϕ, which represents dependent variables, u, v, and θ,

$$\frac{D\phi}{Dt} = \frac{\partial\phi}{\partial t} + u\frac{\partial\phi}{\partial r} + v\frac{\partial\phi}{\partial y} \tag{36}$$

$$\nabla^2\phi = \frac{1}{r}\frac{\partial}{\partial r}\left(\frac{\partial\phi}{\partial r}\right) + \frac{\partial^2\phi}{\partial y^2} \tag{37}$$

also

$$\mathrm{Re}_v = \frac{\rho_o u_o l_o}{\mu_v}; \quad \mathrm{Pr}_v = \frac{\nu_v}{\alpha_v}; \quad \mathrm{Ra}_l = \frac{g\beta_l(T_{\mathrm{sat}} - T_\infty)l_0^3}{\nu_l\alpha_l};$$

$$\hat{\rho} = \frac{\rho_v}{\rho_l}; \quad \hat{\mu} = \frac{\mu_v}{\mu_l}; \quad \hat{\alpha} = \frac{\alpha_v}{\alpha_l}.$$

In carrying out numerical simulation the characteristic length, l_o, and characteristic growth rate frequency ω_o are defined in Eq. (19). The characteristic time, t_o, characteristic velocity, u_o, and ''most dangerous frequency'' ω_d are defined as

$$t_o = \sqrt{\frac{l_o}{g}}; \quad u_o = \frac{l_o}{t_o}; \quad \omega_d = 0.62 \times \omega_o. \tag{38}$$

The characteristic time, t_o, is obtained by combining the gravitational acceleration and the characteristic length, whereas the characteristic velocity, u_o, is obtained by combining characteristic length and characteristic time.

The dimensionless temperatures are defined as

$$\theta_v = \frac{T_v - T_{\mathrm{sat}}}{\Delta T_w}; \quad \theta_l = \frac{T_l - T_\infty}{\Delta T_{\mathrm{sub}}}, \tag{39}$$

where T_v and T_l denote the vapor and liquid temperature variables, respectively. The dimensionless pressures are defined as

$$p_v = \frac{p_v^* + \rho_v g y}{\rho_v u_o^2}; \quad p_l = \frac{p_l^* + \rho_l g y}{\rho_l u_o^2}, \tag{40}$$

and p_v^* and p_l^* denote the static pressures, respectively. It is to be noted that p is defined as a pressure whose gradient is subtracted by a gravitational head which otherwise would appear in momentum equations. Also, the degree of superheat ΔT_w and degree of subcooling ΔT_{sub} are defined as

$$\Delta T_w = T_{\text{wall}} - T_{\text{sat}}; \quad \Delta T_{\text{sub}} = T_{\text{sat}} - T_\infty,$$

where, T_{sat} is the saturation temperature of the test fluid and T_∞ is the temperature of the liquid phase far away from the vapor-liquid interface.

For complex geometries, the solution procedure of governing equations are simplified by transformation to generalized, nonorthogonal, curvilinear coorodinates. This provides flexibility in improving resolution in desired regions of the domain of solution. Since two-phase flow with a complex interface is difficult to solve in (x, y) coordinates, the following coordinate transformation is used:

$$\xi = \xi(x,y,t); \quad \eta = \eta(x,y,t). \tag{41}$$

When the interface is deformed largely, interior grid points are difficult to determine algebraically. As such a grid system aligned with a complex interface is generated numerically by solving Poisson's equations (Thompson et al. [12]).

At the interface, $\theta_v = 0$ or $T_v = T_{\text{sat}}$ and $\theta_l = 1$ or $T_l = T_{\text{sat}}$. At the rigid wall

$$u_v = 0; \quad v_v = 0 \tag{42}$$

$$T_v = T_{\text{wall}}, \tag{43}$$

where, T_{wall} is the wall temperature. At the locations of symmetry with respect to y-axis and the centerline

$$u_v = 0; \quad \frac{\partial v_v}{\partial r} = 0$$

$$u_l = 0; \quad \frac{\partial v_l}{\partial r} = 0 \tag{44}$$

$$\frac{\partial \theta_v}{\partial r} = 0 \tag{45}$$

$$\frac{\partial \theta_l}{\partial r} = 0. \tag{46}$$

Far away from the interface

$$\frac{\partial u_l}{\partial r} = 0; \quad \frac{\partial v_l}{\partial y} = 0; \quad \theta_l = 0. \tag{47}$$

At the interface, the matching conditions for velocities and stresses are (see, e.g., Shyy [13]):

$$u_l - u_v = (1-\hat{\rho}) \frac{y_\xi \dot{m}}{\sqrt{x_\xi^2 + y_\xi^2}}$$

$$v_l - v_v = -(1-\hat{\rho}) \frac{x_\xi \dot{m}}{\sqrt{x_\xi^2 + y_\xi^2}}. \tag{48}$$

For shear stress and pressure

$$\frac{1}{\hat{\mu}} \tau_l - \tau_v = 0 \tag{49}$$

$$\frac{1}{\hat{\rho}} p_l - p_v = \frac{2}{\text{Re}_v} \left(\frac{1}{\mu} \sigma_l - \sigma_v \right) + (1-\hat{\rho}) \frac{\dot{m}^2}{r^2 (x_\xi^2 + y_\xi^2)} + \frac{(1-\hat{\rho})}{\hat{\rho}} (y - y_o) - \frac{(1-\hat{\rho})}{\hat{\rho}} \frac{1}{R_s}. \tag{50}$$

In the above equations

$$\dot{m} = \frac{\text{Ja}_v}{\text{Pr}_v \, \text{Re}_v} \frac{r(x_\xi^2 + y_\xi^2)}{J} \left(\theta_{v\eta} - \frac{\overset{*}{Ja}_l}{\overset{*}{Ja}_v} \frac{\hat{\alpha}}{\hat{\rho}} \theta_{l\eta} \right) \tag{51}$$

$$J_{a_v}^* = \frac{C_{p_v} \Delta T_w}{h_{fg}} \tag{52}$$

$$\overset{*}{Ja}_l = \frac{C_{p_l} \Delta T_{\text{sub}}}{h_{fg}} \tag{53}$$

$$\sqrt{x_\xi^2 + y_\xi^2}\, \tau = \frac{x_\xi^2 + y_\xi^2}{J} \overline{u}_\eta - \frac{x_\xi x_\eta + y_\xi y_\eta}{J} \overline{u}_\xi + \frac{x_\xi u_\xi - y_\xi u_\xi}{\sqrt{x_\xi^2 + y_\xi^2}} - \frac{x_\xi^2 + y_\xi^2}{J} \left[\left(\frac{x_\xi}{\sqrt{x_\xi^2 + y_\xi^2}} \right)_\eta u + \left(\frac{y_\xi}{\sqrt{x_\xi^2 + y_\xi^2}} \right)_\eta v \right] + \frac{x_\xi x_\eta + y_\xi y_\eta}{J} \left[\left(\frac{x_\xi}{\sqrt{x_\xi^2 + y_\xi^2}} \right)_\xi u + \left(\frac{y_\xi}{\sqrt{x_\xi^2 + y_\xi^2}} \right)_\xi v \right] \tag{54}$$

$$\sigma = -c \frac{u}{r} - \frac{x_\xi u_\xi + y_\xi v_\xi}{x_\xi^2 + y_\xi^2}$$

$$\frac{1}{R_s} = -\frac{x_\xi y_{\xi\xi} - y_\xi x_{\xi\xi}}{(x_\xi^2 + y_\xi^2)^{3/2}} - c \frac{y_\xi}{r \sqrt{x_\xi^2 + y_\xi^2}}. \tag{55}$$

In carrying out the computations, the energy equation is solved prior to the momentum equations because initially only θ is unknown in Eqs. (31) and (35). In this study, the discretized equations are solved by an iterative method rather than by direct inversion of matrix. To enhance the rate of convergence of iterations, a relaxation factor obtained from orthogonal-residual method (Streett and Hussaini [14]) is used.

The numerical model employed in this study is similar to that given by Banerjee [15] and Son and Dhir [16]. For the details (about the discretization of the governing equations, coordinate transformation, numerical grid generation and solution procedure for contravariant velocity vectors employed in this study—using second order projection method and orthogonal residual method) the reader is referred to the above mentioned references.

An explicit scheme was used for marching in time. The time steps during computations were varied in the range 10^{-3} to 10^{-5} to satisfy the CFL (<1) condition for a grid size of 42×64 in the fluid region. The time step was varied, in accordance with the CFL condition, due to reduction in the minimum size of the nonuniform grid as the bubble evolved. The smallest grid dimension varied from 5×10^{-2} to $2 \times 10^{-3} l_o$. It took about 8–10 hours of CPU time on CRAY C90 to calculate one cycle of bubble evolution.

The numerical model was tested for its accuracy by comparing with the numerical results of Son [5] for saturated film boiling of water. The results were in agreement with the numerical predictions of Son [5]. The numerical method was also tested for its accuracy by comparing the predicted early growth rate of the interface with that determined from the linear instability theory for a two-dimensional interface. For a rigid adiabatic wall, the numerical error was found to be less than 1 percent. The sensitivity of the results to grid size was also tested. When the number of grid points was doubled the difference in the calculated Nusselt numbers based on area and time averaged heat transfer coefficients were in agreement with each other within 1 percent. As such, all of the results reported in this work were obtained with the number of grids noted earlier.

3 Results and Discussion

Before proceeding with the numerical simulation of an evolving interface, it is necessary to determine the computational domain. The extent of the computational domain depends on the dominant wavelength. As such we first discuss the results obtained from the dispersion relation, Eq. (26).

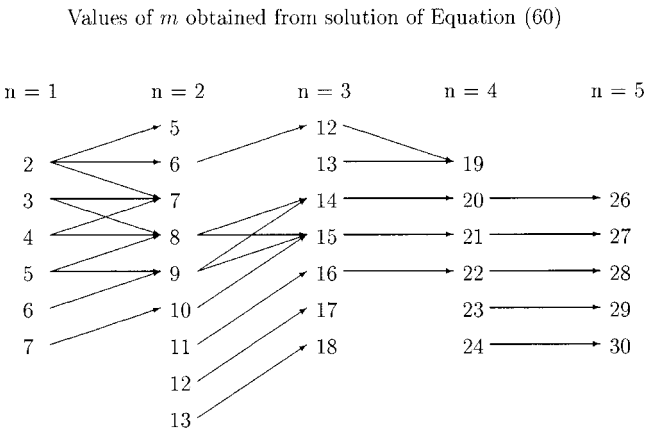

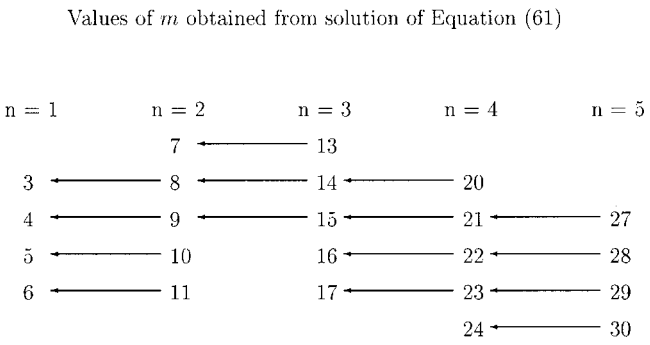

Fig. 1 Values of *m* obtained from solution of Eqs. (60) and (61) for spatial distribution of wave peaks corresponding to wave number k_{n_d} both in the radial and in the circumferential directions

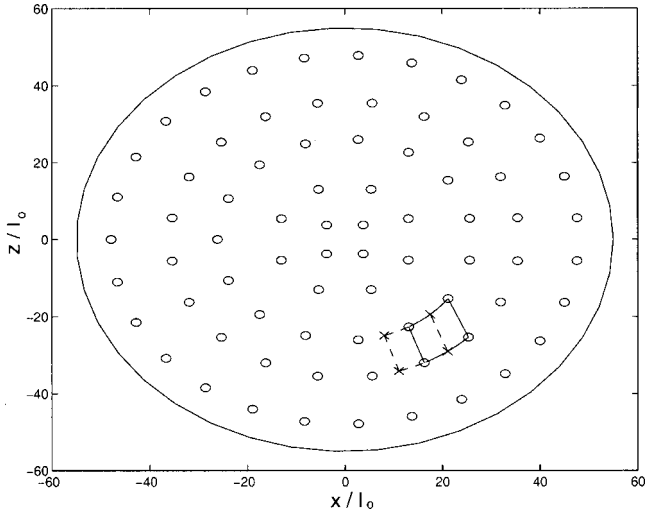

Fig. 2 Plot of crests of the three-dimensional Taylor wave on a circular plate for (*m*,*n*) values of (4, 1), (8, 2), (15, 3), (21, 4), and (27, 5). The circular plate, radial rings and wave crests are shown elliptical in the figure.

Table 1 Number of peaks supported by the region between consecutive rings

n	$n+1$	(Number of wave crests)/ λ_{d2}^2
1	2	0.8
2	3	1.1
3	4	1
4	5	0.98

3.1 Dominant Wavelength. The dispersion relation, Eq. (26) involves three unknowns, namely *m*, *n*, and *r*. Thus two additional relations are needed to determine the wavenumbers corresponding to critical or ''most dangerous'' wavelength. A second relation is provided by Eq. (13). Since in film boiling, no preference is expected to be given to perturbations that grow either in radial or azimuthal directions, we obtain the third relation by assuming that the dominant wavelength in the azimuthal direction is the same as in the radial direction:

$$r_{n+1}-r_n=\frac{2\pi r_n}{m}, \tag{56}$$

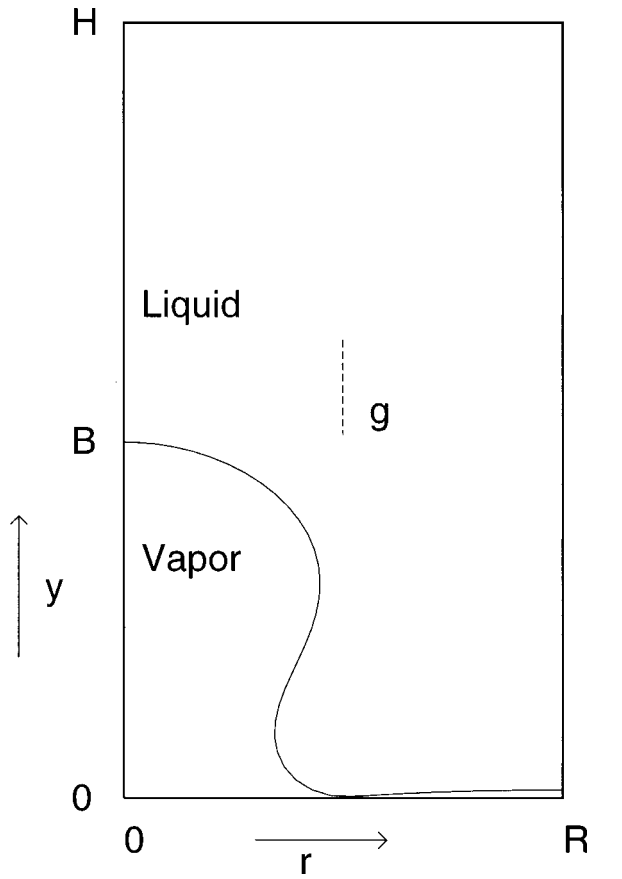

Fig. 3 Computational domain for solution of fluid side governing equations. In the computations *H* was set to 15, *R* was set to 4.34. The value of *B* changed as the height of the vapor bubble changed with time. The number of grids used in the vapor side was 42×22, with 42 grid points along the radial direction. The number of grids used in the liquid side was 42 ×42 in simulation runs for saturated film boiling and 42×77 in simulation runs for subcooled film boiling.

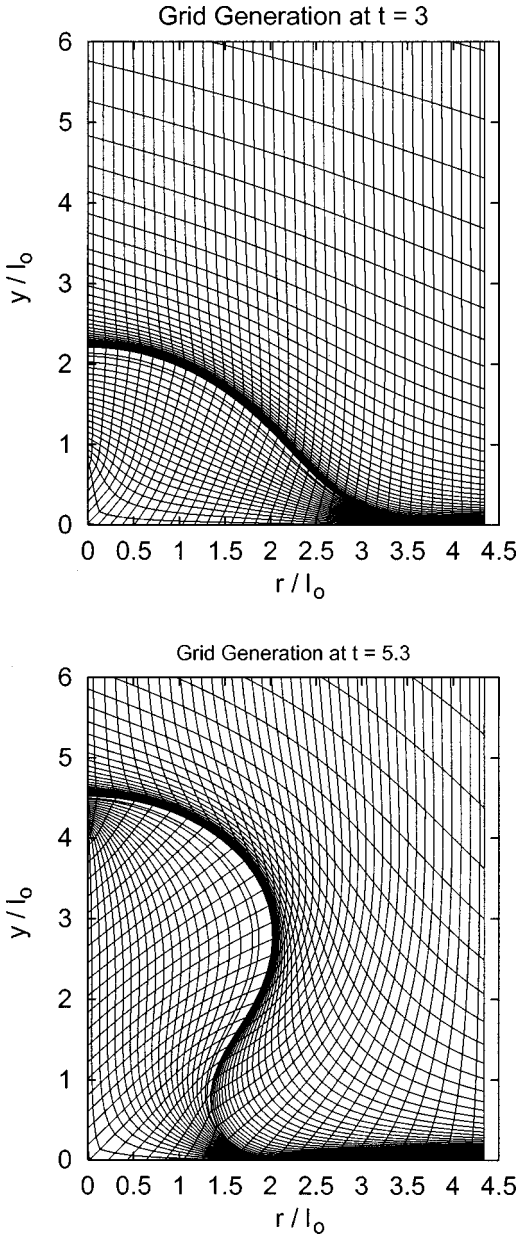

Fig. 4 Plot of grid locations for film boiling of saturated PF-5060 at $Ja_l^*=0.77$, and $Ja_v^*=0.133$, i.e., $\Delta T_W=100°C$, and $\Delta T_{sub}=10°C$. The radial and vertical distances are non-dimensionalized with respect to l_o. Time t is non-dimensionalized with respect to t_o.

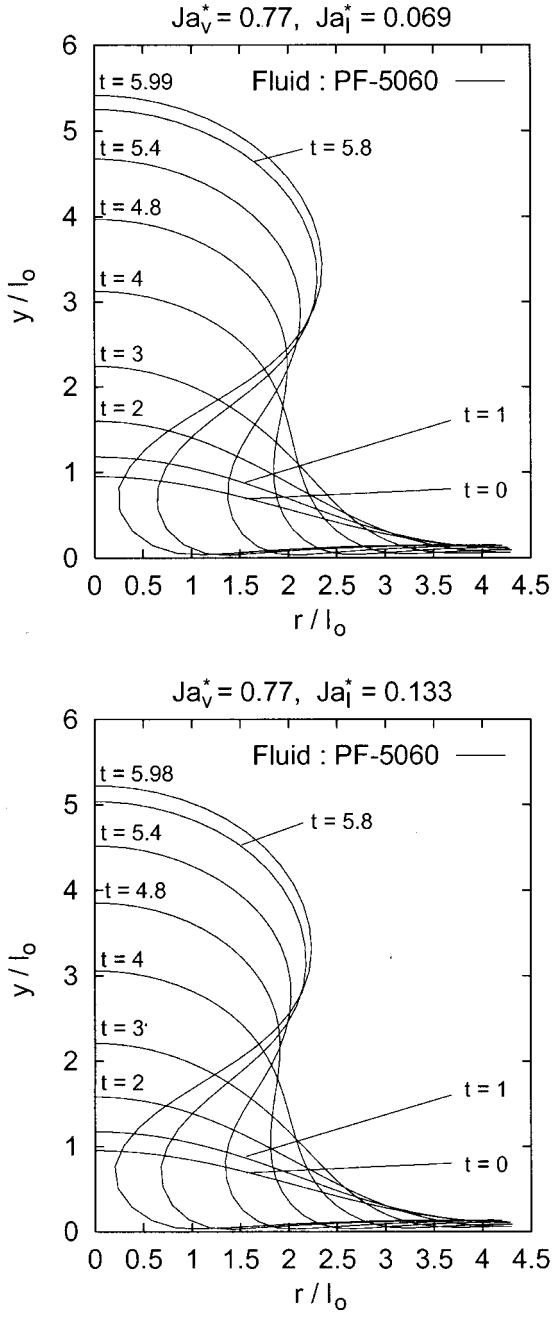

Fig. 5 Numerical predictions for temporal evolution of the liquid-vapor interface for wall superheat, $\Delta T_W=100°C$ and $\Delta T_{sub}=5°C$ and 10°C. The radial distances and interface heights are non-dimensionalized with respect to l_o. Time t is non-dimensionalized with respect to t_o.

where n and $n+1$ are the ring numbers of circumferential arrangement of wave peaks as we move radially out from the center. Similarly if one moves radially inwards, the relation becomes:

$$r_n - r_{n-1} = \frac{2\pi r_n}{m}. \tag{57}$$

Using Eq. (13) in Eqs. (56) and (57) the following relations are obtained, respectively:

$$\frac{\alpha_{m',n+1}}{k_{n+1}} - \frac{\alpha_{m,n}}{k_n} = \frac{2\pi}{m} \times \frac{\alpha_{m,n}}{k_n} \tag{58}$$

or,

$$\frac{\alpha_{m,n}}{k_n} - \frac{\alpha_{m',n-1}}{k_{n-1}} = \frac{2\pi}{m} \times \frac{\alpha_{m,n}}{k_n}, \tag{59}$$

where m' denotes the number of wave nodes at the preceeding or succeeding ring from ring n.

It can be shown from the dispersion relation Eq. (26) that the wavenumber k_n becomes independent of radius, r within a short distance from the origin. The asymptotic value of k_n is reached before the occurrence of the first concentric ring of the wave nodes. Hence in the above equations, it can be assumed that $k_{n+1}=k_n=k_{n-1}$. This enables a solution for m for a given n which is coupled with the solution of m' at ring number $n+1$ (or $n-1$). Therefore, we obtain from Eqs. (58) and (59), respectively, as follows:

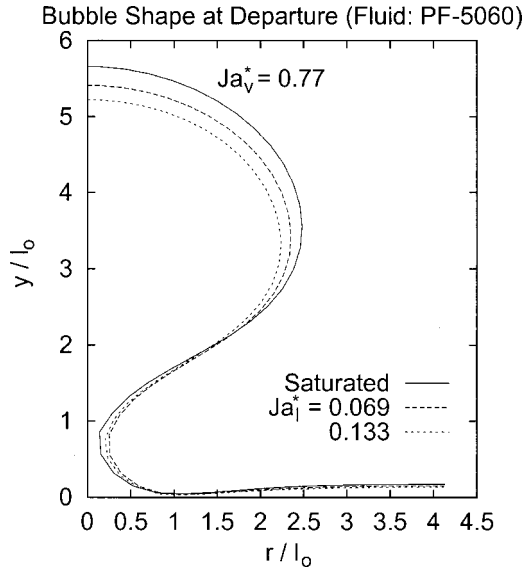

Fig. 6 Comparison of interface shape at bubble departure for wall superheat, ΔT_W=100°C, and liquid subcoolings, ΔT_{sub} =0°C, 5°C, and 10°C. The interface height and radius are non-dimensionalized with respect to l_o.

$$m = \frac{2\pi\alpha_{m,n}}{\alpha_{m',n+1} - \alpha_{m,n}} \tag{60}$$

or,

$$m = \frac{2\pi\alpha_{m,n}}{\alpha_{m,n} - \alpha_{m',n-1}}. \tag{61}$$

The above two equations describe implicit solutions for the *probable* values of m for a given n. Hence, either of the values of m obtained from the above equations are possible. This yields a set of solutions for (m, n) which provide a spatial distribution of wave peaks which are equidistant in the radial and circumferential directions.

Figure 1 shows the values of m for each ring number n obtained from Eqs. (60) and (61) assuming that the distance between the wave amplitude peaks (crests) correspond to the most dangerous wave number, k_{n_d}. In the figure, each column corresponds to the number of concentric ring. For example, when $n=1$, the minimum possible value of m is 2, according to Eq. (60). Hence, 2 is listed under first column for the solution of Eq. (60). When $m=2$ and $n=1$ the possible values of m for $n=2$ are 5, 6, and 7, according to Eq. (60). Hence arrows have been drawn in Fig. 1 from 2 in the first column pointing to 5, 6, and 7 in the second column. When $m=5$ and $n=2$ no solution is possible to Eq. (60) for values of m at $n=3$, so that the inter-crest separation distance

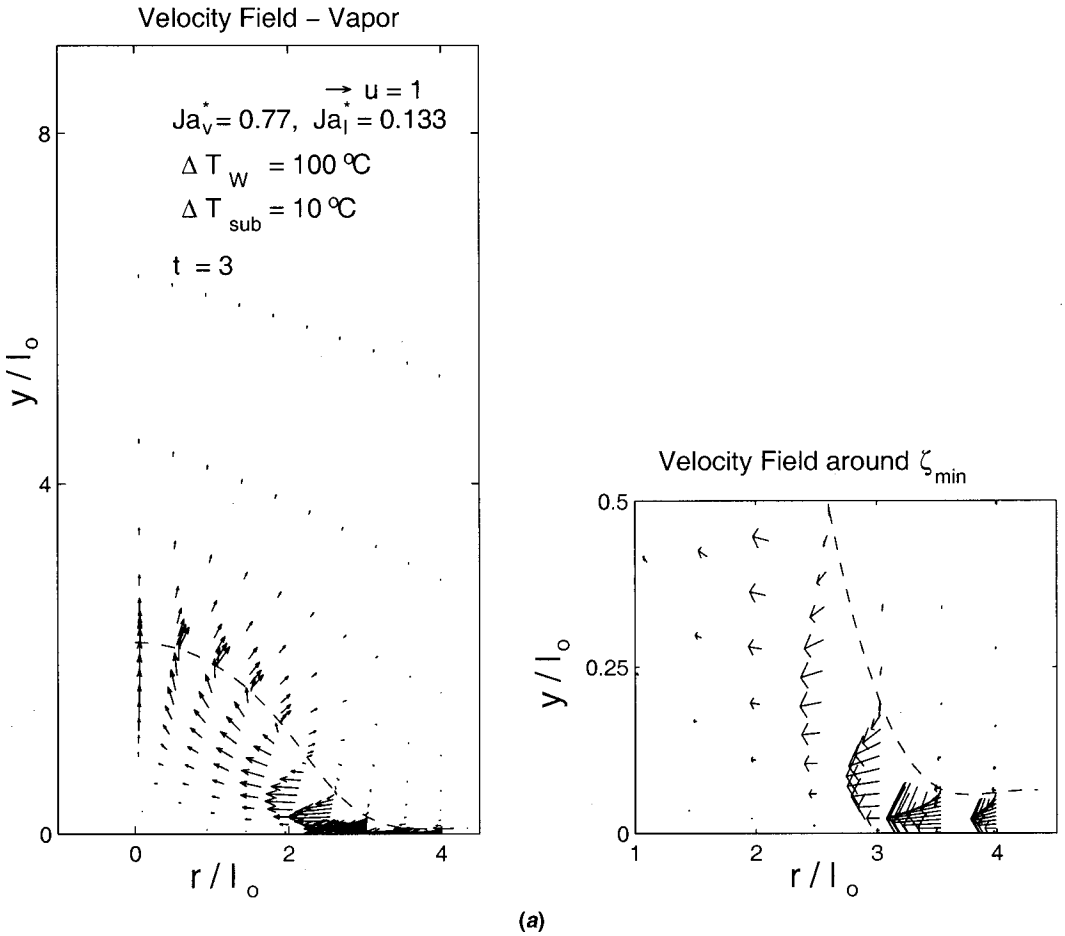

(*a*)

Fig. 7 (*a*) Spatial distribution of velocity vectors for ΔT_W=100°C, ΔT_{sub}=10°C and t=3. Time is non-dimensionalized with respect to t_o and velocity is non-dimensionalized with respect to u_o. The length of arrows plotted in the figure at the right are 2 times the respective length of arrows in the figure on the left; (*b*) spatial distribution of isotherms (θ) for ΔT_W=100°C and ΔT_{sub}=10°C at t=3. Time is non- dimensionalized with respect to t_o.

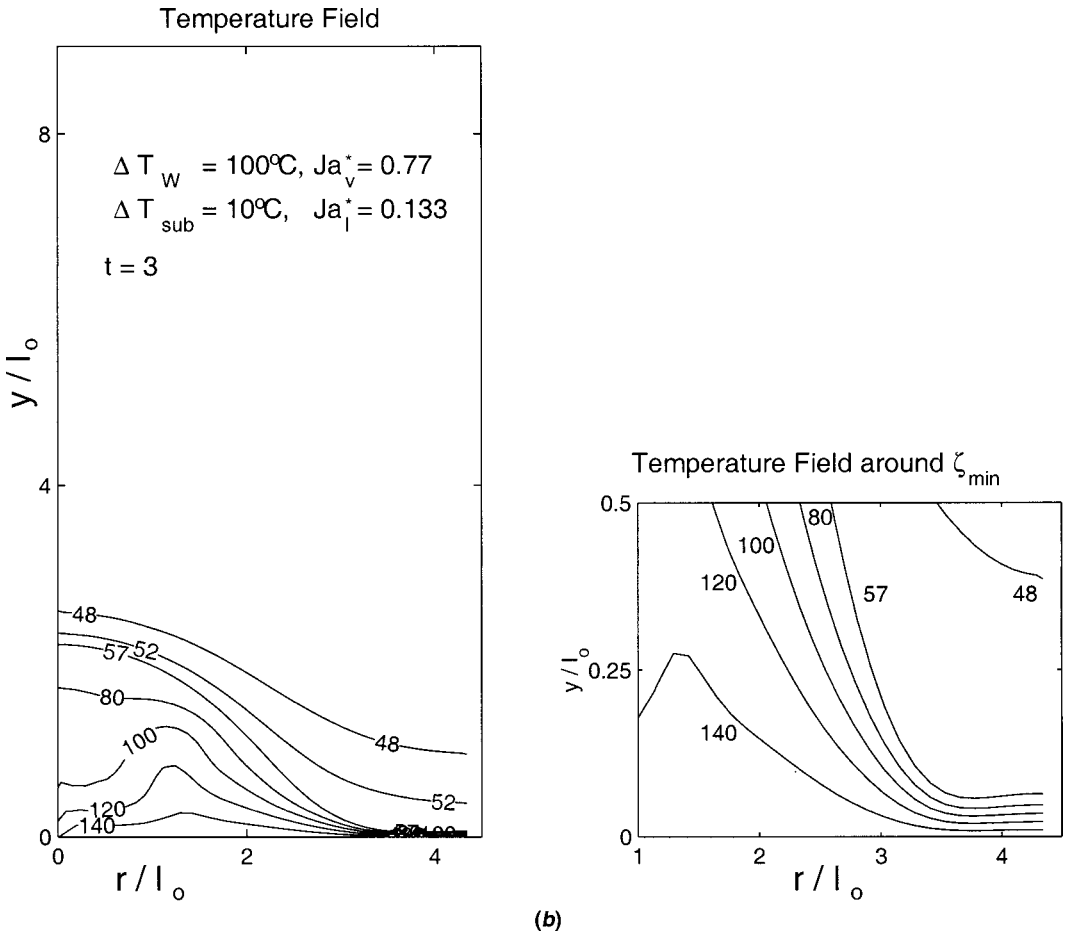

(*b*)

Fig. 7 (***Continued***)

corresponds to k_{n_d}. Hence, no arrows originate from $m=5$ in the second column. When $m=6$ and $n=2$ the only possible value of m for $n=3$ is 12, according to Eq. (60). Hence an arrow has been drawn from 6 in the second column pointing to 12 in the third column in Fig. 1. The possible values of m for succeeding values of n have been listed in the figure, in the columns that follow. A set of arrows are drawn in Fig. 1 to depict the relations akin to those mentioned above. Solution of Eq. (61) yields similar relationships which are also shown in Fig. 1.

From Fig. 1 the most probable solution corresponding to Eq. (60) is found as:

$n=1$	$n=2$	$n=3$	$n=4$	$n=5$
4 or **5**	**8**	**15**	**21**	**27** ’

whereas corresponding to Eq. (61) it is:

$n=1$	$n=2$	$n=3$	$n=4$	$n=5$
4	**9**	**15**	**21**	**27** .

Thus the two formulations give nearly identical solutions with small differences in the number of nodes that are accommodated in the inner rings. Figure 2 shows the location of wave crests (small ellipses) on concentric rings (also shown elliptical). The outer ring denoted by the solid line, and depicted as a large ellipse, represents the outer edge of the circular heater. The radius of each ring (the spacing between each ring being equal to the most dangerous wavelength) is obtained from Eqs. (60) and (61). Since in film boiling vapor bubbles are expected to be released alternatively from nodes and antinodes of the Taylor wave during each half of the cycle, in Fig. 2 the antinodes are depicted by crosses. It is interesting to note that starting with the first ring ($n=1$), the dominant wavelength in the radial and azimuthal directions obtained from the three-dimensional analysis is found to be equal to the ‘‘most dangerous’’ wavelength, λ_{d2}, obtained from two-dimensional Cartesian analysis. Table 1 shows the number of wave peaks supported per λ_{d2}^2 area in the region between consecutive rings. It is seen that about one wave peak is expected to exist over an area equal to square of two dimensional Taylor wavelength.

Next question to be answered before proceeding with the numerical simulation of the evolution of the interface is the extent of the computational domain for the axisymmetric analysis, although the process is three dimensional. Son [5] modeled the alternate release of bubbles from the node and antinode during each half of the cycle from an area equal to λ_{d2}^2. He did so by considering two interacting circular regions of area $\lambda_{d2}^2/2$ that surrounded the node and the antinode (locations of bubble release during the first half and the second half of a cycle, respectively). The analysis revealed that the essential physics of the process could still be retained if either of the circular regions surrounding the node or the antinode was considered and a condition of symmetry was imposed at the outer edge of these areas. The latter approach simplifies the numerical simulations and is utilized here, although the area and time averaged heat transfer coefficients in the latter approach are about 10 percent higher.

3.2 Evolution of the Interface During Subcooled Film Boiling. Figure 3 shows the computational domain used in the present analysis. The dimensionless outer radius, R, of the computational domain has a value of $\sqrt{6\pi}$ or 4.34. The dimensionless height H, of the computational domain was chosen to be 15. Com-

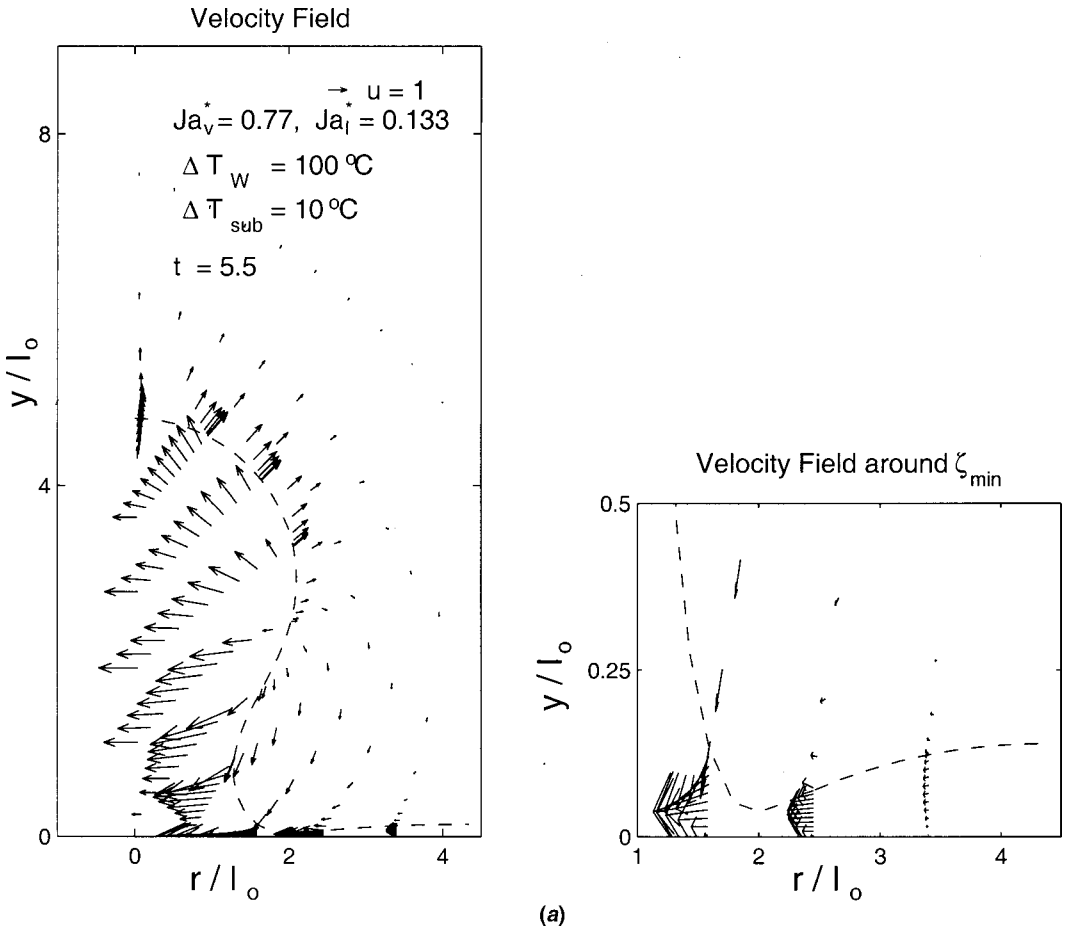

Fig. 8 (*a*) **Spatial distribution of velocity vectors for $\Delta T_W = 100°C$ and $\Delta T_{sub} = 10°C$ at $t = 5.5$. Time is non-dimensionalized with respect to t_o and velocity is non-dimensionalized with respect to u_o. The length of arrows plotted in the figure at the right are 2 times the respective length of arrows in the figure on the left;** (*b*) **spatial distribution of isotherms (θ) for $\Delta T_W = 100°C$ and $\Delta T_{sub} = 10°C$ at $t = 5.5$. Time is non-dimensionalized with respect to t_o.**

putations were performed for thermophysical properties of PF-5060 for wall superheat, $\Delta T_w = 100°C$ and liquid subcoolings ΔT_{sub} of 5°C, 10°C and 22°C. The vapor properties are evaluated at a vapor mean temperature of $(T_{wall} + T_{sat})/2$ and the liquid properties are evaluated at $(T_\infty + T_{sat})/2$. For thermophysical property values of saturated PF-5060 at atmospheric pressure the values of the characteristic length and growth rate are obtained from Eq. (19) as $l_o = 0.735$ mm and $\omega_o = 114.7$ Hz, respectively. Similarly, the characteristic time and velocity obtained from Eq. (38) are $t_o = 8.65$ ms, and $u_o = 0.085$ m/s, respectively.

Initially a vapor film of uniform thickness was perturbed using a Bessel function distribution as follows:

$$\frac{\zeta}{\zeta_0} = [1 + \epsilon J_0(3.832r/R)], \tag{62}$$

where J_o is the Bessel's function of order 0 and a value of 3.832 is the first root satisfying $dJ_o/dr = 0$ (Daly, [11]), and ϵ was set to 0.1. Here ζ is the location of the vapor-liquid interface in the vertical direction from the wall, while ζ_o is the thickness of the undisturbed vapor layer. [Note: ζ_{max} is the maximum height of the vapor liquid interface from the wall and ζ_{min} is the minimum vapor film thickness]. The initial velocity and pressure profiles were obtained from linear stability analysis, as described by Son [5]. Initially a conduction temperature profile (linear) is specified in the vapor region and in the liquid region an error function distribution of temperature is specified. The thickness of the thermal boundary layer in the liquid is derived by assuming that a semi-infinite liquid layer uniformly at subcooled temperature is brought in contact with the interface at the saturation temperature. The duration of contact is assumed to be equal to half of the time period between two consecutive bubble departures at a particular location.

Prediction of Interface Shape and Growth. The evolution of the interface during one cycle was computed. The grid structure at early and late periods of evolution of the interface is shown in Fig. 4. The computations were terminated after the radius of the neck acquired a value smaller than the size of one mesh. In this work, no attempt was made to track the bubble motion into liquid after pinch off. The shapes of the evolving interface at several discrete times from computations for superheat of 100°C and subcooling of 5°C, and 10°C are shown in Fig. 5. The plotted interface height at different radial positions has been non-dimensionalized with the characteristic length. After the outer interface in the middle attains an amplitude of about 3, a ''neck'' starts to form at the base of the evolving interface. After the ''neck'' formation—the interface continues to move inward until the bubble pinches off. The vapor film is thinnest where the interface appears to attach to the heater surface. The location at which minimum film thickness occurs moves radially inward with time. The minimum vapor film thickness is found to decrease with time until just prior to bubble departure, when at the location of minimum vapor film thickness the interface once again moves away from the wall. This is caused by enhanced evaporation due to superheated vapor accelerating at the location of minimum vapor film thickness.

The bubble shapes just prior to departure for the saturated case

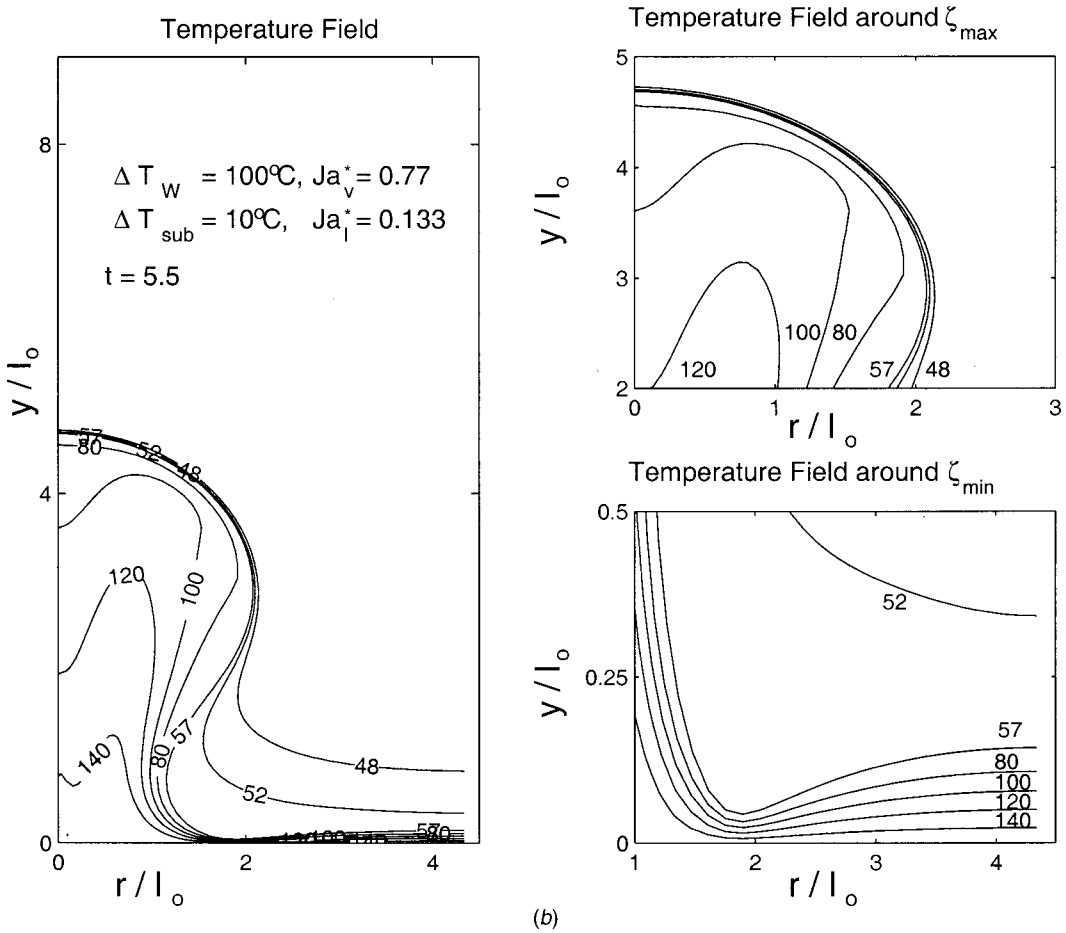

Fig. 8 (***Continued***)

and for subcoolings, $\Delta T_{sub}=5°C$ and 10°C, for a wall superheat of $\Delta T_W=100°C$ are shown in Fig. 6. The effect of liquid subcooling is to reduce the bubble height as well as the sideways growth of the interface. At higher subcooling the liquid drag on the vapor bubble is smaller because of the decrease in growth rate of the interface and correspondingly there is less sideways protrusion of the vapor bubble.

Thermal and Hydrodynamic Analyses. Both vapor and liquid side hydrodynamics significantly modify the heat transfer mechanisms in subcooled film boiling. In Figs. 7 and 8 velocity vectors and isotherms, respectively, have been plotted for a wall superheat of 100°C and for liquid subcooling of 10°C at dimensionless times 3 and 5.5. The figures show that the magnitude of velocities in the vapor phase are much higher than those in the liquid phase. The vapor velocity increases radially inwards in the thin film region because of gradually decreasing flow area as the vapor formed at the interface flows radially inward. The vapor injected into the bubble from the thin film region induces a large convective motion in the bubble. The liquid velocities are higher near the top part of the bubble due to dispacement of the liquid mass by the expanding bubble and diminish in the pool. The radially inward movement of the interface at the neck region causes the liquid from the upper region to flow inward towards the neck region.

The temperature profiles show that the spacing between the isotherms is uniform in the thin film region. This indicates that the energy transfer during film boiling is governed mainly by conduction in the thin film region, rather than by convection. The spacing between isotherms is distorted in the vapor bubble due to large convective motion in the bubble.

It is also observed that the thermal boundary layer is ''squeezed'' at the upper portion of the vapor bubble with rapid evolution of the interface. The thermal boundary layer shrinks as the interface rises at a rate faster than the development of the thermal boundary layer in the liquid. However, the thermal boundary layer in the neck region is quite thick because of lack of upward convective motion.

Heat Flux Partitioning. In contrast to saturated film boiling where liquid side heat transfer is nonexistent, in subcooled film boiling the liquid side heat transfer significantly affects the evapo-

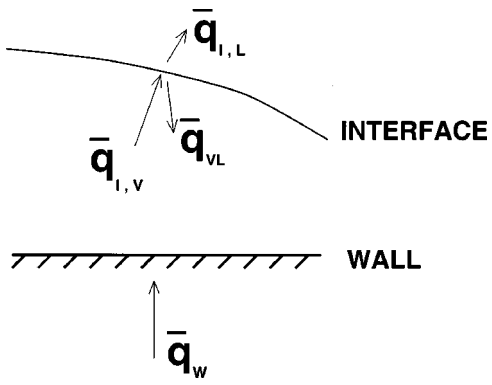

Fig. 9 Schematic of the various heat fluxes at the interface and at the wall in subcooled film boiling

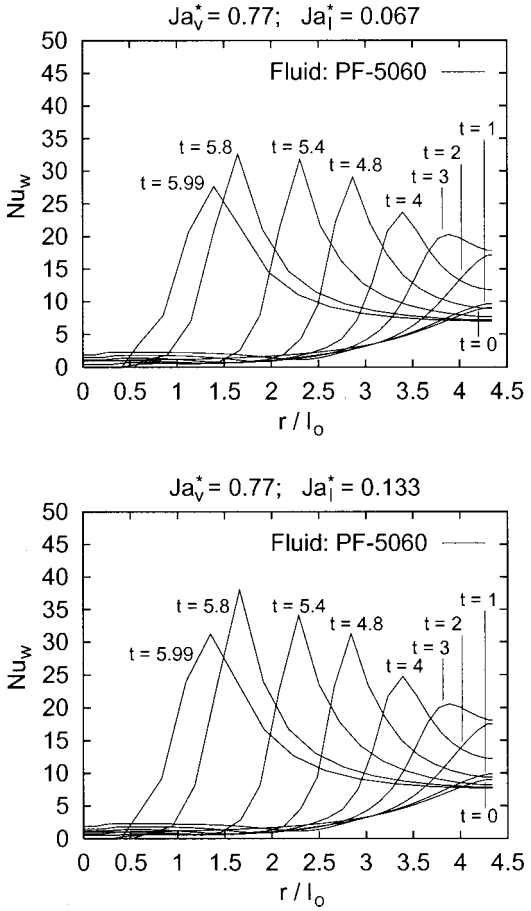

Fig. 10 Plot of temporal variation of local values of wall Nu for wall superheat, ΔT_W=100°C and liquid subcooling, ΔT_{sub} =5°C and 10°C. The radial distances are non-dimensionalized with respect to l_o. Time t is non-dimensionalized with respect to t_o.

ration at the interface and thereby influences the wall heat transfer. Figure 9 shows a schematic representation of the various components of heat flux at the interface. The area averaged heat flux at the wall, $\overline{q_W}$, is partitioned between the sensible heat gained by the vapor (area averaged value), $\overline{q_{VS}}$, and the heat flux at the interface (area averaged) from the vapor side, $\overline{q_{I,V}}$. (The values

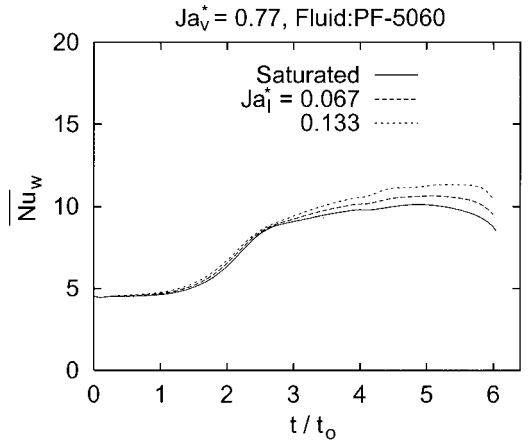

Fig. 11 Temporal variation of area averaged Nu at wall for wall superheat, ΔT_W=100°C and liquid subcooling, ΔT_{sub}=0°C, 5°C, and 10°C. Time is non-dimensionalized with respect to t_o.

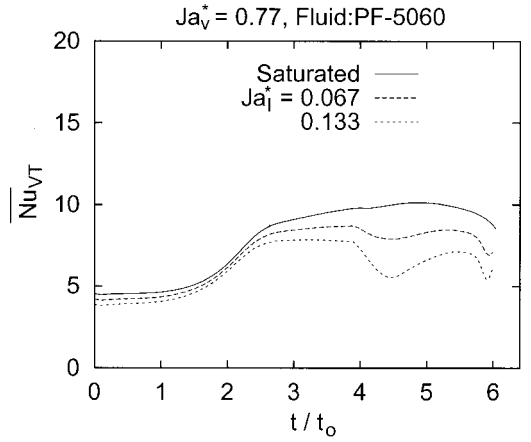

Fig. 12 Temporal variation of area averaged Nu in the vapor phase for wall siperheat, ΔT_W=100°C and liquid subcooling, ΔT_{sub}=0°C, 5°C, and 10°C. Time is non-dimensionalized with respect to t_o.

are averaged over an area bounded by a circle of radius R', where $R'=\lambda_{d2}/\sqrt{2\pi}$.) The area averaged heat flux at the interface from the vapor side $\overline{q_{I,V}}$, is partitioned between area averaged value of heat lost to the liquid at the interface, $\overline{q_{I,L}}$, and the heat flux, $\overline{q_{VL}}$, utilized for vapor production at the interface. Hence the total heat input, $\overline{q_{VT}}$, to the vapor phase as latent heat and sensible heat per unit cell area per unit time, is obtained by summing of $\overline{q_{VS}}$ and $\overline{q_{VL}}$, or

$$\overline{q_W}=\overline{q_{VS}}+\overline{q_{I,V}} \tag{63}$$

$$\overline{q_{I,V}}=\overline{q_{I,L}}+\overline{q_{VL}} \tag{64}$$

$$\overline{q_{VT}}=\overline{q_{VL}}+\overline{q_{VS}}. \tag{65}$$

The above components can be evaluated from the following relationships:

$$\overline{q_W}=\frac{\Delta T_w}{R'^2}\int_{r=0}^{r=R'}-\kappa_v\left(\frac{\partial\theta_v}{\partial y}\right)_{y=0}2rdr \tag{66}$$

$$\overline{q_{I,V}}=\frac{\Delta T_w}{R'^2}\int_{r=0}^{r=R'}-\kappa_v\hat{\mathbf{j}}\cdot\left(\frac{\partial\theta_v}{\partial\hat{\mathbf{n}}}\right)_{y=\eta_0}2rdr \tag{67}$$

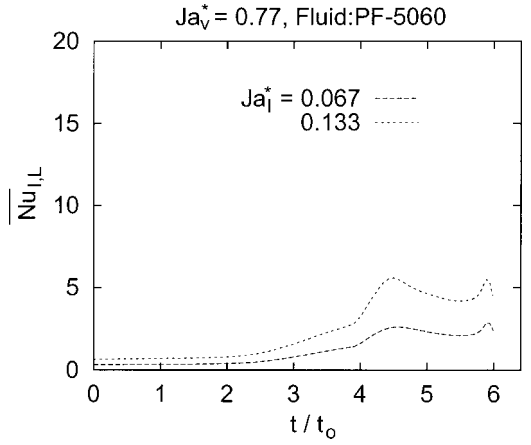

Fig. 13 Temporal variation of component of averaged Nu in the liquid phase for wall superheat, ΔT_W=100°C and liquid subcooling, ΔT_{sub}=5°C and 10°C. Time is non-dimensionalized with respect to t_o.

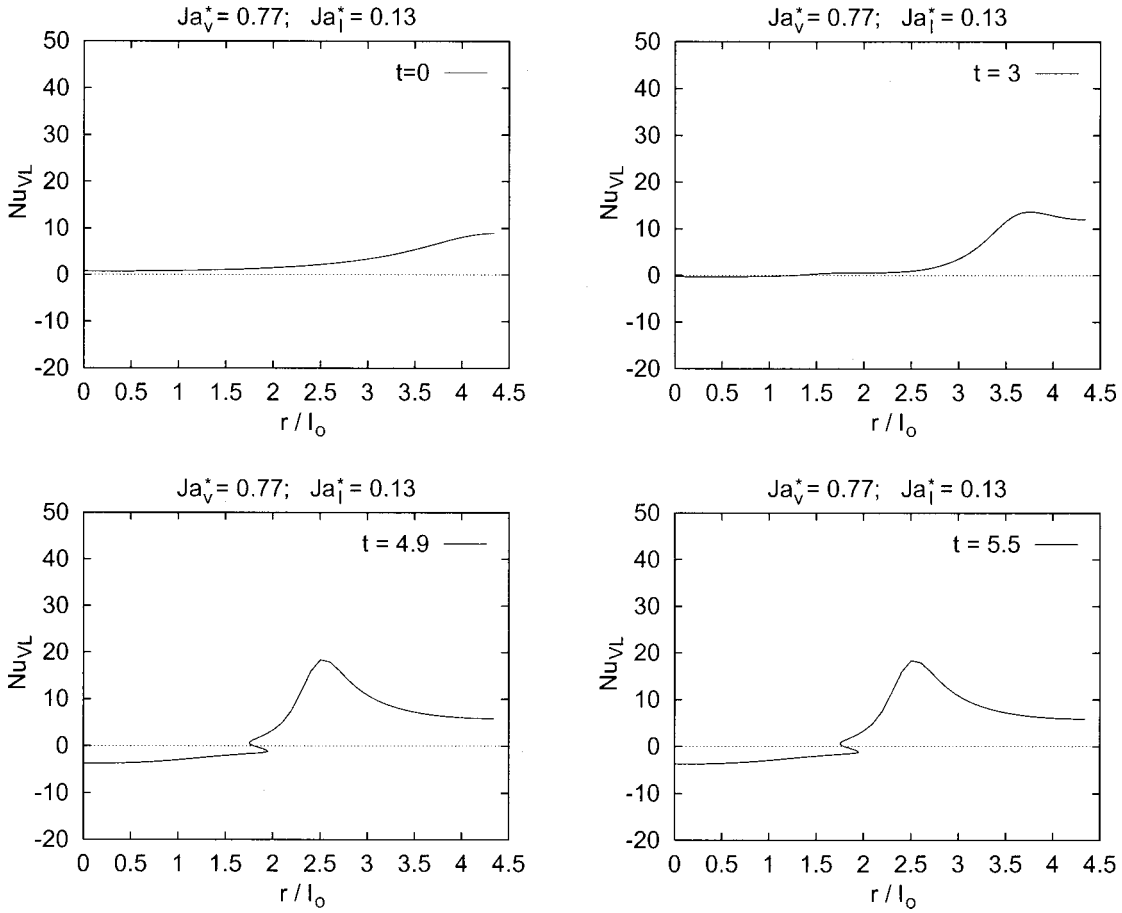

Fig. 14 Plot of local Nu at interface for production of vapor entering the film for $t=0$, 3, 4.9, and 5.5. Time is non-dimensionalized with respect to t_o and radial distance is non-dimensionalized with respect to l_o.

$$\overline{q_{I,L}} = \frac{\Delta T_{\text{sub}}}{R'^2} \int_{r=0}^{r=R'} -\kappa_l \hat{\mathbf{j}} \cdot \left(\frac{\partial \theta_l}{\partial \hat{\mathbf{n}}} \right)_{u=n_0} 2rdr \tag{68}$$

$$\overline{q_{V,L}} = \overline{\dot{m}} h_{fg} \tag{69}$$

where

$$\overline{\dot{m}} = \frac{\rho_v u_0}{R'^2} \int_{r=0}^{r=R'} \dot{m} 2rdr, \tag{70}$$

where $\dot{m}$ is defined in Eq. (51), $\hat{\mathbf{n}}$ is the unit normal vector at any radial location on the interface and $\hat{\mathbf{j}}$ is the unit vector in the y direction. (In saturated film boiling $\overline{q_{I,L}}=0$, and, hence, $\overline{q_{I,V}} = \overline{q_{VL}}$).

The Nusselt number based on area averaged wall heat flux is written as

Table 2 Predictions for $\overline{\overline{\text{Nu}}}_W$ for $\Delta T_W = 100°\text{C}$

$(\Delta T)_{sub}$ (°C)	Ja_l^*	Numerical Prediction
0	0	7.84
5	0.067	8.12
10	0.133	8.45
22	0.293	8.91

$$\overline{\text{Nu}}_W = \frac{\overline{q_W} l_0}{\kappa_v \Delta T_W} = \frac{1}{R'^2} \int_{r=0}^{r=R'} \text{Nu}_W 2rdr. \tag{71}$$

Similar Nu can be defined for $\overline{q_{I,L}}$, $\overline{q_{VT}}$, and $\overline{q_{VL}}$ as

$$\overline{\text{Nu}}_{VT} = \frac{\overline{q_{VT}} l_0}{\kappa_v \Delta T_W} \tag{72}$$

$$\overline{\text{Nu}}_{I,L} = \frac{\overline{q_{I,L}} l_0}{\kappa_v \Delta T_W} \tag{73}$$

$$\overline{\text{Nu}}_{VL} = \frac{\overline{q_{VL}} l_0}{\kappa_v \Delta T_W}. \tag{74}$$

The spatial variation of Nu_W at different times during the evolution of the interface is shown in Fig. 10. Large variations in Nu_W are seen to occur both spatially and temporally. The peak in Nu_W occurs at a point where the vapor film thickness is minimum. The location at which maximum heat transfer (or Nu_W) occurs is seen to move radially inward towards the center with time. Also, the magnitude of maximum heat transfer (or maximum value of Nu_W) increases with time, until prior to bubble departure. Just before bubble departure, the peak value of Nu_W is found to decrease. This result is different from that observed for results from computations when property values of water are used [5]. The value of Ja_v for a wall superheat of 100 °C for PF-5060 is 0.77, and 0.09 for water.

High values of Ja_v imply that liquid can be readily evaporated when exposed to superheated vapor. It is postulated that increase

in the minimum vapor thickness just prior to bubble departure is a result of evaporation induced by the high velocity vapor leaving the film region.

Figure 11 shows the temporal variation of area averaged Nusselt number (or $\overline{\mathrm{Nu}}_W$) computed for the two values of ΔT_{sub}. It is noted that as the interface evolves a significant increase in $\overline{\mathrm{Nu}}_W$ occurs from the initial value. The increase results from the increase in local value of heat transfer coefficient in the thin film region. With increase in liquid subcooling the area averaged heat transfer coefficient increases. However, most of this enhancement occurs in late stages of the evolution of the interface. In order to understand the physics of the process further, we plot in Fig. 12, area averaged Nusselt number based on heat input into the vapor (phase change and sensible heat). It is seen that with increase in liquid subcooling less amount of energy partitions into the vapor. The largest reduction in heat input into vapor occurs when the interfacial area of the evolving interface increase very rapidly. However, subsequently in the later stages of the evolution of the interface some recovery in the total heat input in vapor takes place.

Nusselt number based on area average heat transfer into the subcooled liquid (or $\overline{\mathrm{Nu}}_{I,L}$) is plotted in Fig. 13 as a function of time during the growth period of the interface. At a given time the Nusselt number increases as liquid subcooling is increased. For a given subcooling the Nusselt number remains fairly constant during the initial period but increases very rapidly in the dimensionless time interval between 4 and 5. This is the period during which a rapid reduction in $\overline{\mathrm{Nu}}_{VT}$ was observed. During the bubble growth period as much as five fold variation in liquid side heat transfer is observed. Isotherms in the liquid show that during the period of rapid increase in interfacial area the thermal boundary layer in the upper portion of the bubble thins and in turn leads to an increase in the rate of heat transfer into liquid. However, in the later stages, as the interface slows down, the boundary layer thickens once again and leads to reduced rate of heat transfer into liquid.

In Fig. 14 the Nusselt number based on the energy utilized in producing vapor at the interface is plotted as a function of radial position at different times during the evolution of the interface. It is seen that later periods of the evolution of the interface, negative values of the of the Nusselt number occur at the top portion of the vapor-liquid interface. The negative values imply that heat flux into liquid in the thin thermal layer region is supported by condensation of vapor. At a radial position of about 2, $\overline{\mathrm{Nu}}_{VL}$ is shown to be multi-valued. This is reflection of the shape of the interface and simultaneous evaporation and condensation that occur on different parts of the interface. The maximum value of $\overline{\mathrm{Nu}}_{VL}$ occurs at the location where film is the thinnest.

The calculated values of $\overline{\overline{\mathrm{Nu}}_W}$ based on area and time average heat transfer coefficient at the wall are given in Table 2. As would be expected $\overline{\overline{\mathrm{Nu}}_W}$ increases with increase in Ja_l or liquid subcooling. The enhancement in $\overline{\overline{\mathrm{Nu}}_W}$ results from the fact that wall has to supply not only the energy transferred into the vapor but also into the liquid overlying the thin film region. For the limited range of subcoolings studied in this work, the values listed in the table are correlated as

$$\overline{\overline{\mathrm{Nu}}_W} = \overline{\overline{\mathrm{Nu}}_{W_0}}(1 + 0.5\ \ J^*_{a_l}), \tag{75}$$

where $\overline{\overline{\mathrm{Nu}}_{Wa}}$ is the Nusselt number obtained from the analysis when liquid is saturated. The numerical constant found in Eq. (75) is dependent on wall superheat or $J^*_{a_v}$. The constant will increase nonlinearly as $J^*_{a_v}$ is reduced. For the results presented in Table 2, $J^*_{a_v}$ is 0.77. This value is much higher than that obtained by Dhir and Purohit [17] in their experiments of subcooled film boiling of water. However, Dhir and Purohit's analysis clearly showed a reduction in the constant multiplying $J^*_{a_l}$ as wall superheat was increased. The value of 0.5 obtained in the present work is consistent with that deduced from the results of Dhir and Purohit for high wall superheats.

4 Conclusions

1 Three dimensional Taylor instability analysis in an axisymmetric geometry has been performed. The analysis reveals that most dominant Taylor wavelength during film boiling on a disc is the same as that obtained from 2-D analysis in Cartesian coordinates.

2 Numerical simulation of evolving interface during subcooled film boiling have been performed. The analysis provides the shape and the growth rates of the interface as well as the associated hydrodynamic and thermal behavior.

3 The effect of liquid subcooling is to increase the wall heat flux, mainly because of the heat loss to liquid that occurs in the thin film region. With increased heat loss to the liquid the film becomes thinner.

4 Condensation of vapor occurs on the top portion of the evolving interface whereas evaporation occurs in the thin film region.

Nomenclature

c = constant
c_{pl} = liquid specific heat
c_{pv} = vapor specific heat
g = gravitational acceleration
h = heat transfer coefficient
h_{fg} = latent heat of vaporization
J = Bessel function
Ja* = modified Jacob number
k = wave number
l_o = characteristic length
m = eigen value
n = eigen value
Nu = Nusselt number
p = pressure
Pr = Prandtl number
q = heat flux
R = radius
r = radial coordinate
Ra = Rayleigh number
Re = Reynolds number
R_s = radius of curvature of the interface
t = time
u = radial velocity
v = velocity in the vertical direction
w = velocity in the azimuthal direction
x = coordinate in the horizontal plane
y = vertical coordinate
z = coordinate in the horizontal plane
α = dimensionless wave number
γ = interfacial tension
ΔT_{sub} = liquid subcooling
ΔT_w = wall superheat
κ = thermal conductivity
ζ = interface position from the wall
$\overline{\eta}$ = interface displacement from mean film thickness
θ = dimensionless temperature
λ = wavelength
μ = molecular viscosity
ν = kinetic viscosity
ρ = density
σ = normal stress
τ = shear stress
ϕ = potential function
ω_0 = characteristic growth rate

Subscripts

c = critical
d_2 = most dangerous two-dimensional
IL = interface liquid side
IV = interface vapor side
l = liquid
nc = natural convection
v = vapor
VL = latent heat (vapor phase)
VS = sensible heat (vapor phase)
VT = vapor total
W = wall

References

[1] Berenson, P. J., 1961, ''Film Boiling Heat Transfer From Horizontal Surface,'' ASME J. Heat Transfer, **83**, pp. 351–362.
[2] Hosler, E. R., and Westwater, J. W., 1962, ''Film Boiling on a Horizontal Plate,'' ARS J., **32**, pp. 553–560.
[3] Ramilison, J. M., and Lienhard, J. H., 1987, ''Transition Boiling Heat Transfer and the Film Transition Regime,'' ASME J. Heat Transfer, **102**, pp. 746–752.
[4] Klimenko, V. V., and Shelepen, A. G., 1982, ''Film Boiling On a Horizontal Plate-A Supplementary Communication,'' Int. J. Heat Mass Transf., **25**, pp. 1611–1613.
[5] Son, G., 1996, ''Numerical Simulation of Nonlinear Taylor Instability with Applications to Film Boiling, Melting and Sublimation,'' Ph.D. thesis, University of California, Los Angeles, CA.
[6] Hamill, T. D., and Baumeister, K. J. 1969, ''Effect of Subcooling and Radiation on Film-Boiling Heat Transfer from a Flat Plate,'' NASA TND D-3925.
[7] Dhir, V. K., and Lienhard, J. J., 1973, ''Taylor Stability of Viscous Fluids With Application to Film Boiling,'' Int. J. Heat Mass Transf., **16–11**, pp. 2097–2109.
[8] Bellman, R., and Pennington, R. H., 1954, ''Effects of Surface Tension and Viscosity on Taylor Instability,'' Q. Appl. Math., **12**, pp. 151–161.
[9] Sernas, V., Lienhard, J. H., and Dhir, V. K., 1973, ''The Taylor Wave Configuration During Film Boiling From a Flat Plate,'' Int. J. Heat Mass Transf., **16**, pp. 1820–21.
[10] Jacobs, J. W., 1986, ''Three Dimensional Rayleigh Taylor Instability,'' Ph.D. thesis, University of California, Los Angeles, CA.
[11] Daly, B. J., 1969, ''Numerical Study of the Effect of Surface Tension on Interface Instability,'' Phys. Fluids, **20**, No. 4.
[12] Thompson, J. F., Warsi, Z. U. A., and Mastin, C. W., 1985, *Numerical Grid Generation, Foundations and Applications*, Elsevier Science, North Holland.
[13] Shyy, W., 1994, *Computational Modeling for Fluid Fow and Interfacial Transfer*, Elsevier, NY.
[14] Streett, C. L., and Hussaini, M. Y., 1987, ''Finite Length Effects on Taylor Couette Flow,'' in Stability of Time-Dependent and Spatially Varying Flows, D. L. Dwoyer, and M. Y. Hussaini, eds., Springer-Verlag, New York.
[15] Banerjee, D., 1999, ''Numerical and Experimental Investigation of Subcooled Film Boiling on a Horizontal Plate,'' Ph.D. thesis, University of California, Los Angeles, CA.
[16] Son, G., and Dhir, V. K., 1997, ''Numerical Simulation of Saturated Film Boiling on a Horizontal Surface,'' ASME J. Heat Transfer, **119**, pp. 525–533.
[17] Dhir, V. K., and Purohit, G. P., 1978, ''Subcooled Film-Boiling Heat Transfer From Spheres,'' Nucl. Eng. Des., **47**, No. 1, pp. 49–66.

Study of Subcooled Film Boiling on a Horizontal Disc:[1] Part 2—Experiments

D. Banerjee

V. K. Dhir

Mechanical and Aerospace Engineering Department, University of California, Los Angeles, Los Angeles, CA 90095

Experiments were performed to study subcooled film boiling of performance liquid PF-5060 (made by 3-M Company) on a horizontal copper disc. The experiments were performed for two regimes of film boiling involving departing vapor bubbles (low subcooling) and nondeparting vapor bubbles (high subcooling). By employing high speed digital camera, data were obtained for temporal variation of bubble height, bubble shape and bubble growth rate over one cycle. Heat flux data were deduced from temperatures measured with thermocouples embedded in the solid. The results from the numerical model are compared with experimental data and are found to be in general agreement. Particle Tracking Velocimetry (PTV) experiments were performed for a configuration of non-departing vapor bubbles to study the flow field in the liquid phase. The PTV experiments point to the existence of natural convection flow in the liquid phase and is in qualitative agreement with the predictions available in the literature.
[DOI: 10.1115/1.1345890]

Keywords: Boiling, Film, Heat Transfer, Phase Change, Two-Phase

1 Introduction

In subcooled film boiling the bulk temperature of the liquid phase is lower than the saturation temperature. In such a situation the heat flux at the wall is partitioned at the interface between phase change and convective heat transfer into the subcooled liquid. This results in higher heat transfer compared to saturated film boiling.

Dhir and Purohit [1] observed experimentally that film boiling heat transfer coefficients in subcooled film boiling on a sphere were 50–60 percent higher than those predicted by the laminar plane interface theory. The significant enhancement in liquid side heat transfer was attributed to the alteration of flow field in the liquid by interfacial waves. Experimental results of Vijaykumar and Dhir [2,3] show that degree of subcooling significantly affects the liquid side heat transfer in subcooled film boiling on a flat vertical plate.

Nishio and Ohtake [4] observed that subcooled film boiling in the ''small cylinder diameter'' regime could be divided into two distinct regimes, ''normal'' and ''singular.'' In the ''normal'' regime of film boiling (for R-113 as the test fluid and for heater wire diameter greater than 0.2 mm) the boiling heat transfer coefficient was found to increase with degree of subcooling. In the ''singular'' regime of film boiling (for R-113 as the test fluid and heater wire diameter less than 0.2 mm), the heat transfer coefficients were found to decrease to a minimum with increasing subcooling. However, the authors did not provide any explanation for this peculiar behavior in the ''singular'' regime.

Kikuchi et al. [5] found that in saturated film boiling of water on silver coated spherical and cylindrical probes the liquid-solid (L-S) contacts occurred with a much higher frequency compared to subcooled film boiling, in which the L-S contacts were almost nonexistent. This pointed to the stabilizing influence of subcooling on the vapor-liquid interface in subcooled film boiling. They also found that the L-S contact frequency was lower for a cylinder than for a sphere.

Linear stability analysis performed by Busse and Schubert [6] and also discussed by Busse [7], for a system undergoing first order phase change by heating from below pointed to the existence of different regimes of vapor-liquid interfacial instability. An application of this analysis was in a geothermal situation where, for instance, water can be stably stratified over steam. The results of the aforementioned analysis were experimentally verified by Ahlers et al. [8]. The experiments involved isotropic-nematic phase transition of a liquid crystal. They reported various conditions where conduction temperature profile was obtained in the heavier overlying nematic phase.

Under certain conditions of subcooling and wall heat flux values the vapor film is stably stratified under the liquid pool in subcooled film boiling under pool boiling conditions. Study of such a configuration is helpful in understanding the hydrodynamic aspects of the vapor-liquid interface and heat transfer into the subcooled liquid. Such a situation was reported by Ayazi and Dhir [9], for subcooled film boiling of water on a horizontal cylinder. The authors argued that such a configuration of stationary vapor-liquid interface can exist only when the vapor production rate at the film matches the condensation rate at the bubble interface. Based on the experimental results, the authors proposed a criterion for the onset of collapse of subcooled film boiling on a horizontal cylinder.

Though there is a huge body of literature on subcooled film boiling—very few investigations have been performed to understand the hydrodynamics of film boiling on a horizontal flat plate. Part of the reason can be ascribed to the difficulty in gathering experimental data for evolution of the interface on a flat plate (compared to say, on a horizontal cylinder) and also in proper post processing of the experimental data. The difficulty arises because of obstruction of the view by bubbles departing in front and back of the focal plane. This study was performed to enhance the understanding of subcooled film boiling on a horizontal flat plate under pool boiling conditions. The objectives of the present investigation were to: (1) compare the hydrodynamic and wall heat transfer experimental data with numerical predictions for a configuration of departing bubbles at low subcoolings; and (2) study the occurrence of a stably stratified vapor layer under the liquid pool for subcooled film boiling on a horizontal disc at high subcoolings and compare the results with the numerical predictions of Banerjee et al. [10].

For this purpose, film boiling experiments were performed from low to high subcoolings. In the experiments, spacing of the bubble

[1]This work received support from the National Science Foundation.

Contributed by the Heat Transfer Division for publication in the JOURNAL OF HEAT TRANSFER. Manuscript received by the Heat Transfer Division January 20, 2000; revision received October 31, 2000. Associate Editor: V. Carey.

releasing nodes, bubble shape during the evolution of the interface, bubble growth rate, flow field in the liquid and overall heat transfer rate were measured.

2 Experimental Apparatus

The experimental setup is shown in Fig. 1. The test section consists of a cylindrical test heater block (machined from one end of a 99.99 percent pure solid copper cylinder) placed on a steel base plate and forms the base of a cubic viewing chamber (15 cm each side). The test heater block was machined to a diameter of 88.9 mm and a height of 42.18 mm. Holes were drilled into the copper cylinder from bottom to insert several cartridge heaters. Temperature was measured with thermocouples embedded in the test block. The test liquid was confined to the viewing chamber and was boiled on the copper surface. A cooling coil made of copper tubing was placed just under the free surface of the test liquid. Antifreeze mixture (mixture of ethylene glycol and water) was used as a cooling fluid. The antifreeze mixture was chilled in an external chiller unit to $-15°C$ and pumped through the cooling coil to cool the test liquid and obtain the required degree of subcooling. The temperature drop of the cooling fluid in the chiller tubes was maintained at less than 1°C to ensure uniform cooling at the free surface. Complete details of the apparatus are given by Banerjee [11].

Visualization studies were performed to determine the interface motion. The viewing chamber was illuminated from outside with tungsten filament incandescent light source placed behind optical diffuser plates. Vapor bubbles were photographed with a digital camera (manufactured by HiSys Inc.) at framing rates ranging from 450 to 1024 frames/s. A measuring scale was glued on the side of the steel jacket for calibration of the digital video pictures. Simultaneous acquisition of thermocouple data for heat flux and wall temperature and video pictures for temporal variation of bubble height and bubble spacing was made. A few time exposure still photographs were also recorded on high speed photographic films. Various lense combinations ranging from 35–210 mm were tried for obtaining motion pictures on the video camera as well as for the still photographs. The pictures of the vapor bubbles on the heater were obtained by taking video pictures at an angle from the side of the viewing chamber. The angle of inclination, with respect to the horizontal plane, of the video camera varied from 5 deg to 20 deg. The distance between vapor bubbles was measured for vapor bubbles lying in a plane perpendicular to the viewing axis. This was done to obviate the optical distortions arising from the inclination of the camera.

Particle Tracking Velocimetry (PTV) Measurements. With the objective of studying the flow-field within the liquid pool at high subcoolings, the liquid pool above the heater was seeded with particles and the video pictures of the particle motion were recorded. Since a priori information was available about the optimum particle concentration, proper intensity and lighting techniques as well as the required camera parameters (e.g., magnification, resolution of the digital video camera, exposure time, etc.) for minimizing the errors in the data, the experimental procedure was based on trial and error. The particles used in this experiment were ground fish scales with a metallized coating of Aluminum. The particles had a nominal diameter of 10 μm. Also, the particles had widely varying density distribution—depending on the amount of metallized coating. Hence, particles with similar density as the test fluid (PF-5060) were obtained by floatation separation technique. In following this technique, particles were well stirred in a container of PF-5060. The particles with same density as liquid PF-5060 remained suspended in the liquid and were sucked out with a pipette, thus separating them from the floating particles at the free surface of the liquid and the particle sediments settled at the bottom of the container. This way a slurry of particles in PF-5060 was obtained with the solid particles having the same density as the liquid PF-5060.

The particles were introduced from above into the liquid pool during subcooled film boiling with a pipette and a plunger. The pipette was filled with the slurry of the particles in PF-5060 and was placed in the upper portion of the plane of imaging. The focal plane of the high speed digital camera was aligned with the illuminating plane. Illumination was achieved with a 600W Lowel Omni stage lamp (manufacturer: Omni Inc.) placed behind a collimator arrangement to generate a light sheet of approximately 1 mm thickness. He-Ne lasers of power rating 10mW, 100mW, and 300mW were also tried as illumination sources. However they were found to be unsuitable due to rapid attenuation of the illumination intensity of the light sheet.

To determine the flow field in the liquid, it was necessary to obtain simultaneous image of the particles and the vapor bubbles. Light scattered by the particles was sufficient to obtain an image on the digital video camera placed perpendicular to the light sheet. However, the light reflected by the vapor bubbles was insufficient to obtain an image on the digital video camera. Hence, a 60 W incandescent light source was placed on the side opposite to the camera, along with a set of diffuser plates to obtain a faint outline of the vapor bubbles in the images. This unconventional arrangement (compared to standard two-dimensional PTV) was necessi-

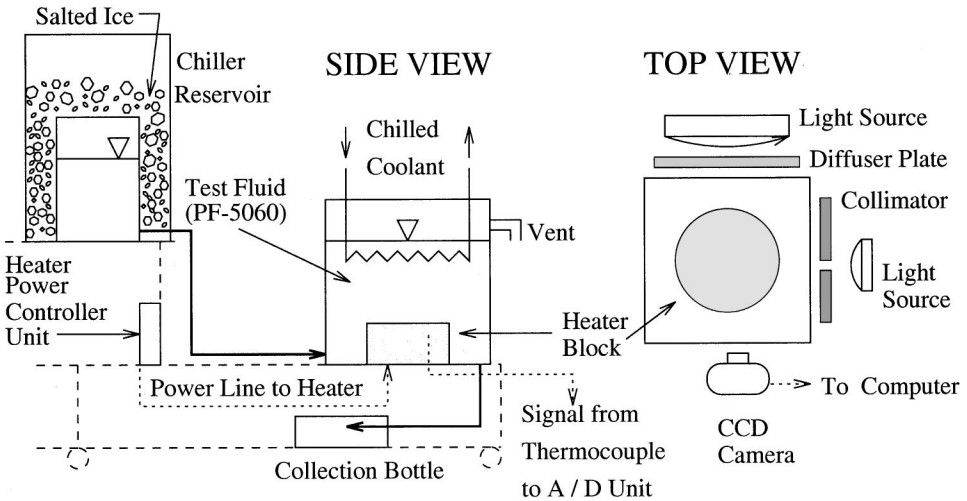

Fig. 1 Schematic diagram of experimental apparatus

tated by the need to obtain uniform background illumination as well as to restrict the illumination intensity to obtain images of particles and vapor bubbles at the same instant.

2.1 Experimental Procedure. The test surface was rubbed with 500 grit emery paper followed by 1000 grit emery paper and cleaned with acetone, prior to any test run. The test surface was heated to a temperature above the required superheat and the viewing chamber was filled with the test liquid to a certain fixed height.

A data acquisition system, consisting of a digital to analog converter and 16 channel data logger (manufacturer: Strawberry Tree), was used to record the signals from the thermocouples placed inside the copper block, on the outer surface of the steel jacket, in the test liquid, and the side walls of the test section.

The wall heat flux was adjusted by a variac to achieve the required superheat for obtaining film boiling under steady-state conditions. Tests were considered to be steady state when the temperature of the test block changed less than ± 1°C in 5 minutes. The liquid temperature changes were less than ± 0.5°C in 1 minute for liquid subcooling upto 20°C. Care was taken to avoid liquid thermal stratification. The liquid thermal stratification was found to be less than 0.5°C in a height of over 5 cm for subcoolings upto 20°C. The liquid subcooling was varied from 0 to 42°C and the wall superheat was varied from 50 to 100°C.

After steady state conditions were established the video camera was focussed on an area on the test surface for video capture of temporal evolution of vapor bubbles. The image of the measuring scale was recorded at the end of each experimental run for calibrating the magnification parameters of the camera and subsequent post processing for calculation of the bubble height.

2.2 Data Reduction

Wavelength Measurements. The radial location of bubbles was measured in pixels from the individual digital frames of the video pictures and converted to the actual distance, by multiplying with camera magnification. This enabled the measurement of the wavelengths in the radial direction. The circumferential direction wavelengths were obtained by counting the number of bubbles in each concentric ring. From this the average bubble separation distance in the circumferential direction was obtained by dividing the circumference of the ring by the number of bubbles.

Bubble Growth Rate Measurements. From the video films the height of the evolving interface was determined as a function of time. The interfacial velocity was obtained by taking the temporal derivative of the bubble height ($\zeta_{\max}$). The interfacial velocity in this situation is given by

$$\frac{d\zeta_{\max}}{dt} = \frac{(\Delta\zeta_{\max})}{(\Delta t)} \tag{1}$$

The growth rate is given by

$$\omega = \frac{\zeta_o}{\zeta_{\max}} \frac{d(\zeta_{\max}/\zeta_o)}{dt} = \frac{d}{dt}(\ln[\zeta_{\max}/\zeta_o]), \tag{2}$$

where, ζ_o is the undisturbed height of the vapor layer from the wall.

Particle Tracking Velocity Measurements. Using the ''pathline method,'' the velocity field in the liquid pool was measured with particles seeded in the liquid. In this method the displacement of a specific particle was measured between two consecutive video frames to obtain the velocity as

$$u = \frac{\Delta s}{S} f, \tag{3}$$

where s is the displacement of the particle, S is the magnification factor of the camera, and f is the framing rate of the video camera. The calculated value of the velocity was assigned to the mid-point between the initial and final locations of the particle.

Heat Flux Measurements. In steady-state tests, surface heat fluxes are readily calculated using the spatial temperature distribution recorded from the thermocouples. One-dimensional heat flow was found to exist inside the test heater block. The temperature distribution in the copper block was linear and the heat flux, q_W, was evaluated from the gradient of the temperature profiles in the copper block, as

$$q_W = \kappa_s \frac{\Delta T}{\Delta y}, \tag{4}$$

where κ_s is the thermal conductivity of heater test block material (copper), ΔT is the temperature differential between two thermocouples lying in the same vertical plane, and Δy is the distance between them. The surface temperature was obtained by simply extrapolating the temperature profile to the surface. Hence, the average wall Nusselt number $\overline{\overline{\mathrm{Nu}}}_W$ and the average heat transfer coefficient in film boiling $\bar{h}$ can be defined as

$$\overline{\overline{\mathrm{Nu}}}_W = \frac{q_W l_o}{\Delta T_W \kappa_v}; \quad \bar{h} = \frac{q_W}{\Delta T_W}. \tag{5}$$

The characteristic length scale, l_o and growth frequency, ω_o, in film boiling are defined as

$$l_o = \left[\frac{\gamma}{(\rho_l - \rho_v)g}\right]^{1/2}; \quad \omega_o = \left[\left(\frac{\rho_l - \rho_v}{\rho_l + \rho_v}\right)\left(\frac{g}{l_o}\right)\right]^{1/2}. \tag{6}$$

2.3 Error Analysis. The uncertainty in heat flux data is estimated to be ± 12 percent whereas the uncertainty in heat transfer coefficient values is estimated to be ± 15 percent. The error in measurement of interface height is estimated to be ± 10 percent, in interface velocity, ± 11 percent and in interface growth frequency ± 16 percent. For details of error analyses the reader is referred to Banerjee [11].

The net error in displacement measurement of particles in the PTV experiments is calculated to be ± 10 percent neglecting the three-dimensional effects of the velocity field. By including the three-dimensional effects in the velocity field this error is estimated to be less than 15 percent. The net error in velocity determination is estimated to be about ± 10.5 percent when neglecting the three-dimensional effects and is estimated to be about ± 15 percent when including the three-dimensional effects.

3 Results and Discussion

Experimental observations of interfacial behavior and wall heat transfer were made for a range of liquid subcoolings. At low liquid subcoolings the interface was observed to evolve as for saturated film boiling and vapor bubbles were released in a regular and cyclic manner from the interface. However, at high subcoolings the interface acquired a static shape. As such, discussion of results is divided into low and high subcooling cases.

3.1 Low Subcooling. For film boiling under subcooled conditions data were taken for dominant wavelength, interface shape, growth of interface, growth rate and for the heat transfer coefficient and comparisons were made with predictions.

Dominant Wavelength. Because of the passage through the pool of the bubbles leaving the interface, it was difficult to capture an unambiguous view of the orientation and location of the bubble releasing nodes at low subcoolings. However, with increased subcooling the interface acquired a nearly static shape, as will be discussed in more detail later. In this situation a clear view of the location of the bubble releasing nodes could be obtained. This is depicted in the photograph in Fig. 2. In this photograph the location of wave peaks in several radial rings and in the azimuthal direction can be clearly seen. It is in this context that Fig. 2 is contained in this section on low subcooling. From such photo-

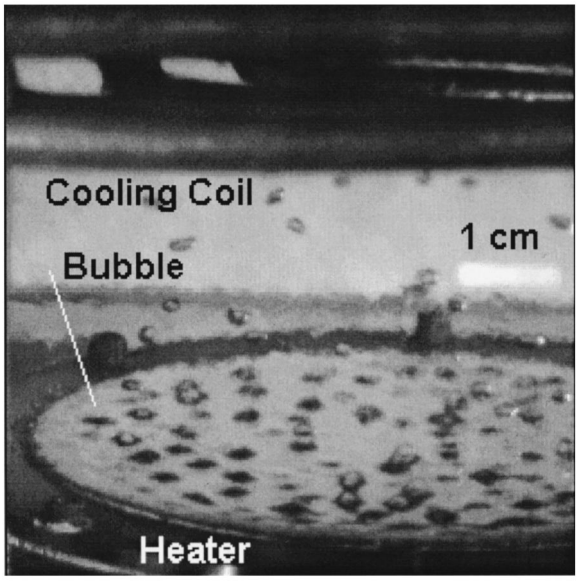

Fig. 2 Digital image of non-departing bubbles arranged on concentric rings on a horizontal circular plate for superheat of 52°C and subcooling of 42°C obtained from a single frame of movie. Camera angle: 10 deg to the horizontal. Test-Fluid: PF-5060. About 5 percent of the bubbles were found to depart by merger of contiguous bubbles caused by natural convection circulation induced into the liquid pool from the side walls.

graphs the ring radius as a function of discrete values of the ring number, n, from the center and the number of wave modes (m) in the n^{th} ring could be obtained. Figure 3 compares with the data the dimensionless value of ring radius as a function of ring number, n, with that predicted from the analysis. It is seen that though there is some variability in the data obtained from different experiments, the predictions are in general agreement with data. A similar comparison of the number of wave modes, m, as function of n is performed in Fig. 4. Although the agreement between predictions from analysis and data is reasonable, the data also show scatter. Some scatter in the data is not unexpected because of some lateral merger of bubbles. Any merger can reduce the number of wave modes by one, until the original pattern re-establishes. Good agreement with analytical predictions of the measured values of r_{n_d}, and m suggest that as assumed in the analysis the dominant

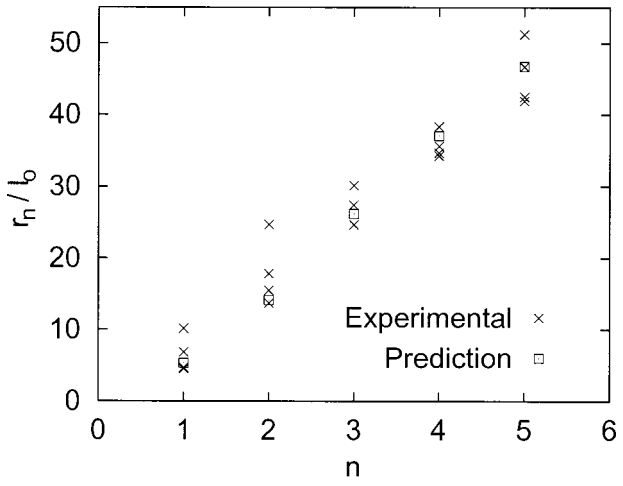

Fig. 3 Comparison of prediction for most probable values of r_n for different rings with the experimental measurements

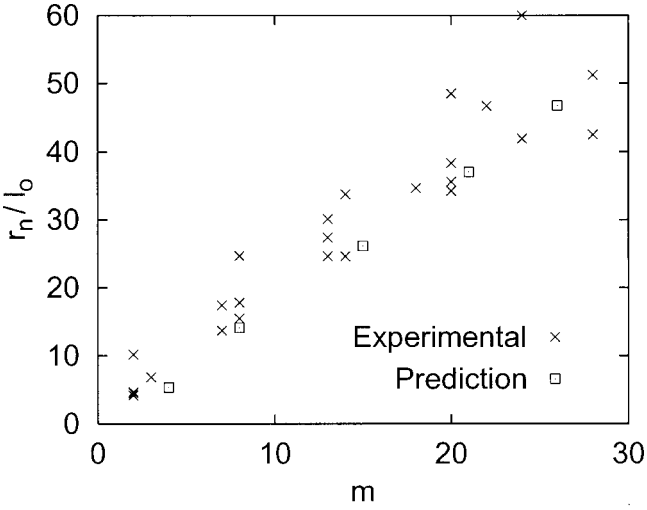

Fig. 4 Comparison of prediction for most probable values of r_n with the experimental measurements of number of crests in a ring

wavelength in the radial and azimuthal directions are the same and are equal to two-dimensional Taylor wavelength, λ_{d2}. By dividing the total surface area of the disc with the number of wave-nodes, the area supported by one node is found to be approximately λ_{d2}^2. This is within ± 5 percent of the predicted values.

Comparison of Interface Shapes. Comparison is made for the interface shape predictions from numerical simulations with vapor bubble pictures taken during experiments and is shown in Fig. 5, for subcooled film boiling of PF-5060 at a wall superheat of $\Delta T_W = 100°C$ and $\Delta T_{\text{sub}} = 10°C$. Three frames prior to bubble departure are shown in Fig. 5 in three separate rows. The picture

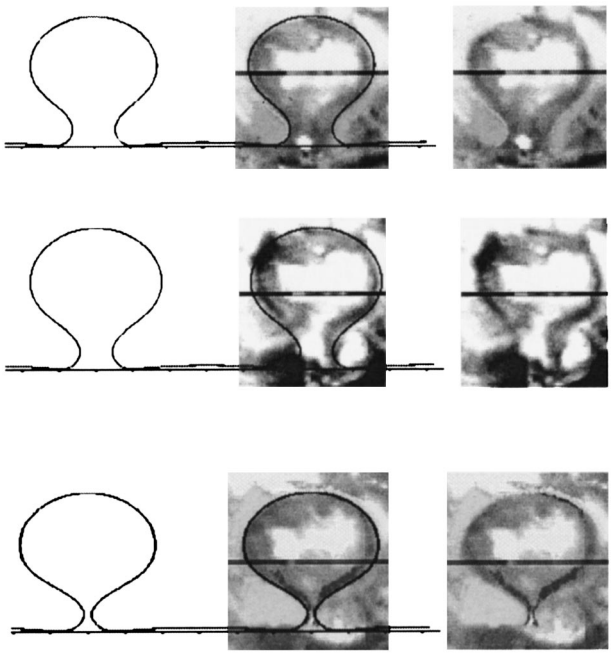

Fig. 5 Comparison of shapes of vapor bubbles obtained from experiments with numerical predictions of interface shape for subcooled film boiling of PF-5060 at a wall superheat of $\Delta T_W = 100°C$ and $\Delta T_{\text{sub}} = 10°C$. The pictures are at 1.2 ms intervals starting at 39.1 ms from the detected formation of the vapor bulge.

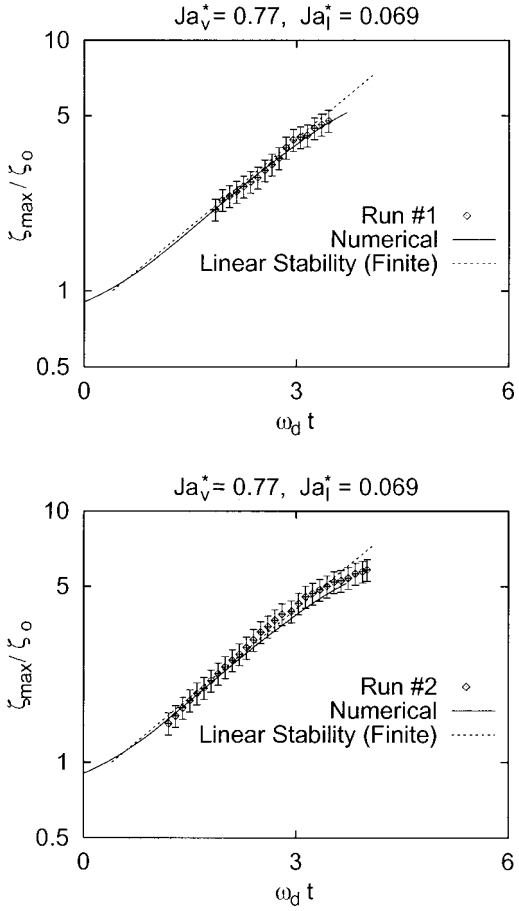

Fig. 6 Comparison of experimental data (denoted by various marker symbols) with numerical predictions (denoted by solid line) for temporal variation of bubble height for wall superheat, $\Delta T_W = 100°C$ and liquid subcoolings, $\Delta T_{sub} = 5°C$. The dotted line represents prediction from linear stability theory.

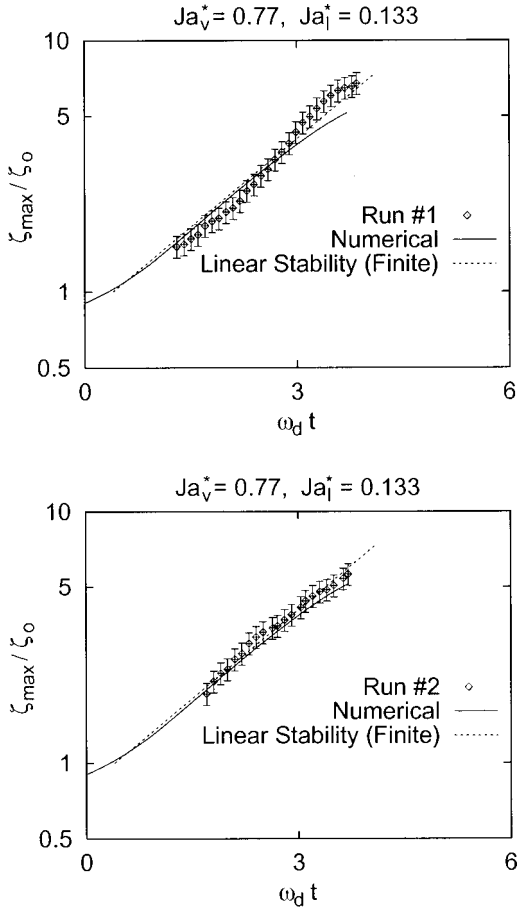

Fig. 7 Comparison of experimental data (denoted by various marker symbols) with numerical predictions (denoted by solid line) for temporal variation of bubble height for wall superheat, $\Delta T_W = 100°C$ and liquid subcoolings, $\Delta T_{sub} = 10°C$. The dotted line represents prediction from linear stability theory.

on the right in each row was obtained from a single frame of the video motion picture recorded from experiments. The left plot in each row is the shape of the bubble obtained from numerical analyses at corresponding time step prior to bubble departure. In the middle of the predicted and observed bubble shapes is their superimposition. It is found that the predicted interfacial shapes agree quite well with the experimental data.

Interface Position. The highest position of the interface from the wall was measured in experiments and is plotted in Figs. 6 and 7 for liquid subcoolings of 5°C ($Ja_l^* = 0.069$) and 10°C ($Ja_l^* = 0.133$), respectively. In both cases data are plotted as a function of time from two different experiments. The interface height is normalized with initial vapor thickness of 0.77 mm and time is normalized with respect to inverse of the growth rate obtained from linear stability analysis for infinite fluid layers. In these figures the solid line represents prediction from the numerical simulations whereas the dotted line is from the linear stability theory. The last point on the solid lines represent the initial height just before departure and at the end of the measured growth period. The numerical simulations correctly predict the nonlinear behavior of the interface during its evolution, especially slowing down of the interface in the later stages of the end of growth period. The model generally tends to underpredict the maximum interface position just prior to bubble pinch off by about 10 percent. However the observed growth periods lie within ±10 percent of the predictions.

Growth Rate. The interface growth rate was obtained from data such as plotted in Figs. 6 and 7 by dividing the displacement at two consecutive times with the time interval between the two. The corresponding frequency normalized with the ''most dangerous frequency'' ($0.62\,\omega_o$) for infinite vapor-liquid layers is plotted in Figs. 8 and 9. In these figures the abscissa is the dimensionless position of the peak of the interface. The dotted line in these figures marks the ''most dangerous frequency'' (ω_{d_f}) where the vapor layer is assumed to have a finite thickness of 0.77 mm (ζ_o). The solid line is the prediction from the numerical simulations. The growth rate is predicted to increase to a maximum value as the interface evolves, acquire a nearly constant value before decreasing again to or below the finite vapor layer value before bubble ''pinch off.'' The predictions are seen to be in general agreement with the data, although the data show significant scatter. Two possible reasons for this large scatter are identified. One is the uncertainty (±16 percent) that exists when the derivative is obtained by taking a ratio of two small quantities. The second originates from the occasional merger of two neighboring bubbles. The merger resulted in the departure of a larger bubble. The wake left behind by the larger bubble distorted the flow field and caused an asymmetric growth rate of the interface in the vicinity.

Wall Heat Transfer. From the wall heat flux measured in steady state experiments and the deduced wall temperature, the heat transfer coefficient and in turn the area and time averaged

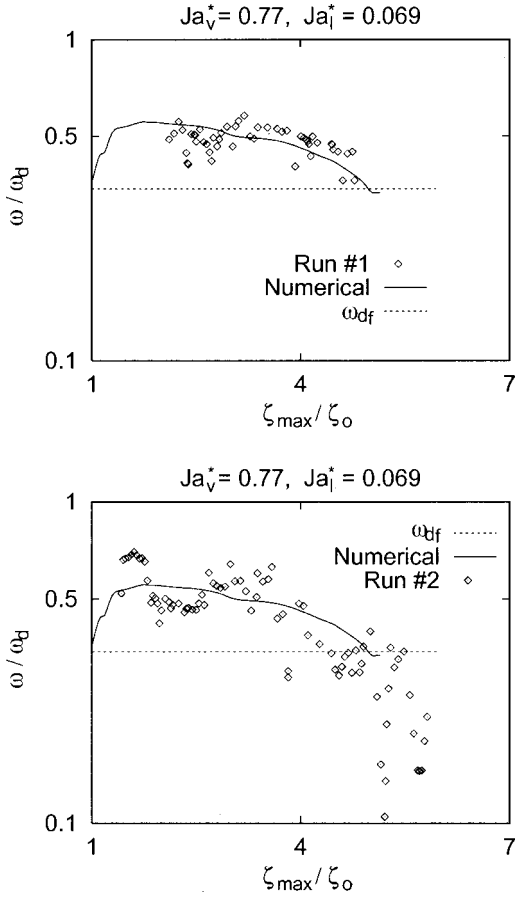

Fig. 8 Comparison of experimental data (denoted by various marker symbols) with numerical predictions (denoted by solid line) for temporal variation of bubble growth rate with bubble height. The dotted line represents prediction of growth rate, ω_{d_f}, from linear stability theory.

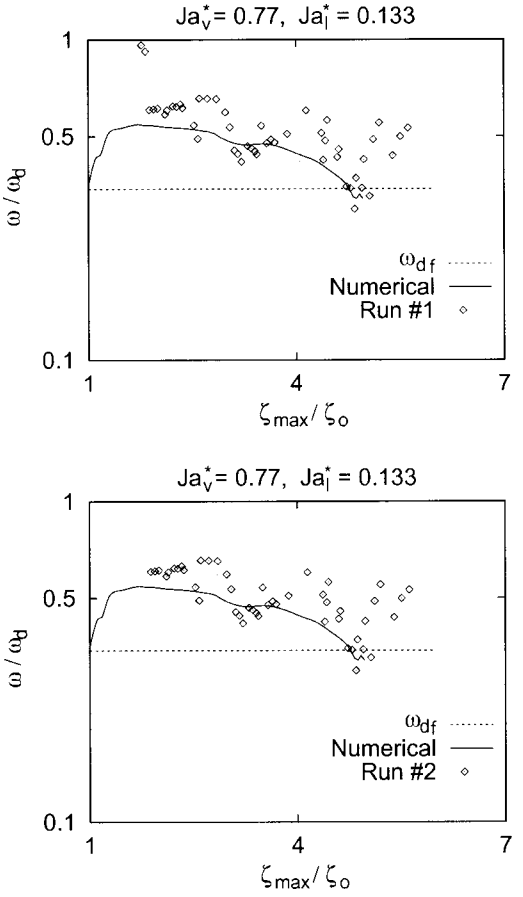

Fig. 9 Comparison of experimental data (denoted by various marker symbols) with numerical predictions (denoted by solid line) for temporal variation of bubble growth rate with bubble height. The dotted line represents prediction of growth rate, ω_{d_f}, from linear stability theory.

Nusselt number, $\overline{\overline{\mathrm{Nu}}}_W$ could be obtained. The values of $\overline{\overline{\mathrm{Nu}}}_W$ obtained in different experiments for liquid subcoolings upto 29.4°C are given in Table 1. In this table the values of $\overline{\overline{\mathrm{Nu}}}_W$ predicted from the numerical simulations are also listed. It should be noted that numerical predictions were made for constant heater surface temperature whereas the experiments were conducted by controlling the wall heat flux. It has been shown by Banerjee et al. [12] that because of spatial and temporal variations of the heat transfer coefficient, local heater surface temperature varies with time. However, for a thick copper surface the temperature variations are not expected to be significant and in turn the difference in the predicted heat transfer coefficient for constant wall temperature and for constant heat flux cases is expected to be quite small.

Figure 10 shows a comparison of the experimentally measured $\overline{\overline{\mathrm{Nu}}}_W$ with the numerical predictions as a function of liquid subcooling. It is found that the predictions are about 20 percent lower than the best fit through the data. Two possible reasons are advanced for this underprediction. One is the uncertainty that exists in the thermophysical properties of PF-5060 vapor, especially thermal conductivity and viscosity. The second is that the numerical simulations are based on a two-dimensional axisymmetric model of the film boiling process. In reality the process is three dimensional.

3.2 High Subcooling. At a wall superheat of 50°C and liquid subcooling greater than 38°C the interface was observed to acquire a near static shape. A photograph of the film boiling phenomena under static conditions of the interface is shown in Fig. 2. Under the static interface condition, however, about 3–5 percent of the vapor bubbles were observed to depart from the heater. Some bubble mergers occurred between the neighboring bubbles on the same ring as well as between bubbles lying on the adjacent rings. The radial as well as azimuthal movement of the bubbles is believed to result from the toroidal single phase convective cells that were present in the liquid. After bubble merger the orderly separation distance between the bubbles was distorted. However, subsequent to bubble departure, new bubble releasing nodes were seen to develop and the node separation distance was found to restore to its original value.

Flow Field. Particle Tracking Velocimetry (two-dimensional) provided the flow field in the liquid pool when the interface was nearly static. Figure 11 shows the liquid field obtained from particle velocimetry at intervals of 4 ms. Since particle density in pool was sparse (to facilitate localized measurements) particle positions from five consecutive video frames were combined together to obtain the information contained in each plot. The particle locations in each frame were mapped and the velocity field was evaluated from displacement of the particles. The viewing area was restricted to an area of 7 mm square in order to achieve the optimum resolution for the video camera. The viewing plane was chosen to begin just above the surface of the heater with the objective of studying the flow field above the interface. However, this placed a constraint on the measurements sincethe particle concentration tended to be lower near the wall due to lesser degree of convective motion just above the thin film region.

It is noted that velocity vectors in general show a downward motion in the region (valley) between two nodes. Above the crests (the larger bubble in Fig. 11) the velocity vectors are pointed

Table 1 Data obtained from low subcooling steady-state experiments.

ΔT_W (°C)	ΔT_{sub} (°C)	$\overline{\overline{Nu_W}}$ Exptl.	$\overline{\overline{Nu_W}}$ Numer.
98.6	0	9.7	
98.6	0	10.4	
102.3	0	9.7	7.94
102.3	0	9.9	
102.1	4.5	11.8	
102.1	4.5	11.5	
100	5	12.0	
102.2	6.2	11.1	
102.2	6.2	12.1	
101.4	7.9	10.7	
101.4	7.9	12.9	
100	10	12	8.45
99.1	11.2	10.1	
99.4	11.7	11.1	
102	14.6	11.1	
102	14.6	12.1	
99.1	21.5	11.1	8.91
99.1	21.5	12.1	
104.6	26.4	12.5	
104.6	26.4	12.0	
96.7	26.7	13.2	
98.9	29.4	14.2	
98.9	29.4	16.9	

upwards. The velocity vectors do show a general motion from right to left. It is believed that the cause of this motion is the toroidal convective cells that were also present in the liquid pool. Highest measured velocities of 100 mm/s are comparable to those predicted from the simulations of Banerjee et al. [10] for convection in a cylindrical cell with a bubble like protrusion at the bottom.

Heat Transfer. The Nusselt numbers based on the area and time averaged heat transfer coefficient obtained under the static mode are listed in Table 2. The data for the static mode was taken over a rather limited range of wall superheats and liquid subcoolings. In the static mode, vapor produced in the thin film region between adjacent bubbles is condensed at the upper surface of the bubble. As a result all of the energy transferred from the wall is dissipated into the pool through single phase natural convection. The vapor liquid interface and the surface of the cooling coils serve as high and low temperature surfaces, respectively. On the interface liquid suction (in the region where evaporation takes place) occurs. However, its effect on the natural convection heat transfer is considered to be small.

In the numerical simulation of the convective process in the circular cell surrounding a bubble, the height of the bubble protrusion was varied parametrically in the study by Banerjee et al. [10]. It was seen that the presence of the protrusion on the lower surface was to enhance the overall heat transfer. However, the effect was not significant, as in the range of parameters studied the enhancement was always less than 20 percent. Also the highest

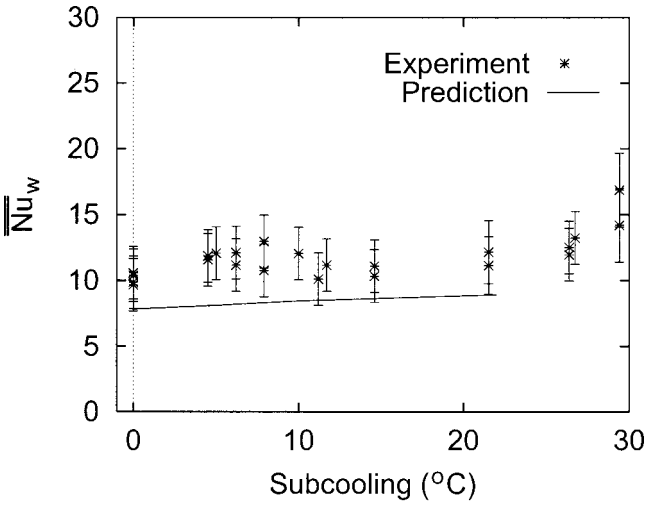

Fig. 10 Comparison of predictions for $\overline{\overline{Nu}}_W$ with experimental data for wall super-heat, $\Delta T_W = 100°C$, and liquid subcooling up to $\Delta T_{sub} = 22°C$

Rayleigh number considered in their work was 10^6. In Fig. 12, the Nusselt numbers predicted from their work are plotted as a function of Rayleigh number. The chainlines represent the extrapolation of their predictions to Rayleigh numbers upto 2×10^8. For the numerical analysis, Rayleigh number was based on the height H of the liquid layer above the interface (which was equal to 4 times the vapor bubble radius). For fluid properties of PF-5060 the value of H is 1.28 cm. In Fig. 12 the Nusselt numbers from Table 1 are also plotted. In plotting these data, the values listed in Table 2 were multiplied by $(\kappa_v/\kappa_l \times H/l_o)$. It is interesting to note that the results predicted from the extrapolated correlations nicely bound the data. Correlations for natural convection in cylinders with heated bottom, cooled top and insulated boundary have been reported by several investigators. Fishenden and Saunders [13] proposed a correlation of the form

$$\overline{\overline{Nu}} = 0.1 Ra^{1/3}, \tag{7}$$

whereas Chavanne et al. [14] proposed the correlation

$$\overline{\overline{Nu}} = 0.17 Ra^{2/7}. \tag{8}$$

In Fig. 12 these correlations are also plotted. It is noted that the observed value of Nusselt number is about 40 percent higher than the prediction from correlation of Fishenden and Saunders [13]. Some underprediction by correlation Eqs. 7 and 8 is expected since they were obtained for rigid bounding wall of the cylinder. In the present work near zero shear stress condition exists at the plane of symmetry between two nodes. Also, these correlations did not account for the presence of a protrusion at the lower surface.

4 Conclusions

1 Experimental validations of the numerical predictions for the evolution of the interface shape, temporal position of the interface, interface growth rates and wall heat flux values were performed. The numerical predictions are found to be in general agreement with the PF-5060 data obtained at low subcoolings.

2 The numerical simulations, generally underpredict the bubble height at departure by about 10 percent. However, the interface shape, interface evolution and interface growth rates prior to bubble departure are predicted within the range of experimental uncertainties. The growth rates of the liquid-vapor interface in subcooled film boiling were found to decrease with increase in subcooling.

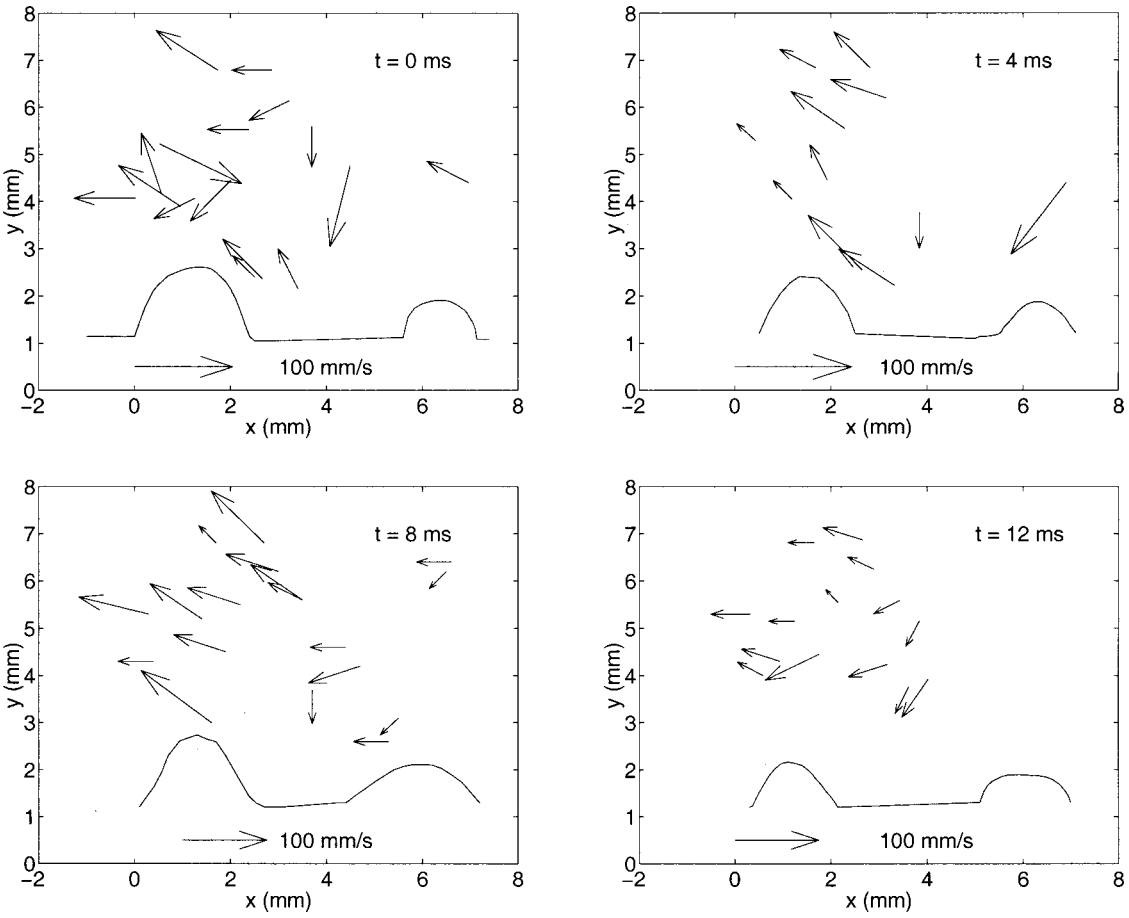

Fig. 11 Sample results from two-dimensional, PTV experiments showing the spatial distribution of velocity vectors at a particular instant. The frames are 4 ms apart. The protrusions depict outline of two vapor bubbles.

3 The wall heat flux values were underpredicted by about 20 percent for steady-state data. However, the model correctly predicts the rate of increase of wall heat transfer with increase in subcooling.

4 At high subcoolings the interface acquires a static shape.

5 The results from two-dimensional PTV experiments qualitatively match the velocity field predictions obtained from the static model of Banerjee et al. [10]. The flow in the liquid pool is towards the valleys and is away from the protrusions.

6 The experimental data for $\overline{\overline{Nu}}_W$ at high liquid subcoolings are bounded by the extrapolated results from the numerical model of Banerjee et al. [10] for the static bubble case. Correlations ob-

Table 2 Heat transfer results for high subcoolings

ΔT_W	ΔT_{sub}	$\overline{\overline{Nu}}_W$	q_W
(°C)	(°C)		$(W/m^2 \times 10^{-4})$
50.1	40	27.5	2.33
53.5	40	26.1	2.35
55	40	25.6	2.38
55	40	25.7	2.39
55	40	25.3	2.36
55.3	40	25.5	2.38
55.4	40	25.1	2.35
52.9	41	27.0	2.41
53.2	41	27.1	2.43
52.4	42	27.2	2.40
53.4	42	26.7	2.41
50.6	43	28.4	2.43
51.7	43	27.9	2.44
52	43	27.9	2.44
50.6	43	28.4	2.43
51.7	43	27.9	2.44
52	43	27.4	2.41

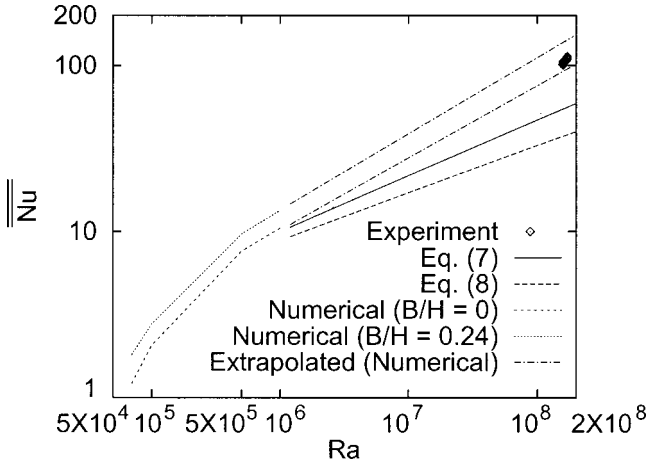

Fig. 12 Comparison of predictions for $\overline{\overline{Nu}}$ from numerical results of Banerjee et al. [10] for $B/H=0$ and $B/H=0.24$ with steady-state experimental data from Table 2. Correlction of Fishenden and Saunders [13] has been plotted as "Eq. (7)" and Correlation of Chavanne et al. [14] has been plotted as "Eq. (8)." Extrapolated trend lines for numerical predictions of Banerjee et al. [10] are also shown.

tained from literature for natural convection in circular cylinders underpredict the experimental values of $\overline{\overline{Nu}}_W$ by about 40 percent.

Nomenclature

B = height of bubble
f = camera framing rate
H = height of liquid pool above heater surface
m = wave number in the azimuthal direction
n = ring number in the radial direction
S = camera magnification factor
s = displacement
κ = thermal conductivity

Subscripts

max = maximum
d = corresponding to ''most dangerous'' or fastest growing wave
f = value obtained from linear stability theory
s = substrate heater property

Superscripts

$^{=}$ = space and time average quantity

References

[1] Dhir, V. K., and Purohit, G. P., 1978, ''Subcooled Film-Boiling Heat Transfer From Spheres,'' Nucl. Eng. Des., **47**, No. 1, pp. 49–66.
[2] Vijaykumar, R., and Dhir, V. K., 1992, ''An Experimental Study of Subcooled Film Boiling on a Vertical Surface-Hydrodynamic Aspects,'' ASME J. Heat Transfer, **114**, No. 1, pp. 161–168.
[3] Vijaykumar, R., and Dhir, V. K., 1992, ''An Experimental Study of Subcooled Film Boiling on a Vertical Surface-Thermal Aspects,'' ASME J. Heat Transfer, **114**, No. 1, pp. 169–178.
[4] Nishio, S., and Ohtake, H., 1992, ''Natural-Convection Film-Boiling Heat Transfer (Film Boiling from Horizontal Cylinders in Middle and Small-Diameter Regions),'' JSME Int. J., Ser. II, **35**, No. 4, pp. 380–388.
[5] Kikuchi, Y., Ebisu, T., and Michiyoshi, I., 1992, ''Measurement of Liquid-Solid Contact in Film Boiling,'' Int. J. Heat Mass Transf., **35**, No. 6, pp. 1589–1594.
[6] Busse, F. H., and Schubert, G., 1971, ''Convection in a Fluid with Two Phases,'' J. Fluid Mech., **46**, Part 4, pp. 801–812.
[7] Busse F. H., 1989, *The Fluid Mechanics of Astrophysics and Geophysics*, Vol. 4, W. R. Peltier, ed., Gordon and Breach, New York.
[8] Ahlers, G., Berge, L. I., Cannell, D. S., 1993, ''Thermal Convection in the Presence of a First-Order Phase Change,'' Phys. Rev. Lett., **70**, No. 16, pp. 2399–2402.
[9] Ayazi, F., and Dhir, V. K., 1987, ''A Thermal and Hydrodynamic Limit for Minimum Heat Flux and Wall Superheat During Subcooled Film Boiling on a Horizontal Cylinder,'' *AIAA 22nd Thermophysics Conference*, June 8–10, Honolulu, Hawaii, Paper No. AIAA-87-1535.
[10] Banerjee, D., Son, G., and Dhir, V. K., 1998, ''Natural Convection in a Cylindrical Section with a Static Protrusion: Numerical Simulation Relevant to Subcooled Film Boiling,'' *Proceedings of the 11th Intl. Heat Tr. Conf.*, **3**, August 23–28, 1998, Kyongju, Korea.
[11] Banerjee, D., 1999, ''Numerical and Experimental Investigation of Subcooled Film Boiling on a Horizontal Plate,'' Ph.D. thesis, University of California, Los Angeles; CA.
[12] Banerjee, D., Son, G., and Dhir, V. K., 1996, ''Conjugate Thermal and Hydrodynamic Analysis of Saturated Film Boiling From a Horizontal Surface,'' Proc. of the 1996 IMECE, Atlanta, GA, Nov. 17–22.
[13] Fishenden, M., and Saunders, O. A., 1950, ''An Introduction to Heat Transfer,'' Oxford University Press, London.
[14] Chavanne, X., Castaing, B., Chabaud, B., Chilla, F., and Hebral, B., 1998, ''Rayleigh Benard Convection at Very High Rayleigh Numbers Close to the ^{4}He Critical Point,'' Cryogenics, **38**, pp. 1191–1198.

Mixed-Convection Laminar Film Condensation on an Inclined Elliptical Tube

M. Mosaad
Professor
e-mail: Mosaad@paaetms.paaet.edu.kw

Department of Mechanical Engineering,
Faculty of Engineering, P.O. Box 52,
Mansoura University 35516, Egypt

The present theoretical study concerns with mixed-convection laminar film condensation outside an inclined elliptical tube with isothermal surface. The assumptions used are as in the classical Nusselt-Rohsenow theory, however, with considering the interfacial vapor shear by extending a circular-tube shear model developed in a previous study. An equivalent diameter, based on equal surface area, is introduced in the analysis to enable comparison with circular tubes. For zero ellipticity, the approach simplifies to the circular tube model developed in our previous work. A numerical solution has been obtained for a wide range of the independent parameters. The results indicate that the heat transfer performance of the inclined elliptical tube enhances with the increase of tube ellipticity compared to an inclined circular tube of equivalent diameter. For forced-convection-dominated film condensation, the rate of this enhancement in the heat transfer coefficient is found smaller than that for pure-free-convection film. [DOI: 10.1115/1.1338136]

Keywords: Condensation, Film, Heat Transfer, Laminar, Mixed Convection

1 Introduction

The problem of laminar film condensation outside elliptical tubes has received considerable attention in recent studies. This is due to the desire for designing more efficient tube condensers.

For a pure-free-convection film condensation on horizontal elliptical tubes, many studies have been made based on the classical assumptions of Nusselt-Rohsenow theory. Cheng and Tao [1] found that the heat transfer performance of a horizontal elliptical tube (with the major axis oriented vertical) is better than that of a horizontal circular tube with the same condensation surface area. Namely, the increase in mean heat transfer coefficient was found about 11 percent for tube eccentricity[1] $\xi=0.4$ (i.e., ellipticity $e \approx 0.92$). Later, Yang and Chen [2] proved theoretically that mean Nusselt number is almost unaffected by surface tension due to surface curvature changing.

A few numbers of recent studies have been focused on the use of inclined elliptical tubes that may serve to thin the condensate film and, consequently, improve the heat transfer performance.

In a Nusselt-type model, Fieg and Roetzel [3] studied the effect of the axial inclination of an elliptical tube from the horizontal on its heat transfer performance during free-convection film condensation mode. They concluded that the use of an inclined elliptical tube enhances the heat transfer performance compared to an inclined circular tube with equivalent condensation surface area.

Recently, Yang and Hsu [4] analyzed the problem of combined free and forced convection film condensation on a horizontal elliptical tube (major ellipse axis oriented vertical) under uniform wall heat flux condition. The classical laminar-film assumptions of Nusselt-Rohsenow theory were adopted in their analysis, however, with considering the effects of vapor shear and pressure gradient. The simple shear model of Shekriladze and Gomelauri [5] was employed to evaluate the vapor shear at the condensate surface. Yang and Hsu concluded that the increase of tube ellipticity enhances the mean heat transfer coefficient compared to an equivalent-area circular tube. This enhancement for pure-forced convection film condensation was found smaller than that for pure-free-convection film. Following Yang and Hsu, Memory et al. [6] analyzed the same problem under isothermal surface condition, however, with considering the effects of surface tension and pressure gradient on the film flow. They concluded that the effects of these two parameters on the mean heat transfer coefficient are insignificant.

However, the problem of mixed-convection laminar film condensation on an inclined elliptical tube (to author's knowledge) has not yet been addressed in the literature. Therefore, in the present work, this problem will be analyzed for the case of being the minor axis of the inclined tube ellipse oriented horizontal. The classical assumptions of Nusselt [7] will be used in the analysis. This is with modeling the interfacial vapor shear by extending the simple shear model of Shekriladze and Gomelauri [5] developed for the horizontal circular tube.

2 Analysis

Consider an elliptical tube inclined at angle φ to the horizontal with the minor axis ''$2b$'' of its cross-sectional ellipse oriented horizontal. A pure saturated vapor flows downward with uniform vertical velocity V_∞ over the external tube surface. The wall temperature T_w is assumed uniform and much lower than the vapor saturation temperature T_s. Thus, continuous condensate film will form on the external surface with simultaneous flow in both axial and peripheral directions. The physical model under consideration is shown in Fig. 1, where the curvilinear coordinates (x,y) are used; with x aligned along the ellipse periphery and y is its normal. The linear coordinate z is taken in the axial direction of tube.

An adequate mathematical formulation of the problem is very complicated. Therefore, the standard Nusselt [7] approximations (including neglecting the effects of inertia, convection, surface tension and pressure gradient) are used, except the interfacial vapor shear is considered.

The above approximations simplify the momentum equation of condensate film in x and z-directions, respectively, as follows:

$$\mu \frac{\partial^2 u}{\partial y^2} + \rho g \sin \phi \cos \varphi = 0 \tag{1}$$

$$\mu \frac{\partial^2 w}{\partial y^2} + \rho g \sin \varphi = 0. \tag{2}$$

Contributed by the Heat Transfer Division for publication in the JOURNAL OF HEAT TRANSFER. Manuscript received by the Heat Transfer Division August 28, 1999; revision received, January 21, 2000. Associate Editor: P. Ayyaswamy.

[1]Eccentricity $\xi=\sqrt{1-e^2}$.

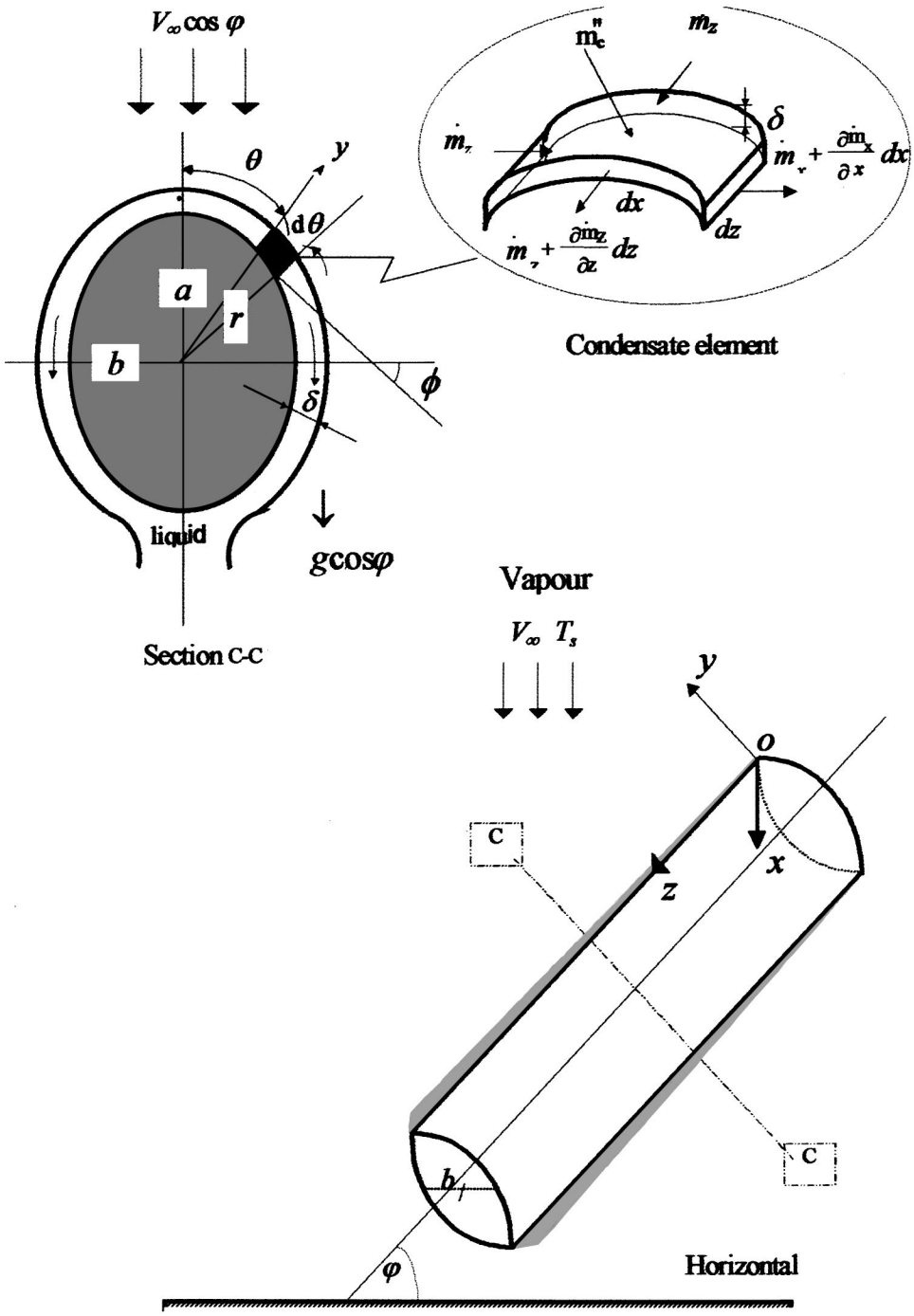

Fig. 1 Physical model and coordinate system

Equations (1) and (2) are subject to the following boundary and interface conditions:

$$\text{at } y=0, \quad u=0, \quad w=0 \tag{3}$$

$$\text{at } y=\delta, \quad \frac{\partial u}{\partial y}=\frac{\tau_{\delta x}}{\mu}, \quad \frac{\partial w}{\partial y}=\frac{\tau_{\delta z}}{\mu}, \tag{4}$$

where u and w are the film velocity components in x and z-directions, respectively. The symbols $\tau_{\delta x}$ and $\tau_{\delta z}$ denote, respectively, to x and z-components of interfacial vapor shear stress, while the symbol δ signs to the local film thickness.

Assuming potential vapor flow with uniform vertical velocity V_∞ over the inclined tube, the vapor velocity at the boundary layer edge may be derived in the x and z-directions, respectively, by

$$V_x = V_\infty(1+\sqrt{(1-e^2)})\sin\phi\cos\varphi \tag{5}$$

$$V_z = V_\infty \sin\varphi. \tag{6}$$

The parameter $e(=\sqrt{a^2-b^2}/a)$ denotes to the ellipse ellipticity. The angle ϕ is measured between the tangent to the tube ellipse at any point (r,θ) and the horizontal.

In a similar way to that made by Shekriladze and Gomelauri [5], the interfacial shear stress can be evaluated (under infinite-condensation-rate condition) in the tangential and axial directions, respectively, by

$$\tau_{\delta x}=m_c''(V_x-u_\delta)\approx m_c''V_x \tag{7}$$

$$\tau_{\delta z}=m_c''(V_z-w_\delta)\approx m_c''V_z, \tag{8}$$

where m_c'' is the local condensation mass flux.

In both Eqs. (7) and (8), the interfacial liquid velocity is considered negligible compared to the vapor velocity, as assumed in the model of Yang and Chen [2].

It is seen from Eqs. (5) and (7) that the peripheral interfacial shear stress $\tau_{\delta x}$ is positive for all values of the peripheral angle ϕ. This means that separation of vapor boundary layer is excluded in the present analysis.

By solving Eqs. (1) and (2) subject to boundary conditions (3) and (4), and substituting Eqs. (5)–(8) to eliminate $\tau_{\delta x}$ and $\tau_{\delta z}$, one gets

$$u=\frac{y}{\mu}\left(m_c''V_\infty(1+\sqrt{1-e^2})-\rho g\left(\frac{y}{2}-\delta\right)\right)\sin\phi\cos\varphi \tag{9}$$

$$w=\frac{y}{\mu}\left(m_c''V_\infty-\rho g\left(\frac{y}{2}-\delta\right)\right)\sin\varphi. \tag{10}$$

A heat balance at the liquid-vapor interface, as in Nusselt theory, gives

$$m_c''=\frac{k\Delta T}{h_{fg}''\delta}, \tag{11}$$

where $h_{fg}''(=h_{fg}+3C_p\Delta T/8)$ is modified latent heat of condensation proposed originally by Rohsenow [8] to account for the effects of heat convection in condensate film.

A mass balance for the condensate element, shown in Fig. 1, yields

$$m_c''=\rho\frac{\partial}{\partial x}\left(\int_0^\delta u dy\right)+\rho\frac{\partial}{\partial z}\left(\int_0^\delta w dy\right). \tag{12}$$

Combining Eqs. (9)–(12) to eliminate m_c'' yields the following partial differential equation for local film thickness:

$$\delta\frac{\partial}{\partial x}\left(\delta\sin\phi\left(2+2\sqrt{1-e^2}+\frac{4\rho g h_{fg}''}{3k\Delta TV_\infty}\delta^2\right)\right)+\tan\varphi\left(1+\frac{2\rho g h_{fg}''}{k\Delta TV_\infty}\delta^2\right)\frac{\partial\delta^2}{\partial z}=\frac{4\nu}{V_\infty\cos\varphi}. \tag{13}$$

Here, it is convenient to express the differential arc length, dx, in polar coordinates. Referring to Fig. 1, dx may be expressed, as in the analysis of Yang and Hsu [4], by

$$dx=(d_e/2)I(\phi)d\phi, \tag{14}$$

where

$$d_e=\frac{2a}{\pi}(1-e^2)\int_0^\pi(1-e^2\sin^2\phi)^{-3/2}d\phi \tag{15}$$

$$I(\phi)=\pi(1-e^2\sin^2\phi)^{-3/2}\Big/\int_0^\pi(1-e^2\sin^2\phi)^{-3/2}d\phi, \tag{16}$$

where d_e is an equivalent circular diameter based on equal outside surface area, which is introduced to enable comparison with circular tubes.

By inserting the arc length dx from Eq. (14) into Eq. (13), one gets (after some rearrangement) the following partial differential equation:

$$\sin\phi\left(\frac{\tilde{\mathrm{Re}}}{2d_e^2}(1+\sqrt{1-e^2})+\frac{\mathrm{Gr}}{d_e^4}\frac{\mu h_{fg}''}{k\Delta T}\delta^2\right)\frac{\partial\delta^2}{\partial\phi}+\frac{d_e}{4}I(\phi)\tan\varphi\left(\frac{\tilde{\mathrm{Re}}}{d_e^2}+\frac{2\,\mathrm{Gr}}{d_e^4}\frac{\mu h_{fg}''}{k\Delta T}\delta^2\right)\frac{\partial\delta^2}{\partial z}+\cos\phi\left(\frac{\tilde{\mathrm{Re}}}{d_e^2}(1+\sqrt{1-e^2})+\frac{2\,\mathrm{Gr}}{3d_e^4}\frac{\mu h_{fg}''}{k\Delta T}\delta^2\right)\delta^2=\frac{I(\phi)}{\cos\varphi} \tag{17}$$

for the local condensate film thickness δ as a function of the two-phase Reynolds number $\tilde{\mathrm{Re}}$, Grashof number Gr, inclination angle φ, peripheral angle ϕ, temperature drop ΔT and axial location z.

By introducing the dimensionless local film thickness Δ,

$$\Delta=\frac{\delta}{2d_e}\sqrt{\tilde{\mathrm{Re}}\cos\varphi} \tag{18}$$

and the dimensionless axial location Z^+

$$Z^+=2z/(d_e\tan\varphi) \tag{19}$$

Equation (17) can be rewritten in the dimensionless form

$$\sin\phi(1+\sqrt{(1-e^2)}+8F\Delta^2)\frac{\partial\Delta^2}{\partial\phi}+I(\phi)(1+8F\Delta^2)\frac{\partial\Delta^2}{\partial Z^+}+2\cos\phi\left(1+\sqrt{(1-e^2)}+\frac{8}{3}F\Delta^2\right)\Delta^2=\frac{I(\phi)}{2} \tag{20}$$

wherein

$$F=(\mathrm{Gr}/(\tilde{\mathrm{Re}}^2\cos\varphi))(\mu h_{fg}''/k\Delta T) \tag{21}$$

is a dimensionless mixed-convection parameter, which gives a measure of the relative importance of gravity force to vapor shear on condensate film motion.

The appropriate boundary conditions are

$$\text{at}\quad Z^+=0;\quad \Delta=0,\quad \pi\geqslant\phi\geqslant0 \tag{22}$$

$$\text{at}\quad \phi=0,\ \phi=\pi;\quad \frac{\partial\Delta}{\partial\phi}=0;\quad \infty\geqslant Z^+\geqslant0 \tag{23}$$

$$\text{at}\quad Z^+\to\infty;\quad \frac{\partial\Delta}{\partial Z^+}=0. \tag{24}$$

The first boundary condition (22) indicates that the film thickness is zero around the ellipse periphery at the upper tube end. The second expresses the symmetry of condensate film and its smoothness at the top ($\phi=0$) and bottom ($\phi=\pi$) points along the inclined tube. The third condition implies that for an inclined tube of infinite length, the thickness of the film after a short length from its start point at $z=0$ becomes nearly as a function of peripheral tube angle ϕ only (Fieg and Roetzel [3]).

Here, it is important to point that application of governing Eqs. (17)–(24) is limited for an inclination angle φ in the range: $0\leqslant\varphi<\pi/2$.

3 Solution

3.1 Special Solutions. First, the following special cases will be considered:

3.1.1 Mixed-Convection Laminar Film on Inclined Circular Tube. For an inclined circular tube ($e=0$ and $I(\phi)=0$), the governing Eq. (20) reduces to that found in a previous study by Mosaad [9]. For more details, the reader can return to this reference.

3.1.2 Forced-Convection Laminar Film on Inclined Elliptical Tube. For this case of $F=0$, Eq. (20) simplifies to that one found previously by Mosaad [10] who solved it analytically by the method of characteristics.

For the simple infinite-tube-length case, the following expression of mean Nusselt number was found

$$\overline{\mathrm{Nu}}_{L\infty}/\sqrt{\widetilde{\mathrm{Re}}\cos\varphi}=\frac{1}{\pi\sqrt{2}}\int_0^{\pi}\sin\phi\left(\int_0^{\phi}(\sin\phi/f(\phi))d\phi\right)^{-1/2}d\phi, \tag{25}$$

where the function $f(\phi)=(1+\sqrt{1-e^2})/I(\phi)$.

For the case of a horizontal circular tube ($e=0$, $\varphi=0$, and $I(\phi)=1$), Eq. (25) simplifies to the known solution of Shekriladze and Gomelauri [5].

3.1.3 Free-Convection Laminar Film on Inclined Elliptical Tube. For this case of $F\to\infty$ or $\widetilde{\mathrm{Re}}=0$, Eq. (17) reduces to a simpler one that can be written in the following dimensionless form:

$$\frac{\partial\beta}{\partial Z^+}+\frac{\sin\phi}{I(\phi)}\frac{\partial\beta}{\partial\phi}=\frac{4}{3}\left(1-\frac{\cos\phi}{I(\phi)}\beta\right), \tag{26}$$

where β is a dimensionless film thickness defined by

$$\beta=\frac{2\delta^4}{3d_e^4}\frac{\mathrm{Ra}}{\mathrm{Ja}}\cos\varphi, \tag{27}$$

wherein Ra is Rayleigh number and Ja is Jakob number.

For $e=0$ and $I(\phi)=1$ (inclined circular tube), Eq. (26) simplifies to the same result found previously by Hassan and Jakob [11].

For the more special case of infinite-tube-length, the term $\partial\beta/\partial Z^+$ in Eq. (26) can be neglected compared to the term $\partial\beta/\partial\phi$, following Fieg and Roetzel [3]. Hence, Eq. (26) reduces to one that can be solved analytically, for $\partial\beta/\partial\phi\to0$ as $\phi\to0$, to yield

$$\beta=\frac{4/3}{\sin^{4/3}\phi}\int_0^{\phi}I(\phi)\sin^{1/3}\phi d\phi. \tag{28}$$

By using Eqs. (27) and (28), the local Nusselt number Nu ($=d_e/\delta$) is found to be calculated by

$$\mathrm{Nu}/\sqrt[4]{(\mathrm{Ra/Ja})\cos\varphi}=\sin^{1/3}\phi\left(2\int_0^{\phi}I(\phi)\sin^{1/3}\phi d\phi\right)^{-1/4}. \tag{29}$$

Consequently, the mean ''overall'' Nusselt number is calculated from

$$\overline{\mathrm{Nu}}_{L\infty}/\sqrt[4]{(\mathrm{Ra/Ja})\cos\varphi}=\frac{1}{\pi}\int_0^{\pi}\sin\phi\left(2\int_0^{\phi}I(\phi)\sin^{1/3}\phi d\phi\right)^{-1/4}d\phi. \tag{30}$$

Using the relation: $\mathrm{Ra/Ja}=\widetilde{\mathrm{Re}}^2\cos\varphi F$ (cf. Eq. (21)), the above equation can be rewritten in the alternative form:

$$\overline{\mathrm{Nu}}_{L\infty}/\sqrt{\widetilde{\mathrm{Re}}\cos\varphi}=F^{1/4}\frac{1}{\pi}\int_0^{\pi}\sin\phi\left(2\int_0^{\phi}I(\phi)\sin\phi d\phi\right)^{-1/4}d\phi. \tag{31}$$

From the above relation, it is noted that

1 For $\varphi=0$, Eq. (30) simplifies to the solution of Yang and Hus [4] for a horizontal elliptical tube with isothermal surface.
2 For $\varphi=0$ and $e=0$, calculating the left-hand-side of Eq. (30) yields constant value$=0.728$, i.e., the solution reduces to that found by Nusselt [7] for a horizontal circular tube.

All special cases discussed above prove validity of the proposed approach.

3.2 General Solution. Next, solution of Eq. (20) subject to boundary conditions (22)–(24), which represents the general solution, will be considered here. This solution can be found numerically to calculate Δ at any point (ϕ,Z^+) on the tube surface, for certain values of ellipticity e and mixed-convection parameter F. Then, the local peripherally averaged Nusselt number can be calculated from

$$\mathrm{Nu}(z)/\sqrt{\widetilde{\mathrm{Re}}\cos\varphi}=\frac{1}{\pi}\int_0^{\pi}\frac{1}{2\Delta(\phi,Z^+)}d\phi, \tag{32}$$

and mean Nusselt number for whole tube surface from

$$\overline{\mathrm{Nu}}_L/\sqrt{\widetilde{\mathrm{Re}}\cos\varphi}=\frac{1}{\pi L^+}\int_0^{L^+}\int_0^{\pi}\frac{1}{2\Delta(\phi,Z^+)}d\phi dZ^+, \tag{33}$$

where L^+ is the dimensionless tube length.

For the case of the infinite-tube-length, the z-derivative term in Eq. (20) can be omitted, as made in the analysis of Mosaad [9] for an inclined circular tube with infinite length. Hence, the values of Δ, calculated numerically from the reduced equation, can be used to calculate the mean Nusselt number from

$$\overline{\mathrm{Nu}}_{L\infty}/\sqrt{\widetilde{\mathrm{Re}}\cos\varphi}=\frac{1}{\pi}\int_0^{\pi}\frac{1}{2\Delta(\phi)}d\phi. \tag{34}$$

A fourth-order Runge-Kutta integration procedure has been used to evaluate numerically the integral terms in Eqs. (32)–(34). Step sizes of $\Delta\phi=0.05°\mathrm{C}$ and $\Delta Z^+=0.1$ were chosen to achieve high accuracy solution. The problem that Δ (calculated numerically from Eq. (20)) goes to infinity as $\phi=\pi$, could be overcome by substituting ϕ by a value very close to π. Preliminary numerical calculations proved that by setting the upper limit of $\phi=3.128$, good accuracy solution could be achieved. The known analytical solutions of circular tube were used as a reference to assess the accuracy of the numerical procedure. The maximum relative errors in numerically calculated Nusselt numbers were less than 0.1 percent.

4 Results and Discussion

First, the simple case of the inclined elliptical tube of infinite length is considered. The variations of local Nusselt number and dimensionless film thickness, Δ, around the ellipse periphery of the tube are shown, respectively, in Figs. 2 and 3, for different values of tube ellipticity e and mixed convection parameter F.

For free convection film condensation ($F\to\infty$), where the gravity force is dominated, Fig. 2 shows that an increase in ellipticity e, results in a thinner film in the front part of the ellipse. This is due to the associated increase in gravity force effect with an increase in e. This will lead to a high condensation rate in this front part, with the consequence of rapid development in the film thickness in the rear part. However, the increased effect of gravity force in this rear region due to the changing in the curvature of ellipse surface, will result in a thinner film in this rear portion compared to a circular tube ($e=0$). The present circular tube solution is the same as that of Hassan and Jakob [11].

For a pure forced convection film condensation ($F\to0$), the shear force is the dominating factor, which plays the role of gravity force in pure free convection film mode. Therefore, the variation in Δ around the tube ellipse periphery takes somewhat similar feature to that of free convection film. However, the effect of ellipticity is more noticeable compared to that in the case of a pure free convection film mode. This may be attributed to the difference in the influence degrees of gravity force and vapor shear.

For mixed convection film mode of $0<F<\infty$, the variation of

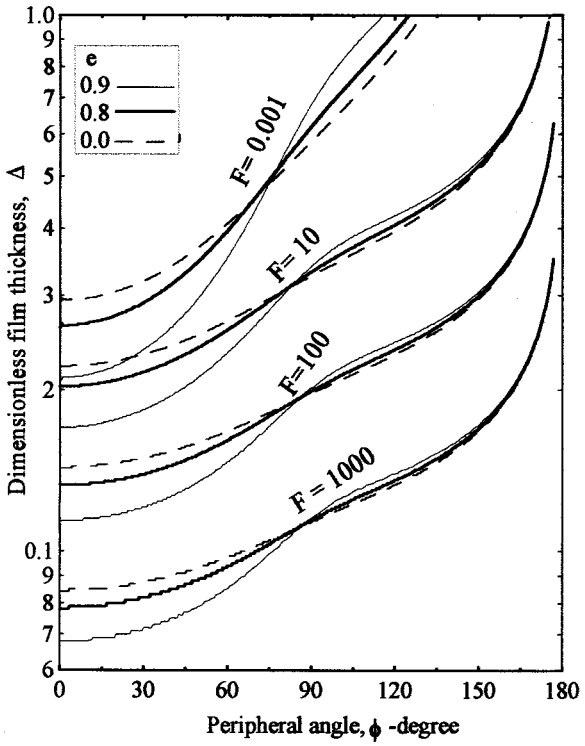

Fig. 2 Variation of dimensionless film thickness around the ellipse periphery of inclined tube with infinite length

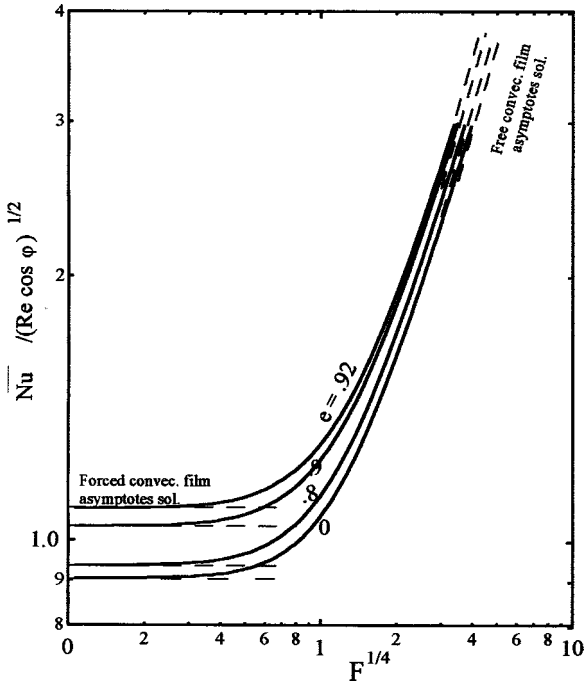

Fig. 4 Dependence of mean Nusselt number of an infinite-length inclined elliptical tube on parameter *F*

Δ around the tube takes a profile lying between the two profiles of low ($F\to 0$) and high ($F\to\infty$) extremes depending on the magnitude of F value. This explains the physical significance of parameter F, which gives a measure of the relative importance of gravity force to vapor shear on film motion.

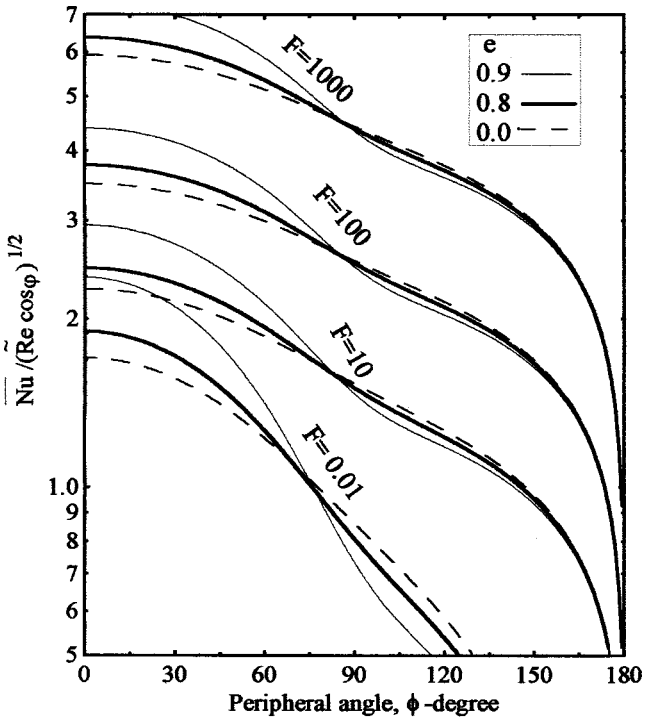

Fig. 3 Variation of local Nusselt number around the ellipse periphery of inclined tube with infinite length

As the local Nusselt number is proportional to the reciprocal of local dimensionless film thickness, it exhibits qualitatively the reversed behavior of Δ, as shown in Fig. 3.

Figure 4 shows the effect of the dimensionless mixed-convection parameter F on the mean Nusselt number. In general, $\overline{\mathrm{Nu}}_{L\infty}/\sqrt{\widetilde{\mathrm{Re}}\cos\varphi}$ increases with increasing F and also with an increase in ellipticity. On the limit $F\to\infty$, the solution assumes the free convection asymptotes (plotted by inclined dashed lines) calculated by Eq. (31). On the opposite extreme limit $F\to 0$, the solution assumes the forced convection asymptotes (horizontal dashed lines) calculated by Eq. (25). For certain F, the mean Nusselt number enhances with an increase in tube ellipticity e. For the inclined circular tube ($e=0$), the present solution agrees within ± 0.1 percent of Mosaad's solution [9].

The enhancement in mean Nusselt number due to an increase in ellipticity is more clearly displayed in Fig. 5, where the ratio $\overline{\mathrm{Nu}}_e/\overline{\mathrm{Nu}}_c$ of mean Nusselt numbers of elliptical and circular inclined tubes is plotted versus ellipticity, for the two extremes of $F=0$ and ∞. It is seen that for $e<0.25$, there is no significant enhancement in the heat transfer performance of the elliptical tube compared to a circular tube of equivalent diameter, provided that both tubes are inclined with the same angle within the applicable range: $0\leqslant\varphi<\pi/2$. The results show that, for a pure forced convection film ($F=0$), the ratio $\overline{\mathrm{Nu}}_e/\overline{\mathrm{Nu}}_c$ decreases, at first, by nearly 1–2 percent as e goes from 0.25 to 0.7, then increases as e exceeds the value of 0.7. This increase reaches about 14 percent as $e=0.92$. However, for a pure free convection film ($F\to\infty$), this Nusselt numbers ratio increases from about 1 percent to 15 percent as e increases from 0.25 to 0.92. Further enhancement in heat transfer coefficient was found as the ellipticity exceeds the value 0.92; however, the present solution was limited to the practical manufacturing range of ellipticity: $0\leqslant e\leqslant 0.92$.

Figure 6 shows that for the inclined elliptical tube of a finite length, a significant enhancement in overall Nusselt number is found with an increase in ellipticity within the range from 0.8 to 0.92, and this enhancement becomes more pronounced for higher F. This confirms the results of Fig. 5. It is also noted that as $L^+\to\infty$, or more exactly, as L^+ exceeds 30, the normalized mean

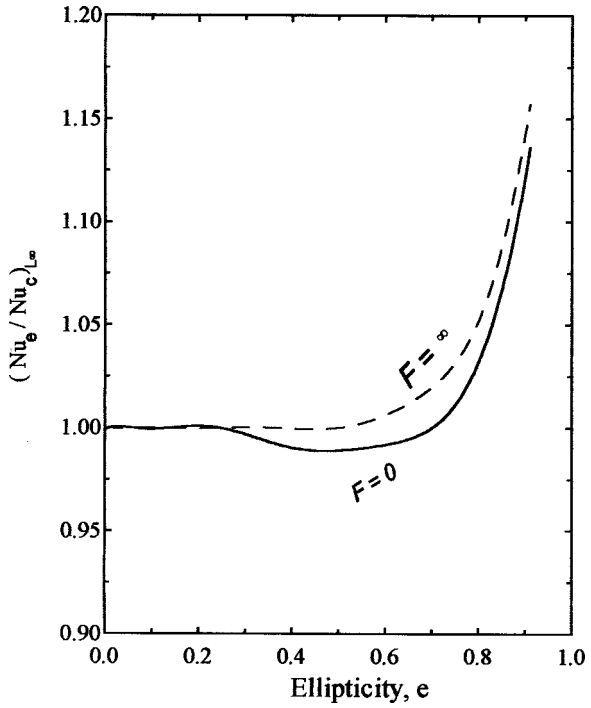

Fig. 5 Ratio of mean Nusselt numbers of elliptical and circular inclined tubes as a function of ellipticity

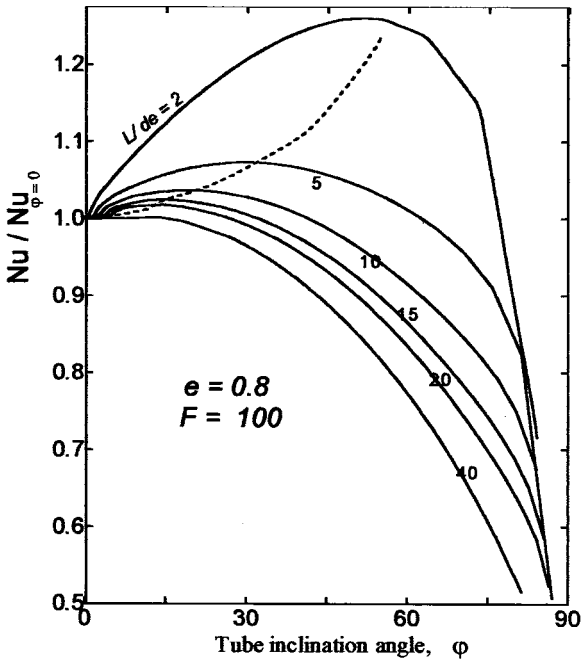

Fig. 7 Ratio of mean Nusselt numbers of inclined and horizontal elliptical tubes as a function of inclination angle φ and aspect ratio L/d_e, for $e=0.8$, and $F=100$

Nusselt number $\overline{\mathrm{Nu}}/\sqrt{\widetilde{\mathrm{Re}}\cos\varphi}$ assumes the corresponding constant values of the infinite-length solution plotted in Fig. 4.

For clarifying the effect of tube inclination angle φ in a more explicit way, the ratio $\overline{\mathrm{Nu}}/\overline{\mathrm{Nu}}_{\varphi=0}$ of Nusselt numbers for inclined and horizontal elliptical tubes is plotted in Fig. 7 versus tube inclination angle φ, for different aspect ratio L/d_e. The results show that there is an optimum inclination angle at which the ratio $\overline{\mathrm{Nu}}/\overline{\mathrm{Nu}}_{\varphi=0}$ takes a maximum value. This optimum angle is found as a function of tube aspect ratio L/d_e. The higher this ratio, the smaller the optimum inclination angle will be. A dashed line in the figure plots the curve of this optimum angle.

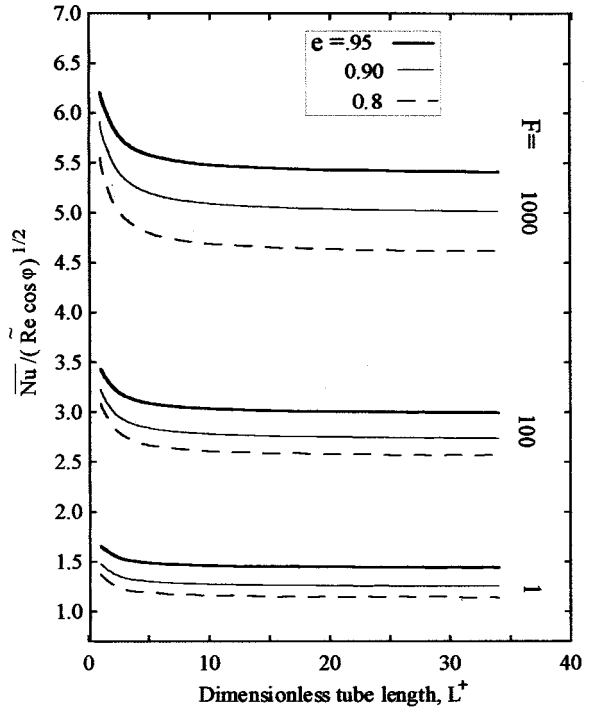

Fig. 6 Overall Nusselt number of inclined elliptical tube as a function of total tube length

5 Conclusions

Based on the classical approximations of Nusselt-Rohsenow theory and the simple shear model of Shekriladze-Gomelauri, which were found consistent for most condensation applications, laminar film condensation outside an inclined elliptical tube has been analyzed under the combined effects of gravity force and vapor shear on the film motion. In addition, two special cases have been treated, namely: pure free convection and pure forced convection film condensation. The main points that can be concluded from this study are:

1 For the mode of mixed-convection laminar film condensation, the heat transfer performance of an inclined elliptical tube (with the minor axis of tube ellipse oriented horizontal) is better than that of an inclined circular tube with the equivalent diameter.

2 For an inclined elliptical tube with infinite length, mean Nusselt number $\overline{\mathrm{Nu}}_{L\infty}$ enhances (compared to a circular tube) with the increase of ellipticity above the value 0.25. Namely, for a pure free convection film mode, this enhancement rises from about 1 percent to 15 percent as e increases from 0.25 to 0.92. However, for a forced convection dominated film, $\overline{\mathrm{Nu}}_{L\infty}$ decreases, at first, by nearly 1–2 percent as e goes from 0.25 to 0.7, then increases with further increase in e value above 0.7. The enhancement in $\overline{\mathrm{Nu}}_{L\infty}$ reaches about 14 percent as e goes to 0.92.

3 Results indicate that the inclined elliptical tubes of usual practical proportions (namely: $L^+>30$) behave as infinite-length tubes, for which the analytical expressions (25) and (30) can be used with acceptable accuracy for calculating mean Nusselt numbers of pure forced convection and pure free convection film condensation, respectively.

4 The present solution is restricted for large Prandtl numbers. However, for small Pr numbers, it is valid only for small values of Jakob number, i.e., similar to Nusselt–Rohsenow-type models.

Nomenclature

a = semi-major axis of ellipse
b = semi-minor axis of ellipse
C_p = specific heat of condensate film at constant pressure
d_e = equivalent circular diameter of elliptical tube, cf. Eq. (15)
e = ellipticity $= (\sqrt{a^2-b^2}/a)$
F = dimensionless mixed-convection parameter, cf. Eq. (21)
g = acceleration of gravity
Gr_d = Grashof number for tube $= g\rho^2 d_e^3/\mu^2$
$I(\phi)$ = function defined by Eq. (16)
h_{fg} = latent heat of condensation
h''_{fg} = modified latent heat of condensation
Ja = Jakob number $= C_p \Delta T/h''_{fg}$
k = thermal conductivity of condensate film
L = tube length
L^+ = dimensionless tube length $= 2L/(d_e \tan \varphi)$
m''_c = condensation mass flux
Nu = local Nusselt number
$\mathrm{Nu}(z)$ = local peripherally averaged Nusselt number $= \alpha_z d_e/k$
$\overline{\mathrm{Nu}}_L$ = mean Nusselt number for whole tube surface $= \overline{\alpha} d_e/k$
$\overline{\mathrm{Nu}}_{L\infty}$ = mean Nusselt number for infinite-length tube $= \overline{\alpha} d_e/k$
Ra = Rayleigh number $= GrPr$
$\tilde{\mathrm{R}}\mathrm{e}$ = two-phase Reynolds number $= V_\infty d_e/v$
u = condensate velocity component in x-direction
w = condensate velocity component in z-direction
V_∞ = free-stream vapor velocity
x = peripheral coordinate measured from top point of tube ellipse
z = axial coordinate
Z^+ = dimensionless axial coordinate, cf. Eq. (19)

Greek Symbols

α = local heat transfer coefficient $= k/\delta$,
$\overline{\alpha}$ = mean heat transfer coefficient for whole tube surface
δ = local thickness of condensate film
Δ = dimensionless local film thickness, cf. Eq. (18)
ΔT = temperature drop across condensate film $= (T_s - T_w)$
β = dimensionless local film thickness, cf. Eq. (27)
ρ = density of condensate
θ = peripheral angle measured from top point of tube ellipse
ϕ = angle between the tangent to tube ellipse at any point (r, θ) and the horizontal
φ = tube inclination angle with the horizontal
μ = dynamic viscosity of condensate
ν = kinematic viscosity of condensate
$\tau_{\delta x}$ = interfacial vapor shear in x-direction
$\tau_{\delta z}$ = interfacial vapor shear in z-direction.

Subscripts

s = saturation
w = wall
x = x-direction
z = z-direction
δ = interface

References

[1] Cheng, S., and Tao, J., 1988, ''Study of Condensation Heat Transfer for Elliptical Pipes in a Stationary Saturated Vapor,'' ASME J. Heat Transfer, **96**, pp. 405–408.
[2] Yang, S., and Chen, C., 1994, ''Laminar Film Condensation on a Horizontal Elliptical Tube With Variable Wall Temperature,'' Int. J. Heat Mass Transf., **116**, pp. 3135–3141.
[3] Fieg, G. P., and Roetzel, W., 1994, ''Calculation of Laminar Film Condensation in/on Inclined Elliptical Tubes,'' Int. J. Heat Mass Transf., **37**, pp. 619–624.
[4] Yang, S., and Hus, C., 1997, ''Mixed-Convection Laminar Film Condensation on a Horizontal Elliptical Tube With Uniform Surface Heat Flux,'' Numer. Heat Transfer, **32**, pp. 85–95.
[5] Shekriladze, I. G., and Gomelauri, V. I., 1966, ''Theoretical Study of Laminar Film Condensation of Flowing Vapour,'' Int. J. Heat Mass Transf., **9**, pp. 581–591.
[6] Memory, S. B., Adams, V. H., and Marto, P. J., 1997, ''Free and Forced Convection Laminar Film Condensation on Horizontal Elliptical Tubes,'' Int. J. Heat Mass Transf., **40**, pp. 3395–3406.
[7] Nusselt, W., 1916, ''Des Oberflachenkondensation des Wasserdamfes,'' Z. Vereines Deutsch. Ing., **60**, pp. 541–564, 569–575.
[8] Rohsenow, E. M., 1956, ''Heat Transfer and Temperature Distribution in Laminar Film Condensation,'' Trans. ASME, **78**, pp. 1648–1654.
[9] Mosaad, M., 1999, ''Combined Free and Forced Convection Laminar Film Condensation on an Inclined Circular Tube With Isothermal Surface,'' Int. J. Heat Mass Transf., **42**, No. 21, pp. 4017–4025.
[10] Mosaad, M., 1999, ''Theoretical Study of Forced Convection Film Condensation on an Inclined Elliptical Tube,'' The 5th ASME/JSME Thermal Engineering Joint Conference, San Diego, California, Vol. II, pp. 645–651.
[11] Hassan, K. E., and Jakob, M., 1958, ''Laminar Film Condensation of Pure Saturated Vapor on Inclined Cylinders,'' ASME J. Heat Transfer, **80**, pp. 887–897.

Heat Transfer and Pressure Drop Characteristics During R22 Evaporation in an Oval Microfin Tube

Man-Hoe Kim
Department of Mechanical and Industrial Engineering, University of Illinois at Urbana-Champaign, 1206 West Green Street, Urbana, IL 61801
e-mail: mankim1@uiuc.edu

Jeong-Seob Shin
Department of Mechanical Engineering, Pohang University of Science and Technology, San 31 Hyoja-Dong, Pohang, Kyungbuk 790-784, Korea

Clark W. Bullard
Department of Mechanical and Industrial Engineering, University of Illinois at Urbana-Champaign, 1206 West Green Street, Urbana, IL 61801

An experimental study on R22 evaporating heat transfer in round and oval microfin tubes has been performed. The oval tube was an elliptic tube of axis ratio 1:1.5, which was fabricated from the round tube with an outer diameter of 9.52 mm and 18 deg helix angle counterclockwise. The test section was a straight horizontal tube of 0.6 m in length and was heated electrically by a tape heater wound on the tube surface. Heat flux of 12 kW/m^2 was maintained constant and the range of refrigerant quality was 0.2–0.8. The tests were conducted for evaporation at 15 °C for 30–60 kg/h mass flow rate (mass flux based on the oval tube: 150–300 kg/m^2s) and the installation angles of the oval tube were varied between 0 and 135 deg in the circumferential direction. The local and average heat transfer and pressure drop characteristics for the oval tube were compared to those for the baseline round tube. The average two-phase heat transfer coefficients for the oval tube were 2–12 percent higher than that for the round tube and pressure drops for both tubes are similar. The single heat transfer coefficient and friction factor correlations for the round and oval microfin tubes are developed within the rms errors of ±5.6 percent and ±10.0 percent, respectively. [DOI: 10.1115/1.1351894]

Keywords: Enhancement, Evaporation, Heat Transfer, Heat Exchangers, Two-Phase

Introduction

Heat exchangers in air conditioning and heat pump applications have an important effect on system efficiency and physical size, and on environmental impacts. Finned round tube heat exchangers are usually used for the evaporator and condenser for residential air-conditioning systems. The air-side thermal resistance of the heat exchangers dominates the total thermal resistance. To improve the thermal performance of finned tube heat exchangers, it is necessary to reduce air-side thermal resistance. When a round tube is used, heat transfer degradation and large pressure drop are caused by re-circulating flow in the wake, and noise problems may be caused by non-uniform flow at the outlet of heat exchangers. Oval tubes are one option for solving these problems. Therefore, several studies of air-side thermal performance of oval tube heat exchanger have attracted researchers [1–5]. To investigate the overall performance of the oval tube heat exchangers, however, tube-side heat transfer and pressure drop behaviors as well as air-side performance must be considered simultaneously. Several investigators [6–13] performed studies on evaporation in microfin round tubes.

Yasuda et al. [6] developed ''THERMOFIN-HEX TUBE'', which was 9.52 mm o.d. microfin tube with 18 deg helix angle, to improve the evaporation performance of room air conditioners. They reported R22 evaporation heat transfer coefficient had a maximum at mass flux of 200–250 kg/m^2s. Schlager et al. [7] investigated evaporation and condensation heat transfer and pressure drop characteristics in three horizontal 12.7 mm microfin tubes with R22. They found evaporation and condensation heat transfer coefficients in the microfin tubes were 1.6–2.2 and 1.5–2.0 times, respectively, larger than those in the smooth tubes. Kandlikar [8] presented a flow boiling heat transfer correlation for enhanced tubes by modifying his smooth tube correlation, and Christoffersen et al. [9] investigated local evaporation heat transfer and pressure drop characteristics for R22, R134a, and R32/R125 (60/40 percent) in smooth and microfin tubes. Kaul et al. [10] conducted a study on the horizontal evaporation heat transfer performance of R22 and several alternative refrigerants in a fluid heated microfin tube and they developed correlations of heat transfer coefficients for each refrigerant. Chamra et al. [11] presented R22 evaporation heat transfer and pressure drop data for new microfin geometries applied to the inner surface of 15.88 mm o.d. tubes. Kuo et al. [12] reported the effect of heat flux, mass flux and evaporation pressure on the heat transfer coefficients using 9.52 mm o.d. microfin and plain tubes. Liu [13] performed a study of evaporation and condensation heat transfer and pressure drop behaviors of R134a and R22 in a 9.52 mm o.d. axially grooved tube and presented heat transfer coefficient and pressure drop correlations for each refrigerant. Dunwoody and Iqbal [14] investigated single-phase laminar heat transfer characteristics in elliptical tubes having different ratios of major and minor axis. They reported that the heat transfer and pressure drop for the elliptic tube are larger than those of a round tube. However, there is no published data in the open literature for refrigerant evaporation in an oval microfin tube.

This study investigates local and average two-phase heat transfer and pressure drop characteristics during R22 evaporation in a horizontal oval microfin tube. The test results are compared to those for a round tube of the same circumferential length. The effect of installation angle on the evaporation characteristics of the oval tube is also reported. Finally, the heat transfer enhancement factors for the oval tube are addressed and the heat transfer and pressure drop correlations are developed.

Experiments

Test Apparatus. Figure 1 shows schematic diagram of the test apparatus. It consists of circulation loops for the refrigerant and heat transfer fluids and data acquisition system. The refrigerant circulation loop includes a gear pump, a mass flow meter, a pre-heater, a test section, a stabilizer, a sub-cooling unit and a receiver. The refrigerant is delivered to the test section by the

Contributed by the Heat Transfer Division for publication in the JOURNAL OF HEAT TRANSFER. Manuscript received by the Heat Transfer Division April 28, 2000; revision received November 15, 2000. Associate Editor: H. Bau.

magnetic gear pump. The refrigerant flow rate was measured using a coriolis-type Micromotion mass flow meter (Model D12) with a nominal flow range of 0–135 kg/h and an accuracy of ±0.15 percent of full scale. The refrigerant quality at the inlet of the test section is regulated through heat exchange between the refrigerant and the hot water in the pre-heater. Table I describes geometrical parameters for the test tubes, compared to those of ACRC [9] and NIST [10]. Figure 2 shows the cross-sectional configuration of the microfin tube tested. The test section has an effective length of 600 mm and the oval tube tested was fabricated using 9.52 mm o.d. round microfin tube with 18 deg helix angle counterclockwise. The oval tube is an elliptic copper tube with axis ratio of 1.5 (major axis: D_m = 11.20 mm, minor axis: D_n = 7.47 mm), so its cross sectional area is about 10 percent smaller. A variable power supply was connected to the sheathed heater wound on the tube surface to control the heat flux of the test section. Thermocouples and pressure transducers are inserted in the inlet and outlet of the test tube and a differential pressure sensor is connected between them. The measured saturation temperatures were in good agreement with the temperature calculated based on the measured saturated pressure within ±0.3°C. To measure the tube surface temperatures, twelve thermocouples were attached on the outer surface of the tube at three locations along the length of the tube, mounted at the top, bottom, right and left of the tube in the circumferential direction. The entire refrigeration circulation loop including the test section was wrapped with 40 mm thick foam insulation to minimize heat transfer between refrigerant and the environment.

The hot and cold water circulation loops to control the state of the refrigerant include a pre-heater and a sub-cooler. Thermocouples were inserted to measure the temperatures at the inlet and outlet of the sub-cooler and pre-heater, and thermopiles were attached to measure the temperature differences between the inlet and outlet of the hot and cold water. Heat transfer rate of the pre-heater was regulated by water flow rate measured using a coriolis-type Micromotion mass flow meter (Model D40) with a nominal flow range of 0–1225 kg/h and an accuracy ±0.15 percent of full scale. The test data were collected using a hybrid recorder and analyzed in real time with a PC running the data reduction program. All the information about test conditions and test data during the test, were displayed on the monitor and test conditions were changed based on this information.

Test Conditions and Methods. Prior to the evaporation test, the energy balance between the heater and tube-side was checked using water at the proper heat flux, and the results showed agreement within 3 percent as shown in Table 2. The test conditions described in Table 3 span the range of operating conditions of an evaporator for a residential air conditioning system. The tests are conducted for evaporation at 15°C for 30, 45, and 60 kg/h mass flow rate with R22. The refrigerant flow rate (mass flux of the oval tube: 150–300 kg/m^{2}s) is changed by regulating the input power of the variable speed magnetic gear pump. Constant heat flux of 12 kW/m^2 based on the average inside tube surface area is maintained through all the tests. The quality of the refrigerant entering the test section is controlled through the heat exchange rate in the pre-heater, and the heat flux was maintained by modulating the power of the sheathed heater. The installation angles of the oval tube are varied between 0 and 135 deg in the circumferential direction for investigating the effect of gravitational force on evaporation. Figure 3 defines installation angle. Installation angle of 0 deg designates that the major axis of the oval tube is horizontal, normal to the direction of the gravitational force. The test conditions and data to be collected were monitored throughout the test, and data sets of 60–100 were recorded and averaged over 6–10 minutes after test conditions reached the steady state.

Refrigerant flow rates, rather than mass fluxes, were held constant during the experiments to maximize usefulness of the data for designers who seek the air-side benefits of substituting oval for

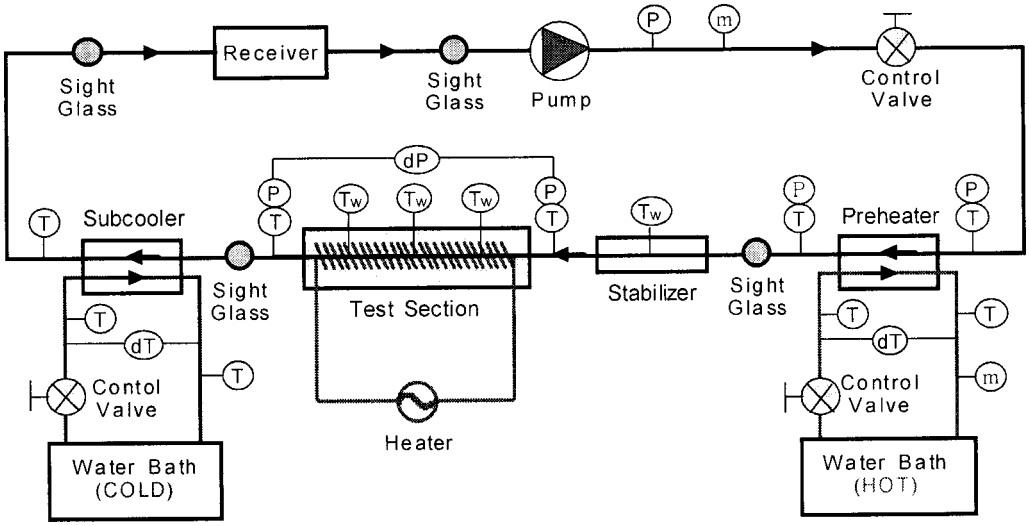

Fig. 1 Schematic diagram of test rig

Table 1 Geometrical parameters for the test tubes

Tube type	D_o/D_r (mm)	D_m/D_n (mm)	T_b/T_m (mm)	H_f (mm)	β/α (°)	Number of fins	D_h (mm)	A_c (mm^2)	A/A_p
Oval	-	11.2/7.47	0.3/0.36	0.2	18/40	60	5.0	55.6	1.6
Baseline	8.8/8.92	-	0.3/0.36	0.2	18/40	60	5.5	60.8	1.6
ACRC [9]	8.71/8.89	-	0.32/0.41	0.18	18/25	60	5.66	59.6	1.54
NIST [10]	8.8/8.92	-	0.3/0.4	0.2	18/50	60	5.45	60.8	1.6

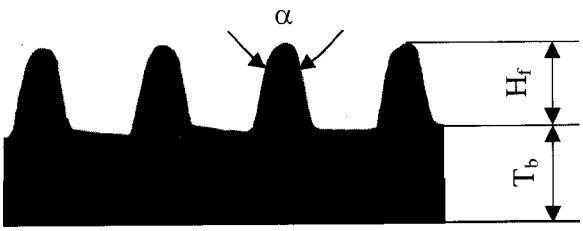

Fig. 2 Cross-sectional geometry of the microfin tube tested

Table 2 Test results for the energy balance

Heater	Heat flux (kW/m^2)	12
	Heat transfer rate (kW)	0.215
Water	Flow rate (kg/s)	0.0278
	Inlet temperature (^{o}C)	25.2
	Outlet temperature (^{o}C)	27.1
	Heat transfer rate (kW)	0.220

round tubes, and wish to understand the refrigerant-side impacts. In this paper, results are presented and comparisons are made in terms of mass flux wherever possible.

Data Reduction. The inlet and average qualities of the refrigerant at the test section were calculated from the energy balance in the preheater and the test section, respectively

$$x_i = \frac{1}{i_{fg}}\left(\frac{Q_{ph}}{m_r} - (i_f - i_{ph,i})\right) \tag{1}$$

$$x = x_i + \frac{Q_{ts}}{2m_r i_{fg}}. \tag{2}$$

The evaporation heat transfer coefficients were calculated as

$$h = \frac{q_i''}{T_w - T_r}, \tag{3}$$

where q_i'' is heat flux, and T_w and T_r are inside wall and refrigerant temperatures, respectively. Heat flux was determined using inside tube wall area, based on the average of root and minimum inner diameters and power input supplied to the heater. T_w was

Table 3 Test conditions

Refrigerant		R22		
Evaporating temperature (^{o}C)		15		
Mass flow rate (kg/h)		30	45	60
Mass flux (kg/m^{2}s)	Round tube	137	206	274
	Oval tube	150	225	300
Heat flux (kW/m^2)		12		
Quality range		0.2-0.8		
Installation angle (^{o})		0, 45, 90, 135 (-45)		

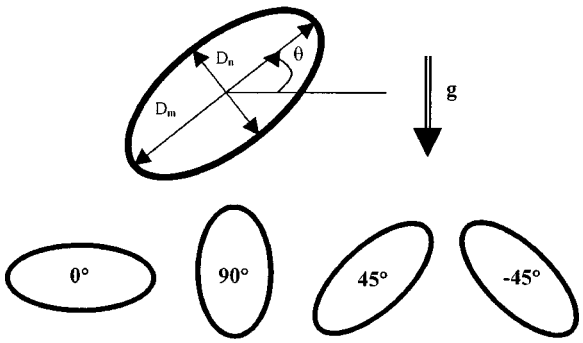

Fig. 3 Definition of installation angle

Table 4 Estimated uncertainties

Sensors	Temperature	±0.1 ^{o}C
	Pressure	±0.25 %
	Mass flow	±0.15 %
Parameters	Heat flux	±5.5 %
	Refrigerant quality	±2.8 ± 6.0 %
	Refrigerant mass flux	±0.8 ± 1.2 %
	Average heat transfer coefficient	±5.9 ± 10.3 %
	Friction factor	±8.5 ± 10.7 %

calculated from the temperature measured at the outside tube wall using the one-dimensional conduction equation, approximated as Cartesian geometry. Pressure drop data were obtained simultaneously from the differential pressure transducer with 0.17 kPa accuracy and two absolute pressure transducers installed at the inlet and outlet of the test section, and two values were in good agreement. Average heat transfer coefficient and pressure drop data were obtained, respectively, from the average values of the integral of the local heat transfer coefficient and pressure drop, which were fitted over the quality ranges of 0.2–0.8. Refrigerant properties were calculated using REFPROP [15]. Accounting for all instrument errors, uncertainties for the average heat transfer coefficients and pressure drops were estimated ±10.3 percent and ±10.7 percent (see Table 4), respectively using the standard method [16].

Results and Discussion

Before considering heat transfer behaviors, experimental flow patterns (Fig. 4) are presented on the Taitel-Dukler map [17] since two-phase heat transfer is strongly dependent on flow pattern. Modified Froude numbers (F) in Fig. 4 were calculated using different length scales (D_e) for each installation angle (θ); $D_e = D_n$ for $\theta = 0$ deg and $D_e = D_m \sin\theta$ for 90 deg and ±45 deg

$$F = \left(\frac{\rho_g}{D_e g(\rho_f - \rho_g)}\right)^{0.5}\left(\frac{Gx}{\rho_g}\right). \tag{4}$$

For mass flow rates of 45 and 60 kg/h, the flow patterns for most of test data are in the annular flow regime except at very low quality ($x < 0.2$). On the other hand, for the lowest mass flow rate ($m = 30$ kg/h) and low refrigerant quality, the flow regimes are in the stratified wavy flow region or close to the boundary between the annular and stratified wavy flow.

Figures 5–7 compare temperature variations along the circumferential direction for the round and oval tubes with 0 deg and 90 deg installation angles. Figure 5 shows wall temperature profiles for the round tube at the mass flow rates of 30 kg/h and 60 kg/h for ease of comparison with oval tube data obtained at the same

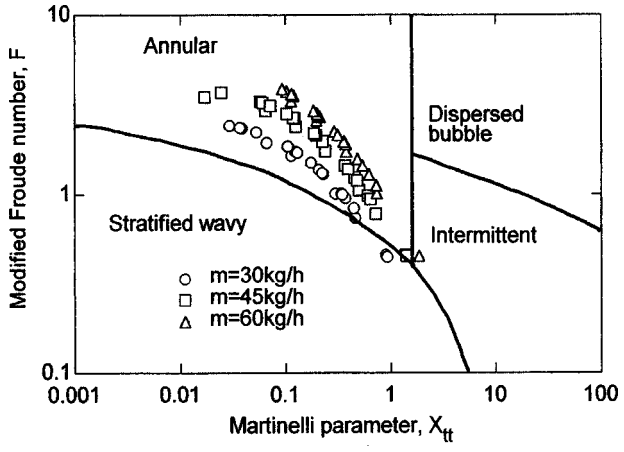

Fig. 4 Experimental flow patterns on the Taitel-Dukler map

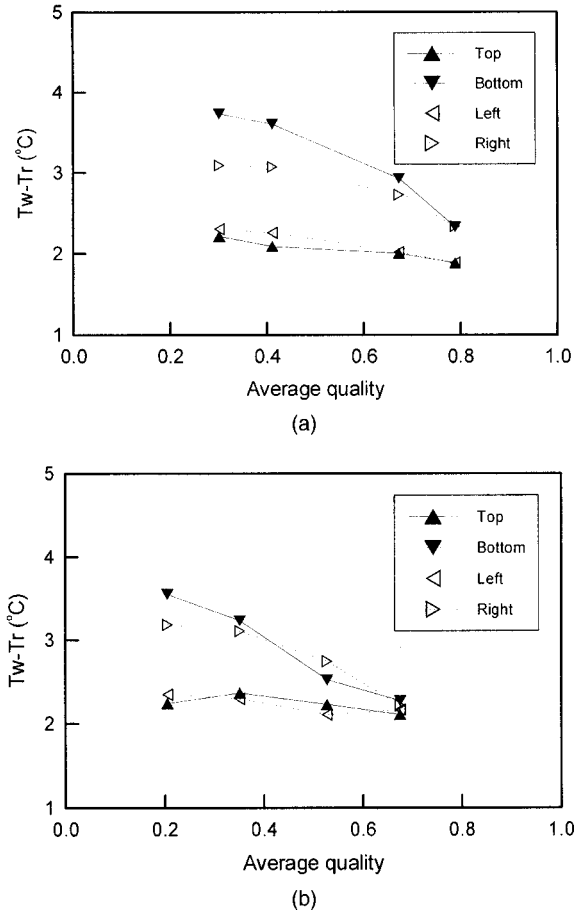

Fig. 5 Circumferential variations of wall temperatures for the round tube: (*a*) mass flow rate: 30 kg/h; (*b*) mass flow rate: 60 kg/h.

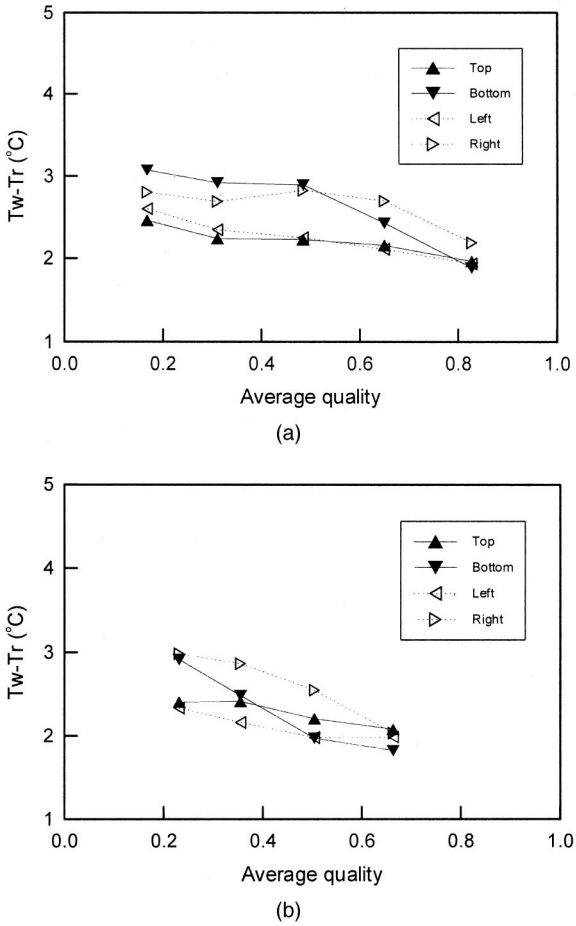

Fig. 6 Circumferential variations of wall temperatures for the oval tube (0 deg installation angle): (*a*) mass flow rate: 30 kg/h; (*b*) mass flow rate: 60 kg/h.

mass flow rates. The temperatures of the bottom and right walls are relatively higher than those of the top and left walls, since liquid film layers are thicker due to gravity and the counterclockwise helix [18]. As expected, temperature variations along the circumference decrease as refrigerant mass flux and quality increase since the gravity and helix angle effects become relatively less important as the flow pattern changes from stratified wavy flow to annular flow.

Figure 6 presents the circumferential wall temperature distribution for the oval tube at $\theta = 0$ deg, where the major axis is horizontal. Compared to $\theta = 90$ deg (Fig. 7), the temperature variation along the circumference is relatively small, and so is the temperature difference between the surface and refrigerant, which may explain the relatively higher heat transfer. It is observed that the top of the tube has a higher temperature difference than the bottom at $x > 0.8$, 0.6, and 0.4 for $G = 150$, 225, and 300 kg/m^{2}s, respectively. This consistent trend in the data suggests that dryout occurs earlier when the mass flux increases and the increased vapor velocity causes the thinner liquid film at the top region of the tube to break down and become entrained as droplets in the vapor core of the flow [19]. This could explain the higher temperature difference at the top of the tube.

Figure 7 shows the wall temperature distribution for the oval tube at for $\theta = 90$ deg. The wall temperature variation along the circumference is similar to that for the round tube and it indicates that the flow regime is stratified wavy flow for low mass flux over the whole quality range except for $x > 0.7$. However, as the refrigerant mass flux increases and flow regime changes to annular flow, the temperature variation along the circumference decreases.

Heat Transfer Results. Figure 8 presents local heat transfer behaviors with the refrigerant quality and mass flow rate. The local heat transfer coefficients are increased with refrigerant quality as expected except at low mass flux and low quality region, where flow regime is stratified wavy flow and heat transfer coefficients are relatively constant with quality. The effect of installation angle on the heat transfer coefficient decreases with increasing the refrigerant quality and mass flux. This behavior may be partly due to the flow regime transition from stratified wavy flow to annular flow and more complete wall wetting and thinning of the liquid film [9].

Figure 9 shows how average heat transfer coefficients vary with mass flux and installation angle. Average heat transfer coefficients for the oval tube are consistently 2–12 percent higher than that for the round tube for all mass fluxes considered in the study. The heat transfer coefficients had maximum values at the refrigerant flow rate of around 45 kg/h, where mass fluxes of round and oval tubes are 206 and 225 kg/m^{2}s, respectively. This behavior is consistent with the test result for the study of Yasuda et al. [6] who used the same round microfin tube. These phenomena suggest again that dryout occurred earlier and therefore the heat transfer coefficient decreased as mass flux increased.

Heat transfer enhancement factors defined by

$$\eta_h = \frac{h_{\text{oval}}}{h_{\text{round}}}, \tag{5}$$

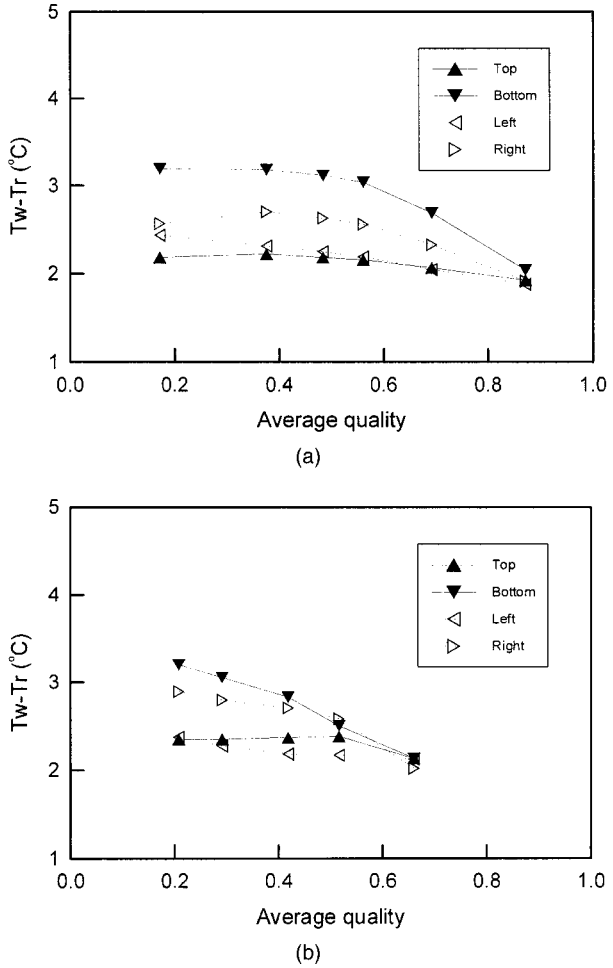

Fig. 7 Circumferential variations of wall temperatures for the oval tube (90 deg installation angle): (*a*) mass flow rate: 30 kg/h; (*b*) mass flow rate: 60 kg/h.

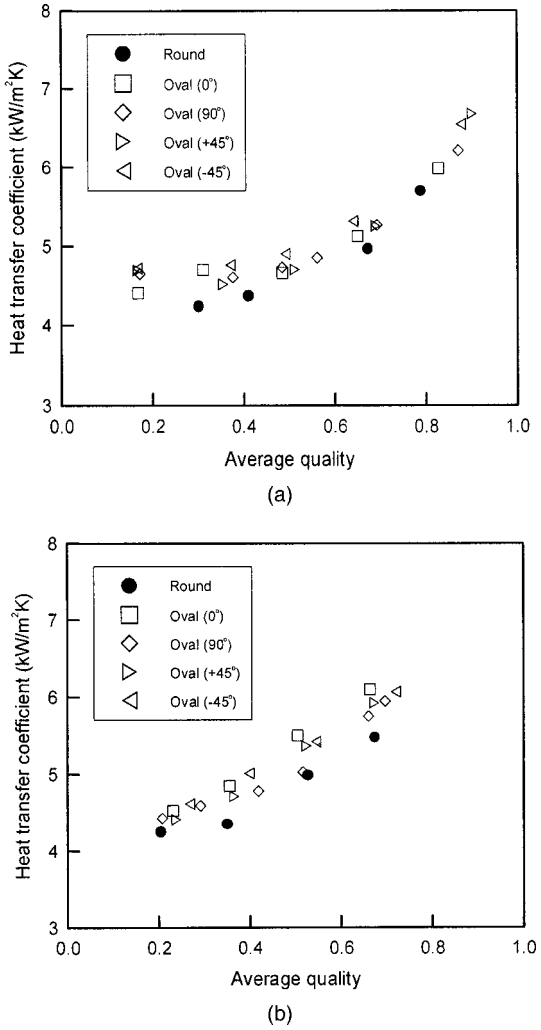

Fig. 8 Local heat transfer coefficients: (*a*) mass flow rate: 30 kg/h; (*b*) mass flow rate: 60 kg/h.

where h_{oval} and h_{round} are the average heat transfer coefficients for the oval and round tubes and they are fitted using third-order polynomial function of mass flux, G.

$$h = aG + bG^2 + cG^3 \tag{6}$$

The polynomial coefficients a, b, and c are shown in Table 5 for the round and oval tubes. Table 6 shows the heat transfer enhancement factors obtained from Eqs. (5) and (6) at the mass fluxes (G = 150, 225, and 300 kg/m^{2}s) considered in the study. For the round tube, η_h is 1. The heat transfer enhancement factor for 135 deg (-45 deg) installation angle is larger than that for 45 deg installation angle, suggesting the symmetry plane of the liquid film thickness is rotated counterclockwise, in the same direction as the grooved helix [18].

The heat transfer enhancement factors η_h determined from the experiments are expected to depend strongly on tube geometry, especially at low refrigerant qualities and mass fluxes where helix angle and gravitational effects are strongest. Additional experiments with different tubes will be needed to quantify this dependence. Eventually the enhancement factor can be included as a multiplier in heat transfer correlations, such as the one illustrated below, which begins by modifying the round tube evaporation correlation proposed by Kaul et al. [10].

$$\text{Nu}_{\text{oval}} = \text{Nu}_{\text{round}}\,\eta_h \frac{D_{h,\text{oval}}}{D_{h,\text{round}}} \tag{7}$$

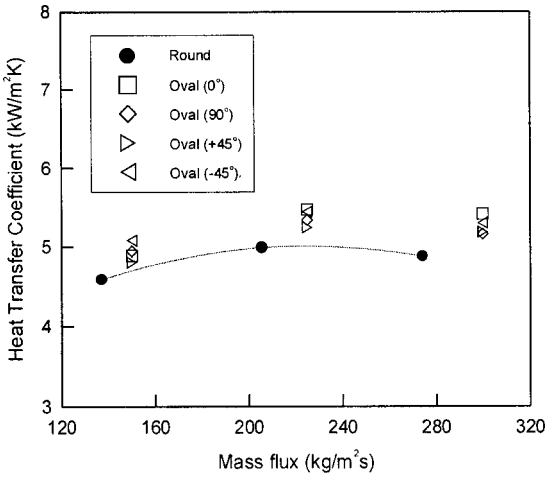

Fig. 9 Average heat transfer coefficients with variation of mass flux

Table 5 Polynomial coefficients in Eq. (6)

	Round tube	Oval tube (installation angle, °)			
		0	45	90	-45
a	0.060	0.055	0.058	0.060	0.063
b*10^4	-2.34	-1.78	-2.06	-2.14	-2.34
c*10^7	2.89	1.79	2.39	2.42	2.80

Table 6 Heat transfer enhancement factors (η_h)

Mass flux (kg/m^2s)	Installation angle (°)			
	0	45	90	-45
150	1.03	1.02	1.05	1.08
225	1.09	1.06	1.08	1.10
300	1.12	1.09	1.09	1.12

Table 7 Data sets used in the study

	Tube	Data points	T_{evap} (°C)	q_i'' (kW/m^2)	G (kg/m^2s)
Present	Round oval	75	15	12	137-274 150-300
ACRC [9]	Round	60	5	2.0-38.7	50-505
NIST [10]	Round	150	4.4	3.4-29.2	43-1800

$$\mathrm{Nu}_{\mathrm{round}}=\frac{h_{\mathrm{round}}D_{h,\mathrm{round}}}{k_f}=45.85\mathrm{Bo}^{\alpha}\mathrm{Re}_{lo}^{\beta}\mathrm{Pr}_f^{0.4} \tag{8}$$

$$\alpha=0.475-0.476x+0.197x^2,\quad \beta=0.599-0.474x+0.282x^2, \tag{9}$$

where D_h is the hydraulic diameter as defined in Kedzierski and Goncalves [20]. The quadratic exponents in Eq. (9) have been shown to be very successful for correlating convective boiling with a single expression [10,21].

Equations (7) and (8) can now be combined into a single heat transfer correlation for the round and oval tubes

$$\mathrm{Nu}=\frac{hD_h}{k_f}=45.85\eta_h\left(\frac{D_h}{D_{h,\mathrm{round}}}\right)\mathrm{Bo}^{\alpha}\mathrm{Re}_{lo}^{\beta}\mathrm{Pr}_f^{0.4}. \tag{10}$$

Figure 10 compares the present test data and correlation with ACRC [9] and NIST data [10], in which tube configurations are similar to the baseline round tube as shown in Table 1. The present correlation [Eq. (10)] predicts well the present test data within rms errors ±5.6 percent, and ACRC and NIST data ±15.9 percent and ±10.2 percent, respectively. The latter studies included a wider range of test conditions as shown in Table 7, and the ACRC tube geometry had significantly different apex angle (see Table 1). The heat transfer correlation [Eq. (10)] can be used for the round and oval microfin tubes within the test conditions indicated in Table 7.

Pressure Drop Results. Figures 11–13 show pressure drop results. As shown in Fig. 11, local pressure drops for both round and oval tubes increase with quality as expected. However, incremental rate decreases over certain quality and it varies with mass flow rate. For lower mass flow rate (30 and 45 kg/h), incremental rates decrease over vapor quality of 0.65, while for 60 kg/h mass flow rate it decreases over quality of 0.55. As the quality or mass flux increases and the liquid layer becomes thinner, the roughness of the liquid-vapor interface decreases and therefore, pressure drop decreases [9]. Figure 12 shows how average total (frictional and acceleration) pressure drops in the round and oval tubes vary with refrigerant mass flux, and increase systematically with mass flux as expected. The average pressure drop of the oval tube is smaller or the same as the round tube at the same mass flux, essentially indistinguishable within range of experimental error. However at the same mass flow rate, the average total pressure drop in the oval tube varies from 3 percent to 20 percent greater than that in the round tube as mass flux increases, consistent with other published data for a round microfin tube [9]. The cross sectional area (55.6 mm^2) of the oval tube is about 10 percent smaller than that of the round tube (60.8 mm^2), since the oval tube has a smaller hydraulic diameter.

Considering that the pressure drop is a characteristic of the friction with the vapor flow [9,13], it can be expressed using friction factor (f), mass flux (G), quality (x), and vapor density (ρ_g):

$$\Delta P=f\frac{\Delta l}{D_h}\frac{(Gx)^2}{2\rho_g}, \tag{11}$$

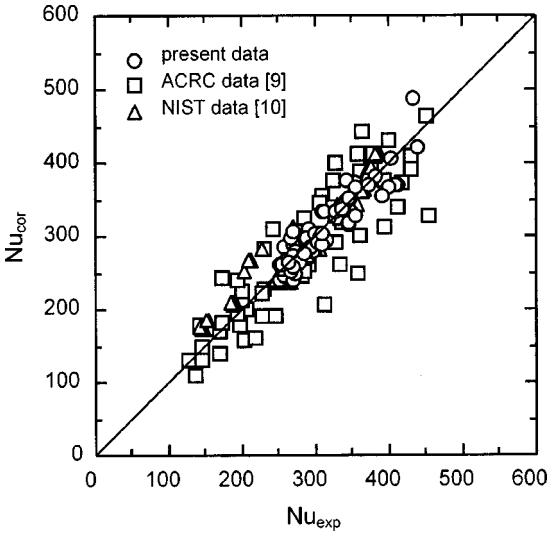

Fig. 10 Comparison of experimental data and Nu correlation

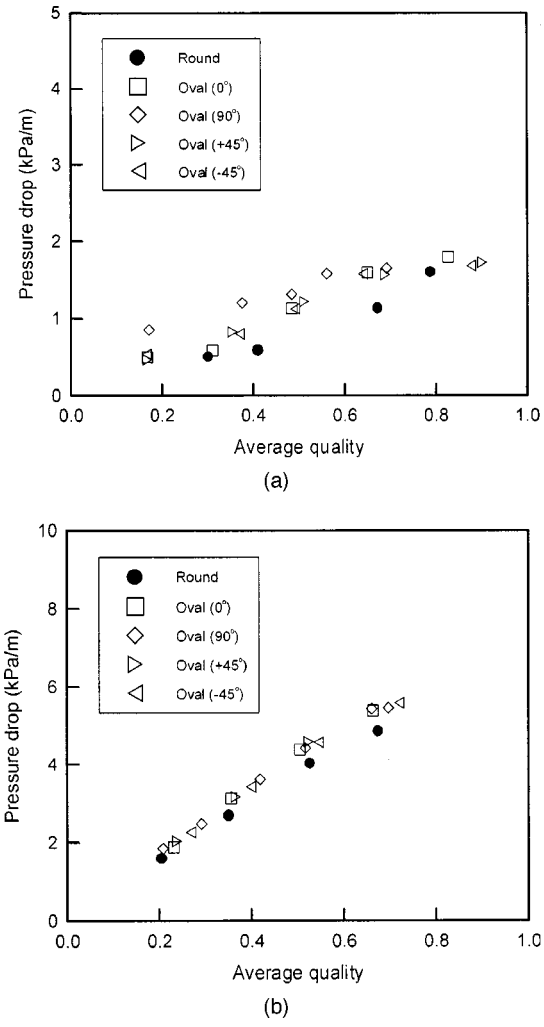

Fig. 11 Local pressure drops (*a*) mass flow rate: 30 kg/h; (*b*) mass flow rate: 60 kg/h.

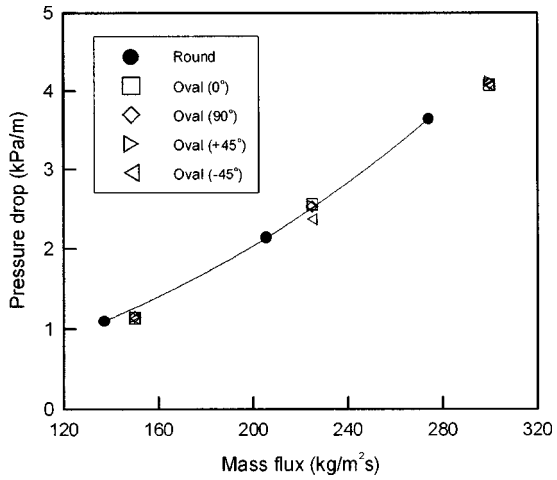

Fig. 12 Average total pressure drops with variation of mass flux

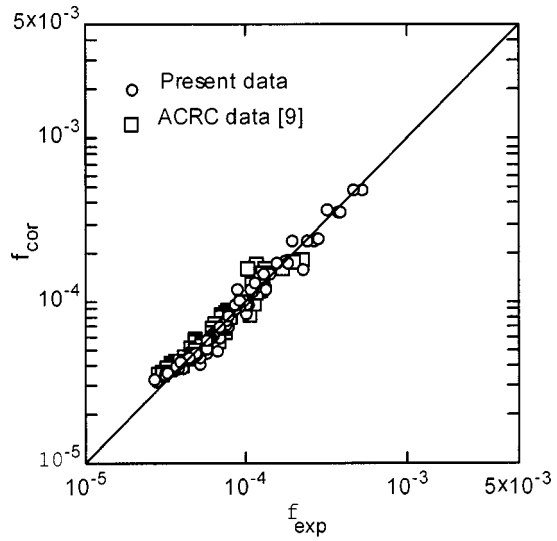

Fig. 13 Comparison of experimental data and friction factor correlation

where f is the friction factor and its single correlation for the round and oval tubes is developed using the vapor Reynolds number (Re_g) and average quality (x):

$$f = 0.212\,\mathrm{Re}_g^{-0.112} x^{-1.035}. \tag{12}$$

The correlation predicts the present and ACRC data [9] within rms errors of ± 10.0 percent and ± 15.5 percent, respectively. The pressure drop correlation developed here can be used for the oval and round microfin tubes in the range of test conditions as shown in Table 7.

Concluding Remarks

Evaporation heat transfer and pressure drop characteristics of R22 in a microfin oval tube have been investigated. The average heat transfer coefficients in an oval tube were 2–12 percent larger than that in the round tube with the same microfin and circumference, while the average pressure drops for both tubes were similar, based on the mass flux. The installation angle of the oval tube did not affect significantly the evaporation behaviors. The heat transfer enhancement factor for the oval tube was defined based on the round microfin tube, and the quality dependent exponents enabled the single correlation to predict most of two-phase heat transfer coefficients. The single heat transfer coefficient and friction factor correlations for the round and oval microfin tubes were developed within rms errors of ± 5.6 percent and ± 10.0 percent, respectively. Their applicability to oval tubes having different helix angles and aspect ratios needs to be generalized as additional tube geometries are examined in similar experiments.

Acknowledgments

We are grateful for supporting of this study to Samsung Electronics Co., Ltd. and the 25 member companies of the Air Conditioning and Refrigeration Center (ACRC) at the University of Illinois at Urbana-Champaign. We are also grateful to Dr. Mark A. Kedzierski of NIST for providing the valuable data and comments.

Nomenclature

A = heat transfer area, mm^2
A_c = heat transfer area, mm^2
A_p = heat transfer area for corresponding plain tube, mm^2
a,b,c = polynomial coefficients in Eq. (6)
B_o = boiling number (q_i''/Gi_{fg})
D_a = average diameter, mm
D_e = characteristic length, mm
D_h = hydraulic diameter, mm
D_m = major axis, mm
D_n = minor axis, mm
D_r = root diameter, mm
f = friction factor
F = modified Froude number
g = gravitational acceleration, m/s^2
G = refrigerant mass flux, kg/m^{2}s
h = heat transfer coefficient, W/m^{2}K
H_f = fin height, mm
i = enthalpy, J/kg
i_f = saturation liquid enthalpy in the preheater, J/kg
i_{fg} = latent heat of evaporation, J/kg
k = thermal conductivity, W/mK
l = tube length, m
m = refrigerant mass flow rate, kg/s
Nu = Nusselt number (hD_h/k)
ΔP = pressure drop, Pa
Pr = Prandtl number
q_i'' = heat flux, W/m^2
Re = Reynolds number
Re_{lo} = liquid Reynolds number based on hydraulic diameter (GD_h/μ_f)
Re_g = vapor Reynolds number based on hydraulic diameter ($GD_h x/\mu_g$)
T = temperature, K
T_b = bottom wall thickness, mm
T_m = mean wall thickness, mm
x = refrigerant vapor quality or average quality

Greek Letters

α = apex angle, deg, or quadratic exponent defined in Eq. (9)
β = helix angle, deg, or quadratic exponent defined in Eq. (9)
η_h = heat transfer enhancement factor
θ = installation angle, deg.
ρ = density, kg/m^3

Subscripts

evap = evaporation
f = liquid
g = vapor

i = inlet
oval = oval tube
ph = preheater
r = refrigerant side
round = round tube
ts = test section
w = tube wall

References

[1] Brauer, H., 1964, ''Compact Heat Exchanger,'' Chemical and Process Engineering pp. 451–460.

[2] Ota, T., Nishiyama, H., and Takao, Y., 1984, ''Heat Transfer and Flow Around an Elliptic Cylinder,'' Int. J. Heat Mass Transf., **27**, No. 10, pp. 1771–1779.

[3] Chen, Y., Fiebig, M., and Mitra, N. K., 1998, ''Conjugate Heat Transfer of a Finned Oval Tube Part A: Flow Patterns,'' Numer. Heat Transfer, Part A, **33**, pp. 371–385.

[4] Chen, Y., Fiebig, M., and Mitra, N. K., 1998, ''Conjugate Heat Transfer of a Finned Oval Tube Part B: Heat Transfer Behaviors,'' Numer. Heat Transfer, Part A, **33**, pp. 387–401.

[5] Choi, Y.-H., Kim, S.-T., and Sohn, D.-Y., 1998, ''Navier-Stokes Code Development for Performance Assessment of Fin-Tube Heat Exchanger,'' Ajou University Report 1998A1546, Suwon, Korea.

[6] Yasuda, K., Ohizumi, K., Hori, M., and Kawamata, O., 1990, ''Development of Condensing Thermofin-HEX-C Tube,'' Hitachi Cable Review, No. 9, pp. 247–252.

[7] Schlager, L. M., Pate, M. B., and Bergles, A. E., 1990, ''Evaporation and Condensation Heat Transfer and Pressure Drop in Horizontal, 12.7-mm Microfin Tubes With Refrigerant 22,'' J. Heat Transfer, **122**, pp. 1041–1047.

[8] Kandlikar, S. G., 1991, ''A Model for Correlating Flow Boiling Heat Transfer in Augmented Tubes and Compact Evaporators,'' J. Heat Transfer, **113**, pp. 966–972.

[9] Christoffersen, B. R., Chato, J. C., Wattelet, J. P., and Souza, A. L., 1993, ''Heat Transfer and Flow Characteristics of R22, R32/R125, and R134a in Smooth and Microfin Tubes,'' ACRC Technical Report 47, University of Illinois at Urbana-Champaign, Urbana, IL.

[10] Kaul, M. P., Kedzierski, M. A., and Didion, D. A., 1996, ''Horizontal Flow Boiling of Alternative Refrigerants Within a Fluid Heated Microfin Tube,'' *Process, Enhanced and Multiphase Heat Transfer: A Fesischrift for A. E. Bergles*, Begell House, Inc., New York, pp. 167–173.

[11] Chamra, L. M., Webb, R. L., and Randlett, M. R., 1996, ''Advanced Microfin Tubes for Evaporation,'' Int. J. Heat Mass Transf., **39**, No. 9, pp. 1827–1996.

[12] Kuo, S. C., and Wang, C. C., 1996, ''In-Tube Evaporation of HCFC-22 in a 9.52 mm Microfin/Smooth Tube,'' Int. J. Heat Mass Transf., **39**, No. 12, pp. 2559–2569.

[13] Liu, X., 1997, ''Condensing and Evaporating Heat Transfer and Pressure Drop Characteristics of HFC-134a and HCFC-22,'' J. Heat Transfer, **119**, pp. 158–163.

[14] Shah, R. K., and London, A. L., 1978, *Laminar Flow Forced Convection in Ducts*, Academic Press, San Diego, CA, pp. 247–252.

[15] Huber, M., Gallagher, J., McLinden, M., and Morrison, G., 1996, NIST Thermodynamic Properties of Refrigerants and Refrigerant Mixtures Database—REFPROP, Version 5.1, NIST, USA.

[16] Moffat, R. J., 1988, ''Describing the Uncertainties in Experimental Results,'' Exp. Therm. Fluid Sci., **1**, pp. 3–17.

[17] Taitel, Y., and Dukler, A. E., 1976, ''A Model for Predicting Flow Regime Transitions in Horizontal and Near Horizontal Gas-Liquid Flow,'' AIChE J., **22**, No. 1, pp. 47–55.

[18] Shedd, T. A., Shurig, R., and Newell, T., 2000, ''An Investigation of Two-Phase Flow in Microgrooved Tubes,'' *Proceedings of the 2000 International Refrigeration Conference at Purdue*, pp. 193–200.

[19] Pettersen, J., Riberer, R., and Munkejord, S. T., 2000, ''Heat Transfer and Pressure Drop Characteristics of Evaporating Carbon Dioxide in Microchannel Tubes,'' *Proceedings of 4th IIR-Gustav Lorentzen Conference on Natural Working Fluids at Purdue*, pp. 107–114.

[20] Kedzierski, M. A., and Goncalves, J. M., 1999, ''Horizontal Convective Condensation of Alternative Refrigerants Within a Microfin Tube,'' Enhanced Heat Transfer, **6**, pp. 161–178.

[21] Kedzierski, M. A., and Kim, M. S., 1998, ''Convective Boiling and Condensation Heat Transfer With a Twisted-Tape Insert for R12, R22, R152a, R134a, R290, R32/134a, R32/R152a, R290/R134a, R134a/R600a,'' Therm. Sci. Eng., **6**, No. 1, pp. 113–122.

Ken-ichi Yoshida
Former Graduate Student,
Keio University,
Yokohama, Japan

Yoshiyuki Abe
Electrotechnical Laboratory,
Tsukuba, Japan
e-mail: y.abe@etl.go.jp

Toshiharu Oka
Research Institute,
Ishikawajima-Harima Heavy Industries Co., Ltd.,
Yokohama, Japan

Yasuhiko H. Mori

Akira Nagashima
Professor, Mem. ASME

Keio University,
Yokohama, Japan

Spray Cooling Under Reduced Gravity Condition

The present paper reports on the results of a series of authors' parabolic flight experiments on spray cooling in addition to ground-based experiments in which the influence of heater orientation and the behavior of rebounded droplets were especially studied in detail. Water and FC-72 (perfluorocarbon) were employed alternatively as a test liquid sprayed from a single full-cone nozzle onto a Cr-plated surface of an electrically heated copper block for transient cooling experiments or onto a transparent ITO (indium tin oxide) coated surface of a glass block for steady state experiments in a relatively low superheat region. Each experimental run was accomplished within some 15 sec through which a stable reduced gravity condition (0.01 times the terrestrial gravity) was maintained in the aircraft. Cooling curves were obtained over a wide range of each of the following parameters: the wall superheat, the spray volume flux and the Weber number for the spray droplets. It is demonstrated that the gravity dependency of the spray cooling characteristics varies with the spray volume flux and the droplet Weber number. Qualitative interpretations of the observed gravity dependency are provided.
[DOI: 10.1115/1.1345887]

Introduction

Spray cooling has been widely applied to many industrial processes in which controlled rapid and effective cooling performance is required. Because of its capability for intensive and accurately controlled heat removal, spray cooling is considered to be one of the key technologies for developing thermal management systems for use in space. In fact, flash evaporators were developed for the Space Shuttles [1], and they have been operated for years of the Space Shuttle missions. In addition, spray cooling should have potential applicability to various space technologies such as emergency cooling, microelectronics cooling, quenching and rapid cooling in microgravity materials processing, etc. Despite the mass of literatures on spray cooling, however, the present understanding of the influence of gravity on spray cooling characteristics is considerably limited.

Choi and Yao [2] examined the effect of heater orientation by the experiments on both horizontal and vertical sprays impacting onto vertical and horizontal heater surfaces, respectively. Their results showed a higher rate of heat transfer for the vertical spray in the film boiling region due to the secondary contacts of spattered droplets, and a higher heat transfer for the horizontal spray in the transition boiling region most likely due to easier vapor removal from the heater surface. Qiao and Chandra [3] observed a detailed impact behavior of free-falling single droplets on a heated surface under a low gravity condition, though the experimental time available with a 15 mm free-fall was only 55 ms. They noted that water droplets could not be maintained on the heater in Leidenfrost evaporation in low gravity condition. As for the heat transfer in the nucleate boiling region, however, no appreciable influence of the reduction in gravity was found. Another important finding in their work was a difference in boiling behavior between water and an organic liquid (*n*-heptane), which is presumably ascribable to the differences in surface tension and wetting angle between the two liquids. The effects of such differences may become more prominent with the reduction in gravity.

The present authors' previous work on pool boiling also showed a difference in the boiling behavior and boiling heat transfer between organic liquids and water in microgravity conditions [4]. It is likely that spray cooling characteristics might show a similar different behavior between organic liquids and water. It is expected that the influence of gravity may be mostly emphasized in film boiling region under low Weber number conditions, because, according to the We-based criterion of droplet impinging behavior [5], the rebounding motion of droplets on the heater surface in reduced gravity conditions must be considerably different from that in the normal gravity.

Although most of previous works studied on post-impact behavior of spray droplets, the thermal interaction between spray droplets and air (or vapor) during pre-impact may also have a significant influence on the heat transfer in spray cooling. The interaction between spray and buoyant jet arising from the heated surface was experimentally and theoretically investigated, and a considerable reduction in droplet velocities due to the counterflowing buoyant vapor jet was pointed out [6]. In addition to all these previous findings indicating the influence of gravity, the thickness of a liquid film on the heater surface [7,8] may be under an influence of gravity as long as the flooding condition takes place on the heater surface. Deb and Yao [9] analyzed the film boiling heat transfer, taking account of three different heat transfer mechanisms: drop contact heat transfer including local vapor convection and local entrained air convection, bulk convection and radiation. The previous studies outlined above allow us to presume that gravity should play an important role in the spray cooling particularly in the film boiling region. Nevertheless, none of these studies provided us with an indisputable experimental evidence for the influence of gravity on the spray cooling characteristics.

In this context, the present authors initiated an experimental approach, using parabolic flights of a Japanese aircraft, MU-300. The results of the first experiments in this project has been reported elsewhere [10]. These experiments were performed with water and CFC-113 each sprayed onto a Ni-plated surface of a copper block heater of 19 mm in diameter. Water and CFC-113 were selected, noting significant differences in physical properties (e.g., latent heat of vaporization, surface tension, contact angle on metal, etc.) between them. In view of substantial differences in pool boiling behavior between water and some organic liquids

Contributed by the Heat Transfer Division for publication in the JOURNAL OF HEAT TRANSFER. Manuscript received by the Heat Transfer Division February 3, 2000; revision received July 19, 2000. Associate Editor: T. Avedisian.

observed in previous microgravity experiments of the present authors [4], it was expected that water and CFC-113 may show appreciably different spray cooling characteristics. Later CFC-113 was replaced by FC-72 (perfluorocarbon), and the Ni-plated heater was also replaced by a hard Cr-plated surface of a copper block heater, which was 50 mm in diameter. As for the heater surface characteristics, the hard Cr-plated heater surface employed in the present study showed very stable cooling characteristics throughout the present experiments due to its high resistivity against oxidization, though we have experienced rather poor stability of Ni-plated surfaces, mirror-finished Cr-plated surface, and gold-plated surfaces. At the same time, a metallized (ITO) surface of a transparent glass heater was also employed in a relatively low superheat region, i.e., nucleate boiling region, for the observation of the behavior of liquid droplets impinging onto the transparent heater covered with a liquid film [11]. Note that recent experimental data for spray cooling characteristics with CFC-113 [12] and FC-72 [13] are available, and FC-72 is regarded as a coolant in the thermal management systems for both the Expose Facility in the JEM (Japanese Experiment Module) in the ISS (International Space Station) Alpha and Japanese un-manned space vehicle under development. The results obtained in the present authors' preceding studies [11] may be briefly summarized as follows.

For Water. At spray volume fluxes below 3.0×10^{-4} $m^3/(m^2\cdot s)$, the heat transfer in the high temperature region beyond the MHF (minimum heat flux) point was degraded by about 30 percent with a decrease in gravity. At spray volume fluxes higher than 2.0×10^{-3} $m^3/(m^2\cdot s)$, a reduction in gravity caused a slight increase in the CHF (critical heat flux). The observation of the transparent heater surface from its rear side revealed that the droplets fed onto the surface at lower spray volume fluxes completely vaporized there, without showing mutual interactions, if the heat flux imposed on the heater was so raised as to approach the CHF.

For CFC-113 and FC-72. At spray volume fluxes above 5.0×10^{-4} $m^3/(m^2\cdot s)$, a reduction in gravity yielded a slight increase in the CHF. When a heat flux close to the CHF was imposed on the heater surface, droplets having impinged on the surface integrated into quite thin liquid films, which were immediately swept away.

The above results indicate some gravity dependency of the spray-cooling heat transfer characteristics, which is qualitatively consistent with the results of the previous terrestrial spray-cooling experiments on the influence of the heater-surface orientation [2]. However, the following issues are still remained to be clarified: (1) the variation of gravity dependency of spray cooling heat transfer with a change in spray volume flux conditions; and (2) the variation of gravity dependency of spray cooling heat transfer over a wide range of *We* conditions particularly in the film boiling region.

This paper reports on the results of a succeeding series of parabolic-flight experiments, which were performed with an intention to clarify the issues listed above. Special attention was paid to cover wide ranges of wall superheating and *We*, respectively. A Laser Doppler Velocimeter (LDV) with a frequency shifter was employed for the evaluation of the velocities of liquid droplets before impinging on the heater surface and rebounding from it. The range of the spray volume flux in the present study does not cover the liquid flooding regime but is limited to the drop-wise evaporation regime. The authors believe that spray cooling should not be used in the liquid flooding regime as far as the application of spray cooling in space is concerned, because the liquid flooding regime presumably yields complicated bulk liquid/vapor interaction in microgravity conditions with erratic and/or indefinite *g*-jitters from various sources. It should also be noted that, in space, the liquid to be sprayed needs to be saved, without causing a substantial degradation of spray cooling performance. The objective of the present study is, therefore, not to pursue higher CHF's but to obtain experimental knowledge of the effects of gravity on spray cooling in various spray conditions.

Experimental

Apparatus. Figure 1 schematically illustrates the assembly of the apparatus. Since the apparatus was designed for parabolic flight experiments, the systems were essentially closed. The liquid contained in a pressure vessel was continuously squeezed out by a plunger being replaced by dry nitrogen gas at a constant pressure, 0.2–0.7 MPa, so that the liquid could be sprayed at a constant volume flux into a spray chamber from a nozzle installed at the top of the chamber. No attempt was made to control the liquid temperature at a prescribed level; the liquid was thermally equilibrated with the ambience both in the ground-based and parabolic flight experiments. The subcoolings of water and FC-72 alternatively used as the test liquid were, therefore, 68–79 K and 29–37 K, respectively. The liquid thus sprayed onto the surface of a heater installed in the chamber vaporized completely or partly. The vapor filling the chamber and, if any, a residual liquid were then discharged into an external reservoir to be stored there. In reduced gravity conditions, this draining procedure was maintained with the aid of a small auxiliary pump. The pressure vessel was a 0.01 m^3 in volume, and hence one filling-up of the vessel allowed for one series of parabolic flight experiments, i.e., the experiments performed in ten successive parabolic flights, which were succeeded in one hour.

Two different heaters, namely a copper block heater and a transparent glass heater, were prepared for use in two different classes of experiments, transient experiments and steady-state experiments, respectively. Figure 2 illustrates the structure of the upper portion of the copper block heater, which had a hard Cr-plated circular surface of 50 mm in diameter. The heater required a relatively large test surface and, at the same time, such a small heat capacity as to allow rapid temperature control during parabolic flights. The present heater design was a compromise between these two requirements. The positions of twelve sheathed chromel-alumel thermocouples inserted into the copper block are indicated in Fig. 2. These thermocouples, 0.25 mm in diameter, were calibrated in advance, and the uncertainty in the temperature measurements with these thermocouples was evaluated to be ±0.1 K. Before each experiment, the copper block was heated up to a prescribed temperature (up to 400°C) by seven 1 kW cartridge heaters embedded in the block from its bottom. The copper block was then cooled down transiently by spraying a liquid onto its surface. The junctions of those thermocouples were fixed at four different depths from the top surface of the block and at three different radial locations—just on the central axis of the block, and 8 and 15 mm, respectively, offset from the central axis. Each

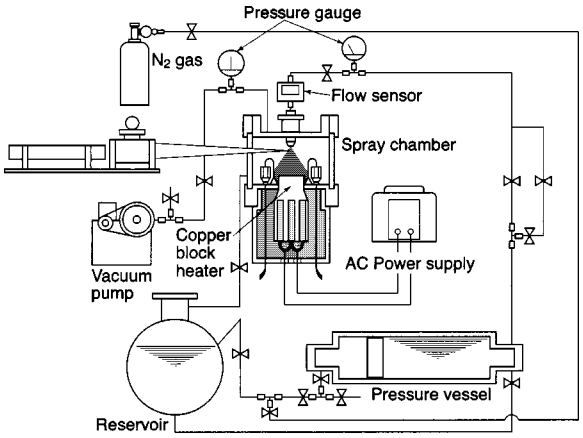

Fig. 1 Spray cooling experimental apparatus

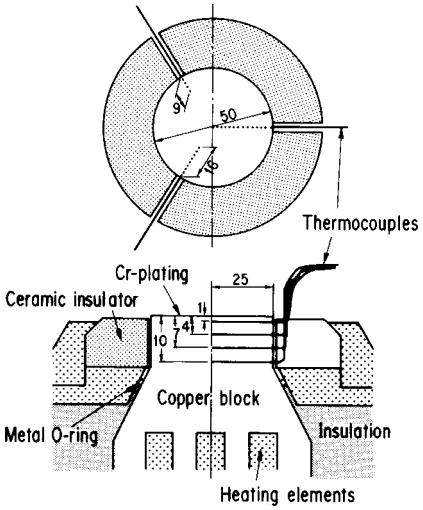

Fig. 2 Structure of copper block heater

thermocouple was stuck into a 0.35 mm-diameter hole with a thermal-resistant alumina/silica cement. The cooling of the block was monitored simultaneously with the twelve thermocouples. The surface heat flux and the surface temperature at each instant were deduced from the instantaneous temperature distribution inside the block detected by those thermocouples, assuming one-dimensional conduction in the cylindrical copper block and taking into account of the temperature dependency of the thermal conductivity of copper. After the experiments, the copper block was cut, and the maximum discrepancies of the actual locations of the thermocouple junctions from their nominal locations were found to be ± 0.05 mm in the axial direction and ± 0.2 mm in the radial direction. The relative uncertainty in the heat flux was the largest at the MHF point for FC-72; it was estimated to be ± 10 percent. The transient experiments using this copper block heater enabled us to obtain the heat transfer characteristics throughout the film, transition and nucleate boiling regions, thereby permitting us to determine the CHF and the MHF.

Figure 3 illustrates another heater assembly which was used for observing the behavior of liquid droplets on the heater surface. A Pyrex block shaped into an anomalous prism configuration was substituted for the copper block. An 18 mm $\times$18 mm area on the top surface of the glass prism was plated with a thin (100–500 nm in thickness) transparent ITO (indium tin oxide) film which could serve as the source of Joule-heat generation. Since the electric resistance of the ITO film increases with an increase in temperature with a fairly good and stable linearity, the area-averaged heater surface temperature could be evaluated by measuring the resistance of the ITO film. The uncertainty in the temperature

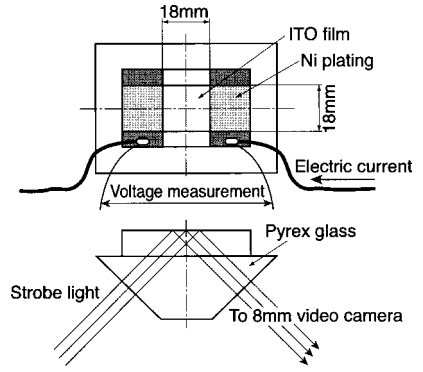

Fig. 3 Structure of transparent glass heater

determination was estimated to be within ± 1 K. All the experiments with this glass-prism heater were performed under a steady-state thermal condition in contrast with the transient cooling experiments with the copper block heater, and were limited to the nucleate boiling region to prevent the ITO film from possible thermal destruction at high heat fluxes close to the CHFs.

Three different full-cone nozzles (Uni-jet type TG, Spraying Systems Co., Ltd) were used alternately to spray water or FC-72 onto the heater surface in the chamber filled with nitrogen gas nearly held at the normal atmospheric pressure. The spray volume flux could be changed either by exchanging the nozzle in use for another one or by changing the pressure of nitrogen gas supplied to the pressure vessel storing the test liquid, water or FC-72. Any nozzle put to use was fixed at a position 100 mm above the heater surface so that it was pointed at the center of the surface.

In the experiments on the ground, the spray chamber was so installed that the heater surface was facing either upward or downward to examine the dependency of the heat transfer characteristics on the heater orientation.

Spray Parameters. The spray volume flux at the heater surface was calibrated, on the ground, for different levels of the pressure imposed on the liquid to be sprayed out from each nozzle. In the calibration, the heater in the spray chamber was replaced by a honeycomb-structured droplet receiver such that the top surface of the latter was located at the same position as that of the former in the spray cooling. This enabled us to know the spatial distribution of the spray volume flux. It was found that the volume flux under each prescribed condition was nearly uniform within a diameter of some 30 mm about the axis of the spray but significantly radius-dependent over the peripheral region. Thus, the volume flux averaged over the central area of the heater within 30 mm in diameter was used as D, the nominal spray volume flux, in this paper.

The diameters and velocities of droplets sprayed out from the nozzles were measured with the aid of a PDPA (Phase Doppler Particle Analyzer) at a plane 100 mm below the nozzle tip, which corresponds to the position of the heater surface in the spray cooling experiments. The droplet velocities thus measured under each experimental condition showed a typical Gaussian distribution in the radial direction with the maximum velocity at the center. The mean velocity averaged over the central area, within 30 mm in diameter in the heater surface, was defined as v, the nominal droplet velocity, in this paper. The difference between the mean velocity and the maximum velocity was within ± 3 percent, and the uncertainty in the mean velocity was within ± 0.5 m/s. The droplet diameter measurements also showed a slight spatial distribution, but the difference in diameter between the center and the edge of the heater surface was within ± 6 percent. In the present study, the arithmetic diameter at the center of the heater surface is defined as the droplet diameter. The spray characteristics thus measured are summarized in Table 1. The specifications of the nozzles employed in the present experiments and the liquid pressures are also summarized in Table 1. These PDPA measurements were carried out exclusively on the ground. The LDV system on board the aircraft was different from the PDPA system used on the ground.

Procedure of Flight Experiments. The LDV system including a 15-mW He-Ne laser and a frequency shifter was also on board to measure, through a side window of the spray chamber, the velocities of droplets impinging upon, and rebounding from, the heater surface. The measuring point was 15 mm above the heater surface. Compared to the PDPA measurements on the ground, the velocities measured with the LDV on the aircraft showed a wider scattering; the difference between the maximum and the minimum velocity in the area of the heater surface was within ± 10 percent. The measurements of the rebounded droplets velocities were also schemed during the flight experiments. However, the measurements in reduced gravity condition were seri-

Table 1 Spray parameters

Coolant	Nozzle	Pressure MPa	Spray volume flux D, $m^3/(m^2 \cdot s)$	Droplet diameter (arithmetic mean) d, μm	Droplet velocity v, m/s	Weber number We
Water	TG 0.4	0.2	0.000142	68	5.6	30
Water	TG 0.3	0.4	0.000136	92	5.1	33
Water	TG 0.4	0.4	0.000197	60	5.8	28
Water	TG 2	0.1	0.000370	386	10.8	622
FC-72	TG 0.3	0.3	0.000225	60	5.8	283
FC-72	TG 0.4	0.2	0.000217	54	2.8	59

ously hindered by the vapor condensation and the creeping up of the residual liquid on the sight glass, and, hence, no reliable data were obtained.

The whole experimental apparatus was installed in three standard racks (700 mm×450 mm×900 mm) for the parabolic flights in the MU-300 aircraft. The spray chamber and the main part of the experimental hardware were mounted on one rack (the main rack), and the LDV and the optical signal processing systems were arranged in the second rack next to the main rack. The data acquisition and control systems were accommodated in the third rack.

A series of spray cooling experiments were conducted under a reduced gravity condition (0.01 times the terrestrial gravity g_e), 1 g_e and an elevated gravity condition (2 g_e) during each parabolic maneuver. 1 g_e reference experiments were also conducted on ground before take-off. We confirmed that both cooling characteristics obtained in these 1 g_e situations were in complete agreement. Although the reduced or elevated gravity period during one parabolic trajectory lasts some 15~20 seconds, the only data in the last 6 seconds in that period were employed for the present evaluation of the heat transfer characteristics because of a better stability of the gravity level in the later part of the period. The data composing one boiling curve for a particular experimental condition were taken through one series of parabolic flights, i.e., normally successive 10 parabolas. In the case of water, for instance, starting at 400 K, the copper block heater was gradually cooled down approximately by 5–20 K during each parabola. The rate of cooling depended on the spray condition selected in each series of parabolic flights, and it varied with time in the course of cooling, primarily depending on the boiling regime prevailing on the heater surface at each instant. The experimental data then covered a whole boiling curve after 10 parabolas.

The data sampling frequency was set at 1 Hz while the heater surface temperature (in other words the wall superheat) was in the film boiling region. The frequency was increased to 10 Hz when the surface temperature fell in the transition or the nucleate boiling region.

Results and Discussion

Ground-Based Experiments

Water

(a) Steady state experiments and observation from the rear side of the heater.

Before the flight experiments, a number of reference experiments, especially those for different heater orientation, i.e., upward-facing (1 g_e) and downward-facing (-1 g_e) orientations, were conducted in the normal gravity condition at different spray volume fluxes. Figure 4 compares the heat transfer characteristics for both heater orientations in the nucleate boiling regime with the transparent heater. Here we find that the downward-facing orientation gave a higher heat flux at any degree of the wall superheat irrespective of the spray volume flux. This fact may be explained with the aid of the visual observations of the surface of the transparent heater from its rear side, which are described below.

When the spray volume flux was held at a relatively low level, 1.356×10^{-4} $m^3/(m^2 \cdot s)$, the fraction of the downward-facing heater surface covered by liquid films at the highest heat flux was found to be lower than the corresponding fraction for the upward-facing surface by about 20 percent. On the contrary, the former was higher than the latter by about 20 percent when the spray volume flux was held at a higher level, 4.3×10^{-4} $m^3/(m^2 \cdot s)$. Figure 5 shows typical rear-side views of the heater surface under a low spray volume flux condition, where dark parts and bright parts represent liquid films and dry areas on the heater surface, respectively.

When the spray volume flux was low, it was observed that impinging water droplets formed a number of small (island-like) liquid films which partly covered the heater surface, and that the droplets impinging on the residual dry area immediately evaporated. The authors presume that each isolated island-like film was rather flattened in the 1 g_e condition due to gravitational force, which resulted in a higher liquid occupancy at 1 g_e. It turned out from this behavior of droplet/heater interaction that the lower occupancy of the downward-facing surface by liquid films favors the evaporation of the impinging droplets, thereby yielding a better heat transfer characteristics.

In contrast to this, when the spray volume flux was high, the heater surface was mostly covered by enlarged liquid films, and vigorous nucleate boiling took place in these liquid films. Due to

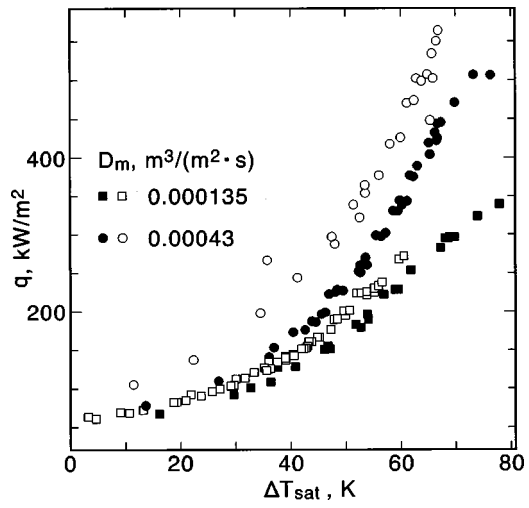

Fig. 4 Comparison of spray cooling characteristics for water with different orientation of transparent heater (Solid circles: 1 g_e, Open circles: -1 g_e)

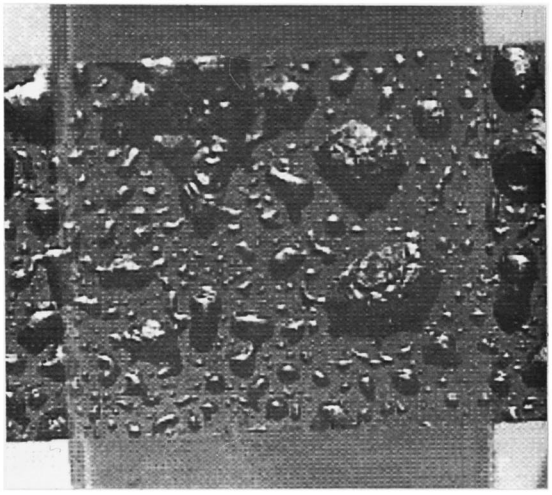

(*a*)

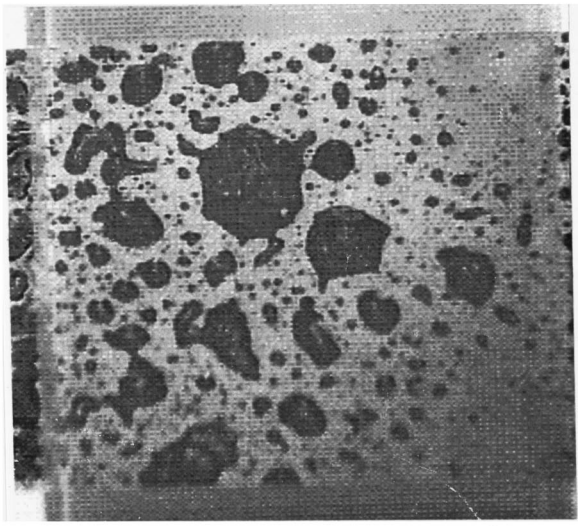

(*b*)

Fig. 5 Observation of water-sprayed heater surface from rear side (*a*) $1\,g_e$, $D=1.97\times10^{-4}$ m^3/(m^2·s), $q=430$ kW/m^2 (*b*) $-1\,g_e$, $D=1.97\times10^{-4}$ m^3/(m^2·s), $q=450$ kW/m^2

flattening of the liquid films in the $1\,g_e$ condition, the in-film nucleate boiling is considered to decrease the liquid occupancy more strongly in the $1\,g_e$ condition than in the case of $-1\,g_e$, downward-facing orientation. Thus the higher fraction of liquid-film-covered area in the downward-facing surface should yield a larger contribution of the in-film nucleate boiling to the heat transfer, thereby resulting in a better heat transfer characteristics. However, the mechanism underlying the variation in liquid film occupancy of the heater surface depending on its orientation is yet-to-be clarified.

The data obtained in the nucleate boiling region in the steady state experiments were found to be well correlated as,

$$q \propto (\Delta T_{\mathrm{sat}})^m, \tag{1}$$

where q and ΔT_{sat} denote the heat flux and the wall superheat, respectively, and m is a dimensionless index falling in the range 1.7–2.0. The above correlation follows the form of empirical correlations reported in some previous studies [14,15].

(***b***) ***Transient experiments and the behavior of rebounded droplets in different* We *conditions***.

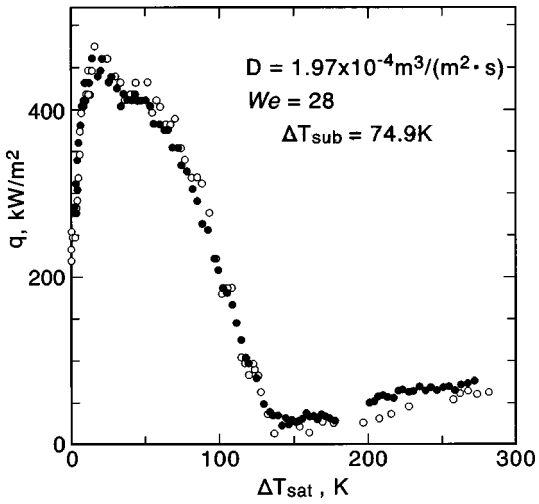

Fig. 6 Comparison of spray cooling characteristics for water with different orientation of copper block heater (Solid circles: $1\,g_e$, Open circles: $-1\,g_e$)

In contrast to the substantial dependency of the heat transfer in the nucleate boiling region on the heater orientation, no significant orientation dependency was observed in the CHF and the transition boiling region. Figure 6 shows the results of the transient experiments with the copper block heater in a low spray volume flux condition. Although Fig. 4 shows an appreciable effect of heater orientation on the heat transfer in the nucleate boiling region, Fig. 6 hardly shows such an effect. This difference is presumably ascribable to the difference in the surface characteristics between the transparent heater used in the steady state experiments and the copper block heater used in the transient cooling experiments. The transparent glass heater has a very smooth surface coated by ITO, while the copper block heater has a relatively rough hard Cr-plated surface. As a result of its higher surface smoothness, the glass heater allows the nucleate boiling to take place in a wider superheat range [16]. It is also presumed that the ITO-coated surface of the glass heater has a higher wettability with water. The impinging droplets easily form either isolated or integrated liquid films on the glass heater, and this particular behavior is presumably relevant to the considerable difference in the nucleate boiling heat transfer characteristics between the upward-facing orientation and the downward-facing orientation.

In Fig. 6 we find a considerable orientation dependency in the film boiling region including the MHF point, where the heat transfer from the downward-facing heater surface was deteriorated by about 30 percent, compared to that from the upward-facing surface. The heat transfer deterioration detected with the downward-facing surface is considered to be caused by the lack of the contribution of rebounded droplets in the low *We* condition ($We=28$); i.e., impinging droplets do not spread out but are rebounded away from the downward-facing heater surface.

According to Shoji et al. [17], the behavior of liquid droplets sprayed onto a heater surface in the film boiling region was classified into the following two categories with respect to the *We*: when $We>80$, each droplet having impinged upon the heater surface is crashed to disintegrate into small fragments; when $We<80$, each droplet is subject to a deformation at the impingement on the heater surface but it soon recovers its spherical shape and then rebounds from the surface due to the predominant role of surface tension and the bulk motion of vapor generated from the droplets. Since *We* in the experimental conditions in Fig. 6 was as low as 28, liquid droplets inevitably rebounded. Each of these droplets once rebounded from the heater surface facing upward possibly repeated such a rebounding motion, thereby continually contributing to the heat removal from the heater surface. On the

Table 2 Results of LDV measurements for rebounded droplets

Coolant	Spray volume flux D, $m^3/(m^2 \cdot s)$	Droplet velocity at heater center v, m/s Downward	Upward	Ratio of rebounded droplets at heater center	Droplet velocity at 15 mm from heater center v, m/s Downward	Upward	Ratio of rebounded droplets at 15 mm from heater center
Water	0.00014	7.8	-2.1	0.54	6.2	-1.2	0.60
Water	0.00020	12.5	-2.7	0.56	10.0	-1.3	0.57
Water	0.00043	10.6	-1.9	0.15	9.5	-1.3	0.13
FC-72	0.00005	3.1	-1.2	0.16	3.3	-1.2	0.16
FC-72	0.00007	4.7	-0.8	0.15	4.4	-1.3	0.17
FC-72	0.00011	3.4	-1.1	0.15	2.7	-1.3	0.13
FC-72	0.00019	5.5	-1.3	0.23	5.3	-1.2	0.14

other hand, it is not likely that the droplets once rebounded from the downward-facing surface interact with the surface again. Thus, the deterioration in heat transfer in the high wall-superheat region observed with the downward-facing surface is reasonably ascribable to the above-mentioned difference in droplet-rebounding behavior between the two surface orientations.

In fact, the velocities of rebounding droplets were measured with the LDV, and it was found that those rebounded droplets had an upward-direction velocity in the range 1.3~2.7 m/s. Detailed measurements revealed that 55–60 percent of droplets were rebounded from the heater when $We=30$. The percentage of the rebounded droplets reduced to about 15 percent when $We=108$ (Table 2). When $We=622$, however, rebounded droplets could not be monitored since all the droplets spread out at the heater surface. A similar situation is expected in the reduced gravity condition.

Figure 7 plots the CHF versus spray volume flux data for water obtained under the terrestrial condition. Also indicated in Fig. 7 are q_{max} versus D relation, where q_{max}, assuming the ideal evaporation of sprayed liquid, is expressed as

$$q_{max}=\rho D(L+c_p\Delta T_{sub}), \tag{2}$$

and an empirical correlation due to Monde [18].

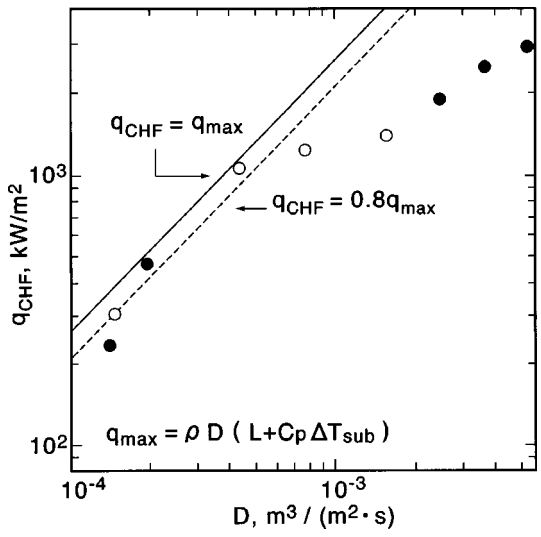

Fig. 7 Relation of CHF and spray volume flux for water in 1 g_e (open circles represent the data obtained in the previous study (Sone et al. [11]))

$$q_{CHF}\approx 0.8q_{max}, \tag{3}$$

where ρ the density of the sprayed liquid, D the mean spray volume flux, L the latent heat of evaporation of liquid, c_p the specific heat, and ΔT_{sub} the subcooling of liquid. The authors' experimental data showed a tendency to deviating from any linear q_{max} versus D relation in a high D range, $D>7\times10^{-4}$ $m^3/(m^2\cdot s)$, and the increase of q_{CHF} with an increasing D was significantly depressed in this range. It is reasonable to assume that the gravity effect may change with a variation in liquid/heater contact mode, which in turn may vary as to whether D is lower or higher than the critical volume flux, $D_{cr}\approx 7\times10^{-4}$ $m^3/(m^2\cdot s)$. Thus, two spray volume flux regions are distinguished here for the convenience of discussing the gravity effect on spray-cooling heat transfer in a later part of this paper: the low spray volume flux region ($D<D_{cr}$) in which droplets having impinged upon the heater surface hardly interact each other and completely vaporize, and the high spray volume flux region ($D>D_{cr}$) in which droplets integrate into liquid films spread over the heater surface.

It may be said alternatively that the low spray volume flux region defines the D range in which q_{CHF} is approximated by Monde's correlation with a reasonable accuracy, and that the high spray volume flux region is the residual D range in which q_{CHF} is no longer approximated by Monde's correlation because of an incompleteness of vaporization of the liquid on the heater surface.

FC-72.

(*a*) ***Steady state experiments and observation from the rear side of the heater.***

In general, a relatively large scattering appeared in the experimental data for FC-72 compared to those for water; this is presumably ascribable to a poor heat transfer characteristics in spraying FC-72 due to its low latent heat. The steady state experiments with the transparent heater showed that the downward-facing heater surface gave a slightly better heat transfer than the upward-facing surface in the nucleate boiling region. From the rear side of the heater, it was observed that an extended liquid film covered the heater surface almost entirely and vigorously flowed over the surface. No nucleation site was clearly observed in the film. This behavior considerably different from that in water spraying is considered to come from the lower surface tension, the lower viscosity and the lower latent heat of FC-72 as well as a higher wettability of the heater surface with FC-72.

(*b*) ***Transient experiments and the behavior of rebounded droplets in different We conditions.***

In the transient cooling experiments, the heat transfer characteristics for downward-facing heater orientation showed an appreciable heat transfer deterioration in the transition and film boiling regions (Fig. 8). Accordingly, both CHF and MHF were deterio-

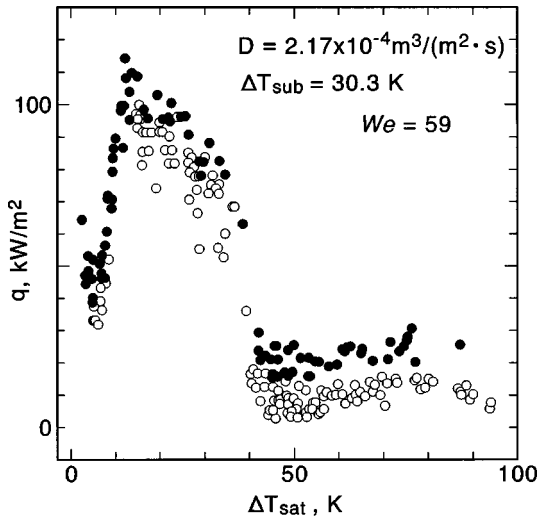

Fig. 8 Comparison of spray cooling characteristics for FC-72 with different orientation of copper block heater (Solid circles: 1 g_e, Open circles: -1 g_e)

rated with the downward-facing orientation. The reduction in the CHF was about 10 percent, and those in the heat fluxes in the film boiling region were 25 percent and 40 percent when $We=283$ and 59, respectively. Just the same as in the water spray cooling, such heat transfer deterioration observed with the downward-facing heater surface is ascribable to no contribution of rebounded droplets to the heat removal from the surface. Detailed LDV measurements indicated that the velocity of the rebounded droplets was 0.8–1.3 m/s (Table 2). As a whole, 15–20 percent of impinging droplets rebounded from the heater surface even at relatively high *We* conditions ($We=140$); this is much lower than the corresponding percentage of rebounded droplets in water spraying. This fact is reasonably ascribable to the surface tension of FC-72 being lower than that of water. The most significant effect of heater orientation on the spray cooling heat transfer with FC-72 was found in the MHF. When $We=59$, the reduction in the MHF for the downward-facing orientation was as large as some 70 percent, compared to the MHF obtained with the upward-facing orientation.

When the CHF data are plotted against D as shown in Fig. 9, we find that the data are approximated by the following correlation in the range $D<4\times10^{-4}$ m^3/(m^2·s):

$$q_{\mathrm{CHF}}\approx 0.4q_{\max}. \tag{5}$$

This correlation indicates that the spray cooling with FC-72 is considerably less effective than that with water (cf. Fig. 7 and Eq. (3)).

Parabolic Flight Experiments

Water.

(*a*) ***Steady state experiments and observation from the rear side of the heater***.

Steady-state experiments in the nucleate boiling region with the transparent heater were carried out at two spray volume fluxes, 3.7×10^{-3} m^3/(m^2·s) and 1.4×10^{-4} m^3/(m^2·s), higher and lower than the critical volume flux D_{cr}, 7×10^{-4} m^3/(m^2·s), respectively. Unexpectedly, the heat transfer characteristics obtained in these experiments showed no appreciable change due to the reduction in gravity. Also we found little change in the behavior on the heater surface observed from the rear side of the transparent heater depending on the magnitude of the gravity. At the highest heat fluxes set in the experiments, presumably very close to the CHFs, the fractions of the heater surface covered by liquid films were 90 percent and 44–49 percent when the spray volume flux was high (3.7×10^{-3} m^3/(m^2·s) and low (1.4×10^{-4} m^3/(m^2·s)), respectively, irrespective as to whether the gravity was reduced, normal or elevated.

(*b*) ***Transient experiments and the behavior of rebounded droplets in different* We *conditions***.

The cooling characteristics obtained in the transient experiments at a spray volume flux, 1.4×10^{-4} m^3/(m^2·s), less than the critical volume flux D_{cr} are presented in Fig. 10. As already described, we conducted 0.01 g_e, 1 g_e and 2 g_e experiments in the same series of parabolic flights. Since the experimental data at 1 g_e were always between those at 0.01 g_e and 2 g_e, we compare only 2 g_e data with 0.01 g_e data in the figures to emphasize the effect of gravity. We find no appreciable difference in the heat transfer near the CHF point between the reduced and the elevated gravity conditions. On the other hand, we find a significant heat transfer deterioration in the film boiling region under the reduced gravity, which exceeds 30 percent of the heat flux under 2 g_e condition over the major portion of the film boiling region. The

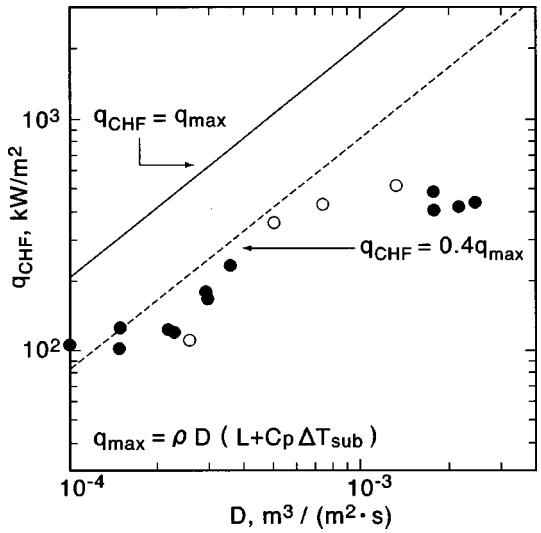

Fig. 9 Relation of CHF and spray volume flux for FC-72 in 1 g_e (open circles represent the data obtained in the previous study (Sone et al. [11]))

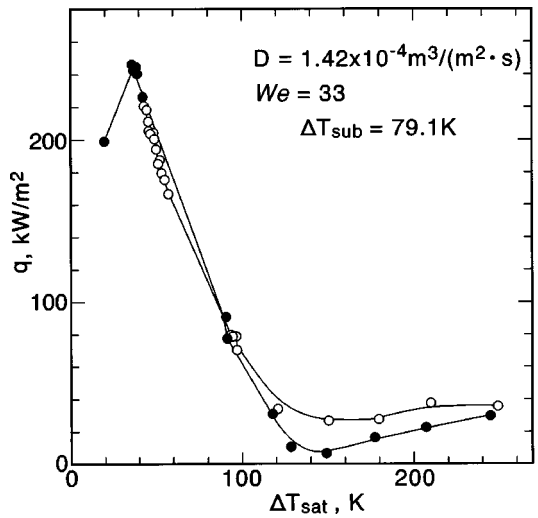

Fig. 10 Spray cooling characteristics for water with copper block heater in parabolic flight experiments in low *We* and *D* (Solid circles: 0.01 g_e, Open circles: 2 g_e)

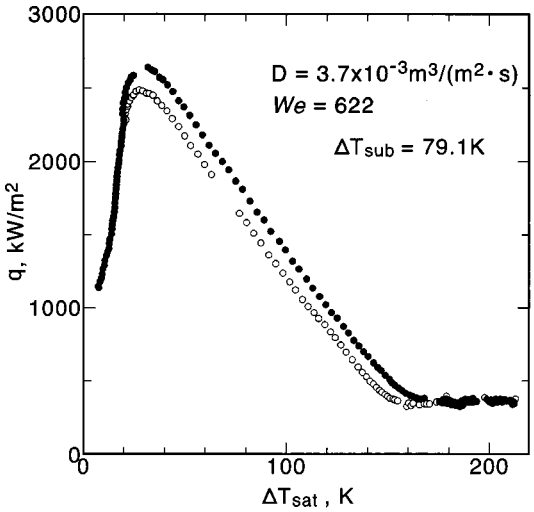

Fig. 11 Spray cooling characteristics for water with copper block heater in parabolic flight experiments in high *We* and *D* (Solid circles: 0.01 g_e, Open circles: 2 g_e)

MHF under the reduced gravity also fell down to about 25 percent of that under 2 g_e. The above facts are generally consistent with the heater orientation dependency of the heat transfer observed in the experiments on the ground, and they are ascribed to a variation of droplets/heater-surface interaction with a change in the surface superheating, which is discussed below.

In a superheating range not far from the CHF point, liquid droplets of 50–100 μm in diameter vaporize immediately after their impingement onto the heater surface. Most of these droplets neither coalesce each other nor fall into a rebounding motion before they vaporize away. Thus, it is unlikely that any change in gravity alters the droplets/heater-surface interaction near the CHF point as long as the spaying condition is in the low spray volume flux region. In the film boiling region, on the other hand, droplets spayed onto the heater surface rebound in a low *We* condition; note that $We=33$ in the experiments of present interest. Those droplets possibly keep continual interaction with the heater surface in the presence of gravity working toward the heater surface. Such a continual droplets/heater-surface interaction must be lost with the reduction in gravity.

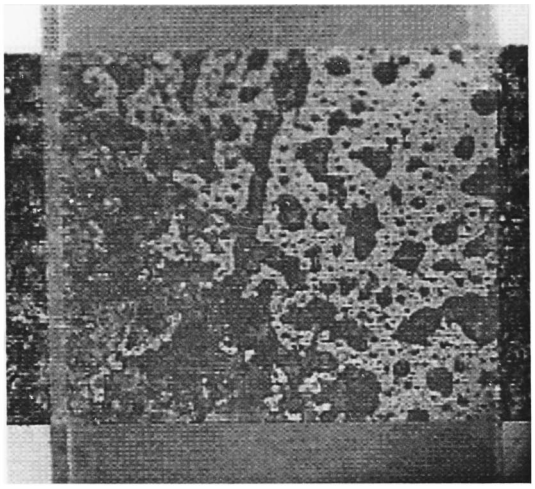

(*a*)

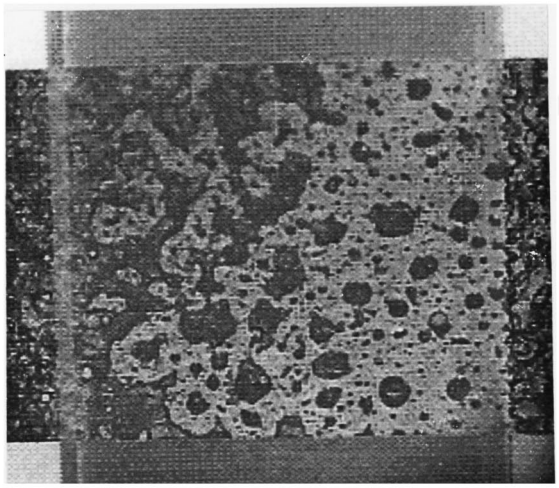

(*b*)

Fig. 13 Observation of FC–72-sprayed heater surface from rear side: (*a*) 0.01 g_e; (*b*) 2 g_e.

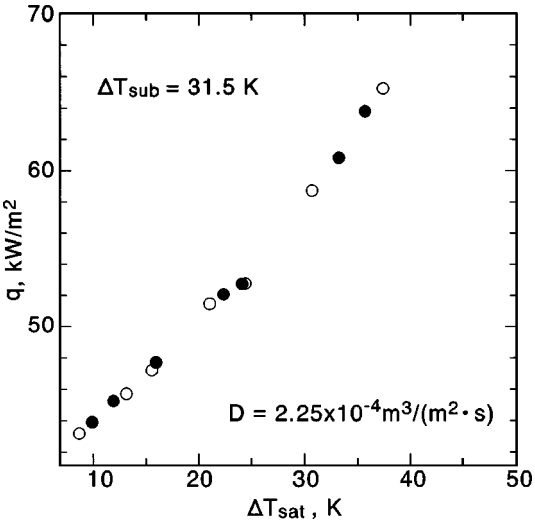

Fig. 12 Spray cooling characteristics for FC-72 with transparent heater in parabolic flight experiments (Solid circles: 0.01 g_e, Open circles: 2 g_e)

The spray cooling characteristics at a higher spray volume flux, 3.7×10^{-3} $m^3(m^2\cdot s)$, exceeding the critical volume flux are presented in Fig. 11. Here we find that the CHF under the reduced gravity is raised above the one under 2 g_e by about 10 percent. This gravity dependency prevails in the transition boiling region, but it is lost in the film boiling region. These facts are well consistent with the results of on-the-ground experiments in which the heater orientation was varied [10]. When the spray volume flux is sufficiently high, droplets having impinged on the heater surface coalesce each other and form liquid films covering a significant proportion of the surface even in a superheat range close to the CHF point. Because of the dimensions of those liquid films far exceeding those of impinging droplets, the configurations and behavior of the films are presumably under the influence of gravity. If this is the case, the heat transfer in a liquid-film-dominating region including the CHF point should inevitably be dependent on gravity. In the film boiling region, droplets sprayed onto the heater surface split into tiny fragments instead of coalescing each other; note that $We>600$ in the experiments of the present concern. Those fragments, or disintegrated droplets, presumably evaporate

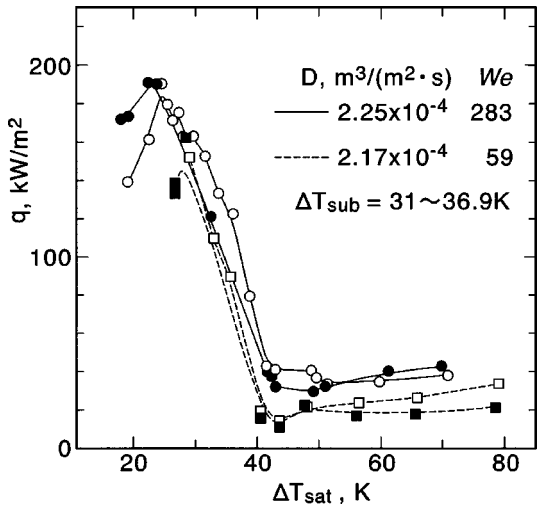

Fig. 14 Spray cooling characteristics for FC-72 with copper block heater in parabolic flight experiments (Solid symbols: 0.01 g_e, Open symbols: 2 g_e)

away in the vicinity of the heater surface irrespective of the level of gravity. Consequently gravity effect is vanishing in the film boiling region.

FC-72

(*a*) ***Steady state experiments and observation from the rear side of the heater***.

Figure 12 compares the heat transfer characteristics for a steady state experiment with the transparent heater under reduced and elevated gravity conditions at the same spray volume flux 2.25×10^{-4} m^3/(m^2·s), which is lower than the critical spray volume flux, $D_{cr}=4\times10^{-4}$ m^3/(m^2·s). The range of the experiments was limited to the nucleate boiling region below the CHF point. Here we hardly recognize any gravity effect on the heat transfer.

Figure 13 shows two rear-side views of the heater surface upon which a heat flux close to the CHF was imposed. Although no appreciable difference in the heat transfer characteristics was detected, the fraction of liquid-film covered area on the heater surface evaluated from the rear side pictures showed slight variations depending on the gravity level, i.e., 53 percent in the reduced gravity, 60 percent in the normal gravity, and 64 percent in the elevated gravity. It seems that droplets having impinged on the heater surface form thin, discrete liquid-films which immediately evaporate, rarely causing mutual interaction and thereby experiencing little gravity effect.

(*b*) ***Transient experiments and the behavior of rebounded droplets in different We conditions***.

Figure 14 compares the results of four different transient cooling experiments performed at nearly the same volume fluxes around 2.2×10^{-4} m^3/(m^2·s). The parameters of interest here are the gravity level and *We*. The heat transfer in the film boiling region suffers a substantial deterioration with the reduction in gravity when *We* is low (less than 80), but does not when *We* is rather high. These results are consistent with those for water exemplified in Fig. 10 ($We=33$) and Fig. 11 ($We=622$), and it is believed that the contribution of rebounded droplets yields such difference.

Concluding Remarks

A series of spray cooling experiments were carried out, using water and FC-72 as the coolants, under a reduced gravity condition. Corresponding ground-based experiments were also performed to examine the effect of the heater surface orientation on the spray cooling characteristics. In either class of the experiments, two different heaters, a transparent glass heater for heater surface observation and a copper block heater for obtaining heat transfer data in a wide range of wall superheat, were employed. The behavior of rebounded droplets in the film boiling region was studied in detail on the ground with the aid of an LDV. Throughout these experiments, special attention was paid to the two spray parameters—the spray volume flux and the droplet Weber number.

In the nucleate boiling region, no particular effect of gravity was observed with either fluid, though the experiments using water on the ground showed that the downward-facing orientation of the heater surface gave an appreciably higher heat flux than the upward-facing orientation did at any given wall superheat on the heater surface. The heat transfer in the nucleate boiling region was found to be well correlated as, $q\propto(\Delta T_{sat})^m$, where $m=1.7-2.0$ for water and $m=0.5$ for FC-72.

The relation between the CHF and the spray volume flux D was found to change at D_{cr}, a critical level of D, which is about 7×10^{-4} m^3/(m^2·s) for water and about 4×10^{-4} m^3/(m^2·s) for FC-72. The difference in the CHF versus D relation between the low D region and the high D region bordered by D_{cr} is considered to be caused by the difference in the liquid/heater contact behavior between these regions, i.e., the droplets impinging upon the heater surface completely vaporize, hardly interacting each other in the low D region, while the droplets integrate into liquid films covering the heater surface in the high D region. In the case of low spray volume flux, heater surface is not covered by such liquid film flow, but liquid films cover heater surface entirely in the case of high spray volume flux. Neither gravity nor heater orientation affected the CHFs in the low D region. In the high D region, on the other hand, the CHFs were found to be under the influence of both gravity and heater orientation; the influence of gravity and heater orientation was maintained in the transition boiling region.

The most significant influence of gravity and heater orientation appeared in the MHF and the heat transfer in the film boiling region in low *We* conditions, $We<80$, in which impinging droplets did not spread out on the heater surface but rebound from the surface. It was found that both in the reduced gravity condition and the terrestrial gravity condition in which the heater surface was facing downward, the heat transfer at such low *We*'s was considerably deteriorated throughout the film boiling region because of the lack of secondary impingement, on the heater surface, of rebounded droplets which could otherwise contribute appreciably to the heat transfer.

In conventional applications, spray cooling systems are quite often operated in the film boiling region. If this is also the case in space applications, operations at high *We* conditions are strongly recommended in view of the results of the present study.

Acknowledgments

The authors would like to express their sincere gratitude to Prof. S. Nishio of University of Tokyo for helpful discussion, and to the staff of the Diamond Air Service and Mr. N. Saito of IHI for their faithful assistance in the course of the parabolic flight campaign. The main part of the present study was financially supported by the Science and Technology Agency, Japan.

Nomenclature

c_p = specific heat of spray liquid (kJ/kg·K)
d = droplet diameter (m)
D = spray volume flux (m^3/(m^2·s))
L = latent heat of evaporation (kJ/kg)
g_e = terrestrial value of gravitational acceleration (9.8 m/s^2)
q = heat flux (kW/m^2)
q_{CHF} = critical heat flux (kW/m^2)
v = droplet velocity (m/s)
ΔT_{sat} = wall superheat (K)
ΔT_{sub} = subcooling of spray liquid (K)

ρ = density of spray liquid (kg/m^3)
σ = surface tension of spray liquid (N/m)
We = Weber number ($=v^2 d\rho/\sigma$)

References

[1] Vought Corp. 1976, *Flash Evaporator Systems Test Final Report*, NASA-CR-151222.
[2] Choi, K. J., and Yao, S. C., 1987, ''Mechanism of Film Boiling Heat Transfer of Normally Impacting Spray,'' Int. J. Heat Mass Transf., **30**, No. 2, pp. 311–318.
[3] Qiao, Y. M., and Chandra, S., 1996, ''Boiling of Droplets on a Hot Surface in Low Gravity,'' Int. J. Heat Mass Transf., **39**, pp. 1379–1393.
[4] Oka, T., Abe, Y., Mori, Y. H., and Nagashima, A., 1995, ''Pool Boiling of *n*-Pentane, CFC-113, and Water Under Reduced Gravity,'' ASME J. Heat Transfer, **117**, pp. 408–417.
[5] Wachters, L. H. J., and Westerling, N. A. J., 1966, ''The Heat Transfer From a Hot Wall to Impinging Water Drops in the Spheroidal State,'' Chem. Eng. Sci., **21**, pp. 1047–1056.
[6] González, J. E., and Black, W. Z., 1997, ''Study of Droplet Sprays Prior to Impact on a Heated Horizontal Surface,'' ASME J. Heat Transfer, **119**, pp. 279–287.
[7] Grissom, W. M., and Wierum, F. A., 1981, ''Liquid Spray Cooling of a Heated Surface,'' Int. J. Heat Mass Transf., **24**, pp. 261–271.
[8] Yang, J., Chow, L. C., and Pais, M. R., 1996, ''Nucleate Boiling Heat Transfer in Spray Cooling,'' ASME J. Heat Transfer, **118**, pp. 668–671.
[9] Deb, S., and Yao, S. C., 1989, ''Analysis on Film Boiling Heat Transfer of Impacting Sprays,'' Int. J. Heat Mass Transf., **32**, No. 11, pp. 2099–2112.
[10] Kato, M., Abe, Y., Mori, Y. H., and Nagashima, A., 1995, ''On the Spray Cooling Characteristics Under Reduced Gravity,'' J. Thermophysics and Heat Transfer, **9**, No. 2, pp. 378–381.
[11] Sone, K., Yoshida, K., Oka, T., Abe, Y., Mori, Y. H., and Nagashima, A., 1996, ''Spray Cooling Characteristics of Water and FC-72 Under Reduced and Elevated Gravity for Space Application,'' *Proc. 31st IECEC*, **2**, pp. 1500–1505.
[12] Ghodbane, M., and Holman, J. P., 1991, ''Experimental Study of Spray Cooling With Freon-113,'' Int. J. Heat Mass Transf., **34**, pp. 1163–1174.
[13] Mudawar, I., and Estes, K. A., 1996, ''Optimizing and Predicting CHF in Spray Cooling of a Square Surface,'' ASME J. Heat Transfer, **118**, pp. 672–679.
[14] Ishigai, S., Nakanishi, S., and Ochi, T., 1980, *Mist Cooling of a Hot Surface* (in Japanese), *Proc. 16th Symposium Heat Transfer Society of Japan*, pp. 316–318.
[15] Nishio, S., and Endo, T., 1979, ''An Experimental Study on Heat Transfer to Impinging Sprayed Jet,'' (in Japanese), Seisan-Kenkyu, Monthly J. of Institute of Industrial Science, Univ. of Tokyo, **31**, No. 10, pp. 697–700.
[16] Berenson, P. J., 1962, ''Experiments on Pool-Boiling Heat Transfer,'' Int. J. Heat Mass Transf., **5**, No. 10, pp. 985–999.
[17] Shoji, M., Wakunaga, T., and Kodama, K., 1984, ''Heat Transfer of Impinging Subcooled Droplets on Superheated Surface,'' (in Japanese), Trans. Jpn. Soc. Mech. Eng., Ser. B, **50**, No. 451, pp. 716–723.
[18] Monde, M., 1979, ''Study of Mist Cooling at Critical Heat Flux,'' (in Japanese), Trans. Jpn. Soc. Mech. Eng., Ser. B, **45**, No. 394, pp. 849–858.

Predicting the Onset of a Low-Frequency, Limit-Cycle Type of Oscillatory Flow Instability in Multitube Condensing Flow Systems

C. J. Kobus
Assistant Professor of Engineering
Mem. ASME
e-mail: cjkobus@oakland.edu

G. L. Wedekind
John F. Dodge Professor of Engineering
Mem. ASME
e-mail: wedekind@oakland.edu

B. L. Bhatt
Professor and Associate Dean of Engineering and Computer Science
Mem. ASME
e-mail: bhatt@oakland.edu

Oakland University
Rochester, MI 48309

A means was developed for extending the predictive capability of the Equivalent Single-Tube Model (ESTM) to accurately predict the onset of a self-sustained oscillatory flow instability for a multitube condensing flow system. The model includes the effects of compressibility, subcooled liquid inertia, and thermal and flow distribution asymmetry. Previously, liquid inertia, a necessary mechanism for the instability, had not been modeled for a multitube system. Extensive experimental data was obtained for a two-tube system that verifies not only the predictive capability of the ESTM, but also its accuracy and its wide range of applicability. [DOI: 10.1115/1.1338132]

Keywords: Condensation, Heat Transfer, Instability, Phase Change, Two-Phase

Introduction

Background. The research presented in this paper is associated with a low-frequency, limit-cycle type of oscillatory condensing flow instability in multitube condensing flow systems. This research is important because large flow oscillations of the condensate in multitube systems could substantially affect the performance, control and safety of these and other associated systems. To the best knowledge of the authors, there do not appear to be any models in the archival literature predicting the conditions under which such an instability might exist for *multitube* systems. The focus of the present research, therefore, is the development and verification of such a model.

Bhatt and Wedekind [1] and Bhatt et al. [2] studied this type of instability for *single-tube* condensing flow systems. Given the complexity of the physical mechanisms involved in *multitube* systems, and the fact that most of them are coupled in some way, a significant step is involved between successfully modeling this instability in a *single-tube* condenser and having the same level of success when the condenser is *multitube*. The task is made even more difficult when thermal and flow distribution asymmetry exists within the tube bundle. In the aforementioned *single-tube* studies, the physical parameters and mechanisms found to be responsible for this particular type of unstable flow behavior included condenser heat flux, liquid inertia, upstream and two-phase vapor compressibility, two-phase pressure drop and downstream flow resistance. When thermal and flow distribution asymmetry exists in *multitube* systems, each of the tubes would have a different condensing length, two-phase pressure drop, two-phase vapor compressibility and a different amount of liquid inertia.

Constructing a rational bridge between the single-tube instability model and a viable multitube model required a sequence of planned research studies. These studies were designed to investigate various modeling techniques for describing each of the above multitube complexities in such a manner that each technique could be validated experimentally. This type of sequential approach is important when attempting to sort out the complex physical mechanisms associated with systems or processes with multiple and coupled phenomena. Also, consistent with the previous work of the authors, the goal of the research was to keep the final model as ''user friendly'' as possible, so that parametric studies could be carried out on typical ''spread-sheet'' software.

The first step in constructing this rational bridge was the theoretical development and experimental verification of an Equivalent Single-Tube Model (ESTM) [18]. This model demonstrated the feasibility of modeling transient flow surges associated with multitube condensing flow systems. The most salient feature of the ESTM is its simplicity—being able to accurately describe multitube condensing phenomena in terms of an *equivalent* single-tube condensing flow system. At that point in time, however, the ESTM was limited to incompressible flow. To further evaluate the model, the predictive capability of the ESTM was extended to predict the frequency-response characteristics [3,4] of multitube condensing flows systems, again under the conditions when compressibility effects are negligible.

Wedekind et al. [5] developed the means to further extend the concept of an ESTM to predict the transient flow surge phenomenon in multitube condensing flow systems, when compressibility effects are significant. This was a necessary step in understanding how to model compressibility effects for a multitube system, since it is one of the dominant energy storage mechanisms responsible for the instability under consideration. The effects of thermal and flow distribution asymmetry were also considered. These effects included the pressure drop and the vapor volume in the two-phase region—both of which may vary from one tube to another, depending on the magnitude of the asymmetry.

Since the focus of the current paper is a limit-cycle type of flow instability, a technique was needed for modeling two additional physical mechanisms for multitude systems—liquid inertia and the influence of compressibility on the effective point of complete condensation. Neither of these two mechanisms were of significance in the earlier multitube studies, but both are necessary for the instability to exist.

The research reported in this paper extends the existing ESTM concept to include the effects of compressibility on the dynamics of the effective point of complete condensation in each tube, and the effects of liquid inertia. Liquid inertia involves an appropriate combination of the inertia due to liquid within each individual

Contributed by the Heat Transfer Division for publication in the JOURNAL OF HEAT TRANSFER. Manuscript received by the Heat Transfer Division September 2, 1999; revision received, June 10, 2000. Associate Editor: P. S. Ayyaswamy.

condenser tube and within and downstream of the exit manifold. The effective point of complete condensation and the amount of liquid inertia may also vary significantly from one tube to another, depending on the magnitude of thermal and flow distribution asymmetry. Such interaction adds considerable complexity to the problem.

Other Relevant Research. Certain condensation-induced instabilities are known to have a dramatic effect during the by-pass phase of the PWR loss of coolant accident [6,7]. They are also associated with countercurrent (reflux) and cocurrent condensation inside the steam generator tubes of the PWR, during a small break (without scram) loss of coolant accident [8]. Steam chugging within the condensation pipes of a pressure suppression system of a BWR [9,10] is also due to condensation-induced instabilities. Also, in a study involving a multitube condenser for space application [11], substantial pressure drop fluctuations were observed in each of the condenser tubes. Some of these fluctuations were as high as 50 percent of the mean value. Therefore, such instabilities are expected to play a significant role in the operation of the overall system. Boyer et al. [12] observed an oscillatory-type of flow instability in condensing steam in a vertical annular passage. Condensing flow instabilities are also important in ocean thermal energy conversion systems and a host of other applications in refrigeration, chemical processing and electronic component cooling [13].

To the best knowledge of the authors, the ESTM represents the only developed model in the archival literature capable of predicting transient phenomena in *multitube* condensing flow systems. The purpose of this paper is to show how the ESTM concept can be *extended* to have the capability of predicting the onset of self-sustained oscillatory flow instabilities in *multitube* systems, and to verify this capability experimentally.

Formulation of Governing Differential Equations

A schematic of a two-tube horizontal condensing flow system is depicted in Fig. 1. The mass flowrate, heat flux, and cross-sectional geometry of each channel is allowed to be different; however, the length of the channels is assumed to be the same. Viscous dissipation, longitudinal heat conduction, and changes in kinetic energy are considered negligible. The spatially-averaged heat flux for each tube is assumed to be time-invariant. Since thermodynamic equilibrium is assumed to exist in the two-phase region, all thermodynamic properties are assumed to be saturated properties, independent of axial position, and evaluated at the mean condensing system pressure, which is, however, allowed to vary with time. The local flow quality and local area void fraction are allowed to vary within the two-phase region with both axial position and time. The region upstream of the two-phase region, in/and upstream of the individual condenser tubes, is assumed to be adiabatic and saturated. Also, the inlet flow quality into each individual tube is assumed to be unity, and complete condensation is assumed to take place in each condenser tube.

In the subsequent analysis, the effect of property variations with pressure changes is considered negligible. In previous research [5], it was important to retain this effect because of the amplification characteristics of condensing flow systems, where very large transient flow surges would be accompanied by significant pressure changes in the upstream vapor volume. However, the purpose of this research is to model the *stability boundary, not* the instability itself. It will be seen later in this paper that, under certain conditions, very large self-sustained oscillations may occur in the outlet liquid flowrate, which are accompanied by significant oscillations in the condensing pressure. At the *stability boundary*, however, these oscillations are not present and the condensing flow system operates in what is normally referred to as steady-state conditions, even though stochastic fluctuations inherent to all

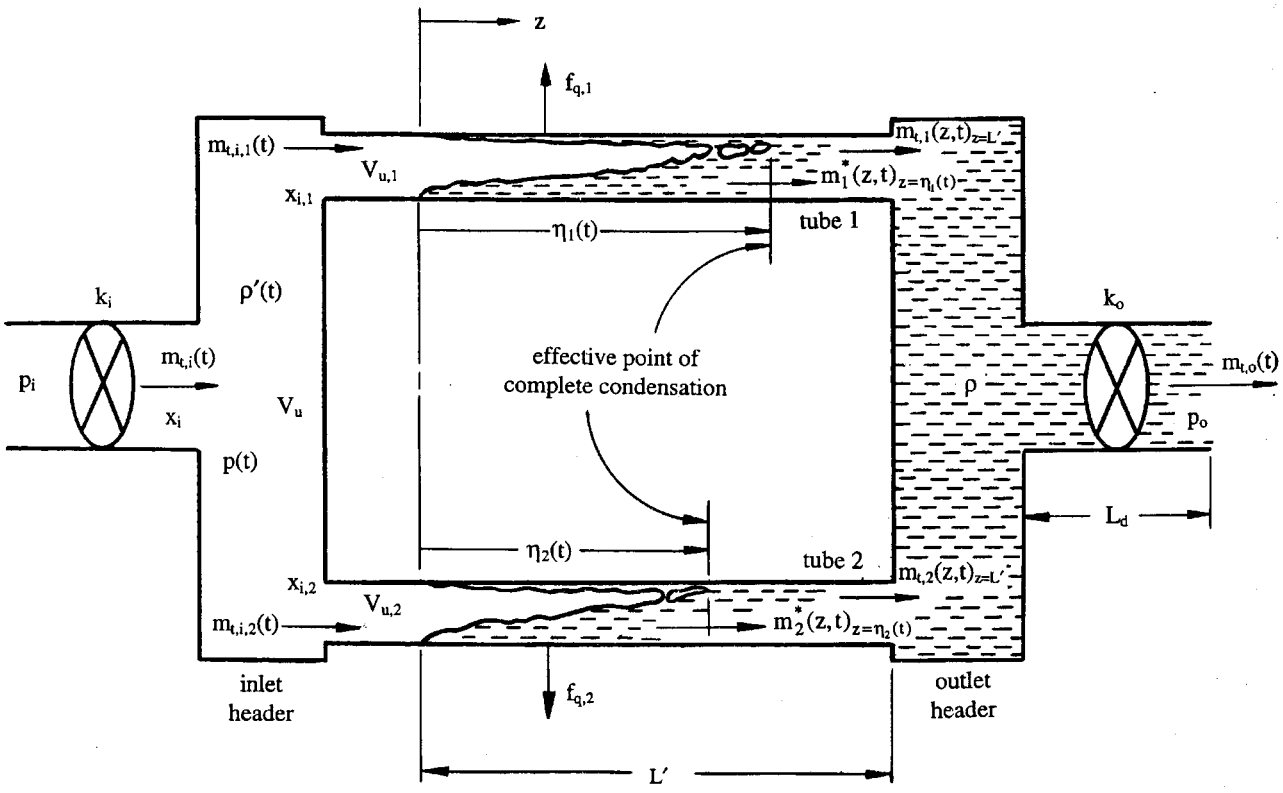

Fig. 1 Schematic of horizontal two-tube condensing flow system

two-phase flow systems are still present. In this situation, the condensing pressure remains virtually constant, and in turn, the thermodynamic property variations would be negligible.

Central in the development of the governing equations is the System Mean Void Fraction (SMVF) Model, which is a one-dimensional, two-fluid, distributed parameter *integral model* describing the primary physical mechanisms within the two-phase region, and[1] which incorporates the concept of a non-fluctuating system mean void fraction, $\overline{\alpha}$.

System Mean Void Fraction Model. The SMVF Model, developed in previous research, is a way of modeling the transient characteristics of the effective point of complete condensation, $\eta(t)$. It is obtained by application of the conservation of mass and energy principles to the two-phase region. The differential equation governing the effective point of complete condensation for a representative j^{th} tube, $\eta_j(t)$, was developed by Wedekind et al. [5] and is expressed as

$$\tau_{c,j}\frac{d\eta_j(t)}{dt}+\eta_j(t)=\frac{(h'-h)}{\overline{f}_{q,j}P_j}\gamma_j m_{t,i}(t)-\frac{(h'-h)}{\overline{f}_{q,j}P_j}\{V_{u,j}+\gamma_j V_u+V_{2\phi,j}\}\frac{d\rho'}{dt}, \tag{1}$$

where the condensing flow system time constant for the j^{th} tube, $\tau_{c,j}$, is expressed as

$$\tau_{c,j}=\frac{\rho'(h'-h)\overline{\alpha}A_{t,j}}{\overline{f}_{q,j}P_j}. \tag{2}$$

It should be pointed out that the last term in Eq. (1) has in prior research been negligible. In this research, however, the effects of compressibility on the motion of the effective point of complete condensation, $\eta_j(t)$, is a critical and necessary coupling mechanism in successfully modeling the stability boundary. The system mean void fraction, $\overline{\alpha}$, is defined in terms of the local area void fraction, $\alpha(z,t)$, and represents the integral form of the mean value theorem; thus,

$$\overline{\alpha}\equiv\frac{1}{\eta(t)}\int_{z=0}^{\eta(t)}\alpha(z,t)dz. \tag{3}$$

It had been determined in previous research [14] that, for most applications, the system mean void fraction is essentially time-invariant. Physically, this requires the redistribution of liquid and vapor within the two-phase region to occur at a rate faster than that of the deterministic flow transient, and is mathematically guaranteed by being able to establish a similarity relationship. This simplification has the effect of uncoupling the conservation of mass and energy principles, *in the two-phase region*, from the *transient* form of the momentum principle; thus, only the *steady-state* form of the momentum principle is required. For this situation, the system mean void fraction, $\overline{\alpha}$, can be obtained by the following model:

$$\overline{\alpha}=\frac{1}{(1-a)}+\frac{a\text{Ln}(a)}{(1-a)^2};\quad a=(\rho'/\rho)^{2/3}. \tag{4}$$

The time invariance of the *system mean* void fraction does *not* preclude transient changes in the *local* area void fraction affecting the deterministic flow transient. Time invariance only applies to the *mean value* of the void fraction from the point where condensation begins, $z=0$, to the effective point of complete condensation, $\eta_j(t)$. The particular void fraction model used here is that proposed by Zivi [15]. It was chosen for its simplicity and proven accuracy for these types of flow problems. Any void fraction-flow quality relationship, however, that is valid over the full range of flow qualities would yield similar results [14].

Vapor Compressibility. The vapor compressibility can be obtained from the transient momentum principle [1,16]; thus,

$$\frac{d\rho'}{dt}=\gamma^* k_o^*\frac{dm_{t,o}(t)}{dt}+\gamma^*\left(\frac{L_o^*}{A_{t,o}}\right)_{\text{eq}}\frac{d^2m_{t,o}(t)}{dt^2}, \tag{5}$$

where

$$k_o^*=k_o'\overline{m}=\frac{2k_o}{\rho A_{t,o}^2}\overline{m};\quad k_o'=\frac{\Delta p_o}{\overline{m}^2} \tag{6}$$

$$\left(\frac{L_o^*}{A_{t,o}}\right)_{\text{eq}}=\left\{\frac{L_d}{A_{t,o}}+\frac{1}{n^2}\sum_{j=1}^{n}\frac{L_j^*}{A_{t,j}}\right\}. \tag{7}$$

$$L_j^*=(L'-\overline{\eta}_j);\quad \overline{\eta}_j=\frac{(h'-h)}{\overline{f}_{q,j}P_j}\overline{m}_j \tag{8}$$

Although Eq. (5) is similar to what was presented by Wedekind et al. [5], the second term on the r.h.s. represents the effect of liquid inertia, which was not considered in the above mentioned research. The effective outlet flow resistance coefficient, k_o^*, includes the flow resistances downstream of the condenser tube bundle and the *equivalent* resistance of the multitube bundle itself, including two-phase pressure drop.[2] The parameter $(L_o^*/A_{t,o})_{eq}$ represents an equivalent liquid inertia length for the condenser tube bundle and is formulated in the following section.

Equivalent Liquid Inertia Length. A more general expression to that in Eq. (7) was first obtained from the inertia term in the momentum principle, and is seen to consist of a downstream portion and an equivalent value for the multitube condenser bundle, which in turn involves the liquid inertia length and resistances in the individual condenser tubes[3]; thus,

$$\left(\frac{L_o}{A_{t,o}}\right)_{\text{eq}}=\left\{\frac{L_d}{A_{t,o}}+\left(\frac{L_j}{A_{t,j}}\right)_{\text{eq}}\right\}, \tag{9}$$

where

$$\left(\frac{L_j}{A_{t,j}}\right)_{\text{eq}}=\sum_{j=1}^{n}\left(\frac{k'_{\text{eq}}}{k'_{t,j}}\right)\frac{[L'-\eta_j(t)]}{A_{t,j}}. \tag{10}$$

Also, the equivalent flow resistance coefficient for the multitube condenser bundle, k'_{eq}, is expressed [5] as

$$k'_{\text{eq}}=\frac{k'_n}{n^2}. \tag{11}$$

It is reasonable to assume that the flow resistance coefficient in a representative j^{th} tube, $k'_{t,j}$, is approximately the same value as that of the entire tube bundle, k'_n, because, with common headers, the pressure drop across any tube and the entire tube bundle is the same. The ratio of flow resistance coefficients seen in Eq. (10), between that of the entire bundle and a single representative j^{th} tube, can therefore be reduced to

$$\left(\frac{k'_{\text{eq}}}{k'_{t,j}}\right)=\frac{1}{n^2}\left(\frac{k'_n}{k'_{t,j}}\right)\approx\frac{1}{n^2}. \tag{12}$$

[1]The System Mean Void Fraction Model is in the same category as that of von Karman's integral model for describing the viscous effects within a viscous boundary layer.

[2]The inclusion of the two-phase pressure drop in the outlet flow resistance is described in detail in footnote 14 in the paper by Wedekind et al. [5].

[3]This analysis is analogous to the way electrical circuits are handled. The flow resistance coefficient would be analogous to the electrical resistance, inertia to electrical inductance, pressure drop to voltage drop and mass flowrate to electrical current. Therefore, a multitube condensing flow system would be analogous to parallel electrical circuits, each consisting of a resistor and an inductor, this parallel system being in series with a resistor and inductor representing the downstream side of the system.

Eq. (10) in turn reduces to

$$\left(\frac{L_j}{A_{t,j}}\right)_{\text{eq}} = \frac{1}{n^2}\sum_{j=1}^{n}\frac{L_j'}{A_{t,j}}, \tag{13}$$

where

$$L_j' = [L' - \eta_j(t)] \approx [L' - \overline{\eta_j}] = L_j^*. \tag{14}$$

The average value of the effective point of complete condensation, $\overline{\eta_j}$, obtained from Eq. (8), is used to compute the linearized inertia length for that tube, L_j^*. Therefore, the linearized equivalent liquid inertia length for the entire multitube system can be expressed as

$$\left(\frac{L_o^*}{A_{t,o}}\right)_{\text{eq}} = \left\{\frac{L_d}{A_{t,o}} + \frac{1}{n^2}\sum_{j=1}^{n}\frac{L_j^*}{A_{t,j}}\right\}. \tag{15}$$

If the number of individual condenser tubes in the multitube bundle, n, is large and/or the length of the subcooled liquid region in each tube, L_j^*, is small, then the equivalent inertia length is essentially just the length of the downstream liquid region; thus,

$$\left(\frac{L_o^*}{A_{t,o}}\right)_{\text{eq}} = \frac{L_d}{A_{t,o}}. \tag{16}$$

This may in fact be true in many industrial applications because, in part, excessive subcooling of the liquid in each of the condenser tubes may lead to certain types of instabilities in the multitube system. Rabas and Minard [17] point out that, due to the possibility of certain instabilities occurring in multitube systems, many condensers are designed to minimize subcooling of the liquid by minimizing the length of the individual condenser tubes.

Outlet Liquid Flowrate. The differential equation governing the transient outlet liquid flowrate, $m_{t,o}(t)$, is similar to what was presented by Wedekind et al. [5], but with an additional term due to the effects of inertia, effects which were not considered in the prior research; thus,

$$\tau_{i,s}\tau_{f,s}\frac{d^2m_{t,o}(t)}{dt^2} + \tau_{f,s}\frac{dm_{t,o}(t)}{dt} + m_{t,o}(t) = \left(\frac{\rho}{\rho'}\right)m_{t,i}(t) - \left[\left(\frac{\rho}{\rho'}\right) - 1\right]\sum_{j=1}^{n}\frac{\overline{f}_{q,j}P_j\eta_j(t)}{(h'-h)}, \tag{17}$$

where the system inertia and compressible flow system time constants, $\tau_{i,s}$ and $\tau_{f,s}$, are respectively expressed as

$$\tau_{i,s} = \frac{1}{k_o^*}\left(\frac{L_o^*}{A_{t,o}}\right)_{\text{eq}} \tag{18}$$

$$\tau_{f,s} = \left(\frac{\rho}{\rho'}\right)\{V_{u,t} + V_{2\phi}\}\gamma^* k_o^* \tag{19}$$

and, where

$$V_{u,t} = V_u + \sum_{j=1}^{n} V_{u,j} \tag{20}$$

$$V_{2\phi} = \sum_{j=1}^{n} V_{2\phi,j} = \sum_{j=1}^{n} A_{t,j}\overline{\alpha\eta_j}. \tag{21}$$

Equation (17), governing the outlet liquid flowrate, $m_{t,o}(t)$, is similar to that presented by Wedekind et al. [5], but with the addition of the first term, related to inertia effects, which results in this differential equation being of second order, rather than first order. This equation is seen to be dependent on the effective point of complete condensation in each tube, $\eta_j(t)$, Eq. (1), which in turn is dependent on the outlet mass flowrate through the mechanism of vapor compressibility, Eq. (5); thus the *two-way coupling*. This set of governing differential equations can be combined to yield n-coupled, second-order differential equations governing the response of the outlet liquid flowrate, $m_{t,o}(t)$, to an inlet vapor flowrate variation, $m_{t,i}(t)$, which, when added together and rearranged result in the following third-order differential equation governing the outlet liquid flowrate, $m_{t,o}(t)$:

$$\left[\tau_{i,s}\sum_{j=1}^{n}\tau_{c,j}\tau_{f,j}\right]\frac{d^3m_{t,o}(t)}{dt^3} + \left[\sum_{j=1}^{n}\tau_{c,t}\tau_{f,j} + \tau_{i,s}(\tau_{f,s} - \tau_{2w,s})\right]\frac{d^2m_{t,o}(t)}{dt^2} + (\tau_{f,s} - \tau_{2w,s})\frac{dm_{t,o}(t)}{dt} + m_{t,o}(t) + \sum_{j=1}^{n}\left\{\tau_{c,j}\frac{dm_{t,j}(z,t)_{z=L'}}{dt}\right\} = m_{t,i}(t) + \left(\frac{\rho}{\rho'}\right)\left[\sum_{j=1}^{n}\gamma_j\tau_{c,j}\right]\frac{dm_{t,i}(t)}{dt}, \tag{22}$$

where

$$\tau_{2w,s} = [(\rho/\rho') - 1][V_{u,t} + V_{2\phi}]\gamma^* k_o^* \tag{23}$$

and where the flow distribution parameter, γ_j, is defined as

$$\gamma_j \equiv \frac{m_{t,i,j}(t)}{m_{t,i,c}(t)}; \quad m_{t,i,c}(t) = \sum_{j=1}^{n} m_{t,i,j}(t). \tag{24}$$

The time constant $\tau_{2w,s}$, defined in Eq. (23), represents a two-way coupling between the outlet liquid flowrate and the effective point of complete condensation, borne from the inclusion of the influence of compressibility on the effective point of complete condensation, Eq. (1). As mentioned earlier, this influence has been negligible in prior multitube research [3–5], but is essential in the prediction of the stability boundary. Stated another way, neglecting this effect, by dropping the last term in Eq. (1), or $\tau_{2w,s}$ in Eq. (22), the forthcoming analysis would predict that the instability in the current research cannot exist under any operating conditions.

Referring to Eq. (24), the flow distribution parameter, γ_j, is physically defined as the fraction of the total mass flowrate entering tube j. A flow distribution parameter $\gamma_j = 1/n$ assures flow distribution symmetry in an n-tube system. Also, the sum of the flow distribution parameters for all of the condenser tubes is unity. This is a consequence of its definition and the conservation of mass principle. The parameter, β_j, is the product of the heat flux ratio between a reference tube (usually designated as tube 1) and any tube in the system, and a geometrical ratio between any tube and the same reference tube [18]. In general, $\beta_j \geqslant 0$, and $\beta_j = 1$ signifies thermal/geometrical symmetry of the multitube system. Although the model does allow for cross-sectional geometrical variations in the individual tubes, they will not be considered here, and β_j will therefore be considered a *thermal asymmetry* parameter; thus,

$$\beta_j = (\overline{f}_{q,1}/\overline{f}_{q,j}). \tag{25}$$

Both the thermal and flow distribution asymmetry parameters, γ and β, respectively, are considered system parameters in the classical sense [5].

Equation (22) cannot, in general, be solved in its present form because there are $(n-1)$ too many unknowns, except for the situation where thermal *symmetry* exists. Thermal symmetry would result in the condensing flow system time constant of each individual condenser tube, $\tau_{c,j}$, being the same. Such a solution, however, would obviously be incapable of providing any insight into the effects of thermal asymmetry. Utilizing the approximation technique embodied in the concept of the Equivalent Single-Tube Model (ESTM), however, Eq. (22) can be simplified considerably.

Equivalent Single-Tube Model (ESTM). The ESTM is an *approximation technique* which has been successfully employed in predicting various transient characteristics associated with multitube two-phase condensing flow systems [5,18]. This approximation technique has the effect of reducing the governing differential equation, Eq. (22), which contains summations, to an *approximation* of Eq. (22) where the summations are eliminated. The resulting equation is of the same *form* as that of a single-tube condensing flow system [1]; thus the term *equivalent* single-tube. The ESTM incorporates an equivalent single-tube condensing flow system time constant, $\tau_{c,s}$, which is a weighted average of the condensing flow system time constants associated with each individual tube, $\tau_{c,j}$; thus,

$$\tau_{c,s}=\sum_{j=1}^{n}\gamma_j\tau_{c,j}=\tau_{c,1}\sum_{j=1}^{n}\gamma_j\beta_j. \tag{26}$$

Utilizing the above approximation, Eq. (22) can be reduced by substituting $\tau_{c,s}$ for every $\tau_{c,j}$ and rearranging; thus,

$$\tau_{i,s}\tau_{c,s}\tau_{f,s}\frac{d^3m_{t,o}(t)}{dt^3}+(\tau_{c,s}\tau_{f,s}+\tau_{i,s}\tau_{f,s}-\tau_{i,s}\tau_{2w,s})\frac{d^2m_{t,o}(t)}{dt^2}+(\tau_{c,s}+\tau_{f,s}-\tau_{2w,s})\frac{dm_{t,o}(t)}{dt}+m_{t,o}(t)=m_{t,i}(t)+(\rho/\rho')\tau_{c,s}\frac{dm_{t,i}(i)}{dt}. \tag{27}$$

Although the above equation is of the same *form* as that for a single-tube [1], the physical meaning of the various terms in the equation is considerably different.

If a flow instability is to occur, oscillations in the inlet vapor flowrate, $m_{t,i}(t)$, must be coupled in some way to the oscillations in the outlet liquid flowrate, $m_{t,o}(t)$. Therefore, the inlet vapor flowrate needs to be modeled. The pressure drop across the outlet flow resistance, obtained from the momentum principle [1], is given by

$$p(t)-p_0=k_o^*m_{t,o}(t)+\left(\frac{L_o^*}{A_{t,o}}\right)_{\text{eq}}\frac{dm_{t,o}(t)}{dt}. \tag{28}$$

Referring to Fig. 1, there is a corresponding pressure drop across an inlet resistance where the vapor flowrate, $m_{t,i}(t)$, enters the system. Neglecting the inertia of the inlet vapor flowrate,

$$p_i-p(t)=k_i^*m_{t,i}(t), \tag{29}$$

where

$$k_i^*=k_i'\overline{m}=\frac{k_i}{\rho_v'A_{t,i}^2}\overline{m};\quad k_i'=\frac{\Delta p_i}{\overline{m}^2}. \tag{30}$$

Adding Eqs. (28) and (29), an expression for the total pressure drop across the entire condensing flow system, (p_i-p_o), is expressed as

$$(p_i-p_o)=k_i^*m_{t,i}(t)+k_o^*m_{t,o}(t)+\left(\frac{L_o^*}{A_{t,o}}\right)_{\text{eq}}\frac{dm_{t,o}(t)}{dt}. \tag{31}$$

Solving Eq. (31) for the inlet vapor flowrate, $m_{t,i}(t)$, and substituting this expression back into Eq. (27), a differential equation may be obtained governing the transient outlet liquid flowrate, $m_{t,o}(t)$; thus,

$$\tau_{i,s}\tau_{c,s}\tau_{f,s}\frac{d^3m_{t,o}(t)}{dt^3}+\left\{\tau_{c,s}\tau_{f,s}+\tau_{i,s}\tau_{f,s}+\left(\frac{\rho}{\rho'}\right)\tau_{c,s}\tau_{i,s}\left(\frac{k_o^*}{k_i^*}\right)-\tau_{i,s}\tau_{2w,s}\right\}\frac{d^2m_{t,o}(t)}{dt^2}+\left\{\tau_{c,s}+\tau_{f,s}+\left(\frac{\rho}{\rho'}\right)\tau_{c,s}\left(\frac{k_o^*}{k_i^*}\right)-\tau_{2w,s}\right\}\frac{dm_{t,o}(t)}{dt}+\left[1+\left(\frac{k_o^*}{k_i^*}\right)\right]m_{t,o}(t)=\frac{(p_i-p_o)}{k_i^*}. \tag{32}$$

Prediction of the Onset of Flow Instability. It should be noted that the parameters appearing in Eq. (32) are *multitube* parameters. Thus, the former single-tube governing equation was incapable of predicting the behavior of a multitube system. The above multitube equation can be non-dimensionalized and, utilizing Routh's stability criterion, an expression can be obtained to *predict* the conditions under which the system would be stable, in terms of several dimensionless numbers, each involving various system parameters [1]; thus,

$$N_c+N_i\geqslant N_o \tag{33}$$

where

$$N_c=\frac{\tau_{c,s}}{(V_{u,t}+V_{2\phi})\gamma^*k_i^*}=\left(\frac{\tau_{c,s}}{\tau_{f,s}}\right)\left(\frac{\rho}{\rho'}\right)\left(\frac{k_o^*}{k_i^*}\right) \tag{34}$$

$$N_i=\frac{k_o^*\tau_{c,s}}{\left(\frac{L_o^*}{A_{t,o}}\right)_{\text{eq}}}=\left(\frac{\tau_{c,s}}{\tau_{i,s}}\right) \tag{35}$$

$$N_o=\left\{\left[\left(\frac{\rho}{\rho'}\right)\left(\frac{k_o^*}{k_i^*}\right)+1\right]^{-1}-\left(\frac{\rho'}{\rho}\right)\right\}. \tag{36}$$

Both N_c and N_i are directly proportional to the condensing flow system time constant, $\tau_{c,s}$. Thus, an examination of Eqs. (33) through (35) indicates that the instability would be most prevalent when $\tau_{c,s}$ is small, corresponding to the case of high heat flux in the individual condenser tubes. Also, the role of subcooled liquid inertia becomes clear by examining Eq. (35). The equivalent inertia length for the multitube system, which would mainly be due to the inertia of the downstream portion of the system, is seen to be in the denominator. Therefore, a long inertia length would tend to destabilize the system. It may well be that the length of the subcooled liquid region downstream of the multitube condenser bundle cannot be controlled. The amount of compressibility, however, usually can be. An examination of Eq. (34) reveals that the dimensionless number N_c is inversely proportional to the vapor volume and downstream flow resistance. Although the upstream vapor volume may be beyond the control of the design engineer, the downstream flow resistance is more readily controlled. Increasing the downstream flow resistance would then have the effect of stabilizing the system, but at the expense of pressure drop.

The natural frequency of oscillation associated with the above set of equations can also be obtained [1]; thus,

$$\omega_n=\left\{\frac{\left[\left(\frac{k_o^*}{k_i^*}\right)+\left(\frac{\rho'}{\rho}\right)\right]}{(V_{u,t}+V_{2\phi})\gamma^*\left(\frac{L_o^*}{A_{t,o}}\right)_{\text{eq}}}\right\}^{1/2}=\left\{\left[\left(\frac{k_o^*}{k_i^*}\right)+\left(\frac{\rho'}{\rho}\right)\right]\frac{(\rho/\rho')}{\tau_{f,s}\tau_{i,s}}\right\}^{1/2}. \tag{37}$$

Again, the *form* of the above predictions for both the stability boundary and corresponding natural frequency *appear* identical to that reported by Bhatt and Wedekind [1]. It should again be

pointed out, however, that the parameters in the above equations are *multitube* parameters, parameters that were *not* considered in the earlier single-tube study. The former single-tube model, therefore, is incapable of predicting the stability characteristics of *multitube* systems.

Experimental Verification

Because of the nature of the ESTM, the equivalent single-tube condensing flow system time constant being a weighted average of the condensing flow system time constants associated with each individual tube, Eq. (26), it seems intuitive that the ESTM approximation would improve with an increasing number of tubes. Thus, a two-tube system with significant thermal asymmetry may very well represent a worst-case situation for the ESTM [5]. Therefore, consistent with previous multitube research, the multitube system utilized in the current experimental phase of the research also consists of two parallel tubes connected to common headers.

Experimental Apparatus and Measurement Techniques. A schematic of the experimental apparatus is shown in Fig. 2. Refrigerant-12 vapor is generated in the high-pressure reservoir (vapor generator) by circulating temperature-regulated hot water in the finned tubes coiled inside the shell of the reservoir. The high-pressure vapor first passes through the flow-control module, essentially consisting of a manually operated throttling valve. Both the flow control module and the orifice flowmeter are heated so as to prevent any condensation from occurring. Downstream of the orifice flowmeter, the refrigerant vapor passes through a superheater (to prevent premature condensation), a variable-area flowmeter, and then splits into two individual feeder tubes. It then passes through a turbine flowmeter in each feeder tube and finally through an additional heat exchanger (pre-condenser), which is used to adjust the inlet flow quality, x_i, for each condenser. Sight-glass sections at the outlet of the pre-condenser are used to visually confirm the existence or non-existence of liquid prior to entering the condenser test sections.

The test sections are horizontal, copper, concentric-tube condensers approximately 5 meters long, where the inner tubes are single, uninterrupted tubes with inner and outer diameters of 8.0 mm (0.315 in) and 9.5 mm (0.375 in), respectively. Chilled water is circulated through the annulus and is counterflow to the incoming refrigerant-12 vapor. The outer tube has an inner diameter of 17.3 mm (0.68 in). The temperature of the chilled water is controlled for each tube as is the flowrate, which is measured by variable-area flowmeters. A series of thermocouples are positioned at equal spacing intervals axially along each test section and are used to experimentally locate the position of the effective point of complete condensation. This experimentally measured effective point of complete condensation, $\eta(t)$, agreed to within 10 percent of that predicted by the empirical model of Bhatt and Wedekind [19], which was used to predict the spatially average condensing heat flux, $\overline{f_q}$.

Downstream of the test sections, the liquid refrigerant leaving the condenser tubes combines at the outlet manifold, after which this combined flow passes through a precalibrated variable-orifice flowmeter, which also doubles as the major variable flow resistance controller, into the low-pressure reservoir, maintained at a constant pressure by circulating temperature-regulated cold water in the finned-tubes coiled inside the shell of the reservoir. Liquid refrigerant is pumped back to the high-pressure reservoir through a small, variable-speed, positive-displacement gear pump. In this way, the condensing flow experimentation is continuous.

Prior to each test, static calibration of the pressure transducers is carried out with refrigerant-12 vapor at a pressure below the saturation level to ensure that no condensation takes place during calibration. The transducers are carefully calibrated against a very accurate digital pressure transducer. A four-channel continuous chart recorder documents the voltage output signal traces as a function of time for the differential pressure transducer associated with the inlet orifice vapor flowmeter, the output signal for both inlet vapor turbine flowmeters, and the differential pressure transducer located across the variable-orifice liquid flowmeter at the system outlet.

Measurement Uncertainties. Uncertainties in differential pressure measurements were less than ± 0.138 kPa (± 0.02 psi) because, prior to every test, all pressure transducers were calibrated against the above mentioned digital pressure transducer

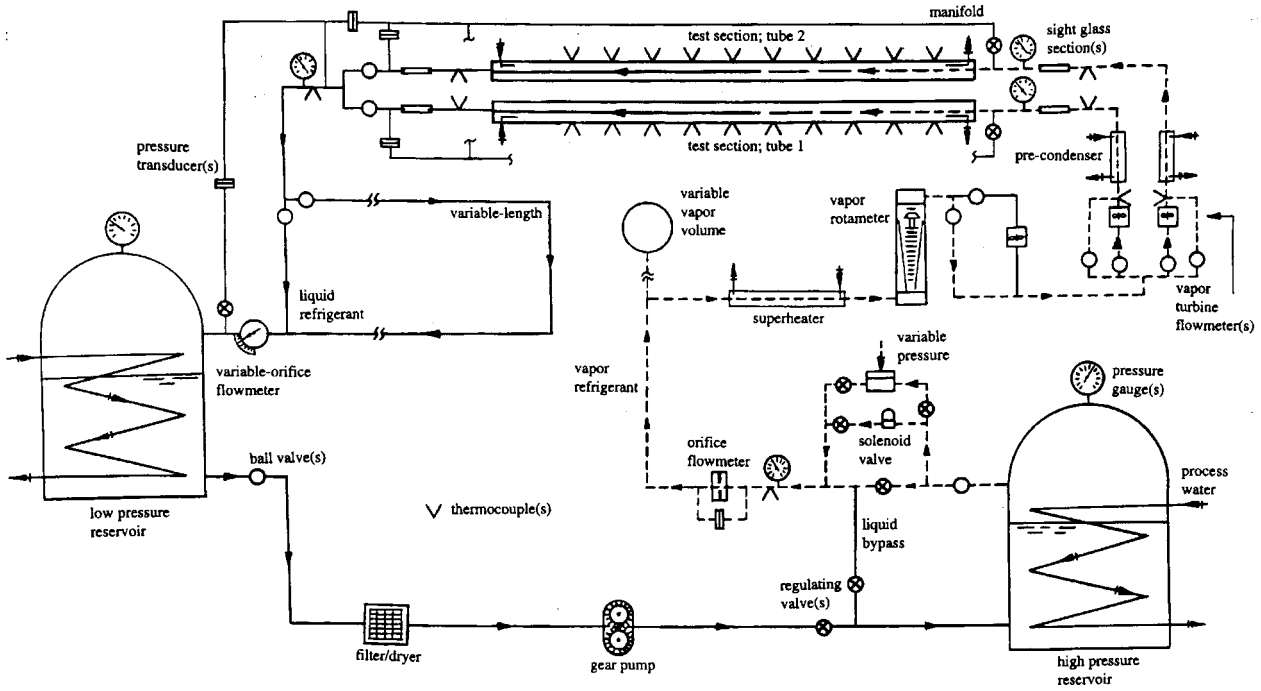

Fig. 2 Schematic of experimental apparatus; two-tube condensing flow system

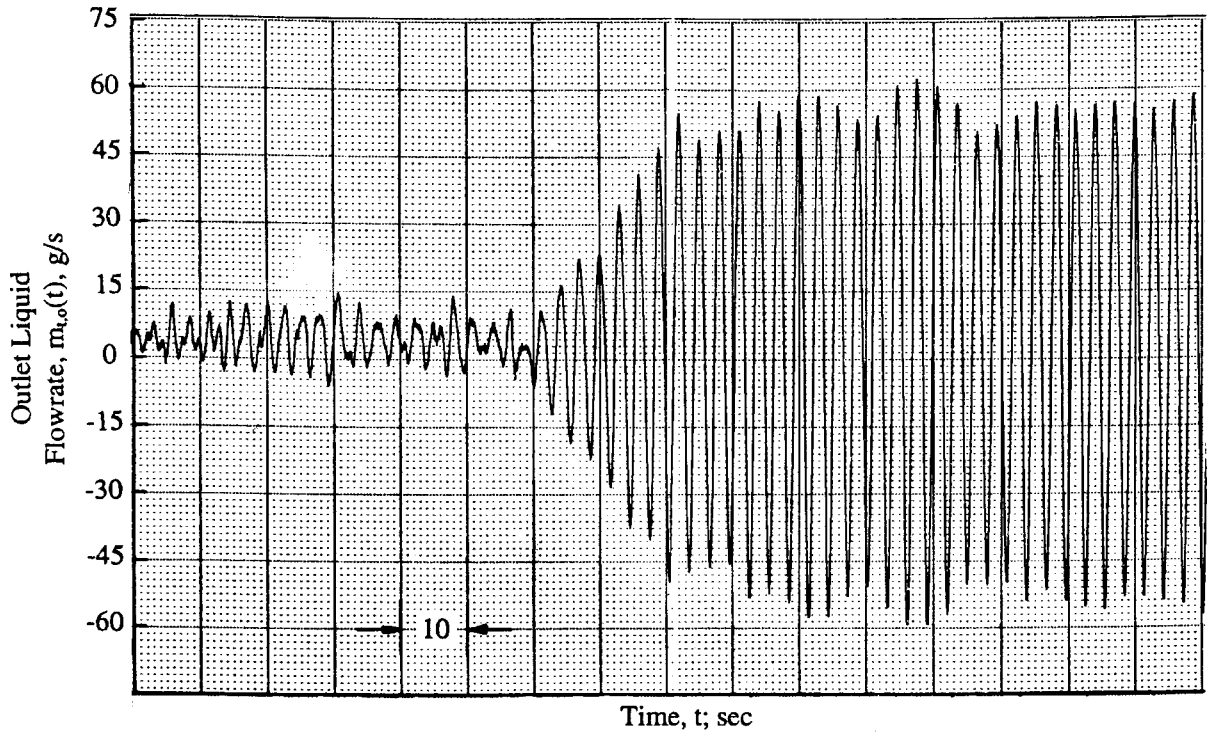

Fig. 3 Experimentally measured transient outlet liquid flowrate demonstrating the growth of a self-sustained limit-cycle type oscillatory flow instability in a two-tube condensing flow system

(Mensor model 14000 digital pressure gauge), whose accuracy was better than ±0.069 kPa (±0.01 psi). Uncertainties in absolute pressure measurements were ±1.38 Pa (±0.2 psig). Temperature measurement uncertainties were ±0.42°C (±0.75°F). The standards that were used for flow measurement calibration were liquid and vapor turbine type flowmeters, which had an accuracy of ±2 percent of flow.

Special measurements were carried out to calibrate the orifice vapor flowmeter at the system inlet, and the variable-orifice liquid flowmeter at the system outlet. The calibration curve for the inlet

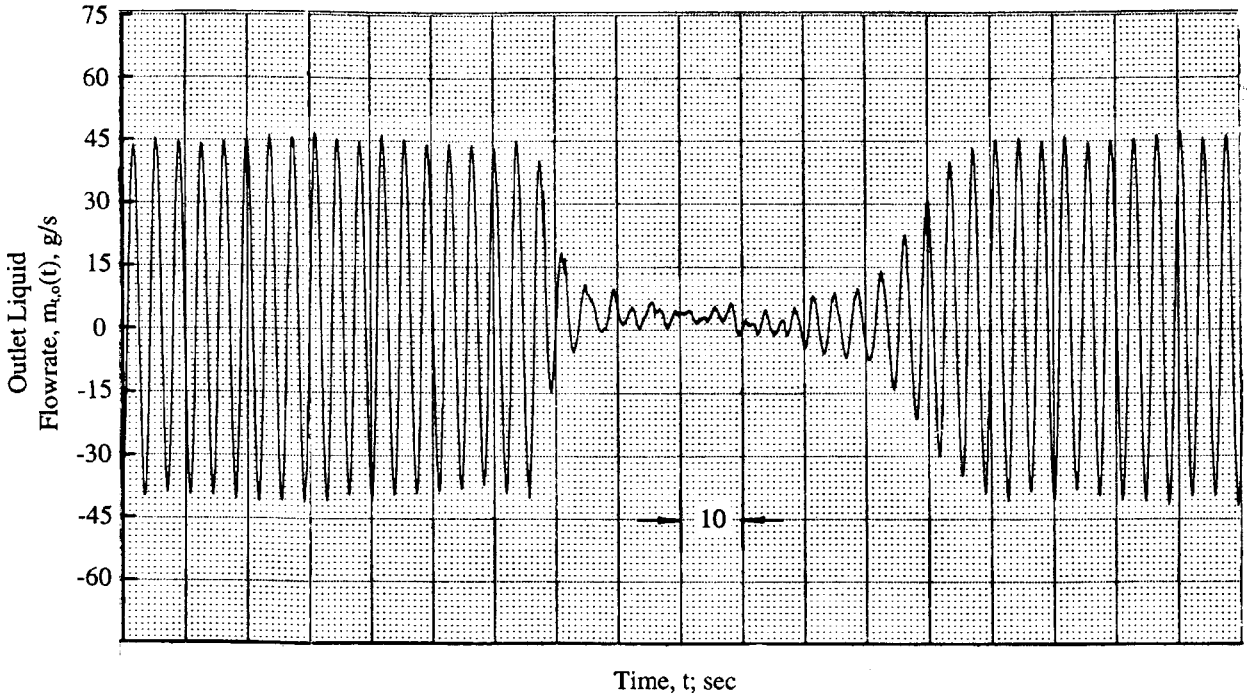

Fig. 4 Experimentally measured transient outlet liquid flowrate demonstrating the decay and growth of a self-sustained limit-cycle oscillatory flow instability in a two-tube condensing flow system

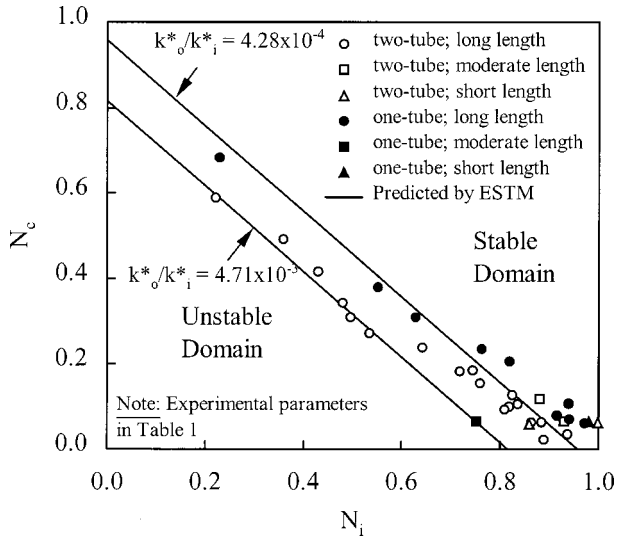

Fig. 5 Comparison of experimentally measured stability boundary of a self-sustained limit-cycle type oscillatory flow instability and boundary predicted by the ESTM

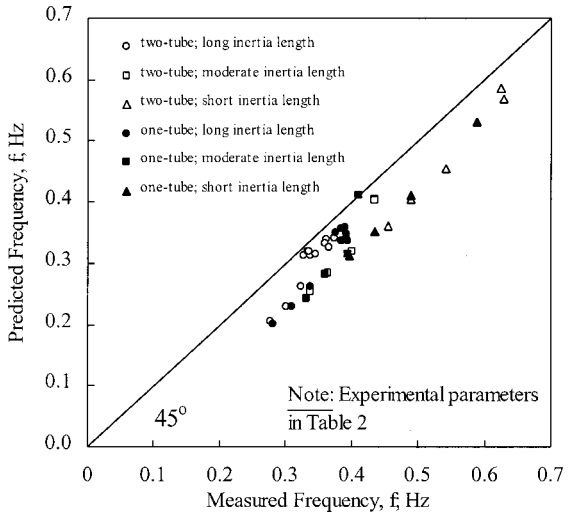

Fig. 6 Comparison between experimentally measured frequency of oscillation of the self-sustained limit-cycle type flow instability and that predicted by the ESTM

orifice vapor flowmeter was accurate to within ±5 percent of the flowrate, whereas the outlet variable-orifice liquid flowmeter had a slightly higher uncertainty of ±7–8 percent. However, steady-state tests showed that the inlet orifice vapor flowmeter measured the flowrate to within 3 percent of that measured by the combined vapor turbine flowmeters in the two feeder tubes for a wide range of flowrates and flow distribution asymmetries. In fact, the vapor turbine flowmeter traces were recorded continuously during every test run along with the orifice flowmeter, in part to continuously monitor the flow distribution, and in part as a redundant flow measurement device for the orifice vapor flowmeter. For steady-state tests, the outlet variable-orifice liquid flowmeter agreed with the inlet orifice vapor flowmeter to within ±7 percent, again affirming the quality of the flow calibration process.

The major uncertainty associated with the flow instability, however, is not due to the aforementioned measurement uncertainty, but rather is in the experimental determination of the stability boundary. The criterion for determining this boundary involved the observation of a degree of the inherent randomness in the outlet liquid flowrate, $m_{t,o}(t)$. Although some subjectivity in this determination is unavoidable, great care was taken to apply the criterion consistently throughout the experimentation. In many cases, although the outlet liquid flowrate appeared mostly random,

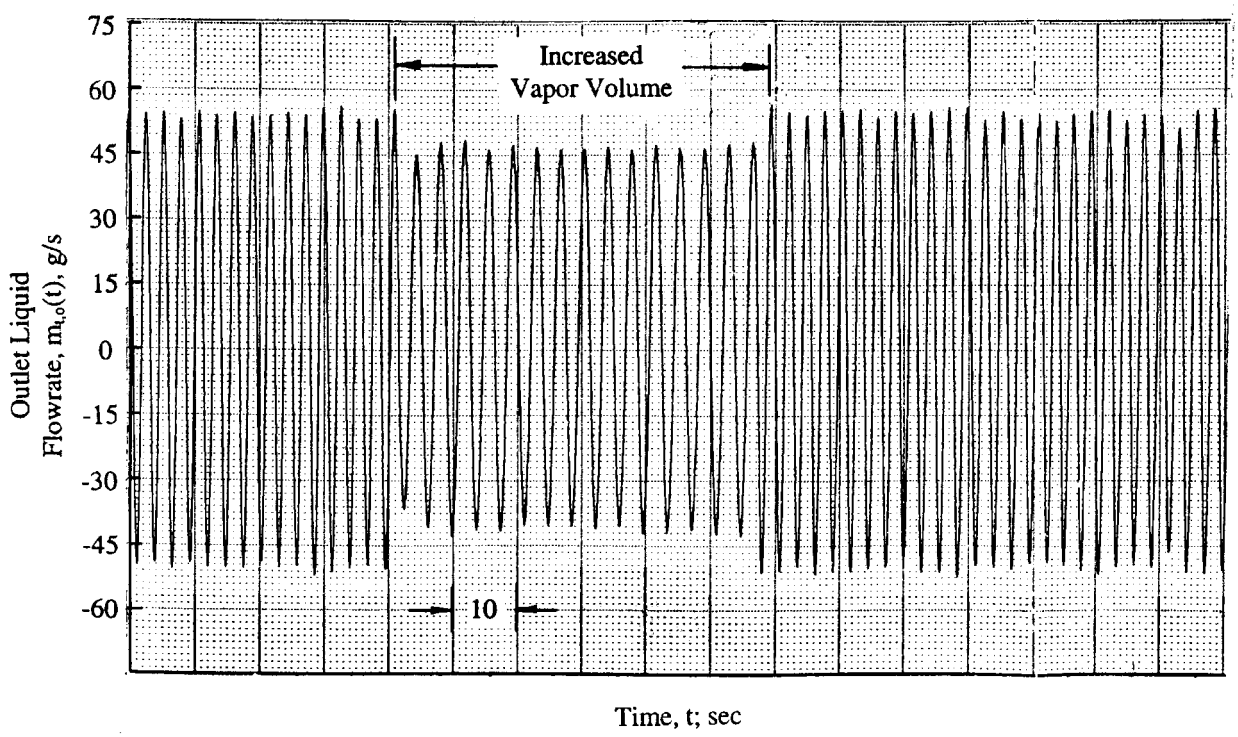

Fig. 7 Experimentally measured instability in a two-tube condensing flow system demonstrating the influence of vapor volume on frequency of oscillation

Table 1 Physical properties and parameters for stability boundary

data point designation	pressure p [kN/m²]	density ratio ρ/ρ'	SMVF [ ]	heat flux $f_{q,1}$ [kW/m²]	mass flowrate [g/s]	thermal asym β_2	flow asym γ_1	$\tau_{c,1}$ [s]	V_u [cm³]	$V_{2\phi,1}$ [cm³]	$V_{2\phi,2}$ [cm³]	k_o^* [N-s /cm⁴kg]	(k_o^*/k_i^*) x10³ [ ]	$\tau_{c,s}$ [s]	$\tau_{f,s}$ [s]	L_{sd} [m]	$(L^*_o/A_{t,o})$ equiv. [1/cm]	$\tau_{t,s}$ [s]	N_c [ ]	N_i [ ]	N_o [ ]
2u-818-3	639.83	35.87	0.835	17.02	4.61	1.00	0.50	0.497	314.73	31.26	31.26	9.408	4.28	0.497	0.129	0.84	546	0.003	0.059	0.859	0.957
2u-818-5	637.28	36.04	0.835	16.78	7.11	1.00	0.50	0.503	314.73	49.05	49.05	27.309	21.85	0.503	0.395	6.73	1676	0.003	0.100	0.819	0.899
2u-911-1	608.39	37.89	0.839	15.89	4.38	1.00	0.50	0.513	314.73	32.21	32.21	28.953	13.62	0.513	0.419	6.73	1716	0.003	0.063	0.864	0.925
2u-911-2	609.77	37.80	0.839	15.95	4.46	1.00	0.50	0.512	314.73	32.05	32.05	20.185	9.83	0.512	0.292	3.70	1112	0.002	0.065	0.930	0.938
2u-911-3	600.12	38.46	0.840	15.52	4.38	1.00	0.50	0.519	314.73	33.06	33.06	10.412	4.85	0.519	0.153	0.84	542	0.002	0.063	0.998	0.957
2u-911-7	607.01	37.99	0.839	15.83	4.38	1.00	0.50	0.514	314.73	32.37	32.37	16.532	38.17	0.514	0.241	6.73	1716	0.004	0.309	0.496	0.847
2u-911-8	600.12	38.46	0.840	15.54	3.93	1.00	0.50	0.519	314.73	29.59	29.59	7.398	37.01	0.519	0.107	6.73	1722	0.010	0.589	0.221	0.849
2u-911-9	582.19	39.74	0.842	14.86	4.38	1.00	0.50	0.530	314.73	34.82	34.82	15.527	38.46	0.530	0.237	6.73	1710	0.005	0.342	0.481	0.842
2u-916-1	580.81	39.84	0.842	14.80	4.31	1.00	0.50	0.531	314.73	34.92	34.99	17.171	33.86	0.531	0.264	6.73	1710	0.004	0.272	0.535	0.856
2u-916-2	580.81	39.84	0.842	14.85	4.16	1.00	0.50	0.529	314.73	32.99	32.99	13.974	41.75	0.529	0.212	6.73	1714	0.005	0.415	0.430	0.832
2u-916-3	580.81	39.84	0.841	14.94	4.99	1.00	0.50	0.526	314.73	39.62	39.62	11.600	42.14	0.526	0.180	6.73	1699	0.006	0.491	0.359	0.831
2u-916-4	596.67	38.70	0.840	15.80	4.38	1.00	0.50	0.508	314.73	32.54	32.54	21.738	38.95	0.508	0.321	6.73	1716	0.003	0.238	0.643	0.843
2u-916-5	591.84	39.04	0.841	15.56	4.84	1.00	0.50	0.513	314.73	36.64	36.64	23.930	33.13	0.513	0.362	6.73	1706	0.003	0.183	0.720	0.860
2u-916-6	587.71	39.34	0.841	15.30	4.31	1.00	0.50	0.518	314.73	33.19	33.19	18.815	16.37	0.518	0.284	3.70	1110	0.003	0.118	0.881	0.914
2u-918-1	573.92	40.36	0.843	6.88	3.55	0.44	0.35	1.133	314.73	42.18	34.99	20.916	7.28	0.720	0.328	6.73	1701	0.004	0.064	0.885	0.946
2u-918-2	580.81	39.84	0.842	7.19	5.97	0.46	0.34	1.090	314.73	67.03	59.02	19.546	12.20	0.703	0.325	6.73	1644	0.004	0.105	0.837	0.929
2u-918-3	580.81	39.84	0.842	7.46	3.55	0.47	0.35	1.053	314.73	38.75	18.15	20.368	10.41	0.687	0.306	6.73	1725	0.004	0.093	0.810	0.935
2u-918-4	580.81	39.84	0.842	7.36	5.75	0.47	0.34	1.068	314.73	63.11	56.24	18.084	16.69	0.694	0.297	6.73	1652	0.004	0.155	0.760	0.913
2u-918-5	578.74	40.00	0.842	7.46	3.33	0.47	0.35	1.051	314.73	36.62	32.70	20.550	14.56	0.687	0.316	6.73	1711	0.004	0.127	0.826	0.920
2u-918-6	580.81	39.84	0.842	7.39	5.22	0.46	0.34	1.064	314.73	83.71	38.91	17.810	19.92	0.688	0.294	6.73	1648	0.004	0.185	0.745	0.901
2u-923-2	573.99	40.35	0.843	14.54	3.93	1.00	0.50	0.536	625.38	31.88	31.88	30.049	11.10	0.536	0.674	6.73	1717	0.002	0.036	0.937	0.932
2u-923-3	564.33	41.10	0.844	14.16	3.78	1.00	0.50	0.543	1197.62	31.88	31.88	28.131	9.94	0.543	1.015	6.73	1717	0.003	0.022	0.889	0.936
1u-911-4	608.39	37.89	0.839	15.93	3.48	n/a	n/a	0.511	486.08	51.17	n/a	38.087	13.26	0.511	0.419	6.73	2003	0.002	0.061	0.972	0.926
1u-911-5	607.01	37.99	0.839	15.87	3.48	n/a	n/a	0.512	486.08	51.67	n/a	20.459	7.52	0.512	0.226	3.70	1396	0.003	0.065	0.752	0.946
1u-911-6	607.01	37.99	0.839	15.87	3.48	n/a	n/a	0.512	486.08	51.67	n/a	15.801	5.82	0.512	0.175	0.84	829	0.002	0.065	0.980	0.952
1u-925-1	568.13	40.80	0.843	15.00	3.33	n/a	n/a	0.516	486.08	52.97	n/a	36.443	14.50	0.516	0.433	6.73	1995	0.002	0.070	0.941	0.920
1u-925-2	568.13	40.80	0.843	15.01	3.18	n/a	n/a	0.515	486.08	50.52	n/a	35.712	15.93	0.515	0.422	6.73	2007	0.002	0.079	0.916	0.914
1u-925-3	568.13	40.80	0.843	15.07	2.65	n/a	n/a	0.513	486.08	41.53	n/a	37.447	22.44	0.513	0.436	6.73	2049	0.002	0.108	0.939	0.892
1u-925-4	568.13	40.80	0.843	14.97	3.55	n/a	n/a	0.516	486.08	56.24	n/a	31.419	36.81	0.516	0.376	6.73	1980	0.003	0.206	0.820	0.845
1u-925-5	568.13	40.80	0.843	14.99	3.40	n/a	n/a	0.516	486.08	53.74	n/a	29.501	39.26	0.516	0.351	6.73	1992	0.003	0.235	0.764	0.837
1u-925-6	575.02	40.80	0.843	15.33	3.25	n/a	n/a	0.509	486.08	50.68	n/a	24.843	43.78	0.509	0.290	6.73	2006	0.003	0.309	0.630	0.826
1u-925-7	575.02	40.80	0.843	15.33	3.25	n/a	n/a	0.509	486.08	50.68	n/a	21.829	47.13	0.509	0.255	6.73	2006	0.004	0.379	0.553	0.816
1u-925-8	575.02	40.80	0.843	15.40	2.65	n/a	n/a	0.507	486.08	40.55	n/a	9.316	35.60	0.507	0.106	6.73	2054	0.010	0.683	0.229	0.850

Two-tube system

$V_{u,1}$ [cm³]	$V_{u,2}$ [cm³]
148.46	148.46

Both systems

x_i [ ]	d [cm]
1	0.80

intermittent growth and decay of the flow oscillation was observed.[4] Therefore, the criterion for determining whether or not the system was stable was that the outlet liquid flowrate consisted of mostly random fluctuations and furthermore showed no potential for even intermittent flow oscillation growth. Thus, the maximum uncertainty associated with experimentally determining the stability boundary is approximately 15 percent.

Experimental Verification of Stability Criterion. The experimental procedure that was followed for experimentally verifying the stability criterion, predicted by the ESTM, consisted of initially establishing obtainable operating conditions that represent a suitable point well within the *unstable* domain. An instability in the outlet liquid flowrate was indicated by an initial growth in the amplitude of the inherent stochastic flow fluctuations, which would subsequently become fully-developed oscillations of fixed amplitude. The final stage is a self-sustained, limit-cycle type of flow instability. Figure 3 depicts a typical strip-chart trace of the outlet liquid flowrate, $m_{t,o}(t)$, and shows the inherent stochastic fluctuations, the growth and eventual limit-cycle type of behavior.

A subsequent means of stabilizing the system was achieved by varying one or more system parameters seen in Eqs. (34) through (36), such as the heat flux, the mean system flowrate, or the outlet flow resistance. Although several other parameters could be changed to stabilize or destabilize the system, changing the outlet flow resistance or the total mean flowrate were the most convenient in most instances. System *stability* is indicated by a decay in the amplitude of the oscillations in the flowrate and the reappearance of the inherent stochastic fluctuations. Figure 4 depicts the stabilization of the flowrate from an initial unstable behavior. In this condition, measurements were taken and used to determine the parameters, and in turn the dimensionless numbers N_i, N_o, and N_c, which locate the position of the data point on the stability plot. The transient decay of the oscillations and the reappearance of the inherent fluctuations was faster than that of the growth cycle, which was depicted in Fig. 3. The amplitude of the oscillations in Figs. 3 and 4 is very large, as much as 12 times the mean flowrate. As can be seen, significant flow reversals exist. The system could be *de*stabilized, as seen in Fig. 4, by adjusting the one or more system parameters, initially changed to stabilize the system, back to their original values.

In Figs. 3 and 4, the magnitude of the inherent stochastic fluctuations appears to be large. The variable orifice flowmeter that measures the transient outlet liquid flowrate, $m_{t,o}(t)$, is also used as the major control mechanism of flow resistance. In the above figures, to initiate a flow instability, or to terminate an existing instability, the outlet flow resistance had to be decreased, or increased, respectively. By changing the flow resistance, however, the value of the calibration constant for the variable orifice flowmeter also changes. Therefore, in Figs. 3 and 4, what is referred to as the stable condition, where the inherent stochastic fluctuations are present, the actual flowrates are somewhat less in magnitude than the scale depicts.

The experimental data indicating the onset of unstable flow are shown by the data points in Fig. 5. The data include many different flow conditions and configurations, such as two-tube data with varying degrees of thermal and flow distribution asymmetry; both configurations being run with different vapor volumes and inertia lengths. Superimposed on this graph is the stability criterion, predicted by the ESTM, Eq. (33), which is shown by the solid straight lines that represent the boundary between the stable and

[4]It is noteworthy to point out that the intermittent flow oscillations observed, when the system was near the stability boundary, is conceptually similar to turbulent flow in a tube, as the Reynold's number is decreased towards the critical value for transition to laminar flow. In the transition region between laminar and turbulent flow, but closer to the laminar boundary, the laminar flow is still unstable and generates intermittent ''bursts'' of turbulent fluctuations [20].

Table 2 Physical properties and parameters for frequency of oscillation

data point designation	pressure p [kN/m^2]	density ratio ρ/ρ'	SMVF [ ]	heat flux $f_{q,1}$ [kW/m^2]	mass flowrate [g/s]	thermal asym β_2	flow asym γ_1	$\tau_{c,1}$ [s]	V_u [cm^3]	$V_{2\phi,1}$ [cm^3]	$V_{2\phi,2}$ [cm^3]	k_o^* [N-s /cm^{2}kg]	(k_o^*/k_i^*) x10^{-4} [ ]	$\tau_{c,s}$ [s]	$\tau_{r,s}$ [s]	L_d [m]	$(L^*_o/A_{t,o})$ equiv. [1/cm]	$\tau_{i,s}$ [s]	f [Hz]
2f-818-3	639.83	35.87	0.835	17.02	4.61	1.00	0.50	0.497	314.73	31.26	31.26	9.408	4.28	0.497	0.129	0.844	546	0.003	0.586
2f-818-5	637.28	36.04	0.835	16.78	7.11	1.00	0.50	0.503	314.73	49.05	49.05	27.309	21.85	0.503	0.395	6.730	1676	0.003	0.336
2f-911-1	608.39	37.89	0.839	15.89	4.38	1.00	0.50	0.513	314.73	32.21	32.21	28.953	13.62	0.513	0.419	6.730	1716	0.003	0.327
2f-911-2	609.77	37.80	0.839	15.95	4.46	1.00	0.50	0.512	314.73	32.05	32.05	20.185	9.83	0.512	0.292	3.696	1112	0.002	0.404
2f-911-3	600.12	38.46	0.840	15.52	4.38	1.00	0.50	0.519	314.73	33.06	33.06	10.412	4.85	0.519	0.153	0.844	542	0.002	0.568
2f-911-7	607.01	37.99	0.839	15.83	4.38	1.00	0.50	0.514	314.73	32.37	32.37	16.532	38.17	0.514	0.241	6.730	1716	0.004	0.341
2f-916-1	580.81	39.84	0.842	14.80	4.31	1.00	0.50	0.531	314.73	34.92	34.99	21.738	38.95	0.531	0.321	6.730	1710	0.003	0.339
2f-916-5	591.84	39.04	0.841	15.56	4.84	1.00	0.50	0.513	314.73	36.64	36.64	23.930	33.13	0.513	0.362	6.730	1706	0.003	0.333
2f-916-6	587.71	39.34	0.841	15.30	4.31	1.00	0.50	0.518	314.73	33.19	33.19	18.815	16.37	0.518	0.284	3.696	1110	0.003	0.402
2f-918-1	573.92	40.36	0.843	6.88	3.55	0.44	0.35	1.133	314.73	42.18	34.99	20.916	7.28	0.720	0.328	6.730	1701	0.004	0.313
2f-918-2	580.81	39.84	0.842	7.19	5.97	0.46	0.34	1.090	314.73	67.03	59.02	19.546	12.20	0.703	0.325	6.730	1644	0.004	0.312
2f-918-3	580.81	39.84	0.842	7.46	3.55	0.47	0.35	1.053	314.73	38.75	18.15	20.368	10.41	0.687	0.306	6.730	1725	0.004	0.319
2f-918-4	580.81	39.84	0.842	7.36	5.75	0.47	0.34	1.068	314.73	63.11	56.24	18.084	16.70	0.694	0.297	6.730	1652	0.004	0.315
2f-918-5	578.74	40.00	0.842	7.46	3.33	0.47	0.35	1.051	314.73	36.62	32.70	20.550	14.56	0.687	0.316	6.730	1711	0.004	0.319
2f-923-1	578.74	40.00	0.842	7.46	3.33	0.47	0.35	1.051	314.73	36.62	32.70	7.946	3.05	0.687	0.228	6.730	1711	0.009	0.229
2f-923-2	573.99	40.35	0.843	14.54	3.93	1.00	0.50	0.536	625.38	31.88	31.88	30.049	11.10	0.536	0.674	6.730	1717	0.002	0.262
2f-923-3	564.33	41.10	0.844	14.16	3.78	1.00	0.50	0.543	1197.62	31.88	31.88	28.131	9.94	0.543	1.015	6.730	1717	0.003	0.206
2f-923-4	564.33	41.10	0.844	14.15	3.86	1.00	0.50	0.543	1197.62	32.05	32.05	7.855	2.93	0.543	0.283	3.696	1113	0.006	0.253
2f-923-5	571.23	40.56	0.843	14.59	3.70	1.00	0.50	0.532	625.38	30.25	30.25	7.307	2.72	0.532	0.164	3.696	1117	0.007	0.319
2f-923-6	571.23	40.56	0.843	14.59	3.86	1.00	0.50	0.532	886.97	31.06	31.06	7.581	2.85	0.532	0.217	3.696	1115	0.006	0.284
2f-923-7	570.47	40.62	0.843	14.50	3.86	1.00	0.50	0.535	886.97	31.23	31.23	4.567	1.78	0.535	0.131	0.844	547	0.005	0.404
2f-923-8	571.23	40.56	0.843	14.54	3.86	1.00	0.50	0.534	625.38	31.23	31.23	8.494	3.22	0.534	0.192	0.844	547	0.003	0.456
2f-923-9	567.78	40.83	0.843	14.42	3.86	1.00	0.50	0.536	1197.62	31.56	31.56	4.749	1.76	0.536	0.170	0.844	547	0.005	0.361
1f-911-4	608.39	37.89	0.839	15.93	3.48	n/a	n/a	0.511	486.08	51.17	n/a	38.087	13.26	0.511	0.419	6.730	2003	0.002	0.347
1f-911-5	607.01	37.99	0.839	15.87	3.48	n/a	n/a	0.512	486.08	51.67	n/a	20.459	7.52	0.512	0.23	3.696	1396	0.003	0.411
1f-911-6	607.01	37.99	0.839	15.87	3.48	n/a	n/a	0.512	486.08	51.67	n/a	15.801	5.82	0.512	0.18	0.844	829	0.002	0.532
1f-923-10	574.68	40.30	0.843	14.38	3.25	n/a	n/a	0.542	1346.08	53.63	n/a	14.614	4.60	0.542	0.467	6.730	1992	0.006	0.202
1f-923-11	582.95	39.69	0.842	15.01	3.25	n/a	n/a	0.525	1035.43	51.34	n/a	13.792	4.35	0.525	0.337	6.730	2003	0.006	0.230
1f-923-12	578.81	39.99	0.842	14.80	3.33	n/a	n/a	0.530	773.83	52.81	n/a	14.431	4.58	0.530	0.270	6.730	1996	0.006	0.263
1f-923-13	580.19	39.89	0.842	14.65	3.25	n/a	n/a	0.536	773.83	52.65	n/a	14.248	4.49	0.536	0.265	3.696	1393	0.004	0.315
1f-923-14	608.39	37.89	0.839	15.93	3.48	n/a	n/a	0.511	1035.43	51.17	n/a	14.066	4.90	0.511	0.327	3.696	1399	0.004	0.282
1f-923-15	567.78	40.83	0.843	14.27	3.25	n/a	n/a	0.541	1346.08	54.28	n/a	25.209	7.96	0.541	0.814	3.696	1385	0.002	0.242
1f-923-16	564.33	41.10	0.844	14.14	3.33	n/a	n/a	0.544	773.83	55.43	n/a	12.970	4.04	0.544	0.248	0.844	812	0.003	0.411
1f-923-17	564.33	41.10	0.844	14.15	3.25	n/a	n/a	0.544	1035.43	54.61	n/a	12.513	3.93	0.544	0.316	0.844	817	0.003	0.353
1f-923-18	571.23	40.56	0.843	14.49	3.25	n/a	n/a	0.536	1346.08	53.14	n/a	11.965	3.78	0.536	0.383	0.844	823	0.003	0.312
1f-925-1	568.13	40.80	0.843	15.00	3.33	n/a	n/a	0.516	486.08	52.97	n/a	36.443	14.50	0.516	0.43	6.730	1995	0.002	0.336
1f-925-2	568.13	40.80	0.843	15.01	3.18	n/a	n/a	0.515	486.08	50.52	n/a	35.712	15.93	0.515	0.42	6.730	2007	0.002	0.337
1f-925-3	568.13	40.80	0.843	15.07	2.65	n/a	n/a	0.513	486.08	41.53	n/a	37.447	22.44	0.513	0.44	6.730	2049	0.002	0.341
1f-925-4	568.13	40.80	0.843	14.97	3.55	n/a	n/a	0.516	486.08	56.24	n/a	31.419	36.81	0.516	0.38	6.730	1980	0.003	0.351
1f-925-6	575.02	40.80	0.843	15.33	3.25	n/a	n/a	0.509	486.08	50.68	n/a	24.843	43.78	0.509	0.29	6.730	2006	0.003	0.357
1f-925-7	575.02	40.80	0.843	15.33	3.25	n/a	n/a	0.509	486.08	50.68	n/a	21.829	47.13	0.509	0.26	6.730	2006	0.004	0.359

Two-tube system

$V_{u,1}$ [cm^3]	$V_{u,2}$ [cm^3]
148.46	148.46

Both systems

x_i [ ]	d [cm]
1	0.80

unstable domains.[5] The intercept on the abscissa and ordinate in Fig. 5 is the dimensionless number N_o, Eq. (36). The two parallel lines depicted in Fig. 5 represent the *extremes* of the predicted stability boundary for *all* of the experimental data presented, due to variations in the outlet-to-inlet flow resistances, (k_o^*/k_i^*).

A comparison of the experimental data with the theoretical stability boundary predicted by the ESTM indicates a high degree of agreement, especially in light of the uncertainty in pinpointing the exact location at which the system stabilizes or destabilizes. This degree of agreement is even more significant when consideration is given to the complexity of the many different physical mechanisms involved, and the simplicity of the ESTM, complete with its ability to accurately predict the effects of thermal and flow distribution asymmetry for a *multitube* system.

Experimental Verification of Natural Frequency. The experimental data, shown in Fig. 6, represent the natural frequency of the self-sustained limit-cycle oscillations. The degree of agreement between the natural frequency, predicted by the ESTM, Eq. (37), and the experimentally measured frequency, is quite good, and covers as wide a range as was possible with the existing experimental apparatus, $0.3 \leqslant f \leqslant 0.7$ Hz.

The range of natural frequencies presented was made possible by changes in the upstream vapor volume and inertia length. As can be seen in the schematic of the experimental apparatus in Fig. 2, a variable vapor volume in the upstream portion of the apparatus allowed for the total upstream vapor volume, V_u, to be changed readily. The variable vapor volume was heated so as to prevent condensation from occurring within the added volume. Figure 7 depicts the experimentally measured flow instability when a sudden increase in upstream vapor volume is made. This increased vapor volume caused a sudden decrease in the natural frequency of oscillation. After the system was allowed to operate in this mode for some time, the additional variable vapor volume was then isolated from the apparatus, and the previous oscillation frequency was regained very quickly. The difference in the natural frequency between the two unstable conditions is quite apparent.

As can be seen in Fig. 6, the ESTM predicted slightly lower natural frequencies than what was measured experimentally. However, the correspondence between the predictive capability of

[5]It should be pointed out that a favorable feature of the present ESTM is that the stability boundary is valid for any number of tubes in the condensing flow system, as is indicated in Fig. 5 by being able to display both two-tube and single-tube data together on the same plot.

the ESTM and direct experimental data is again quite good, especially considering the physical complexity involved, and the model's simplicity.

Summary and Conclusions

The research presented in this paper is a theoretical and experimental investigation of a low-frequency, self-sustained, limit-cycle type of oscillatory instability in the outlet condensate flowrate. The oscillations are of large amplitude and may include flow reversals. This instability normally exists under conditions of high heat flux and low outlet flow resistance.

The primary physical parameters responsible for this particular type of unstable behavior include the condenser heat flux, downstream inertia of the subcooled liquid, compressibility in the upstream vapor volume, and flow resistance; with the liquid-to-vapor density ratio being the primary physical parameter responsible for the amplitude of the oscillations. A means was developed for extending the Equivalent Single-Tube Model (ESTM), based on the System Mean Void Fraction (SMVF) Model, to predict the stability boundary for a multitube system. This predictive capability was verified experimentally for a two-tube system, which may well be a worst-case situation for the accuracy of the ESTM. The corresponding natural frequency of oscillation also compared favorably with the experimental data. The upstream compressible vapor volume and downstream liquid inertia appear to be the dominant energy-storage mechanisms responsible for this unstable behavior.

The experimental data presented in this research directly verifies the predictive capability of the ESTM, and, in turn, that of the SMVF Model. The true value and utility of the ESTM can only be comprehended when consideration is given to the complexity of the numerous physical mechanisms involved in multitube condensing flow systems, and the high degree of accuracy of such a relatively simple model; a model which can be solved, and graphically demonstrated, on typical 'spread-sheet' software.

Acknowledgments

The authors would like to acknowledge the National Science Foundation, Thermal Transport and Thermal Processing Program, Division of Chemical and Transport Systems, for its part in the support of this research under Grant No. CTS-9420853.

Nomenclature

$A_{t,o}$ = total cross-sectional area of system outlet, m^2
$\bar{f}_{q,j}$ = spatially average heat flux from tube j, W/m^2
h = enthalpy of standard liquid, J/kg
k_o = lumped effective outlet orifice coefficient, $\Delta p/\rho v^2$
k' = flow resistance coefficient, $N\cdot s^2/m^2\cdot kg^2$
k_o^* = linearized flow resistance at system outlet, $kN\cdot s/m^2\cdot g$
k_i^* = linearized flow resistance at system inlet, $kN\cdot s/m^2\cdot g$
L_d = downstream length, m
L' = length of condenser tube bundle, m
L_o^* = linearized subcooled liquid inertia length, m
$\bar{m}$ = mean total flowrate, kg/s
$m_{t,i}(t)$ = total time-dependent mass flowrate at system inlet, kg/s
$m_{t,o}(t)$ = total time-dependent mass flowrate at system outlet, kg/s
n = number of individual condenser tubes in multitube system
$p(t)$ = condensing flow system pressure, N/m^2
p_c = average condensing pressure, N/m^2
p_i = pressure at condensing flow system inlet, N/m^2
P = inside periphery, m
p_o = pressure at condensing flow system outlet, N/m^2
V_u = upstream vapor volume in inlet header assembly, m^3
$V_{u,t}$ = total upstream vapor volume, m^3
$V_{2\phi}$ = total two-phase vapor volume in multitube system, m^3
x_i = quality of flow entering at the system inlet
z = axial position coordinate from beginning of condensation process, m

Greek Symbols

$\alpha(z,t)$ = local area mean void fraction
$\bar{\alpha}$ = system mean void fraction
β = thermal asymmetry parameter
Δp = pressure prop, N/m^2
γ = flow distribution asymmetry parameter
γ^* = vapor compressibility coefficient; $d\rho'/dp$, $kg/m\cdot kN$
$\bar{\eta}$ = mean position of effective point of complete condensation, m
$\eta_j(t)$ = position of effective point of complete condensation in j^{th} tube, m
ρ = density of saturated liquid, kg/m^3
$\tau_{c,s}$ = effective condensing flow system time constant for entire multitube system, s
$\tau_{f,s}$ = effective compressible flow system time constant for entire multitube system, s
$\tau_{i,s}$ = effective inertia time constant for entire multitube system, s
$\tau_{2w,s}$ = effective two-way coupling time constant for entire multitube system, s
ω_n = natural frequency, 1/s

Subscripts and Superscripts. Primed ($'$) symbols of quantities refer to saturated vapor. A subscript (j) usually refers to quantities for the arbitrary representative j^{th} tube. Symbols of quantities generally refer to time-averaged quantities where the averaging time is small enough so as to just eliminate the inherent fluctuations but not interfere with the deterministic transient.

References

[1] Bhatt, B. L., and Wedekind, G. L., 1980, ''A Self-Sustained Oscillatory Flow Phenomenon in Two-Phase Condensing Flow Systems,'' ASME J. Heat Transfer, **102**, No. 4, pp. 695–700.
[2] Bhatt, B. L., Wedekind, G. L., and Jung, K., 1989, ''Effects of Two-Phase Pressure Drop on the Self-Sustained Oscillatory Instability in Condensing Flow,'' ASME J. Heat Transfer, **111**, pp. 538–545.
[3] Kobus, C. J., Wedekind, G. L., and Bhatt, B. L., 1998, ''Application of an Equivalent Single-Tube Model for Predicting Frequency-Response Characteristics of Multitube Two-Phase Condensing Flow Systems with Thermal and Flow Distribution Asymmetry,'' ASME J. Heat Transfer, **120**, No. 2, pp. 528–530.
[4] Kobus, C. J., Wedekind, G. L., and Bhatt, B. L., 2000, ''Predicting the Influence of Compressibility and Thermal and Flow Distribution Asymmetry on the Frequency-Response Characteristics of Multitube Two-Phase Condensing Flow Systems,'' ASME J. Heat Transfer, **122**, No. 1, pp. 196–200.
[5] Wedekind, G. L., Kobus, C. J., and Bhatt, B. L., 1997, ''Modeling the Characteristics of Thermally Governed Transient Flow Surges in Multitube Two-Phase Condensing Flow Systems with Compressibility and Thermal and Flow Distribution Asymmetry,'' ASME J. Heat Transfer, **119**, No. 3, pp. 534–543.
[6] Lahey, R. T., and Drew, D. A., 1980, ''An Assessment of the Literature Related to LWR Instability Modes,'' NUREG/CR-1414, prepared for U.S. Nuclear Regulatory Commission, Washington D.C. 20555, NRC FIN NO:B6461.
[7] Block, J. A., 1980, ''Condensation-Driven Fluid Motion,'' Int. J. Multiphase Flow, **6**, pp. 113–129.
[8] Calia, C., and Griffith, P., 1981, ''Modes of Circulation in an Inverted U-Tube Array with Condensation,'' Thermal-Hydraulics in Nuclear Power Technology, ASME HTD-15, *20th National Heat Transfer Conference*, Milwaukee, Wisconsin, pp. 35–43, August 2–5.
[9] Pitts, J. H., 1980, ''Steam Chugging in a Boiling Water reactor Pressure-Suppression System,'' Int. J. Multiphase Flow, **6**, pp. 329–344.
[10] Wang, S. S., Sargin, D. A., Stuhmiller, J. H., and Masiello, P. J., 1981, ''Numerical Simulation of Condensation Phenomena in Reactor Steam Suppression Systems,'' AIChE Symposium, Series No. 208, **77**, pp. 180–190.
[11] Soliman, M., and Berenson, P. J., 1970, ''Flow Stability and Gravitational Effects in Condenser Tubes,'' *Proceedings of the Fourth International Heat Transfer Conference*, Paris, France, VI, Paper No. Cs 1.8.
[12] Boyer, D. B., Robinson, G. E., and Hughes, T. G., 1995, ''Experimental Investigation of Flow Regimes and Oscillatory Phenomena of Condensing Steam in a Single Vertical Annular Passage,'' Int. J. Multiphase Flow, **21**, No. 1, pp. 61–74.

[13] Kishimoto, T., and Harada, A., 1992, ''Two-Phase Thermal Siphon Cooling for Telecom Multichip Modules,'' *Advances in Electronic Packaging, First Joint ASME/JSME Conference on Electronic Packaging*, Milpitas, CA, pp. 135–141, April.
[14] Wedekind, G. L., and Bhatt, B. L., 1977, ''An Experimental and Theoretical Investigation into Thermally Governed Transient Flow Surges in Two-Phase Condensing Flow,'' ASME J. Heat Transfer, **99**, pp. 561–567.
[15] Zivi, S. M., 1964, ''Estimation of Steady-State Steam Void Fraction by Means of the Principle of Minimum Entropy Production,'' ASME J. Heat Transfer, **86**, p. 247.
[16] Kobus, C. J., 1998, ''Application of the System Mean Void Fraction Model in Formulating an Equivalent Single-Tube Model for Predicting Various Transient and Unstable Flow Phenomena Associated with Horizontal Multitube Two-Phase Condensing Flow Systems with and without the Effects of Compressibility, Inertia, and Thermal and Flow Distribution Asymmetry,'' Ph.D. thesis, Oakland University, Rochester, Michigan.
[17] Rabas, T. J., and Minard, P. G., 1987, ''Two types of Flow Instabilities Occurring inside Horizontal Tubes with Complete Condensation,'' Heat Transfer Eng., **8**, No. 1, pp. 40–49.
[18] Wedekind, G. L., and Bhatt, B. L., 1989, ''Modeling the Thermally Governed Transient Flow Surges in Multitube Condensing Flow Systems with Thermal and Flow Distribution Asymmetry,'' ASME J. Heat Transfer, **111**, No. 3, pp. 786–791.
[19] Bhatt, B. L., and Wedekind, G. L., 1984, ''An Experimental and Theoretical Study into the Determination of Condensing Length,'' *Basic Aspects of Two-Phase Flow and Heat Transfer, 22nd National Heat Transfer Conference*, V. K. Dhir and V. E. Schrock, eds., Niagara Falls, NY, pp. 179–183.
[20] White, F. M., 1984, *Heat Transfer*, Addison-Wesley, Reading, MA, pp. 216–217.

Extinction and Scattering Properties of Soot Emitted From Buoyant Turbulent Diffusion Flames

S. S. Krishnan[1]

K.-C. Lin[2]

G. M. Faeth
Professor,
Fellow ASME,
e-mail: gmfaeth@umich.edu

Department of Aerospace Engineering,
The University of Michigan,
Ann Arbor, MI 48109-2140

Extinction and scattering properties at wavelengths of 250–5200 nm were studied for soot emitted from buoyant turbulent diffusion flames in the long residence time regime where soot properties are independent of position in the overfire region and characteristic flame residence times. Flames burning in still air and fueled with gas (acetylene, ethylene, propane, and propylene) and liquid (benzene, toluene, cyclohexane, and n-heptane) hydrocarbon fuels were considered. Measured scattering patterns and ratios of total scattering/absorption cross sections were in good agreement with predictions based on the Rayleigh-Debye-Gans (RDG) scattering approximation in the visible. Measured depolarization ratios were roughly correlated by primary particle size parameter, suggesting potential for completing RDG methodology needed to make soot scattering predictions as well as providing a nonintrusive way to measure primary soot particle diameters. Measurements of dimensionless extinction coefficients were in good agreement with earlier measurements for similar soot populations and were independent of fuel type and wavelength except for reduced values as the near ultraviolet was approached. The ratios of the scattering/absorption refractive index functions were independent of fuel type within experimental uncertainties and were in good agreement with earlier measurements. The refractive index function for absorption was similarly independent of fuel type but was larger than earlier reflectometry measurements in the infrared. Ratios of total scattering/absorption cross sections were relatively large in the visible and near infrared, with maximum values as large as 0.9 and with values as large as 0.2 at 2000 nm, suggesting greater potential for scattering from soot particles to affect flame radiation properties than previously thought. [DOI: 10.1115/1.1350823]

Keywords: Combustion, Fire, Flame, Heat Transfer, Radiation

Introduction

The extinction and scattering properties of soot at visible and infrared wavelengths must be known in order to develop *in situ* optical techniques for measuring soot properties and to obtain reliable estimates of the radiation properties of soot. Past studies have made significant progress toward resolving the extinction and scattering properties of soot, see Charalampopoulos [1], Faeth and Köylü [2], Julien and Botet [3], Tien and Lee [4], and Viskanta and Mengüc [5]. This work has shown that soot consists of nearly monodisperse spherical primary particles collected into mass fractal aggregates, that primary soot particle diameters and the number of primary particles per aggregate vary widely whereas soot fractal properties are relatively universal, that soot optical properties can be approximated by Rayleigh-Debye-Gans (RDG) scattering from polydisperse mass fractal aggregates (called RDG-PFA theory) at visible wavelengths and that accurate estimates of soot optical properties are mainly limited by uncertainties about soot refractive index properties. Earlier work in this laboratory due to Krishnan et al. [6] sought to improve understanding of soot refractive index properties in the visible by completing *in situ* measurements of soot extinction and scattering coefficients and interpreting these results using RDG–PFA theory. The objective of the present investigation was to extend this research, concentrating on additional measurements and analysis of soot extinction and scattering properties in the near ultraviolet, visible and infrared wavelength ranges (wavelengths of 250–5200 nm).

Earlier studies of soot extinction and scattering properties are reviewed by Wu et al. [7]; therefore, the following discussion will be limited to the findings of the companion study of Krishnan et al. [6]. Krishnan et al. [6] carried out *in situ* measurements of the optical properties of soot at wavelengths of 351.2–800.0 nm, considering soot in the overfire region of large buoyant turbulent diffusion flames burning in still air at standard temperature and pressure (STP) and at long characteristic flame residence times where soot properties are independent of position and characteristic flame residence time for a particular fuel [8], considering soot in flames fueled with a variety of gaseous and liquid hydrocarbons (acetylene, ethylene, propylene, butadiene, benzene, cyclohexane, toluene, and n-heptane). Extinction and scattering were interpreted to find soot optical properties using RDG–PFA theory after establishing that this theory was effective over the test range. Effects of fuel type on soot optical properties were comparable to experimental uncertainties. Dimensionless extinction coefficients were relatively independent of wavelength for wavelengths of 400–800 nm and yielded a mean value of 8.4 in good agreement with earlier measurements of Dobbins et al. [9], Choi et al. [10], Mulholland and Choi [11], and Zhou et al. [12] who considered similar overfire soot populations. Measurements of the refractive index function for absorption, $E(m)$, were in good agreement with earlier *ex situ* reflectometry measurements of Dalzell and Sarofim [13], and Stagg and Charalampopoulos [14]. On the other hand, measured values of the refractive index function for scatter-

[1]Graduate Student Research Assistant; now with Maurice J. Zucrow Laboratories, Purdue University, West Lafayette, IN.

[2]Research Fellow, now with Taitec, Inc., Wright-Patterson AFB, OH.

Contributed by the Heat Transfer Division for publication in the JOURNAL OF HEAT TRANSFER. Manuscript received by the Heat Transfer Division April 18, 2000; revision received November 3, 2000. Associate Editor: W. Webb.

ing, $F(m)$, only agreed with these earlier measurements for wavelengths of 400–550 nm but otherwise increased with increasing wavelength more rapidly than the rest. These measurements also showed that refractive index functions increased rapidly with increasing wavelength in the visible, yielding large levels of scattering as the infrared wavelength range was approached. This behavior raises concerns about approximations of modest refractive index values in the infrared that are required by RDG–PFA theory [9,15,16]; as well as concerns about the common assumption that scattering from soot in the infrared can be neglected when estimating flame radiation properties [4,5]. Finally, these results showed that soot refractive index properties do not approach a resonance condition in the near ultraviolet that is observed for graphite, see Chang and Charalampopoulos [17]; instead, refractive indices declined continuously with decreasing wavelength as the near ultraviolet was approached, similar to the findings of Vaglieco et al. [18] for amorphous carbon and soot.

The present study sought to extend the measurements of Krishnan et al. [6] into both the infrared and the near ultraviolet in order to help resolve concerns about soot optical properties in these spectral regions. Other issues that were considered included evaluating scattering predictions in the visible and infrared based on RDG–PFA theory, developing information about depolarization ratios in the visible that is needed to properly close scattering predictions based on RDG–PFA theory, and exploiting RDG–PFA theory to evaluate the potential importance of scattering from soot on flame radiation properties in the infrared. The following description of the study is brief; more details and a complete tabulation of data can be found in Krishnan [19].

Experimental Methods

The experimental arrangement was the same as Krishnan et al. [6]. The apparatus consisted of either a water-cooled gas-fueled burner having a diameter of 50 mm, or uncooled liquid-fueled burners having diameters of 51 and 102 mm, all injecting fuel gases vertically upward. The burners were located within an enclosure having a hood with a 152 mm diameter vertical exhaust duct at the top. Measurements were made at the exit of the exhaust duct where flow properties were nearly uniform. All operating conditions involved buoyant turbulent diffusion flames in still air within the long residence time regime where soot in the fuel-lean (overfire) region is independent of both position and characteristic flame residence time [8].

Many of the properties of the present overfire soot were available from earlier measurements by [6–8,20–23], as follows: density, composition, volume fractions (gravimetrically), primary particle diameters, aggregate size properties ($\bar{N}, N_g, \sigma_g$), aggregate fractal dimensions, scattering and extinction properties in the visible, and refractive index properties in the visible. Present measurements emphasized extinction within the wavelength range of 250–5200 nm. The wavelengths that were considered and the light sources that were used are as follows: 351.2, 457.9, 488.0, and 514.5 nm using an argon-ion laser (4W, Coherent Innova 90-4); 632.8 nm using a He-Ne laser (28 mW, Jodon HN10G1R); 248.0, 303.0, 405.0, 436.0, 546.0, and 578.0 nm using a mercury lamp (100W, Oriel 6281); 600.0, 800.0, 1100.0, 1550.0, and 2017.0 nm using a Quartz-Tungsten Halogen (QTH) lamp (100W, Oriel 6333); and 3980.0 and 5205.0 nm using an IR emitter source (Oriel 6363). Two detectors were used, as follows: 351.2–800.0 nm using a silicon detector (Newport 818-UV), and 248.0-303.0 nm and 1100.0–5205.0 nm using a pyrodetector (Oriel 70128). Interference filters having 10 nm bandwidths were used for wavelengths up to 1550.0 nm; interference filters having bandwidths of 90–160 nm were used for wavelengths larger than 1600.0 nm. The optical arrangement was designed following Manickavasagam and Mengüc [24] to reduce contributions of forward scattering to extinction measurements to less than 1 percent. Calcium fluoride lenses were used for spatial filtering and collimating the incident light due to the large range of wavelengths considered. The light was modulated by an enclosed chopper (Oriel 75155) before passing through the soot-containing exhaust flow. The output of the detector was passed through lock-in amplifiers prior to sampling and storage using a laboratory computer. Sampling was done at 2 kHz for a time period of 60s, averaging results for three sampling periods at each wavelength. Experimental uncertainties (95 percent confidence) of the extinction measurements are estimated to be less than 5 percent. Experimental uncertainties of other measurements will be presented when they are discussed.

The test conditions were the same as Krishnan et al. [6]. A brief summary of the fuels considered, and the corresponding structure properties of the overfire soot, is presented in Table 1. This range of fuels provides evaluation of soot optical properties for H/C atomic ratios of 1.00–2.28.

Table 1 Summary of soot structure properties[a]

Fuel[b]	d_p (nm)	$\bar{N}$	N_g	σ_g
Toluene (f)	51	526	252	3.2
Benzene (f)	50	552	261	3.5
Acetylene (g)	47	417	214	3.3
Butadiene (g)	42[c]	---	---	---
Propylene (g)	41	460	227	3.0
Cyclohexane (f)	37[c]	---	---	---
n-Heptane (f)	35	260	173	2.4
Ethylene (g)	32	467	290	2.7

[a]Soot in the overfire region of buoyant turbulent diffusion flames burning in still air in the long residence time regime with ambient pressures and temperatures of 99 ± 0.5 kPa and 298 ± 3 K, respectively. Soot density of 1880 kg/m^3 from Wu et al. [7]; $k_f = 8.5$ with a standard deviation of 0.5 from Köylü et al. [23]; $D_f = 1.79$ with a standard deviation of 0.05 from Krishnan et al. [6]. Values of d_p, $\bar{N}$, N_g and σ_g from Köylü and Faeth [8,23] except when noted otherwise. Listed in order of decreasing primary particle diameter.

[b]Parameter in parentheses denotes gas (g) or liquid (f) fuel.

[c]From Krishnan et al. [6].

Theoretical Methods

RDG–PFA Theory. Analysis of the extinction and scattering measurements to find soot optical properties was based on RDG–PFA theory. Portions of this theory used during the present investigation are briefly summarized in the following, see Julien and Botet [3], Dobbins and Megaridis [15], and Köylü and Faeth [21] for more details.

The main assumptions of RDG–PFA theory are as follows: individual primary particles are Rayleigh scattering objects, aggregates satisfy the RDG scattering approximations, primary particles are spherical and have constant diameters, primary particles just touch one another, the number of primary particles per aggregate satisfies a log-normal probability distribution function, and aggregates are mass fractal objects that satisfy the following relationship [3]:

$$N = k_f (R_g / d_p)^{Df}. \tag{1}$$

These approximations have proven to be satisfactory during past evaluations of RDG–PFA theory for a variety of conditions, including soot populations similar to the present study, see Krishnan et al. [6], Wu et al. [7], and Köylü and Faeth [21,22,25]; nevertheless, the theory was still evaluated during the present investigation before applying it to find soot optical and scattering properties.

The following formulation will be in terms of volumetric optical cross sections; these can be converted to optical cross sections, as follows:

$$\overline{C}_j^a = \overline{NQ}_j^a / n_p; \quad j = vv, hh, s, a, e. \tag{2}$$

The volumetric extinction cross section is simply the sum of the volumetric absorption and total scattering cross sections,

$$\overline{Q}_e^a = \overline{Q}_a^a + \overline{q}_s^a = (1 + \rho_{sa}) \overline{Q}_a^a, \tag{3}$$

where the last expression introduces the total scattering/absorption cross section ratio:

$$\rho_{sa} = \overline{Q}_s^a / \overline{Q}_a^a. \tag{4}$$

Based on RDG–PFA theory, ρ_{sa} can be computed given the structure and refractive index properties of the soot population, when effects of depolarization are small, as follows:

$$\rho_{sa} = 2 x_p^3 F(m) \overline{N^2 g} / (3 E(m) \overline{N}). \tag{5}$$

The specific expression for the aggregate total scattering factor, $g(kR_g, D_f)$, and the method of computing $\overline{N^2 g}$ from known *aggregate* structure properties, are described by Köylü and Faeth [21].

In order to complete predictions of soot extinction and scattering properties using RDG–PFA theory, measurements of soot volume fractions (gravimetrically) and primary particle diameters (by thermophoretic sampling and transmission electron microscopy, TEM) were used to compute primary particle density, as follows:

$$n_p = 6 f_v / (\pi d_p^3). \tag{6}$$

Present extinction and scattering measurements in the visible yield $\overline{Q}_e^a$ and $\overline{Q}_s^a$ directly, so that $\overline{Q}_a^a$ can be found from Eq. (3) and ρ_{sa} from Eq. (4). Then the refractive index functions can be computed from the RDG–PFA formulation, as follows:

$$E(m) = k^2 \overline{Q}_a^a / (4 \pi x_p^3 n_p) \tag{7}$$

$$F(m) = k^2 (q d_p)^{D_f} \overline{Q}_{vv}^a (q d_p) / (k_f x_p^6 n_p), \tag{8}$$

where $q d_p$ must be large enough so that scattering is in the large-angle (power-law) regime where Eq. (8) is appropriate. This last requirement was readily satisfied because power-law scattering dominated the scattering properties of the present large soot aggregates, see Wu et al. [7]. The fractal properties needed to apply Eq. (8) also were known for the present soot populations, see Table 1. Finally, combining Eqs. (6) and (7) yields a useful expression for $\overline{Q}_a^a$, as follows:

$$\overline{Q}_a^a = 6 \pi E(m) f_v / \lambda. \tag{9}$$

Large soot aggregates exhibit effects of depolarization which influence $\overline{Q}_{hh}^a$ and thus estimates of $\overline{Q}_s^a$ and ρ_{sa}. Unfortunately, effects of depolarization cannot be predicted using RDG–PFA theory and must be handled empirically instead. This was done as suggested by Köylü and Faeth [21] by defining a depolarization ratio, ρ_v, and using it analogous to Rayleigh scattering theory, see Rudder and Bach [26]. Thus, values of $\overline{Q}_{hh}^a(\theta)$ were found, as follows:

$$\overline{Q}_{hh}^a(\theta) = [(1 - \rho_v) \cos^2 \theta + \rho_v] \overline{Q}_{vv}^a(\theta). \tag{10}$$

It follows immediately from Eq. (10) that [21,27]

$$\rho_v = \overline{Q}_{hh}^a(90°) / \overline{Q}_{vv}^a(90°) \tag{11}$$

so that ρ_v could be obtained directly from present measurements in the visible.

The formulation of Eqs. (1)–(11) was used in several ways during the present investigation. First of all, normalized parameters, e.g., $\overline{Q}_{vv}^a(\theta) / \overline{Q}_{vv}^a(90 \text{ deg})$ and $\overline{Q}_{hh}^a(\theta) / \overline{Q}_{vv}^a(90 \text{ deg})$, yield scattering patterns that are independent of refractive index properties from Eqs. (7)–(11) and can be used to evaluate RDG–PFA predictions and find values of ρ_v from the measurements. In addition, all quantities on the right hand sides of Eqs. (7) and (8) were known in the visible so that these equations could be used to find $E(m)$ and $F(m)$ in the visible as discussed by Krishnan et al. [6]. Effects of depolarization on predictions of total scattering cross sections were small so that Eq. (5) could be used to predict ρ_{sa} in the visible, given values of $E(m)$ and $F(m)$, providing a means of testing combined effects of RDG–PFA predictions and refractive index property measurements. Then, Eq. (5) was used to estimate ρ_{sa} in the infrared (after finding a correlation for $F(m)/E(m)$ in the infrared to be discussed later) so that $E(m)$ could be found from present measurements of $\overline{Q}_e^a$ using Eqs. (3) and (9). Finally, Eq. (5) in conjunction with values of $E(m)$ and $F(m)$ developed from the measurements, were used to estimate the potential importance of scattering from soot on the properties of flame radiation.

Dimensionless Extinction Coefficients. For conditions where soot properties are uniform along an optical path, the dimensionless extinction coefficient, K_e, provides a simple relationship between extinction and soot volume fractions, as follows [9]:

$$K_e = -\lambda \ln(I/I_0) / (L f_v). \tag{12}$$

Soot properties, including f_v, were nearly constant over the present optical path; nevertheless, an appropriate average value of f_v was used to evaluate K_e from Eq. (12) based on several gravimetric measurements of f_v along the optical path. The volumetric extinction cross section for a uniform path of length L is given by [21]:

$$\overline{Q}_e^a = -\ln(I/I_0)/L. \tag{13}$$

Then, introducing the volumetric absorption coefficient from Eq. (3), and combining Eqs. (12) and (13), yields the following:

$$K_e = \lambda (1 + \rho_{sa}) \overline{Q}_a^a / f_v. \tag{14}$$

Finally, substituting for $\overline{Q}_a^a$ from Eq. (9) yields

$$K_e = 6 \pi E(m) (1 + \rho_{sa}). \tag{15}$$

Equation (15) implies that variations of the dimensionless extinction coefficient with wavelength result from variations of both $E(m)$ and ρ_{sa} with wavelength.

Results and Discussion

Scattering Patterns. Typical examples of measured and predicted scattering patterns of ethylene soot at wavelengths of 351.2–632.8 nm appear in Fig. 1, see Krishnan et al. [6], Wu et al. [7] and Köylü and Faeth [21] for other examples involving similar overfire soot populations. Experimental uncertainties (95 percent confidence) of the normalized scattering properties illustrated in Fig. 1, are estimated to be smaller than 10 percent, except for the *hh* component near 90 deg, where small values of this ratio make uncertainties somewhat larger. The agreement between measurements and predictions is excellent with discrepancies smaller than experimental uncertainties. In particular, there is no deterioration of predictions at small wavelengths where relatively large values of x_p create concerns about the validity of RDG–PFA theory [6]. Similarly, there is no deterioration of performance at large wavelengths where progressively increasing values of the real and imaginary parts of the refractive indices of soot with increased wavelength also cause concerns about the validity of RDG–PFA theory [6]. Similar performance was achieved at other conditions implying acceptable use of RDG–PFA theory for soot at values of x_p as large as 0.46. This general behavior, involving variations of both wavelength and refractive indices to justify the use of RDG–PFA theory, agrees with the detailed computational evaluations of Farias et al. [28] concerning the range of validity of RDG–PFA theory.

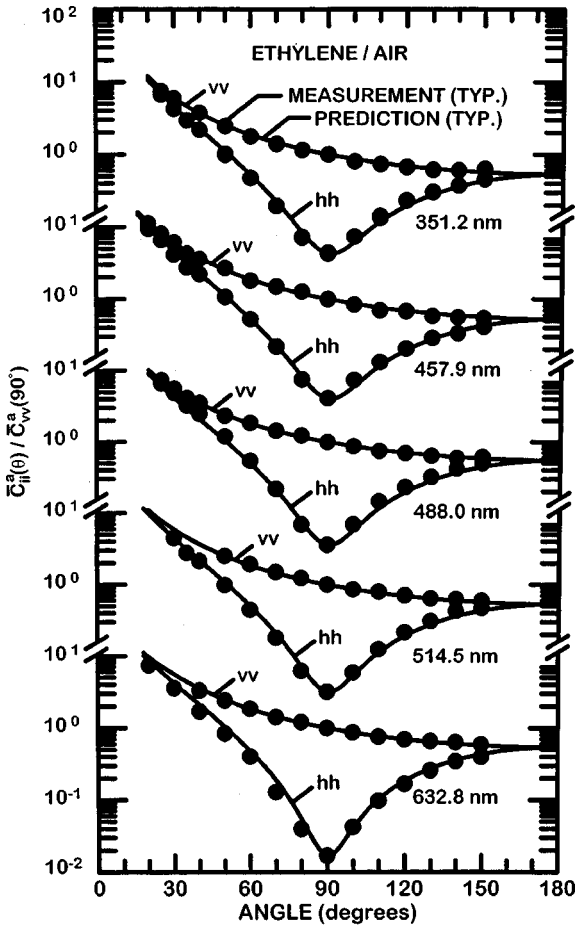

Fig. 1 Measured and predicted scattering patterns for soot in ethylene/air flames at wavelengths in the visible (351.2–632.8 nm)

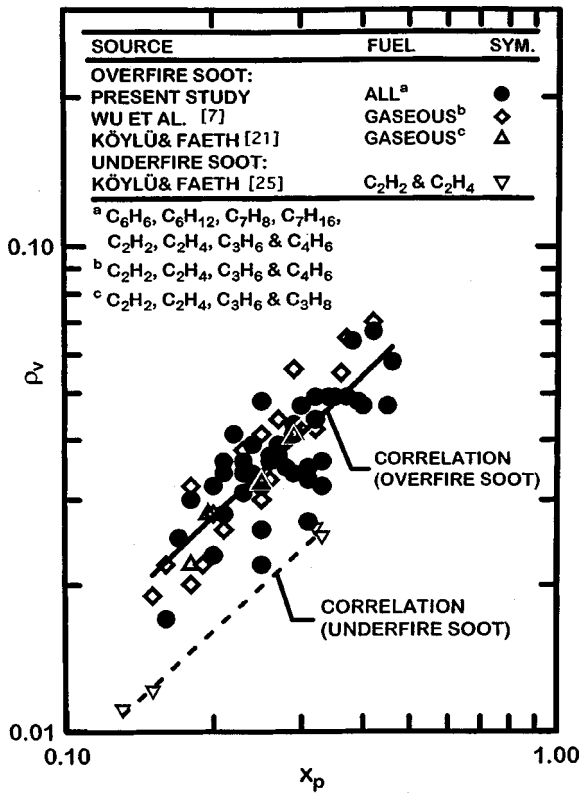

Fig. 2 Measurements of depolarization ratios for various fuels as a function of primary particle size parameter in the visible (351.2–632.8 nm). Measurements of Wu et al. [7], Köylü and Faeth [21,25], and the present investigation.

Depolarization Ratios. A limitation of RDG–PFA theory is that it provides no estimates of depolarization ratios that are needed to accurately compute $\overline{Q}^a_{hh}(\theta)$ from Eq. (10). Thus, measurements of ρ_v were completed so that computations to find ρ_v in the near infrared could be undertaken. This work involved exploiting the available data base of scattering patterns in the literature, using Eq. (11) to find ρ_v. Available measurements of ρ_v are plotted as a function of x_p in Fig. 2. Measurements illustrated in the plot include results from Krishnan et al. [6], Wu et al. [7], Köylü and Faeth [21,25], and the present investigation. Experimental uncertainties (95 percent confidence) of these determinations are somewhat larger than those of $\overline{Q}^a_{vv}(\theta)/\overline{Q}^a_{vv}$ (90 deg) due to the small magnitude of ρ_v but are still estimated to be smaller than 20 percent. Results for soot in the overfire region of buoyant turbulent diffusion flames in the long residence time regime, due to Krishnan et al. [6], Wu et al. [7], Köylü and Faeth [21], and the present investigation, are in reasonable agreement with each other, yielding the following correlation for ρ_v:

$$\rho_v = 0.14 x_p, \tag{16}$$

which also is shown on the plot. The standard error of the power of x_p in Eq. (16) is 0.1, the standard error of the coefficient is 0.03, and the correlation coefficient of the fit is 0.83, which is reasonably good. This is not surprising because relationships between the size of scattering objects and depolarization ratio have been recognized for some time [26,27], including recent observations of diStasio [29] of a relationship between primary soot particle diameter and depolarization ratio analogous to the present findings. In contrast, the measurements for underfire soot in laminar diffusion flames due to Köylü and Faeth [25] are consistently smaller (by roughly 35 percent) than results for the overfire soot, although the variation of ρ_v with x_p is similar. This behavior suggests that the coefficient of Eq. (16) may be a function of aggregate size because the underfire soot involved $\overline{N}$ in the range 30–80 whereas the overfire soot involved $\overline{N}$ in the range 260–552 (see Table 1 for the latter). Finally, the values of ρ_v for soot aggregates illustrated in Fig. 2 are roughly an order of magnitude larger than typical values of ρ_v for Rayleigh scattering from gases, see Rudder and Bach [26]. This behavior is consistent with the much smaller values of x_p for gases than for soot.

Total Scattering/Absorption Ratios. Predictions of RDG–PFA theory were further evaluated using present measurements of total scattering/absorption ratios, ρ_{sa}, in the visible. Values of ρ_{sa} were found by integrating measured differential scattering cross sections to find $\overline{Q}^a_s$ and then applying Eq. (3) and the measured value of $\overline{Q}^a_e$ to find $\overline{Q}^a_a$ and Eq. (4) to find ρ_{sa}. Experimental uncertainties of ρ_{sa} (95 percent confidence) are estimated to be smaller than 20 percent, with uncertainties tending to be largest at 632.8 nm for n-heptane and at 351.2 nm for the rest of the fuels because ρ_{sa} reaches minimum values at these conditions. Predictions of ρ_{sa} were obtained from measured soot structure properties using Eq. (5). Values of the soot refractive index function ratio, $F(m)/E(m)$, needed to make these determinations in the visible were obtained from the measurements of Krishnan et al. [6] for the same soot populations.

Measured and predicted values of ρ_{sa} are illustrated for wavelengths of 351.1–632.8 nm in Fig. 3. These results are for overfire soot in large buoyant turbulent diffusion flames burning n-heptane, benzene, toluene, ethylene, propylene, and acetylene in still air. Measured values of ρ_{sa} are relatively large, in the range 0.1–0.9, tending to increase with increasing propensity to soot as

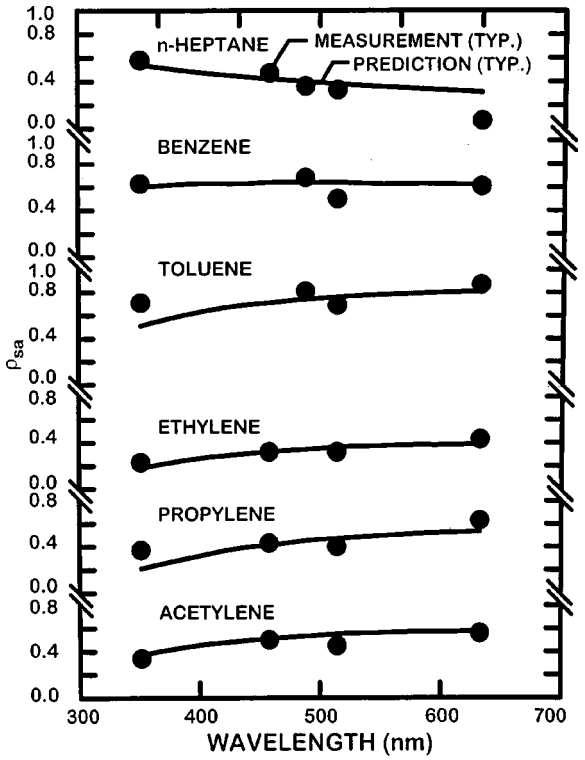

Fig. 3 Measured and predicted total scattering/absorption cross section ratios for various fuels as a function of wavelength in the visible (351.2–632.8 nm)

indicated by increasing primary particle diameters. These results suggest significant effects of scattering for the conditions of the present measurements, which is expected in view of the relatively large aggregates found in the overfire region of large buoyant diffusion flames. Finally, RDG–PFA theory is in reasonably good agreement with the measurements.

An interesting feature of the results illustrated in Fig. 3 is that ρ_{sa} increases with increasing wavelength for all the fuels except n-heptane. This behavior is related to aggregate size, noting that n-heptane has the smallest aggregates of all the fuels considered in Fig. 3, e.g., the overfire soot produced by this fuel has the smallest value of N all the fuels by a wide margin and nearly the smallest value of d_p, see Table 1. These properties imply that the optical properties of n-heptane soot tend to approach Rayleigh scattering to a closer extent than the other fuels, where ρ_{sa} can be formulated, as follows [21]:

$$\rho_{sa}=(2\pi^3/3)(F(m)/E(m))(d_p/\lambda)^3, \quad \text{Rayleigh scattering.} \tag{17}$$

The general expression for ρ_{sa} for RDG–PFA scattering, Eq. (5), is more complex than Eq. (17), however, it can be simplified considerably at the limit of large aggregates and wavelengths where scattering is dominated by the large angle regime. Such conditions are representative of the large aggregates considered in Fig. 3, as a limit. At the large aggregate limit, ρ_{sa} is independent of the specific distribution of N (the scattering properties of the aggregates saturate) and the theory yields the following asymptotic expression [21]:

$$\rho_{sa}=D(F(m)/E(m))\times(d_p/\lambda)^{(3-Df)}, \quad \text{saturated RDG–PFA scattering,} \tag{18}$$

where D is a fractal factor that is independent of wavelength, defined as follows:

$$D=\frac{\pi^3 k_f}{3(4\pi)^{D_f}}\left[\frac{4}{(2-D_f)}-\frac{24}{(6-D_f)(4-D_f)}\right]. \tag{19}$$

Adopting fractal properties typical of soot, $D_f=1.8$ and $k_f=8.5$ yields $D=16.06$ and the expression for ρ_{sa} for large soot aggregates from Eq. (18) becomes:

$$\rho_{sa}=D(F(m)/E(m))\times(d_p/\lambda)^{1,2}, \quad \text{saturated RDG–PFA scattering.} \tag{20}$$

Based on Eqs. (17) and (20), it is evident that small soot aggregates, such as n-heptane soot, exhibit a relatively rapid reduction of ρ_{sa} with increasing wavelength compared to large soot aggregates, given similar variations of $F(m)/E(m)$ with wavelength. Thus, it is plausible that increases of $F(m)/E(m)$ with increasing wavelength that are sufficient to cause ρ_{sa} to increase with increasing wavelength for large aggregates are still not sufficient to cause corresponding increases of ρ_{sa} for small aggregates that approach the Rayleigh scattering limit.

Dimensionless Extinction Coefficients. The experimental uncertainties (95 percent confidence) of measurements of dimensionless extinction coefficients are estimated to be less than 14 percent for a best case with laser sources, where uncertainties were dominated by uncertainties of soot volume fraction distributions, to a maximum of 26 percent at long wavelengths for other sources where optical signal-noise ratios become a factor, e.g., ethylene-fueled flames at 2017 nm. Similar to Krishnan et al. [6], effects of fuel type on dimensionless extinction coefficients were comparable to experimental uncertainties. As a result, present measurements were limited to the gas-fueled flames, in order to check this behavior, with the following measurements presented as averages over all the gas-fueled flames, for conciseness. The resulting values of K_e are plotted as a function of wavelength in Fig. 4. Other measurements for overfire soot in the long residence time regime for various fuels, due to Krishnan et al. [6], Dobbins

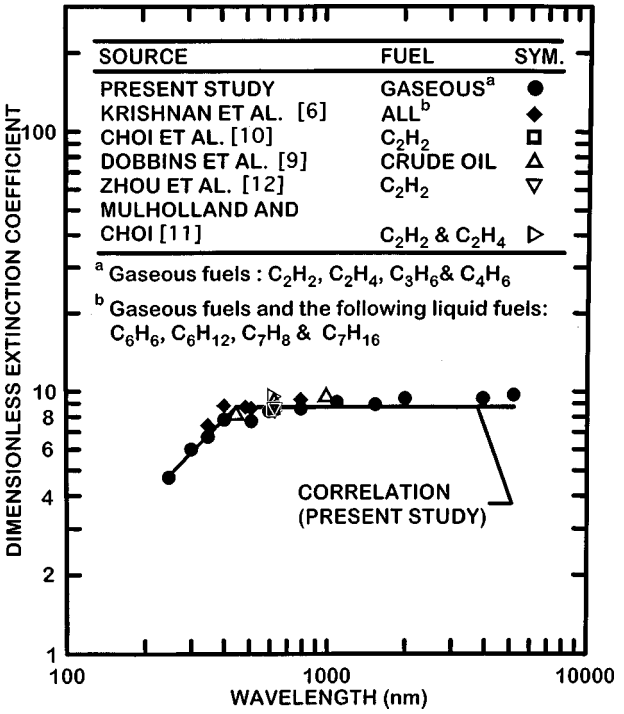

Fig. 4 Measured dimensionless extinction coefficients of soot for various fuels at wavelengths of 250–5200 nm. Measurements of Krishnan et al. [6], Dobbins et al. [9], Choi et al. [10], Mulholland and Choi [11], Zhou et al. [12] and the present investigation.

et al. [9], Choi et al. [10], Mulholland and Choi [11], and Zhou et al. [12] are plotted on the figure for comparison with the present measurements. This relative independence of K_e on soot type, however, should not be assumed for all flame conditions. For example, Dobbins et al. [9] and Colbeck et al. [30] review measurements of specific extinction coefficients which readily yield values of K_e that exhibit significant differences among soot in large diffusion flames, in premixed flames, and in smoldering flames.

Values of K_e illustrated in Fig. 4 increase rapidly with increasing wavelength in the near ultraviolet, at wavelengths smaller than 400 nm, which agrees with the observations of Vaglieco et al. [18] for amorphous carbon and soot in the near ultraviolet. In contrast, graphite approaches a resonance condition which causes extinction levels to increase in the near ultraviolet [4]. For wavelengths in the range 400–5200 nm, however, values of K_e are relatively constant, yielding an average value over all fuels and wavelengths for the measurements of Krishnan et al. [6] and the present investigation of 8.7 with a standard deviation of 1.5 which is plotted in the figure. This mean value is slightly larger than the value of 8.4 with a similar standard deviation for wavelengths of 400–800 nm found by Krishnan et al. [6]. The present slightly larger value of K_e reflects the relatively slow increase of K_e with increasing wavelength over the wavelength range 400–5200 nm seen in Fig. 4.

It is of interest to examine the relative variation of K_e with wavelength for the conditions illustrated in Fig. 4, resulting from the predictions of RDG–PFA theory. These considerations can be based on Eq. (15) with the wavelength variation of ρ_{sa} estimated from Eq. (20) for large soot aggregates because values of K_e were only obtained for the gaseous fuels (and not for n-heptane) over the full wavelength range illustrated in Fig. 4. Based on these considerations, $K_e/E(m)$ varies proportional to λ° to $\lambda^{-1.2}$ as ρ_{sa} varies from small to large values compared to unity. Thus, the behavior of K_e seen in Fig. 4 requires a relatively rapid increase of $E(m)$ with increasing wavelength in the near ultraviolet at wavelengths smaller than 400 nm, followed by a more gradual increase with increasing wavelength for wavelengths in the range 400–5200 nm, with the rate of increase tending to be larger for soot having relatively large values of ρ_{sa} in this wavelength range, such as the overfire soot considered during the present investigation. This observation will be helpful for interpreting values of $E(m)$ and $F(m)$ to be considered next.

Refractive Index Functions. Values of $F(m)/E(m)$ and $E(m)$ are needed to find spectral radiation properties and to carry out nonintrusive measurements of soot volume fractions, see Eqs. (5), (7), (8), (9), and (15). Values of $F(m)/E(m)$ for wavelengths of 350–9000 nm are illustrated in Fig. 5. Results shown include the *ex situ* reflectometry measurements of Dalzell and Sarofim [13], Stagg and Charalampopoulos [14], and Felske et al. [31], and the *in situ* absorption and scattering measurements in the visible of Krishnan et al. [6] and Wu et al. [7]. The measurements of Dalzell and Sarofim [13] are averages of their results for acetylene and propane-fueled flames. The measurements of Wu et al. [7] have been adjusted to correct an error in their gravimetric determinations of soot volume fractions by matching their dimensionless extinction coefficients to the present measurements at 514.5 nm as discussed by Krishnan et al. [6]. Other measurements due to Chang and Charalampopoulos [17], Vaglieco et al. [18], Batten [32], and Lee and Tien [33] have not been included on the plot due to concerns about methods used to interpret measurements as discussed by Krishnan et al. [6]. Finally, two empirical correlations of the measurements are illustrated on the plot: one for the measurements of Krishnan et al. [6] for wavelengths of 350–650 nm and one for all the measurements for wavelengths 350–6000 nm.

The measurements of $F(m)/E(m)$ illustrated in Fig. 5 involve various fuels, sources and methods and are in remarkably good agreement. Exceptions involve the early *ex situ* reflectometry

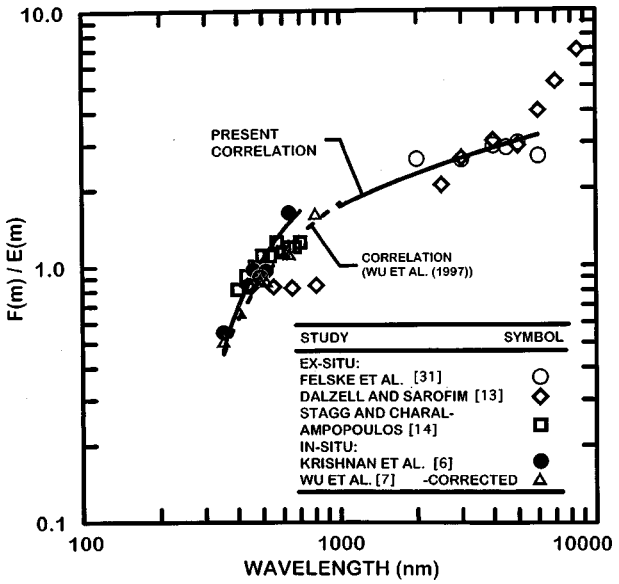

Fig. 5 Measurements of the refractive index function ratios, $F(m)/E(m)$, for various fuels as a function of wavelength for wavelengths of 250–9000 nm. *Ex situ* measurements of Dalzell and Sarofim [13], Stagg and Charalampopoulos [14]; *in situ* measurements of Krishnan et al. [6], and Wu et al. [7].

measurements of Dalzell and Sarofim [13]; they provide low estimates in the visible which may be due to the fact that corrections were not made for effects of surface voids on scattering properties which are important in the visible [31]; and they provide high estimates in the far infrared at wavelengths larger than 6000 nm where small scattering levels and corresponding poor signal-to-noise ratios may be a factor. The relatively good agreement among the measurements at other conditions is no doubt promoted by the fact that $F(m)/E(m)$ involves ratios of scattering to absorption cross sections which tends to normalize the measurements and reduce errors compared to measurements of absorption and scattering alone and the fact that corrections of the *ex situ* results for effects of surface roughness should be relatively small in the infrared [31]. Nevertheless, in view of past criticism of the *ex situ* measurements of Dalzell and Sarofim [13] and Felske et al. [31] their measured velocity values of $F(m)/E(m)$ in the infrared clearly merit reconsideration.

The absorption and scattering measurements of Krishnan et al. [6] and the corrected absorption and scattering measurements of Wu et al. [7], both in the visible, provide complete information needed to find ρ_{sa} and $E(m)$ in the visible using Eqs. (7) and (8). In addition, ρ_{sa} becomes small at the largest wavelengths considered during the present investigation so that present measured values of $Q_e^a \approx Q_a^a$ and $E(m)$ can be found directly from Eq. (7). At intermediate wavelengths, however, RDG–PFA theory was used to estimate values of ρ_{sa} so that Q_a^a could be found from the extinction measurements and then $E(m)$ from Eq. (7). These estimates of ρ_{sa} were obtained using the correlation of $F(m)/E(m)$ illustrated in Fig. 5, the known structure properties of the present soot and the RDG–PFA results of Eq. (5). Another set of *in situ* measurements of $E(m)$ was obtained from the earlier extinction measurements of Köylü and Faeth [22]: this was done by matching values of $E(m)$ from Krishnan et al. [6] with these results at 514.5 nm and then using present measurements and estimates of ρ_{sa} in the visible and infrared to find $E(m)$ from Eq. (7). Finally, the *ex situ* reflectometry measurements of Dalzell and Sarofim [13], Stagg and Charalampopoulos [14], and Felske et al. [31] directly provide values of $E(m)$.

The various determinations of $E(m)$ for wavelengths of 350–9000 nm are illustrated in Fig. 6. The various *in situ* measure-

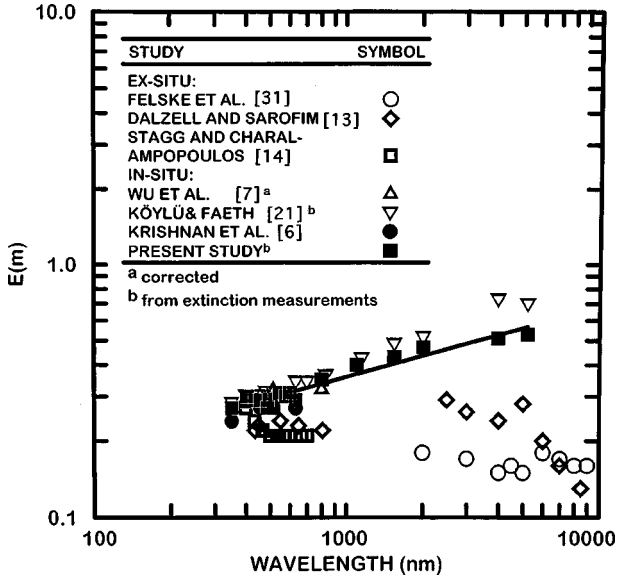

Fig. 6 Measurements of the refractive index function for absorption, $E(m)$, as a function of wavelength for wavelengths of 250–9000 nm. *Ex situ* results of Dalzell and Sarofim [13], Stagg and Charalampopoulos [14], and Felske et al. [31]; *in situ* results of Krishnan et al. [6], Wu et al. [7], and Köylü and Faeth [21], and the present investigation.

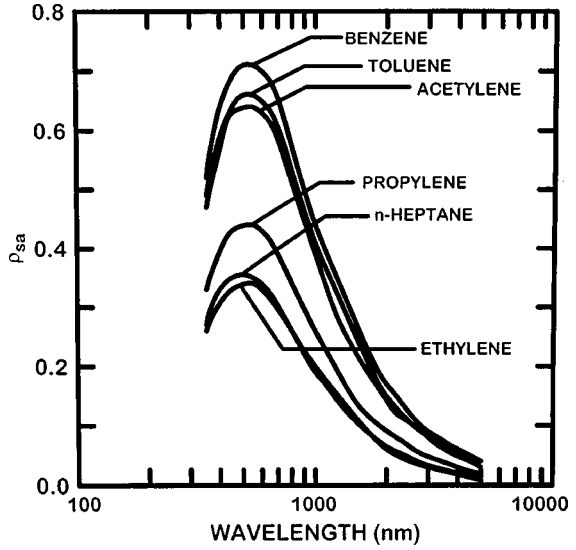

Fig. 7 Estimates of total scattering/absorption cross section ratios for various fuels as a function of wavelength for wavelengths in the visible and infrared (350–5200 nm)

ments of $E(m)$ agree within experimental uncertainties over the entire wavelength range of the measurements which is encouraging. The *in situ* and *ex situ* measurements of $E(m)$ in the visible agree within experimental uncertainties, with the somewhat smaller values of $E(m)$ for the *ex situ* measurements attributed to uncorrected effects of surface voidage, at least for the measurements of Dalzell and Sarofim [13]. More disconcerting, however, are the unusually small values of $E(m)$ found from the *ex situ* reflectometry measurements of Dalzell and Sarofim [13] and Felske et al. [13] in the infrared at wavelengths of 2000–9000 nm. In particular, it is difficult to see how trends of constant or progressively decreasing values of $E(m)$ with increasing wavelength could yield the slightly increasing values of K_e with increasing wavelength in the infrared seen in Fig. 4 for RDG scattering objects. In contrast, present values of $E(m)$ expressly yield the trends of K_e illustrated in Fig. 4 due to the method used to find $E(m)$. Nevertheless, resolving the differences between the *in situ* and *ex situ* determinations of $E(m)$ seen in Fig. 6 merits priority because these differences clearly can have a large impact on the radiative properties of soot-containing flames which are dominated by continuum radiation from soot in the infrared.

Soot Scattering Predictions. Given the RDG–PFA scattering and refractive index properties of the present overfire soot aggregates, it is of interest to estimate the potential importance of scattering from such soot in flame environments. This was done by finding ρ_{sa} for the six fuels where required structure properties were known. Values of ρ_{sa} were computed using Eq. (5) and the correlation of $F(m)/E(m)$ illustrated in Fig. 5 along with the appropriate structure properties. The results of these computations are illustrated in Fig. 7.

Referring to Fig. 5, the general correlation for $F(m)/E(m)$ is not as steep in the visible as specific correlations for the present measurements; therefore, values of ρ_{sa} in Fig. 7 begin to decrease with increasing wavelength somewhat sooner than corresponding results for present test conditions illustrated in Fig. 3. The results shown in Fig. 7 indicate maximum values of ρ_{sa} for wavelengths of 450–600 nm, with n-heptane soot reaching a maximum before the rest as discussed earlier. The progressive increase of $F(m)/E(m)$ with increasing wavelength seen in Fig. 5, however, tends to maintain relatively large values of ρ_{sa} well into the infrared, particularly for the very large soot aggregates resulting from the combustion of benzene, toluene and acetylene, where scattering is still roughly 20 percent of absorption at wavelengths approaching 2000 nm. This behavior suggests that scattering should be considered for accurate estimates of continuum radiation from soot in flame environments, at least for large soot aggregates similar to those considered during the present investigation and representative of natural fires.

Conclusions

The extinction and scattering properties of soot were studied using *in situ* methods at wavelengths of 250–5200 nm. Test conditions were limited to soot in the fuel-lean (overfire) region of buoyant turbulent diffusion flames in the long residence time regime where soot properties are independent of position in the overfire region and characteristic flame residence times. Flames burning in still air and fueled with eight liquid and gaseous hydrocarbon fuels were considered to provide atomic H/C ratios in the range 1.00–2.28. RDG–PFA theory was used to interpret the measurements based on successful evaluation of this theory over the test range (values of x_p up to 0.46). The major conclusions of the study are as follows:

1 Present dimensionless extinction coefficients were relatively independent of fuel type, they increased rapidly with increasing wavelength in the near ultraviolet but became relatively independent of wavelength over the range 400–5200 nm. Present measurements were in good agreement with earlier measurements for similar soot populations due to Dobbins et al. [9], Choi et al. [10], Mulholland and Choi [11], and Zhou et al. [12].

2 Present *in situ* measurements of the ratios of the scattering/absorption refractive index function, $F(m)/E(m)$, were independent of fuel type and were in good agreement with earlier *ex situ* measurements in the literature. Present *in situ* measurements of the refractive index function for absorption, $E(m)$, were also independent of fuel type and were in good agreement with earlier *in situ* measurements but were somewhat larger than earlier *ex situ* reflectometry measurements in the infrared.

3 Measured depolarization ratios yielded a somewhat scattered but simple correlation in terms of the primary particle size parameter alone as suggested in recent work of diStasio [29]. Given a correlation along these lines, the methodology needed to compute

scattering properties according to RDG–PFA theory would be completed and a simple nonintrusive diagnostic to measure particle diameter would be feasible. Effects of aggregate size on this correlation were observed, however, and merit further study in the future before these methods can be reliably used.

4 Ratios of total scattering/absorption cross sections, ρ_{sa}, were relatively large in the visible (reaching maximum values as large as 0.9), whereas values of ρ_{sa} remain as large as 0.2 at wavelengths approaching 2000 nm suggesting potential for greater effects of scattering from soot particles on the properties of flame radiation than previously thought.

Extending these conclusions to other types of soot should be approached with caution. In particular, the present soot has been exposed to oxidation in flame environments and involves relatively large soot aggregates due to large characteristic flame residence times; thus, such soot may not be representative of unoxidized and weakly aggregated soot typical of fuel-rich soot growth regions.

Acknowledgments

This research was supported by the Building and Fire Research Laboratory of the National Institute of Standards and Technology, Grant Nos. 60NANB4D-1696 and 60NANB8D0084, with H. R. Baum serving as Scientific Officer and by NASA Grants NAG3-1878 and NAG3-2048 under the technical management of D. L. Urban and Z.-G. Yuan of the NASA Glenn Research Center. The authors also would like to acknowledge useful discussions with D. Snelling of the National Research Council of Canada.

Nomenclature

C = optical cross section
d_p = primary particle diameter
D = fractal factor, Eq. (19)
D_f = mass fractal dimension
$E(m)$ = refractive index function for absorption $= Im((m^2-1)/(m^2+2))$
f_v = soot volume fraction
$F(m)$ = refractive index function for scattering $= |(m^2-1)/(m^2+2)|^2$
$g(kR_g, D_f)$ = aggregate total scattering factor
i = $(-1)^{1/2}$
I = light intensity
k = wave number $= 2\pi/\lambda$
k_f = fractal prefactor
K_e = dimensionless extinction coefficient
L = light path length
m = soot refractive index $= n + i\kappa$
n = real part of soot refractive index
n_p = mean number of primary particles per unit volume
N = number of primary particles per aggregate
N_g = geometric mean of the number of particles per aggregate
q = modulus of scattering vector $= 2k \sin(\theta/2)$
Q = volumetric optical cross section
R_g = radius of gyration of an aggregate
x_p = primary particle size parameter $= \pi d_p/\lambda$
θ = angle of scattering from forward direction
κ = imaginary part of soot refractive index
λ = wavelength of radiation
ρ_{sa} = ratio of total scattering to absorption cross sections
ρ_v = depolarization ratio
σ_D = standard deviation of D_f
σ_g = standard deviation of number of particles per aggregate from geometric mean

Subscripts

a = absorption
av = average value
e = extinction
h = horizontal polarization
ij = incident (i) and scattered (j) polarization directions
s = total scattering
v = vertical polarization
o = initial value

Superscripts

a = aggregate property
$\underline{p}$ = primary particle property
$\langle\ \rangle$ = mean value over a polydisperse aggregate population

References

[1] Charalampopoulos, T. T., 1992, ''Morphology and Dynamics of Agglomerated Particulates in Combustion Systems Using Light Scattering Techniques,'' Prog. Energy Combust. Sci., **18**, pp. 13–45.
[2] Faeth, G. M., and Köylü, Ü. Ö., 1995, ''Soot Morphology and Optical Properties in Nonpremixed Turbulent Flame Environments,'' Combust. Sci. Technol., **108**, pp. 207–229.
[3] Jullien, R., and Botet, R., 1987, *Aggregation and Fractal Aggregates*, World Scientific, Singapore, pp. 45–60.
[4] Tien, C. L., and Lee, S. C., 1982, ''Flame Radiation,'' Prog. Energy Combust. Sci., **8**, pp. 41–59.
[5] Viskanta, R., and Mengüc, M. P., 1987, ''Radiation Heat Transfer in Combustion Systems,'' Prog. Energy Combust. Sci., **13**, pp. 511–524.
[6] Krishnan, S. S., Lin, K. C., and Faeth, G. M., 2000, ''Optical Properties in the Visible of Overfire Soot in Large Buoyant Turbulent Diffusion Flames,'' ASME J. Heat Transfer, **122**, pp. 517–524.
[7] Wu, J.-S., Krishnan, S. S., and Faeth, G. M., 1997, ''Refractive Indices at Visible Wavelengths of Soot Emitted from Buoyant Turbulent Diffusion Flames,'' ASME J. Heat Transfer, **119**, pp. 230–237.
[8] Köylü, Ü. Ö., and Faeth, G. M., 1992, ''Structure of Overfire Soot in Buoyant Turbulent Diffusion Flames at Long Residence Times,'' Combust. Flame, **89**, pp. 140–156.
[9] Dobbins, R. A., Mulholland, G. W., and Bryner, N. P., 1994, ''Comparison of a Fractal Smoke Optics Model with Light Extinction Measurements,'' Atmos. Environ., **28**, pp. 889–897.
[10] Choi, M. Y., Mulholland, G. W., Hamins, A., and Kashiwagi, T., 1995, ''Comparisons of the Soot Volume Fraction Using Gravimetric and Light Extinction Techniques,'' Combust. Flame, **102**, pp. 161–169.
[11] Mulholland, G. W., and Choi, M. Y., 1998, ''Measurement of the Mass Specific Extincion Coefficient for Acetylene and Ethene Smoke Using the Large Agglomerate Optics Facility,'' *Proceedings of the Combustion Institute*, **27**, pp. 1515–1522.
[12] Zhou, Z.-Q., Ahmed, T. U., and Choi, M. Y., 1998, ''Measurements of Dimensionless Soot Extinction Constant Using a Gravimetric Sampling Technique,'' Exp. Therm. Fluid Sci., **18**, pp. 27–32.
[13] Dalzell, W. H., and Sarofim, A. F., 1969, ''Optical Constants of Soot and Their Application to Heat Flux Calculations,'' ASME J. Heat Transfer, **91**, pp. 100–104.
[14] Stagg, B. J., and Charalampopoulos, T. T., 1993, ''Refractive Indices of Pyrolytic Graphite, Amorphous Carbon, and Flame Soot in the Temperature Range 25° to 600°C,'' Combust. Flame, **94**, pp. 381–396.
[15] Dobbins, R. A., and Megaridis, C. M., 1991, ''Absorption and Scattering of Light by Polydisperse Aggregates,'' Appl. Opt., **30**, pp. 4747–4754.
[16] Köylü, Ü. Ö., and Faeth, G. M., 1993, ''Radiative Properties of Flame-Generated Soot,'' ASME J. Heat Transfer, **111**, pp. 409–417.
[17] Chang, H. Y., and Charalampopoulos, T. T., 1990, ''Determination of the Wavelength Dependence of Refractive Indices of Flame Soot,'' Proc. R. Soc. London, Ser. A, **A430**, pp. 577–591.
[18] Vaglieco, B. M., Beretta, F., and D'Alessio, A., 1990, ''In Situ Evaluation of the Soot Refractive Index in the UV-Visible from the Measurements of Scattering and Extinction Coefficients in Rich Flames,'' Combust. Flame, **79**, pp. 259–271.
[19] Krishnan, S., 2000, ''Optical Properties of Soot Emitted from Buoyant Turbulent Diffusion Flames,'' Ph.D. thesis, The University of Michigan, Ann Arbor, MI.
[20] Köylü, Ü. Ö., 1992, ''Emission, Structure and Optical Properties of Overfire Soot from Buoyant Turbulent Diffusion Flames,'' Ph.D. thesis, The University of Michigan, Ann Arbor, MI.
[21] Köylü, Ü. Ö., and Faeth, G. M., 1994, ''Optical Properties of Overfire Soot in Buoyant Turbulent Diffusion Flames at Long Residence Times,'' ASME J. Heat Transfer, **116**, pp. 152–159.
[22] Köylü, Ü. Ö., and Faeth, G. M., 1996, ''Spectral Extinction Coefficients of Soot Aggregates from Turbulent Diffusion Flames,'' ASME J. Heat Transfer, **118**, pp. 415–421.
[23] Köylü, Ü. Ö., Faeth, G. M., Farias, T. L., and Carvalho, M. G., 1995, ''Fractal and Projected Structure Properties of Soot Aggregates,'' Combust. Flame, **100**, pp. 621–633.

[24] Manickavasagam, S., and Mengüc, M. P., 1993, ''Effective Optical Properties of Coal/Char Particles Determined from FT-IR Spectroscopy Experiments,'' Energy Fuels, **7**, pp. 860–869.
[25] Köylü, Ü. O., and Faeth, G. M., 1994, ''Optical Properties of Soot in Buoyant Laminar Diffusion Flames,'' ASME J. Heat Transfer, **116**, pp. 971–979.
[26] Rudder, R. R., and Bach, D. R., 1968, ''Rayleigh Scattering of Ruby-Laser Light by Neutral Gases,'' J. Opt. Soc. Am., **58**, pp. 1260–1266.
[27] Bohren, C. F., and Huffman, D. R., 1983, *Absorption and Scattering of Light by Small Particles*, Wiley, New York, pp. 477–482.
[28] Farias, T. L., Köylü, Ü. O., and Carvalho, M. C., 1996, ''The Range of Validity of the Rayleigh-Debye-Gans Theory for Optics of Fractal Aggregates,'' Appl. Opt., **35**, pp. 6560–6567.
[29] di Stasio, S., 2000, ''Feasibility of an Optical Experimental Method for the Sizing of Primary Spherules in Sub-Micron Agglomerates by Polarized Light Scattering,'' Appl. Phys., **B70**, pp. 635–643.
[30] Colbeck, I., Atkinson, B., and Johar, Y., 1997, ''The Morphology and Optical Properties of Soot Produced by Different Fuels,'' J. Aerosol Sci., **28**, pp. 715–723.
[31] Felske, J. D., Charalampopoulos, T. T., and Hura, H., 1984, ''Determination of the Refractive Indices of Soot Particles from the Reflectivities of Compressed Soot Pellets,'' Combust. Sci. Technol., **37**, pp. 263–284.
[32] Batten, C. E., 1985, ''Spectral Optical Constants of Soots from Polarized Angular Reflectance Measurements,'' Appl. Opt., **24**, pp. 1193–1199.
[33] Lee, S. C., and Tien, C. L., 1980, ''Optical Constants of Soot in Hydrocarbon Flames,'' *Proceedings of the Combustion Institute*, **18**, pp. 1159–1166.

Phonon Heat Conduction in Thin Films: Impacts of Thermal Boundary Resistance and Internal Heat Generation

Taofang Zeng

Gang Chen
Mem. ASME

Mechanical and Aerospace Engineering Department,
University of California,
Los Angeles, CA 90095-1597

The measured thermal resistance across a thin film deposited on a substrate often includes the internal thermal resistance within the film and the thermal boundary resistance (TBR) across the film-substrate interface. These two resistances are frequently lumped and reported as an equivalent thermal conductivity of the film. Two fundamental questions should be answered regarding the use of this equivalent thermal conductivity. One is whether it leads to the correct temperature distribution inside the film. The other one is whether it is applicable for thin films with internal heat generation. This paper presents a study based on the Boltzmann transport equation (BTE) to treat phonon heat conduction inside the film and across the film-substrate interface simultaneously, for the cases with and without internal heat generation inside the film. Material systems studied include SiO_2 and diamond films on Si substrates, representative of thin-film materials with low and high thermal conductivity. It is found that for a SiO_2 film on a Si substrate, the film thermal conductivity and TBR can be treated independently, while for a diamond film on a Si substrate, the two are related to each other by the interface scattering. When the free surface behaves as a black phonon emitter, the TBR for thin diamond films with internal heat generation is the same as that without the internal heat generation. When the free surface is adiabatic, however, the TBR increases and approaches the value of the corresponding black surface as the film thickness increases. Results of this study suggest that great care must be taken when extending the effective thermal conductivity measured for thin films under one experimental condition to other application situations.
[DOI: 10.1115/1.1351169]

1 Introduction

Heat conduction in dielectric or semiconductor thin films has attracted great attention in the past [1]. It is now well accepted that when the film thickness becomes comparable to, or smaller than, the phonon mean free path (MFP), size effect becomes significant. In experiments and device applications, a thin film often comes with a substrate. The measured thermal resistance of the thin film in the cross-plane direction usually consists of two parts: one is the thermal resistance within the thin film, the other is the thermal boundary resistance (TBR) across the interface [2,3]. Heat conduction and the thermal conductivity of thin films in both the in-plane and the cross-plane directions are often modeled based on the Boltzmann transport equation [4,5]. The modeling in the in-plane direction is relatively straightforward since local thermal equilibrium can be established on a length scale much smaller than the in-plane film length. However, the phonon transport in the cross-plane direction could deviate far from equilibrium as manifested in the temperature jump at interfaces [4]. This temperature jump is of the same origin as the TBR, which has been a subject of intense study in the past [3,6].

Many measurements were performed in the past for the cross-plane thermal conductivity of thin films on substrate systems. Examples include SiO_2 and SiN_x on Si [7,8] and diamond on Si [9]. Usually, the TBR and the thin-film thermal conductivity are lumped together as the equivalent thermal conductivity, while there are also efforts to separate the TBR from the thermal conductivity of the film [7]. The observed thickness dependence of the equivalent thin-film thermal conductivity was explained as a result of the change of the relative contribution of the internal thermal conductivity of the film and the TBR at the interface [7]. The former depends on the film thickness while the latter is generally considered thickness independent. At macroscale, these two quantities are not correlated. At microscale, however, when the phonon mean free path becomes comparable to the film thickness, both the TBR and the film thermal conductivity depend on how phonons are scattered at the substrate/film interface as well as at the other surface/interface of the film. In this case, both the effective thermal conductivity inside the film and the thermal boundary resistance depend on the interface conditions, and they should be treated on a unified basis, i.e., with the BTE, as demonstrated by Chen [10] for superlattices. For a thin-film-on-substrate system, Jen and Chieng [11] recently reported a study considering this problem. Their treatment assumed that the interface thermalizes the incoming phonons. This assumption may be valid for interfaces with highly disordered interfacial layers. The nonequilibrium states of phonons at interfaces, however, should be considered for other practical applications.

In the measurement of the thermal conductivity of a thin film, a heat flux is typically applied at the boundaries, i.e., surfaces or ends of thin films. In practice, heat could also be generated inside film devices. For example, there have been considerable efforts to dope diamond for making high temperature devices [12]. In thermoelectric thin film devices, internal heat generation is an important factor determining the device performance [13]. A fundamental issue is whether the thermal resistance measured under the surface-flux boundary condition is still applicable for the case with internal heat generation.

The objectives of this study are two-fold. One is to investigate the effects of the interface phonon scattering on the effective cross-plane thermal conductivity of thin films. The relation be-

Contributed by the Heat Transfer Division for publication in the JOURNAL OF HEAT TRANSFER. Manuscript received by the Heat Transfer Division February 23 1999; revision received November 21, 2000. Associate Editor: A. Majumdar.

tween the thermal resistance inside the film and the TBR to the interface scattering processes will be examined based on solving the BTE on a unified basis. The other objective is to examine the applicability of the TBR and the equivalent thermal conductivity, obtained from experiments with surface heat flux conditions, to the case with internal heat generation. Two systems, diamond films on silicon and silicon dioxide films on silicon, representative of the high and low thermal conductivity spectra of solid materials, are investigated. Several interface scattering mechanisms are assumed to account for the interface properties. The TBR is computed for the cases with and without internal heat sources, and the temperature distributions are compared using different definitions of the effective thermal conductivities of the film. It was found that the TBR dominates the thermal resistance for diamond on silicon. In this case, the thermal boundary resistance is no longer an intrinsic property of the two materials joined together. Instead, it depends on the film thickness, the surface/interface conditions, and the heating conditions.

2 Physical Models and Analyses

This study focuses on phonon transport through a thin film and its substrate as shown in Figs. 1(*a*) and (*b*). To include the effect of the substrate on the heat conduction inside the film and the TBR, while excluding the complication of the heat conduction process in the bulk substrate, it is assumed that phonons are emitted at a uniform temperature from the substrate and travel towards the interface. These phonons can be thought of as coming from within one MFP of the substrate side. The rest of the substrate could be treated based on the Fourier heat conduction theory. Though a thin film is studied, it is approximated here that the phonon spectrum of the film is the same as that of its bulk material. Thus the phonon wave effect can be excluded. It is also approximated that the internal scattering rate in the film can be represented by an average MFP. The validity of those two approximations has been discussed in detail by Chen [10,14].

Under the above conditions, the phonon transport across the film and the interface can be approximated by the BTE, which is, under the intensity representation [4]

$$\mu \frac{dI}{dz} = \frac{I^0 - I}{\Lambda}, \tag{1}$$

where I is the total phonon intensity, I^0 the equilibrium phonon intensity approximated as

$$I^0 = \frac{1}{4\pi} Cv(T - T_{\text{ref}}) + I^0_{\text{ref}} \tag{2}$$

and Λ is the average MFP in the corresponding bulk material, $\mu(=\cos\theta)$ is the directional cosine, C is the volumetric specific heat, and v is the magnitude of the phonon group velocity. It should be emphasized that the temperature in Eq. (2) may represent a highly non-equilibrium situation and it is best regarded as a quantity representing local total phonon energy [10].

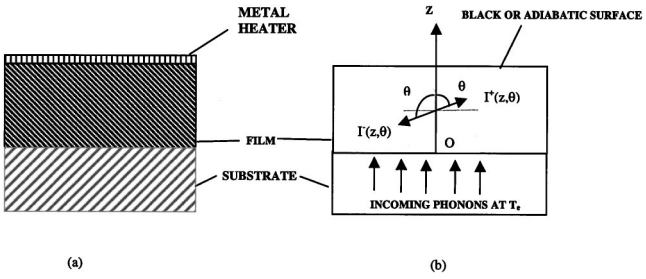

Fig. 1 Schematic diagram of the film/substrate system, (*a*) a typical experimental configuration, and (*b*) physical model in this study. The upper surface is a black phonon emitter or an adiabatic surface.

The solution of the above equation was well-documented [15]

$$I^+(\xi,\mu) = I^+(0,\mu)\exp\left(-\frac{\xi}{\mu}\right) + \frac{1}{\mu}\int_0^{\xi} I^0 \exp\left(\frac{\xi_1 - \xi}{\mu}\right) d\xi_1 \quad (\text{for } 0 < \mu < 1) \tag{3}$$

$$I^-(\xi,\mu) = I^-(\xi_h,\mu)\exp\left(\frac{-\xi + \xi_h}{\mu}\right) - \frac{1}{\mu}\int_{\xi}^{\xi_h} I^0 \exp\left(\frac{\xi_1 - \xi}{\mu}\right) d\xi_1 \quad (\text{for} -1 < \mu < 0), \tag{4}$$

where ''+'' and ''−'' represent the forward and backward propagating phonons in correspondence with the directional cosine, ξ $(=z/\Lambda)$ is the dimensionless coordinate, and $\xi_h(=h/\Lambda)$ is the dimensionless film thickness. The local heat flux can be obtained by integration over the solid angle as

$$q(\xi) = \int_{\Omega=4\pi} I\cos\theta d\Omega = 2\pi\int_0^1 [I^+(\xi,\mu) - I^-(\xi,-\mu)]\cdot\mu d\mu, \tag{5}$$

where $d\Omega(=2\pi\sin\theta d\theta)$, is the differential solid angle. The local temperature distribution can be obtained by using the condition of energy conservation

$$\frac{dq}{dz} = S, \tag{6}$$

where S is the heat generation per unit volume. The detailed heat generation mechanisms are neglected in this work, and a uniform volumetric heat generation rate is assumed. Equations (5) and (6) lead to

$$2I^0(\xi) = \int_0^1 I^+(0,\mu)\exp\left(-\frac{\xi}{\mu}\right) d\mu + \int_0^1 I^-(\xi_h,-\mu)\exp\left(\frac{\xi_h - \xi}{-\mu}\right) d\mu + \int_0^{\xi_h} I^0 E_1(|\xi - \xi_1|) d\xi_1 + S\Lambda/2\pi. \tag{7}$$

Boundary and Interface Conditions. To solve for the temperature distribution in the film and the TBR from Eqs. (3), (4) and (7), boundary conditions at the surface of the film and the film-substrate interface need to be defined. The interface condition will be discussed and two different surface conditions will then be introduced.

Film/Substrate Interface. Phonon reflection at interfaces is the fundamental reason for the existence of the TBR. There exist two prevailing models for the phonon reflection and transmission at interfaces: the acoustic mismatch model and the diffuse scattering model. The acoustic mismatch theory is applicable for elastic scattering at specular interfaces [6], i.e., when the scattered phonons are of the same frequency as the incident phonons. However, if the roughness of the interface is comparable to the wavelength of the phonon, the diffuse scattering at the interface will be significant [16]. A diffuse scattering model has been developed for this case [3]. In real situations, the interface may be neither perfectly specular nor perfectly diffuse. In the latest study, Chen [10] combined the specular and diffuse interface scattering models and demonstrated that the specularity of the interface is important in determining the TBR as well as size effect in superlattice structures. For a partially diffuse and partially specular interface, the phonon intensity leaving the interface can be written as

$$I^+(0,\mu)=P[R_{s12}I^-(0,-\mu)+t_{s21}I^0(T_e)]+(1-P)\times\left[2R_{d12}\int_0^1 I^-(0,-\mu)\mu d\mu+T_{d21}I^0(T_e)\right], \quad (8)$$

where P is the interface specularity parameter that represents the fraction of specularly reflected/transmitted phonons, and

$$t_{s21}=T_{s21}(\mu_2)\mu_2 d\mu_2/(\mu_1 d\mu_1) \quad (9)$$

accounts for the solid angle change upon phonon refraction. $R_{s12}(\mu_1)$ and $T_{s21}(\mu_2)$ are the specular reflectivity and transmissivity, respectively, for phonons incident from layer 1 at an angle of μ_1 and from layer 2 at μ_2, and R_{d12} and T_{d21} are the diffuse reflectivity and transmissivity, respectively. Those four parameters will be discussed in the next subsection. The first two terms in the right hand side of Eq. (8) represent contributions from the specular part, while the last two terms represent contributions from the diffuse part. It is worthwhile to point out that, while the incoming phonon from the substrate is $I^0(T_e)$, the equilibrium temperature in the substrate side of the interface is not at T_e. The latter is determined by the phonon intensity transmitted from the film and the intensity of the emitted phonons.

Surface Condition. Two simplified surface conditions are investigated. One is the constant-temperature black surface. In this case, the free surface is assumed to emit phonons with intensity $I(T_2)$. The boundary condition is thus defined as

$$I^-(\xi_h,-\mu)=I(T_2). \quad (10)$$

The other situation is an adiabatic, diffuse surface with the corresponding boundary condition as

$$I^-(\xi_h,-\mu)=2\int_0^1 I^+(\xi_h,\mu)\mu d\mu. \quad (11)$$

Clearly, to represent the true experimental configuration with a metal film heater, the top surface should be treated as an interface between the metal film and the dielectric film. Equation (10) is a quite stringent simplification, but it allows for focusing on the physics of one interface. It is anticipated that similar phenomena observed for the film-substrate interface can happen for the metal heater-film interface.

Interface Properties. The phonon reflectivity and transmissivity have been a subject of intense study for many years related to the TBR phenomena [3,6], particularly at low temperatures. Approximations proposed by Chen [10] for different interface phonon transport processes at room temperature and higher are used in this study.

Diffuse Scattering Model. The diffuse scattering model is based on the assumption that the scattered phonons completely lose its origin. In this limit, the reflectivity phonons can also be thought as transmitted from the other side, thus [3],

$$T_{d12}=R_{d21}=1-T_{d21}. \quad (12)$$

Expressions for the transmissivity and reflectivity in the low temperature limit were given by Swartz and Pohl [3]. Based on this assumption, Chen extended it to room temperature and higher as [10]

$$T_{d21}=\frac{C_1 v_1}{C_1 v_1+C_2 v_2}. \quad (13)$$

By adopting these two equations, one assumes that phonons of all frequencies can transmit through the interface. Since the phonons at the two sides generally have different spectra, these expressions imply that inelastic scattering occurs at the interface, i.e., phonons can change their frequency through splitting or combining into several phonons, as in the case of three phonon scattering in bulk materials.

Elastic Acoustic Mismatch. The acoustic mismatch model represents the limit that phonons are specularly scattered. When the reflected and transmitted phonons are at the same frequency as the incident phonons, i.e., in the case of elastic scattering, simplified formulas for the interface reflectivity and transmissivity from the acoustic mismatch model are used

$$R_{s21}(\mu_2)=\left|\frac{Z_1\mu_1-Z_2\mu_2}{Z_1\mu_1+Z_2\mu_2}\right| \quad (14)$$

$$T_{s21}(\mu_2)=\frac{4Z_1Z_2\mu_1\mu_2}{(Z_1\mu_1+Z_2\mu_2)^2}, \quad (15)$$

where, $Z_i(=\rho_i v_i)$ is the acoustic impedance and

$$T_{s12}(\mu_1)=\frac{C_2 v_2^3}{C_1 v_1^3}T_{s21}(\mu_2). \quad (16)$$

Equations (13)–(16) are valid when the incident angle is less than the critical angle. Above the critical angle, total internal reflection occurs, thus

$$R_{s21}(\mu_2)=1 \quad \text{and} \quad T_{s21}(\mu_2)=0. \quad (17)$$

By adopting the above equations, it is assumed that the maximum acoustic-phonon frequency or phonon group velocity in medium 2(substrate) is lower than that in medium 1(thin film), which is valid for the two example systems in this study. Phonons in medium 1 with frequencies above the maximum frequency in medium 2 are confined in medium 1 if only elastic scattering occurs at the interface. Thus, Eqs. (14) and (15) are valid for the specular reflectivity and transmissivity in medium 2.

Inelastic Acoustic Mismatch. If phonons in medium 1 are not confined but escape into medium 2 through inelastic scattering, the above elastic acoustic mismatch model can no longer be applied. The diffuse mismatch model as given by Eqs. (12) and (13) includes the inelastic scattering but assumes total loss of directionality during scattering. To take into consideration the possibility that the directionality can be maintained during inelastic scattering, Chen [10] proposed the following modification to Snell's law

$$\frac{\sin\theta_1}{\sin\theta_2}=\left(\frac{C_2 v_2^3}{C_1 v_1^3}\right)^{1/2}. \quad (18)$$

With this modification, the reflectivity and transmissivity from medium 2 into medium 1 can still be calculated from Eqs. (14) and (15), and $T_{s12}=T_{s21}$ in the whole frequency range. This is referred to as the inelastic acoustic mismatch model

Thermal Boundary Resistance, Internal and External Thermal Conductivity

By definition, the TBR is the ratio of the temperature difference between the two sides of the interface to the heat flux across the interface

$$R=\frac{T^0(\xi=0)-T^*}{q}, \quad (19)$$

where the heat flux, q, can be derived and calculated from Eq. (5). T^* is the equilibrium phonon temperature of the substrate at the interface, which can be calculated from Eq. (*A*3) in Appendix A. The internal thermal conductivity of the thin film is defined as

$$K_{\text{int}}=\frac{qh}{T^0(\xi_h)-T^0(\xi=0)}. \quad (20)$$

The external thermal conductivity is the equivalent thermal conductivity of the internal thermal conductivity and the TBR

$$K_{\text{ext}}=\frac{qh}{T^0(\xi_h)-T^*}=\frac{1}{\dfrac{1}{K_{\text{int}}}+\dfrac{R}{h}}. \tag{21}$$

Temperature Distribution With Internal Heat Source. To quantify the difference between the temperature distributions predicted by using the BTE and the Fourier law, calculations for a diamond film on a Si substrate with an internal heat source in the diamond film are performed using both methods. The diamond surface is considered as a free surface and two cases are investigated. One is an adiabatic free surface as specified by Eq. (11), the other a black surface as defined by Eq. (10). The BTE for the case with an internal heat source is Eq. (7). The final equations used to calculate the intensity distribution for an adiabatic surface are provided in Appendix B. Note that the equilibrium intensity $I^0(\xi)$ is now directly related to the intensity at the free surface $I^+(\xi_h,\mu)$. The temperature distribution with an adiabatic condition using Fourier's law is derived as

$$\frac{T-T^*}{S\Lambda^2/K_{\text{ext}}}=\left(\xi\xi_h-\frac{1}{2}\xi^2\right). \tag{22}$$

The equation for the temperature distribution with a black boundary condition using Fourier's law can be written as

$$\frac{T-T^*}{T_2-T^*}=\frac{\xi}{\xi_h}-\frac{1}{2}\frac{S\Lambda^2}{K_{\text{ext}}\cdot(T_2-T(\xi=0))}(\xi^2-\xi\xi_h). \tag{23}$$

Numerical Method

The intensity Eqs. (3) and (4), the energy balance Eq. (7), and the boundary-conditions, Eqs. (8) and (9), should be solved simultaneously. This can only be achieved numerically. There are five unknowns: $I^+(\xi_h,\mu)$, $I^-(\xi_h,-\mu)$, $I^+(0,\mu)$, $I^-(0,-\mu)$, and $I^0(\xi)$. Those five equations can be reduced to two equations after substitution and rearrangement. The two unknowns are $I^+(\xi_h,\mu)$ and $I^0(\xi)$. Detailed equations are given in Appendix A. These two integral equations are discretized using the Gauss-Legendre quadrature. Equation (*A*1) is solved first to obtain $I^0(\xi)$. Then $I^0(\xi)$ is substituted into Eq. (*A*2) to obtain $I^+(\xi_h,\mu)$. Attention was paid to the discretization of angles in the film and in the substrate by converting the angles in the substrate to the film side, which are related to each other by Snell's law.

In the calculation, the two intensities, $I^0(\xi)$ and $I^+(\xi)$ are normalized by $I^0(T_2)$. Since the interest of this study is on the heat transfer from the free surface to the substrate, temperature T_2 is set to be larger than T_e. Because the two cosines μ_1 and μ_2 are related to each other according to Snell's law, and the calculation for Eqs. (*A*1) and (*A*2) is only for layer 1 (thin film), the reflectivity $R_{s21}(\mu_2)$ and the transmissivity $T_{s21}(\mu_2)$ are converted to μ_1 in layer 1. The validity of the calculation is tested by setting the film thickness as large as possible to examine the asymptotic behavior. The calculated internal thermal conductivity approaches the bulk value as the thickness became larger but the total nondimensional thickness ξ_h is limited to 15. The accuracy of the numerical results is also tested by doubling the number of integration points.

The solution for the equations with the internal heat source is more complicated, because $I^0(\xi)$ and $I^-(\xi_h,-\mu)$ are now correlated in Eqs. (*B*1) and (*B*2). Those two equations are discretized, and the obtained discrete equations can be written in the form of a matrix equation

$$\begin{pmatrix} A_{m\times m} & B_{n\times n} \\ C_{m\times m} & D_{n\times n}\end{pmatrix}\begin{pmatrix} I^0_{m\times 1} \\ I^+_{n\times 1}\end{pmatrix}=\begin{pmatrix} E \\ F\end{pmatrix}. \tag{24}$$

By analyzing Eqs. (*B*1) and (*B*2), it is found that matrices A and D are almost diagonal and ill-conditioned for a thick film ($\xi_h \geqslant 5$). An iteration scheme is developed to obtain the solution to Eqs. (*B*1) and (*B*2). First, Eq. (24) is solved to obtain an initial guess for I^0 and I^+, and then the data for I^0 are substituted into the following equation:

$$D_{n\times n}I^+=F-C_{m\times m}I^0 \tag{25}$$

to calculate I^+. Those new values of I^+ are used to calculate I^0. The iterations are performed until the relative error for two consecutive iterations is smaller than 0.1 percent.

Table 1 Parameters used in the calculation

	Specific heat X 10^6 J/m^{3}K	Group velocity m/s	Mean free path Å	Density kg/m^3
SiO_2	1.687[a]	4400[b]	5.58[c]	2278[d]
Si	.93[e]	1804[e]	2604[e]	2330[f]
Diamond	calculated[g]	13200[h]	calculated[i]	3520[j]

[a]Touloukian [19], Vol. 5, p. 215.
[b]Cahill and Pohl [20], p. 4071.
[c]Calculated from $\Lambda=3K/Cv$ at 300°K by using K=1.38W/mK from Touloukian [19], Vol. 2, p. 193.
[d]Touloukian [19], Vol. 5, p. 214.
[e]Chen [10] by using the dispersion model.
[f]Shackelford [21], p. 46.
[g]Method from Jen and Chieng [11] and Goodson [17], and data from Touloukian [19], Vol. 5, p. 8.
[h]Goodson [18], p. 281.
[i]Method from Jen and Chieng [11] and Goodson [18], depends on thickness.
[j]Brady and Clauser [22], p. 257.

Parameters Used in the Calculation

Two very different systems, SiO_2/Si and diamond/Si, representing the low and the high film phonon mean free path limits, are investigated. The input parameters are the bulk properties of those materials including the specific heat, the phonon velocity, and the phonon MFP. Those parameters are presented in Table 1. In the table, the MFP of SiO_2 is estimated from the kinetic equation, $K=Cv\Lambda/3$, because the phonon spectrum for SiO_2 is not available. It should be cautioned that this kinetic model for amorphous materials may be over-simplified. The heat conduction mechanism is still a topic under intense study [17]. The properties of Si are estimated by using the method from Chen [10], where the contribution of optical phonons to the bulk thermal conductivity is neglected, because optical phonons have a very low group velocity.

The average phonon MFP in polycrystalline diamond films is determined by considering phonon scattering due to defects as well as the inherent phonon-phonon Umklapp scattering processes through the following approximation of Matthiessen's rule

$$\frac{1}{\Lambda}=\frac{1}{\Lambda_U}+\frac{1}{\Lambda_{GB}}. \tag{26}$$

The average $\Lambda_U(\tau_U)$ was calculated directly from the bulk diamond by using $\Lambda_U=3K/Cv$, where $K=1350$ W/mk for type IIb diamond. The average grain boundary scattering MFP(Λ_{GB}) is estimated from the frequency dependent scattering rate of grain boundaries, which depends on the density of imperfections and the thickness of the film. The same approach as in Ref. [18] is used in this calculation, and the details are omitted here.

3 Results and Discussion

Figures 2–4 show the results for the case without an internal heat source, and Fig. 5 shows the results for the case with an internal heat source. Both diamond/Si and SiO_2/Si systems are studied, and the results for the diamond/Si system, however, are presented in more detail because of the stronger size effect.

Figures 2(*a*) and 2(*b*) show the distribution of the dimensionless equilibrium temperature, $\Theta=Cv(T-T_e)/(4\pi q)$, where q is the heat flux, based on the elastic acoustic mismatch model and the inelastic acoustic mismatch model, respectively. The temperature inside the substrate is uniform because no scattering inside the substrate is considered. The temperature jump at the film sub-

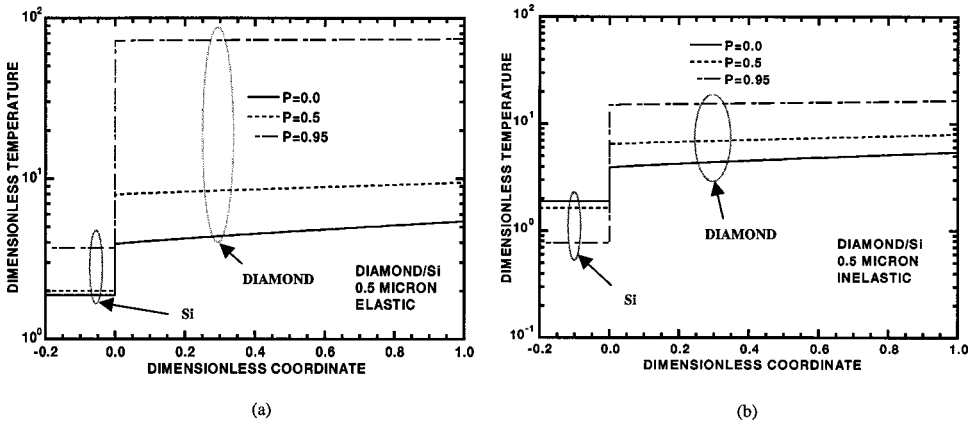

Fig. 2 Distribution of dimensionless temperature [$\Theta = C\nu(T-T_e)/4\pi q$] as a function of dimensionless coordinate (z/h)

strate interface is the smallest for diffuse interfaces ($P=0$). The temperature drop at the free surface of the film is, however, always very small (less than 2 percent, not shown in the figure), because of the assumption of a black emitting surface. For the case with $P=0.95$, nearly all the temperature drop is at the interface, while the internal temperature distribution is nearly uniform within the film. Not surprisingly, the inelastic model predicts a slightly smaller temperature drop at the interface, because of a larger phonon transmissivity predicted under this model.

Figures 3(*a*) and 3(*b*) show the results of TBR as a function of the film thickness. Both the elastic and inelastic acoustic mismatch models are used to approximate the TBR. From Fig. 3(*a*), it can be seen that for the diamond/Si system the TBR does not change much with thickness for the same specularity parameter, because the phonon temperature inside the film is nearly uniform. For the SiO_2/Si system, the TBR changes for small thickness when the incident phonons originate from locations with different temperatures.

Note that the totally diffuse interface with $P=0$ has the smallest TBR for the same film while the difference of the TBR values between the elastic and the inelastic mismatch models increases as the interface becomes increasingly specular. This is because of the relatively large transmissivity for phonons incident from the diamond or SiO_2 film into the silicon substrate calculated under the diffuse mismatch model, according to Eqs. (12) and (13). It should be pointed out that Eqs. (12) and (13) are based upon the argument that in the diffuse limit, it is impossible to distinguish which side phonons are originated. This model is at best estimation of the limiting case. The diffuse phonon interface scattering associated with the TBR phenomenon is poorly understood at this stage. For specular interfaces, the transmissivity is dependent on the incident angles as well as the physical properties of the two materials. The mismatch between diamond and Si is much larger than that between SiO_2 and Si, thus the diamond/Si system has a larger TBR, and the two systems behave quite differently with the elastic and inelastic mismatch model under the same specularity parameter value.

The effects of film thickness on the thermal conductivity of thin films are described in Figs. 4(*a*)–(*d*). Both internal thermal conductivity and external thermal conductivity are presented for the diamond/Si system in Figs. 4(*a*) and (*b*). Figures 4(*c*) and (*d*) depict the external thermal conductivity for the SiO_2/Si system. In measurements, external thermal conductivity is usually obtained, which changes with different substrates. In this study, the external thermal conductivity is much smaller than the internal one for the diamond film in the diamond/Si system, obviously due to the dominance of TBR.

Because of the interface scattering, the internal film thermal conductivity is lowered when the thickness is comparable to the MFP. When the film becomes thicker, its thermal conductivity approaches the bulk value as expected. Due to the computational limit of the computer used in this study, the film thickness used in the calculation for SiO_2 films cannot be very large. Nevertheless, it is still useful to compare the calculation with the measurement. The measured external thermal conductivity of PECVD SiO_2 is between 0.8 and 1.0 W/mK at 300K [7], when the film thickness

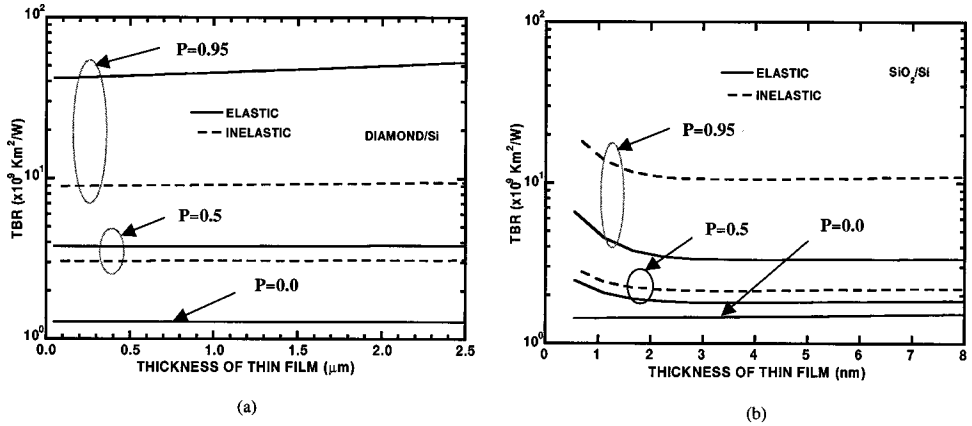

Fig. 3 Thickness dependence of the thermal boundary resistance, (*a*) for diamond/Si, (*b*) for SiO_2/Si

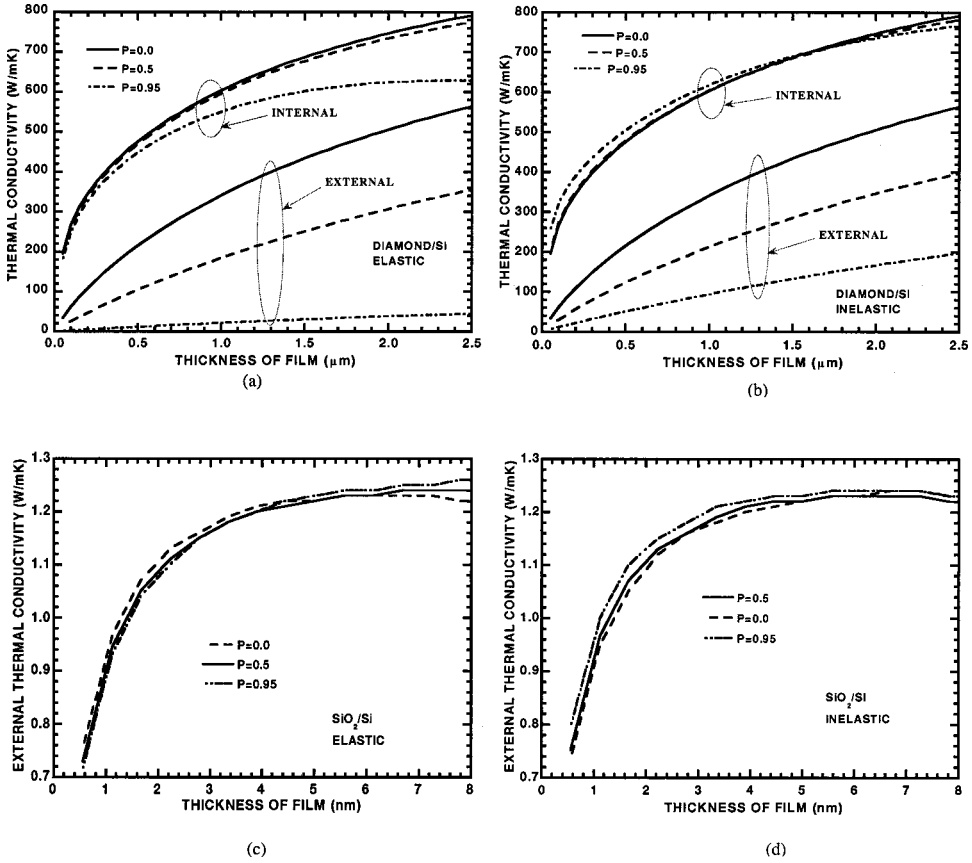

Fig. 4 Thickness dependence of thermal conductivity, (*a*) and (*b*) for diamond/Si, (*c*) and (*d*) for SiO_2/Si

is between 32 and 190 nm. The measured results cannot be explained using the size effect nor the intrinsic TBR as calculated here. Possible reasons for the observed reduction of the thermal conductivity of SiO_2 films include the porosity and a larger TBR probably caused by the increased disorder at the film/interface [8]. It is also worthwhile to point out that the heat conduction mechanisms in amorphous materials are not clear at this stage and the BTE based picture may be inappropriate. Cahill and Pohl [20] and Morath et al. [23] explained the heat conduction in amorphous solids on the atomic scale in terms of the transport by a random walk of energy rather than by propagating phonons.

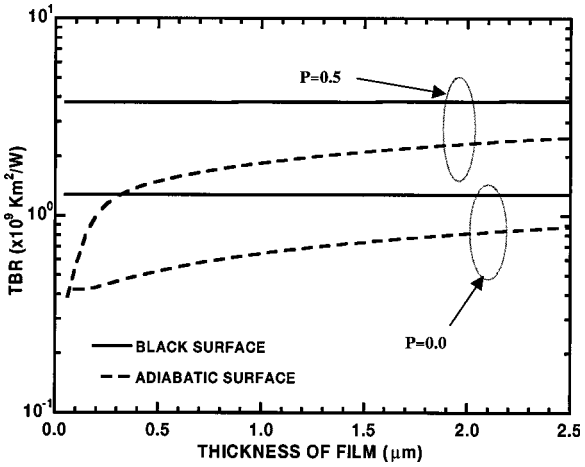

Fig. 5 Thickness dependence of TBR with and without internal heat generation

It is also noted that in Fig. 4(*b*) the internal thermal conductivity value for $P=0$ are smaller than the values for $P=0.95$, for the films with a thickness below 1.5 μm. This trend, predicted by the inelastic model, is reversed for films with a thickness greater than 1.5 μm for diamond/Si system. This behavior can be connected to Fig. 3(*a*), which shows a slight increasing trend of TBR as the film becomes thicker. This trend is caused by the fact that phonons reaching the interface come from different locations adjacent to the boundary. For the diamond/Si system, the large interface reflectivity accumulates more hot phonons originated further away from the interface, creating a larger TBR and a smaller internal thermal conductivity.

Figure 5 shows the TBR of the diamond/Si interface with internal heat sources. Two types of interface conditions are studied with $P=0.0$ and $P=0.5$. The free surface was set to be (1) black with a fixed temperature and (2) adiabatic. When the free surface is black, the TBR obtained for the case with internal heat generation is the same as that without internal heat generation. In other words, if the free surface of the film is still a black phonon emitter, the internal heat generation has no effect on the TBR. This is because the profile of the phonon intensity incident onto the interface is the same except that the whole curve of phonon intensity moves up. However, when the free surface is adiabatic, phonons incident onto the interface are affected by the reflection at the free surface. More phonons which are originally reflected can transmit through the interface due to multiple reflection, producing a smaller TBR. The TBR increases with increasing film thickness and approaches the value for black surface when the thickness is very large.

Figure 6 compares the temperature distributions for the diamond film with an internal heat source by using both Fourier's law and the BTE. The temperature distributions determined by Fourier's law are calculated in two ways: one is with the internal

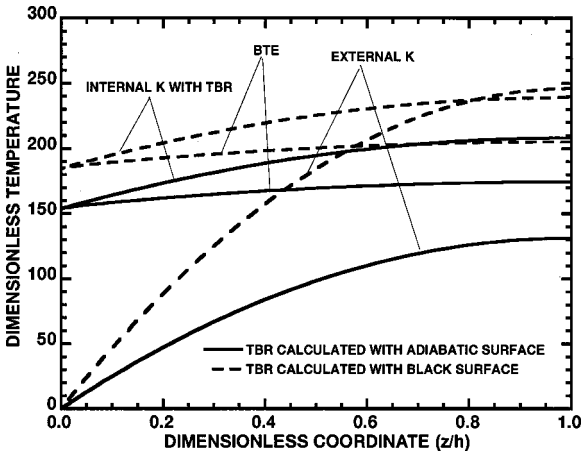

Fig. 6 Distribution of dimensionless temperature as a function of dimensionless coordinate for diamond/Si. The temperatures are normalized to heat flux.

thermal conductivity plus a TBR determined from the solution of the BTE, the other one is with the external thermal conductivity. Results for both a black surface boundary condition and an adiabatic surface boundary condition are presented. It can be seen that the BTE method predicts a lower temperature profile than Fourier's law using the internal conductivity, while the profile is higher than that using the external thermal conductivity. The difference of the temperature predicted by the BTE and Fourier's law means that the states of the phonons deviate from equilibrium states.

4 Conclusions

This work develops a unified model based on the BTE and interface scattering mechanisms to study the interplay between the size effects and the TBR. The major results can be summarized as follows:

1 The total thermal resistance across a film consists of two parts: one is the effective thermal resistance within the film, and the other one is the thermal boundary resistance at the interface. Both resistances may be dependent upon the film thickness and the physical properties of the two adjacent materials.

2 For the diamond/Si system, it is found that both the effective thermal resistance and the TBR are strongly dependent on the interface specularity. Thus the total thermal resistance is mainly determined by the interface conditions. The results indicate that the TBR is a dominant factor in the cross-plane thermal conductivity of diamond thin films.

3 For the SiO_2/Si system, the effective thermal conductivity of the film is independent of the specularity parameter, because SiO_2 and Si have very similar physical properties and because the short phonon MFP inside SiO_2. Neither the size effect nor the interface specularity is important for this system.

4 The temperature profile for diamond films with internal heat generation predicted by the Fourier theory using the internal thermal conductivity and TBR calculated from the BTE is closer to, but higher than, that obtained directly from solving the BTE. The temperature profile calculated by using the external thermal conductivity, which is often obtained from experimental measurement, deviates far from that by the BTE, especially at the interface. Large temperature jumps occur at the interface for the diamond/Si system because of the interface mismatch. The presence of the internal heat generation affects the TBR and thus the external thermal conductivity when the film is thin.

From this study, it is clear that extreme care must be taken when applying the thermal conductivity measurement results for thin films obtained under one configuration to other situations.

Acknowledgments

This project is partially supported through an NSF Young Investigator Award to GC and DOD MURI grant on thermoelectrics.

Nomenclature

C = volumetric specific heat [J/m^{3}K]
E_i = exponential integral function
h = thickness of film [m]
I = phonon intensity [W/m^2.sr]
K = thermal conductivity [W/mK]
P = interface specularity parameter
R = thermal boundary resistance [Km^2/W]
R_{12} = phonon reflectivity
S = internal heat source [W/m^3]
T = temperature [K]
T_e = emitting temperature of phonons [K]
v = group velocity [m/s]
z = coordinate
Λ = mean free path [m]
Θ = dimensionless temperature
θ = angle [rad]
ρ = density [kg/m^3]
μ = directional cosine [$=\cos(\theta)$]
χ = dimensionless phonon frequency
τ = relaxation time [s]
ξ = dimensionless coordinate
η = dimensionless scattering strength

Subscripts

d = diffuse
s = specular
U = Umklapp scattering
1 = medium 1
2 = medium 2
12 = from medium 1 to medium 2

Superscripts

0 = equilibrium
+ = positive direction
− = negative direction

Abbreviations

MFP = mean free path
TBR = thermal boundary resistance

Appendix A

Intensity Equations for Black Surface. Equations used to calculate intensity/temperature distributions and thermal conductivities are simplified as

$$2I^0(\xi)=PI^0(T_2)\int_0^1 R_{s12}e^{-(\xi+\xi_h)/\mu}d\mu+(1-P)T_{d21}E_2(\xi)I_2(T_e)$$
$$+E_2(\xi_h-\xi)I^0(T_2)+2(1-P)R_{d12}E_2(\xi)\left[E_3(\xi_h)I^0(T_2)\right.$$
$$\left.+\int_0^{\xi_h} I^0(\xi_1)E_2(\xi_1)d\xi_1\right]$$
$$+P\int_0^{\xi_h} I^0(\xi_1)\int_0^1 e^{-(\xi+\xi_1)/\mu}R_{s12}\frac{1}{\mu}d\mu d\xi_1$$
$$+PI^0(T_e)\int_0^1 t_{s21}e^{-\xi/\mu}d\mu+\int_0^{\xi_h} I^0(\xi_1)E_1(|\xi_1-\xi|)d\xi_1 \quad (A1)$$

$$I^+(\xi_h,\mu)=\frac{1}{\mu}PR_{s12}e^{-\xi_h/\mu}\int_0^{\xi_h}I^0(\xi_1)e^{-\xi_1/\mu}d\xi_1$$
$$+PR_{s12}e^{-2\xi_h/\mu}I^0(T_2)+Pt_{s21}e^{-\xi_h/\mu}I^0(T_e)$$
$$+2(1-P)R_{d12}e^{-\xi_h/\mu}E_3(\xi_h)I^0(T_2)$$
$$+\frac{1}{\mu}\int_0^{\xi_h}I^0(\xi_1)e^{(\xi_1-\xi_h)/\mu}d\xi_1$$
$$+(1-P)T_{d12}e^{-\xi_h/\mu}I^0(T_e)$$
$$+2(1-P)R_{d12}e^{-\xi_h/\mu}\int_0^{\xi_h}I^0(\xi_1)E_2(\xi_1)d\xi_1. \quad (A2)$$

For room temperature and higher, the phonon intensity can be expressed as $I^0(T)=I^0(T_e)+Cv/4\pi(T-T_e)$. In the calculation, the above two equations are simplified by setting $T_e=0$, which can be justified as follows. Suppose that the whole system is at equilibrium with T_e (this can be achieved by letting $T_2=T_e$), the above two equations still hold. By subtracting the two equilibrium equations from (*A*1) and (*A*2), and dividing all terms by $Cv/4\pi(T_2-T_e)$, two new equations are obtained. These two new equations can be written down by replacing $I^+(\xi_h)$ with $4\pi I^+(\xi_h)/Cv(T_2-T_e)$, $I^0(\xi)$ with $T-T_e/T_2-T_e$, $I^0(T_2)=1$, and $I^0(T_e)=0$.

The equilibrium temperature at the substrate side of the interface, T^*, should be calculated from the phonon intensities coming from the free surface of the substrate and those phonons penetrating through the interface from the film side:

$$2I^0(T^*)=I^0(T_e)+P\int_0^1(R_{s21}I^0(T_e)+t_{s12}I^-(0,-\mu))d\mu$$
$$+(1-P)\left(R_{d21}I^0(T_e)+2T_{d12}\int_0^1 I^-(0,-\mu)\mu d\mu\right). \quad (A3)$$

Appendix B

Intensity Equations for Adiabatic Surface. The two equations used to calculate the temperature/intensity profiles with an internal heat source are

$$2I^0(\xi)=2P\int_0^1 R_{s12}e^{-(\xi+\xi_h)/\mu}d\mu\int_0^1 I^+(\xi_h,\mu)\mu d\mu$$
$$+PI^0(T_e)\int_0^1 t_{s21}e^{-\xi/\mu}d\mu$$
$$+P\int_0^{\xi_h}I^0(\xi_1)\int_0^1 e^{-(\xi+\xi_1)/\mu}R_{s12}\frac{1}{\mu}d\mu d\xi_1$$
$$+2(1-P)R_{d12}E_2(\xi)\left[2E_3(\xi_h)\int_0^1\mu I^+(\xi_h)d\mu\right.$$
$$\left.+\int_0^{\xi_h}I^0(\xi_1)E_2(\xi_1)d\xi_1\right]+2E_2(\xi_h-\xi)$$
$$\times\int_0^1 I^+(\xi_h,\mu)\mu d\mu+\int_0^{\xi_h}I^0(\xi_1)E_1(|\xi_1-\xi|)d\xi_1$$
$$+(1-P)T_{d21}E_2(\xi)I^0(T_e)+S\Lambda/4\pi \quad (B1)$$

$$I^+(\xi_h,\mu)=\frac{1}{\mu}PR_{s12}e^{-\xi_h/\mu}\int_0^{\xi_h}I^0(\xi_1)e^{-\xi_1/\mu}d\xi_1$$
$$+2PR_{s12}e^{-\xi_h/\mu}\int_0^{\xi_h}\mu I^+(\xi_h,\mu)d\mu+4(1-P)$$
$$\times R_{d12}e^{-\xi_h/\mu}E_3(\xi_h)\int_0^1\mu I^+(\xi_h,\mu)d\mu$$
$$+\frac{1}{\mu}\int_0^{\xi_h}I^0(\xi_1)e^{(\xi_1-\xi_h)/\mu}d\xi_1+Pt_{s21}e^{-\xi_h/\mu}I^0(T_e)$$
$$+2(1-P)R_{d12}e^{-\xi_h/\mu}\int_0^{\xi_h}I^0(\xi_1)E_2(\xi_1)d\xi_1$$
$$+(1-P)T_{d21}e^{-\xi_h/\mu}I^0(T_e). \quad (B2)$$

The reference point is set at T^*, the equivalent phonon temperature of the substrate at the interface. The intensities are normalized against $S\Lambda$.

References

[1] Tien, C. L., Majumdar, A., and Gerner, F., 1998, *Microscale Energy Transport*, Taylor and Francis, New York.
[2] Cahill, D. G., Fischer, H. E., Klitsner, T., Swartz, E. T., and Pohl, R. O., 1988, ''Thermal Conductivity of Thin Films: Measurements and Understanding,'' J. Vac. Sci. Technol. A, **7**, pp. 1259–1266.
[3] Swartz, E. T., and Pohl, R. O., 1989, ''Thermal Boundary Resistance,'' Rev. Mod. Phys., **61**, pp. 605–668.
[4] Majumdar, A., 1993, ''Microscale Heat Conduction in Dielectric Thin Films,'' ASME J. Heat Transfer, **115**, pp. 7–16.
[5] Chen, G., and Tien, C. L., 1993, ''Thermal Conductivities of Quantum Well Structures,'' J. Thermophys. Heat Transfer, **7**, pp. 311–318.
[6] Little, W. A., 1959, ''The Transport of Heat Between Dissimilar Solids at Low Temperatures,'' Can. J. Phys., **37**, pp. 334–349.
[7] Lee, S.-M., and Cahill, D. G., 1997, ''Heat Transport in Thin Dielectric Films,'' J. Appl. Phys., **81**, pp. 2590–2595.
[8] Goodson, K. E., Flik, M. I., Su, L. T., and Antoniadis, D. A., 1993, ''Annealing-Temperature Dependence of the Thermal Conductivity of LPCVD Silicon-Dioxide Layers,'' IEEE Electron Device Lett., **14**, pp. 490–492.
[9] Goodson, K. E., Kading, O. W., Rosler, M., and Zachai, R., 1995, ''Experimental Investigation of Thermal Conduction Normal to Diamond-silicon Boundaries,'' J. Appl. Phys., **77**, pp. 1385–1392.
[10] Chen, G., 1998, ''Thermal Conductivity and Ballistic-Phonon Transport in the Crossplane Direction of Superlattices,'' Phys. Rev. B, **57**, pp. 14958–14973.
[11] Jen, C.-P., and Chieng, C.-C., 1998, ''Microscale Thermal Characterization for Two Adjacent Dielectric Thin Films,'' J. Thermophys. Heat Transfer, **12**, pp. 146–152.
[12] Gaze, J., Oyanagi, N., Yamamoto, I., and Izawa, H., 1998, ''Laser Ablation Doping Process for the Synthesis of Conductive Diamond Thin Film,'' Thin Solid Films, **322**, pp. 28–32.
[13] Min, G., and Rowe, D. M., 1999, ''Cooling Performance of Integrated Thermoelectric Microcooler,'' Solid-State Electron., **43**, No. 5, pp. 923–929.
[14] Chen, G., 1997, ''Size and Interface Effects on Thermal Conductivity of Superlattices and Periodic Thin-Film Structures,'' ASME J. Heat Transfer, **119**, pp. 220–229.
[15] Siegel, R., and Howell, J., 1993, *Thermal Radiation Heat Transfer*, Hemisphere, Washington, D.C.
[16] Ziman, J. M., 1960, *Electrons and Phonons*, Clarendon Press, Oxford, England.
[17] Shen, P., and Zhou, M., 1991, ''Heat Conduction of Amorphous Solids: Simulation Results on Model Structure,'' Science, **253**, pp. 539–542.
[18] Goodson, K. E., 1996, ''Thermal Conduction in Nonhomogeneous CVD Diamond Layers in Electronic Microstructures,'' ASME J. Heat Transfer, **118**, pp. 279–286.
[19] Touloukian, Y. S., Powell, R. W., Ho, C. Y., and Klemens, P. G., 1970, *Thermophysical Properties of Matter*, IFI/Plenum, New York.
[20] Cahill, D. G., and Pohl, R. O., 1987, ''Thermal Conductivity of Amorphous Solids Above the Plateau,'' Phys. Rev. B, **35**, pp. 4067–4072.
[21] Shackelford, J. F., ed., 1994, *CRC Materials Science and Engineering Handbook*, 2nd Ed., CRC Press, Boca Raton, FL.
[22] Brady, G. S., and Clauser, H. R., 1986, *Materials Handbook*, 20th Ed., McGraw-Hill, New York.
[23] Morath, C. J., Maris, H. J., Cuomo, J. J., Pappas, D. L., Grill, A., Patel, V. V., Doyle, J. P., and Saenger, K. L., 1994, ''Picosecond Optical Studies of Amorphous Diamond and Diamond-Like Carbon: Thermal Conductivity and Longitudinal Sound Velocity,'' J. Appl. Phys., **76**, pp. 2636–2640.

Heat Rate Predictions in Humid Air-Water Heat Exchangers Using Correlations and Neural Networks

Arturo Pacheco-Vega
Gerardo Díaz
Mihir Sen
E-mail: Mihir.Sen.1@nd.edu
K. T. Yang
Rodney L. McClain

Department of Aerospace
and Mechanical Engineering,
University of Notre Dame,
Notre Dame, IN 46556

We consider the flow of humid air over fin-tube multi-row multi-column compact heat exchangers with possible condensation. Previously published experimental data are used to show that a regression analysis for the best-fit correlation of a prescribed form does not provide an unique answer, and that there are small but significant differences between the predictions of the different correlations thus obtained. It is also shown that it is more accurate to predict the heat rate directly rather than through intermediate quantities like the j-factors. The artificial neural network technique is offered as an alternative technique. It is trained with experimental values of the humid-air flow rates, dry-bulb and wet-bulb inlet temperatures, fin spacing, and heat transfer rates. The trained network is then used to make predictions of the heat transfer. Comparison of the results demonstrates that the neural network is more accurate than conventional correlations.
[DOI: 10.1115/1.1351167]

Keywords: Artificial Intelligence, Condensation, Convection, Heat Transfer, Heat Exchangers

1 Introduction

For the design of a thermal system it is often necessary, for selection purposes, to predict the heat transfer rates of heat exchangers under specific operating conditions. Heat exchangers are complex devices, the complexity being due both to the geometry and to the physical phenomena involved in the transfer of heat. For a heat exchanger operating with humid air, e.g., in refrigeration and air-conditioning applications, some of the moisture in the air may condense on the fins and tubes. Condensing heat exchangers have been studied by Jacobi and Goldschmidt [1], Srinivasan and Shah [2], Ramadhyani [3], and Jang et al. [4], among others, using heat and mass transfer coefficients. Physical processes related to the latent heat and modification of the flow field by the water film or droplets increase the computational difficulty of the problem, and numerical calculations entirely based on first principles are not possible. Experiments must be carried out, usually by the manufacturers for each of their models, to determine the heat rates as functions of the system parameters like the flow rates, inlet temperatures and fin spacing. The experimental information must then be transferred in some way to the user of the information who needs it to predict the heat rates under different operating conditions. One way is to provide the heat transfer coefficients. However, these are not constant but vary considerably with operating conditions, and can thus provide only very rough approximations. A better and more common procedure is to compress information about the heat transfer coefficients by means of correlations so that variations with respect to the operating parameters can be taken into account through standard nondimensional groups. Usually the form of the correlation cannot be totally justified from first principles; it is selected on the basis of simplicity and common usage. Estimated errors in heat rates from correlations are normally larger than the experimental error, being mainly due to the data compression that occurs through the correlation process. Another reason for inaccuracy in predictions is that, for most forms of correlating functions that are used, a least-squares analysis of the error gives multiple sets of values for the constants indicating that a local, rather than a global, optimum set of values may have been found.

The problem of accuracy in condensing heat exchangers predictions is addressed by an alternative approach using artificial neural networks (ANNs). ANNs have been developed in recent years and used successfully in many application areas, among them thermal engineering [5]. Some examples are heat transfer data analysis [6], manufacturing and materials processing [7,8], solar receivers [9], convective heat transfer coefficients [10], and HVAC control [11]. Previous work on the prediction of heat rates in heat exchangers without condensation has been reported by Zhao et al. [12] and Diaz et al. [13]. The most attractive advantage of the method is that it allows the modeling of complex systems without requiring detailed knowledge of the physical processes.

In the present work, we are interested in using ANNs for the prediction of the performance of heat exchangers with condensation. There is a body of published experimental data related to this problem that we will use. First, the procedure for obtaining correlations using a least-squares regression analysis will be studied with special regard to the multiplicity of the result. Second, we will consider the advantages of predicting the heat rate directly, instead of using *j*-factors to determine the transfer coefficients from which the heat rates have to be calculated, as is usually done. Finally, the heat rate will be computed using artificial neural networks.

2 Published Data and Correlations

Extensive experimental data from five different multiple-row multiple-column plate-fin type heat exchangers with staggered tubes were obtained and published by McQuiston [14,15]. Because of their importance to applications such as air-conditioning and refrigeration these data and the corresponding correlations have become standards in the field. The fluids used were atmospheric air flowing through the fin passages and water inside the tubes. The conditions were such that, for certain cases, condensation would occur on the fins. The nature of the air-side surface, i.e., whether dry, covered with condensed water droplets, or covered with a water film, was determined by direct observations and recorded. All five heat exchangers had a nominal size of $127\ \text{mm} \times 305\ \text{mm}$, were geometrically similar but with different fin spacings. A schematic with the geometrical parameters and dimensions is shown in Fig. 1. It must be noted that, even when there is no condensation, analysis of the data shows that the specific humidities at the inlet and outlet vary by as much as 150

Contributed by the Heat Transfer Division for publication in the JOURNAL OF HEAT TRANSFER. Manuscript received by the Heat Transfer Division January 12, 2000; revision received October 3, 2000. Associate Editor: R. Mahajan.

percent. This discrepancy may be due to heat losses between the locations at which the temperatures were measured and the heat exchanger. The data for dropwise and film condensation could also have been similarly affected.

McQuiston [15,16] was interested in predicting the air-side heat transfer. He used high Reynolds-number turbulent flow on the water side so that its heat transfer coefficient, which could be estimated from the Dittus-Boelter correlation, was much higher than that on the air side and thus introduced little error. He defined the air-side heat transfer coefficients using the log-mean temperature difference for the dry surface. A similar procedure was followed for determining the air-side heat transfer coefficients under condensing conditions using the enthalpy difference as the driving potential. The correlations that were obtained are

$$j_s = 0.0014 + 0.2618\,\mathrm{Re}_D^{-0.4}\left(\frac{A}{A_{tb}}\right)^{-0.15} f_s(\delta) \tag{1}$$

$$j_t = 0.0014 + 0.2618\,\mathrm{Re}_D^{-0.4}\left(\frac{A}{A_{tb}}\right)^{-0.15} f_t(\delta), \tag{2}$$

where

$$f_s = \begin{cases} 1.0 & \text{for dry surface} \\ (0.90 + 4.3\times 10^{-5}\,\mathrm{Re}_\delta^{1.25})\left(\dfrac{\delta}{\delta - t}\right)^{-1} & \text{for dropwise condensation} \\ 0.84 + 4.0\times 10^{-5}\,\mathrm{Re}_\delta^{1.25} & \text{for filmwise condensation} \end{cases} \tag{3}$$

$$f_t = \begin{cases} 1.0 & \text{for dry surface} \\ (0.80 + 4.0\times 10^{-5}\,\mathrm{Re}_\delta^{1.25})\left(\dfrac{\delta}{\delta - t}\right)^{4} & \text{for dropwise condensation} \\ (0.95 + 4.0\times 10^{-5}\,\mathrm{Re}_\delta^{1.25})\left(\dfrac{\delta}{\delta - t}\right)^{2} & \text{for filmwise condensation} \end{cases} \tag{4}$$

$$j_s = \frac{h_a}{G_c c_{p,a}}\mathrm{Pr}_a^{2/3}, \quad j_t = \frac{h_{t,a}}{G_c}Sc_a^{2/3} \tag{5}$$

$$\mathrm{Re}_D = \frac{G_c D}{\mu_a}, \quad \mathrm{Re}_\delta = \frac{G_c \delta}{\mu_a}, \quad \frac{A}{A_{tb}} = \frac{4}{\pi}\frac{x_a}{D_h}\frac{x_b}{D}\sigma_f, \tag{6}$$

where j_s is the Colburn j-factor for the sensible heat and j_t is that for the total heat. Of course, in the dry case the two are the same. The range of validity of the correlation was also given.

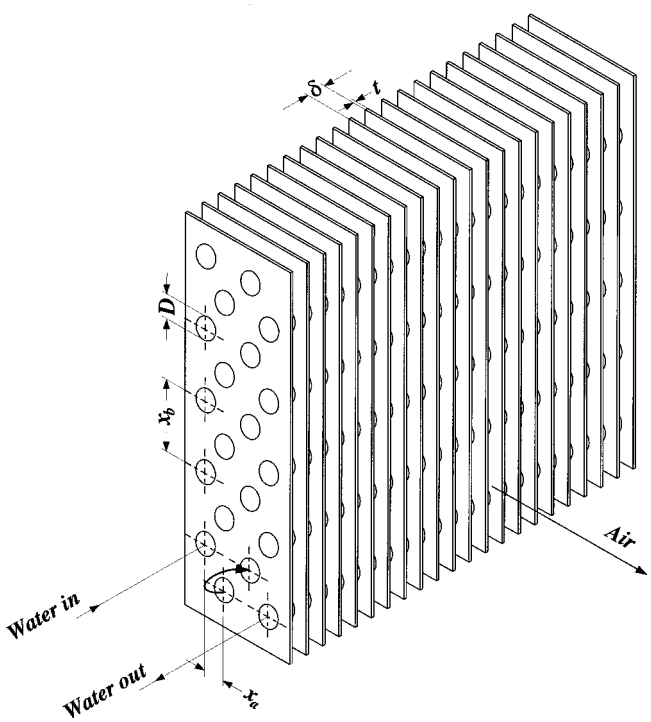

Fig. 1 Schematic of a compact fin-tube heat exchanger

Gray and Webb [17] added data from other sources to find a different correlation

$$j_s = 0.14\,\mathrm{Re}_D^{-0.328}\left(\frac{x_b}{x_a}\right)^{-0.502}\left(\frac{\delta - t}{D}\right)^{0.0312} \quad \text{for dry surface} \tag{7}$$

with its corresponding range of applicability.

3 Multiplicity of ''Best'' Correlations

Let us look at a regression analysis to find the best correlation for the dry surface, the procedure for the other cases being similar. The general form of this correlation, as proposed by McQuiston [16], is

$$j_s = a + b\,\mathrm{Re}_D^{-c}\left(\frac{A}{A_{tb}}\right)^{-d}. \tag{8}$$

In a least-squares method the difference between the measured and the predicted values of j_s is minimized to determine the constants a, b, c, and d in the above equation. This is done by calculating the variance of the error defined as

$$S_{j_s} = \frac{1}{M_1}\sum_{i=1}^{M_1}[(j_s)_i^e - (j_s)_i^p]^2, \tag{9}$$

where $(j_s)_i^e$, for $i = 1,...,M_1$, are the experimental measurements and $(j_s)_i^p$, for $i = 1,...,M_1$, are the values predicted by Eq. (8). $S_{j_s}(\mathbf{C})$ is a smooth manifold in a five-dimensional space, where $\mathbf{C} = (a,b,c,d)$ is the vector of unknown constants, and a search must find $\mathbf{C}$ such that $S_{j_s}(\mathbf{C})$ is a minimum.

This procedure was carried out for the M_1 data sets. It was found that S_{j_s} had multiple local minima, the following two being examples.

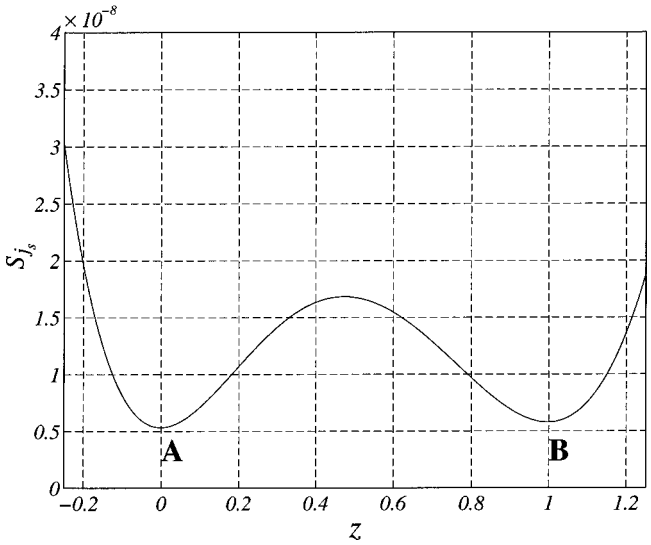

Fig. 2 Section of the surface $S_{j_s}(a,b,c,d)$; A is the global minimum; B is a local minimum

$$\text{Correlation A:}\quad j_s = -0.0218 + 0.0606\,\mathrm{Re}_D^{-0.0778}\left(\frac{A}{A_{tb}}\right)^{-0.0187} \tag{10}$$

$$\text{Correlation B:}\quad j_s = -0.0057 + 0.0562\,\mathrm{Re}_D^{-0.1507}\left(\frac{A}{A_{tb}}\right)^{-0.0436} \tag{11}$$

Superficially, the two correlations appear to be quantitatively different, and are both different from Eq. (1).

Figure 2 shows a section of the S_{j_s} surface that passes through the two minima, *A* and *B*. For clarity the location coordinate *z* is such that $\mathbf{C}=\mathbf{C}_A(1-z)+\mathbf{C}_B z$, where $\mathbf{C}_A=(a,b,c,d)_A$ and $\mathbf{C}_B=(a,b,c,d)_B$ correspond to the two minima. These two minimum values of S_{j_s} are within 17.1 percent of each other and the corresponding j_s predictions are within 3.7 percent. Thus the error in heat rate prediction would increase somewhat if the higher minimum is chosen instead of the lower one.

Multiplicity of minima of the error surface comes from the mathematical form of the correlating function assumed, Eq. (8), and the nonlinearity of the function S_{j_s}, Eq. (9), to be minimized. Faced with this, it is natural to search for the global minimum among the various local minima of S_{j_s} which would then be *the* best correlation. One of the ways in which this can be done is by a genetic algorithm [18]. In fact, correlation A above is found to be the global minimum.

Table 1 Comparison of percentage errors in j_s, j_t, and $\dot{Q}$ predictions between various correlations and the ANN

Surface	*Prediction method*	j_s	j_t	$\dot{Q}$
Dry	McQuiston (1978b)	14.57	14.57	6.07
	Gray & Webb (1986)	11.62	11.62	4.95
	Eq. (10)	8.1	8.1	3.84
	Eq. (15)	9.3	9.3	3.84
	ANN	1.002	1.002	0.928
Dropwise	McQuiston (1978b)	8.50	7.55	8.10
	Minimizing S_j	9.12	9.43	9.91
	Minimizing $S_{\dot{Q}}$	–	17.76	4.27
	ANN	3.32	3.87	1.446
Filmwise	McQuiston (1978b)	9.01	14.98	10.25
	Minimizing S_j	8.32	10.89	10.44
	Minimizing $S_{\dot{Q}}$	–	18.97	4.34
	ANN	2.58	3.15	1.960
Combined	ANN	4.58	5.05	2.69

The same global search procedure has been followed to find the best correlations for dropwise and film condensation by first fixing the constants found for the dry surface and then searching for the additional constants that Eqs. (3) and (4) have. The results of the correlations for the dry surface are shown in Table 1 as ''Eq. (10),'' and for the wet surfaces as ''Minimizing S_j.'' The table shows the ability of the correlations to predict the same data from which they were derived. The errors indicated are the root-mean-square (rms) values of the percentage differences between the predicted and experimental data. The results of the correlations of McQuiston [16] for all surfaces and Gray and Webb [17] for dry surfaces only are also shown; as claimed, the latter is seen to perform better than the former. The correlations found here using the global search technique are much better than the previous correlations for the dry surface, slightly worse for dropwise and slightly better for filmwise condensations. Some of the differences could be due to possible elimination of outliers by previous investigators; none of the published data has been excluded here.

4 Direct Correlation of Heat Rate

Using the method of the previous section to determine the heat rate, which is what the user of the information is usually interested in, one must find the *j*-factor first, then the heat transfer coefficient, and finally the heat rate. The procedure gives some generality to the results since different fluids and temperatures can be used. If accuracy is the goal, however, it may be better to correlate the heat rate directly, as will be investigated in this section. The dry-surface case is discussed in some detail, and for the wet surfaces the procedure is similar.

Using the water-side heat transfer coefficient defined on the basis of the log-mean temperature difference [15], the heat rate is

$$\dot{Q} = (T_w^{\text{in}} - T_a^{\text{in}})\,\frac{1-\exp\{UA[(\dot{m}_w c_{p,w})^{-1}-(\dot{m}_a c_{p,a})^{-1}]\}}{(\dot{m}_a c_{p,a})^{-1}-(\dot{m}_w c_{p,w})^{-1}\exp\{UA[(\dot{m}_w c_{p,w})^{-1}-(\dot{m}_a c_{p,a})^{-1}]\}}, \tag{12}$$

where

$$U = \left(\frac{A}{A_w h_w} + \frac{Pr_a^{2/3}}{\eta G_c c_{p,a} j_s}\right)^{-1} \tag{13}$$

and j_s is given in Eq. (8). To find the constants in the correlation, the mean square error of the heat transfer rates

$$S_{\dot{Q}} = \frac{1}{M_1}\sum_{k=1}^{M_1}[\dot{Q}_k^e - \dot{Q}_k^p]^2 \tag{14}$$

must be minimized. A genetic-algorithm based global search results in a correlation, which when converted to a *j*-factor is

$$j_s = -0.0479 + 0.0971\,\mathrm{Re}_D^{-0.0631}\left(\frac{A}{A_{tb}}\right)^{-0.0137}, \qquad (15)$$

which is different from Eqs. (1), (10), and (11), all of which have been obtained from the same data.

The results of using direct correlation of the heat rate are also shown in Table 1 as ''Eq. (15).'' The percentage error is 3.84 percent, which is the same as that given by Eq. (10). However, if we compare the absolute, dimensional rms error, direct correlation of heat rate shows an error of only 158.6 W, compared to an error of 272 W from the *j*-factor correlation; this is an improvement of 41.7 percent. The global minimization of S_j does not necessarily imply the global minimization of $S_{\dot{Q}}$. The difference of the predictions in j_s is 14.8 percent between the two methods.

A similar procedure was followed to find the correlations for j_t under wet-surface conditions, and the errors are given in Table 1 under ''Minimizing $S_{\dot{Q}}$''. The direct correlation of dimensional heat rate gives predictions that have 56.9 percent less error compared to the *j*-factor correlation for dropwise condensation and 58.6 percent for film condensation. Thus, predicting the heat rate rather than *j*-factors gives more accurate predictions. This is somewhat expected since the *j*-factor assumes the existence of the heat transfer coefficient, while $\dot{Q}$ does not.

5 Artificial Neural Networks

ANNs offer an attractive alternative to the correlation method discussed in the previous sections to predict the performance of heat exchangers. Although there are many different types of neural networks, the feedforward configuration has become the most widely used in engineering applications [19]. This consists of a series of layers, each with a number of nodes, the first and last layers being the input and output layers while the remaining are hidden layers. The nodes of each layer are connected only to those of the layer before and the one after. The connections are associated with weights and the nodes with biases. These can be adjusted during the training procedure using known data: for a given input the actual output is compared with the target output, and the weights and biases are repeatedly adjusted using the backpropagation algorithm [20] until the actual differs little from the target output. All variables are normalized to be within the [0.15, 0.85] range. Further details are in Sen and Yang [5].

5.1 Separation of Data for Training and Testing. The ANN structure chosen for the present analysis consists of four layers: the input layer at the left, the output layer at the right and two hidden layers. This 5-5-3-1 configuration, where the numbers stand for the number of nodes in each layer, is similar to the schematic shown in Fig. 4 which is used in the next section for the heat exchanger analysis, the only difference being that the fourth layer has only one output, the heat rate. The inputs to the network correspond to the air-flow Reynolds number Re_D, inlet air dry-bulb temperature $T_{a,db}^{\mathrm{in}}$, inlet air wet-bulb temperature $T_{a,wb}^{\mathrm{in}}$, inlet water temperature T_w^{in}, and fin spacing δ. The output is the total heat rate $\dot{Q}$. For testing the trained ANN, the variables Re_D, $T_{a,db}^{\mathrm{in}}$, $T_{a,wb}^{\mathrm{in}}$, T_w^{in}, and δ are input and the corresponding $\dot{Q}^p$ are predicted.

A total of $M=327$ experimental runs were reported by McQuiston [15] for three different surface conditions. The data can be separated in different ways into training and testing data. Díaz et al. [13], for example, used 75 percent of the total data sets available for training and the rest for testing. This has two disadvantages: first, the data set available for training is smaller than the total amount of information available so that the predictions are not the best possible, and second, if the training data do not include the extreme values the predictions fall in the extrapolated range and are hence less reliable. The issue of separating the complete data into training and testing sets is further analyzed in the following way.

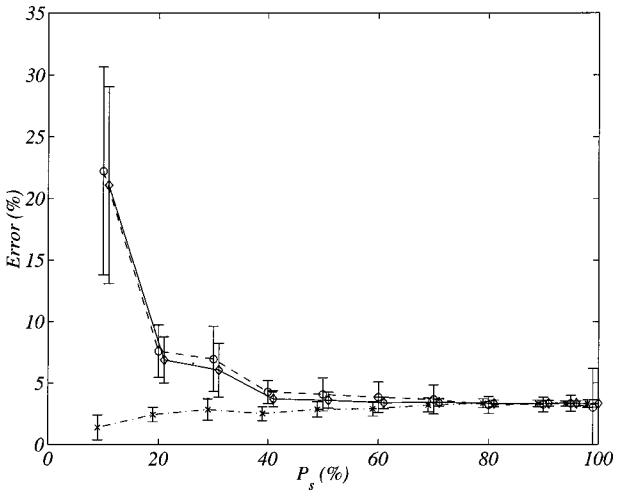

Fig. 3 ANN prediction errors versus percentage of data used for training; –×– error E_a using training data; –○– error E_b using data not used for training; –◇– error E using complete data. Error bars indicate standard deviations. The E_a and E curves have been shifted horizontally by −1 percent and 1 percent, respectively, for clarity.

The M available sets of experimental data are first randomly sorted to avoid introducing any bias in the selection process and their order is then fixed. Only the first M_a of these are chosen for training and the rest $M_b = M - M_a$ kept aside for the moment. The fraction used for training is thus $P_s = M_a/M$. The rms values of the relative output errors

$$S_{e_{\dot{Q}}} = \left[\frac{1}{M_a}\sum_{i=1}^{M_a}\left(\frac{\dot{Q}_i^p - \dot{Q}_i^e}{\dot{Q}_i^e}\right)^2\right]^{1/2} \qquad (16)$$

are calculated at each cycle of the training process in order to evaluate the performance of the network and to update the weights. Here $i=1,...,M_a$, where $\dot{Q}^p$ are the predictions, and $\dot{Q}^e$ are the experimental values of the heat rates. A reasonably low level of error, $S_{e_{\dot{Q}}}$, in the training process is obtained with 250,000 cycles, which is the same for the rest of the procedure.

After the training is finished, three different data sets are tested: (*a*) the same M_a data that were used for training are tested, (*b*) the M_b data left out of the training process are tested, and (*c*) the complete M data sets are tested. In each case the percentage error between the predicted and experimental values are calculated, being E_a, E_b, and E, respectively. Without reordering the M data sets the procedure described above is repeated for different values of the percentage of splitting, i.e., $P_s = 10$ percent, 20 percent,..., 90 percent, 95 percent, and 99 percent. The exact shape of the error versus P_s curve depends on the initial order of the data sets, but some general features can be identified.

To get the overall characteristics of the error, the curves were calculated ten times and the results averaged to remove the influence of the initial random ordering of the data sets. Figure 3 shows the average error in prediction calculated in the three different ways as a function of the training fraction P_s. The error bars indicate the standard deviations, σ_a, σ_b, and σ corresponding to E_a, E_b, and E, respectively, that resulted from the ten different curves. From this figure, it can be seen that as P_s increases the prediction errors for all three cases asymptote, on the average, to approximately the same values. For any P_s, E_a is always small since the training and testing data are identical. At small values of P_s, E_b, and E are both very large indicating that an insufficient fraction of the data has been used for training. As we increase M_a, better predictions are obtained. Beyond $P_s = 60$ percent approximately the differences in the prediction errors

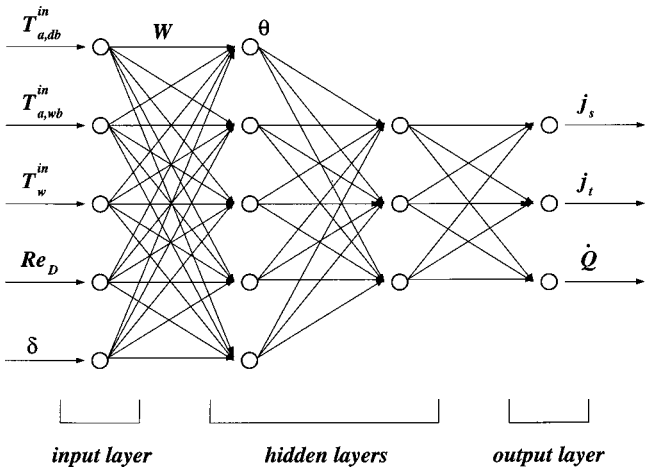

Fig. 4 A 5-5-3-3 neural network used

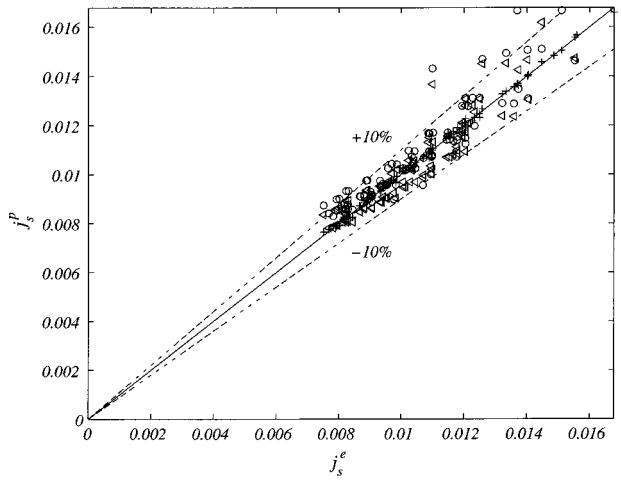

Fig. 5 Experimental versus predicted j_s for heat exchanger with dry surface; + ANN; ◁ McQuiston [16]; ○ Gray and Webb [17]. Straight line is the perfect prediction.

for all data sets are small. The same trend is observed for the σs which become smaller as $P_s \rightarrow 100$ percent, indicating that the prediction is somewhat insensitive to the initial random ordering of the data. Near the end, however, at $P_s = 99$ percent for example, σ_b becomes large again because now M_b is very small and the error depends greatly on the data set that is picked for testing.

From this exercise one can deduce that, in this case at least, if more than 60 percent of the available data is used for training, the results will be essentially the same. In the rest of the paper we use all of the available data for training, and use the same for testing. This gives us the best prediction over the widest parameter range. For the correlations also, as is commonly done, the entire data set was used for finding the correlation and testing its predictions.

5.2 Heat Exchanger Analysis. From the total of $M = 327$ experimental runs were reported by McQuiston [15], $M_1 = 91$ corresponded to dry-surface conditions, $M_2 = 117$ corresponded to dropwise condensation, and $M_3 = 119$ to film condensation. Figure 4 shows a schematic of the feedforward neural network configuration used for the present analysis. There are four layers in this configuration. The inputs to the network correspond to the same physical variables described in the previous section. The outputs correspond to j_s, j_t, and the total heat rate $\dot{Q}$. Thus, j_s, j_t, and $\dot{Q}$ are functions of Re_D, $T^{\mathrm{in}}_{a,db}$, $T^{\mathrm{in}}_{a,wb}$, T^{in}_{w}, and δ. For testing the trained ANN, the physical variables are input and the corresponding j_s^p and j_t^p and $\dot{Q}^p$ are predicted. The j-factors are not necessary for the heat rate predictions, but are calculated here merely for the purpose of comparison with the other methods.

As mentioned before, the performance of the network is evaluated by computing the rms values of the output errors

$$S_e = \left[\frac{1}{M_k} \sum_{i=1}^{M_k} \left(\frac{O^p_{i,k} - O^e_{i,k}}{O^e_{i,k}} \right)^2 \right]^{1/2} \tag{17}$$

at each stage of the training. Now $i = 1,...,M_k$, $k = 1,2,3$, where $O^p_{i,k} = \{j_s, j_t, \dot{Q}\}^p$ are the set of predictions, and $O^e_{i,k} = \{j_s, j_t, \dot{Q}\}^e$ are the experimental output values. Several ANN configurations were tested, as in Díaz et al. [13], and the best results were given by the fully-connected 5-5-3-3 configuration which was chosen. A number of 800,000 cycles was selected for training to assure a reasonably low level of error S_e.

6 Artificial Neural Network Results

The ANN results are also shown in Table 1 along with those of correlations previously discussed. For all three surfaces, the ANN predictions are much better than any of the correlations. It is of

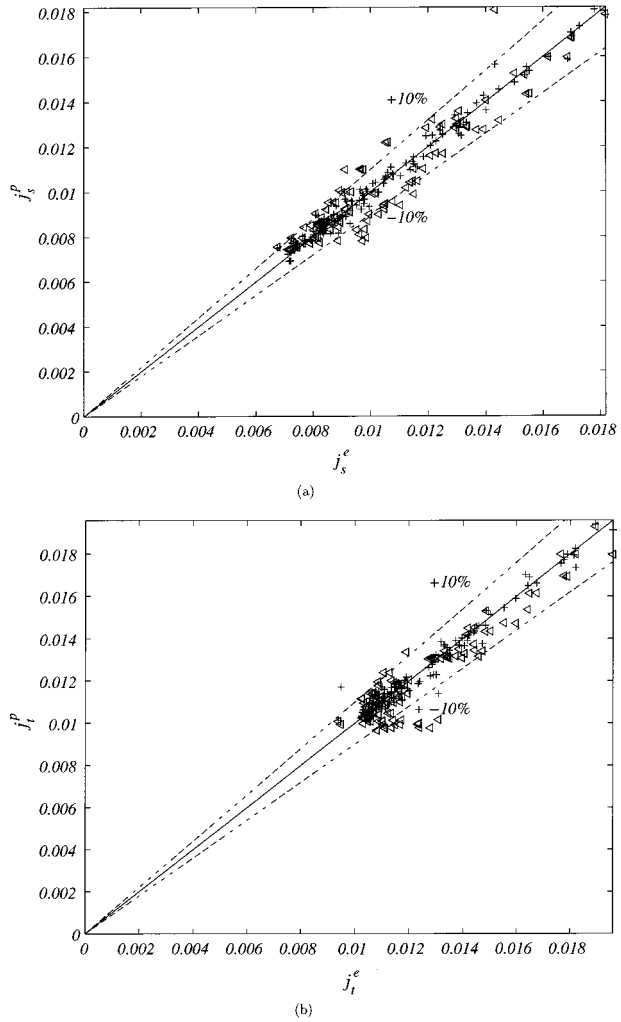

Fig. 6 Experiments versus predictions for heat exchanger with dropwise condensation; + ANN; ◁ McQuiston [16]. Straight line is the perfect prediction: (*a*) sensible heat j_s; (*b*) total heat j_t.

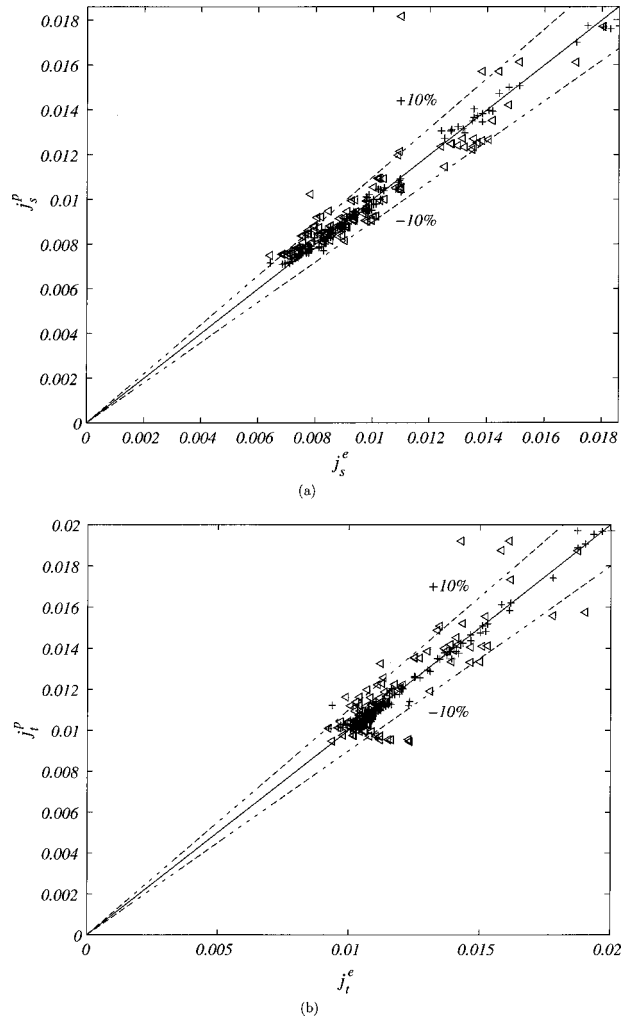

Fig. 7 Experiments versus predictions for heat exchanger with film condensation; +ANN; ◁ McQuiston [16]. Straight line is the perfect prediction: (*a*) sensible heat j_s; (*b*) total heat j_t.

interest to note that the ANN gives better prediction for dry surfaces than for wet. This is expected since the physical phenomena associated with condensation are more complex.

To determine whether the network based on training data separated by some physical condition would perform better than another trained with the combined data set, the entire set of runs M was combined to train a single ANN. The error, shown in Table 1 under ''Combined,'' is larger than the ANN predictions for individual cases, indicating that this ANN has more difficulty in differentiating between the different physics involved. However, even then the predictions of the total heat rate have errors of the order of only 2.7 percent.

Comparisons of j_s and j_t under dry and wet-surface conditions between the previously published correlations and the ANN results are shown in Fig. 5–7. For the dry surface there is only one j-factor, but under condensing conditions both j_s and j_t are shown. In all the figures, the straight lines indicate equality between prediction and experiment. The accuracy and precision given by the ANN is remarkable. There are some data points in Fig. 5–7 that are outliers and can clearly be eliminated to improve the predictions, if desired.

Table 2 Percentage of data sets of different surface conditions that fall in different clusters

Surface	I	II	III
Dry	89.01	10.99	0.00
Dropwise	0.00	29.06	70.94
Filmwise	0.00	18.49	81.51

The experimental measurements reported by McQuiston [15] were classified according to a visual procedure. For dry surface conditions this method is relatively reliable, but under wet conditions it is very difficult to distinguish between different forms of condensation by simple observation. One can ask if this visual information is really necessary, or if the data can be separated using some pattern recognition procedure. One of the simplest is numerical clustering using a k-means algorithm [21]. We use this method to classify the data into three groups, with all variables normalized in the [0, 1] range.

Table 2 shows the percentage of data sets of all three surface conditions that belong to a particular cluster I, II, or III. These results show that cluster I clearly corresponds to dry surface conditions, while the situation is less crisp for clusters II and III. The difference between the dry and wet wall data would have been sharper if only two clusters (dry and wet wall) had been used. Each of the three clusters is analyzed separately to train three ANNs using their respective data sets, $M_{\mathrm{I}}=81$ for cluster I, $M_{\mathrm{II}}=66$ for cluster II and $M_{\mathrm{III}}=180$ for cluster III. The total heat rate errors given by the ANN procedure are 0.866 percent for cluster I, 1.626 percent for cluster II and 1.242 percent for cluster III which are of the same order for data separated by visual observation. Visual information is thus not really necessary and the clustering technique is a viable alternative that produces equally good predictions.

7 Conclusions

Correlations found from heat exchanger experimental data using a regression procedure are often non-unique. In this case a global error minimization algorithm, rather than a local procedure, should be used. We have shown that there can be small but significant differences between the two. Furthermore, the correlation that is obtained can only be as good as its assumed functional form. It must also be pointed out that heat transfer coefficients are defined upon the assumption of a characteristic temperature difference and their usefulness depends on the similarity of the temperature profiles. In other words, if the temperature distributions are always identical except for a constant, this constant is the only quantity needed to determine the heat flux at the wall. With property variations, condensation, laminar and turbulent flows, and many other phenomena present, this is often not the case. The situation is worse for mass transfer during condensation, since its rate is clearly not proportional to the enthalpy difference. Thus it is better to develop correlations to predict the heat rates directly, rather than intermediate quantities like the j-factors that assume the existence of transfer coefficients. In addition, the user of the information is usually interested only in the overall heat rate and not in intermediate variables like the heat transfer coefficients.

Artificial neural networks do not have the drawbacks of correlations, and are an attractive alternative that can be used to accurately model the thermal behavior of heat exchangers without need to assume a functional form for the correlation nor an accurate mathematical model of the details of the process. We have shown that they can predict the behavior of heat exchangers under dry and wet conditions and their predictions are remarkably more accurate than those from correlations. The network is able to catch the complex physics in a heat exchanger very well. In the end, the error in the predictions of the neural network is probably of the same order as the uncertainty in the measurements, which is the best that can be expected.

ANNs also have some limitations. They do not provide any physical insight into the phenomena in which they are used, but then neither do correlations. The training of the network may be computationally expensive though its subsequent use for predic-

tion purposes is not. For users with PCs, which is how most design is currently done, it is quick and easy to use. One issue that needs to be looked at in greater detail is the range of validity of the predictions as a function of the range and density of the training data set. Though research in this and related areas is ongoing, the neural network technique is currently a viable and accurate alternative to conventional correlations.

Nomenclature

A = total air-side heat transfer area [m^2]
A_{tb} = surface area of tubes without fins [m^2]
A_w = water-side heat transfer area [m^2]
a, b, c, d = correlation constants
$\mathbf{C}$ = vector of unknown constants
c_p = specific heat [J/kg K]
D = tube outer diameter [m]
D_h = hydraulic diameter [m]
E = error corresponding to procedure (c)
E_a = error corresponding to procedure (a)
E_b = error corresponding to procedure (b)
f_s, f_t = functions
G_c = air mass velocity based in free-flow area [kg/m^2 s]
h = heat transfer coefficient [W/m^2 K]
h_t = total (enthalpy) heat transfer coefficient [kg/m^2]
j = Colburn j-factor
M = total number of experimental data sets
M_a = number of data sets used for training
M_b = number of data sets used not used for training
M_1 = number of data sets with dry surface
M_2 = number of data sets with dropwise condensation
M_3 = number of data sets with film condensation
$\dot{m}$ = mass flow rate [kg/s]
$O_{i,k}$ = $\{j_s, j_t, \dot{Q}\}$ for run i
Pr = Prandtl number
P_s = percentage of splitting [percent]
$\dot{Q}$ = heat transfer rate between fluids [W]
Re_D = Reynolds number based in the diameter
Re_δ = Reynolds number based in the fin spacing
Sc = Schmidt number
$S_e, S_{e_{\dot{Q}}}$ = root mean square error
$S_{\dot{Q}}$ = variance of total heat transfer rate error
S_j = variance of the Colburn j-factor error
T = fluid temperature [C]
t = fin thickness [m]
U = overall heat transfer coefficient [W/m^2 K]
W = synaptic weight between nodes
x_a = tube spacing in the longitudinal direction [m]
x_b = tube spacing in the transverse direction [m]
z = section coordinate in S_{j_s} surface

Greek Symbols

δ = fin spacing [m]
θ = bias
η = fin effectiveness
μ = dynamic viscosity of fluid [kg/m s]
σ = standard deviation in procedure (c)
σ_a = standard deviation in procedure (a)
σ_b = standard deviation in procedure (b)
σ_f = ratio of free-flow cross-sectional area to frontal area

Subscripts and Superscripts

a = air side
db = dry bulb
e = experimental value
in = inlet
p = predicted value
s = sensible
t = total
w = water side
wb = wet bulb

Acknowledgments

A. P.-V. is the recipient of a CONACyT-Fulbright Fellowship from Mexico for which we are grateful. We also acknowledge the support of Mr. D. K. Dorini of BRGD-TNDR for this and related projects in the Hydronics Laboratory.

References

[1] Jacobi, A. M., and Goldschmidt, V. W., 1990, ''Low Reynolds Number Heat and Mass Transfer Measurements of an Overall Counterflow, Baffled, Finned-Tube, Condensing Heat Exchanger,'' Int. J. Heat Mass Transf., **33**, No. 4, pp. 755–765.

[2] Srinivasan, V., and Shah, R. K., 1997, ''Condensation in Compact Heat Exchangers,'' Journal of Enhanced Heat Transfer, **4**, No. 4, pp. 237–256.

[3] Ramadhyani, S., 1998, ''Calculation of Air-Side Heat Transfer in Compact Heat Exchangers Under Condensing Conditions,'' in *Computer Simulations in Compact Heat Exchangers*, **1**, Computational Mechanics Publications, B. Sunden and M. Faghri editors, South Hampton, UK., pp. 151–168.

[4] Jang, J. Y., Lai, J. T., and Liu, L. C., 1998, ''The Thermal-Hydraulic Characteristics of Staggered Circular Finned-Tube Heat Exchangers Under Dry and Dehumidifying Conditions,'' Int. J. Heat Mass Transf., **41**, pp. 3321–3337.

[5] Sen, M., and Yang, K. T., 1999, ''Applications of Artificial Neural Networks and Genetic Algorithms in Thermal Engineering,'' *CRC Handbook of Thermal Engineering, F. Kreith*, ed., Section 4.24 pp. 620–661.

[6] Thibault, J., and Grandjean, B. P. A., 1991, ''A Neural Network Methodology for Heat Transfer Data Analysis,'' Int. J. Heat Mass Transf., **34**, No. 8, pp. 2063–2070.

[7] Mahajan, R. L., and Wang, X. A., 1993, ''Neural Network Models for Thermally Based Microelectronic Manufacturing Processes,'' J. Electrochem. Soc., **140**, No. 8, pp. 2287–2293.

[8] Marwah, M., Li, Y., and Mahajan, R. L., 1996, ''Integrated Neural Network Modeling for Electronic Manufacturing,'' J. Electron. Manufact., **6**, No. 2, pp. 79–91.

[9] Fowler, M. M., Klett, D. E., Moreno, J. B., and Heermann, P. D., 1997, ''Using Artificial Neural Networks to Predict the Performance of a Liquid Sodium Reflux Pool Boiler Solar Receiver,'' in *Proceedings of the International Solar Energy Conference*, pp. 93–104.

[10] Jambunathan, K., Hartle, S. L., Ashforth-Frost, S., and Fontama, V. N., 1996, ''Evaluating Convective Heat Transfer Coefficients Using Neural Networks,'' Int. J. Heat Mass Transf., **39**, No. 11, pp. 2329–2332.

[11] Jeannette, E., Assawamartbunlue, K., Curtiss, P. S., and Kreider, J. F., 1998, ''Experimental Results of a Predictive Neural Network HVAC Controller,'' in ASHRAE Trans., **104**, Part 2, pp. 192–197.

[12] Zhao, X., McClain, R. L., Sen, M., and Yang, K. T., 1995, ''An Artificial Neural Network Model of a Heat Exchanger,'' in *Symposium on Thermal Science and Engineering in Honor of Chancellor Chang-Lin Tien*, pp. 83–88.

[13] Díaz, G., Sen, M., Yang, K. T., and McClain, R. L., 1999, ''Simulation of Heat Exchanger Performance by Artificial Neural Networks,'' Int. J. HVAC Res., **5**, No. 3, pp. 195–208.

[14] McQuiston, F. C., 1976, ''Heat, Mass and Momentum Transfer in a Parallel Plate dehumidifying Exchanger,'' in ASHRAE Trans., **82**, Part 2, pp. 87–106.

[15] McQuiston, F. C., 1978, ''Heat, Mass and Momentum Transfer Data for Five Plate-Fin-Tube Heat Transfer Surfaces,'' ASHRAE Trans., **84**, Part 1, pp. 266–293.

[16] McQuiston, F. C., 1978, ''Correlation of Heat, Mass and Momentum Transport Coefficients for Plate-Fin-Tube Heat Transfer Surfaces With Staggered Tubes,'' ASHRAE Trans., **84**, Part 1, pp. 294–309.

[17] Gray, D. L., and Webb, R. L., 1986, ''Heat Transfer and Friction Correlations for Plate Finned-Tube Heat Exchangers Having Plain Fins,'' in *Proceedings of the Eighth International Heat Transfer Conference*, **6**, pp. 2745–2750.

[18] Pacheco-Vega, A., Sen M., Yang, K. T., and McClain, R. L., 1998, ''Genetic-Algorithm-Based Predictions of Fin-Tube Heat Exchanger Performance,'' in *Proceedings of the Eleventh International Heat Transfer Conference*, **6**, pp. 137–142.

[19] Zeng, P., 1998, ''Neural Computing in Mechanics,'' Appl. Mech. Rev., **51**, No. 2, pp. 173–197.

[20] Rumelhart, D. E., Hinton, G. E., and Williams, R. J., 1986, ''Learning Internal Representations by Error Propagation,'' in *Parallel Distributed Processing: Explorations in the Microstructure of Cognition*, MIT Press, Cambridge, MA.

[21] Theodoridis, S., and Koutroumbas, K., 1999, *Pattern Recognition*, Academic Press, San Diego, CA.

Influence of Flow Regime, Heat Flux, and Mass Flux on Electrohydrodynamically Enhanced Convective Boiling

J. E. Bryan
Outokumpu Copper,
Franklin, KY 42134

J. Seyed-Yagoobi
Department of Mechanical Engineering,
Texas A&M University,
College Station, TX 77843-3123

The influence of quality, flow regime, heat flux, and mass flux on the electrohydrodynamic (EHD) enhancement of convective boiling of R-134a in a horizontal smooth tube was investigated in detail. The EHD forces generated significant enhancements in the heat transfer coefficient, but the enhancements were highly dependent on the quality, flow regime, heat flux, and mass flux. The experimental data provided evidence that an optimum EHD enhancement exists for a given set of these variables with a specific electrode design. However, experimental data also provided evidence that the EHD forces can drastically reduce the rate of heat transfer at certain conditions.
[DOI: 10.1115/1.1316782]

Introduction

Passive and active enhancement methods for improving convective boiling heat transfer are continuously being developed and researched. An active method, which has been recently investigated utilizes the elctrohydrodynamic (EHD) phenomena. EHD enhanced pool boiling has been investigated for over 30 years. However, there have been only a few researchers in the last ten years to investigate EHD enhanced convective boiling. The limited amount of research is, in part, due to an incomplete fundamental knowledge on EHD enhanced heat transfer.

EHD enhancement of convective boiling heat transfer features several distinct advantages over conventional passive methods. One is the ability to vary or control the boiling heat transfer coefficient by changing the applied voltage. Another is a significant enhancement in the boiling heat transfer can be achieved with EHD. Furthermore, the EHD enhancement process contains no moving parts and the electric power input is usually negligible.

The largest EHD convective boiling enhancements achieved in six of the seven cited references are shown in Table 1 and information on the experimental parameters are given in Table 2. The maximum EHD enhancements range from 1000 percent locally to an average of 100 percent achieved by Salehi et al. [1] and Yabe et al. [2], respectively. The large enhancements achieved by Salehi et al. [1] were for convective boiling in a downward flowing micro-channel. Salehi et al. [1] classified their channels as microscale; however, the hydraulic diameter of these channels was 1.5 mm. This is the only research on EHD enhanced convective boiling in mm-size channels. All the other references focus on EHD enhancements in tubes of the order of 10 mm in diameter in a horizontal flow configuration. There are two primary reasons that the enhancement by Salehi et al. [1] was so significant. First, downward flow eliminates stratification of the liquid in the channel and creates a more unstable flow due to vapor and liquid density differences. Second, the applied electric field was locally higher on the heat transfer surface (microfin tube) because of the enhanced surface geometry and size of the cylindrical energized electrode. This higher electric field focused the EHD force on the heat transfer surface. All of the maximum enhancements, except for those achieved by Singh et al. [3], occurred at very low mass fluxes. Also, all the maximum enhancements were measured at heat fluxes of 10 kW/m^2 or less except that by Salehi et al. [1] which was at 25 kW/m^2. The occurrence of the maximum enhancements at different qualities for the different researchers is primarily due to the electrode designs, the geometry of the heat transfer surface, and the operating conditions (refer to Table 2).

A study by Norris et al. [4] showed that, as the inlet quality of R-134a into a 1500-mm test section increased, the EHD enhancement decreased and in some cases the EHD forces caused premature dryout. The test section was 12.7 mm in diameter in which a 3.2-mm-diameter rod electrode was suspended. The premature dryout was attributed to the dielectrophoretic force component (discussed in the next section) causing the liquid at the tube surface to be attracted to the energized electrode at the center of the tube.

Recently, Bryan and Seyed-Yagoobi [5] developed a theoretical relationship between the radial EHD pressure and axial momentum flux and investigated its influence on heat transfer enhancement and pressure drop in EHD enhanced convective boiling. It was shown that the amount of heat transfer enhancement and the pressure drop penalty were dependent upon the size of the radial EHD pressure relative to the rate of the axial momentum flux.

The results, obtained by the various researchers in the cited references, show the range of EHD enhanced heat transfer in convective boiling. However, the fundamental understanding is incomplete on how the EHD enhancements are affected by changes in mass flux, quality, flow regime, heat flux, operating temperature, and geometrical characteristics of the heat transfer surface. The research to date, except for the study by Norris et al. [4] and Bryan and Seyed-Yagoobi [5] has only focused on demonstrating the EHD enhancement and measuring the average EHD enhanced heat transfer coefficient. The results presented in this study will improve the knowledge of how the EHD enhancement is achieved and how it is affected by quality, flow regime, heat flux, and mass flux for a given fluid and electrode design.

Electrohydrodynamic (EHD) Phenomena

The EHD phenomena involve the interaction of electric fields and flow fields in a dielectric fluid medium. This interaction, under certain conditions, will result in electrically induced fluid motion and/or interfacial instabilities, which are caused by an electric body force. The electric body force density acting on the molecules of a fluid in the presence of an electric field consists of three terms.

Contributed by the Heat Transfer Division for publication in the JOURNAL OF HEAT TRANSFER. Manuscript received by the Heat Transfer Division, Mar. 14, 1999; revision received, May 15, 2000. Associate Editor: C. T. Avedisian.

Table 1 Comparison of EHD enhanced convective boiling results from different researchers. Shown are the different operating conditions, fluid, applied electric field, EHD power consumption, and the resulting heat transfer coefficient with and without EHD.

Reference	Fluid	G kg/m^{2}s	x kg/kg	q'' kW/m^2	h_{o_2} W/m^{2}K	h_{EHD} W/m^{2}K	$E_E(10^6)$ V/m	$E_G(10^6)$ V/m	Q_{EHD} W
Yabe et al. [2]	R123/R134a	33	0.2–0.6	4[b,f]	500–1000	1050–2000	4.04[c]	2.02	N/A
Singh et al. [19]	R123	75	0[a]	5[b,f]	800	3800	5.83	1.86	0.34
Singh et al. [3]	R134a	200	0[a]	5[b,f]	2100	4600	5.83	1.86	0.23
Singh [20]	R134a	50	0.1[a]	5[g]	2000	13900	2.22[c]	1.84[c]	0.36
Salehi et al. [21]	R404A	50	0.3[a]	10[g]	3000	7000	1.66[c]	1.38[c]	0.01[d]
Salehi et al. [1]	R134a	50[e]	0.6[a]	25[g]	5000	50000	4.55	4.04[c]	0.01[d]

[a]Measured at inlet to test section and different from local change of quality in the test section.
[b]Average heat flux; this is not constant along test section.
[c]Electric field is based on radius; local electric field is different due to geometrical shape of surface.
[d]Power was estimated from power ratio presented by researchers.
[e]Estimated from Reynolds number presented by researchers; based on cross-sectional area of micro-channel.
[f]Test section heated by hot water.
[g]Test section heated by resistive electrical heater.

Table 2 Experimental parameters investigated by the various researchers for the comparison given in Table 1

Reference	Tube	D_o mm	L m	Electrode	D_E mm	T_{sat} °C	G range kg/m^{2}s	x range kg/kg	q'' range kW/m^2
Yabe et al. [2]	smooth	10	3.75	perforated tube	5	30	33 & 66	0–0.9	4[c]
Singh et al. [19]	smooth	9.4	1.22	cylindrical	3	25	50–400	0–0.5[b]	5–20[c]
Singh et al. [3]	smooth	9.4	1.22	cylindrical	3	25	50–400	0–0.5[b]	5–20[c]
Singh [20]	microfin	12.7	0.3	helical	9.8	25	50–150	0–0.8[b]	5–30
Salehi et al. [21]	microfin	12.7	0.3	helical	9.8	25	50–200	0–0.8[b]	5, 10
Salehi et al. [1]	microfin	12.7[a]	0.11	cylindrical	9.5[a]	25	50 & 100	0–0.6[b]	25

[a]Annulus resulting from tube and cylindrical electrode is separated into 12 micro-channels, each with a hydraulic diameter of 2 mm.
[b]Measured at inlet to test section and different from test section quality.
[c]Heat flux is averaged and is not constant along test section.

$$\mathbf{f}_e = \rho_e \mathbf{E} - \frac{1}{2} E^2 \nabla \varepsilon + \frac{1}{2} \nabla \left[E^2 \rho \left(\frac{2\varepsilon}{\partial \rho} \right)_T \right]. \quad (1)$$

Melcher [6] derived Eq. (1) through a thermodynamic approach, with the assumption that the polarization is a linear function of the applied electric field and it is dependent on the fluid density. The three terms in Eq. (1) stand for two primary force densities acting on the fluid. The first term represents the force acting on the free charges in the presence of an electric field and is known as the Coulomb force. The second and third terms represent the polarization force induced in the fluid. Seyed-Yagoobi and Bryan [7] provide a more detailed discussion on the electrostatic equations supporting Eq. (1).

Figure 1 shows four examples of induced forces on a dielectric fluid medium, which can result from the application of a nonuniform electric field. The electric body force density components defined in Eq. (1) are responsible for the induced forces on the dielectric fluid medium. Schematic (*a*) in Fig. 1 is a representation of fluid motion resulting from the Coulomb force. A charged body in a nonuniform or uniform electric field will move along the electric field lines and impart momentum to the surrounding fluid. Free charges can be introduced into the fluid medium by direct injection from an energized sharp electrode resulting in a net charge in the fluid. Free charges can also be induced within the fluid without a net charge build up. This charge induction takes place in the presence of an electric field due to a nonuniformity in the electric conductivity of the fluid. A nonuniformity in the electric conductivity can be a result of a temperature gradient and/or an inhomogeneous fluid. It is important to note that the motion of the charged body will depend on whether the charged body is created by direct injection or induction, the strength of the applied electric field, and whether the applied field is d.c. or a.c. The life of the charged body will be dependent on the fluid charge relaxation time, τ_e, which is a ratio of the electric permittivity to the electric conductivity of the fluid.

Schematic (*b*) in Fig. 1 represents translational motion, often identified as dielectrophoresis, resulting from the generation of the

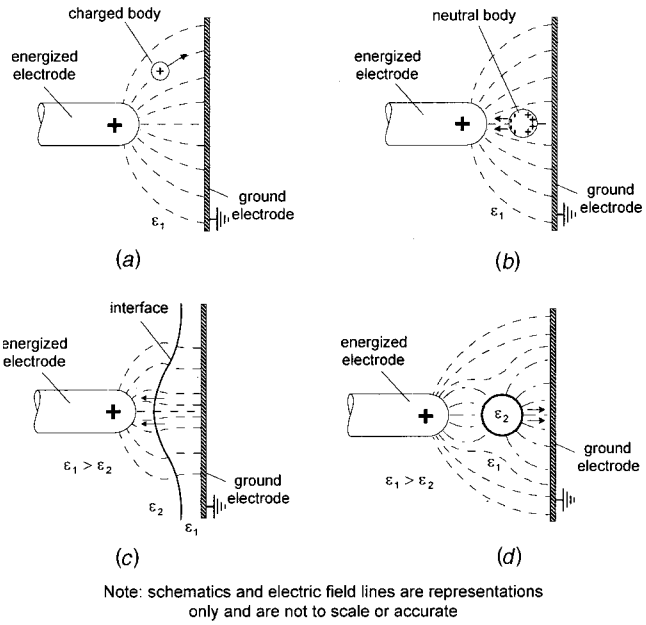

Fig. 1 Simple representations of electric body force density components with ε_1 and ε_2 representing the liquid vapor permittivity, respectively. (*a*) Coulomb force, (*b*) dielectrophoresis (type of polarization force), (*c*) and (*d*) are additional variations of the polarization force.

polarization force in a nonuniform electric field. For the fluid to experience a net polarization force over a given region, there must be a relative displacement of positive and negative bound charges in a body by applying an electric field. An induced dipole, resulting from the displacement of the positive and negative bound charges in a neutral body by applying an electric field, will expe-

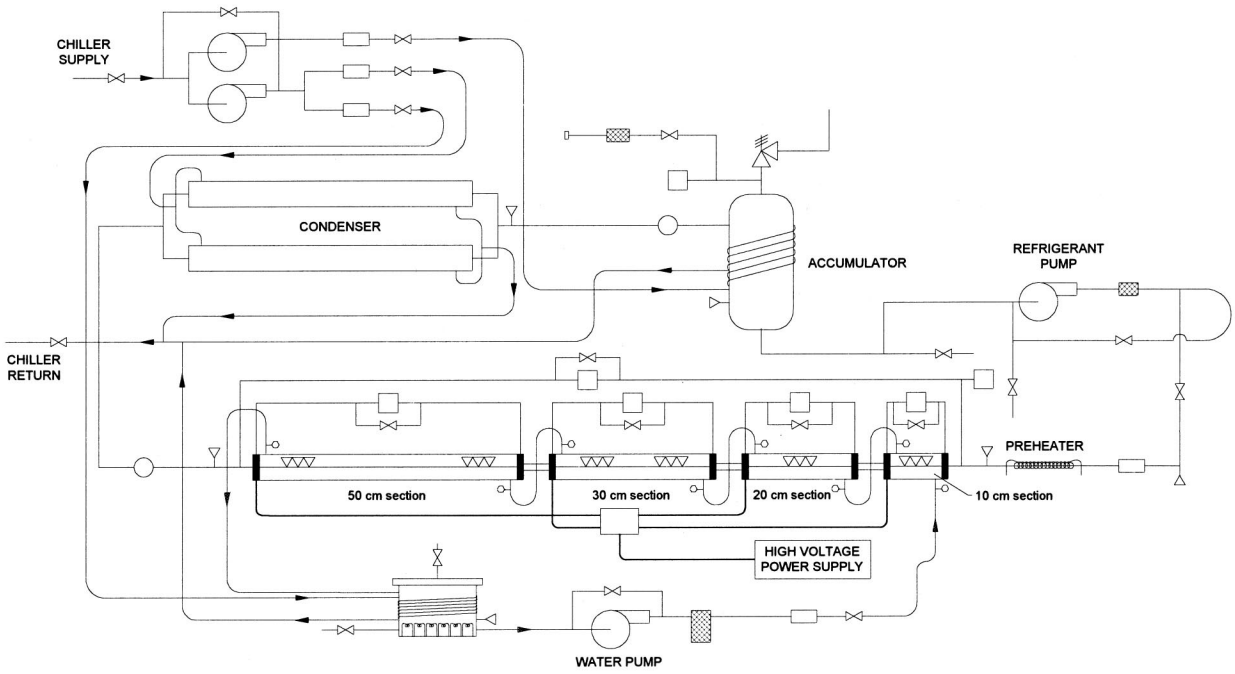

Fig. 2 Schematic of experimental apparatus

rience a net unidirectional force in a nonuniform electric field. One end (the negative end in the sketch) of this dipole in a nonuniform electric field experiences a higher force than the other end (the positive end in the sketch), resulting in a net translation of the polarized body towards the higher electric field.

There are two ways in which a fluid, which is isotropic (per phase) both before and after an electric field is applied, can become polarized. The fluid can be inhomogeneous, in the sense that the permittivity is a function of position, or it can vary with density. The second term in Eq. (1) is due to inhomogeneities, while the last term is due to variations in the fluid density. Since the last term provides a coupling between the fluid density and the electric field, it is called the electrostriction force density ([6]). Discussion has persisted over the years with respect to the electrostriction force density term in Eq. (1) and whether it can be responsible for translational motion.

The last two schematics, (*c*) and (*d*), in Fig. 1 are additional representations of polarization forces due to the application of a nonuniform electric field. If an interface exists, such as between a liquid and vapor, in a nonuniform electric field, an attraction force is created which draws the fluid of higher permittivity (liquid) toward the region of higher electric field strength, as shown in schematic (*c*) and (*d*) in Fig. 1. The bubble in schematic (*d*), which is of lower permittivity than the surrounding liquid, will be forced to the region of lower electric field strength, as defined by the second term in Eq. (1). It should be noted that Jones [8] has classified the force acting on the bubble, shown in Fig. 1(*d*), as the dielectrophoretic force. The polarization attraction force will occur whether or not a d.c. or a.c. nonuniform field is applied. However, the potential accumulation of charge at the interface can influence the polarization force. Locally, if the charge accumulation is large enough, space charge effects can become significant and the Coulomb force can be influential.

The application of EHD to two-phase heat transfer problems is quite complicated. The simple representations shown in Fig. 1 were described individually. However, when an electric field is applied in a region where two-phase heat transfer is occurring, the force descriptions shown in Fig. 1 will interact and occur simultaneously. All three components of the EHD force density can be significant or one can dominate over the others. In convective boiling all three forces will be present, however, the second term of Eq. (1) will dominate as the quality and heat flux increase, which will be shown in the results.

Experimental Apparatus

The experimental apparatus, shown in Fig. 2, was a closed loop in which refrigerant was pumped with a positive displacement gear pump instead of a compressor. The refrigerant flowed from the pump through a flow regulating valve and preheat section and then through four evaporator test sections of 10, 20, 30, and 50 cm in length. The refrigerant then flowed to the condenser and accumulator where it was condensed and subcooled before reentering the pump. The heat removal and operating temperature setpoint of the apparatus were maintained with a low-temperature recirculating chiller. The refrigerant flow rate was measured with a turbine flowmeter located upstream of the preheater (see Fig. 2). The temperature upstream of the flowmeter was monitored with a T-type thermocouple probe to ensure that the flow entering the flowmeter was subcooled. The working fluid used in all experiments was R-134a. Complete details on the experimental apparatus and test procedures are provided by Bryan [9].

The four test sections, shown in Fig. 2, were connected in series and heat was provided to each by a recirculating hot water loop. The different test sections were used to allow for the measurement of the local heat transfer coefficients and heat fluxes within each test section. Each test section, as shown in Fig. 3, consisted of a smooth copper boiling tube (inside diameter = 14.1 mm and outside diameter = 15.9 mm) surrounded by an acrylic tube (inside diameter 38.1 mm) in which the hot water flowed. A high-pressure Pyrex tube (inside diameter 12.7 mm) was placed in between each test section so the flow entering and leaving each test section could be observed. The test sections were connected in a parallel flow configuration with respect to the hot water flow direction to allow the highest heat fluxes to occur in the 10-cm section where evaporation would first take place and nucleate boiling would be the greatest. Also, the parallel configuration did not allow for potential premature local dryout in the 50-cm section at certain operating conditions. The inlet and outlet water temperature to each test section was measured with thermistors so that

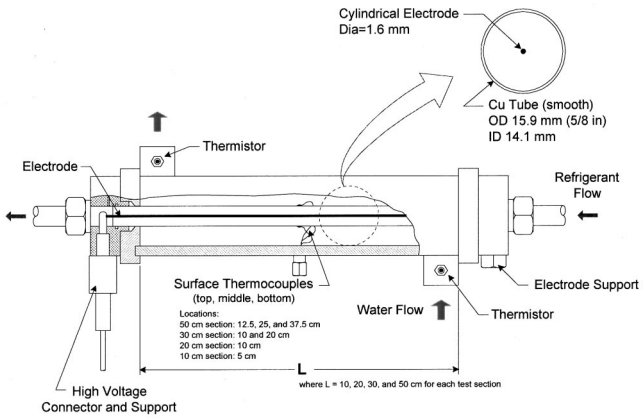

Fig. 3 Drawing of test section

in all experiments the temperature difference across each test section could be accurately measured and maintained to 1°C or less. The water flow rate to the test sections was controlled and measured with a turbine flowmeter.

T-type thermocouples were soldered to the outer surface of the boiling tubes at the top, middle, and bottom in each test section. Figure 3 gives the exact location of thermocouples in each test section. Two T-type thermocouple probes were used to measure the refrigerant saturation temperature. The thermocouple probe temperature measurement was verified with the saturation temperature measurement obtained from the absolute pressure gage during calibration. During experiments the thermocouple probes were used to monitor the saturation temperature, because the absolute pressure gage was only accurate to ±0.4°C. In all experiments the maximum pressure drop across the test sections corresponded to less than 0.4°C drop in the saturation temperature. One thermocouple probe was located just upstream of the absolute pressure tap at the inlet to the 10-cm section and just down stream of the preheater (see Fig. 2). The other thermocouple probe was located downstream of the 50-cm test section.

The electrode geometry used in the experiments was a brass rod 1.6 mm in diameter (see Fig. 3). The brass electrode was suspended in the center of each test section and held in tension by two electrode supports, one at the entrance and one at the exit of the test section. In all experiments the brass electrode was energized with a positive d.c. high voltage while the copper boiling tube was grounded.

Data Reduction and Uncertainty Analysis

The heat transfer coefficient in convective boiling experiments is often determined from the Wilson plot approach. However, in this research an understanding of how the EHD forces influence the local and overall heat transfer is of interest. Thus, in all experiments the heat flux, heat transfer coefficient, and quality were calculated from direct measurements using the following equations.

$$q'' = \frac{\dot{m} c_p (T_{\text{in}} - T_{\text{out}})}{\pi D_i L} \tag{2}$$

Uniform heat flux to the tube surface was assumed and this will be discussed further when the local heat transfer results are presented.

The local heat transfer coefficient at each location inside the tube was calculated from

$$h = \frac{\dot{m} c_p (T_{\text{in}} - T_{\text{out}})}{\pi D_i L (T_{w_i} - T_{\text{sat}})}. \tag{3}$$

Table 3 Maximum total uncertainties, measured and calculated

	Total Uncertainty	
Measurements	**Average**	**Maximum**
Surface temperature	±0.09°C	±0.41°C
Inlet and outlet refrigerant temperature	±0.13°C	±0.17°C
Inlet and outlet water temperature	±0.06°C	±0.09°C
Refrigerant mass flux	±4.2 kg/m^{2}s	±4.3 kg/m^{2}s
Water mass flow rate	±0.0027 kg/s	±0.0027 kg/s
Calculated Quantities[a]	**Average**	**Maximum**
Quality	±13.8%	±20.5%
Heat flux	±13.1%	±20.0%
Heat transfer coefficient	±13.4%	±39.2%

[a]Uncertainties were smallest on 10-cm section and greatest on 50-cm section and increased as heat load increased.

The local inside wall temperature, T_{w_i}, was calculated through a one-dimensional conduction analysis, knowing the measured local outside surface temperature. The conduction through the wall was accounted for even though its influence was very small.

The flow quality was determined from

$$x = \frac{(\dot{m} c_p (T_{\text{in}} - T_{\text{out}})/\dot{m}_r)}{h_{fg}}. \tag{4}$$

The point in each test section at which the quality was determined corresponded to the location of each surface thermocouple station. In all experiments proper preheating was provided to ensure that the liquid entering the first test section was at a saturated state.

All the temperature instruments were calibrated against a NIST traceable thermometer, which was accurate to 0.02°C, in a constant temperature bath. The temperature instruments were calibrated end to end, that is all wiring, connections, terminal strips, and the data acquisition were connected when the calibration was made. The turbine flowmeters were also calibrated in place. The accuracy uncertainty of the calibration was less than 0.5 percent for the refrigerant flowmeter and 0.7 percent for the water flowmeter over the entire calibration range. The flowmeters were, also, calibrated at various temperatures to account for any temperature dependencies. All instruments were calibrated over a range large enough to cover all planned test conditions.

A total uncertainty analysis was performed for all the measured data and calculated quantities based on methods described by Kline and McClintock [10] and Taylor [11]. The average and maximum total uncertainties are shown in Table 3 for the different measured and calculated quantities. The maximum uncertainties occurred when EHD was applied at a low heat flux and quality because the measured temperature differences were small.

An energy balance was performed to check that the sum of the heat loads to the individual test sections was within the total uncertainty of the electrical energy input. It was determined that for all conditions the sum of the energy to the test sections was within the uncertainty of the measured electrical energy input. Refer to Bryan [9] for additional details.

Results and Discussion

Verification of Experimental Data. The experimental data were compared to existing data from Wattelet et al. [12] for one case of $G = 300.7$ kg/m^{2}s and $T_{\text{sat}} = 5.0$°C and the heat transfer coefficients were within 17 percent. The data trends compared quite well considering the test sections used by Wattelet et al. [12] were electrically heated allowing for constant heat flux. The experimental data were also compared to two correlations because of the limited experimental data available at similar operating conditions. Since correlations are developed from large data bases they can be used to further check the validity of the experimental data. The two correlations used were by Kandlikar [13] and Wattelet [14]. The comparison of the two correlations to the experi-

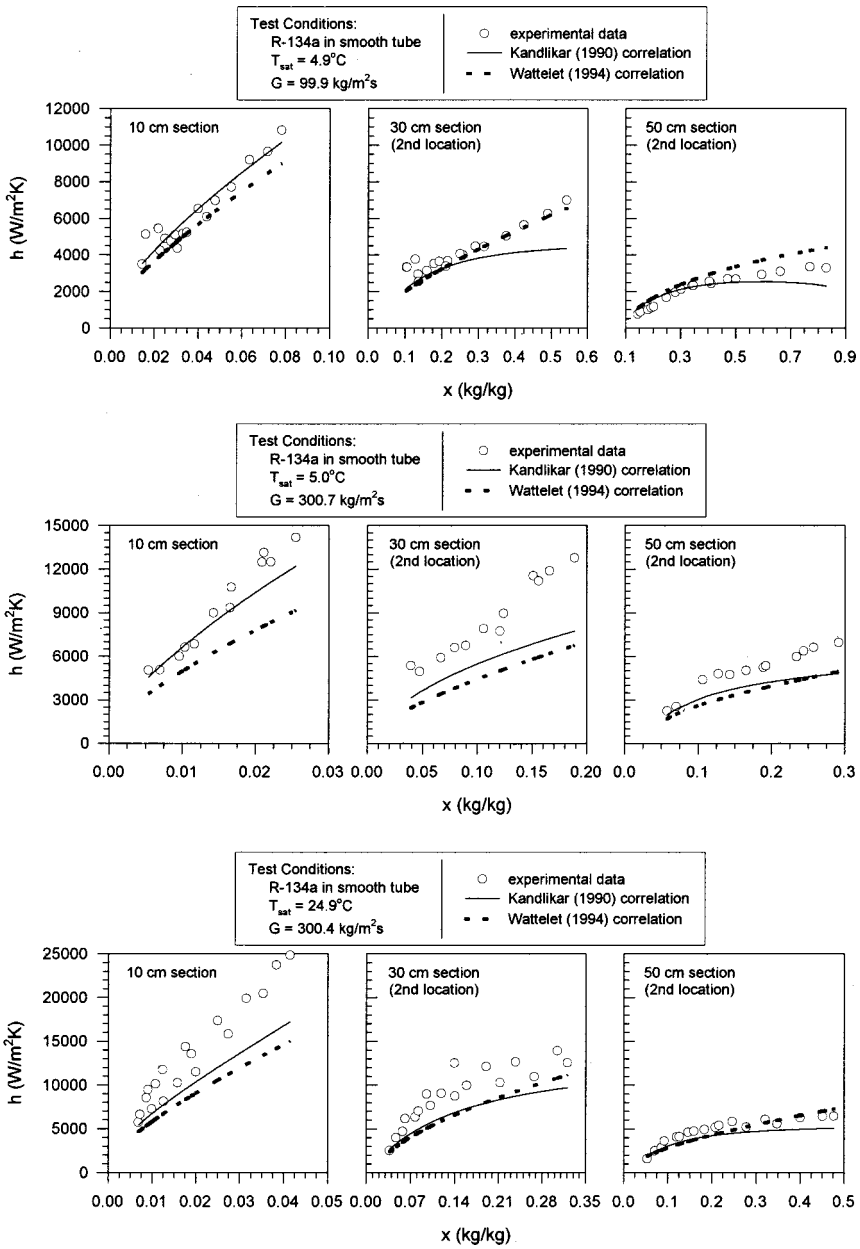

Fig. 4 Comparison of experimental data to correlations by Kandlikar [13] and Wattelet [14] for three operating conditions

mental data for three different test conditions, with the electrode in place, is shown in Fig. 4. In general the correlations and experimental data compare well. The comparison is best for the mass flux of 99.9 kg/m^{2}s, but varies at the high mass fluxes. The correlations under predict the heat transfer for the higher mass fluxes at low qualities, but the correlations compare better to the experimental data, as the quality increases.

The presence of the electrode did not influence the heat transfer coefficient significantly. Table 4 shows some average heat transfer coefficient data with and without the electrode. Except for two cases of around 30 percent difference, the effect of the electrode was within the experimental uncertainty. The increase in the heat transfer coefficient due to the electrode was evident, but the enhancement was small.

Electrohydrodynamic (EHD) Enhancement Results. Before the results are discussed, the issue of constant and uniform heat flux and the local heat transfer coefficient should be addressed. A temperature difference of 1°C or less was maintained across each test section in order to approximate a constant heat flux to the tube surface. Electrical heating would have been the correct way to maintain a constant heat flux, but results were needed for the case that more closely resembled an industrial application. Also in all experiments the circumferential heat flux was assumed uniform. However, the local heat flux, circumferentially, is nonuniform because the resistance to heat transfer around the inside of the tube is nonuniform, which is due to the changing quality and flow regime in the presence or absence of EHD. When the local heat transfer coefficient is low, the resistance to heat transfer is high and the calculated heat flux (which is assumed circumferentially uniform) is higher than the true local heat flux. When the local heat transfer coefficient is high, the resistance to heat transfer is low and the calculated heat flux is lower than the true local heat flux. Thus, the circumferential EHD enhanced or suppressed heat transfer coefficients presented here will be, re-

Table 4 Selected results showing the influence of electrode presence on heat transfer

Refrigerant	Electrode	T_{set}(°C)	G(kg/m^{2}s)	q''_{avg}(kW/m^2)	x_{in}(kg/kg)	x_{out}(kg/kg)	h_{avg}(W/m^{2}K)	%dif
R-134a	no	25.2	102.2	22.5	0.00	0.43	4057	12.9
	yes	25.1	101.4	23.0	0.00	0.45	4582	
R-404A	no	25.7	101.3	27.4	0.00	0.67	4768	0.1[a]
	yes	25.4	101.2	27.8	0.00	0.68	4762	
R-134a	no	25.0	248.8	70.8	0.00	0.11	9974	1.2[a]
	yes	25.1	252.4	69.7	0.00	0.10	9849	
R-134a	no	25.0	248.8	31.1	0.27	0.38	4874	28.3
	yes	25.1	252.4	33.9	0.28	0.40	6255	
R-404A	no	25.0	250.3	59.3	0.00	0.58	7567	7.2
	yes	24.9	250.3	61.0	0.00	0.60	8120	
R-404A	no	25.0	299.6	71.8	0.00	0.59	8863	7.1
	yes	24.9	299.9	72.6	0.00	0.60	9492	
R-134a	no	25.0	399.4	109.2	0.00	0.10	14989	27.7
	yes	24.8	401.4	105.9	0.00	0.09	19138	

[a]no measurable influence due to the electrode

spectively, lower or higher than those of the true local values. The local surface temperatures were measured in order to determine local heat transfer coefficients to study the influence of the EHD forces on the convective boiling heat transfer. The local surface temperature measurement is used to calculate the heat transfer coefficient for that specific location based on the uniform heat flux assumption and approximation.

The first set of results is shown in Figs. 5–7 for an average mass flux of 99.9 kg/m^{2}s and an average saturation temperature of 4.9°C. The convective boiling begins in the 10-cm section and proceeds through the 50-cm section. Experimental results shown in Figs. 5–7 are for the 10-cm section, second downstream location (20 cm from inlet to test section) in the 30 cm section, and second downstream location (37.5 cm from inlet to test section) in the 50-cm section, respectively. The above test section locations were chosen because they showed the most pronounced influence of the EHD forces on the heat transfer enhancement or suppression. The results, in each figure, are presented in five plots. Plot (*a*) shows the experimental data at 0 kV on the flow map by Taitel and Dukler [15]. The flow map provides acceptable information on the flow regime structure without EHD. This is to say that the flow regimes were visually observed both with and without the

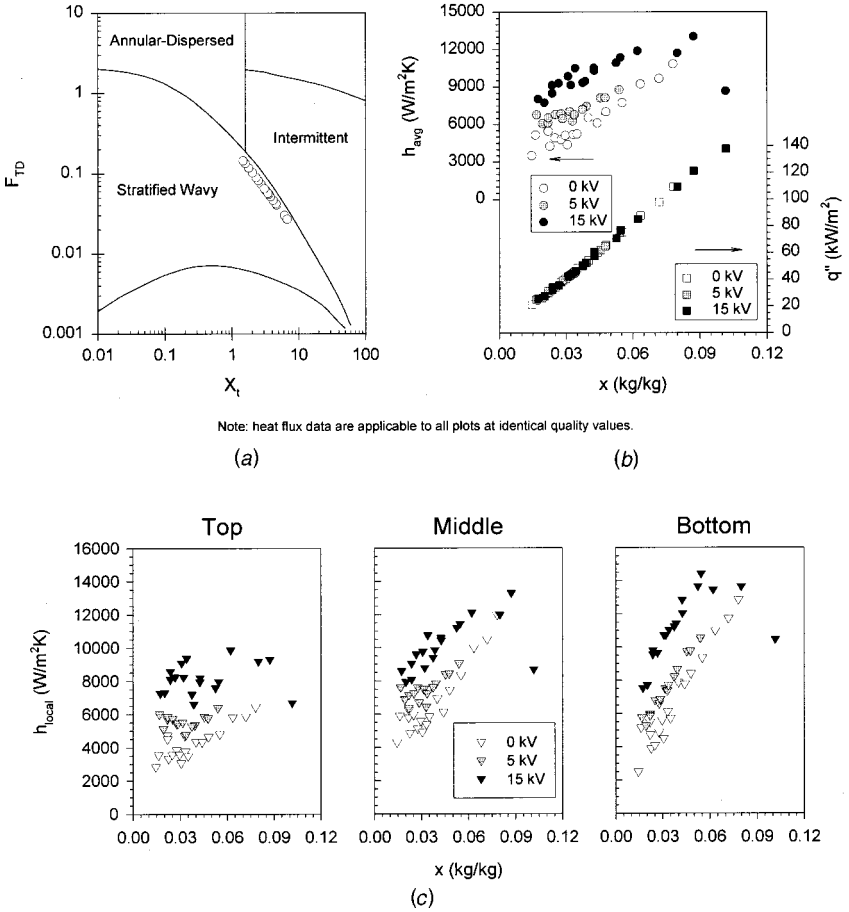

Fig. 5 Results with R-134a in a smooth tube for the 10-cm section at T_{sat}=4.9°C and G=99.9 kg/m^{2}s: (*a*) the flow map, (*b*) average heat transfer coefficient data, and (*c*) local heat transfer coefficient data

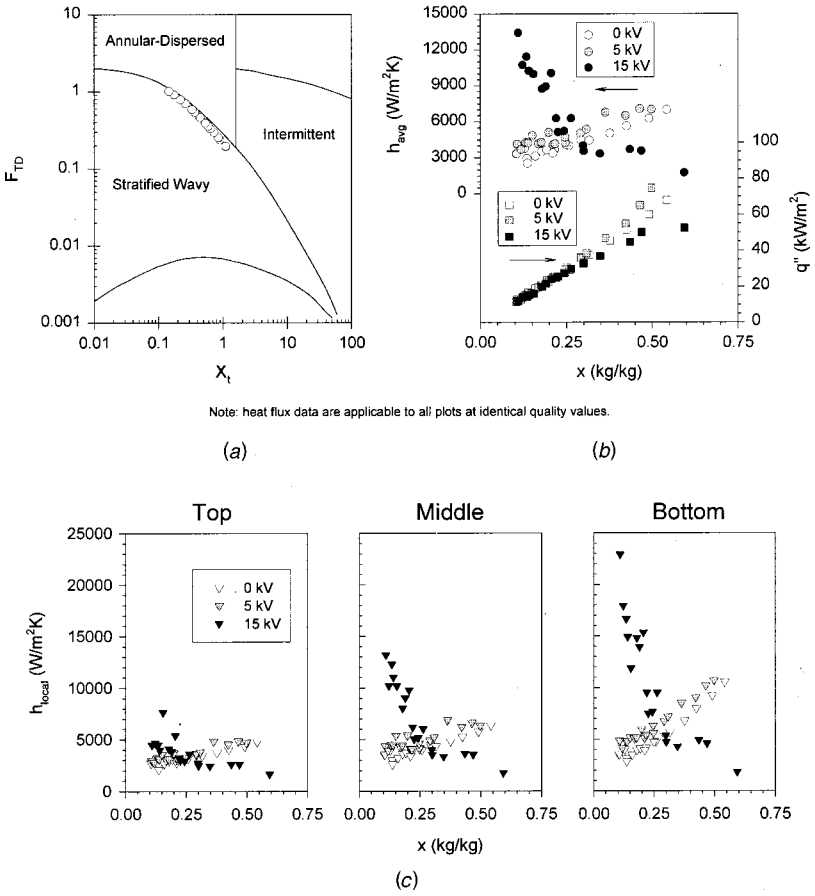

Fig. 6 Results with R-134a in a smooth tube for second location (20 cm from inlet to test section) on the 30-cm section at T_{sat}=4.9°C and G=99.9 kg/m^{2}s: (*a*) the flow map, (*b*) average heat transfer coefficient data, and (*c*) local heat transfer coefficient data

electrodes in place to be within the region plotted on the flow map by Taitel and Dukler [15]. However, these observations were only qualitative and the flow map is only meant to provide a basis to compare the measured results. The local heat transfer coefficients calculated from the experimental data, at the top, middle, and bottom of the boiling tube, provided additional verification of the flow regimes observed at the exit of the test section and determined by the flow map. For example, for stratified wavy flow as shown in Fig. 5, the heat transfer coefficient is expected to be greatest on the bottom and lowest on the top as the quality increases because vapor occupies the top portion of the tube. Plot (*b*) shows the average heat transfer coefficient and heat flux versus quality. Plot (*c*) shows the remaining three graphs of the local heat transfer coefficients versus quality for the top, middle, and bottom of the boiling tube. The average heat transfer coefficient shown in the plot (*b*) is the average of the top, middle, and bottom local heat transfer coefficients. The heat flux versus quality shown in the plot (*b*) is also applicable to the local heat transfer coefficient data at the identical quality value.

The behavior of two-phase heat transfer without EHD in the different test section locations should be addressed before the influence of the EHD forces is addressed. The stratification of the flow can be seen in the local heat transfer coefficients for the 0 kV data. As the heat flux increases, the heat transfer coefficients begin to differ between the top, middle, and bottom of the boiling tube as seen in Figs. 5(*c*)–7(*c*). This is evidence of flow stratification, because the vapor is collecting in the top portion of the tube and is beginning to reduce the rate of heat transfer at the top of the tube.

At the low heat fluxes and low qualities, primarily in the 10-cm section, there is scatter in the heat transfer data. The scatter is due to the variation in the active nucleation sites where each local heat transfer coefficient was measured. Although these measurements were made under the same operating conditions and at the same location, the experiments were performed with increasing heat flux and other times with decreasing heat flux, which resulted in variations in the number and location of active nucleation sites.

The application of the EHD force density to the convective boiling produces some very significant and different results as the flow regime and heat flux change. This is very evident as the flow proceeds and changes from the 10-cm section to the 50-cm section. In the 10-cm section, as shown in Fig. 5(*b*), the average EHD enhancement at 5 and 15 kV is evident throughout the heat flux range except at the highest two heat fluxes at 15 kV. The local maximum EHD enhancement is about 100 percent, 60 percent, and 80 percent at 15 kV for the top, middle, and bottom of the tube, respectively, for a heat flux range from 20 to 80 kW/m^2. In this heat flux range, the EHD enhancement is consistent with the EHD enhancement seen in pool boiling (refer to Seyed-Yagoobi et al., [16]). At the highest two heat fluxes, the EHD forces are suppressing the heat transfer. The polarization forces (see Figs. 1(*c*) and 1(*d*)) are beginning to dominate and cause the heat transfer suppression at 15 kV. With the current electrode design, the suppression is attributed to the attraction of the liquid refrigerant to the high voltage electrode (high electric field strength), which is in the center of the tube and forcing the vapor bubbles, as they are formed, to be pressed to the grounded boiling tube surface (low electric field strength). This has been observed in pool boiling experiments [17] where the vapor bubbles are held in place by

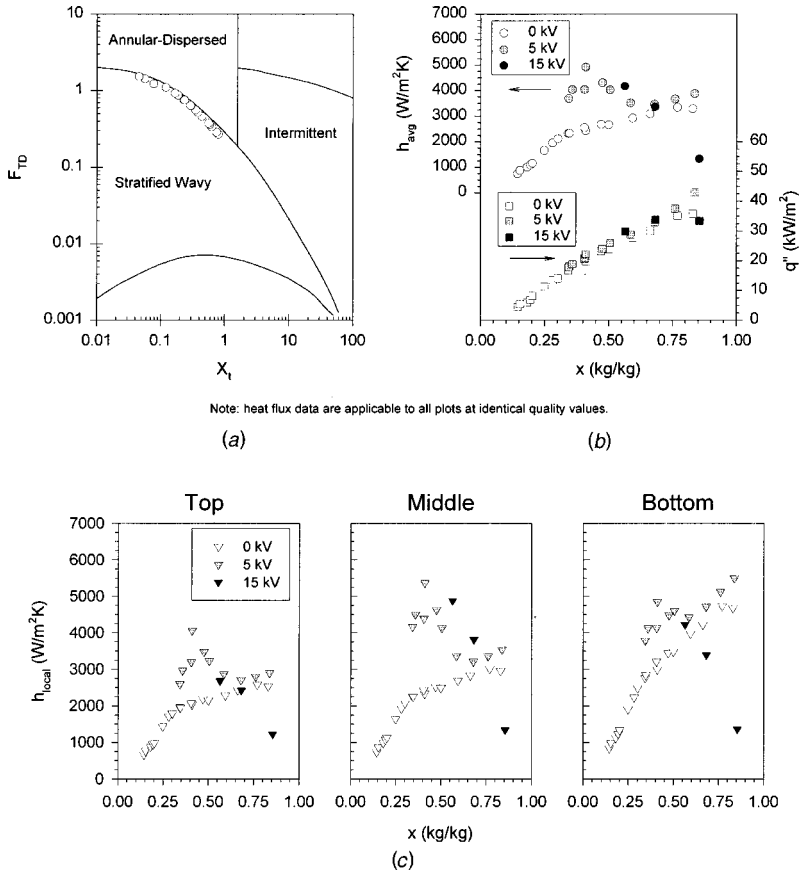

Fig. 7 Results for R-134a in a smooth tube for second location (37.5 cm from inlet to test section) on the 50-cm section at $T_{sat}=4.9°C$ and $G=99.9$ kg/m^{2}s: (*a*) the flow map, (*b*) average heat transfer coefficient data, and (*c*) local heat transfer coefficient data

the polarization forces against the tube as they form and grow, thus decreasing the local heat transfer and increasing the wall temperature. It is important to realize that forcing vapor bubbles back to the heated surface where they were formed and sweeping them around the surface (due to the polarization forces and the asymmetric electric field distribution) has been shown to promote enhanced nucleate boiling heat transfer since the sweeping improved the heat transfer from the evaporation micro layer to the bubble ([18]). However, in convective boiling where the fluid (liquid and vapor) is confined in the tube, the polarization forces can redistribute the liquid and vapor, forcing more vapor at the tube wall and attracting the liquid to the tube center. When the heat flux is high, this redistribution of the liquid and vapor due to the polarization forces can cause the resistance to heat transfer to increase at the tube wall as more vapor bubbles are produced.

Moving further downstream to the second location on the 30-cm section, the flow regime has transitioned to stratified-annular flow, as seen in the flow map without EHD in Fig. 6(*a*). The most pronounced influence of the EHD forces can be seen in Figs. 6(*b*) and (*c*). This is a point in the flow where it can be seen that the flow regime has a significant impact on the EHD enhancement potential. At 5 kV some heat transfer enhancement is occurring at each tube location. Increasing the applied voltage to 15 kV changes the enhancement behavior significantly. At the low heat flux and quality, there is some enhancement at the top of the tube, but the enhancement increases substantially towards the bottom of the tube. The maximum local EHD enhancement at 15 kV on the bottom of the tube is a significant 650 percent at the lowest heat flux, but the decrease is extreme as the heat flux increases. The EHD forces on the bottom of the boiling tube generate an enhanced heat transfer coefficient of 22,733 W/m^{2}K at a heat flux of 11.8 kW/m^2 and a suppressed heat transfer coefficient of 1798 W/m^{2}K at 52.7 kW/m^2. The EHD forces are only providing enhancement for this location at heat fluxes below 25 kW/m^2. Above 25 kW /m^2, the EHD forces are continuously suppressing the heat transfer as much as 380 percent on average and over 500 percent locally at the highest heat fluxes.

It is evident that the flow regime is influencing the EHD enhancement around the tube. At the low heat fluxes, the EHD forces produce substantial heat transfer enhancement at 15 kV. The Coulomb force and primarily the polarization force together are producing the significant enhancement, because a mixture of liquid and vapor is present and the wall superheat is low enough that the nucleation at the tube surface is not too substantial. At this point, the EHD forces are generating secondary fluid motion and the polarization forces are acting at the liquid-vapor interface to move the bubbles around the tube surface as they are formed. However, as the heat flux increases, more nucleation occurs at the tube wall, and the polarization forces attract the remaining liquid and force the bubbles to stay at the tube surface. This leads to decreased enhancement at the bottom of the tube and suppression at the top and middle of the tube. When more energy is added to the flow and the quality increases, the flow transitions to the annular regime. In this regime, the thinner liquid layer at the top of the tube can be removed by the polarization forces. By removing the liquid layer, the heat transfer is reduced and in some cases local dryout can be initiated. On the bottom of the tube, initially the EHD forces thin the liquid layer and thus increase the heat transfer because the layer is of sufficient thickness to cause improved vaporization. However, as the heat flux increases, the liq-

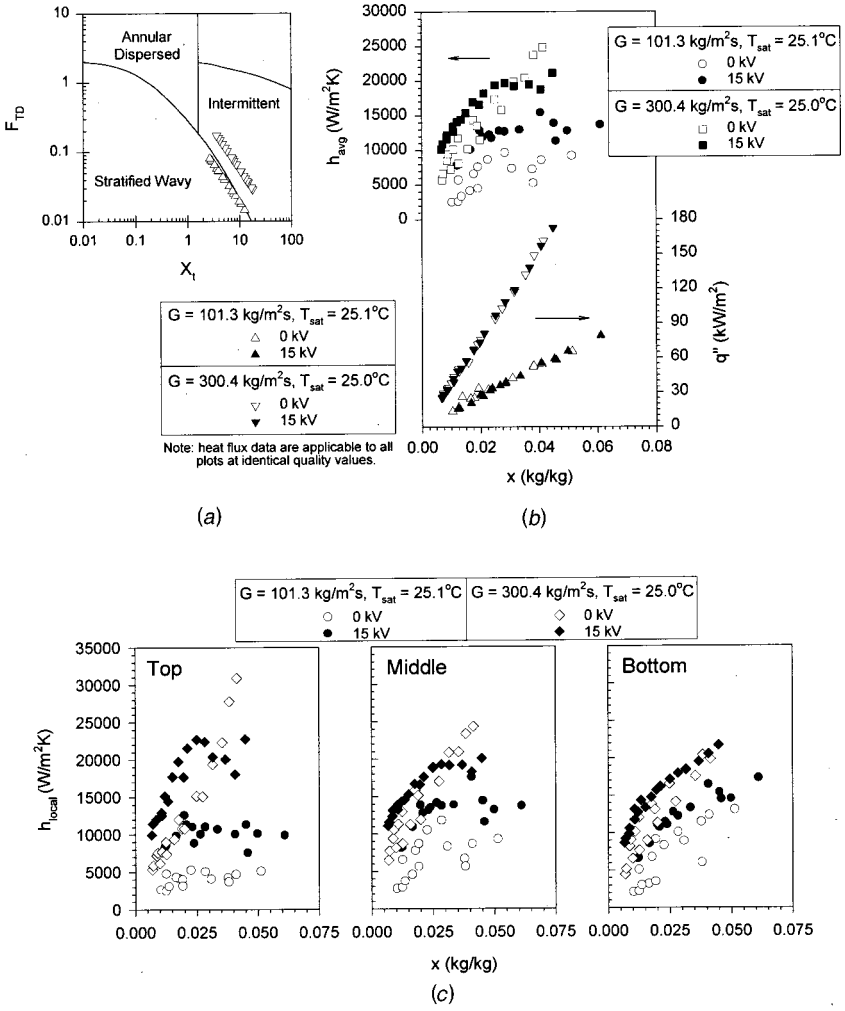

Fig. 8 Mass flux comparison in intermittent flow regime for R-134a in a smooth tube at a T_{sat} of 25°C: (*a*) the flow map, (*b*) average heat transfer coefficient data, and (*c*) local heat transfer coefficient data

uid layer is thinned further and the vapor bubbles that form on the wall are being pressed to the wall due to the EHD forces, resulting in a decrease in the heat transfer coefficient. In the 30-cm test section it can be seen how the EHD forces can drastically enhance the heat transfer at one heat flux level and quality and suppress the heat transfer at another. The strength of the EHD forces will determine how drastic this behavior will be, as seen when the applied voltage is increased from 5 kV to 15 kV. This suggests that the enhancement can be optimized, but it will be highly dependent on the quality, heat flux, and flow regime.

Moving to the last test section, the EHD enhancement at 5 kV becomes more significant compared to the other test sections, as seen in Figs. 7(*b*) and (*c*). Limited data were obtained at 5 kV at low heat fluxes and 15 kV throughout most of the heat flux range, due to arcing in the test section. It is important to note that the arcing was an electrode connection problem and not due to the convective boiling conditions. In the 50-cm section the flow was observed to be completely in the stratified-annular regime for the results shown in Fig. 7. At 5 kV, optimum conditions appear to occur and the enhancement reaches a peak of over 90 percent at a quality and heat flux of 0.41 kg/kg and 21 kW/m^2, respectively. The few data points at 15 kV show the rapid decay from enhancement to suppression at the high heat fluxes.

The influence of the mass flux for some selected results is presented in Figs. 8 and 9, showing heat transfer results for the intermittent and annular flow regimes, respectively, at mass fluxes of 101.3 and 300.4 kg/m^{2}s at a saturation temperature of 25°C. The flow at a mass flux of 101.3 kg/m^{2}s was stratified as discussed earlier in the flow maps without EHD and the flow at 300.4 kg/m^{2}s was not stratified. However, the vapor bubbles, as they formed, tended to migrate toward the top of the tube even at the higher mass flux, because the flow is horizontal. The plots shown in Figs. 8 and 9 are in the same format as Figs. 5–7.

In the intermittent (bubbly and slug) flow regime, as shown in Fig. 8(*a*), the effect of the two different mass fluxes can be seen in the difference in the local heat transfer coefficients at 0 kV. For the mass flux of 300.4 kg/m^{2}s, the local heat transfer coefficients without EHD are highest at the top of the tube and decrease to the bottom of the tube as the heat flux increases. The opposite occurs for the mass flux of 101.3 kg/m^{2}s. The liquid motion in the top portion of the tube is greater at 300.4 kg/m^{2}s compared to 101.3 kg/m^{2}s, but there is still less liquid in the top portion of the tube compared to the bottom, since the vapor bubbles are migrating toward the top of the tube. Greater evaporation is most likely occurring in the top of the tube at 300.4 kg/m^{2}s, due to the greater percentage of vapor in the top portion of the tube resulting in a thin liquid film at the wall.

The prime reason the heat transfer coefficients are lower at 101.3 kg/m^{2}s is that the heat flux is lower (see Fig. 8). As mentioned earlier, the heat transfer at these mass fluxes is nucleate boiling dominated. This is verified by examining the data shown

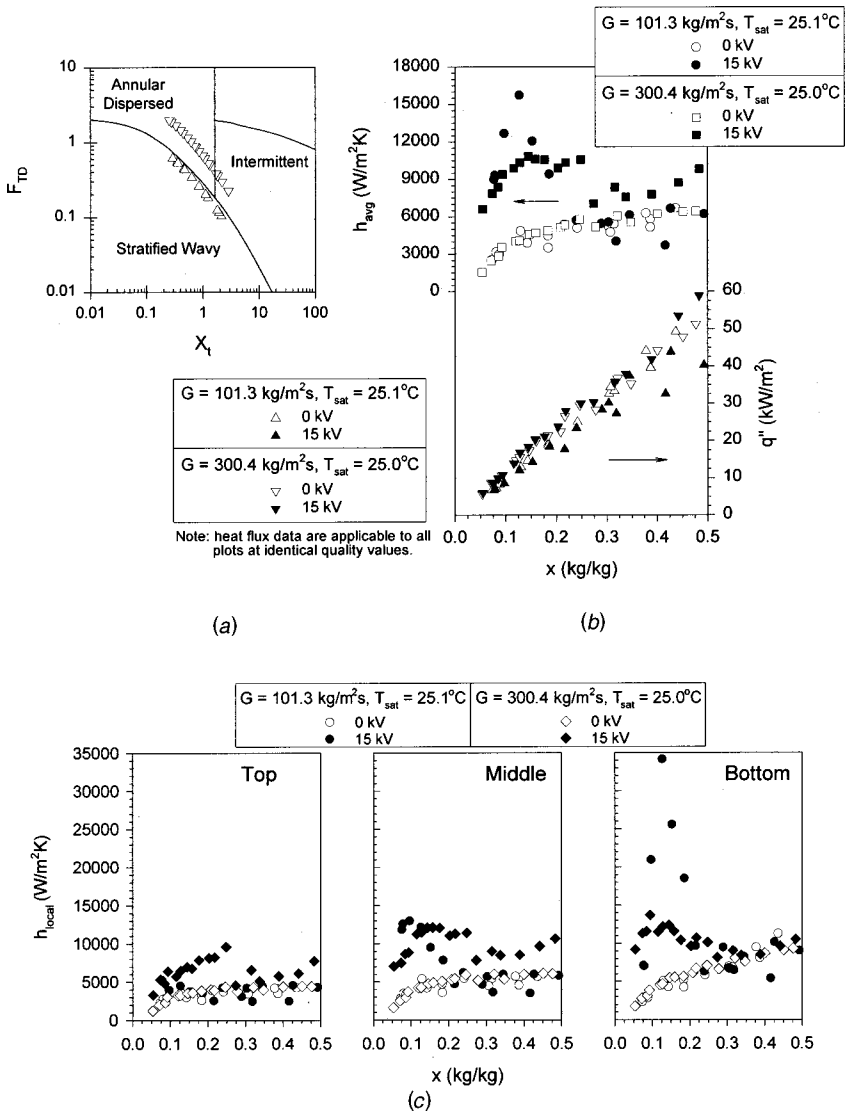

Fig. 9 Mass flux comparison from intermittent to annular flow regimes for R-134a in a smooth tube at a T_{sat} of 25°C: (*a*) the flow map, (*b*) average heat transfer coefficient data, and (*c*) local heat transfer coefficient data

in Fig. 9, where flow regime is primarily annular and the heat transfer coefficient and heat flux are the same at 0 kV for both mass fluxes throughout the quality range.

The EHD enhancement has decreased in the intermittent flow regime with the increased mass flux, as seen in Figs. 8(*b*) and (*c*). This would be expected because the EHD forces are acting primarily in the radial direction with this electrode design and, as the mass flux is increased, the fluid momentum is increasing in the axial direction. Therefore, the EHD forces, which are generating secondary fluid motion, attracting the liquid to the energized electrode and repelling the vapor bubbles toward the tube wall, are smaller relative to the axial momentum force at the higher mass flux. However, the EHD forces are still large enough to cause some suppression at the higher heat fluxes. This concept was theoretically confirmed recently by Bryan and Seyed-Yagoobi [5].

In the annular flow regime, as shown in Figs. 9(*b*) and (*c*), the EHD enhancement is also influenced by the change in mass flux. The EHD enhancement at 101.3 kg/m^{2}s is high at low heat fluxes and decreases with increasing heat flux to the point of suppressing the heat transfer at the highest heat fluxes. This is the same behavior, except for low heat fluxes on the tube bottom, as shown in Figs. 5–7 for the mass flux of 99.9 kg/m^{2}s and saturation temperature of 4.9°C. The EHD enhancement at 300.4 kg/m^{2}s is quite different. The local heat transfer coefficients, at 15 kV, increase, reach a peak, and then decrease as heat flux increases, but they are never lower than the local heat transfer coefficients at 0 kV. This is similar behavior to the 5 kV results shown in Figs. 7(*b*) and (*c*) and provides more support that there exists an optimum quality, flow regime, heat flux, and mass flux for a specific applied voltage and electrode design where the EHD forces will produce the greatest enhancements. This optimum is much more pronounced at 101.3 kg/m^{2}s, but only on the bottom of the tube. The reason that there are EHD enhancements for 300.4 kg/m^{2}s at the higher qualities and heat fluxes is believed to be related to the EHD forces relative to the axial momentum. The ability of EHD force to extract the liquid from the tube wall decreases as the axial momentum increases due to the increase in mass flux (also see Bryan and Seyed-Yagoobi [5]). However, the EHD forces are strong enough to generate instabilities at the liquid-vapor interface, thus enhancing the heat transfer.

One might expect that the application of the EHD forces would only provide enhancement at low qualities and suppression at higher qualities from the results presented in Figs. 5–9. This is not necessarily true for two reasons. First and most important is that

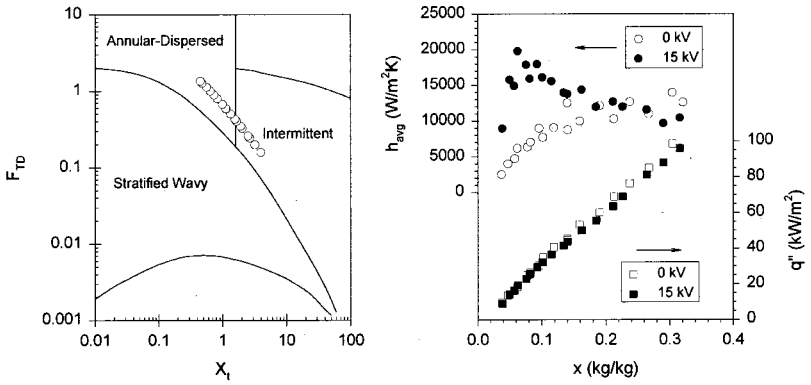

(*a*) second location (20 cm from inlet to test section) on the 30 cm section

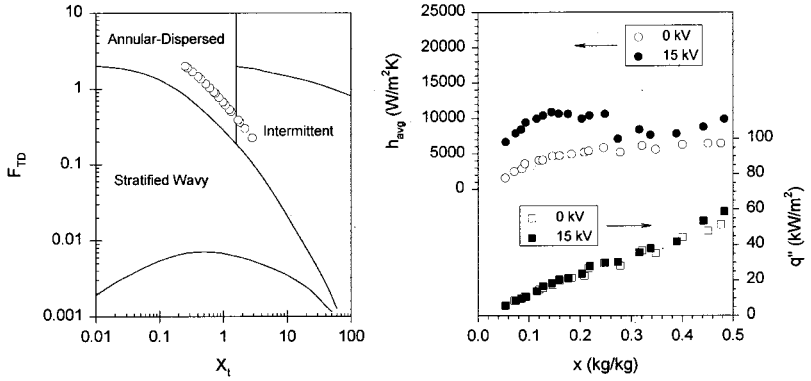

(*b*) second location (37.5 cm from inlet to test section) on the 50 cm section

Fig. 10 Influence of heat flux on EHD enhanced heat transfer for R-134a in a smooth tube at $G=300.4$ kg/m^{2}s and $T_{sat}=25.0°$C: (*a*) second location (20 cm from inlet to test section) on the 30-cm section, (*b*) second location (37.5 cm from inlet to test section) on the 50-cm section

the change in quality was achieved by increasing the heat flux. Therefore, when the EHD forces were suppressing the heat transfer at the higher qualities, primarily in the annular flow regimes, the heat flux was also high. Refrigeration applications on average operate at heat fluxes lower than 30 kW/m^2, and most of the suppression due to the EHD forces occurred above 30 kW/m^2. The high heat flux appears to be a significant contributing factor to the suppression. This can be seen by examining the data shown in Figs. 10 and 11. The heat transfer coefficient and heat flux for two locations at $G=300.4$ kg/m^2 and $T_{sat}=24.9°$C and at $G=101.3$ kg/m^2 and $T_{sat}=25.1°$C are shown in Figs. 10 and 11, respectively. What is interesting is that the suppression occurs in the 30-cm section as shown Fig. 10(*a*), where the heat flux is much higher, but not in the 50-cm section as shown in Fig. 10(*b*), at $G=300.4$ and 101.3 kg/m^2, which is further downstream from the 30-cm section and at a higher quality. When the heat flux is high, the rate of bubble nucleation at the tube surface is high. This can make it easier for the polarization force to remove the smaller amount of liquid from the tube surface, thus suppressing the heat transfer. The strength of the EHD forces relative to the structure of the convective boiling flow is also important and is the second reason that heat transfer enhancement does not necessarily occur only at low qualities. As shown in Fig. 9 there is an optimum enhancement that can occur for a given electric field strength and electrode design.

The experimental data presented in this work provide additional insight into the influence of the EHD forces on convective boiling heat transfer. Some of the observations presented and discussed in this paper were verified in a theoretical analysis, which was performed by Bryan and Seyed-Yagoobi [5] to relate the radial EHD pressure to the change in the axial momentum flux. They showed that the heat transfer enhancement and pressure drop penalty were directly proportional to the ratio of the radial EHD pressure to the change in the axial momentum flux. Finally, pressure drop and EHD power consumption were not presented in this work. However, detailed pressure drop and EHD power consumption can be obtained from Bryan [9].

Conclusions

From the experimental data, it is evident that the EHD forces can generate significant enhancements in the convective boiling heat transfer coefficient. However, the enhancements are highly dependent on the quality, flow regime, heat flux, mass flux, and the strength of the radial EHD forces relative to the flow axial momentum. In many cases the EHD forces can even drastically reduce the rate of heat transfer as is evident in the data at high heat fluxes and qualities. The primary mechanism of the EHD force density, which is generating the enhancement or suppression is the force resulting from the local change in permittivity between the liquid and vapor. This force, as depicted in Fig. 1, will attract the liquid towards the higher electric field strength, the electrode in the center of the tube, and force vapor bubbles to the lower electric field strength, the tube wall in the present design. When this force is enhancing heat transfer it is thinning and/or destabilizing the liquid layer, depending on the mass flux. However, this force can thin the liquid layer to a point of removing it and can drastically reduce the heat transfer, especially at low mass fluxes and high heat fluxes.

As the evaporation process progressed through the test sections, a flow regime was being approached in which the electrode design used in this work produced the highest heat transfer enhance-

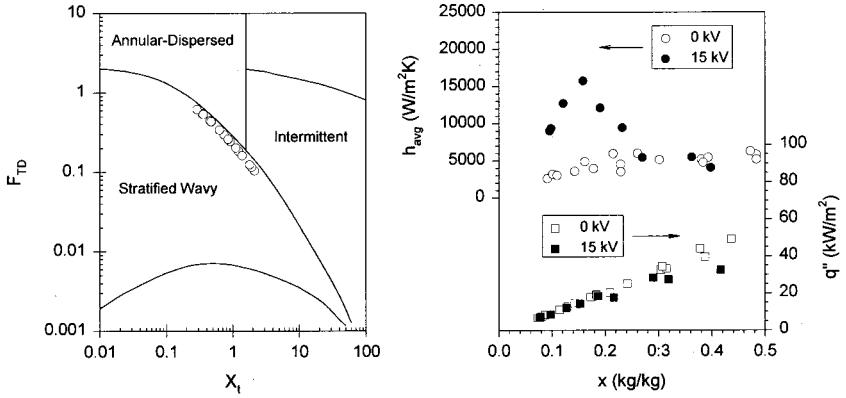

(*a*) second location (20 cm from inlet to test section) on the 30 cm section

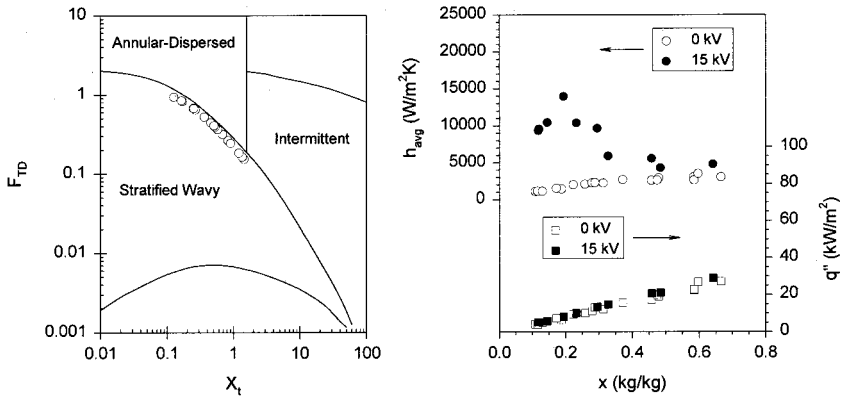

(*b*) second location (37.5 cm from inlet to test section) on the 50 cm section

Fig. 11 Influence of heat flux on EHD enhanced heat transfer for R-134a in a smooth tube at $G=101.3$ kg/m^{2}s and $T_{sat}=25.1°$C: (*a*) second location (20 cm from inlet to test section) on the 30-cm section, (*b*) second location (37.5 cm from inlet to test section) on the 50-cm section

ments. The experimental data provided evidence that an optimum EHD enhancement exists for a given quality, flow regime, heat flux, and mass flux for a specific electrode design. The electrode design used in this work is a simple design and it is not the optimum design to achieve the highest overall heat transfer enhancement. It is evident from the results that EHD enhancement of convective boiling has some promise. However, as the heat flux and quality continued to increase, the heat transfer enhancement decreased and eventually resulted in heat transfer suppression under certain operating conditions. Therefore, the electrodes must be properly designed with respect to the quality, flow regime, heat flux, and mass flux ranges to be experienced. It is important to note that the electrode design, applied voltage, and electrical properties of the fluid will also affect the EHD enhancement.

Acknowledgment

The authors gratefully acknowledge the financial support of this research by ASHRAE and NASA Lyndon B. Johnson Space Center. The authors, also, gratefully acknowledge DuPont for providing the refrigerant used in the experiments and Wolverine Tube, Inc. for providing the boiling tubes.

Nomenclature

c_p = specific heat (J/kgK)
D_E = electrode diameter (mm)
D_i = boiling tube inside diameter (mm)
D_o = boiling tube outside diameter (mm)
E = electric field strength (V/m)
E_E = electric field strength at electrode (V/m)
E_G = electric field strength at ground (V/m)
f_e = EHD force density (N/m^3)
F_{TD} = Taitel and Dukler flow parameter $[G^2x^2/\rho_v(\rho_l-\rho_v)D_ig]^{1/2}$
G = mass flux (kg/m^{2}s)
g = gravitational acceleration
h = heat transfer coefficient (W/m^{2}K)
h_{EHD} = heat transfer coefficient with EHD (W/m^{2}K)
h_{fg} = latent heat of vaporization (J/kg)
h_o = heat transfer coefficient without EHD (W/m^{2}K)
L = length of test section (cm)
$\dot{m}$ = mass flow rate of water (kg/s)
$\dot{m}_r$ = mass flow rate of refrigerant (kg/s)
Q_{EHD} = EHD power (W)
q'' = heat flux (kW/m^2)
T_{in} = inlet hot water temperature (°C)
T_{out} = outlet hot water temperature (°C)
T_{sat} = refrigerant saturation temperature (°C)
T_{wi} = tube inside surface temperature (°C)
T_{wo} = tube outside surface temperature (°C)
x = quality (kg/kg)
X_t = Martinelli parameter
ε = permittivity (pF/m)
ρ = density (kg/m^3)
ρ_e = charge density (C/m^3)

References

[1] Salehi, M., Ohadi, M. M., and Dessiatoun, S., 1995, ''EHD-Enhanced Convective Boiling of R-134a in Grooved Channels-Application to Compact Heat Exchangers,'' ASME J. Heat Transfer, **119**, pp. 805–809.

[2] Yabe, A., Taketani, T., Maki, H., Takahshi, K., and Nakadai, Y., 1992, ''Experimental Study of Electrohydrodynamically Enhanced Evaporator for Non-azeotropic Mixtures,'' ASHRAE Trans., **98**, No. 2, pp. 455–461.
[3] Singh, A., Ohadi, M. M., Dessiatoun, S., and Salehi, M., 1995, ''In-tube Boiling Enhancement of R-134a Utilizing the Electric Field Effect,'' *ASME/JSME Thermal Engineering Joint Conference*, Maui, Hawaii, Vol. 2, pp. 215–223.
[4] Norris, C., Cotton, J. S., Shoukri, M., Smith-Pollard, T., and Chang, J. S., 1997, ''Inlet Quality Effects on Horizontal Convective Boiling Under the Electrohydrodynamic (EHD) Effect,'' *Proceedings of ESA-IEJ Joint Symposium on Electrostatics*, Vol. 2, pp. 76–94.
[5] Bryan, J. E., and Seyed-Yagoobi, J., 2000, ''Electrohydrodynamically Enhanced Convective Boiling: Relationship between Electrohydrodynamic Pressure and Momentum Flux,'' ASME J. Heat Transfer (in press).
[6] Melcher, J. R., 1981, *Continuum Electromechanics*, MIT Press, Cambridge, Massachusetts.
[7] Seyed-Yagoobi, J., and Bryan, J. E., 1999, ''Enhancement of Heat Transfer and Mass Transport in Single-phase and Two-phase Flows with Electrohydrodynamics,'' Adv. Heat Transfer, **33**, pp. 95–186, Academic Press.
[8] Jones, T. B., 1977, ''Bubble Dielectrophoresis,'' J. Appl. Phys., **48**, No. 4, pp. 1412–1417.
[9] Bryan, J. E., 1998, ''Fundamental Study of Electrohydrodynamically Enhanced Convective and Nucleate Boiling Heat Transfer,'' Ph.D. Dissertation, Texas A&M University, College Station.
[10] Kline, S. J., and McClintock, F. A., 1953, ''Describing Uncertainties in Single Sample Experiments,'' Mech. Eng. (Am. Soc. Mech. Eng.), **75**, pp. 3–8.
[11] Taylor, J. R., 1982, *An Introduction to Error Analysis*, University Science Books, Mill Valley, California.
[12] Wattelet, J. P., Chato, J. C., Souza, A. L., and Christoffersen, B. R., 1994, ''Evaporative Characteristics of R-12, R-134a, and a Mixture at Low Mass Fluxes,'' ASHRAE Trans., **100**, No. 1, pp. 603–615.
[13] Kandlikar, S. G., 1990, ''A General Correlation for Saturated Two-Phase Flow Boiling Heat Transfer Inside Horizontal and Vertical Tubes,'' ASME J. Heat Transfer, **112**, pp. 219–228.
[14] Wattelet, J. P., 1994, ''Heat Transfer Flow Regimes of Refrigerants in a Horizontal-Tube Evaporator,'' Ph.D. Dissertation, University of Illinois, Urbana-Champaign, Illinois.
[15] Taitel, Y., and Dukler, A. E., 1976, ''A Model for Predicting Flow Regime Transitions in Horizontal and Near Horizontal Gas-liquid Flow,'' AIChE J., **22**, pp. 47–55.
[16] Seyed-Yagoobi, J., Geppert, C. A., and Geppert, L. M., 1996, ''Electrohydrodynamically Enhanced Heat Transfer in Pool Boiling,'' ASME J. Heat Transfer, **118**, pp. 233–237.
[17] Geppert, C. A., 1994, ''Electrohydrodynamically Enhanced Heat Transfer in Pool Boiling,'' Technical Report, Department of Mechanical Engineering, Texas A&M University, College Station, Texas.
[18] Ogata, J., and Yabe, A., 1993, ''Augmentation of Boiling Heat Transfer by Utilizing the EHD Effect-EHD Behavior of Boiling Bubbles and Heat Transfer Characteristics,'' Int. J. Heat Mass Transf., **36**, No. 3, pp. 783–791.
[19] Singh, A., Ohadi, M. M., Dessiatoun, S., and Chu, W., 1994, ''In-tube Boiling Enhancement of R-123 Using the EHD Technique,'' ASHRAE Trans., **100**, No. 2, pp. 818–825.
[20] Singh, A., 1995, ''Electrohydrodynamic (EHD) Enhancement of In-Tube Boiling and Condensation of Alternative (Non-CFC) Refrigerants,'' Ph.D. Dissertation, University of Maryland, College Park.
[21] Salehi, M., Ohadi, M. M., and Dessiatoun, S., 1996, ''The Applicability of the EHD Technique for Convective Boiling of Refrigerant Blends—Experiments with R-404A,'' ASHRAE Trans., **102**, No. 1, pp. 839–844.

Transport Phenomena During Solidification Processing of Functionally Graded Composites by Sedimentation

J. W. Gao

C. Y. Wang
e-mail: cxw31@psu.edu

Department of Mechanical and Nuclear Engineering,
The Pennsylvania State University,
University Park, PA 16802

A combined experimental and numerical investigation of the solidification process during gravity casting of functionally graded materials (FGMs) is conducted. Focus is placed on understanding the interplay between the freezing front dynamics and particle transport during solidification. Transparent model experiments were performed in a rectangular ingot using pure water and succinonitrile (SCN) as the matrix and glass beads as the particle phase. The time evolutions of local particle volume fractions were measured in situ by bifurcated fiber optical probes working in the reflection mode. The effects of important processing parameters were explored. It is found that there exists a particle-free zone in the top portion of the solidified ingot, followed by a graded particle distribution region towards the bottom. Higher superheat results in slower solidification and hence a thicker particle-free zone and a higher particle concentration near the bottom. The higher initial particle volume fraction leads to a thinner particle-free region. Lower cooling temperatures suppress particle settling. A one-dimensional multiphase solidification model was also developed, and the model equations were solved numerically using a fixed-grid, finite-volume method. The model was then validated against the experimental results and subsequently used as a tool for efficient computational prototyping of an Al/SiC FGM. [DOI: 10.1115/1.1339976]

1 Introduction

The recently developed functionally graded materials (FGMs) have been highly considered as candidate materials for applications in severe environments confronting modern technologies. Among various FGMs, metal matrix composite FGMs are of great practical interest. Metal matrix composite FGMs feature gradual compositional variations from ceramic at one surface to metal at the other, leading to the unique advantages of a smooth transition in thermal stresses across the thickness and minimized stress concentration at the interface of dissimilar materials. As a result, such FGMs are rapidly finding applications in aggressive environments with steep temperature gradients such as turbine components and rocket nozzles.

Presently, there is no reliable and inexpensive way of fabricating FGMs that allows for bulk production of large parts. Current methods of fabrication include solidification processing, chemical vapor deposition, plasma spray and powder metallurgy techniques [1]. Of these, perhaps the most economical and attractive processing route is gravity or centrifugal casting. The process involves the addition of a reinforcing particle phase to a liquid metal matrix and mixing them uniformly, followed by segregation of particles and liquid under gravity or in a centrifugal field to create a desired gradient in the particle concentration, and finally preservation of the spatially graded structure by solidification. Various FGMs such as metal-intermetallic compounds, metal-ceramics and metal alloy-ceramics have been successfully synthesized by this method [2–4].

A wealth of complex transport phenomena may occur in solidification processing of FGMs, including the transport of fluid, heat and solute, which governs the migration of particles in a liquid matrix, the interactions of particles with the advancing solidification front, and finally the incorporation of particles within the solidifying matrix. In order to create a desired particle distribution in the solidified part, the solidification time must be controlled such that it will be long enough to create the particle gradient but short enough to ''freeze'' the graded particle distribution in place. Therefore, it is of paramount importance to understand the solidification process with particle motion.

Particle sedimentation without solidification has been studied extensively in both fluidized bed and aqueous systems, but only a few investigations have addressed this problem in liquid metals. Hanumanth et al. [5] studied the sedimentation behavior of high volume fraction (as high as 0.30) of 90 μm diameter SiC particles in liquid aluminum using an electrical resistance probe to measure the in situ particle volume fraction. A multiphase hydrodynamic model was developed to describe the sedimentation. Using the same resistance probe, settling and clustering of 14 μm SiC particles in Al melts were monitored and analyzed by Irons and Owusu-Boahen [6]. From their analysis, the observed settling rates were consistent with that of 38 μm clusters containing ~42 percent particles by volume within the clusters. It was concluded that intense stirring prior to settling would result in smaller clusters.

Solidification of particle-reinforced metal-matrix composites (SiC particle in an aluminum alloy) was recently studied by Hanumanth and Irons [7] both numerically and experimentally. A one-dimensional enthalpy model was developed. In their model, particle velocity was simply estimated from the Richardson-Zaki hindered settling correlation [8], without solving the coupled momentum and continuity equations. This approach implies that the counter-current displacement flow of liquid due to particle sedimentation was not accounted for, which could lead to substantial overestimation of the particle phase velocity (i.e. by a factor of $1/(1-\varepsilon_p)$, where ε_p is the particle volume fraction). The mushy zone evolution was described using the Scheil equation. The effects of cooling rate and thermal conductivity of SiC particles were explored. It was proposed that the SiC particle thermal conductivity should be on the order of the single crystal value for accurate representation of cooling rates and particle settling, although very little settling was found to occur for the prescribed cooling condition. Feller and Beckermann [9] developed a multi-

Contributed by the Heat Transfer Division for publication in the JOURNAL OF HEAT TRANSFER. Manuscript received by the Heat Transfer Division February 29, 2000; revision received October 11, 2000. Associate Editor: D. A. Kaminski.

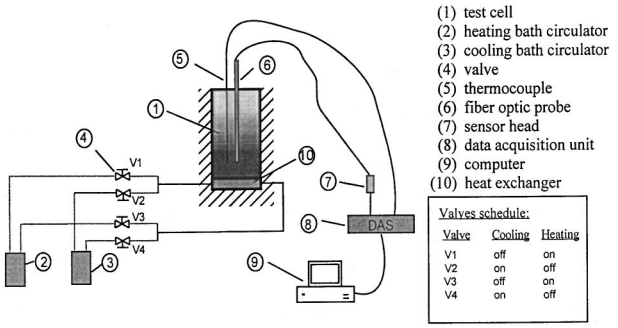

Fig. 1 Schematic of experimental setup

phase model for the alloy solidification of metal-matrix particulate composites with convection. The Happel [10] hindered settling function was used. The model was applied to various one and two-dimensional Al-7 wt pct Si/SiC systems. Good agreement was found between the simulation and available experimental sedimentation results in A356 systems containing clustering and non-clustering SiC particles.

The previous studies focused mainly on the final distribution of particles, whereas virtually no information on the time evolution of the coupled solidification and sedimentation events was revealed. Therefore, detailed mechanisms for particle segregation in a solidifying matrix, which are of paramount importance for the design of FGMs, remain elusive. Also, limited experimental work in the past has not provided detailed data on time evolution of the particle concentration distribution during matrix solidification. The availability of these data during processing is necessary to rigorously validate any sophisticated model describing FGM solidification. The present work is thus aimed at studying the detailed solidification process during gravity casting of FGMs by means of in situ measurements of both temperature and particle volume fraction. Transparent model experiments were performed using pure substances as the matrix and glass beads as the particle phase. Local particle volume fractions were measured by fiber optic probes, making it possible to obtain the volume fraction changes with time during settling and solidification. Subsequently, a one-dimensional numerical model, derived from the general multiphase solidification model of Wang [11], was developed and validated against the experimental results. The validated code was used as a tool for ''computational prototyping'' of as-cast FGMs.

2 Experimental Setup and Procedures

The experimental setup is schematically shown in Fig. 1. The rectangular test cell consists of a stainless steel heat exchanger cold plate as the bottom wall, a Plexiglas top wall and center section. Cooling was accomplished by passing a mixture of ethylene glycol and water (1:1) through the heat exchanger.

The glass beads supplied by MO-SCI Corporation were used as the particle phase. The mean diameter of the particles was found to be 30 μm with a standard deviation of 9 μm. The matrix liquids were succinonitrile from Alfa Aesar (purity: 98^+ percent, melting temperature 58°C) and distilled water, respectively.

A. Temperature Measurement. Temperature measurements were performed using copper-constantan (type-T) thermocouples that were mounted through the top panel of the test cell. Modular plug-in thermocouples (Omega Model number TMQSS-020-6) were used, calibrated to an accuracy of ± 0.3°C. Four thermocouples were placed at different height in the test cell, with positioning uncertainty of ± 1 mm. Each experiment was repeated three times by varying the horizontal position of each thermocouple at fixed height. The maximum temperature difference along the horizontal plane was found to be 0.5°C.

B. Particle Volume Fraction Measurement. There are a number of techniques for the measurement of solid concentrations in multiphase flows [12]. Among these techniques, fiber optic probes working in reflection mode are extensively used, especially for gas/solid flows in circulating fluidized beds. In the reflection mode, light is carried by the emitting fiber into a measuring volume and reflected back by the particles to the receiving fiber. Therefore, the reflection mode is especially suitable for measurements of dense suspensions.

Characteristics of Fiber Optical Probes. Plastic bifurcated fiber optic probes (model PBP26U) from Banner Engineering Corporation were used in this study. The probe has two parallel plastic optical fibers of 0.5 mm core size, bifurcated and shielded by annealed stainless steel. The probe was connected to an analog Umni-Beam sensor head (model OASBFP, Banner), which contains a light source (visible red $\lambda = 650$ nm) for the emitting fiber and a photodetector for the receiving fiber to convert the reflected light intensity to voltage signals. The time constant of the sensor is 2 ms, rendering the probes sufficiently fast for transient experiments. Subsequent signal sampling and processing were made by a PowerMac computer. More details can be found in Gao et al. [13].

Calibration. Each probe was calibrated before being used in the experiments. Detailed calibration procedures are described in Gao et al. [13]. The calibrations were first made in water/glass-bead suspensions. It was found that the measurement can be described by

$$\Delta U = U - U_0 = a\varepsilon_p^b, \tag{1}$$

where U is the output of the sensor at a particle volume fraction of ε_p, and U_0 represents the reading obtained in the same fluid without particles. This correlation is consistent with those shown by Hartge et al. [14] and Nieuwland et al. [12]. It is also found that the exponent b depends only on the properties of the particles and probes whereas the factor a depends on the carrier fluid (i.e., the liquid matrix here). Since the exponent b is independent of the type of fluids, the values of b determined in water/glass-bead suspension can be used in other glass-bead suspensions with transparent carrier fluids. This offers great advantages for the calibration of probes, especially for those carrier fluids that are solid at room temperature such as succinonitrile (SCN). Several suspensions of SCN/glass-bead with known particle volume fractions, namely 15 percent, 20 percent, and 40 percent, were used to obtain the numerical factors. These calibrated values along with complete calibration curves are given in detail in Gao et al. [13].

During the solidification and sedimentation experiments, the probes were inserted into the test cell through the top wall and were positioned by a scale, with positioning uncertainty of ± 1 mm.

C. Experimental Procedures. Suspensions were prepared by mixing particles with a liquid matrix. Before the experiments, the mixture was preheated to a certain superheat by pumping the working fluid from the heating circulator through the heat exchanger. At the desired temperature, the melt was stirred to form a homogenous suspension. At the same instant when stirring was stopped, the fiber optic probes and thermocouples were quickly inserted into the test cell. At this point, the coolant with preset temperature was run through the heat exchanger and the data acquisition system was initiated, with the sampling rate of 0.5 Hz for both temperature and particle volume fraction measurements.

3 Numerical Modeling

A. Model Formulation. A general multiphase modeling framework developed by Wang [11] is used to build the present model. The following assumptions are invoked:

Table 1 Thermophysical properties of succinonitrile/glass-bead

Quantity	Symbol	Value	Units	Reference
Liquid density	ρ_l	986.7	kg/m^3	[20]
Solid density	ρ_s	986.7	kg/m^3	assumed
Particle density	ρ_p	2500	kg/m^3	MO-SCI Inc.
Liquid viscosity	μ_l	2.56×10^{-3}	kg/m s	[20]
Liquid specific heat	C_{pl}	2000	J/kg K	[19]
Solid specific heat	C_{ps}	1910	J/kg K	[19]
Particle specific heat	C_{pp}	745	J/kg K	[17]
Liquid thermal conductivity	k_l	0.223	W/m K	[20]
Solid thermal conductivity	k_s	0.223	W/m K	[20]
Particle thermal conductivity	k_p	1.40	W/m K	[17]
Latent heat of fusion (pure SCN)	Δh	4.62×10^4	J/kg	[19]
Melting temperature (pure SCN)	T_m	331.0	K	[19]

Data from Refs. [17], [19], [20].

1 One-dimensional planar solidification.

2 The model treats particles, liquid and forming solid as separate phases.

3 The motion of particles is slow and reaches the terminal velocity instantaneously. This assumption is appropriate due to the small size of the particles.

4 Local thermal equilibrium exists, which is justified by the typically large thermal conductivities of metals.

5 Particle pushing at the solid/liquid interface does not occur due to the relatively high advancing velocity of the solidification front in the present study as compared to the critical velocity for pushing, as shown by Gao et al. [13]. This fact is also well supported by our experimental observations.

6 The particles are rigid and spherical, and do not react chemically with the matrix.

7 Volume change during solidification is negligible.

8 All thermophysical properties are assumed to be constant as given in Tables 1 and 2.

With the preceding assumptions, a working model can be formulated from the general multiphase model as follows.

Mass Conservation Equations

$$\text{Particle:}\quad \frac{\partial}{\partial t}(\rho_p\varepsilon_p)+\frac{\partial}{\partial y}(\rho_p\varepsilon_p v_p)=0 \tag{2}$$

$$\text{Solid:}\quad \frac{\partial}{\partial t}(\rho_s\varepsilon_s)=\Gamma_s \tag{3}$$

Table 2 Thermophysical properties of Al/SiC

Quantity	Symbol	Value	Units	Reference
Liquid density	ρ_l	2390	kg/m^3	[21]
Solid density	ρ_s	2550	kg/m^3	[21]
Particle density	ρ_p	3200	kg/m^3	[21]
Liquid viscosity	μ_l	1.26×10^{-3}	kg/m s	[18]
Liquid specific heat	C_{pl}	1079.5	J/kg K	[21]
Solid specific heat	C_{ps}	1176.5	J/kg K	[21]
Particle specific heat	C_{pp}	840	J/kg K	[21]
Liquid thermal conductivity	k_l	95	W/m K	[21]
Solid thermal conductivity	k_s	210	W/m K	[21]
Particle thermal conductivity	k_p	16	W/m K	[22]
Latent heat of fusion (pure Al)	Δh	3.97×10^5	J/kg	[21]
Melting temperature (puer Al)	T_m	933.6	K	[21]

Data from Refs. [18], [21], [22].

$$\text{Liquid:}\quad \frac{\partial}{\partial t}(\rho_l\varepsilon_l)+\frac{\partial}{\partial y}(\rho_l\varepsilon_l v_l)=-\Gamma_s \tag{4}$$

Momentum Conservation Equations

$$\text{Particle:}\quad -\varepsilon_p\frac{\partial p}{\partial y}-\rho_p\varepsilon_p g+M_p^d=0 \tag{5}$$

$$\text{Liquid:}\quad -\varepsilon_l\frac{\partial p}{\partial y}-\rho_l\varepsilon_l g-M_p^d=0 \tag{6}$$

Energy Conservation Equation

$$\begin{aligned}&\frac{\partial}{\partial t}[(\rho_s\varepsilon_s C_{ps}+\rho_p\varepsilon_p C_{pp}+\rho_l\varepsilon_l C_{pl})T]\\&+\frac{\partial}{\partial y}[(\rho_p\varepsilon_p C_{pp}v_p+\rho_l\varepsilon_l C_{pl}v_l)T]\\&=\frac{\partial}{\partial y}\left[(\varepsilon_s k_s+\varepsilon_p k_p+\varepsilon_l k_l)\frac{\partial T}{\partial y}\right]+\Gamma_s[\Delta h+(C_{ps}-C_{pl})T_m]\end{aligned} \tag{7}$$

Boundary Conditions

$$y=0\quad T=T_w,\quad \frac{\partial\varepsilon_p}{\partial y}=\frac{\partial\varepsilon_l}{\partial y}=0,\quad v_p=v_l=0$$

$$y=l\quad \frac{\partial T}{\partial y}=0,\quad \frac{\partial\varepsilon_p}{\partial y}=\frac{\partial\varepsilon_l}{\partial y}=0,\quad v_p=v_l=0$$

Initial Conditions

$$T=T_i\quad \varepsilon_p=\varepsilon_{pi}\quad \varepsilon_s=\varepsilon_l=0\quad \text{at } t=0$$

Constitutive Equation

$$\varepsilon_p+\varepsilon_s+\varepsilon_l=1 \tag{8}$$

Following Wang [11], the liquid-particle drag term M_p^d in a multiparticle system can be modeled as

$$M_p^d=\frac{18(1-\varepsilon_l)\mu_l C_\varepsilon}{d^2}\varepsilon_l^2(v_l-v_p), \tag{9}$$

where the settling ratio for a multiple particle system, C_ε, accounts for all departures from the idealized single solid sphere settling as described by Stokes law. In this study, the well established hindered settling function of Richardson and Zaki [8] was utilized,

$$C_\varepsilon=(1-\varepsilon_p)^{-4.65}. \tag{10}$$

Further manipulation of momentum Eqs. (5) and (6) by incorporating Eqs. (2)–(4) and (9) gives:

$$v_p=-\frac{(\rho_p-\rho_l)\varepsilon_p g d^2}{18\mu_l(1-\varepsilon_l)C_\varepsilon(\varepsilon_p+\varepsilon_l)^2}\quad v_l=-\frac{\varepsilon_p v_p}{\varepsilon_l}. \tag{11}$$

Equation (11) is valid in the free particle regime, whereas for the packed bed regime both v_p and v_l are set to be zero.

B. Numerical Procedures. The conservation equations are solved simultaneously using a fixed-grid, single-domain numerical solution procedure. A fully-implicit, control-volume based finite difference method is utilized to discretize the conservation equations (2), (3), and (7), with the finite-difference coefficients

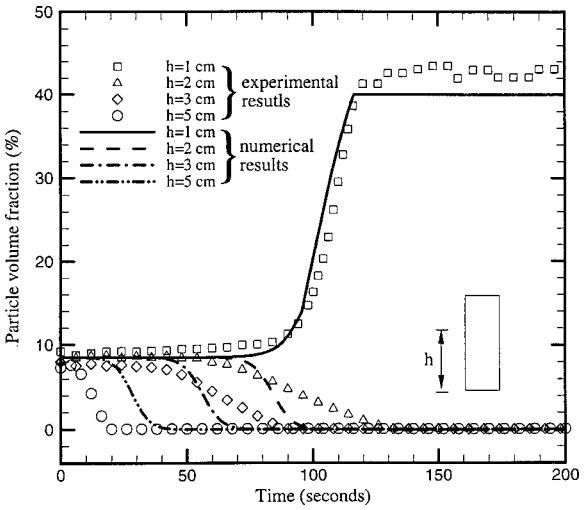

Fig. 2 Sedimentation curve for a water/glass-bead system (ε_{pi}=8.5 percent at room temperature)

evaluated by the upwind scheme. The discretized equations are solved iteratively. The detailed procedures can be found in the literature [13].

Stringent numerical tests were performed to ensure that solutions were independent of the grid size and time step. For a typical water/glass-bead solidification system, the maximum difference in temperature and particle volume fraction is less than 0.02°C and 0.1 percent, respectively for a grid size containing 40 to 150 control volumes. Virtually no difference was found in the results for time steps ranging from 0.02 s to 5 s. It was found that a grid containing 60 control volumes in the *y*-direction with a single control volume in the *x*-direction provides sufficient spatial resolution. Previous experience has also shown that such a grid is able to capture all dynamic solidification features at a reasonable computational cost [11]. A time step of 0.5 s was utilized for all simulations reported in the following.

4 Results and Discussion

A. Model Validation

Sedimentation. A mixture of water and 8.5 percent volume fraction of glass beads was poured into the test cell to produce a melt height of 6 cm. The sedimentation results are plotted in Fig. 2. It can be seen that in general, the model prediction agrees well with the experimental results, which show the characteristics of one-dimensional batch sedimentation, as depicted in the literature [7,15]. That is, a particle-free zone starts to form from the top and a layer of sediment on the bottom; in the middle portion of the cell, the particle volume fraction remains the initial particle volume fraction for a period of time and then starts to monotonically decrease to zero. Note that within the sediment bed (i.e., 1 cm away from the bottom), the particle volume fraction approaches 40 percent, lower than the random close packing factor of 60 percent. This can be attributed to the fact that the particles may form clusters during sedimentation, resulting in a loosely packed sediment at the bottom. This packing limit will be utilized in all of the numerical simulations. The experimental result for the location 5 cm away from the bottom exhibits faster settling than the model prediction, which may be due to the fact that the vortex motion of the suspension during the stirring persists and hence expedites the settling. This effect is most pronounced on the settling of particles at the top, where the particle-free zone forms before the vortex motion dies out. It is also interesting to notice more gradual decreases of the particle volume fraction in the experimental sedimentation curves at positions 2 and 3 cm away from the bottom. This may be attributed to the particle size distribution of the glass beads used.

It should be pointed out that there are a number of hindered settling functions in the literature [16], obtained mainly from aqueous or gas/solid systems. Among those relations, the Happel and Richardson-Zaki relations have been used most widely. Preliminary simulations showed that if the Happel hindering function was applied in the present model, the predicted settling rate is about half of that with the Richardson-Zaki function, i.e., Eq. (10). Feller and Beckermann [9] used the Happel relation in their model and discussed their results in relation to the study of Hanumanth et al. [5], in which the Richardson-Zaki's function was applied. They concluded that the Richardson-Zaki relation overestimates the settling rate. They attributed the good agreement between the experimental and modeling results in the study of Hanumanth et al. [5] to a larger liquid melt viscosity used. The present study, however, indicates that the Richardson-Zaki function gives more realistic predictions, which is consistent with numerous studies in the literature for aqueous and gas/solid systems [16]. Since the current study was performed for water, whose thermophysical properties are well documented in the literature and can be evaluated accurately, the viscosity is unlikely a factor that affects the above conclusion.

Solidification With Particle Sedimentation. Experiments and simulations were performed to validate the model in dealing with combined solidification and particle settling. For each simulation, the measured wall temperature from the experiments was fitted to a polynomial function, namely $T_w = f(t)$, to give temperature boundary conditions for the energy equation.

The mixture used in the preceding sedimentation experiment was solidified from an initial temperature of 23°C. The cooling curves and time evolution of particle concentrations are plotted in Figs. 3(*a*) and 3(*b*). Good agreement between the experiment and simulation was achieved. It can be seen that due to the large latent heat of water, the solidification is fairly slow and therefore the curves for the particle volume fraction are very similar to those in the pure sedimentation case shown in Fig. 2.

With the same initial temperature, a water/glass-bead suspension with an initial particle volume fraction of 20 percent was solidified. The results are plotted in Figs. 4(*a*) and 4(*b*). The model prediction is in good agreement with the experiment.

One interesting feature is that the wall temperature experiences an increase around 150 seconds into the experiment. This is found in cooling curves for both cases (see Figs. 3(*a*) and 4(*a*)), and can be explained by the fact that freezing occurred at this time instant, releasing a large amount of latent heat and therefore increasing the local temperature. This phenomenon was not observed in the solidification of the SCN/glass-bead system probably due to the much smaller latent heat of succinonitrile.

B. SCN/Glass-Bead Systems. Due to its high specific heat and low freezing temperature, the water/glass-bead system does not allow much room for the investigation of various processing conditions. Therefore, in the subsequent experimental studies, a SCN/glass-bead system was investigated.

The suspensions were prepared by mixing prescribed volume fractions of glass beads with SCN and forming a melt height of 6.35 cm for all experiments. The experimental conditions are summarized in Table 3.

Base Case. Figures 5(*a*) and 5(*b*) show the results for a base case having a 20 percent volume fraction of particles, a cooling temperature of −10°C, and an initial temperature of 63°C. Comparing the experimental and numerical results, reasonable agreement was found for the cooling curve, while agreement for the time evolutions of the particle concentration is only fair. The discrepancy may be attributed to the purity of SCN used in this study, namely 98^+ percent. Under certain cooling conditions, den-

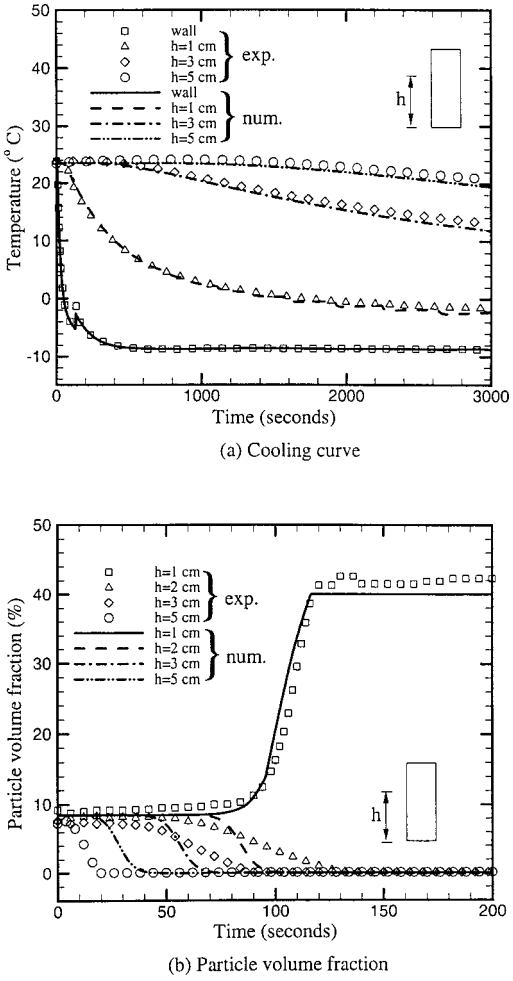

Fig. 3 Solidification of a water/glass-bead suspension (ε_{pi} = 8.5 percent, T_i = 23°C): (*a*) cooling curves; (*b*) time evolution of particle volume fraction

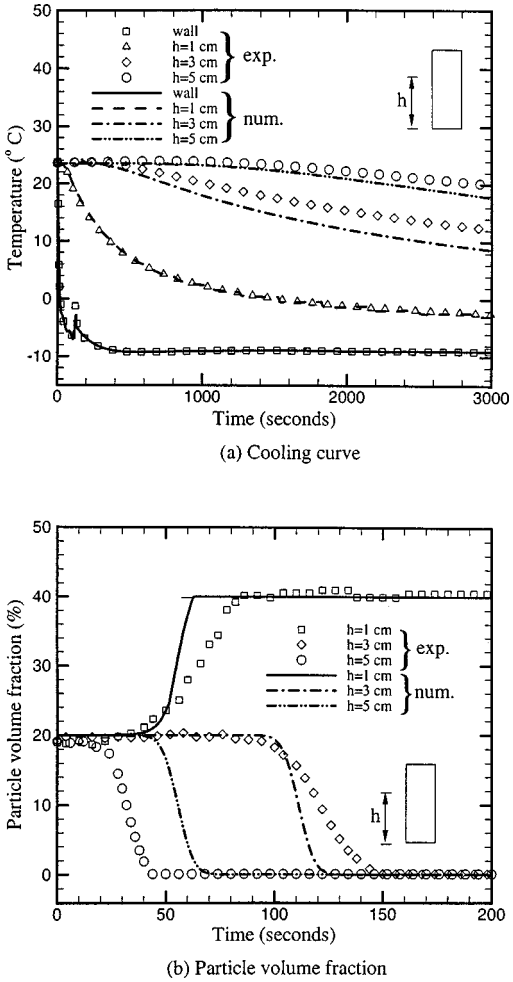

Fig. 4 Solidification of a water/glass-bead suspension (ε_{pi} = 20 percent, T_i = 23°C): (*a*) cooling curves; (*b*) time evolution of particle volume fraction

dritic microstructures were observed that would affect the measurement of particle volume fractions, especially in the solidifying region.

The final particle concentration distributions measured and predicted for the baseline case are shown in Fig. 6(*a*). Upon cooling, the melt close to the wall solidified first so that the particle volume fraction was fixed approximately at its initial value. This occurs relatively quickly, as is shown by the cooling curve for the first thermocouple (at the wall). For subsequent points away from the wall, the particle volume fraction increases due to settling from above before solidification, leading to a higher particle volume fraction. Solidification, however, interrupts the settling process: when the solidification front passes through a certain control volume, it freezes the local particle concentration in place and stops the particle flow from the above. This results in an increasing particle concentration at the location right above it since the control volume at this location only receives particles from its upper neighbor. In the meantime, when moving upward, the solidification front becomes slower, allowing more time for particles to settle. This trend develops as the solidification and settling progresses, resulting in a graded layer of about 7 mm thick from the bottom, with an almost linearly increasing particle concentration across the layer (see Fig. 6). Above this layer, solidification was not fast enough, hence a layer of packed-bed particle volume fraction was formed, followed by a particle-free zone on top of it.

Parametric Study. In this section, effects of different parameters on the final particle concentration distribution are examined.

Figure 6(*a*) also summarizes the effect of increasing superheat of the melt. It is indicated that increasing the superheat (from 5°C to 10°C) slows down the solidification allowing for more particles to settle before freezing occurs. Therefore the final particle distribution is slightly higher throughout most of the test cell with more of the cell being occupied by pure succinonitrile for Case 2.

Figure 6(*b*) shows that increasing the temperature of the bottom cold wall, as expected, produces a slightly thinner graded layer. The higher cooling temperature causes slower solidification, and therefore the particles have more time to settle before solidification, resulting in a thinner graded layer with higher local particle concentration as compared to the corresponding locations in the base case.

Table 3 Experimental conditions for SCN/glass-bead systems

Case #	Initial Particle Volume Fraction (%)	Superheat ΔT (K)	Cooling Temperature (°C)
1 (baseline case)	20	5	-10
2	20	10	-10
3	20	5	5
4	15	5	-10

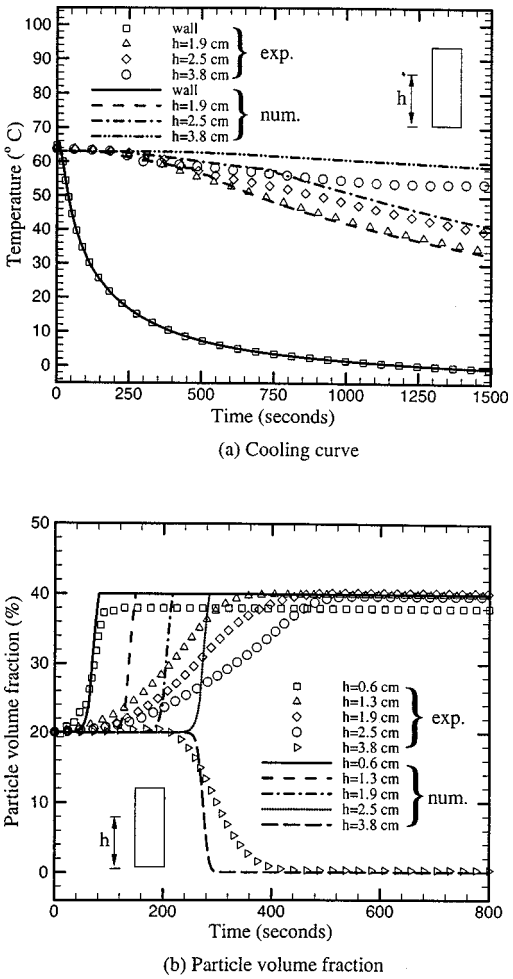

Fig. 5 Solidification of a SCN/glass-bead suspension (ε_{pi} = 20 percent, T_i = 63°C): (*a*) cooling curves; (*b*) time evolution of particle volume fraction

The effects of the initial particle concentration are much more pronounced, as indicated in Fig. 6(*c*). When the initial particle volume fraction is decreased from 20 percent to 15 percent, two of the probes show zero readings, indicating a larger particle-free region at the top. A thicker gradient layer is formed but with generally lower particle concentrations. This is due to the fact that there are fewer particles in the system, requiring a longer time for particles to settle before they become packed.

FGM Solidification Mechanisms. From the above analysis, two factors can be identified to be responsible for creation of the graded structure in a solidified FGM, namely, particle migration and solidification. Particle migration segregates the particles from the liquid melt and thus creates a gradient in their volume fraction. Solidification interrupts the particle migration and alters the segregation process, in such a way that it ''freezes'' the local particle concentration in place and alters the particle migration in the non-solidified regions. In view of the interplay between the two factors, one can tailor a gradient in an FGM by controlling the various processing conditions.

C. Solidification of Al-SiC FGMs. The validated code was applied to simulate the casting of Al-SiC FGMs from a melt 6 cm in height, with the bottom chill surface maintained at a constant temperature. The packed particle volume fraction was set to be 40 percent. Although this value may vary in reality, depending on the degree of particle clustering, the general conclusions are still applicable.

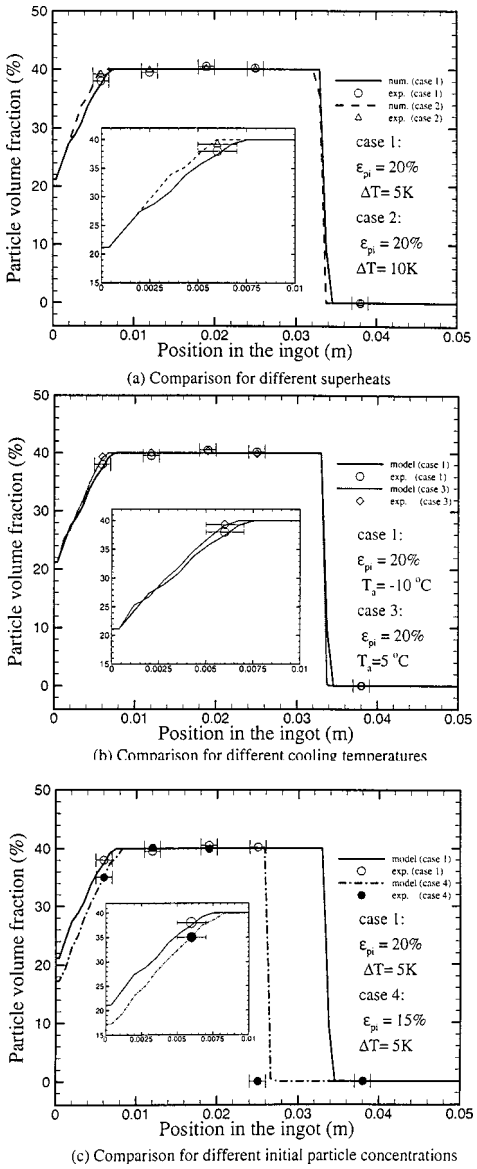

Fig. 6 Particle concentration distribution in a solidified SCN/glass-bead system under different processing conditions

Figure 7(*a*) explores the effect of cooling temperatures for a melt initially containing 20 percent SiC particles of 20 microns. It can be seen that a higher cooling temperature will allow particles to settle, and hence generate a certain gradient in the solidified part. Low cooling temperature freezes the melt quickly due to the large thermal conductivity of aluminum and therefore the particles do not have time to segregate, leading to a nearly homogeneous particle distribution.

Melts containing three different particle sizes are solidified, as shown in Figure 7(*b*). Larger particles settle faster and thus form a packed bed more easily, which is the case for 40 μm particles where a gradient is confined within a 2 cm region towards the bottom with a packed bed of about 1.5 cm in thickness followed. For particles of 10 μm, however, the sedimentation is too slow and the final particle concentration is almost uniform throughout the ingot.

The initial particle volume fraction has a significant effect on the final particle distribution, especially for a larger particle size like 40 μm, as indicated in Fig. 7(*c*). A gradient is formed from the bottom of the ingot in all three cases. The initial particle concentration of 10 percent gives the thickest gradient region and

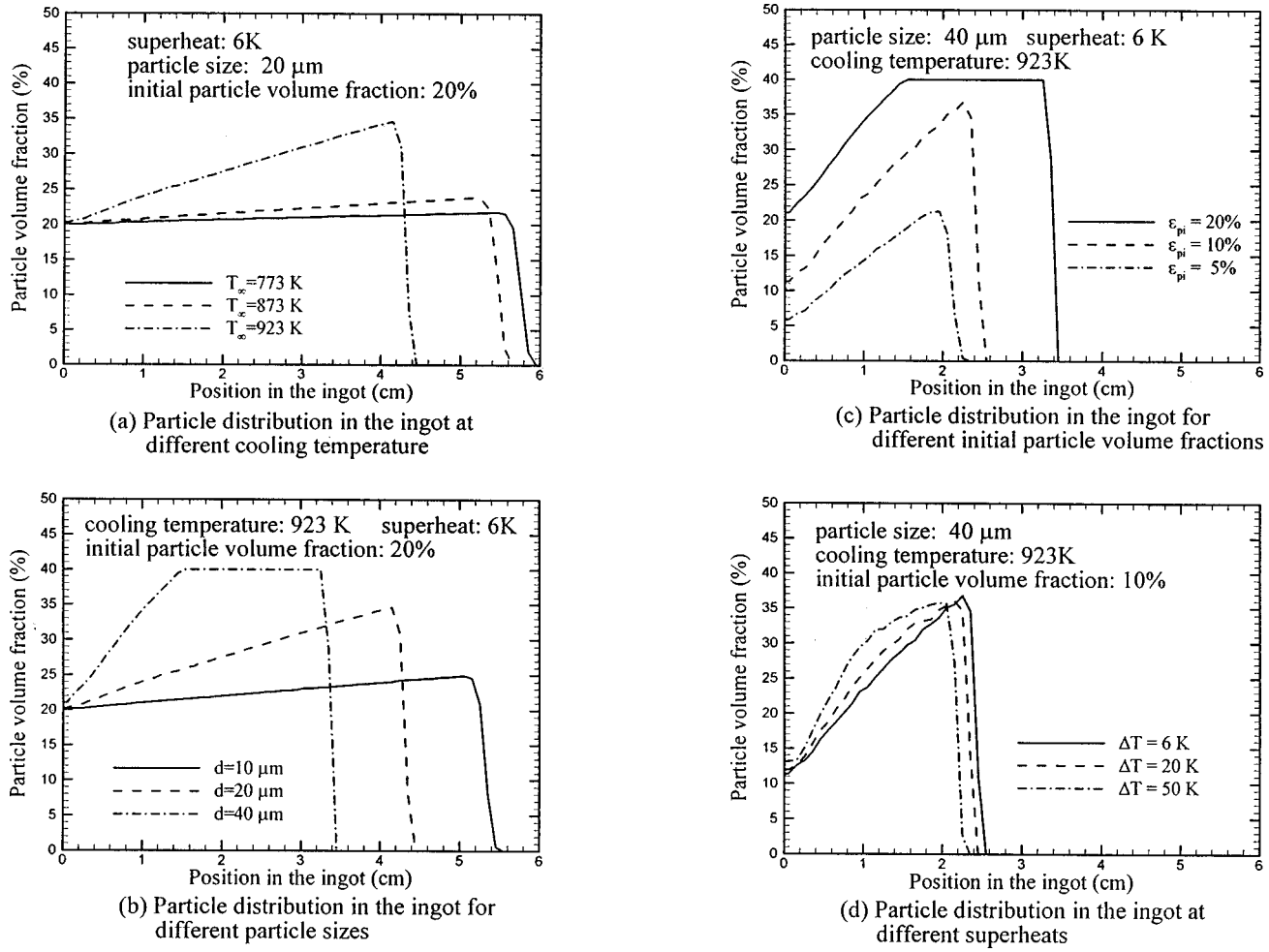

Fig. 7 Particle concentration distribution in a solidified Al/SiC composite under different processing conditions

the steepest gradient. 20 percent initial particle concentration results in a thick packed bed region whereas the 5 percent case simply does not have enough particles to generate a thick gradient layer. Therefore, in the casting practice, there exists an optimized initial particle volume fraction at a specific particle size for a desired particle gradient.

The effect of superheat, however, is not pronounced as can be seen from Fig. 7(*d*), which may be attributed to the large thermal conductivity of aluminum, allowing the superheat to be dissipated quickly upon cooling. A higher superheat allows slightly more time for particles to settle and hence a thinner gradient layer and a higher particle concentration at the same position in the graded zone.

The simulations confirm that the generation of a particle concentration gradient is determined by the competition between the rates of particle sedimentation and matrix solidification. It should be pointed out that in this study the final profiles of particle concentration do not vary monotonically across the entire part. Instead, there exists a layer of increasing particle volume fraction from the initial concentration to the packing limit, followed by a particle-free region on top of it (see Figs. 6 and 7). This is due to the fact that cooling starts instantaneously with the settling process, resulting in a particle concentration being close to the initial value at the cold surface. In order to obtain a monotonically varying particle distribution in the finally solidified part, one could delay the cooling until the maximum particle concentration (i.e., a packed bed) forms at the bottom followed by a layer of decreasing particle concentration upwards. The multiphase model developed in this study can be applied to design such a delayed cooling scheme to achieve the desired gradient. Research is underway to find an optimized set of processing conditions using an inverse problem design methodology.

5 Conclusions

Both experimental and numerical studies have been carried out for solidification of FGMs. Key conclusions from this study are as follows:

1 Fiber optic probes working in the reflection mode were successfully applied to the in situ measurement of particle volume fraction.

2 The experiments were performed to provide benchmark data on the time evolution of the particle distribution during solidification processing as well as to investigate effects of various processing parameters. The interplay between solidification and particle transport was elucidated in relation to creation of gradient structures in FGMs.

3 The multiphase solidification model developed in this study was extensively validated against the experimental results and generally good agreement was found. Simulations for the Al/SiC FGMs indicated that by optimizing the processing conditions, such as particle size, initial particle concentration, cooling rate and superheat, one can engineer a desired gradient in the solidified part.

Future work will focus on other modes of the interactions between particles and the solidification front, e.g., particle pushing and clustering. The model can also be extended to design centrifu-

gally cast FGMs. Research is also underway to investigate multi-dimensional solidification with melt convection in the presence of particles.

Acknowledgment

This work was supported by National Science Foundation under Grant No. CTS-9733662.

Nomenclature

a = coefficient in Eq. (1)
b = exponent in Eq. (1)
C_p = specific heat, J/kg-K
C_ε = hindered settling function
d = diameter of particles, μm
g = gravitational acceleration, m/s^2
k = thermal conductivity, W/mK
l = height of the suspension, m
M_p^d = particle/liquid drag per unit volume, N/m^3
p = pressure, N/m^2
T = absolute temperature, K
T_m = melting temperature, K
T_w = wall temperature, K
t = time, s
U = sensor output, V
v = velocity component in y-direction, m/s
y = y-coordinate in Cartesian system, m

Greek Symbols

ε_k = volume fraction of phase k, $[-]$
ε_{pi} = initial particle volume fraction, $[-]$
Γ_s = phase change rate, kg/m^3-s
μ = dynamic viscosity, N·s/m
ρ = density, kg/m^3
Δh = latent heat of fusion, J/kg

Subscripts

i = initial condition
l = liquid phase
p = particle phase
s = solid phase

References

[1] Mortensen, A., and Suresh, S., 1995, ''Functionally Graded Metals and Metal-Ceramic Composites: Part 1 Processing,'' Int. Mater. Rev., **40**, No. 6, pp. 239–259.
[2] Lajoye, L., and Suéry, M., 1988, ''Modelling of Particle Segregation During Centrifugal Casting of Al-Matrix Composites,'' in *Cast Reinforced Metal Composites*, S. G. Fishman and A. K. Dhingra, Eds., ASM, Materials Park, OH, pp. 15–20.
[3] Fukui, Y., Takashima, K., and Photon, C. B., 1994, ''Measurement of Young's Modulus and Internal Friction of an In Situ Al-Al_3Ni Functionally Gradient Material,'' J. Mater. Sci., **29**, pp. 2281–2288.
[4] Fukui, Y., and Watanabe, Y., 1996, ''Analysis of Thermal Residual Stress in a Thick-Walled Ring of Duralcan-Base Al-SiC Functionally Graded Material,'' Metall. Trans. A, **27A**, pp. 4145–4151.
[5] Hanumanth, G. S., Irons, G. A., and Lafreniere, S., 1992, ''Particle Sedimentation during Processing of Liquid Metal-Matrix Composites,'' Metall. Trans., **23B**, pp. 753–762.
[6] Irons, G. A., and Owusu-Boahen, K., 1995, ''Settling and Clustering of Silicon Carbide Particles in Aluminum Metal Matrix Composites,'' Metall. Trans. B, **26B**, pp. 981–989.
[7] Hanumanth, G. S., and Irons, G. A., 1996, ''Solidification of Particle-Reinforced Metal-Matrix Composites,'' Metall. Trans. B, **27B**, pp. 663–671.
[8] Richardson, J. R., and Zaki, W. N., 1954, ''Sedimentation and Fluidization: I,'' Trans. Inst. Chem. Eng., **32**, pp. 35–53.
[9] Feller, R. J., and Beckermann, C., 1997, ''Modeling of Solidification of Metal-Matrix Particulate Composites with Convection,'' Metall. Trans. B, **28B**, pp. 1165–1183.
[10] Happel, J., 1958, ''Viscous Flow in Multiparticle Systems: Slow Motion of Fluids Relative to Beds of Spherical Particles,'' AIChE J., **4**, pp. 197–201.
[11] Wang, C. Y., 1994, ''Multi-Scale/-Phase Modeling of Dendritic Alloy Solidification,'' Ph.D. thesis, University of Iowa, Iowa City, IA.
[12] Nieuwland, J. J., Meijer, R., Kuipers, J. A. M., and Swaaij, W. P. M., 1996, ''Measurements of Solids Concentration and Axial Solids Velocity in Gas-Solid Two-Phase Flows,'' Powder Technol., **87**, pp. 127–139.
[13] Gao, J. W., White, S. J., and Wang, C. Y., 1999, ''Solidification Processing of Functionally Graded Materials by Sedimentation,'' in *Proc. of IMECE 99*, ASME, Nashville, TN.
[14] Hartge, E. U., Rensner, D., and Werther, J., 1988, ''Solids Concentration and Velocity Patterns in Circulating Fluidized Beds,'' *Proceedings from the 2nd International Conference on Circulating Fluidized Bed Technology*, Basu, J., and Large, J. F., Eds., Pergamon, Oxford, pp. 165–180.
[15] Gidaspow, D., 1994, *Multiphase Flow and Fluidization: Continuum and Kinetic Theory Descriptions*, Academic Press, San Diego, CA.
[16] Davis, R. H., 1996, ''Velocities of Sedimenting Particles in Suspensions,'' *Sedimentation of Small Particles in a Viscous Fluid*, E. M. Troy, ed., Computational Mechanics Publications, UK, pp. 161–198.
[17] Incropera, F. P., and DeWitt, D. P., 1996, *Fundamentals of Heat and Mass Transfer*, 4th Ed., Wiley, New York.
[18] Landolt, H., and Börnstein, R., 1965, *Zahlenwerte und Funkt.*, Springer-Verlag, Berlin, Teil 2, Band IV.
[19] Rubinstein, E. R., and Glicksman, M. E., 1991, ''Dendritic Growth Kinetics and Structure II. Camphene,'' J. Cryst. Growth, **112**, pp. 97–110.
[20] Sekerka, R. F., Coriell, S. R., and McFadden, G. B., 1995, ''Stagnant Film Model of the Effect of Natural Convection on the Dendrite Operating State,'' J. Cryst. Growth, **154**, pp. 370–376.
[21] Smithells, C. J., 1976, *Metals Reference Book*, Butterworth and Co., London.
[22] Stefanescu, D. M., Dhindaw, B. K., Kacar, S. A., and Moitra, A., 1988, ''Behavior of Ceramic Particles at the Solid-Liquid Metal Interface in Metal Matrix Composites,'' Metall. Trans. A, **19A**, pp. 2847–2855.

Lei Li
Graduate Student Researcher,
Mem. ASME

Ted D. Bennett
Assistant Professor,
Mem. ASME
e-mail: bennett@engineering.ucsb.edu

Department of Mechanical and
Environmental Engineering,
University of California,
Santa Barbara, CA 93106

Incandescence Measurement During CO_2 Laser Texturing of Silicate Glass

Laser zone texture is a new approach to improve tribology performance of high aerial density disks made with glass substrates. In this process, nanotexture is introduced to the surface by discrete laser pulses. The topography change is due to the elevation of fictive temperature in the short time and high temperature scales that occur through the laser energy coupling with glass. To exercise better control over this thermal process, knowing the temperature field induced by the laser pulse and the timescale of the thermal cycle are very important. In this paper, emission measurements are made from a laser-heated surface of approximately 300 μm^2 and temporally resolved to 100 ns. Several emission bands are collected in the visible. From emission data, the extensive heat capacity of the heat affected zone is derived, allowing peak surface temperatures to be determined from the pulse energy. Experimental results are compared with a numerical model to determine the validity of earlier calculations and conclusions. [DOI: 10.1115/1.1351166]

Introduction

Today's high-density computer drives require super-smooth disk surfaces for low flying heads. However, this can lead to a severe stiction problem between the head and the disk surface, when they are in contact. Stiction is a capillary force between the lubrication layer on the disk surface and the head. This force changes with the contact area between the surfaces. Laser texture can provide spatially separated bumps on the disk surface that reduce stiction in the head landing zone [1–4].

We have explored the mechanism by which nanotexture is produced on a silicate glass surface with microsecond laser pulses [5,6]. Our investigation suggests that bump formation is the product of a local change in microstructure in the heat affected zone. This change occurs in a region where the thermodynamic temperature exceeds the glass transition temperature. The transition temperature is defined as the temperature above which microstructural relaxation occurs within a given timescale. Consequently, the shorter the timescale, the higher the transition temperature. The ''fictive temperature'' characterizes the microstructural state of the glass, and equals the thermodynamic temperature at which the existing microstructure would be in equilibrium [7]. However, since glass is not in thermodynamic equilibrium, knowledge of both the thermodynamic temperature and the fictive temperature are required to define the state.

Glass laser texture must be able to produce bumps of suitable size and with sufficient control for future hard-drive products. The bump height and diameter are of great interest since they are important parameters affecting the tribology performance of the disk surface. Since topography development is a product of the thermal cycle, acquiring temperature information during the glass evolution is crucial. In theory, the temperature rise resulting from the laser pulse can be calculated using a heat diffusion model. However, in practice this is difficult without an additional experimental investigation because of insufficient glass thermal physical information. Therefore, it is desired to experimentally measure the temperature rise in the glass resulting from a laser pulse.

Many techniques have been used for time resolved temperature measurements during laser heating. They can be broadly classified as either contact methods, in which a temperature sensing device is placed in contact with the sample, or non-contact methods. Examples of contact methods employed for laser heating include the use of thermocouples [8,9] and thermoresistors [10,11]. Optical measurements are the most common non-contact method of temperature sensing, and can be implemented with either active probes or passive measurements. Measuring changes in the optical properties of a surface at the wavelength of a probe beam has been used to time resolve temperature changes during laser processing. Examples include measurements of reflectivity [12], X-ray diffraction [13], Raman scattering [14], and interference [15]. Pyrometry is a passive non-contact measurement of the thermal emission from a heated surface. This is the most widely used non-contact method, and has been used for measuring the temperature rise in many laser heating problems [16–21]. Two- (or more) color methods attempt to determine temperature from the intensity variation with wavelength predicted by Planck's distribution. Alternatively, as done in the present work, one can consider the intensity variation with temperature predicted by Planck's distribution as a way of performing pyrometry.

In the process studied here, laser heating occurs within 1 μs over an area of approximately 300 μm^2. Simultaneously, the surface of the glass is moving at a speed of 1.6 m/s under the laser beam. Due to these constraints, pyrometry is the best choice for the task of temperature measurement. In this work, we have developed a monochromatic pyrometry measurement, suitable for the weak emission inherent to the laser texture process.

Temperature Determination

Under non-ideal conditions, calibration of a pyrometer is challenging. In the present work, we would like to measure temperature in a material that is essentially transparent or semitransparent over the visible and near infrared; that experiences a temperature rise confined to micrometers in spatial scale and microseconds in temporal scale; and that is highly nonisothermal. Experimentally one measures something proportional to the intensity predicted by Planck's distribution. However, in addition to the temperature rise, the collected emission will depend on the emissive properties of the glass and the volumetric extent of the temperature rise, as well as the transmissivity of the optics and the responsivity of the detector. Furthermore, if Plank's distribution is to be used, the temperature rise in the glass must be characterized by an effective value because of the nonisothermal nature of the emission source.

In this experiment, we compare emission collected at different pulse energies but at the same wavelength. The method developed here to determine the temperature rise requires that the measured

Contributed by the Heat Transfer Division for publication in the JOURNAL OF HEAT TRANSFER. Manuscript received by the Heat Transfer Division March 8, 2000; revision received November 21, 2000. Associate Editor: A. Majumdar.

emission signal is proportional to the emission intensity from the glass, and that the emissive properties remain constant over the range of conditions used for measurements at a given wavelength. With these conditions satisfied, an effective emission temperature can be calculated from Planck's distribution if the proportionality constant between the measured signal and the emission intensity is known. To facilitate determining this unknown proportionality constant, we impose a third requirement that the effective emission temperature is proportional to the laser pulse energy. To a good approximation, there is a linear relationship between the temperature rise and the laser pulse energy [6]. Therefore, the third condition is satisfied if the effective emission temperature can properly characterize the temperature rise in the glass. Under these conditions, the proportionality constant between the measured signal and the emission intensity and the proportionality constant between the laser pulse energy and the emission temperature are the only two unknowns.

The emission temperature measured is an effective value reflecting the temperature state in the glass. Emission temperatures are sometimes defined as the temperature for which an isothermal body would give an equivalent amount of emission as the nonisothermal body, at the wavelength being measured. However, this definition suffers from the fact that the size of the equivalent isothermal body influences the value of emission temperature. A judicious choice of volume is required to apply this definition to the laser texture application, since the heat affect volume is small compared with what is in the line of sight of the detector. Instead, we have chosen to define the emission temperature as:

$$T_{\text{emit}}=\frac{\int_{\forall} TK_{a\lambda}I_{\lambda b}e^{-\int k_{a\lambda}dz}d\forall}{\int_{\forall} K_{a\lambda}I_{\lambda b}e^{-\int k_{a\lambda}dz}d\forall}, \tag{1}$$

where $K_{a\lambda}$ is the absorption coefficient at the measured wavelength and $I_{\lambda b}$ is the spectral blackbody intensity.

This definition reflects the fact that the integrated emission comes from elemental volumes at different temperatures in the glass, and defines an effective temperature based on that intensity-weighted average. In Eq. (1), the emission intensity appearing in the integrands contribute significantly to the emission temperature only in regions of high glass temperature. Therefore, integrating over a larger volume has negligible influence on the calculated emission temperature. The difference in emission temperature for these two definitions depends on how the volume for equivalent isothermal body approach is picked.

An extensive heat capacity is defined to relate the emission temperature rise to the pulse energy

$$C_p=\frac{dE}{dT_{\text{emit}}}. \tag{2}$$

Notice that this is an extensive property, since we are considering the whole heat affected volume. If the extensive heat capacity is known, the peak emission temperature can be calculated from

$$T_{\text{emit}}=\frac{E}{C_p}+T_0. \tag{3}$$

Equation (3) is an assertion that, a straight line can be drawn through the glass emission temperature relationship to pulse energy, over a limited range of pulse energies. This will not be the case if the measured temperature range spans a region in which thermophysical properties change rapidly. Therefore, for the purpose of this linear fit, T_o can become offset from the actual initial temperature by phase transitions, or, in the case of glass, by the discontinuity in specific heat at the transition temperature, or, simply due to the temperature dependence of thermophysical properties.

The measured spectral emission is related to Planck's intensity distribution (given in terms of the emission temperature) by an emittance factor ε_f

$$e'_{\lambda,\text{meas}}=\varepsilon_f I_{\lambda b}=\frac{\varepsilon_f C_1/\pi}{\lambda^5\left[\exp\left(\frac{C_2}{\lambda T_{\text{emit}}}\right)-1\right]}, \tag{4}$$

where $C_1=37413\ \text{W}/\mu\text{m}^4/\text{cm}^2$ and $C_2=14388\ \mu\text{mK}$. By combining the Eqs. (3) and (4), the relationship between the measured emission signal and pulse energy is expressed in terms of the unknown extensive heat capacity and the emittance factor. Both can be determined from the experimental data, by fitting a measured trend in peak intensity with respect to pulse energy. Once the extensive heat capacity is determined, the temperature rise in the glass can be calculated from the pulse energy using Eq. (3). The present procedure requires that the emittance factor ε_f does not change rapidly with temperature, compared with the exponential dependence of emission intensity on temperature given by Planck's law. From Eq. (4) it is seen that

$$\frac{\Delta T_{\text{emit}}}{T_{\text{emit}}}\approx-\frac{\lambda T_{\text{emit}}}{C_2}\cdot\frac{\Delta\varepsilon_f}{\varepsilon_f}. \tag{5}$$

For visible emission, a 30 percent change in the emittance factor will lead to a temperature error of less than 9 percent for temperatures less than 6000 K.

For comparison with experimental results, the thermal cycle of the glass is numerically calculated for the laser texture conditions studied here. The diffusion equation for heat transfer is solved by the finite element method. A detailed description of the model is given elsewhere [6]. In the model, laser energy is introduced as a

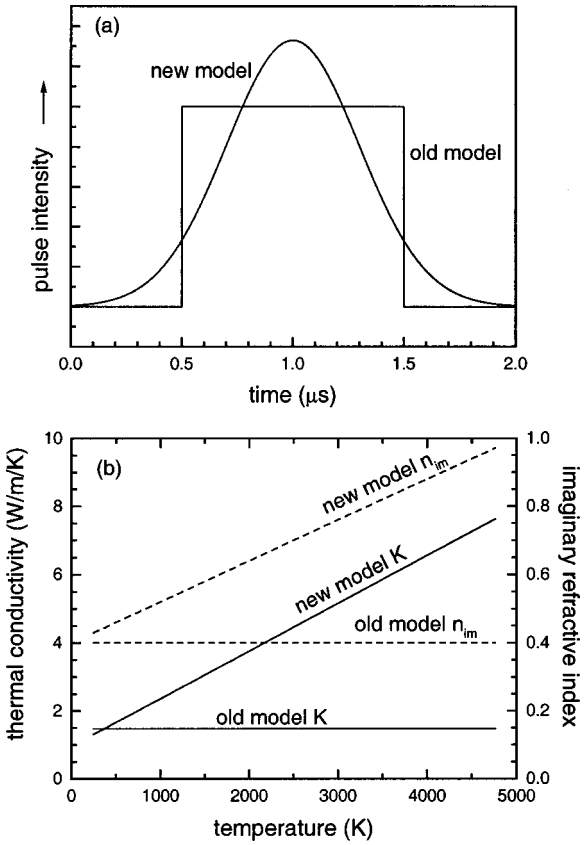

Fig. 1 Comparison between old and new numerical models: (*a*) pulse shape of CO_2 laser pulse; and (*b*) temperature dependence of thermal conductivity (left axis) and imaginary refractive index at the wavelength of the laser (right axis)

volumetric heating source over the optical penetration depth, and is dissipated by diffusion only. Unlike more frequently encountered problems in heat transport through semitransparent materials, the temperature gradients in glass laser texture are of the order of 10^9 K/m. Consequently, conduction dominates over other mechanisms of heat transport. For example, the magnitude of thermal radiative transport is more than 4 orders smaller than conduction heat transfer, and is neglected in the calculation. Although the surface becomes fluid at high temperatures, there is no phase change associated with this process since the material is initially in a glassy state. There is some vaporization from the surface at the peak temperatures in the thermal cycle. However, the impact of vaporization on the overall energy balance that dictates the surface temperature rise can be neglected.

Several significant changes from the original numerical model are made in the present work. First, the temporal profile of the pulse is changed from a rectangular pulse-shape used previously to a Gaussian shape. This is a more accurate description because the short 1 μs pulses used in the present study are approaching the 500 ns response time of the modulator used to shape the temporal profile of the laser pulse. Second, the temperature dependence of thermal conductivity and optical penetration depth is accounted for in this work. A summary of the changes made is given in Fig. 1. Despite these changes, the difference in calculated temperature rise using the current and previous model is small. The reason is that the optical penetration depth of the glass decreases with temperature while the thermal conductivity increases. These two energy transport factors tend to cancel each other during heating. However, the temperature fall at the end of the laser pulse is significantly faster in the new model because of the higher thermal conductivity of the material at elevated temperatures.

Experiment

The laser texture tool uses a CO_2 laser that produces a continuous wave (CW) beam from which part of the energy is dumped with a beam splitter. An acousto-optic modulator is used to chop the CW beam into pulses with variable width and height. The beam is expanded before focusing, to help reduce the spot size. At the $1/e^2$ intensity points, the focused beam diameter is approximately 27 μm [6].

The samples used in this experiment are chemically strengthened aluminosilicate glass (major components are SiO_2 and Al_2O_3). The glass disk is mounted on a variable RPM spindle that is attached to a translation stage. Laser heated spots are patterned in a spiral on the disk during experiments by simultaneous motion of the spindle and the stage. Figure 2 shows an optical microscope image of laser texture bumps made on a glass sample. The CO_2 laser, modulator, spindle and stage are all computer controlled.

The process of visible emission detection is shown schematically in Fig. 3. Thermal emission is collected during laser texture through a spectrally selective coated sapphire plate. The sapphire plate acts as a mirror at the wavelength of the CO_2 laser (10.6 μm) and transmits in the visible. This arrangement permits the laser energy to be delivered to the surface in the same solid angle that emission is collected. A pair of lenses is used to collect emission and image the light into a monochromator. The inlet slit of the monochromator is set at 1 mm, which is sufficient to admit all light transferred by the collection lenses. The front and back slit settings yield a spectral resolution of about 20 nm. The grating used in this work is optimal for wavelengths from 330 nm to 750 nm. A photomultiplier tube (PMT) detects light transmitted by the monochromator. The sensitivity of the PMT is several orders of magnitude higher than other detectors for visible light. A discriminator accepts negative input pulses from the PMT, rejecting those less than an adjustable threshold. A multi-channel scaler is used to record and time resolve photons counted by the PMT. A pulse generator used to drive the acousto-optic modulator also triggers

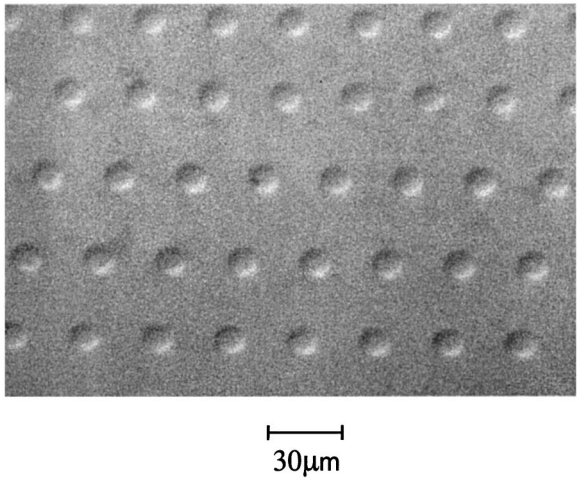

Fig. 2 Optical microscope image of laser texture bumps on silicate glass

the scaler. This synchronizes data collection with the laser pulses. After each trigger, light is collected by the scaler for 20 μs with a temporal resolution of 0.1 μs.

Neutral density (ND) filters are used to keep the peak PMT count rate relatively constant over a range of pulse energies from 9 μJ to 18 μJ. ND filters 0.1, 0.3, and 0.01 are used individually, or in pairs, to attenuate the collected light. This permits emission measurements for which the peak intensity can change by 3 orders of magnitude without the PMT saturating. Unfortunately, using ND filters to increase the peak temperature measurement also increases the minimum temperature that can be measured by raising the detection threshold.

Over the duration of a 1 μs laser pulse, the glass surface moves 6 percent of the spot diameter due to the 1.6 m/s linear surface velocity. It was experimentally determined that the heated spot could move 120 μm before leaving the area imaged by the collection lenses. Consequentially, the thermal cycle can be recorded for a timescale up to 70 μs. This proved not to be a limitation because of the rapid cooling observed.

Emission measurements were made at wavelengths of 400 nm, 475 nm, 550 nm, 625 nm, and 700 nm. For each wavelength, measurements were made at 1 μJ increments over a range of pulse

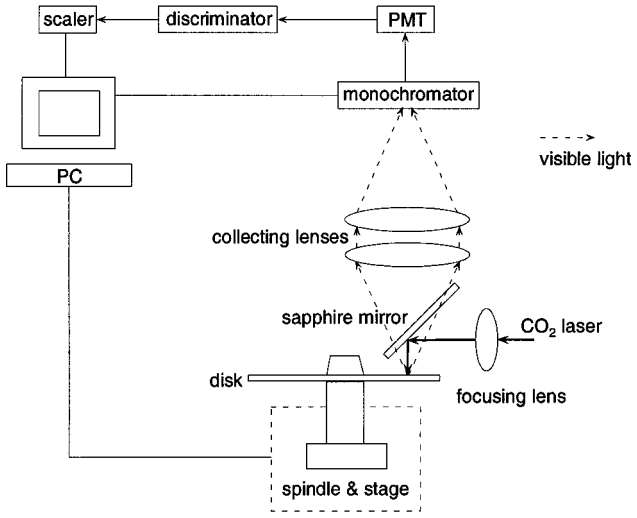

Fig. 3 Experimental setup for visible emission measurements

energies from 9 μJ to 18 μJ. A summation of 62,500 individual time-resolved measurements was used to compensate for low signal levels. Since laser pulses were delivered to the surface at 50 kHz, the total data acquisition time was about 1.25 s for each case.

Results and Discussion

Figure 4 shows time resolved emission intensities at 550 nm from the glass surface heated with different laser pulse energies. For each curve, the peak intensity corresponds to the peak emission temperature occurring from the laser-glass interaction. Figure 5 shows how this peak emission intensity changes as a function of pulse energy for the five different visible wavelengths studied. Using the temperature determination method described in the above section, the reciprocal of extensive heat capacity is obtained from a least square curve fit of the experimental data to Eq. (4). In using the relationship between the emission temperature rise and the pulse energy, Eq. (3), it is assumed that T_o is offset negligibly from the actual initial temperature of 300 K. Figure 6 shows the reciprocal of extensive heat capacity compared with the numerically calculated values for different wavelengths. The numerical calculations are based on the optically thin case of Eq. (5), and the assumption that absorption coefficient is temperature independent at measurement wavelength:

$$T_{\text{emit}}\Big|_{K_{a\lambda}\to 0} = \frac{\int_{\forall} TK_{a\lambda}I_{\lambda b}d\forall}{\int_{\forall} K_{a\lambda}I_{\lambda b}d\forall} = \frac{\int_{\forall} TI_{\lambda b}d\forall}{\int_{\forall} I_{\lambda b}d\forall} \quad (\text{const}\, K_{a\lambda}). \quad (6)$$

Figure 7(*a*) shows the measured peak temperature as a function of pulse energy at each wavelength, using extensive heat capacities found experimentally. It is noticed that the measured peak emission temperature depends on the wavelength of the collected thermal emission. Longer wavelength measurements yield lower emission temperature values because of the spectral shape of Planck's distribution. Figure 7(*b*) shows the emission temperature as a function of wavelength and pulse energy obtained from the numerical model using Eq. (6). Also shown is the calculated surface temperature, which is higher than the emission temperature by about 20 percent. Lower temperatures in the glass contribute more to the measured emission at longer wavelengths. This causes the emission temperature to decrease as the wavelength increases. The spread in measured peak emission temperatures at different wavelengths is greater than what is numerically calculated. The temperatures derived from the emission measurements are mostly within 15 percent of the numerical calculations. However, the measured peak temperature rises more steeply with pulse energy than predicted by the calculations.

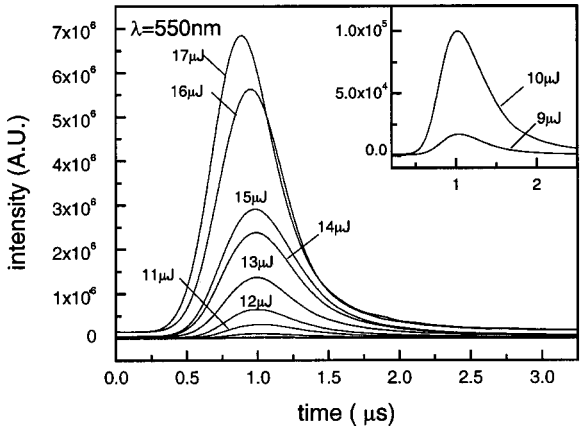

Fig. 4 Time resolved emission measurements at 550 nm for different pulse energies

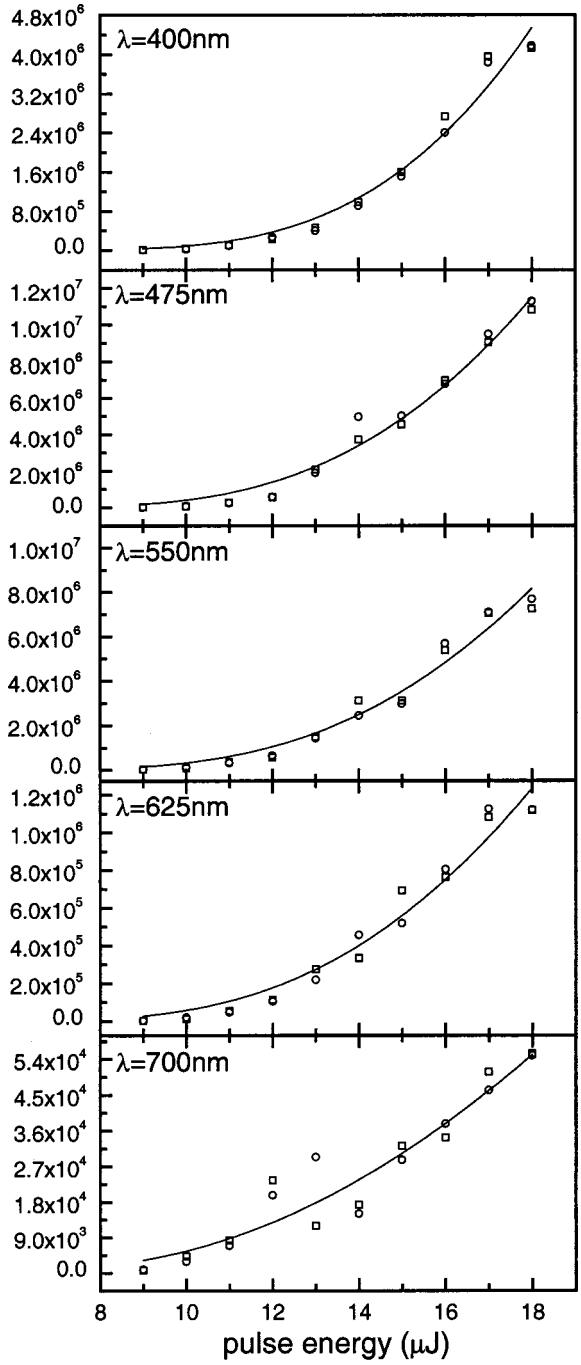

Fig. 5 Peak intensity as a function of pulse energy for different wavelengths. Scattered symbols represent experimental data; solid lines show least square fit to data.

Determining the peak temperature provides the necessary scaling information to transform the intensity signal into a transient temperature measurement using Eq. (4). Representative transient temperatures, corresponding to the intensity measurements presented in Fig. 4, are given in Fig. 8. For the pulse energies used in this study, the highest peak temperature is about 6000 K. The lowest detectable temperature is about 2000 K, observed in measurements made without any ND filters at the lowest pulse energies.

It can be seen that temperature rises with rates of approximately 10^9 K/s during heating. Initially, the cooling process is almost as fast as heating, but slows as the temperature drops. This decline in

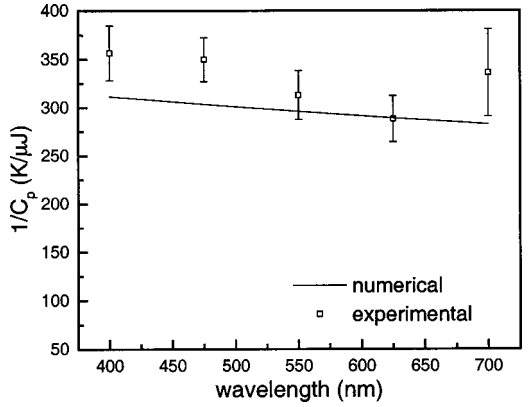

Fig. 6 Reciprocal of extensive heat capacity versus emission wavelength. Experimentally determined values are compared with numerically calculated values based on Eq. (6).

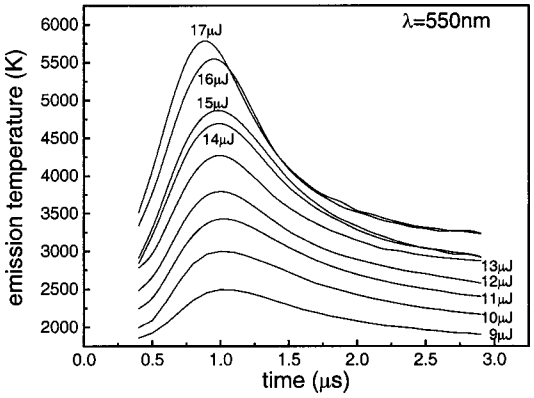

Fig. 8 Transient temperatures for the corresponding emission curves presented in Fig. 4. Experimental uncertainty is approximately 15 percent of the temperature value.

cooling rate is due to the lower temperature gradients at longer times and the decrease in thermal conductivity at lower temperatures. The cooling rate of the glass as it falls below the transition temperature is substantially slower than the heating rate, at the pulse energies studied.

A good agreement between the measured and calculated temperatures is achieved, as shown in Fig. 9. The solid lines represent the calculated emission temperature. The transient temperatures, shown as solid circles, are derived from measurements alone. It should be noted that an individual emission measurement can fall above or below the least square fitted line used to determine heat capacity for a data set (as seen in Fig. 5). Therefore, the transient emission temperature derived from any given measurement can fall above or below the numerical model prediction, although the calculated reciprocal heat capacities are mostly lower than the experimental values. A significant part of the discrepancy between the measured and numerical results is manifested in differences in

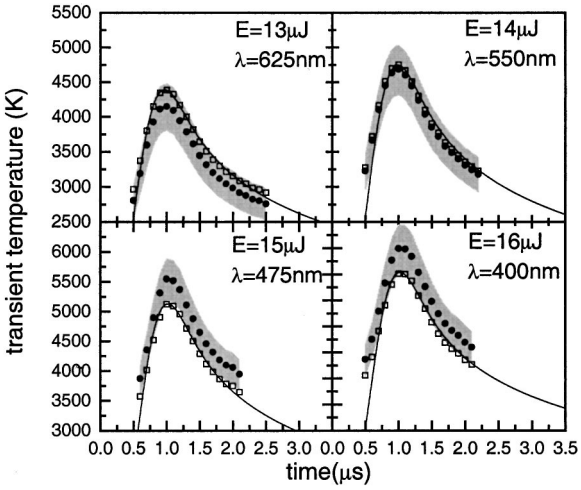

Fig. 9 Comparison of numerically calculated (solid lines) and experimentally measured (solid circles) emission temperatures. For temporal comparison, hollow squares show experimental results scaled with numerical results. Shaded regions show the temperature uncertainty, as derived from the uncertainty in the measured extensive heat capacities reported in Fig. 6.

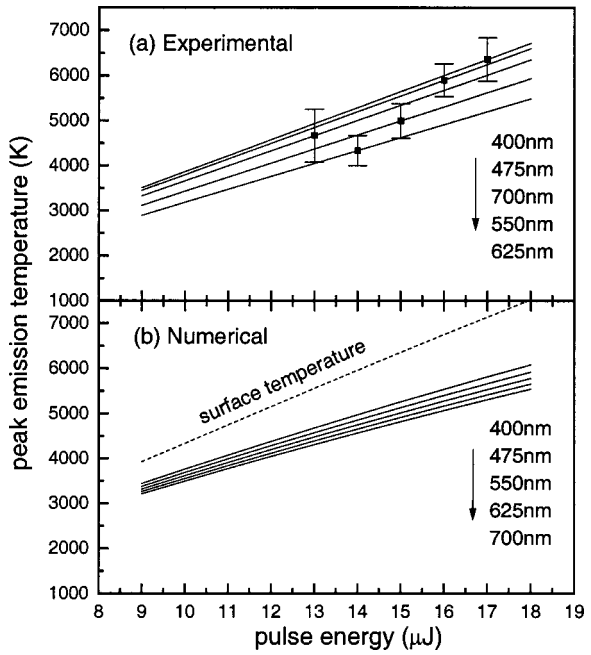

Fig. 7 Peak emission temperature as a function of pulse energy for five wavelengths. Panels (*a*) and (*b*) show experimental and numerical results, respectively. Error bars show the temperature uncertainty, as derived from the uncertainty in the measured extensive heat capacities reported in Fig. 6.

the extensive heat capacities. The comparison improves if the measured transient temperatures are scaled to have the same peak temperature as the numerically calculated temperature, as shown by the hollow squares. However, there is no reason to believe that the numerical model has better absolute temperature accuracy than the measurement.

Conclusion

Laser texture uses the timescale of a rapid thermal cycle to manipulate the transition temperature, and, hence, the final structural state of the glass in the heat affected zone. The transient glass temperature has been measured during laser texture by capturing the emission signal at wavelengths in the visible. To calibrate the emission signal with respect to temperature, the present work experimentally determines an extensive heat capacity related to the heat affected zone. The reciprocal of the extensive heat capacity is defined to be the emission temperature rise over the pulse energy and can be determined from experimental data with a least square fit to the temperature dependence of Planck's distribution.

Because the optical depth for visible emission in silicate glass is long compared with the thermal penetration depth, pyrometric

measurements do not reflect the surface temperature. Rather, the measured emission temperature is an integrated volumetric temperature of the glass in the heat affected zone. However, since the visible emission intensity is heavily weighted toward the highest temperature, the effective emission temperature is only about 20 percent less than the surface temperature. Good agreement was obtained between the experimental measurements and numerical calculations, after the model was improved by taking into account a more realistic temporal pulse profile and the temperature dependence of the laser optical penetration depth and the thermal conductivity were considered.

Acknowledgments

This work was supported by a gift from Laser Data Systems, the UC MICRO Program under Grant No. 99-008, and the National Science Foundation under Grant No. CTS-9875860.

Nomenclature

C_p = extensive heat capacity
E = laser pulse energy
$e'_{\lambda,\mathrm{meas}}$ = measured spectral emission
$I_{\lambda b}$ = spectral blackbody intensity
K = thermal conductivity
$K_{a\lambda}$ = absorption coefficient
n_{im} = imaginary part of the refractive index
T = temperature
T_{emit} = emission temperature

Greek Symbols

ε_f = emittance factor
λ = wavelength

References

[1] Rauch, G. C., Liu, J. J., Lee, S. Y., Boszormenyi, I., Chuan, G., Jing, G., Kuo, D., Marchon, B., Vierk, S., and Malmhall, R., 1996, ''Glass-Ceramic Substrates for 1 Gb/in^2 and Beyond,'' IEEE Trans. Magn., **32**, pp. 3642–3647.
[2] Teng, E., Goh, W., and Eltouhky, A., 1996, ''Laser Zone Texture on Alternative Substrate Disks,'' IEEE Trans. Magn., **32**, pp. 3759–3761.
[3] Kuo, D., Gui, J., Marchon, B., Lee, S., Boszormenyi, I., Liu, J. J., Rauch, G. C., Vierk, S., and Meyer, D., 1996, ''Design of Laser Zone Texture for Low Glide Media,'' IEEE Trans. Magn., **32**, No. 5:1, pp. 3753–3758.
[4] Tam, A. C., Brannon, J., Baumgart, P., and Pour, I. K., 1997, ''Laser Texturing of Glass Disk Substrates,'' IEEE Trans. Magn., **33**, No. 5:1, pp. 3181–3183.
[5] Bennett, T. D., Krajnovich, D. J., Li, L., and Wan, D., 1998, ''Mechanism of Topography Formation During CO_2 Laser Texturing of Silicate Glasses,'' J. Appl. Phys., **84**, No. 5, pp. 2897–2905.
[6] Bennett, T. D., Krajnovich, D. J., and Li, L., 1999, ''Thermophysical Modeling of Bump Formation During CO_2 Laser Texturing of Silicate Glasses,'' J. Appl. Phys., **85**, No. 1, pp. 153–159.
[7] Jones, G. O., and Parke, S., 1971, *Glass*, 2nd ed., Chapman and Hall, London.
[8] Maglic, K. D., and Marsicanin, B. S., 1973, ''Factors Affecting the Accuracy of Transient Response of Intrinsic Thermocouples in Thermal Diffusivity Measurement,'' High Temp.-High Press., **5**, No. 1, pp. 105–110.
[9] Baeri, P., Campisano, S. U., Rimini, E., and Jing Ping, Z., 1984, ''Time Resolves Temperature Measurement of Pulsed Laser Irradiated Germanium by Thin Film Thermocouple,'' Appl. Phys. Lett., **45**, No. 4, pp. 398–400.
[10] Zenobi, R., Hahn, J. H., and Zare, R. N., 1988, ''Surface Temperature Measurement of Dielectric Materials Heated by Pulsed Laser Radiation,'' Chem. Phys. Lett., **150**, No. 5, pp. 361–365.
[11] Shanov, V., Petkov, P., Ivanov, B., Popov, C., and Vodenicharov, C., 1994, ''Sensor for Temperature Measurement of Laser Heated Surfaces,'' Vacuum, **45**, No. 12, pp. 1187–1189.
[12] Xu, X., Grigoropoulos, C. P., and Russo, R. E., 1995, ''Transient Temperature During Pulsed Excimer Laser Heating of Thin Polysilicon Films Obtained by Optical Reflectivity Measurement,'' ASME J. Heat Transfer, **117**, No. 1, pp. 17–24.
[13] Larson, B. C., White, C. W., Noggle, T. S., Barhorst, J. F., and Mills, D. M., 1983, ''Time-Resolved X-Ray Diffraction Measurement of the Temperature and Temperature Gradients in Silicon During Pulsed Laser Annealing,'' Appl. Phys. Lett., **42**, No. 3, pp. 282–284.
[14] Pui-Kwong, C., and Hart, T. R., 1989, ''Raman Scattering Temperature Probe of Laser Disk Marking,'' Appl. Opt., **28**, No. 9, pp. 1685–1691.
[15] Morozova, E. A., Shafeev, G. A., and Wautelet, M., 1992, ''Interferometric Measurement of Lateral Temperature Distribution During Laser-Assisted Processing of Thin Films,'' Meas. Sci. Technol., **3**, No. 3, pp 302–305.
[16] Mann, S. S., Todd, B. D., Stuckless, J. T., Seto, T., and King, D. A., 1991, ''Pulsed Laser Surface Heating: Nanosecond Time-Scale Temperature Measurement,'' Chem. Phys. Lett., **183**, No. 6, pp. 529–533.
[17] Schafer, B., and Bostanjoglo, O., 1993, ''Tracing Fast Changing Temperature on Laser-Pulsed Metal Surfaces by Micropyrometry,'' Rev. Sci. Instrum., **64**, No. 12, pp. 3598–3601.
[18] Holmes, N. C., 1995, ''Fiber-Coupled Optical Pyrometer for Shock-Wave Studies,'' Rev. Sci. Instrum., **66**, No. 3, pp. 2615–2618.
[19] Xu, X., Grigoropoulos, C. P., and Russo, R. E., 1996, ''Nanosecond-Time-Resolution Thermal Emission Measurement During Pulsed Excimer-Laser Interaction With Materials,'' Appl. Phys. A: Mater. Sci. Process., **A62**, No. 1, pp. 51–59.
[20] Nettesheim, S., and Zenobi, R., 1996, ''Pulsed Laser Heating of Surfaces: Nanosecond Timescale Temperature Measurement Using Black Body Radiation,'' Chem. Phys. Lett., **255**, No. 1–3, pp. 39–44.
[21] Otte, D., Kleinschmidt, H., and Bostanjoglo, O., 1997, ''Space and Time Resolved Temperature Measurements in Laser Pulse-Produced Metal Melts,'' Rev. Sci. Instrum., **68**, No. 6, pp. 2534–2537.

Y. P. Wan
Research Scientist
Mem. ASME
Department of Materials Science
and Engineering,
State University of New York at Stony Brook,
Stony Brook, NY 11794-2275
e-mail: Yuepeng.Wan@sunysb.edu

H. Zhang
Assistant Professor
Mem. ASME
Department of Mechanical Engineering,
State University of New York at Stony Brook,
Stony Brook, NY 11794-2300
e-mail: hzhang@pml.eng.sunysb.edu

X. Y. Jiang
Ph.D. Student
e-mail: Xjiang@ic.sunysb.edu

S. Sampath
Associate Professor
e-mail: Ssampath@ms.cc.sunysb.edu

Department of Materials Science
and Engineering,
State University of New York at Stony Brook,
Stony Brook, NY 11794-2275

V. Prasad
Professor, Fellow ASME
Department of Mechanical Engineering,
State University of New York at Stony Brook,
Stony Brook, NY 11794-2300
e-mail: prasad@pml.eng.sunysb.edu

Role of Solidification, Substrate Temperature and Reynolds Number on Droplet Spreading in Thermal Spray Deposition: Measurements and Modeling

Numerical analysis and experimental measurements of the flattening degree of plasma sprayed molybdenum and zirconia droplets deposited on different substrate materials are presented. Investigation is focused on the influence of rate of solidification and wetting angle on droplet spreading. Madejski-Zhang model with one-dimensional treatment of solidification as well as heat transfer in the melt, solidified splat and substrate is employed to perform a numerical analysis. A parametric study is conducted to examine the effects of droplet size, impact velocity, superheating of droplets, substrate temperature, thermal contact resistance, and wetting angle on spreading of the splat and its flattening degree. Numerical results show that the time for solidification can be as small as that for spreading and the rate of solidification can greatly influence the flattening degree. A guideline for when the effect of wetting angle and surface tension on droplet deformation can be neglected is derived. A correlation for the relationship between the flattening degree and Reynolds number with the consideration of solidification is deduced, and a criterion for the effect of droplet solidification on impact dynamics to be negligible is given. The limitations of the assumption of isothermal substrate are also discussed. The numerical predictions agree statistically well with the experimental data.
[DOI: 10.1115/1.1351893]

Introduction

In a thermal spray deposition process, small molten droplets ($\sim$5–100 μm) impact a substrate with very high velocity and form, under certain droplet and substrate conditions, disc-shaped splats as illustrated by the optical image of splat morphology in Fig. 1. Although splats with a perfect disc shape are rather exceptional than common, a clear picture of the physical processes involved in the formation of splats with regular simple shapes serves as a starting point for the understanding of much more complicated morphologies, such as the mechanism of splashing, interlamellar adhesion, etc.

During deposition, the melt solidifies while spreading on the substrate surface. The final shape of the splat is determined primarily by the rates of both spreading and solidification which depend on many factors such as the impact velocity, substrate condition, materials characteristics, etc.. Obtaining data on droplet deformation *in situ* is a challenge and will remain so because of the size of the droplet ($\sim$30 μm) and impact time (a few micro-seconds).

Although some attempts have been made to perform *in situ* measurements of the surface temperature of a spreading splat [1], most of the experiments on deposition of plasma sprayed droplets focus on the morphology of the final splats [1–4], including the flattening degree. Limited data obtained from these experiments do not give a complete picture of the droplet spreading and solidification. However, in conjunction with a reliable theoretical model they can provide valuable information on the formation of plasma sprayed splats. The experiments can help in validating the models that can then be extended to small splats as long as the continuum approximations are valid.

A general practice in the experimental study of this process is to use large size droplets (millimeter) with velocities much lower than that in plasma spraying and to record the impacting and spreading process using high speed cameras [5–8]. The evolution of temperature inside the substrate [9] or at the top of the splat [10] has also been measured for such splats.

Such large-scale experiments help to identify and verify the physics-based models for droplet deposition on a flat substrate. According to the treatment of flow field within a spreading droplet, the available numerical models can be assorted into one-dimensional Madejski-type models [8,11,12] and two or three-dimensional free surface deformation-type models [8,13–15]. The solidification is considered either one-dimensional or two-dimensional and is solved using the heat conduction equation within the melt, solid and substrate. Complex physical phenomena, such as thermal contact resistance, wetting properties, surface

Contributed by the Heat Transfer Division for publication in the JOURNAL OF HEAT TRANSFER. Manuscript received by the Heat Transfer Division May 13, 1999; revision received December 7, 2000. Associate Editor: T. Avedisian.

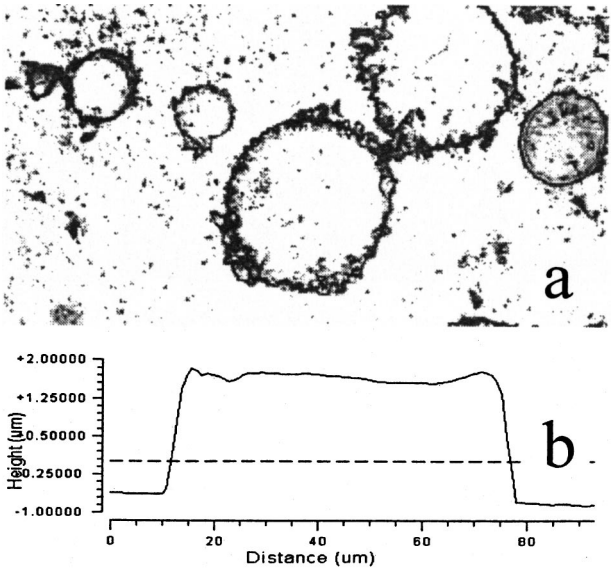

Fig. 1 (*a*) Optical image (using Zygo) showing the morphology of Molybdenum splats on Molybdenum substrate, and (*b*) surface profile of a typical splat

tension, convective heat transfer, and capillary effect, etc., have been incorporated into the mathematical models by different authors. However, it should be noted that most of the model validation has been accomplished only for large-scale (millimeter size) droplets.

It is debatable that the conclusions made from the study of large size droplet impact and deposition, and the models developed and verified based on such investigations can be directly applied to the micro-size droplets in plasma spraying [16]. One disputable problem in characterizing the deposition of plasma sprayed droplets is the role of solidification in splat formation. Although many studies of millimeter-size droplets have demonstrated the importance of solidification rate on the final splat morphology, it is generally concluded that the solidification in plasma spray deposition is much slower than the spreading [17,18]. The major argument for this conclusion is that the thermal contact resistance and the nucleation delay become more important on the heat transfer and solidification rate for the smaller droplets, as summarized by Dykhuizen [18]. A supporting experimental evidence for this conclusion is that many data of the measured splat flattening degree agrees reasonably well with the Madejski correlation (Eq. 20), which considers only the effect of viscous dissipation and neglects the effect of solidification on droplet spreading [3].

However, our recent plasma spray experiments demonstrate that the flattening degree of molybdenum droplets being deposited on a molybdenum or steel substrate is significantly smaller than that on a glass substrate. This indicates that the solidification do affect significantly the spreading of micro-sized droplets with high impacting velocities, which is contradictory to what has been generally believed by the thermal spray researchers. This phenomenon has motivated us to perform the present numerical analysis on relative time scales of the droplet spreading and solidification by simply employing the Madejski-type model. The goal of our analysis is to define the region where solidification plays roll in the deposition of micro-sized droplets processed by plasma spray.

Another important issue that is addressed here is the assumption of isothermal condition for the substrate as employed in many of the numerical analyses [8]. This condition is not valid for many commonly used substrate materials as revealed by our experiments of Mo droplet deposition on a glass substrate. An attempt is also made to develop guidelines for the conditions under which the effect of surface wetting and solidification on droplet deformation can be neglected.

Mathematical Model

The mathematical model employed in the present analysis is basically an extension of the Madejski's splat-quench solidification model [2] together with the modifications by Markworth and Saunders [19] on velocity profile, and by Zhang [12] on wetting angle. As illustrated in Fig. 2, a droplet with initial diameter d_0 impacts with a velocity w_0 on a flat substrate with an initial temperature of T_{sub}. At time t, the deforming splat, which is assumed to have a cylindrical shape, has a radius R, the thickness of the solidified layer is s, and the remaining liquid layer has a thickness b. The conservation of macroscopic mechanical energy leads to the equation for splat radius during the deformation [11,12]. Employing the scales for time, length and velocity as d_0/w_0, d_0, and w_0, respectively, the equation presented by Zhang [12] in its dimensionless form can be written as

$$\frac{d}{d\tilde{t}}\left[\frac{3}{10}\left(\frac{d\tilde{R}}{d\tilde{t}}\right)^2\tilde{b}\left(\tilde{R}^2+\frac{11}{7}\tilde{b}^2\right)+\frac{\tilde{R}}{\mathrm{We}}((1-\cos\phi_0)\tilde{R}+2\tilde{b})\right]+\frac{\tilde{R}^2}{\tilde{b}\,\mathrm{Re}}\left(\frac{d\tilde{R}}{d\tilde{t}}\right)^2\left(\frac{3}{2}+\frac{72}{5}\frac{\tilde{b}^2}{\tilde{R}^2}\right)=0. \tag{1}$$

Here, ϕ_0 is the equilibrium contact angle between the molten droplet and substrate, and $\cos\phi_0$ is known as the wetting coefficient or degree of wetting. The Reynolds number, Re, and Weber number, We, in Eq. (1) are defined as

$$\mathrm{Re}=\rho w_0 d_0/\mu, \quad \text{and} \quad \mathrm{We}=\rho w_0^2 d_0/\sigma_l, \tag{2}$$

where ρ represents the liquid density, μ, the liquid dynamic viscosity, and σ_l, the surface tension of the melt. If the curvature of the melt/solid interface is neglected, the dimensionless thickness of the liquid disk, $\tilde{b}$, which is the only parameter in Eq. (1) explicitly related to solidification, can be determined from mass conservation as [11]

$$\tilde{b}=\frac{1}{6\tilde{R}^2}-\tilde{s}. \tag{3}$$

The initial conditions for Eq. (1) are

$$\tilde{R}_0=\varepsilon, \quad \tilde{b}_0=\frac{1}{6\varepsilon^2}, \quad \left.\frac{d\tilde{R}}{d\tilde{t}}\right|_{\tilde{t}=0}=\left(\frac{3}{5}+\frac{11}{420\varepsilon^6}\right)^{-0.5}, \tag{4}$$

with the value of $\varepsilon=0.74$ [11].

The thickness of the solidified layer, $\tilde{s}$, can be determined by solving either one-dimensional or two-dimensional [11] heat con-

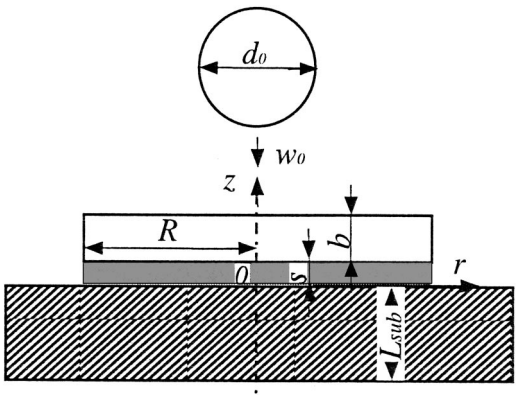

Fig. 2 Schematic of the droplet deposition process and the relevant geometry

duction equation with phase change. Since the goal of the present study is to identify the role of solidification on splat formation and obtain analytical correlation for flattening degree, we have chosen to solve the following one-dimensional heat conduction equation within the melt, solid and substrate with a moving melt/solid interface,

$$\frac{\partial \theta}{\partial \tilde{t}} = \frac{1}{\mathrm{Pe}} \frac{\partial^2 \theta}{\partial \tilde{z}^2}. \tag{5}$$

Here, $\theta = (T - T_{\mathrm{sub}})/(T_m - T_{\mathrm{sub}})$ is the dimensionless temperature, α is the thermal diffusivity of the corresponding material, and the inverse of Peclet number, $1/\mathrm{Pe} = \alpha / w_0 d_0$, represents the dimensionless thermal diffusivity.

In our test calculations, thermal radiation at the melt surface is found to be much smaller than that by conduction, therefore, no heat loss is assumed at the splat surface, i.e.,

$$\left.\frac{\partial \theta}{\partial \tilde{z}}\right|_{\tilde{z}=\tilde{b}+\tilde{s}} = 0. \tag{6}$$

The heat balance at the melt/solid interface can be expressed as

$$\frac{d\tilde{s}}{dt} = \frac{\mathrm{Ja}}{\mathrm{Pe}} \left[\frac{k_s}{k_l} \left.\frac{\partial \theta}{\partial \tilde{z}}\right|_{\tilde{z}=\tilde{s}^-} - \left.\frac{\partial \theta}{\partial \tilde{z}}\right|_{\tilde{z}=\tilde{s}^+} \right], \tag{7}$$

where, k_s and k_l are thermal conductivities of the solid and melt, respectively, $\mathrm{Ja} = c_l (T_m - T_{\mathrm{sub}})/L_m$, is Jakob number with T_m representing the melting point, L_m, the latent heat of fusion, and c_l, the specific heat of melt. No undercooling is considered in the present solidification calculation. Therefore, the temperature at the melt/solid interface is equal to the melting point,

$$\theta|_{\tilde{z}=\tilde{s}} = 1. \tag{8}$$

The heat balance at the splat/substrate interface including the contact resistance, R_t can be written as

$$\left.\frac{\partial \theta}{\partial \tilde{z}}\right|_{\tilde{z}=0^+} = \frac{d_0}{k_s R_t} (\theta_{0^-} - \theta_{0^+}). \tag{9}$$

At the bottom of the substrate in the computational domain, the temperature is considered constant,

$$\theta|_{\tilde{z}=-\tilde{L}_{\mathrm{sub}}} = 0. \tag{10}$$

This is valid if a large thickness of the substrate (3 mm) is considered during the simulation.

By solving the above set of equations for droplet deformation and solidification, we can obtain the thickness of the splat and solidified layer at any time t, as well as the flattening degree, which is defined as

$$\xi_m = 2R/d_0. \tag{11}$$

The ordinary differential equation, Eq. (1) is solved using the fourth-order Runge-Kutta method [20]. A finite volume scheme [21] is employed to solve the heat conduction equation, Eq. (5). At each time-step, the thickness of solid layer is obtained by solving Eq. (5) with a current value of melt thickness, b, and a new melt thickness is then calculated through Eq. (3). The updated melt thickness is then fed back to the solution algorithm of Eq. (1). Since the thickness of the substrate is much larger (3 mm) than that of the melt and solid, a non-uniform grid is used in the substrate layer with total number of grids as 200. A moving uniform grid is used for both the melt and solid layers [22]. A grid of 20 nodes in each layer is found to be enough to produce grid-independent solutions. The dimensionless time-step needs to be adjusted for different cases and a typical value is 10^{-2}.

Experimental Data and Model Validation

Experiments were conducted using two different powder materials, molybdenum and partially stabilized zirconia (PSZ). Mo droplets were deposited on three different substrate materials, molybdenum, glass and steel, under similar substrate and plasma conditions using a Plasma Technik PT-F4 gun. PSZ powders were processed with a Sulzer Metco 9MB plasma gun and deposited on a steel substrate. The detailed experimental conditions are reported by Jiang and Sampath [4] and only the parameters relevant to present analysis are listed in Table 1.

Table 1 Droplet parameters and substrate conditions of the experiments

Droplet-Substrate	T_{sub} (K)	Mean Size (μm)	Velocity, W_0 (m/s)	Temp., T_0 (K)
Mo-Mo	613	30	100-150	2890-3000
Mo-Glass	613	30	100-150	2890-3000
Mo-Steel	613	30	100-150	2890-3000
PSZ-Steel	473	33	170-200	3160-3250

The measured flattening degree is plotted in Fig. 3. The data were obtained by using the Zygo optical non-contact surface profilometer, which measures the volume and diameter of each individual splat. The experimental data shown in Fig. 3 is a number average of a large number of splats (about 100) that have different droplet sizes, impacting velocities and overheating degrees. The standard deviation for the statistics is also shown in the plot, with a value of about 20 percent for each material. The flattening degree for Mo on steel is very similar to that for Mo on Mo, and hence, this data is not plotted in this figure. From Fig. 3, it is evident that the flattening degree for Mo-Mo is significantly smaller than that for Mo-Glass, although the process parameters in both cases are the same. Obviously, the characteristics of substrate material play an important role in droplet spreading and deposition, which is not included in the commonly used Madejski's correlation, Eq. (20). There are two possible mechanisms by which a substrate can affect the droplet characteristics during its deposition, one—the wetting coefficient, and the other—the rate of solidification. Solidification can arrest the droplet spreading and reduce the flattening degree. Which of these mechanisms is the controlling phenomenon in the present case will be clarified in the following section.

A comparison between the predicted values of flattening degree and the experimental data is also presented in Fig. 3. During calculations, we select particles with different sizes (5, 10, 20, 30, 40 μm), assign each droplet with 3 different velocities within the velocity range (i.e., 100, 125, 150 m/s for Mo, 170, 185, and 200 m/s for PSZ), and with 3 different overheating degrees (0, 200,

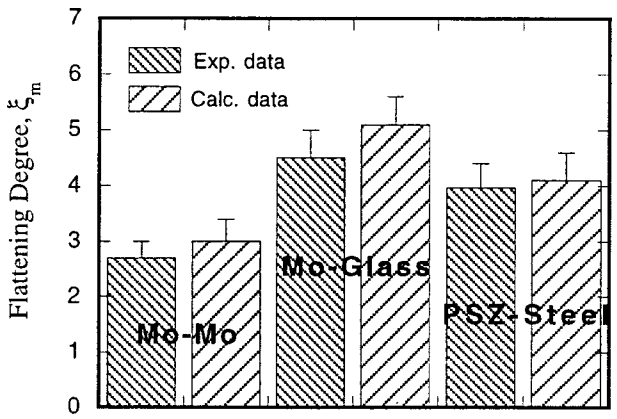

Fig. 3 Statistical comparison between the calculated flattening degree with experimental data for molybdenum on molybdenum, molybdenum on glass and PSZ on steel. (Mo-Steel data are very close to the Mo-Mo data, and hence are not presented here.)

Table 2 Thermo-physical properties of droplet and substrate materials used in calculations

	ρ (kg/m^3)	c_p (J/kg.K)	λ (W/m.K)	σ_l (kg/m^2)	ν (m^2/s)	Source
Mo (liquid)	9.35x10^3	570.	46.	2.25	6.78 x10^{-7}	[23]
(solid)	10.2 x10^3	339.	84.			
PSZ(liquid)	5.7 x10^3	604.	2.32	0.5	6.5 x10^{-6}	[3]
(solid)	5.7 x10^3	604.	2.32			
Glass	2.0 x10^3	900.	1.17			[24]
Steel	7.8 x10^3	400.	30.			

Data from Refs. [23] and [24] included in table.

and 400 K). The fattening degree for each droplet is obtained by solving Eq. (1) and Eq. (5) simultaneously. The thermo-physical properties of droplet and substrate materials are listed in Table 2. The predicted value of flattening degree shown in Fig. 3 is the number average of flattening degree of all the selected droplets. A close agreement between the computation and measurements shows that the Madejski's type deposition model together with one-dimensional treatment of solidification and heat transfer makes a good prediction of the splat flattening degree, at least for the given conditions. It is worth pointing out that the good agreement on just the flattening degree does not mean the perfection of such simple one-dimensional treatment. Many complicated phenomena associated with the deposition, such as splashing, residual stress in splat/coating, adhesion, etc., need to be considered, particularly if a multidimensional approach is adopted. This is out of the scope of the current effort, which focuses on the characteristics of solidification and spreading rather than the model itself.

Numerical and Theoretical Analysis

Characteristics of Droplet Spreading and Solidification. Figure 4 shows the evolutions of the splat thickness and melt/solid interface for Mo droplets on Mo and Glass substrates, and PSZ on Steel substrate obtained by using the numerical model presented earlier. The parameters selected for Mo droplet are: $d_0=30\ \mu$m, velocity, $w_0=150$ m/s, temperature, $T_0=T_m=2883$ K; parameters for PSZ droplet are: $d_0=30\ \mu$m, velocity, $w_0=200$ m/s, temperature, $T_0=T_m=2950$ K.

As shown in Fig. 4, the upper curve characterizes the change of the thickness of a deforming droplet. The thickness decreases rapidly only in the initial time period ($t_{0.9}$ in Eq. (12)). After that time, the thickness does not change much during further spreading. An approximate time for rapid spreading, also called spreading time, defined as the time when spreading reaches 90 percent of its maximum value (without the consideration of solidification), can be estimated using the expression proposed by Trapaga and Szekely [25]

$$t_{0.9}=\frac{2d_0}{3w_0}\mathrm{Re}^{0.2}. \tag{12}$$

As we know, the final thickness is determined by the solidification rate (the lower curve in Fig. 4). Therefore, if the solidification time is short (rapid solidification), the spreading of the droplet is terminated when it experiences rapid decrease in the thickness. For this reason, a small change in the solidification time can have a significant influence on the thickness of the final splat. We call this time domain ($<t_{0.9}$)—the solidification sensitive region. In contrast, the time ($>t_{0.9}$) is the solidification insensitive region, i.e., if the solidification time is longer than this time, a change of the solidification time will not significantly affect the thickness of the final splat.

From the solidification lines it is evident that the solidification of Mo is much faster on Mo substrates than on glass, which is obvious since Mo has much larger thermal conductivity (80 W/m·K) than glass (~1.17 W/m·K).

For the case of a 30 μm Mo droplet, the spreading time predicted by Eq. (12) is about 0.7 μs. After 0.7 μs, the droplet will not experience appreciable changes in splat thickness and its diameter. If the time for splat solidification falls into this time period, i.e., beyond 0.7 μs for Mo, the change in solidification rate, due either to the change in substrate temperature or to droplet overheating or both, will have no significant influence on the final splat size, as shown in Fig. 4 for Mo-Glass. This is also the case for PSZ droplets depositing on a steel substrate, shown in Fig. 4. The spreading time for 30 μm PSZ droplet is about 0.3 μs and the solidification time is about 0.9 μs.

On the other hand, the time available for a Mo droplet to spread on a Mo substrate is less than 0.2 μs because the spreading is arrested by rapid solidification far before the droplet has fully spread out (Fig. 4). Clearly, the rapid solidification plays a critical role in spreading of the droplet and can reduce the spreading, thereby reducing the flattening degree.

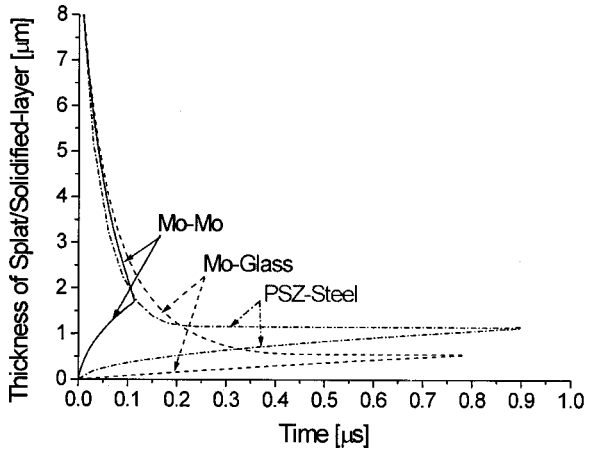

Fig. 4 Change of splat thickness due to spreading (upper part of the curves) and the thickness of solidified layer (lower part) for a molybdenum splat impinging on Mo and glass, respectively, and PSZ on steel

Effect of Wetting Angle. To clarify the role of wetting in flattening of the droplet, we have considered the deposition of Mo droplets on substrates with three different wetting angles, $\phi_0=10$ deg, 90 deg, 160 deg. Results show no appreciable effect on spreading as well as on final flattening degree for given droplet parameters. The maximum difference is within 1 percent. This can be explained by employing the criterion for viscous dissipation dominant regime proposed by Zhang [12],

$$\mathrm{We}>40.0(1-\cos\phi_0)\mathrm{Re}^{0.4}. \tag{13}$$

For Mo droplet parameters used in this calculation, i.e., $d_0=30\ \mu$m and $w_0=150$ m/s, the Reynolds number and Weber number are 6637 and 2805, respectively, which happen to be in the viscous dissipation regime, and therefore, the surface tension and wetting angle effects are minimal.

However, for a droplet with smaller size and/or with lower velocity, the effect of surface tension may become significant. The

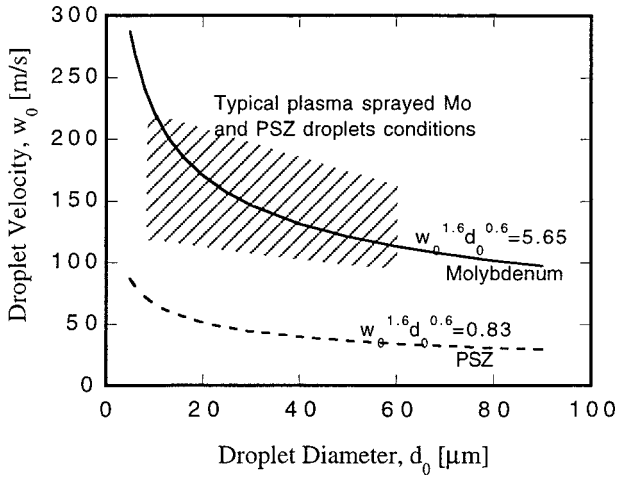

Fig. 5 Viscous dissipation dominating region is above the lines representing the criteria for different materials. The shadowed area represents the typical droplet conditions in plasma spraying.

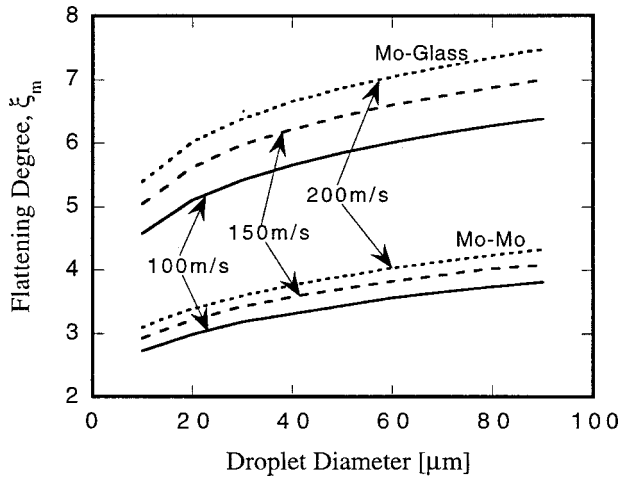

Fig. 6 Dependence of flattening degree on droplet diameter and impacting velocity for molybdenum droplets on two different substrate materials

condition where viscous dissipation and surface tension play equal role in droplet spreading is given by Zhang [12] as

$$\mathrm{We}=6.33(1-\cos\phi_0)\mathrm{Re}^{0.4}. \tag{14}$$

If we reformulate Eq. (13) and Eq. (14) in an explicit relationship for droplet diameter and velocity, we obtain,

$$w_0^{1.6}d_0^{0.6}>40.0(1-\cos\phi_0)\sigma_l/(\rho^{0.6}\mu^{0.4}), \tag{15}$$

and

$$w_0^{1.6}d_0^{0.6}=6.33(1-\cos\phi_0)\sigma_l/(\rho^{0.6}\mu^{0.4}). \tag{16}$$

Setting the limiting value, -1.0, for the wetting coefficient and substituting the appropriate values of thermophysical properties in Eq. (15) gives $w_0^{1.6}d_0^{0.6}>5.65$ for Mo droplets, and $w_0^{1.6}d_0^{0.6}>0.83$ for PSZ droplets. These two criteria are presented in a plot for droplet velocity-versus-droplet diameter (Fig. 5). Also, the typical process values of droplet diameter and velocity range for Mo and PSZ droplets are indicated with a shadowed area, although not all these conditions ensure disc-shaped splats.

As illustrated in Fig. 5, all PSZ particles are in the viscous dissipation dominant regime, which implies that the surface tension and wetting angle effects can be ignored in the case of PSZ. But for many sizes of the Mo droplets, the effect of surface tension may be comparable to the effect of viscous dissipation. Nevertheless, the influence of wetting on flattering degree is not as significant as that of the viscous dissipation. Generally, the spreading of smaller droplets and droplets with lower velocity are more dependent on droplet surface tension and wetting angle.

Effects of Droplet Size and its Velocity. To elucidate the influence of droplet size and velocity on flattening degree, we have chosen the Mo droplets with 10, 20, 30, 40, 50, 60, 70, 80, and 90 μm diameters impacting on Mo and glass substrates with a velocity of 100, 150, and 200 m/s. The computational results for these cases are plotted in Fig. 6. As shown in this plot, the flattening degree is generally larger for bigger droplets and higher velocities. Also, an increase in flattening degree caused by higher velocities and larger sizes is relatively larger in the case of Mo-Glass.

The reason for larger flattening degree at higher velocity is relatively straightforward. If we neglect the convective heat transfer in the melt, as we do in the simple one-dimensional heat conduction and solidification model, the droplet impact velocity should have no influence on its solidification rate. Meanwhile, higher velocity causes faster spreading of the droplet. This corresponds to a steeper spreading line but the same solidification line in Fig. 4. It ends up with a thinner splat, i.e., a larger flattening degree. This explains the slightly larger influence in the case of Mo-Glass than Mo-Mo since the spreading is terminated earlier in the Mo-Mo case by a faster solidification before the difference in thickness caused by the velocity difference reaches its maximum.

To show the influence of the droplet velocity and its diameter on flattening degree, we employ the theoretical correlation of Zhang [12], which gives

$$\frac{1}{\mathrm{Re}}\left(\frac{\xi_m}{1.18}\right)^5+\frac{3(1-\cos\phi_0)(\xi_m^2-1.0)}{\mathrm{We}}+S\left(\frac{\xi_m}{1.15}\right)^{2.5}=1.0, \tag{17}$$

where S indicates the solidification rate and is obtained from

$$\tilde{s}=S\sqrt{\tilde{t}}, \tag{18}$$

if the thickness of the solidified layer is correlated to the square of time.

The second term in Eq. (17) represents the effect of surface tension and wetting angle, and, as we have noted earlier, can be neglected in comparison with the first term, representing the viscous dissipation. Since the solidification rate, S, does not depend on the droplet velocity and its size in one-dimensional heat conduction model, Eq. (17) shows that a larger droplet diameter or higher velocity, that means higher Reynolds numbers, will make the flattening degree larger.

If the solidification rate, S, is appreciable, as in the case of Mo-Mo, the solidification term in Eq. (17) becomes much more important compared to the effect of Re. This explains why the dependence of flattening degree on droplet diameter and velocity is stronger for Mo-Glass than for Mo-Mo.

If we re-plot the data in Fig. 6 in terms of Reynolds number, as shown in Fig. 7, they can be correlated very nicely with Re. A simple relationship between the flattening degree and Re can be derived from Eq. (17) by neglecting the second term (surface tension effects) and approximating $(1.18/1.15)^{2.5}\approx 1.0$,

$$\left(\frac{\xi_m}{1.18}\right)^{2.5}=\sqrt{\mathrm{Re}}\left(\sqrt{\left(\frac{S}{2}\sqrt{\mathrm{Re}}\right)^2+1}-\frac{S}{2}\sqrt{\mathrm{Re}}\right). \tag{19}$$

Since the solidification rate is not dependent on the size and velocity, (or Reynolds number) of the droplet for a fixed substrate condition, the flattening degree should be a function of only Reynolds number. That explains why many researchers succeeded in correlating their experimental data of splat flattening degree using the famous formulation,

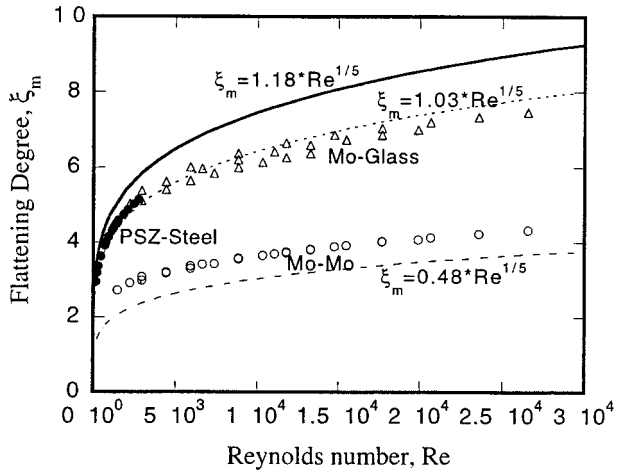

Fig. 7 Relationship between the flattening degree and Reynolds number. Curves represent the correlation, and scattered values are calculated flattening degree for droplets with different sizes and different velocities by solving Eq. (1) and Eq. (5).

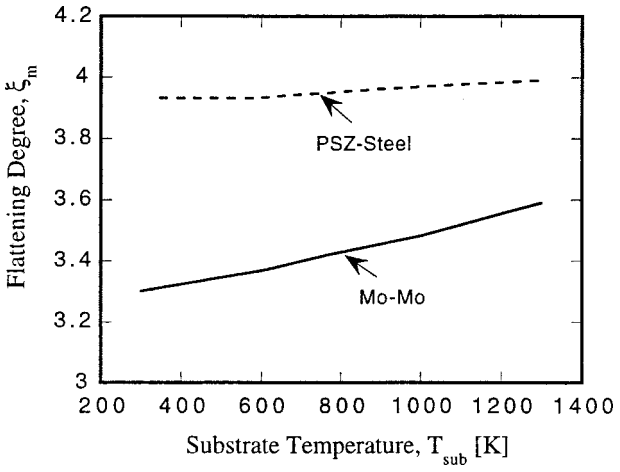

Fig. 8 Dependence of flattening degree on substrate temperature for different materials

$$\xi_m = a\,\mathrm{Re}^{0.2}, \tag{20}$$

with different authors proposing different values for the coefficient a [3], ranging from 0.83 to 1.29; 1.29 being the value obtained by Madejski [2] without solidification. From Eq. (19), a modified version of Madejski's model, the maximum flattening degree without solidification can be expressed as

$$\xi_m = 1.18\,\mathrm{Re}^{0.2}. \tag{21}$$

This curve is also plotted in Fig. 7, which shows the maximum possible flattening degree, and is in close agreement with the PSZ-Steel and Mo-Glass data.

The value of a in Eq. (20) is actually dependent on the rate of solidification that is determined by the thermophysical properties as well as the conditions of both the droplet and substrate. Unfortunately, there is no general analytical correlation for S. Some simple correlations may be derived by making simplifying assumptions. For example, from Eq. (7), under the conditions of constant substrate temperature, a linear temperature distribution within the solidified layer, a small temperature gradient within the melt and a perfect surface contact, the non-dimensional solidification rate, S, can be expressed as [12]:

$$S = \sqrt{\frac{2}{\mathrm{Re}}\frac{\mathrm{Ja}}{\mathrm{Pr}}\frac{k_s}{k_l}}. \tag{22}$$

Substituting Eq. (22) into Eq. (19), we can obtain

$$\xi_m = \left(\sqrt{\frac{\mathrm{Ja}}{2}\frac{k_s}{\mathrm{Pr}\,k_l}+1}-\sqrt{\frac{\mathrm{Ja}}{2}\frac{k_s}{\mathrm{Pr}\,k_l}}\right)^{0.4}(1.18\,\mathrm{Re}^{0.2}). \tag{23}$$

Equation (23) shows that the flattening degree is indeed proportional to $\mathrm{Re}^{1/5}$ even when the solidification influences spreading. The criterion when the solidification effect on flattening can be neglected, then reduces to

$$\frac{\mathrm{Ja}}{2}\frac{k_s}{\mathrm{Pr}\,k_l} \ll 1. \tag{24}$$

This is consistent with the criterion proposed by Pasandideh-Fard et al. [8]. It is worth reminding that Eqs. (23) and (24) are based on the assumption of an isothermal substrate. For substrates with low thermal diffusivity, like glass, these equations will not be applicable.

If Eq. (23) is applied to estimate the flattening degree of Mo-Mo and PSZ-Steel, correlation similar to Eq. (20) with coefficient $a=0.48$ for Mo droplets and $a=1.03$ for PSZ droplets are obtained and plotted in Fig. 7. The correlation for PSZ droplets fits closely to the scattered data for various droplet size and velocity, while the curve for Mo droplets on glass is slightly higher than the computational data and that for Mo-Mo is below the data. The discrepancy comes from the validity of isothermal assumption for the substrate. For PSZ droplets on steel, this assumption reflects quite well the fact that the thermal diffusivity of PSZ is much smaller than that of steel. But for Mo-Mo, heat conduction within the substrate is already comparable to that within the melt and solid, and for Mo-Glass, the isothermal hypothesis is not at all applicable.

Effect of Substrate Temperature, Droplet Overheating, and Thermal Contact Resistance. The substrate temperature, droplet overheating and thermal contact resistance all have direct influence on splat solidification. These parameters affect the flattening degree through the rate of solidification. Since a theoretical expression for solidification rate that includes all of these parameters is very difficult to obtain, a parametric study is performed to demonstrate the effect of each parameter on flattening degree. The droplet size used in this parametric study is 30 μm. The velocity is 150 m/s for Mo droplet and 200 m/s for PSZ droplet.

Figure 8 shows the effect of substrate temperature on flattening degree for Mo-Mo and PSZ-Steel. Generally, a higher substrate temperature increases the flattening degree slightly in all cases,

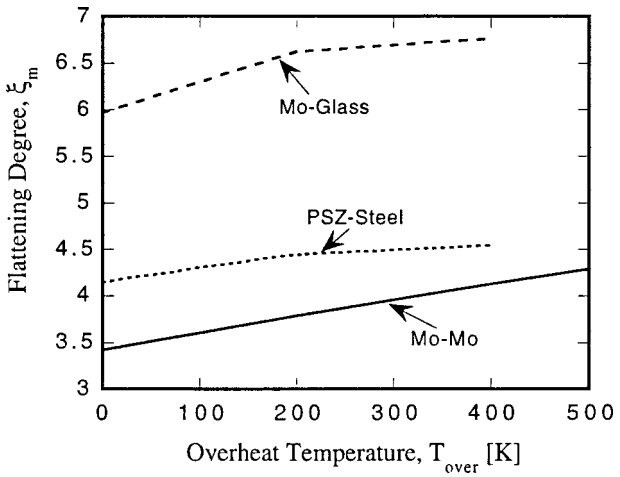

Fig. 9 Dependence of flattening degree on droplet overheating

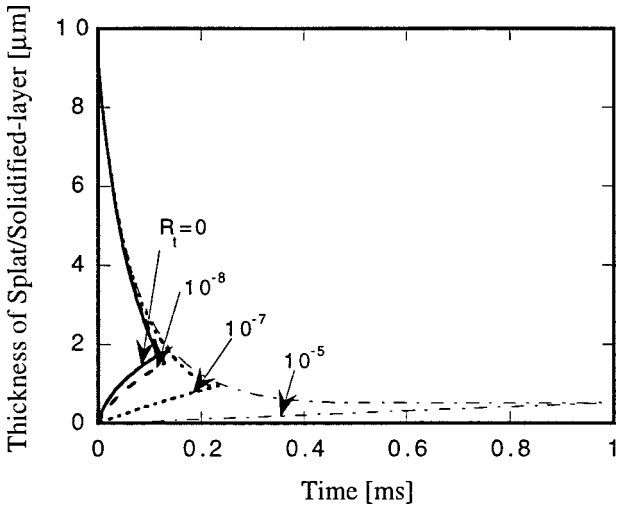

Fig. 10 Thickness of a molybdenum splat and the solidified layer showing the influence of thermal contact resistance (m^2K/W) on spreading and solidification

because a higher substrate temperature causes slower solidification of the droplet. However, since the solidification time for PSZ-Steel is considerably long compared to the spreading time and the intersection between the spreading line and the solidification line falls in the region where the flattening degree is insensitive to solidification rate, as discussed before and shown in Fig. 4, the effect of substrate temperature in the case of PSZ-Steel is less noticeable than in Mo-Mo. Similarly, since the overheating of droplet impedes the solidification of droplet, it also slightly enhances the flattening, as shown in Fig. 9, and the effect is more important for Mo-Mo than for PSZ-Steel.

The effect of thermal contact resistance on splat morphology is also numerically investigated and the results are shown in Fig. 10 for the case of Mo-Mo. The curves for four different values of contact resistance show that the solidification rate, and hence the flattening degree, can be drastically reduced by reducing the thermal contact resistance to $10^{-7}\,m^2\cdot K/W$. Since the flattening degree obtained using $R_t=10^{-8}\,m^2\cdot K/W$ agrees reasonably well with the experimental results (note that the results in Fig. 3 were obtained without contact resistance), it indirectly provides an estimation of the thermal contact resistance which is very difficult, if not impossible, to be measured directly from the experiments. The thermal contact resistance for Mo-Mo should be less than $10^{-8}\,m^2\cdot K/W$.

Conclusions

An experimental and numerical study has been performed to examine the effect of rate of solidification and the size and velocity of plasma-sprayed droplets on splat flattening degree. Four different droplet-substrate combinations, molybdenum-molybdenum, molybdenum-steel, molybdenum-glass and zirconia (PSZ)-steel with varying particle sizes and velocities have been considered. Since solidification is greatly influenced by substrate thermal diffusivity, splat/substrate contact resistance, and superheating of the melt droplet, the effect of all of these parameters is investigated to determine the conditions under which the flattening degree is independent of the rate of solidification.

To perform the theoretical analysis, Madejski-Zhang model for droplet spreading is coupled with a one-dimensional solidification and heat conduction model that incorporates the melt, the solidified splat region and the substrate. The conduction equation is solved iteratively together with the appropriate boundary conditions at various interfaces and equation for droplet spreading. It is demonstrated that the droplet spreading measured by flattening degree is significantly influenced by the rate of solidification that is always higher in the case of substrate with a large thermal diffusivity. Under such conditions, the coefficient ''*a*'' in the popularly used correlation, $\xi_m=a\,\mathrm{Re}^{0.2}$, for flattening degree must be modified to include the effect of the parameters that control solidification. For example, *a* equals 0.48 for Mo-Mo while its value for PSZ-Steel is 1.03, *a* value closer to 1.18 as predicted by the Madejski-Zhang model and 1.29 by the Madejeski model.

The results also show that a lower substrate temperature and/or higher thermal diffusivity reduces the flattening degree by enhancing the rate of solidification and arresting the spreading. On the other hand, a higher thermal contact resistance and superheating of droplet have opposite effect. When all of these effects are accounted for in the formulation, numerical predications agree statistically well with the experimental data for a broad range of materials, droplet size, its velocity, and substrate conditions.

The experimental results support the effect of surface tension and viscous dissipation on droplet spreading as included in the Madejski-Zhang model. They also agree well with the concept and criteria for the surface tension and viscous dissipation regimes as proposed by Zhang [12].

Acknowledgments

This research was supported by the National Science Foundation under the grant No. CTS-9711135 and the MRSEC Program under Award No. DMR-9632570.

Nomenclature

a = coefficient in the correlation of flattening degree, Eq. (20)
b = thickness of the melt, m
c_l = specific heat of the melt, J/kg·K
d_0 = initial droplet diameter, m
Ja = Jakob number, $\mathrm{Ja}=c_l(T_m-T_{\mathrm{sub}})/L_m$
k_l = thermal conductivity of the melt, W/m·K
k_s = thermal conductivity of the solid, W/m·K
L_m = latent heat of fusion, J/kg
L_{sub} = thickness of the substrate, m
Pe = Peclet number, $\mathrm{Pe}=w_0d_0/\alpha_l$
R = radius of spreading splat, m
R_t = thermal contact resistance, $m^2\cdot K/W$
Re = Reynolds number, $\mathrm{Re}=\rho w_0d_0/\mu$
s = thickness of the solidified layer, m
S = dimensionless solidification rate, $S=\tilde{s}/\sqrt{\tilde{t}}$
t = time, s
$t_{0.9}$ = spreading time, s, in Eq. (12)
T = temperature, K
T_0 = initial temperature of impacting droplet, K
T_m = melting point of droplet material, K
T_{sub} = substrate initial temperature, K
w_0 = impacting velocity of droplet, m/s
We = Weber number, $\mathrm{We}=\rho w_0^2d_0/\sigma_l$
z = coordinate in the direction of impact

Greek Symbols

α = thermal diffusivity, m^2/s
α_l = thermal diffusivity of the melt, m^2/s
ε = initial dimensionless radius of splat
ϕ_0 = contact angle (wetting angle), deg
λ = thermal conductivity, w/m·K
μ = dynamic viscosity of the melt, kg/m·s
ν = kinetic viscosity, m^2/s
ρ = density of the melt, kg/m^3
σ_l = surface tension of the melt, kg/s^2
ξ_m = flattening degree

Superscripts

$\sim$ = dimensionless variable

References

[1] Moreau, C., Gougeon, P., and Lamontagne, M., 1995, ''Influence of Substrate Preparation on the Flattening and Cooling of Plasma-Sprayed Particles,'' J. Thermal Spray Technol., **4**, pp. 25–33.

[2] Madejski, J., 1976, ''Solidification of Droplets on a Cold Surface,'' Int. J. Heat Mass Transf., **19**, pp. 1009–1013.

[3] Vardelle, M., Vardelle, A., Legaer, A. C., Fauchais, P., and Gobin, D., 1994, ''Influence of Particle Parameters at Impact on Splat Formation and Solidification in Plasma Spraying Processes,'' J. Thermal Spray Technol., **4**, pp. 50–58.

[4] Jiang, X., and Sampath, S., 1998, ''Effect of Substrate Condition on Splat Formation During Thermal Spray Deposition,'' *Solidification 1998*, S. P. Marsh et al., eds., The Minerals, Metals & Materials Society, pp. 439–448.

[5] Watanabe, T., Kurbayashi, I, Honda, T., and Kanzawa, A., 1992, ''Deformation and Solidification of a Droplet on a Cold Substrate,'' Chem. Eng. Sci., **47**, pp. 3059–3065.

[6] Fukanuma, H., and Ohmori, A., 1994, ''Behavior of Molten Droplets Impinging on Flat Surfaces,'' *Proc. 7th National Thermal Spray Conf.*, pp. 563–568.

[7] Schiaffino, S., and Sonin, A. A., 1997, ''Molten Droplet Deposition and Solidification at Low Weber Numbers,'' Phys. Fluids, **9**, No. 11, pp. 3172–3187.

[8] Pasandideh-Fard, M., Bhola, R., Chandra, S., and Mostaghimi, J., 1998, ''Deposition of Tin Droplets on a Steel Plate: Simulations and Experiments,'' Int. J. Heat Mass Transf., **41**, pp. 2929–2945.

[9] Inada, S., 1988, ''Transient Heat Transfer from a Free-falling Molten Drop of Lead to a Cold Plate,'' J. Chem. Eng. Jpn., **21**, pp. 582–588.

[10] Liu, W., Wang, G. X., and Matthys, E. F., 1995, ''Thermal Analysis and Measurements for a Molten Metal Drop Impacting on a Substrate: Cooling, Solidification and Heat Transfer Coefficients,'' Int. J. Heat Mass Transf., **38**, pp. 1387–1395.

[11] Rangel, R. H., and Bian, X., 1996, ''A Metal-Droplet deformation and Solidification Model with Substrate Remelting,'' *HTD-Vol. 336/FED-Vol. 240, Transport Phenomena in Materials Processing and Manufacturing*, ASME, New York, pp. 265–273.

[12] Zhang, H., 1999, ''Theoretical Analysis of Spreading and Solidification of Molten Droplet During Thermal Spray Deposition,'' Int. J. Heat Mass Transf., **42**, pp. 2499–2508.

[13] Trapaga, G., and Szekely, J., 1991, ''Mathematical Modeling of the Isothermal Impingement of Liquid Droplets in Spraying Processes,'' Metall. Trans. B, **22B**, pp. 901–914.

[14] Liu, H., Lavernia, E. J., and Rangel, R. H., 1993, ''Numerical Simulation of Substrate Impact and Freezing of Droplets in Plasma Spray Processes,'' J. Phys. D, **26**, pp. 1900–1908.

[15] Waldvogel, J. M., and Poulikakos, D., 1997, ''Solidification Phenomena in Picoliter Size Solder Droplet Deposition on a Composite Substrate,'' Int. J. Heat Mass Transf., **40**, No. 2, pp. 295–309.

[16] Jones, H., 1971, ''Cooling, Freezing and Substrate Impact of Droplets Formed by Rotary Atomization,'' J. Phys. D, **4**, pp. 1657–1660.

[17] Bertagnolli, M., Marchese, M., and Jacucci, G., 1995, ''Modeling of Particles Impacting on a Rigid Substrate under Plasma Spraying Conditions,'' J. Thermal Spray Technol., **4**, pp. 41–49.

[18] Dykhuizen, R. C., 1994, ''Review of Impact and Solidification of Molten Thermal Spray Droplets,'' J. Thermal Spray Technol., **3**, pp. 351–361.

[19] Markworth, A. J., and Saunders, J. H., 1992, ''An Improved Velocity Field for the Madejski Splat-Quench Solidification Model,'' Int. J. Heat Mass Transf., **35**, No. 7, pp. 1836–1837.

[20] Chapra, S. C., and Canale, R. P., 1998, *Numerical Methods for Engineers: With Programming and Software Applications*, 3rd Ed., McGraw-Hill, New York.

[21] Patankar, S. V., 1980, *Numerical Heat Transfer and Fluid Flow*, Hemisphere, New York.

[22] Wan, Y. P., Prasad, V., Wang, G.-X., Sampath, S., and Fincke, J. R., 1999, ''Model of Powder Particle Heating, Melting, Resolidification, and Evaporation on Plasma Spraying Processes,'' ASME J. Heat Transfer, **121**, pp. 691–699.

[23] Beer, S. Z., Ed., 1972, *Liquid Metals, Chemistry and Physics*, Marcel Dekker, New York.

[24] Bansal, N. P., and Doremus, R. H., 1986, *Handbook of Glass Properties*, Academic Press, New York.

[25] Trapaga, G., Matthys, E. F., Valencia, J. J., and Szekely, J., 1992, ''Fluid Flow, Heat Transfer, and Solidification of Molten Metal Droplets Impinging on Substrates: Comparison of Numerical and Experimental Results,'' Metall. Trans. B, **23B**, pp. 701–718.

Higher Order Perturbation Analysis of Stochastic Thermal Systems With Correlated Uncertain Properties

A. F. Emery
Department of Mechanical Engineering,
University of Washington,
Seattle, WA 98195-2600
e-mail: emery@u.washington.edu

How the behavior of thermal systems depends on uncertainties in properties and boundary conditions is an important aspect of simulation. This dependence is usually judged by the statistics of the response, i.e., the mean response and its standard deviation which are often determined by perturbation methods, ranging from 1^{st} to 3^{rd} order. The aim of this paper is to be a tutorial for those interested in estimating uncertainties by summarizing the author's experience in using higher order perturbation analysis for thermal problems, detailing the underlying assumptions, and presenting several examples. Problems involving correlated parameters, which occur in almost all thermal experiments, are also treated. It is shown that the scale of correlation has a strong effect upon the statistics of the response and that such correlation should not be ignored. It is recommended that the 1^{st} order estimates of the standard deviation and 2^{nd} order estimates of the mean response be used when characterizing thermal systems with random variables, regardless of the degree of correlation. [DOI: 10.1115/1.1351144]

Keywords: Computational, Heat Transfer, Inverse, Modeling

Introduction

Although most engineering systems are designed by assuming deterministic models, real systems are most often characterized by uncertainty in some or all of the model parameters. These uncertainties can be broadly classified into three categories: (1) uncertainty due to the natural heterogeneity of the material which can lead to a spatial variability of properties, such as in the thermal conductivity, or uncertainty in boundary conditions which may cause a temporal variability, as in the convective heat transfer coefficient; (2) uncertainty due to the limited availability of information about the properties; and (3) uncertainty due to experimental errors which consist of a fixed (bias) component and a random (precision) component [1,2]. Unfortunately it is not easy to incorporate these uncertainties into many thermal analysis programs and most investigators are content with reporting estimated sensitivities of system temperatures and heat transfer to those parameters which are subject to the latter two classes of uncertainty.

Even the most rudimentary literature search will turn up a substantial number of papers and books on uncertainty analysis applied to civil, electrical, and geological engineering [3–5]. Generally the civil and electrical applications are related to stochastic input, noise, or forcing functions. In the civil engineering studies randomness seems to have had its genesis in earthquake, wind loads, and aircraft pressure loadings; in electrical engineering in input and signal noise. In most studies the models are deterministic but the inputs/loads are stochastic. In contrast, in the geological engineering examples, mostly in the water and petroleum acquifer studies, the soil properties are taken to be random, leading to stochastic models. The thermal counterpart to acquifers is porous media in which much work has been done to estimate effective macroscopic properties. This is often accomplished by accounting for the effect of microstructural features on the macroscopic behavior. Reference [6] contains papers relating to porous media, suspensions and inclusions. Surprisingly, until recently, the heat transfer community has not demonstrated an equivalent interest in either stochastic loads or models. I speculate that this may be due to a lack of specificity about the uncertainty and an almost innate acceptance of uncertainty in thermal modeling and apparently the feeling that the lack of specificity mitigates against employing uncertainty analysis in designing or studying thermal systems. While some properties are well characterized, e.g., gas conductivities with reported accuracies of better than 2 percent ([7], pp. 2–87), others are extremely variable and the precision can only be judged from the scatter in the data, e.g., the Reynolds number factor for boiling ([7], pp. 13–39) whose scatter is of the order of ± 50 percent, developing turbulent flow in a duct ([8], pp. 4–73 and 4–79) with scatter of the order of ± 25 percent. Although the scatter can be specified, it is rare that statistical information is provided and correlations are usually derived from least squares fits to the data without assigning statistical weights to the data. Most analyses utilize such correlations and frequently the independent variable, e.g., Reynolds number and Grashof number, can only be estimated. Thus in addition to the uncertainty in the accuracy of the fit, there is an uncertainty in the variable describing the flow regime, which can easily lead to large uncertainties in the convective heat transfer coefficient.

The effect of such uncertainty and randomness in the properties or boundary conditions should be examined. However, a literature search of the last 10 years using the keywords ''stochastic heat transfer'' finds a very limited number of papers in the areas of the following: inverse problems; designing experiments to estimate properties in the presence of uncertainty; consideration of stochastic loads on HVAC and other energy systems; food/grain processing in stochastic environments; and a few papers related to stochastic finite element thermal analyses [9–16]. Madera [17] has used an extension of the usual finite difference procedure in which the coefficients of the algebraic system are not scalars, but stochastic matrices, to solve for the mean temperatures and their covariances.

The statistics, typically the mean value and the standard deviation σ, of the response can be obtained by sampling, usually coupled with some form of variance reduction [18,19] or by per-

Contributed by the Heat Transfer Division for publication in the JOURNAL OF HEAT TRANSFER. Manuscript received by the Heat Transfer Division April 12, 2000; revision received November 3, 2000. Associate Editor: H. Bau.

turbation analysis. Because of the expense associated with sampling, many analyses employ the perturbation approach and it is often assumed that higher order perturbation estimates are more accurate. The problem is, as expected, that these higher order estimates require substantially more computations and are strongly dependent upon the problem being investigated. Even for linear systems, σ is nonlinearly dependent upon the stochastic parameters, and for nonlinear systems—which almost all thermal systems are—the nonlinearity strongly affects the accuracy of the estimates of σ. In this paper we present the basis of the perturbation method and then study several relatively simple, but nonlinear, thermal problems to examine the effectiveness of using higher order estimates. In addition, because thermal systems often are affected by correlated parameters, either in space or time, we examine the effects of correlated random parameters.

Theory

Consider a system with q random parameters, Q_i, $i=1,\ldots,q$, defined by their mean values and covariances. Let the vector of temperatures* at selected points, $\mathbf{\Phi}$, be characterized by its mean and standard deviation defined in terms of the vector of random parameters $\mathbf{Q}$ by Eqs. 1(a) and 1(b). Full details of the statistical derivations, the stochastic finite element procedure for thermal problems, the appropriate references, and a number of examples are described in [20] and [21].

$$E[\mathbf{\Phi}|\mathcal{D}_{\mathcal{Q}}]=\int \mathbf{\Phi}(\mathbf{Q})f(\mathbf{\Phi}|\mathcal{D}_{\mathcal{Q}})d\mathbf{\Phi} \tag{1a}$$

$$\sigma^2[\mathbf{\Phi}|\mathcal{D}_{\mathcal{Q}}]=\int (\mathbf{\Phi}(\mathbf{Q})-E[\mathbf{\Phi}|\mathcal{D}_{\mathcal{Q}}])^2 f(\mathbf{\Phi})d\mathbf{\Phi}, \tag{1b}$$

where $f(\mathbf{\Phi})$ is the probability density distribution of $\mathbf{\Phi}$. From the properties of random variables, $f(\mathbf{\Phi})$ can be written in terms of the joint distribution of Q_i, $f(Q_1,\ldots,Q_q)$, as

$$E[\mathbf{\Phi}|\mathcal{D}_{\mathcal{Q}}]\mathcal{D}_{\mathcal{Q}}=\int\cdots\int \mathbf{\Phi}(\mathbf{Q})f(Q_1,\ldots,Q_q)dQ_1\ldots dQ_q \tag{2a}$$

$$\sigma^2[\Phi|\mathcal{D}_{\mathcal{Q}}]=\int\cdots\int (\mathbf{\Phi}(\mathbf{Q})-\mathbf{E}[\mathbf{\Phi}|\mathcal{D}_{\mathcal{Q}}])^2 f(Q_1,\ldots,Q_q)\times dQ_1\ldots dQ_q. \tag{2b}$$

In Eqs. 1 and 2 the statistics $E[\mathbf{\Phi}]$ and $\sigma[\mathbf{\Phi}]$ are expressed as the conditional statistics $E[\mathbf{\Phi}|\mathcal{D}_{\mathcal{Q}}]$ and $\sigma[\mathbf{\Phi}|\mathcal{D}_{\mathcal{Q}}]$ to emphasize that the results reported herein and the conclusions drawn are conditional and valid only for the specific range of parameters considered in the examples. This will be elaborated on in the section entitled *Accuracy* where $f(\mathbf{\Phi})$ is discussed. Until then, we will drop the conditional notation for convenience.

The values of $E[\mathbf{\Phi}]$ and $\sigma[\mathbf{\Phi}]$ are generally determined by direct numerical integration or perturbation theory. Numerical integration is usually accomplished through straight-forward integration, often using Gaussian quadrature, or limited sampling using Monte Carlo, stratified sampling, importance sampling, or hypercube methods [18]. For very simple problems, even if $\mathbf{\Phi}$ must be determined numerically, the evaluation of Eq. 2 is possible. However, if several random parameters are considered numerical evaluation is rarely practical because of the multiple integrations. The main advantage of sampling methods is that they are applicable to arbitrary probability distributions of $\mathbf{Q}$ but the expense is usually warranted only in unusual circumstances, particularly when $\mathbf{\Phi}(\mathbf{Q})$ is difficult to compute.

The most widely used technique to analyze stochastic systems is the perturbation method in which the response is expressed in a Taylor series with respect to Q as

$$\mathbf{\Phi}=\overline{\mathbf{\Phi}}+\sum_{i=1}^{q}\overline{\mathbf{\Phi}_{Q_i}}\delta Q_i+\frac{1}{2}\sum_{i=1}^{q}\sum_{j=1}^{q}\overline{\mathbf{\Phi}_{Q_iQ_j}}\delta Q_i\delta Q_j+h.o.t., \tag{3}$$

where Q_i represents the i^{th} random variable, overbars represent quantities evaluated at the mean values of the parameters, subscripts represent derivatives, and *h.o.t.* represents higher order terms.

For nonlinear responses, the use of the Taylor series is valid only if (i) the joint pdf, $f(Q_1,\ldots,Q_q)$, is localized in the vicinity of $\overline{Q}$, (ii) $\mathbf{\Phi}$ varies gradually with $\mathbf{Q}$, and (iii) $\mathbf{\Phi}$ is differentiable in the vicinity of Q [22]. When these conditions are not satisfied, then the statistics must be determined through Eq. 1.

Inserting the Taylor series into Eq. 2 and expanding and then retaining the desired order of terms yields the approximations. For example, the results for 2nd order are

$$E[\mathbf{\Phi}]=\overline{\mathbf{\Phi}}+\frac{1}{2}\sum_{i=1}^{q}\sum_{j=1}^{q}\overline{\mathbf{\Phi}_{Q_iQ_j}}Cov[Q_i,Q_j] \tag{4a}$$

$$\begin{aligned}\sigma^2[\mathbf{\Phi}]=Diag\Bigg[&\sum_{i=1}^{q}\sum_{j=1}^{q}\overline{\mathbf{\Phi}_{Q_i}}\ \overline{\mathbf{\Phi}_{Q_j}}^{T}Cov[Q_i,Q_j]\\&+\frac{1}{2}\sum_{i=1}^{q}\sum_{j=1}^{q}\sum_{k=1}^{q}(\overline{\mathbf{\Phi}_{Q_i}}\ \overline{\mathbf{\Phi}_{Q_jQ_k}}^{T}+\overline{\mathbf{\Phi}_{Q_iQ_j}\mathbf{\Phi}_{Q_k}}^{T})\\&\times Cov[Q_i,Q_j,Q_k]\\&+\frac{1}{4}\sum_{i=1}^{q}\sum_{j=1}^{q}\sum_{k=1}^{q}\sum_{l=1}^{q}\overline{\mathbf{\Phi}_{Q_iQ_j}}\ \overline{\mathbf{\Phi}_{Q_kQ_i}}^{T}(Cov[Q_i,Q_j,Q_k,Q_l]\\&-Cov[Q_i,Q_j]Cov[Q_k,Q_l])\\&+\frac{1}{3}\sum_{i=1}^{q}\sum_{j=1}^{q}\sum_{k=1}^{q}\sum_{l=1}^{q}\overline{\mathbf{\Phi}_{Q_i}}\ \overline{\mathbf{\Phi}_{Q_kQ_lQ_j}}^{T}\\&\times Cov[Q_i,Q_j,Q_k,Q_l]\Bigg].\end{aligned} \tag{4b}$$

The results of including terms of order δQ_i and $\delta Q_i\delta Q_j$ in the Taylor series, Eq. 3, are called the 1st and 2nd order approximations, respectively, (referred to by the acronyms FORM and SORM in the reliability literature) but the definition for the 2nd order and 3rd order approximations are not unambiguous. If the Taylor series for $\mathbf{\Phi}$ is truncated at the 2nd order, as suggested by Halder [23], then the equation for $\sigma[\mathbf{\Phi}]$ will not contain the last term of Eq. 4(b).

The evaluation of the 2nd order estimate of $\sigma[\mathbf{\Phi}]$, Eq. 4(b) requires the third and fourth covariances of the random variables and the estimation of 3rd order derivatives. It is rare, particularly when using correlations derived from experimental data, to know more than the mean and the standard deviation of the random variables and it is generally difficult to estimate derivatives higher than the 2nd. For this reason, approximations and simplifications are frequently introduced. Breitung [24] suggested using the theory of asymptotic approximations based only on the principal curvatures, that is retaining only $\mathbf{\Phi}_{Q_iQ_i}$, and ignoring the mixed derivatives. Unfortunately the mixed derivatives are often important in thermal analysis and can not be ignored.

Probably the most common simplification is to assume that the random parameters are normally distributed. In this case, the 3rd order covariances are identically zero and the 4th order covariances can be expressed as products of the 2nd order covariances [25], thus substantially simplifying the analysis. If the random variables are not Gaussian, but their joint pdf is known, Rosenblatt's transformation [26] can be used to derive a set of independent normal variables but frequently this amplifies the nonlinearity of $\mathbf{\Phi}$ with respect to these variables ([23], p. 225).

*Although the development of the equations will be in terms of temperature, the method applies to any quantity of interest, e.g., heat flux, time derivatives.

However, a knowledge of the marginal distribution of the parameters and their covariance matrix is not sufficient to determine the joint pdf unless the random parameters are normal or lognormal [27]. When detailed information about the pdf of the random variables is missing or because of the analytical and computational difficulties in treating Eq. 4 in its full form, analyses are often based upon the assumption of normality.

Most thermal parameters are restricted in their range and thus are not well represented by a normal distribution. For example, the conductivity must be positive and is probably best represented by a lognormal distribution; emissivity is limited to 0 to 1 and a beta, truncated normal, or a uniform distribution could be used. For such non-normal distributions, one may replace the actual distribution by an equivalent normal distribution using the Rackwitz-Fiessler method which is commonly used in reliability analysis ([23], p. 72). For thermal problems in which the parameters are functions of time or temperature, this may require modifying the equivalent normal distribution continuously throughout the simulation. If the parameters are correlated and non-normal, the process is more difficult.

In the case where there is only one normally distributed random parameter, Q, the higher order estimates of the mean and standard deviation are given by

$$E[\mathbf{\Phi}] = \underbrace{\overline{\mathbf{\Phi}}}_{0\text{th}} + \underbrace{\frac{1}{2}\frac{\overline{\partial^2 \mathbf{\Phi}}}{\partial Q^2}\sigma^2[Q]}_{2\text{nd}} \tag{5a}$$

$$\sigma^2[\mathbf{\Phi}] = \underbrace{\left(\frac{\overline{\partial \mathbf{\Phi}}}{\partial Q}\right)^2 \sigma^2[Q]}_{1\text{st}} + \underbrace{\left(\frac{1}{2}\left(\frac{\overline{\partial^2 \mathbf{\Phi}}}{\partial Q^2}\right)^2 + \frac{\overline{\partial \mathbf{\Phi}}}{\partial Q}\frac{\overline{\partial^3 \mathbf{\Phi}}}{\partial Q^3}\right)\sigma^4[Q]}_{2\text{nd}} + \underbrace{\left(\frac{5}{12}\left(\frac{\overline{\partial^3 \mathbf{\Phi}}}{\partial Q^3}\right)^2 + \frac{1}{4}\frac{\overline{\partial \mathbf{\Phi}}}{\partial Q}\frac{\overline{\partial^5 \mathbf{\Phi}}}{\partial Q^5} + \frac{1}{2}\frac{\overline{\partial^2 \mathbf{\Phi}}}{\partial Q^2}\frac{\overline{\partial^4 \mathbf{\Phi}}}{\partial Q^4}\right)\sigma^6[Q]}_{3\text{rd}}, \tag{5b}$$

where the numbers under the braces refer to the order of the approximation. Note that the 2nd order estimate of $\sigma[\mathbf{\Phi}]$ requires solving for $\overline{\mathbf{\Phi}}$, $\overline{\partial \mathbf{\Phi}/\partial Q}$, $\overline{\partial^2 \mathbf{\Phi}/\partial Q^2}$, and $\overline{\partial^3 \mathbf{\Phi}/\partial Q^3}$ all of which may be nonlinear functions of Q and $\mathbf{\Phi}$ and are frequently difficult to compute.

Evaluation of the Derivatives

In order to evaluate Eq. 5, one needs both the statistics of the random parameters and the derivatives of $\mathbf{\Phi}$. These derivatives are usually evaluated by (*a*) finite differencing the temperatures $\mathbf{\Phi}$, and (*b*) solving field equations for the sensitivities.

The simplest and sometimes the most cost effective approach is to use finite differences. Emery and Fadale [28] discuss this method and note that smoothing is generally needed. This point will be elaborated on in the later section on *Computational Effort*.

For strongly nonlinear problems, the solution of the several values of $\mathbf{\Phi}$ needed for the finite differencing may be very costly. Another approach is to use the field equations to solve for the derivatives directly. Consider the semi-discrete transient heat conduction equation,

$$\mathbf{C}\frac{\partial \mathbf{\Phi}}{\partial t} + \mathbf{K}\ \mathbf{\Phi} = \mathbf{q}, \tag{6}$$

with appropriate initial and boundary conditions, both of which may involve random parameters. $\mathbf{C}$, $\mathbf{K}$, and $\mathbf{q}$ are the capacitance, conductance matrices and source vector and many be random. Substituting the Taylor series for $\mathbf{\Phi}$ into Eq. 6 and collecting terms of equal order in δQ yields.

0^{th} Order Equation

$$\overline{\mathbf{C}}\frac{\partial \overline{\mathbf{\Phi}}}{\partial t} + \overline{\mathbf{K}}\ \overline{\mathbf{\Phi}} = \overline{\mathbf{q}} \tag{7a}$$

1^{st} Order Equations

$$\overline{\mathbf{C}}\frac{\partial \overline{\mathbf{\Phi}_{Q_i}}}{\partial t} + \overline{\mathbf{K}}\ \overline{\mathbf{\Phi}_{Q_i}} = \mathbf{f}_{Q_i} \quad i = 1, \ldots, q, \tag{7b}$$

where

$$\mathbf{f}_{Q_i} = \overline{\mathbf{q}_{Q_i}} - \overline{\mathbf{C}_{Q_i}}\frac{\partial \overline{\mathbf{\Phi}}}{\partial t} - \overline{\mathbf{K}_{Q_i}}\ \overline{\mathbf{\Phi}}.$$

In general, the 0^{th} order equation (Eq. 7(*a*)) involves an iterative solution when the properties or boundary conditions are temperature dependent. The solution is the nodal response distribution, denoted as $\overline{\mathbf{\Phi}}$, of the system and is the same as the solution of the direct, deterministic finite element equations [29]. Since, $\overline{\mathbf{C}}$, $\overline{\mathbf{K}}$, and $\overline{\mathbf{f}}$ have been determined in the solution of the 0^{th} order equation, they are now constants and the equations for the higher order derivatives are linear. Similar equations can be derived for the 2^{nd} and higher order derivatives, although the right hand sides become progressively more complicated, particularly if the random variable is a function of temperature [21]. The cost of modifying codes to solve for these derivatives is often the reason that the finite difference approach is used.

We have chosen to examine thermal problems which are simple enough that the integrations involved in Eq. 2 can be numerically computed. The solutions based upon Eq. 2 are referred to as *reference* solutions in the following discussions. Solutions based upon evaluating the statistics of $f(T)$ (see the section on *Accuracy*) are labeled as ''exact.'' These exact values were obtained by using a quadrature with a sufficient number of sampling points to yield an accuracy of better than 99.9 percent. Even for these simple problems, the solution of the field equations, Eq. 6, for the temperatures to be substituted into Eq. 2 must be achieved numerically and the computations can be quite lengthy. The temperatures were calculated with a finite element code with the mesh refined sufficiently so that the computed temperatures agreed with the analytical solution or had converged to an error of less than 0.1 percent. The uncertainty in the parameters was limited to $\sigma[Q]/\overline{Q} = 25$ percent. For a normal distribution this gives a range of $0.25\overline{Q} \leqslant Q \leqslant 1.75\overline{Q}$. A larger value of σ would imply a finite probability of a negative value of Q.

Example 1: Inherent and Strong Linearities in a Transient Conduction Problem. Consider a slab of thickness L with an imposed heat flux of F at $x=0$ and a fixed temperature of T_L at $x=L$ and an initial temperature of T_L. If the conductivity is a constant, k_1, the temperature at $x=0$ is $T(0)-T_L = FL/k_1$ and the Taylor series in terms of k_1 is

$$T(0)-T_L = \overline{T(0)-T_L} - \frac{FL}{\overline{k_1}}\left(\frac{\delta k_1}{\overline{k_1}}\right) + \frac{FL}{\overline{k_1}}\left(\frac{\delta k_1}{\overline{k_1}}\right)^2 - \frac{FL}{\overline{k_1}}\left(\frac{\delta k_1}{\overline{k_1}}\right)^3. \tag{8a}$$

Even for moderate values of $\delta k_1/\overline{k_1}$ the 1^{st} order approximation does not suffice. Figure 1 illustrates the temporal behavior of $\sigma[t_0]$ $(t_0 = (T(0)-T_L)\overline{k_1}/FL)$ for $\sigma[k_1]/\overline{k_1} = 0.1$ and 0.25 with the derivatives computed using both the field equations and finite differences using an implicit time integration.

The dashed lines of Fig. 1(*a*) are the exact steady state values computed by evaluating the pdf of t_0 (see the subsequent section

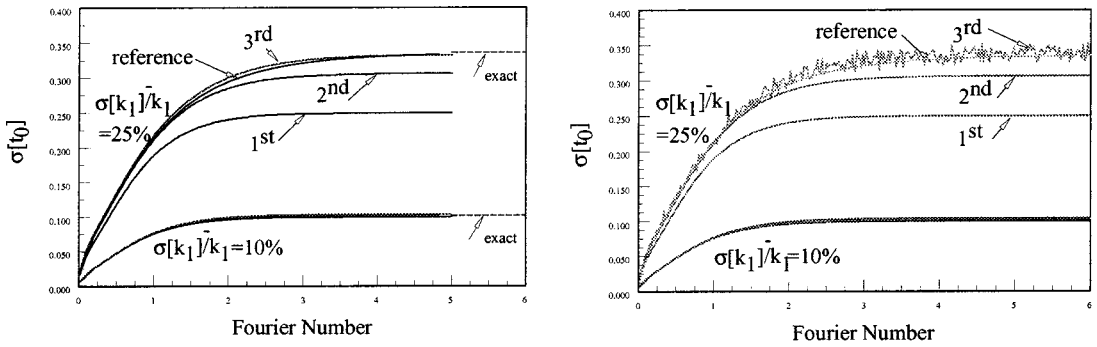

Fig. 1 Temporal behavior of $\sigma[t_0]$ for variations in k_1 computed implicitly: (*a*) using field equations; (*b*) using finite differences.

on *Accuracy*) and the agreement with the 3rd order perturbation solution is excellent. For $\sigma[k_1]/\bar{k}_1=0.1$, the 1st order suffices, but for larger uncertainties the nonlinearity of temperature with respect to k_1 amplifies the uncertainty in t_0. The values based upon the finite differences behave well for moderate values of $\sigma[k_1]/\bar{k}_1$, but as the uncertainty increases the 3rd perturbation displays considerable roughness. If the temperatures are computed explicitly, this roughness often becomes apparent in the 2nd order results.

Let us amplify the nonlinearity by letting the conductivity be temperature dependent according to the linear relationship

$$k(T)=k_1+\beta(T-T_L). \tag{8b}$$

When β is negative, the conductivity decreases with increasing temperature and for a positive flux, F, this causes an increasing gradient, $\partial T/\partial x$, and nonlinearity in the neighborhood of the front surface. The limiting value of $\beta FL/k_1^2$ is -0.5, at which point the conductivity at $x=0$ becomes zero and the gradient infinite. For negative values of β the temperature is more nonlinear in terms of k_1 than indicated by Eq. 8(*a*) and the first few terms of the Taylor series are not a good approximation of the temperature variation with k_1. Figure 2(*a*) displays the temporal behavior for $\beta=0.1$ and -0.1 for $\sigma[k_1]/\bar{k}_1=0.1$. For an increasing conductivity, $\beta=-0.1$, the 1st order suffices, as it did in Fig. 1, but for a decreasing conductivity, $\beta=-0.1$, the uncertainty is amplified to a value approximately equal to that shown in Fig. 1 for $\sigma[k_1]/\bar{k}_1=25$ percent. Figure 2(*b*) displays the steady-state behavior for a range of β.

Example 2: Temperature Dependent Conductivity. An interesting variant of Example 1 is to specify that the conductivity follows the piecewise linear relationship

$$k(T)=\begin{cases} k_1 & T\leqslant T_1 \\ k_1+\dfrac{k_2-k_1}{T_2-T_1}(T-T_1) & T_1\leqslant T\leqslant T_2. \\ k_2 & T>T_2 \end{cases} \tag{9}$$

Piecewise linear relations of this form are frequently used in numerical simulations when conductivities are taken from tabular values. Figure 3 compares the reference and 1st and 2nd order estimates for conductivities which increase ($k_2/k_1>1$) or decrease ($k_2/k_1<1$) with temperature.

Both figures display an abrupt oscillation in the 2nd order perturbation results when the temperature reaches either T_1 or T_2 where the slope of the $k(T)$ curve has a discontinuity. The effect is much stronger for the decreasing conductivity than for the increasing conductivity. In the former case the aberrations occur at both discontinuities, but for the latter only at T_2. Reference [21] provides more details about this problem and the behavior of $\sigma[t_0]$ as a function of F.

Example 3: Radiation From a Fin. Consider a fin which convects and radiates heat to an ambient fluid. The temperature at the base of the fin is T_w, of the ambient fluid is T_∞, and it is thermally insulated at the end $x=L$. The convective heat transfer and radiative loss is chosen such that the thermal performance of the fin is equivalent to an effectiveness of 2 [30]. The convective

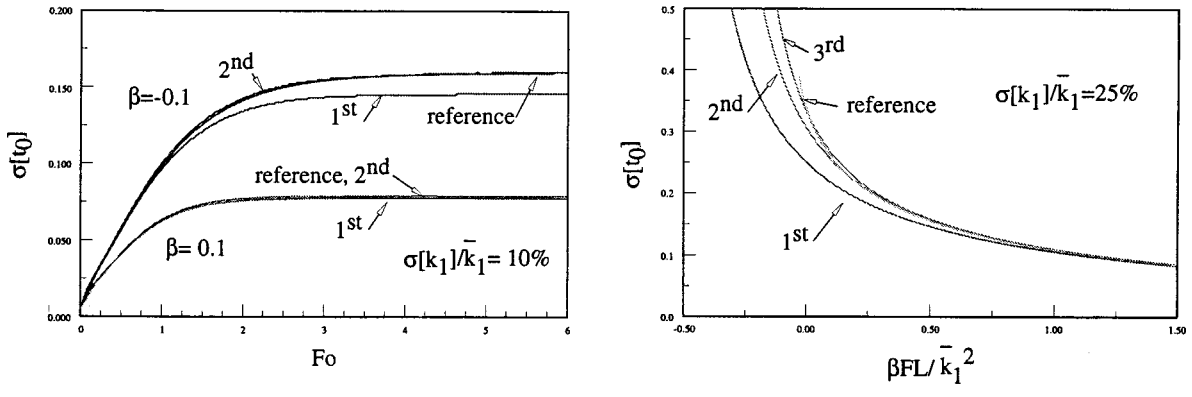

Fig. 2 $\sigma[t_0]$ for $k=k_1+\beta(T-T_L)$ computed implicitly: (*a*) temporal behavior; (*b*) steady state.

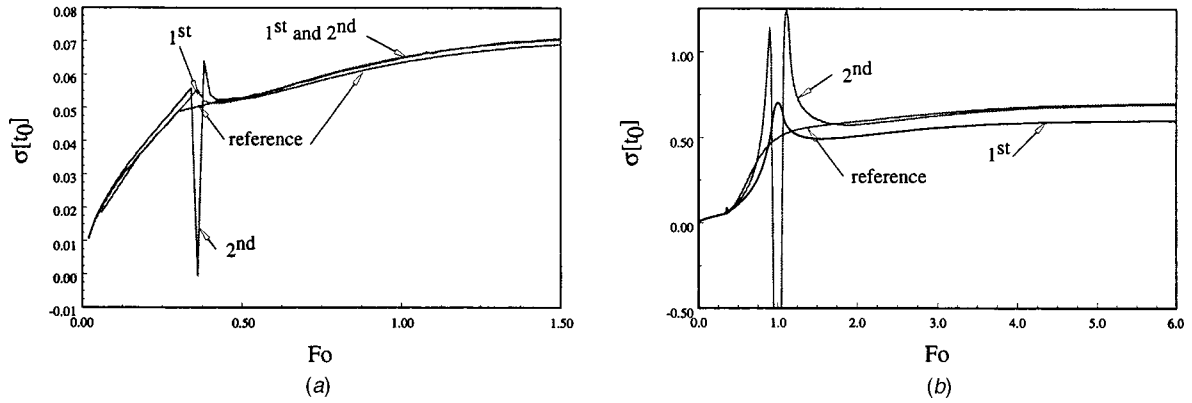

Fig. 3 $\sigma[t_0]$ **for a piecewise definition of** $k(T)$ **and** $\sigma[k_1]/\bar{k}_1=0.1$**: (***a***)** $k_2/k_1=1.5$**; (***b***)** $k_2/k_1=0.5$**.**

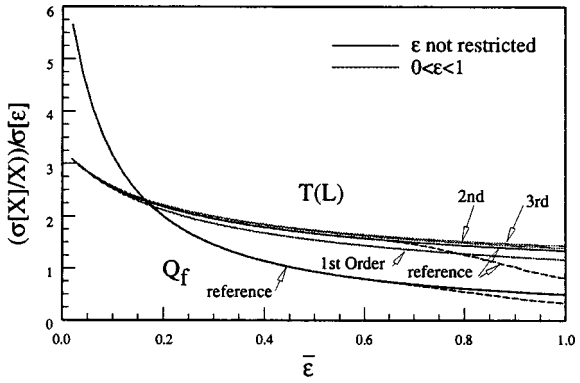

Fig. 4 Standard deviations of Q_f **and** $(T(L)-T_\infty)/(T_w-T_\infty)$ **with respect to** ϵ **for** $\sigma[\epsilon]/\bar{\epsilon}=25$ **percent**

heat transfer coefficient was chosen so that the radiative heat transfer constitutes about 80 percent of the heat transferred to the ambient fluid and we wish to determine the sensitivity of the heat loss and the fin tip temperature, T_L, to the emissivity. Figure 4 displays the standard deviation of these quantities with respect to the emissivity, $\bar{\epsilon}$, for $\sigma[\epsilon]/\bar{\epsilon}=25$ percent computed with a constant, but random emissivity over the surface of the fin (e.g., a uniform distribution). For the heat loss, Q_f, all three orders of the perturbation solution gave essentially the same result and equal to the reference value. For the tip temperature, T_L, the 1st order underestimates, and the 2nd and 3rd slightly overestimate the reference values.

The solid curves on Fig. 4 were computed by assuming that $\bar{\epsilon}$ was unrestricted in its range. In fact, $\bar{\epsilon}$ is limited to the range $0 \leq \bar{\epsilon} \leq 1$. For large values of $\sigma[\epsilon]$, when ϵ approaches 1, the distribution cannot be normal. The dashed curves correspond to a truncated normal distribution. The difference between the perturbation solution and the dashed curves emphasizes one of the major weaknesses of the perturbation approach, namely its insensitivity to the precise form of $f(Q)$.

Correlated Random Variables

Most uncertainty analyses assume that the random parameters are independent, i.e., the covariance matrices are diagonal. For heat transfer problems it is easy to envisage cases where this is not true. For example, consider a simple rectangular fin attached to a wall. Assuming that the fin is thermally infinitely long, the amount of heat transferred from the fin and the wall are given by

$$Q_w=h_wA_w(T_w-T_\infty)$$
$$Q_f=\sqrt{h_fP_fkA_f}(T_w-T_\infty). \tag{8}$$

The heat transfer from both the wall and the fin is controlled by the convection to the ambient fluid. It is easy to imagine the case where an increase in h_w is accompanied by an increase in h_f because of an increased fluid velocity, i.e., a positive correlation. On the other hand it is also possible that the fluid motion may result in a decrease in h_w while h_f increases if the fluid changes its flow pattern to preferentially bathe the fin, i.e., a negative correlation. Letting ρ represent the correlation coefficient between h_w and h_f, the covariance matrix is given by

$$Cov=\begin{bmatrix} \sigma^2[h_f] & \rho\sigma[h_f]\sigma[h_w] \\ \rho\sigma[h_f]\sigma[h_w] & \sigma^2[h_w] \end{bmatrix} \tag{9a}$$

and the standard deviation of the total heat lost Q_t $(=Q_w+Q_f)$ assuming that $\sigma[h_f]=\sigma[h_w]=\sigma[h]$ is given by

$$\frac{\sigma^2[Q_t]}{\bar{Q}_w^2}=\left[1+\rho\frac{\bar{Q}_f}{\bar{Q}_w}+\left(\frac{\bar{Q}_f}{2\bar{Q}_w}\right)^2\right]\frac{\sigma^2[h]}{\bar{h}^2}. \tag{9b}$$

The standard deviation varies strongly with ρ and the effect of the correlation is tied to the value of $\bar{Q}_f/\bar{Q}_w$. For positive correlation the standard deviation of Q_t increases as expected. For negative correlation it decreases since an increase in heat flux at one surface is compensated for by a decrease at the other surface.

Although the example to be discussed involves the spatial correlation of a property, it must be recognized that any information obtained either directly from an experiment or by data reduction which involved a common measuring device, e.g., a data acquisition system, is correlated through the calibration of the device. Smith ([22], pp. 205–209) gives an excellent illustration of this effect and the complications that any uncertainty in the calibration has on the uncertainty of the derived information.

Let us modify the solution of Fig. 4 by assuming that the emissivity is a continuous random field $Q(\vec{x})$. If we consider the discretized random field as an elemental quantity, then the average of the continuous random field of a finite element can be treated as an elemental quantity, but which differs from the stochastic properties of the random field [31]. The local integral over the domain D_i of the finite element of the random field is itself a random variable, referred to as Q_i for the i^{th} element.

$$Q_i=\frac{1}{D_i}\int_{D_i}Q(\vec{x})d\vec{x}. \tag{10}$$

In this example, we assume that the emissivity is a random field with an autocorrelation function of the form $\exp(-x/\theta)$ where θ is the scale of the correlation. The value of the correlation, ρ, between the 1st element at the wall and its neighbor and the last element of the fin as a function of the scale is given in Fig. 5. Uncorrelated elements are characterized by $\theta=0$ and a complete

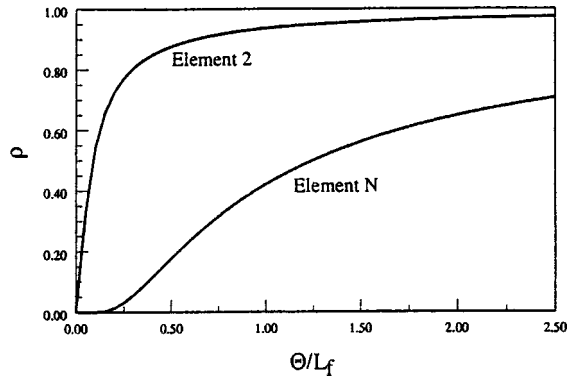

Fig. 5 Correlation between the 1st element at the wall with other elements of the fin

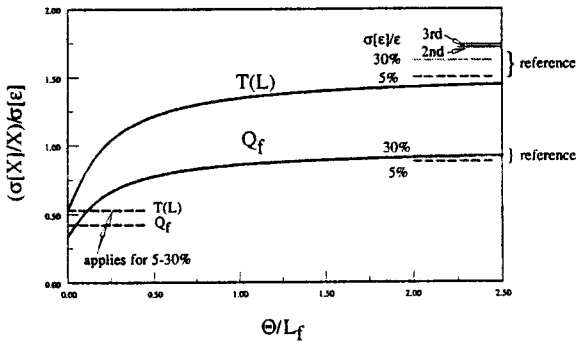

Fig. 6 The effect of correlation scale θ on the 1st order estimate of the standard deviation for $\bar{\epsilon}=0.5$ (dashed lines are the reference values)

correlation (i.e., all elements have the same random parameter) by $\theta=\infty$. While a strong correlation exists between two adjacent elements for moderate values of θ, even for a relatively large value of θ/L_f the correlation between the wall element and the tip element is relatively small.

Figure 6 displays the 1st order estimate of the standard deviation of the fin heat loss, Q_f and the tip temperatures as a function of θ. The 2nd and 3rd order estimates for emissivities which are uniform ($\theta=\infty$) over the fin or uncorrelated ($\theta=0$) are also shown. For Q_f the 1st order estimate agrees very well with the exact solutions as shown by the dashed lines which are essentially independent of the value of $\sigma[\epsilon]$. For the tip temperature, there is a noticeable affect of $\sigma[\epsilon]$ and thus a difference between the 1st and 2nd order estimates.

Consider a fin with no radiation and a fin parameter m ($=\sqrt{h_f P_f/k_f A_f}$). Figure 7(*a*) shows the spatial distribution of $\sigma[T(x)]$. Both the spatial distribution and the accuracy of the perturbation solution are dependent upon the value of m. Figure 7(*b*) compares the 1st order estimate of $\sigma[T(x)]$ with the reference values for $\sigma[h]/\bar{h}=25$ percent. A comparison of Figs. 7(*a*) and 7(*b*) shows that the 1st order estimates are in good agreement with the reference values for both uncorrelated and completely correlated convective heat transfer coefficients for small values of m, but that the agreement deteriorates as m increases.

The results shown in Fig. 7(*a*) are similar to those of Madera [32]. His solution for a uniform distribution of h involved solving Ito's form of the stochastic differential equation by linearizing it with respect to m and assuming a product form for the solution. The resulting equation for the covariance, $cov[T(x_1),T(x_2)]$, was a Poisson equation in the two dimensions, x_1, x_2 and computationally intensive. If the method were to be extended to two dimensional problems it would lead to a biharmonic Poisson equation in x_1, x_2, x_3, x_4. It is not clear that the product form he employed is applicable to thermal problems in general.

Effect of Scale. For problems with N elements, each with its own random property, there are N 1st order derivatives needed for the 1st order estimate of the standard deviation and approximately N^3 triple derivatives needed for the 2nd order estimate. Clearly for large problems one will be restricted to 1st order estimates. However, if the random parameter has a uniform distribution, then Q_i will be identical for each element and there is only one random parameter to consider and only 3 derivatives needed for the 2nd order estimate, Eq. 5. When this condition exists can be determined from the eigenvalues of the covariance matrix and the determination can be made prior to solving the field equations, Eq. 7. Fortunately the covariance matrix is real and symmetric so its eigenvalues are relatively easy to determine without using sophisticated techniques. Figure 8 displays the ratio of the eigenvalues. When the 1st eigenvalue dominates, then only one random parameter need be considered. When the other eigenvalues are important relative to the largest eigenvalue, then all N sensitivities must be determined. Comparing Figs. 5 and 8 suggests that when the 2nd

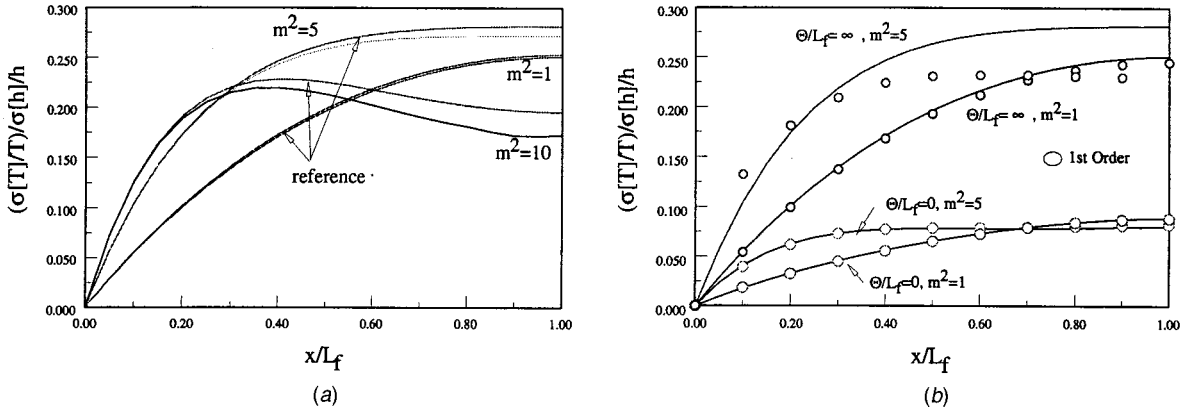

Fig. 7 $\sigma[(T(x)-T\infty)/(T_w-T_\infty)]$ for a fin with $\epsilon=0$ and $\sigma[h]/\bar{h}=25$ percent: (*a*) 2nd order and reference values of $\sigma[T]$ for a Uniformly Distributed h; (*b*) a comparison of the 1st order estimates and the reference values for independently and uniformly distributed h.

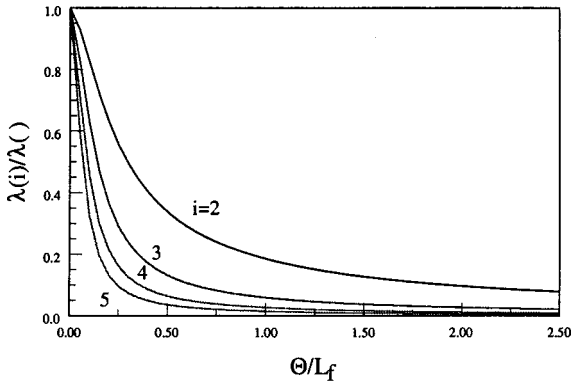

Fig. 8 Eigenvalues for the radiating fin problem

eigenvalue is less than 25 percent of the 1st that the problem can be considered as having a uniformly distributed emissivity.

Accuracy

It is almost axiomatic to assume that the increased accuracy of the higher order perturbation solutions is desirable. This is true only if (*a*) the 1st order perturbation results show trends which are qualitatively different than the exact results or (*b*) if high accuracy in the standard deviation is needed. Both of these reasons need to be examined.

(*a*) In none of the cases studied have we ever seen that the 1st order estimates of $E[T]$ or $\sigma[T]$ differ so much from the exact behavior that the basic behavior of the system is misinterpreted.

(*b*) The standard deviation is useful in determining the spread of the distribution in order to ascertain the probability that specific values of T occur; most importantly the probability that T falls outside of a specific range. Unfortunately this can only be done if $f(T)$ is known. Without $f(T)$, a knowledge of σ is of limited value.

When there is only one random parameter, Q, $f(T)$ is given by

$$f(T)=|J|f(Q),$$

where

$$J=dQ/dT. \tag{11}$$

Using Eq. 11 it is relatively easy to plot $f(T)$, requiring only the evaluation of dT/dQ; but for all values of Q. The exact values quoted in the examples were derived by using Eq. 1 with $f(T)$ obtained from Eq. 11. Figure 9(*a*) depicts $f(t_0)$ for Example 1 along with the equivalent normal distribution based upon $\bar{t}_0$ and $\sigma[t_0]$ and the two distribution differ significantly. The differences are most noticeable in the skewness, the long tail at high values of t_0 and the rapid drop for small values. Because of the skewed distribution, the improved accuracy in determining $\sigma[t_0]$ of the higher order approximations relative to the 1st order is of little value in defining the range of t_0 unless $f(t_0)$ is known. In contrast, Fig. 9(*b*) for the fin shows that the pdf of the tip temperature is very close to normal.

When there is more than one random parameter, e.g., 2, then $f(T)$ is more difficult to determine. One approach is to use

$$f(T)\,\delta T \approx \int\int_{\mathcal{D}_T} f(Q_1,Q_2)\,dQ_1\,dQ_2, \tag{12a}$$

where $\mathcal{D}_T$ is the domain defined by the region δT. The integration is to be taken over all values of Q_1 and Q_2 which lead to values of T that are in $\mathcal{D}_T$. These values can be in discrete but disjoint, ranges of the parameters [4,33]. While T is a single valued function of Q_1 and Q_2, the parameters need not be singled valued functions of T and determining all of the parameter values associated with $\mathcal{D}_T$ is an inverse problem that may be of considerable difficulty, even though the integration may be easy to accomplish.

One could also express Eq. 12(*a*) as

$$f(T)\,\delta T \approx f(Q_1,Q_2)\,\delta Q_1\,\delta Q_2 \tag{12b}$$

and interpret the right hand side of Eq. 12(*b*) as the number of occurrences of T in a bin of size δT. The difficulty with this approach is that δT generally changes size as Q_1 and Q_2 vary and the distribution of the occurrences among the bins is complicated.

If T or the variable of interest can be expressed simply in terms of Q_1 and Q_2 one can employ

$$f(T)=\int_{Q_1} f(T,Q_1)\,dQ_1$$

where

$$f(T,Q_1)=|J|f(T^{-1},Q_1) \tag{12c}$$

and

$$T^{-1}=Q_2(T,Q_1).$$

For example, the heat transfer from the fin is given by $Q_f=\sqrt{(h_f P_f k_f A_f)}(T_w-T_\infty)$ so that $k_f=(Q_f/(T_w-T_\infty))^2/h_f P_f A_f$ and the substitution for k_f in $f(k_f,h_f)$ can be accomplished, although the integration will probably have to be numerical rather than analytical. For more complicated problems, the substitution

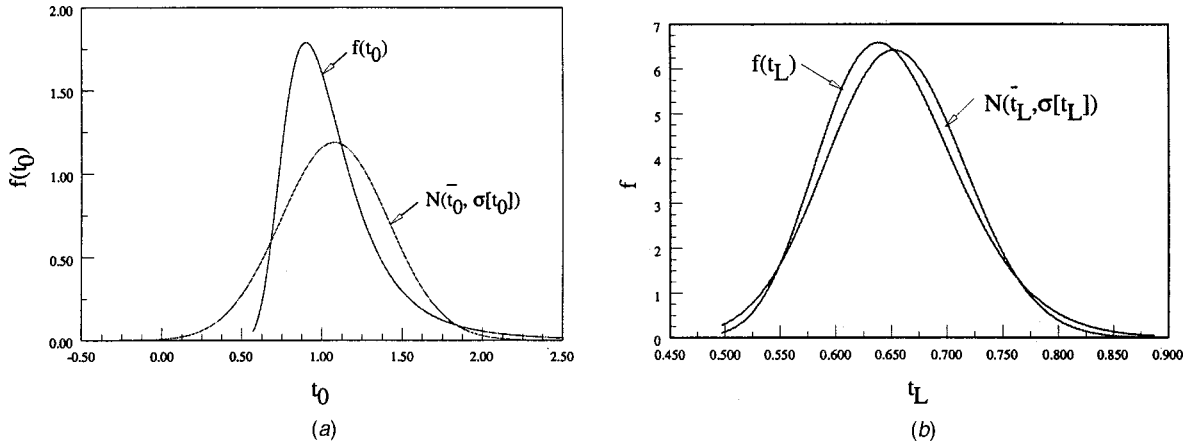

Fig. 9 Probability distributions of t and the Normal distribution based upon $\bar{t}$ and $\sigma[t]$: (*a*) Example 1; (*b*) fin

cannot be made and recourse must be had to Eq. 12(*a*) or (*b*). Methods such as stratified sampling are aimed at reducing the errors in estimating the statistics and will not help in determining $f(T)$, particularly near the tails of the distribution.

Computational Effort

While one can rarely justify using the 3rd order perturbation, it is often valuable to evaluate the 2nd order estimate of $E[\mathbf{\Phi}]$ because the mean value can differ significantly from the 0th order estimate. Haldar [23] recommends using the 2nd order estimate for reliability studies. In the examples presented here and in most of our studies we have found that the 2nd order estimate is generally about 10–15 percent different from the 0th order estimate and within 2–3 percent of the reference value.

The results displayed for the examples herein indicate that 1st order estimate of $\sigma[\mathbf{\Phi}]$ and 2nd order estimate of $E[\mathbf{\Phi}]$ are sufficient for most purposes. Since the 2nd order estimate of $E[\mathbf{\Phi}]$ already requires evaluating $\partial^2 T/\partial Q^2$, it may not be a much greater expense to determine $\partial^3 T/\partial Q^3$ and to evaluate the 2nd order estimate of $\sigma[\mathbf{\Phi}]$. These derivatives can be evaluated either by finite differences or solving the field equations. Figure 1 indicates that using the field equation gives a smooth result while finite differences often produces an erratic curve.

We have found that the derivatives obtained from the field equations are smooth even when an explicit time integration was used. The primary advantage of this approach is that the equations for the derivatives are linear, even for nonlinear problems. The drawback is the need to modify the simulation code with some relatively complex right hand sides, particularly when the random variable is a function of temperature, in which case the matrix on the left side of Eq. 7(*b*) will be non-symmetric [21].

In contrast, the finite difference approach is simpler, requiring only that enough solutions (which may be expensive because they are nonlinear) be obtained to fit the temperature response by a polynomial of the desired order. However, the response curve usually needs to be smoothed by least squares fitting to extract reasonably accurate estimates of the 2nd derivative and particularly so for the 3rd. Figure 10 shows how the derivatives of the smoothed curve vary with the number of points during the transient phase and at steady state for Example 1.

The errors in calculating the derivatives are a combination of the errors in the finite difference approximation and the error in the solution for T. The former can be mollified by reducing δQ, but as the increment gets small, the effect of small errors in calculating T begins to dominate and higher precision simulations must be used. It is clear for this example that 3 points are sufficient to obtain reasonably accurate values of the 1st two derivatives. We have found this to be the case in almost all examples. It is also clear that it may be too expensive to evaluate the 3rd derivative accurately.

Conclusions

For large or complicated problems, calculating the response will require a large number of elements, N. For uniform parameters, these will number q, but for correlated parameters, they will number Nq. With the 2nd order perturbation analysis requiring the evaluation of approximately $q(q+1)/2$ second order derivatives, this means that the 1st order method, which requires computing only the q first order derivatives, is the only practical way to estimate the standard deviation. One can either solve for the sensitivities directly from the field equations, Eq. 7(*b*), or by finite differencing the response. The 1st order estimate suffices for both correlated and uncorrelated random parameters. When the parameter is uniformly distributed, then it is possible to consider higher order estimates. But these higher order estimates are based upon the higher order correlations, whose accuracy is frequently questionable.

The 2nd order estimate of $E[\mathbf{\Phi}]$ can be obtained by using the compact form [20] which sums the effect of all second derivatives (i.e., the 2nd term of Eq. 4(*a*)) and requires only one additional equation to the q equations for the first derivatives. For this reason, we recommend using the 1st order estimate of σ and the 2nd order estimate of the mean. If the higher order correlations are known, one should still compute the 1st order estimate and examine its behavior with respect to Q to see if its behavior justifies computing the higher order derivatives.

The perturbation approach has two fundamental characteristics. First, it is independent of the precise form of the probability density distribution and thus cannot account for parameters which have limited ranges. In this case one must either restrict the range of the parameters or use one of the sampling techniques. We have had most success using the stratified sampling method. Its only drawback is the large number (20–40) of samples necessary to ensure convergence. Second, it is a point estimate (i.e., the derivatives are evaluated at a specific point) of the behavior of the system as compared to the smoothing effect of the integrals of Eq. 1. This effect is most noticeable when discontinuities are present as in the piecewise conductivity-temperature relationship of Example 2. There is little advantage in attempting to obtain a higher accuracy than that of the 1st order estimate, either using the higher order perturbation approach or variance reduction methods, unless the probability density distribution is also determined.

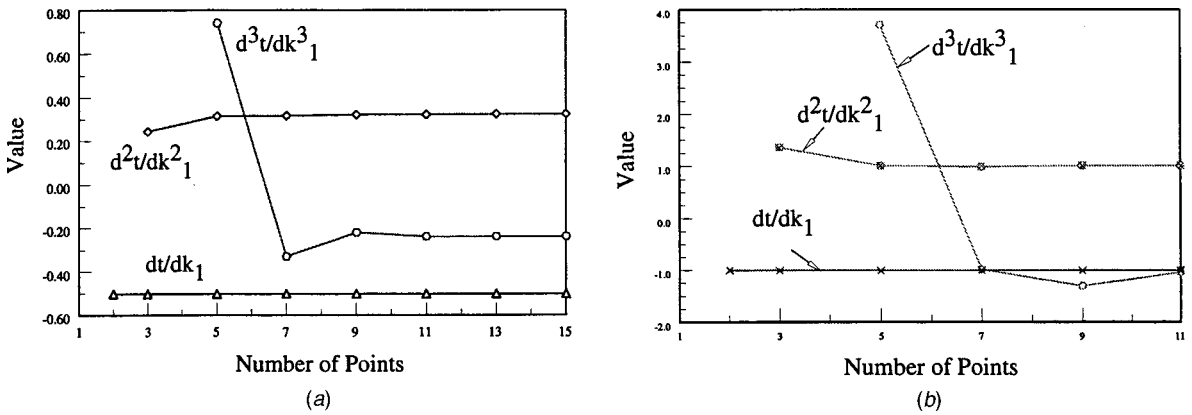

Fig. 10 Finite difference estimates of the derivatives for Example 1 for $\sigma[k_1]/\bar{k}_1 = 25$ percent: (*a*) Fo=0.5; (*b*) steady state

Acknowledgments

I would like to acknowledge the fruitful comments of Drs. J. L. Garbini and T. Fadale and the suggestions of the referees.

Nomenclature

$\mathbf{C}$ = capacitance matrix
D_i = i^{th} elemental domain
$\mathcal{D}$ = domain of stochastic variables
$E[X]$, $\overline{X}$, = expected value operator, mean value of X
$f(Q_1,..,Q_n)$ = joint probability density function of $Q_1,..,Q_n$
$f(\mathbf{\Phi}|\mathcal{D}_Q)$ = probability density function of $\mathbf{\Phi}$ conditional on Q
F = applied heat flux
Fo = Fourier number
h = heat transfer coefficient
h.o.t. = higher order terms
k = thermal conductivity
$\mathbf{K}$ = conductance matrix
L = length
$N[\overline{X},\sigma[X]]$ = normal distribution of X
q = number of random variables
$\mathbf{q}$ = source vector
Q_i = specific outcome of Q
$Q(\vec{x})$ = continuous random field
$\mathbf{Q}$ = random variable vector
t = non-dimensional temperature, time
T = temperature
$\vec{x}$ = position vector
ϵ = emissivity
β = coefficient of conductivity
ρ = correlation coefficient
$\sigma[X]$ = standard deviation of X
θ = scale of correlation
$\mathbf{\Phi}$ = temperature vector
$\mathbf{\Phi}_{Q_i}$ = derivative of $\mathbf{\Phi}$ w.r.t. Q_i
$\mathbf{\Phi}_{Q_iQ_j}$ = derivative of $\mathbf{\Phi}$ w.r.t. Q_i and Q_j *super and subscripts*
T = transpose
w = wall
f = fin
∞ = Ambient temperature

References

[1] Abernethy, R. B., Benedict, R. P., and Dowell, R. B., 1985, ''ASME Measurement Uncertainty,'' ASME J. Fluids Eng., **107**, pp. 161–164.
[2] Moffat, R. J., 1988, ''Describing the Uncertainties in Experimental Results,'' Exp. Therm. Fluid Sci., **1**, pp. 3–17.
[3] Lin, Y. K., 1995, *Probabilistic Structure Dynamics: Advanced Theory and Applications*, McGraw-Hill, New York.
[4] Papoulis, A., 1991, *Probability, Random Variables, and Stochastic Processes*, McGraw-Hill, New York.
[5] Ljung, L., 1999, *System Identification*, Prentice-Hall, New York.
[6] Inan, E., and Markov, K. Z., 1998, *Continuum Models and Discrete Systems*, World Scientific, Singapore.
[7] Rohsenow, W. M., and Hartnett, J. P., 1973, *Handbook of Heat Transfer*, McGraw-Hill, New York.
[8] Kakaç, S., Shah, R. K., and Aung, W., 1987, *Handbook of Single-Phase Convective Heat Transfer*, Wiley, New York.
[9] Andersen, K., Madsen, H., and Hansen, L., 2000, ''Modelling the Heat Dynamics of a Building using Stochastic Differential Equations,'' Energy Build., **31**, pp. 13–24.
[10] Loveday, D., and Craggs, C., 1992, ''Stochastic Modelling of Temperatures Affecting the in situ Performance of a Solar Assisted Heat Pump: The Multivariate Approach and Physical Interpretation,'' Sol. Energy, **49**, pp. 289–298.
[11] Ryniecki, A., and Jayas, D. S., 1992, ''Stochastic Modeling of Grain Temperature in Near-Ambient Drying,'' Drying Technol., **10**, pp. 123–137.
[12] Nicolai, B. M., and De Baerdemaeker, J., 1992, ''Simulation of Heat Transfer in Foods with Stochastic Initial and Boundary Conditions,'' *Inst. Chemical Engineers Symposium Series Food Engineering in a Computer Climate*, pp. 247–252.
[13] Pomraning, G. C., 1998, ''Radiative Transfer and Transport Phenomena in Stochastic Media,'' Int. J. Eng. Sci., **36**, pp. 1595–1621.
[14] Kolditz, O., and Clauser, C., 1998, ''Numerical Simulation of Flow and Heat Transfer in Fractured Crystalline Rocks: Application to the Hot Dry Rock Site in Rosemanowes (U.K.),'' Geothermics, **27**, pp. 1–23.
[15] Hien, T. D., and Kleiber, M., 1997, ''Stochastic Finite Element Modelling in Linear Transient Heat Transfer,'' Comput. Methods Appl. Mech. Eng., **144**, pp. 111–124.
[16] Kieda, S., et al., 1993, ''Application of Stochastic Finite Element Method to Thermal Analysis for Computer Cooling,'' ASME J. Electron. Packag., **115**, pp. 270–275.
[17] Madera, A. G., 1993, ''Modelling of Stochastic Heat Transfer in a Solid,'' Appl. Math. Model., **17**, pp. 664–668.
[18] Emery, A. F., 1999, ''Computing Temperature Variabilities due to Stochastic and Fuzzy Thermal Properties,'' *Proc. 1999 ASME/AIChE National Heat Transfer Conference*, Albuquerque, NM.
[19] Haldar, A., and Mahadevan, S., 2000, *Probability, Reliability, and Statistical Methods in Engineering Design*, Wiley, New York.
[20] Fadale, T. D., and Emery, A. F., 1994, ''Transient Effects of Uncertainties on the Sensitivities of Temperatures and Heat Fluxes using Stochastic Finite Elements,'' ASME J. Heat Transfer, **116**, pp. 808–814.
[21] Emery, A. F., and Fadale, T. D., 1997, ''Handling Temperature Dependent Properties and Boundary Conditions in Stochastic Finite Element Analysis,'' Numer. Heat Transfer, Part B, **31**, pp. 37–51.
[22] Smith, D. L., 1991, *Probability, Statistics, and Data Uncertainties in Nuclear Science and Technology*, American Nuclear Society, LaGrange Part, IL.
[23] Haldar, A., and Mahadevan, S., 2000, *Reliability Assessment Using Stochastic Finite Element Analysis*, J. Wiley & Sons, New York, NY.
[24] Breitung, K., 1984, ''Asymptotic Approximations for Multinormal Integrals,'' J. Eng. Mech., **110**, pp. 357–366.
[25] Anderson, T. W., 1958, *An Introduction to Multivariate Statistical Analysis*, Wiley, New York.
[26] Rosenblatt, M., 1952, ''Remarks on a Multivariate Transformation,'' Ann. Math. Stat., **23**, pp. 470–472.
[27] Bickel, P. J., and Doksum, K. A., 1978, *Mathematical Statistics: Basic Ideas and Selected Topics*, Holden-Day, San Francisco, CA.
[28] Emery, A. F., and Fadale, T. D., 1999, ''Calculating Sensitivities of Thermal Systems with Uncertain Properties using the Stochastic Finite Element Method and Finite Differencing,'' Inverse Problems Eng., **7**, pp. 291–307.
[29] Cook, R. D., Malkus, D. S., and Plesha, M. E., 1989, *Concepts and Applications of Finite Element Analysis*, Wiley, New York.
[30] Incropera, F., and DeWitt, D. P., 1996, *Introduction to Heat Transfer*, Wiley, New York.
[31] Vanmarcke, E., 1984, *Random Fields, Analysis and Synthesis*, The MIT Press, Cambridge, MA.
[32] Madera, A. G., 1996, ''Heat Transfer from an Extended Surface at a Stochastic Heat Transfer Coefficient and Stochastic Environmental Temperatures,'' Int. J. Eng. Sci., **34**, pp. 1093–1099.
[33] Guttman, I., Wilks, S. S., and Hunter, J. S., 1971, *Introductory Engineering Statistics*, Wiley, New York.

Journal of Heat Transfer

Technical Notes

This section contains shorter technical papers. These shorter papers will be subjected to the same review process as that for full papers.

Pool Boiling of FC-72 and HFE-7100

Z. W. Liu

W. W. Lin

D. J. Lee[1]
e-mail: djlee@ccms.ntu.edu.tw

Department of Chemical Engineering, National Taiwan University, Taipei, Taiwan 106, R.O. China

X. F. Peng
Thermal Engineering Department, Tsinghua University, Beijing 100084, P.R. China

This work reported the boiling characteristics of FC-72 and HFE-7100 at atmospheric pressure and at a liquid subcooling of 0–20 K. The FC-72 exhibits a more efficient nucleate boiling mode and a higher critical heat flux (CHF) than the HFE-7100. For film boiling mode, HFE-7100 becomes more efficient.
[DOI: 10.1115/1.1285892]

Keywords: Boiling, Heat Transfer, Instability, Phase Change, Stability, Two-Phase

Introduction

Chlorofluorocarbon (CFC) substitutes are highly promising for electronic cooling applications ([1,2]). This work experimentally elucidates the boiling characteristics of two new CFC-substitutes, FC-72 and HFE-7100, both with zero ozone-depletion potential (ODP) and the potential for electronic cooling applications with phase change.

Experimental

The experimental setup was the same as that employed in Lin et al. [3] and for brevity's sake is not shown here. The upper surface to boiling was a smooth surface with the dimension 80 mm×15 mm. A total of 24 thermocouples were imbedded in the two heating blocks. Heat flux and the wall superheat at the six axial positions on the heating surface were estimated accordingly. The experiment was performed at atmospheric pressure and the liquids used were FC-72 and HFE-7100 (3M Co., USA), both of a purity exceeding 99 percent. Steady-state boiling curves could be constructed based on the extrapolated heater surface temperature and the associated heat flux. There exists no conduction heat transfer between the two heater blocks during the steady-state boiling curve construction.

This work employed Kline and McClintocks' [4] method to estimate the uncertainties of the heat flux and temperature measurements. The bias error of data acquisition system is 0.1 percent. At least this was the data provided by the manufacturer. Any uncertainties are attributed primarily to the thermocouple calibration, which in this study does not exceed 1 K, as well as the employment of thermal conductivity data, which is estimated not to exceed two percent. Thus, the uncertainties existing in the extrapolated heater surface temperature and the associated heat flux when constructing boiling curves are estimated as ±7 percent and ±11 percent, respectively.

Results

Figures 1 and 2 depict the steady-state nucleate boiling and film boiling curves for FC-72 and HFE-7100, respectively, with ΔT_{sub} as a parameter. (Note: the transition boiling curves are omitted here for clarity's sake. A detailed discussion on the difference between ''true'' and ''average'' transition boiling curves is available in Lee and Lu [5].) At fixed heat flux, the nucleate boiling curve slightly shifts to the right with an increasing ΔT_{sub}, while the film boiling curve shifts to the left. Furthermore, at a higher liquid subcooling, both the critical heat flux (CHF) and minimum heat flux (MHF) increased markedly (as indicated by arrows in Figs. 1–2). These observations are consistent with the available literature ([6]).

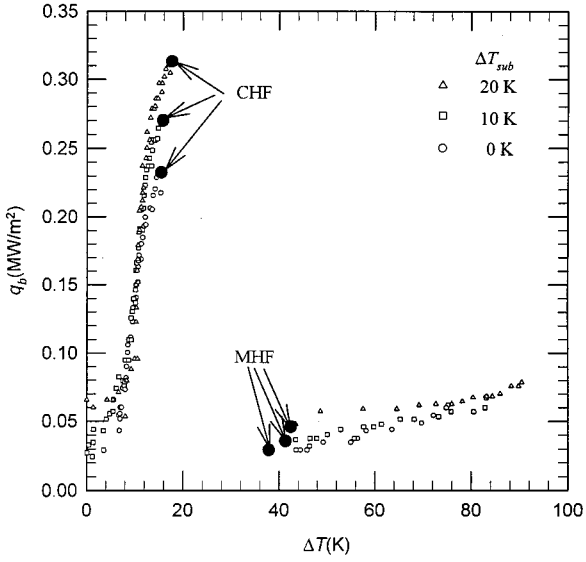

Fig. 1 Nucleate and film boiling curves. Arrows denote the CHF and MHF points. FC-72.

[1]To whom correspondence should be addressed.

Contributed by the Heat Transfer Division for publication in the JOURNAL OF HEAT TRANSFER. Manuscript received by the Heat Transfer Division, Aug. 27, 1999; revision received, Dec. 7, 1999. Associate Editor: D. Poulikakos.

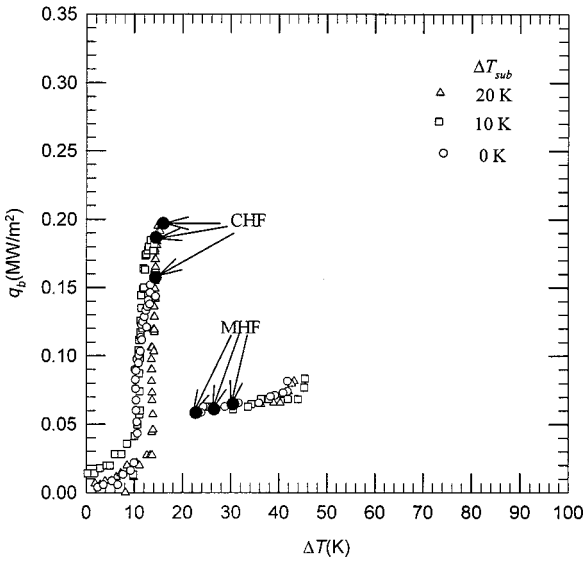

Fig. 2 Nucleate and film boiling curves. Arrows denote the CHF and MHF points. HFE-7100.

Table 1 CHF and MHF data. All values are in MW/m^2. Top to down: ΔT_{sub}=0, 10, and 20 K.

FC-72		HFE-7100	
CHF	MHF	CHF	MHF
0.232	0.030	0.158	0.059
0.270	0.035	0.185	0.061
0.314	0.046	0.196	0.065

Comparing Figs. 1 and 2 clearly reveals two things. First, the nucleate boiling heat transfer coefficients of FC-72 are 10–20 percent higher than those of HFE-7100. Second, the CHF's of FC-72 are at least 50 percent higher than those of the HFE-7100. Table 1 lists the CHF data for reference purposes. (Note: some essential thermophysical properties of FC-72 and HFE-7100 are lacking, thereby preventing comparisons with the classical hydrodynamic theories.) FC-72 is thus superior to HFE-7100 in nucleate boiling mode since it exhibits a more efficient nucleate boiling and can be used at higher heat flux without burnout. Notably, this conclusion is true when the system is subject only to infinitesimal disturbances. However, as Lin and Lee [7] stated, the capability of the system to tolerate a finite-magnitude disturbance relies on relative stability between nucleate and film boiling modes. This work does not discuss this issue.

In addition, Figs. 1 and 2 also suggest that the film boiling heat transfer coefficients of HFE-7100 are approximately 100 percent higher than those of FC-72. Finally, Figs. 1 and 2 show that the HFE-7100 exhibits a greater MHF than the FC-72 does (Table 1 also lists the MHF data). In other words, the heat transfer efficiencies in the film boiling mode follow a trend opposite to that followed in the nucleate boiling mode. Consider a cooled electronic modulus with its outside surface boiled with nucleate boiling at a prescribed heat flux level of 8×10^4 W/m^2. If for some reason local dryout of the heating surface occurred (the nonhydrodynamic burnout), the local surface superheat would shift from 10 K to 40 K for HFE-7100. However, for FC-72 the superheat would reach a markedly higher level, approximately 90 K. Restated, the more efficient the film boiling of HFE-7100 implies a safer thermal environment for electronic cooling applications than does the FC-72 if burnout incidentally occurred.

Conclusions

This work elucidated the boiling characteristics of two CFC substitutes from 3M Co., namely FC-72 and HFE-7100, at atmospheric pressure and at a liquid subcooling of 0–20 K. FC-72 exhibited a more efficient nucleate boiling mode and a higher critical heat flux (CHF) than the HFE-7100 did. However, for the film boiling mode, this trend reverses.

References

[1] You, S. M., Simon, T. W., and Bar-Cohen, A., 1992, ''A Technique for Enhancing Boiling Heat Transfer with Application to Cooling of Electronic Equipment,'' IEEE Trans. CHMT, **15**, pp. 823–831.

[2] Chang, J. Y., and You, S. M., 1996, ''Heater Orientation Effects on Pool Boiling of Micro-Porous-Enhanced Surfaces in Saturated FC-72,'' ASME J. Heat Transfer, **118**, pp. 937–943.

[3] Lin, W. W., Yang, J. C., and Lee, D. J., 1998, ''Boiling Stability Characteristics of Methanol Flowing over a Non-Uniformly Heated Surface,'' Int. J. Heat Mass Transf., **41**, pp. 4009–4023.

[4] Kline, S. J., and McClintock, F. A., 1953, ''Description of Uncertainties in Single Sample Experiments,'' Mech. Eng., **75**, Jan., pp. 3–8.

[5] Lee, D. J., and Lu, S. M., 1992, ''Two-Mode Boiling on a Horizontal Heating Wire,'' AIChE J., **38**, pp. 1115–1128.

[6] Lienhard, J. H., 1987, *A Heat Transfer Textbook*, 2nd Ed. Prentice-Hall, Englewood Cliffs, NJ.

[7] Lin, W. W., and Lee, D. J., 1997, ''Relative Stability Between Nucleate and Film Boiling on a Nonuniformly Heated Flat Surface,'' ASME J. Heat Transfer, **119**, pp. 326–331.

Diameter Effects on Nucleate Pool Boiling for a Vertical Tube

Myeong-Gie Kang

Department of Mechanical Engineering Education, Andong National University, 388 Songchun-dong, Andong-city, Kyungbuk 760-749, Korea

Diameter effects on nucleate pool boiling heat transfer for a tube with vertical orientation have been obtained experimentally. According to the results (1) the heat transfer coefficient decreases as the tube diameter increases and the trend is more notable with a rougher surface, and (2) the experimental data is in good agreement with the Cornwell and Houston's correlation within a ±20 percent scatter range. [DOI: 10.1115/1.1351163]

Keywords: Boiling, Experimental, Heat Transfer, Nuclear, Tubes

Introduction

Throughout the last several decades, pool boiling heat transfer has been studied by many researchers worldwide. Nowadays, it has been investigated widely in nuclear power industry since advanced light water reactors have several passive heat exchanges [1,2]. As already mentioned by Cornwell et al. [3] and Cornwell and Houston [4], one of the most important parameters in pool boiling heat transfer is the tube diameter (D). A detailed analysis of the effects of tube diameter on pool boiling heat transfer is useful for the design of very efficient heat exchangers.

Although some authors have reported results for other cases, to the author's knowledge, Cornwell et al. [3] is the first to specifically establish the relation between nucleate pool boiling heat transfer coefficient (h_b) and tube diameter. Cornwell et al. suggested a very simple and convenient empirical correlation for

Contributed by the Heat Transfer Division for publication in the JOURNAL OF HEAT TRANSFER. Manuscript received by the Heat Transfer Division December 5, 1999; revision received July 20, 2000. Associate Editor: P. Ayyaswamy.

Table 1 Previous works about tube diameter effects on pool boiling heat transfer

Author	Results
Cornwell et al. (1982)	- tubes (D=6~32mm) of several materials - liquid: water, refrigerants, and organics - orientation: horizontal - correlation: $\mathrm{Nu}=C_{tb}Re_b^{2/3}$, $Re_b=\frac{q''D}{\mu_f h_{fg}}$ - h_b decreases with increasing diameter ($6<D\leq 30$mm) - h_b increases slightly with diameter ($30\text{mm}<D$)
Cornwell and Houston (1994)	- tubes (D=8~50mm) of several materials - liquid: water, refrigerants, and organics - orientation: horizontal - correlation: $\mathrm{Nu}=AF(p)Re_b^{0.67}\mathrm{Pr}^{0.4}$ $A=9.7p_c^{0.5}$, $F(p)=1.8p_r^{0.17}+4p_r^{1.2}+10p_r^{10}$, $p_r=p/p_c$ - improved Cornwell et al.'s correlation
Chun and Kang (1998)	- stainless steel tubes (D=9.7~25.4mm) - liquid: water - orientation: horizontal and vertical - correlation: $h_b=0.015\varepsilon^{0.084}\Delta T^{4.508}/D^{1.318}$ (horizontal) $h_b=0.024\varepsilon^{0.672}\Delta T^{3.862}/D^{1.656}$ (vertical) - h_b decreases with increasing diameter

horizontal tubes as shown in Table 1. Cornwell and Houston [4] improved upon Cornwell et al.'s result by introducing a pressure ratio ($p_r=p/p_c$) and Prandtl number (Pr) into the correlation. However, Cornwell et al. [3] and Cornwell and Houston [4] did not quantitatively identify the effect of surface roughness (ε) on pool boiling heat transfer. Chun and Kang [5] empirically investigated the effect of surface roughness on pool boiling outside tubes. They also suggested two empirical correlations (one for horizontal tubes and the other for vertical tubes) which contain the effect of surface roughness as a parameter. Some experimental studies for the diameter effects of horizontal wires on pool boiling heat transfer have been reported by Stralen and Sluyter [6] and Hahne and Feurstein [7].

Through a review of the published results, it can be concluded that in this context a study of tubes with a vertical orientation is rarely found. Although Chun and Kang [5] offered some results for vertical tubes, a more detailed analysis is warranted. The present study is aimed at the determination of diameter effects on nucleate pool boiling heat transfer for a tube with a vertical orientation. The experimental results are compared with the well-known Cornwell and Houston's correlation to verify its applicability to vertical tubes.

Experiments

A schematic view of the present experimental apparatus is shown in Fig. 1. The water storage tank is made of stainless steel and has a rectangular cross section (790×860 mm) and a height of 1000 mm. This tank has a glass view port (595×790 mm) which permits viewing of the tubes and photographing. The heat exchanger tubes are simulated by resistance heaters made of stainless steel tubes. The outer surface of the tube (for the case, D = 19.05 mm) was instrumented with five thermocouples. The thermocouple tip (about 10 mm) is bent at a 90 deg angle, and the bent tip is brazed onto the tube wall. The first and the fifth thermocouples are placed at 115.25 mm from the ends of the heating element and the spacing between the other thermocouples is 75 mm. The temperature of the water is measured with five thermocouples that are located 20, 30, 160, 460, and 760 mm from the tank bottom.

The water storage tank is filled with water until the initial water level reaches 730 mm. The water is then heated using pre-heaters (for this case, three 3.5 kW electric heaters). When the water temperature reaches the saturation value (i.e., 100°C since all the tests are run at atmospheric pressure condition), it is boiled for 30 minutes at this saturation temperature (T_{sat}) to remove the dissolved air. The power supply to the pre-heaters are shut off and the temperatures of test tube surface are measured when they

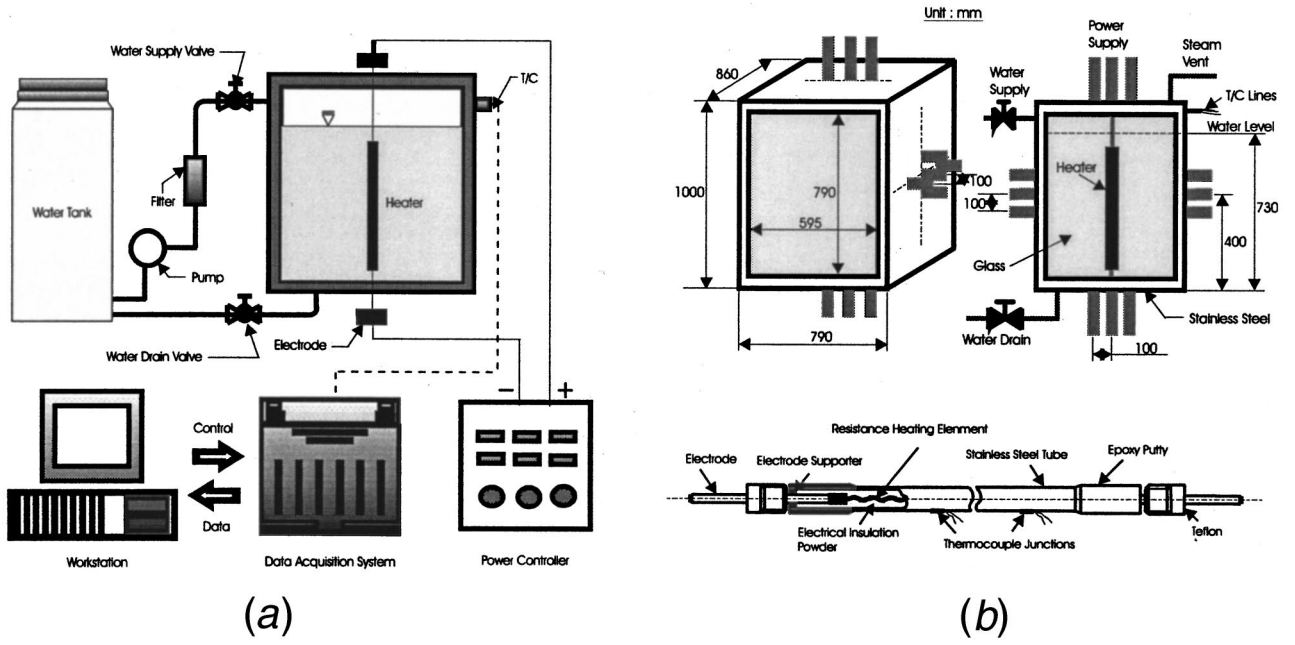

Fig. 1 Schematic Diagram of the experimental apparatus (*a*) overall arrangement; (*b*) water storage tank and heated tube

reach steady state. Measurements are repeated while controlling the heat flux (q'') on the tube surface with input power (q). In this manner a series of experiments has been performed for various combinations of tube diameters (D = 9.7~25.4 mm), surface roughness (ε=15.1~60.9 nm), and dimensionless lengths (H = 11.81~30.93). The uncertainties (errors in measurement, instruments, and in the specification of environmental conditions) of the heat flux and surface roughness are estimated to be ±1.0 percent and ±5.0 nm, respectively. The uncertainty in the measured temperature is estimated to be ±0.7°C including errors from thermocouple compensation (±0.1°C), multiplexer reading (±0.1°C), and thermocouple sensing (±0.5°C).

The heat flux from the electrically heated tube surface is calculated from the measured values of the power input as follows:

$$q'' = \frac{q}{A} = \frac{VI}{\pi DL} = h_b(T_w - T_{sat}) = h_b \Delta T, \quad (1)$$

where V and I are the supplied voltage (in volt) and current (in ampere), and D and L are the outside diameter and the length of the heated tube, respectively. The tube surface temperature T_w used in Eq. (1), on the other hand, is the arithmetic average value of the temperatures measured by thermocouples brazed onto the tube surface.

Experimental data was obtained as the heat flux changed (i.e., increase or decrease). After sufficient (more than six times) series of experiments were carried out for a given condition, data sets for heat flux changes were depicted as h_b versus ΔT curves. From the graphs, it was concluded that there was no visible hysteresis due to heat flux increase and decrease, and sets of data for increasing and decreasing heat flux are combined together in the present study.

Results and Discussion

With a vertical tube, the boiling mechanism on the tube surface is different from that for a horizontal tube. The effect of tube orientation on boiling heat transfer must be considered before analyzing tube diameter effects. One of the most important parameters to be considered for vertical tubes is the tube length [2]. In Chun and Kang's analysis [5], the focus was on the development of empirical correlations; the relation between tube length and heat transfer coefficients was not analyzed in detail. The effect of vertical tube length on pool boiling heat transfer was first investigated by Kang [2]. According to the results, there exists a relation between the boiling heat transfer coefficient and the dimensionless tube length of the form $h_b \propto 1/H^{0.072}$. The experimental data for the heat flux versus tube wall superheat ($\Delta T = T_w - T_{sat}$) have been corrected in advance to remove length effects. Boiling heat transfer coefficients (h_{bc}) have been evaluated for the tubes using the correlation suggested by Kang [2]. For the case, the standard value used for correction is H = 27.85. Figure 2 shows the ratio between the calculated and the corrected heat transfer coefficients versus the dimensionless tube length. In the figure, specific values for heat transfer coefficients are suggested according to the tube diameters used in the experiments.

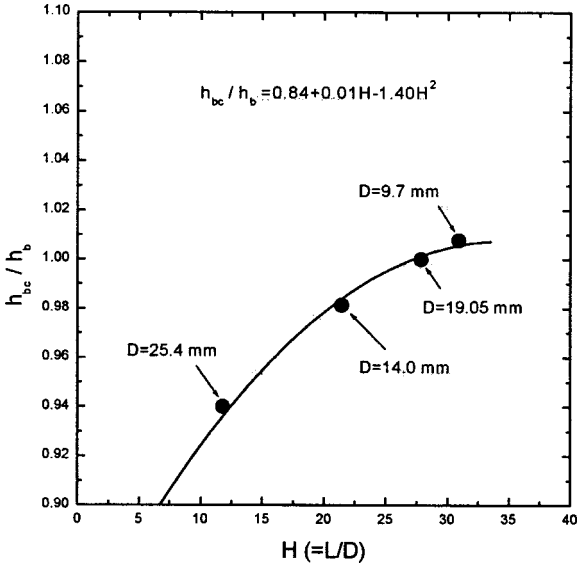

Fig. 2 h_{bc}/h_b versus H to include tube length effect

Figure 3 shows the corrected nucleate pool boiling heat transfer coefficient versus wall superheat for various vertical tubes with different surface roughness. Figures 3(*a*) and 3(*b*) show the results

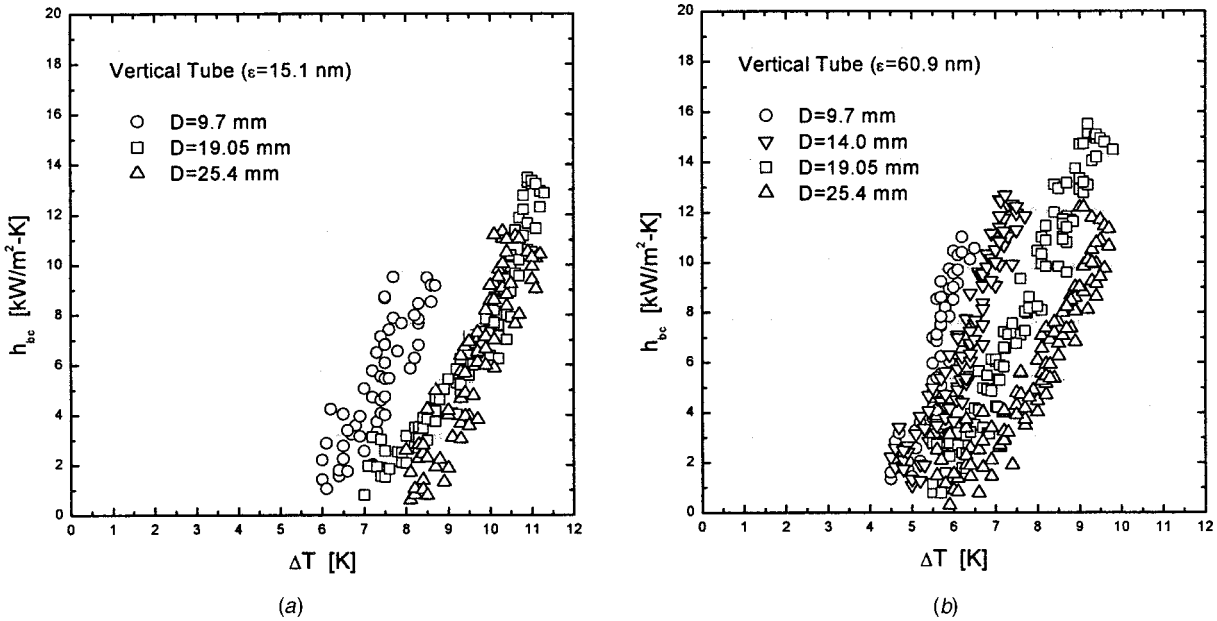

(*a*) (*b*)

Fig. 3 The corrected heat transfer coefficient versus wall superheat for various vertical tubes with different surface roughness: (*a*) smooth surface (ε = 15.1 nm); (*b*) rough surface (ε = 60.9 nm)

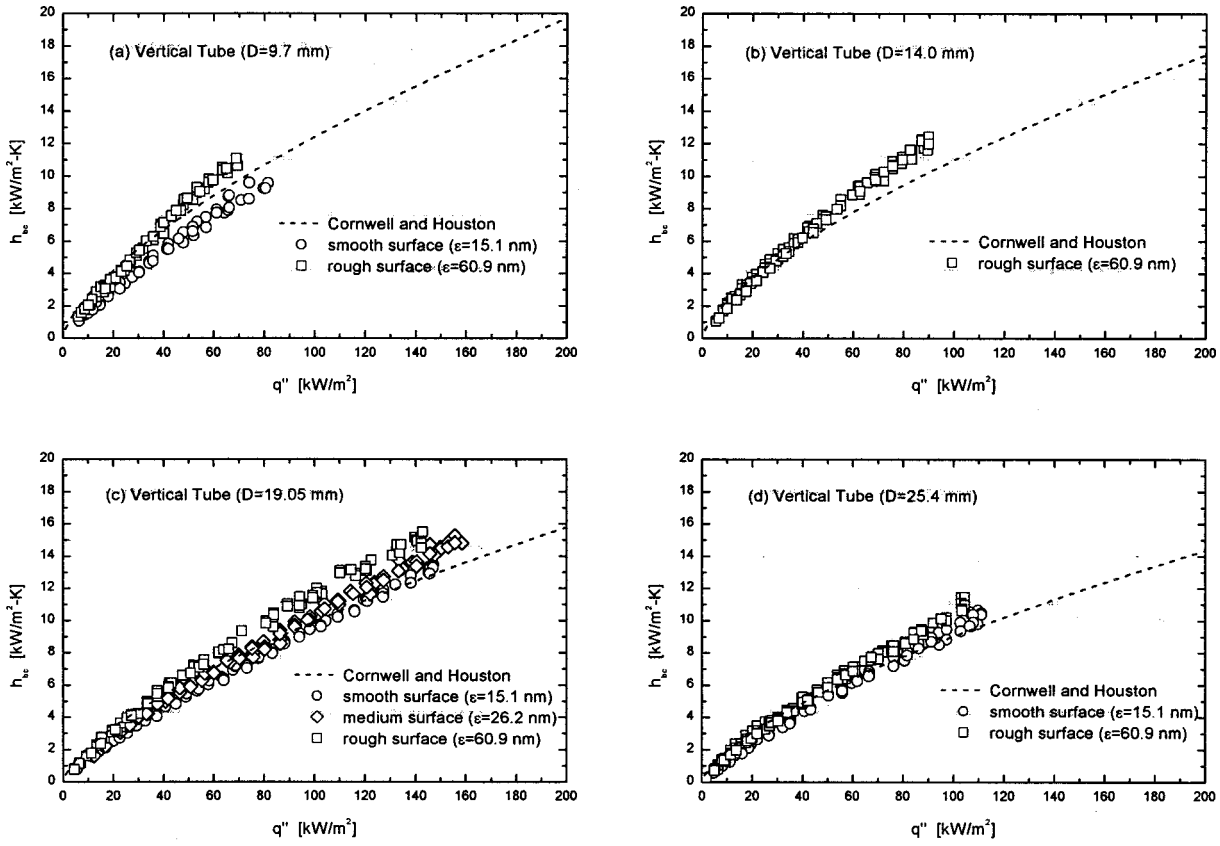

Fig. 4 Comparison of the present experimental data for vertical tubes with Cornwell and Houston's empirical correlation

for the smooth tube (i.e., $\varepsilon = 15.1$ nm) and the rough tube (i.e., $\varepsilon = 60.9$ nm), respectively. The general trend is similar to those of horizontal tubes. The heat transfer coefficient decreases as the tube diameter increases. For the rough surface case, as shown in Fig. 3(*b*), 162 percent increase in tube diameter (i.e., from 9.7 to 25.4 mm) results in 59 percent increase in tube superheat (i.e., from 5.8 K to 9.2 K) for an heat transfer coefficient of 10 kW/m^2-K. Although the effect of tube diameter on pool boiling heat transfer shows similar trend, the magnitude of ΔT to achieve the same h_{bc} is different. In other words, the difference between tube superheats for the different diameters (i.e., 9.7 and 25.4 mm) depends on the tube surface condition. If $h_{bc} = 8$ kW/m^2-K, the difference between tube superheats for $D = 9.7$ and 25.4 mm is about 2.5 K for smooth conditions. This difference increases to 3.4 K for the same tube diameters if rougher tubes were selected. Once a tube diameter has been increased from 9.7 mm to 25.4 mm (i.e., 162 percent), the corrected boiling heat transfer coefficient for rough surface decreases from 10 kW/m^2-K to 1.5 kW/m^2-K (i.e., 85 percent) with $\Delta T = 6.0$ K. The main causes for the decrease in the heat transfer coefficient with the increase in the tube diameter are due to the formation of bubble slugs and rapid convective flow in the vicinity of top regions of the tube. If the tube diameter is increased, more bubbles are generated, and these bubbles form bubble slugs which prevent sufficient liquid access to the heating surface. The bubble slugs also generate a very rapid convective flow on the tube surface due to buoyancy and prevent the generation of fully developed bubbles on the surface. Although the slugs agitate the liquid to increase heat transfer, the effect is relatively small in comparison to the effects of two-heat transfer, the effect is relatively small in comparison to the effects of two-heat transfer decreasing mechanisms. The net effect of an increase in tube diameter is to decrease heat transfer coefficients. Since more bubble generation is expected for a rougher surface, greater decrease in the heat transfer coefficient is to be expected.

The experimental data for vertical tubes are compared with values calculated using Cornwell and Houston's correlation as shown in Fig. 4. As shown in the figure, several data points for the smooth, medium, and rough surface conditions show good agreement with the correlation. For a statistical analysis, the calculated

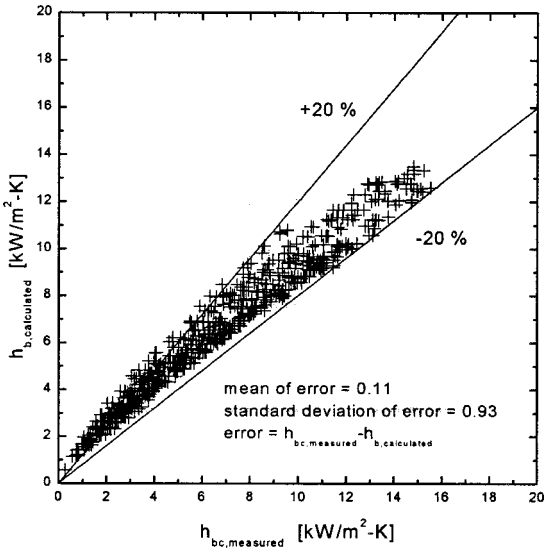

Fig. 5 Calculated heat transfer coefficient versus measured heat transfer coefficient for vertical tubes

heat transfer coefficients were compared with the measured heat transfer coefficients and the results are shown in Fig. 5. This figure indicates that the standard deviation of the error (i.e., $h_{bc,\text{measured}} - h_{b,\text{calculated}}$) is 0.93. The scatter of the present experimental data is between +20 percent and −20 percent, with some exceptions, from a curve fit of Cornwell and Houston's correlation. The scatter in the present data is of similar magnitude to those found in other existing pool boiling data. Although Cornwell and Houston's correlation has been developed for horizontal tubes, its application to vertical tubes (based on the present experimental data) can be said to be reasonable.

Conclusions

An experimental parametric study with vertical tubes has been carried out for saturated water at atmospheric pressure to determine the effects of tube diameter on nucleate pool boiling heat transfer. Based on this study of various tube diameters ($D = 9.7 \sim 25.5$ mm), surface roughness ($\varepsilon = 15.1 \sim 60.9$ nm), and dimensionless lengths ($H = 11.81 \sim 30.93$), following conclusions can be drawn:

1 The heat transfer coefficient decreases as the tube diameter increases and the trend is more notable with a rougher surface.
2 The experimental data is in good agreement with the Cornwell and Houston's correlation within a ±20 percent scatter range.

Nomenclature

A = heat transfer area
D = tube outer diameter
H = dimensionless tube length (L/D)
h_b = boiling heat transfer coefficient
h_{bc} = modified boiling heat transfer coefficient
I = supplied current
L = tube length
p = fluid pressure
p_c = critical pressure
p_r = pressure ratio (p/p_c)
Pr = Prandtl number
q = input power
q'' = heat flux
T_{sat} = saturated water temperature
T_w = tube wall temperature
ΔT = degree of superheat of the heating surface ($T_w - T_{\text{sat}}$)
V = supplied voltage
ε = average tube surface roughness in rms value

References

[1] Corletti, M. M., and Hochreiter, L. E., 1991, ''Advanced Light Water Reactor Passive Residual Heat Removal Heat Exchanger Test,'' *Proc. of the 1st JSME/ASME Joint International Conference on Nuclear Engineering*, Tokyo, Japan, pp. 381–387.
[2] Kang, M. G., 1998, ''Experimental Investigation of Tube Length Effect on Nucleate Pool Boiling Heat Transfer,'' Ann. Nucl. Energy **25**, Nos. 4–5, pp. 295–304.
[3] Cornwell, K., et al., 1982, ''The Influence of Diameter on Nucleate Boiling Outside Tubes,'' *Proc. of the 7th International Heat Transfer Conference*, Munchen, Germany, pp. 47–53.
[4] Cornwell, K., and Houston, S. D., 1994, ''Nucleate Pool Boiling on Horizontal Tubes: A Convection-Based Correlation,'' Int. J. Heat Mass Transf. **37**, Suppl. 1, pp. 303–309.
[5] Chun, M. H., and Kang, M. G., 1998, ''Effects of Heat Exchanger Tube Parameters on Nucleate Pool Boiling Heat Transfer,'' ASME J. Heat Transfer, **120**, pp. 468–476.
[6] van Stralen, S. J. D., and Sluyter, W. M., 1969, ''Investigations on the Critical Heat Flux of Pure Liquids and Mixtures under Various Conditions,'' Int. J. Heat Mass Transf. **12**, pp. 1353–1384.
[7] Hahne, E., and Feurstein, G., 1977, ''Heat Transfer in pool Boiling in the Thermodynamic Critical Region: Effect of Pressure and Geometry,'' in *Heat Transfer in Boiling*, E. Hahne and U. Grigull, eds., chap. 8, pp. 159–206.

Forced Convection in a Porous Channel With Discrete Heat Sources

C. Cui

X. Y. Huang
e-mail: mxhuang@ntu.edu.sg

C. Y. Liu

School of Mechanical and Production Engineering, Nanyang Technological University, Nanyang Avenue, Singapore 639798

An experimental study was conducted on the heat transfer characteristics of flow through a porous channel with discrete heat sources on the upper wall. The temperatures along the heated channel wall were measured with different heat fluxes and the local Nusselt numbers were calculated at the different Reynolds numbers. The temperature distribution of the fluid inside the channel was also measured at several points. The experimental results were compared with that predicted by an analytical model using the Green's integral over the discrete sources, and a good agreement between the two was obtained. The experimental results confirmed that the heat transfer would be more significant at leading edges of the strip heaters and at higher Reynolds numbers.

[DOI: 10.1115/1.1351176]

Keywords: Forced Convection, Heat Transfer, Porous Media

Introduction

The demand for execution speed and memory capacity for modern computers causes the increasing circuit density per chip and high power dissipation per unit volume [1]. For reliable operation, the temperature of electronic package must be below the manufacturer's specification, and some electronic devices require the more uniform surface temperature distribution among the chips or within the devices [2]. With the large increase in heat transfer rate, it was proposed by several researchers to use the channels packed with high-conductivity porous or fibrous material as an effective alternative way to enhance heat transfer. Koh and Colony [3] analyzed the temperature distribution in a channel packed with porous materials. Their results showed that the wall temperature and the temperature difference between the wall and the coolant were drastically reduced by inserting a high-conductivity porous material in the channel. Hwang and Chao [4] utilized porous channels filled with sintered bronze beads to enhance forced convective cooling for potential application to electronic cooling. It was found that forced air heat transfer coefficient could be increased from 0.01 to 0.5 W/cm^2 °C using porous heat sinks with particle diameter of 0.72 mm. Based on the Brinkman-extended Darcy model, Kaviany [5] studied the behavior of forced convection in a porous channel bounded by isothermal parallel plates. It was indicated that the fully developed velocity profile changes gradually from parabolic to uniform as the Darcy number decreases, and the entrance length decreases linearly with the decrease of the Darcy number. Vafai and Kim [6] investigated the fully developed forced convection in a porous channel bounded by parallel plates with a constant heat-flux boundary condition and obtained analytical solutions for velocity and temperature

Contributed by the Heat Transfer Division for publication in the JOURNAL OF HEAT TRANSFER. Manuscript received by the Heat Transfer Division September 23, 1999; revision received July 20, 2000. Associate Editor: M. Hunt.

fields. It was shown that for a high permeability porous medium the thickness of the momentum boundary layer depended on both the Darcy number and the inertia parameter, while for a low permeability porous medium, the inertia effect was weak and the momentum boundary layer depends only on the Darcy number. The velocity profile in a low permeability porous channel can be approximately assumed to be uniform across the channel. Hung and Tien [7] investigated the effects of thermal dispersion in fibrous media experimentally and demonstrated that the heat transfer increase by several times was achievable. Among these studies, the heat transfer of a porous channel with discrete sources was of special interest due to its applications on cooling of electronics [8,9]. Hadim [10] performed a numerical study to analyze steady laminar forced convection in a porous channel containing discrete heat sources on the bottom wall. His results were based on the Brinkman-Forchheimer-extended Darcy model. A significant increase in heat transfer rate was observed as the Darcy number was decreased, especially at the leading edge of each heat source. He suggested that the low permeability porous medium could be used as an effective technique for electronic cooling.

This paper presents some preliminary results from an experiment on the forced convection in a porous channel with discrete heat sources on the top surface. The temperature along the heated wall and the temperature distribution inside the channel were measured for different heat fluxes and flow rates, and the local Nusselt numbers were calculated. The experimental results were verified with the prediction by an analytical model, and good agreement between the two was obtained.

Experimental Setup

The experimental rig consists of a test section, a water supply system and a data acquisition system. The test section, which had a length of 686 mm and a cross-sectional of 70 mm by 20 mm, was made of 20 mm thick perspex and consisted of an entrance, a heater section and an exit. The entrance was constructed entirely of perspex and at its end was a section of 54 mm long porous material to ensure a fully developed flow in the measuring section. As indicated by Hadim [10] the length of the momentum boundary layer of the developing flow was shorter than the height of porous channel H, the effect of entrance region was therefore negligible in this experiment by placing the heater section far away from the entrance. Duocel Silicon Carbide Foam, a kind of fibrous porous, was used as the porous medium and the structure under microscope is shown in Fig. 1. The material was isotropic, uniform in pore spacing and was cut in such a way that the sides were flush with the channel walls for a good contact. The porosity of the Silicon Carbide Foam was 0.88. The permeability was experimentally determined of about 6.67×10^{-9} m^2 and the Darcy Number was about 1.67×10^{-5}. There were 5 strip heaters mounted on the upper wall of the heater section which was made of teflon, shown in Fig. 1. The heaters were 15 mm in width and were placed with intervals of 15 mm on the top of 5 equal size copper plates which were flushed with the teflon wall to ensure a good contact to the porous channel. A teflon plate was clamped on the top of heaters to fasten the heaters firmly on the copper plates, and also to provide heat insulation. In addition, a guard heater was mounted on the teflon plate to maintain a temperature difference between the two sides of the teflon insulation less than 0.1 degree, so that heat loss from the strip heaters through the top teflon plate was minimum and the heat was approximately conducted to the porous channel through the copper plates. There were 26 thermocouples placed along the interface of the porous media and the upper channel wall; the arrangement of the thermocouples is shown in Fig. 1. Two pairs of thermocouples were located on each strip heater and the averaged value was taken as the surface temperature on heaters, and the surface temperatures between the strip heaters were taken by the thermocouples at the center. The temperatures of the inlet and outlet were measured by two thermocouples, and additional 5 sheathed thermocouples, which had a diameter of 0.3 mm, were inserted inside the porous channel to measure the temperature distribution. The exit was located far from the heater section so that the effects of outflow boundary condition on flow and heat transfer were negligible.

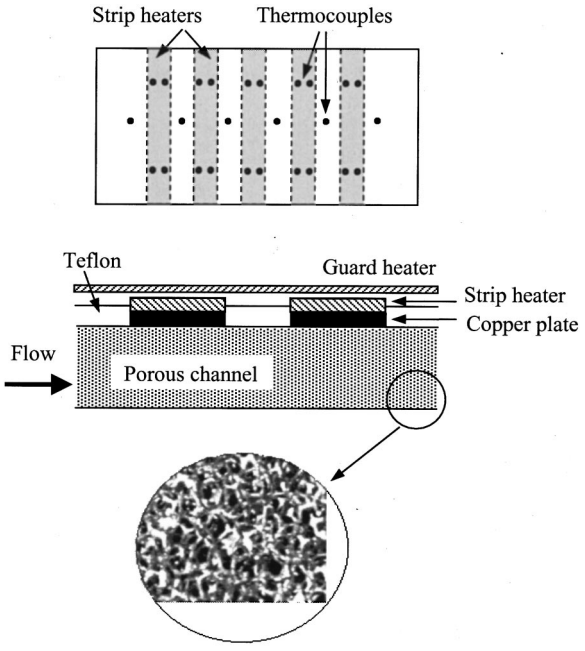

Fig. 1 The test section

A water supply system was used in the experiment. The flow rate of the water entering the section was measured by a rotameter that had a factory calibrated accuracy of ±2.0 percent full scale. Two pressure taps were located before and after the porous foam and connected to pressure transducers, which measured the differential pressure across the porous medium. The output of the thermocouples and the pressure transducers were transmitted to a HP-34970A data acquisition system and processed in PC. The voltage across the heaters as well as the current were read from J&D 1000 voltage meters and current meters and were used to calculate the electrical power input to the heaters. For normal tests, the electrical power to the heaters was adjusted to a desired level using variable voltage transformers, while the flow rate and inlet flow temperature were simultaneously maintained at the desired condition. The raw data were collected every 20 seconds, and the steady state was assumed to have been reached when the variation in the wall temperature measurements was within ±0.2 °C over a period of 2 minutes. The fluid properties were based on the average flow temperature in each test. For the forced convection, the effective thermal conductivity is a combination of the stagnant conductivity, k_o, and the dynamic thermal dispersion conductivity, k_d [11,12]. The dispersion conductivity will be discussed later on, while the stagnant thermal conductivity was obtained by performing a number of one-dimensional conduction heat transfer experiments on the porous channel which was saturated with water. The stagnant thermal conductivity k_o was found about 6.74 W/mK. This was done by measuring the heat flux and the temperature difference in the thickness direction, when the porous channel was filled with water and was supplied a constant heat flux from the upper surface. The measured thermal conductivity was used in the analytical calculations for the comparison with the experimental results.

An uncertainty approximation of the experimental data was conducted using the method described in JHT [13]. The uncertainty in the temperature measurement was estimated to be ±1°C. The maximum percentage of errors for the channel wall temperature, the flow rate, the porous permeability and the stagnant heat

conductivity were estimated as ±7 percent, ±1 percent, ±5 percent, and ±8 percent, respectively. Within the temperature and flow range in the experiment, the maximum uncertainty for the Nusselt number and the Reynolds number were 12 percent and 5 percent, respectively.

Theoretical Modeling

The temperature distribution for the forced convection in a low permeability porous channel with a point heat source, located at $(X_0,\ Y_0,\ Z_0)$ in the channel, was previously obtained [14] in a form of the Green's function, $G(X,Y,Z|X_0,Y_0,Z_0)$. In general, if the geometrical distribution function of the heat sources, say $S(X,Y,Z)$, is known, the non-dimensional temperature field, $\theta=(T-T_{\text{in}})/(q\cdot H/k_f)$, generated by the heat sources can be obtained by using the Green's integral:

$$\theta(X,Y,Z)=\frac{1}{\Delta}\int\int\int_V S(X_0,Y_0,Z_0)\times G(X,Y,Z|X_0,Y_0,Z_0)dX_0dY_0dZ_0, \quad (1)$$

where

$$\Delta\int\int\int_V S(X,Y,Z)dXdYdZ.$$

In the present experiment, the corresponding dimensionless distribution function for the strip heat sources at the upper wall of the channel is

$$S(X_0,Y_0,Z_0)=\delta(Y_0-1)\cdot\begin{cases}0 & 2n<X_0<2n+1, \quad n=0,1,2,3,4.\\ 1 & 2n+1\leqslant X_0\leqslant 2n+2, \quad n=0,1,2,3,4.\end{cases} \quad (2)$$

All assumptions of the fluid and the porous channel were the same as for the point heat source. The channel walls were assumed to be adiabatic except the portions in contact with the heat sources. Thus the temperature distribution in the porous channel and on the wall surface can be obtained by evaluating the Green's integral (1) with the distribution function (2). For the sake of brevity, the calculated temperature field will be directly given in the following discussion.

Results and Discussion

The experiments were conducted with the input heat flux $q=5$ W/cm^2, 10 W/cm^2, and 19.5 W/cm^2, and the Reynolds number Re=250, 400, and 600. The results were presented in terms of the upper wall temperature along the channel, the local Nusselt numbers and the temperature field inside the porous channel.

In order to compare experimental data with analytical predictions, the same parameters for the heat, flow and the porous medium, as well as the channel dimensions were used in the analytical calculation. The effect of dispersion, though it was small, was taken into account in the present study by calculating the dispersion conductivity in fibrous porous [7]:

$$k_d=\rho c_p\gamma u_x\sqrt{K}, \quad (3)$$

where ρ and c_p are the fluid density and heat capacity, γ is the dispersion coefficient which has the empirically determined value of 0.025, K is the permeability of the porous medium and u_x is the flow velocity along the channel. Thus, in the bulk of porous medium, the effective conductivity is equal to the sum of the stagnant and dispersion terms,

$$k_e=k_o+k_d=k_o+\rho c_p\gamma u_x\sqrt{K}. \quad (4)$$

The stagnant conductivity k_o was measured in the experiment.

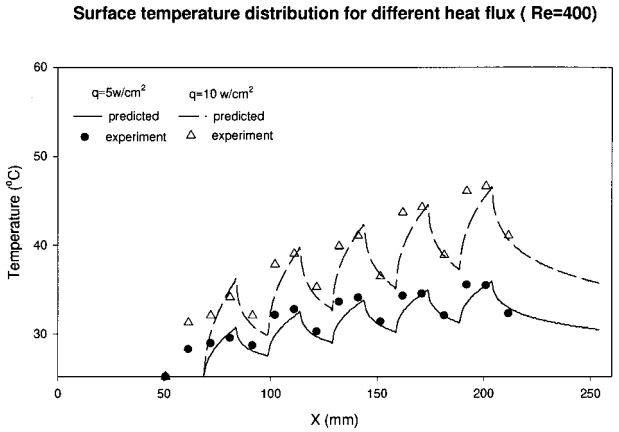

Fig. 2 The surface temperature distributions on the surface of the heated wall at the Reynolds number Re=400

Figure 2 shows the temperature distribution on the inner surface of the heated channel wall for different heat flux. The triangles and the solid circles are the measured results, and the dashed and solid lines are the calculated temperature distributions. It is seen that the temperature over each heater increases along the channel in the flow direction, and over the adiabatic portions between the heaters, the temperature decreases due to heat transfer from the wall to the fluid flow. The overall temperature on the surface is high for the high input heat flux. It is also seen that the predicted temperature distributions agree well within the experimental values along the channel wall. The analytical model used in the prediction was previously verified with Hadim's [10] numerical model for the Darcy number about 10^{-6} [14]. The comparison with the experiment data demonstrates that the discrepancy between the experimental results and the analytical values is also acceptable when the Darcy number is about 10^{-5} in the present case. The variation of local Nusselt number for different Reynolds numbers is shown in Fig. 3. The circles and pulses are the measured values, and the solid and dashed lines are the calculated values. The local Nusselt number is defined as

$$\text{Nu}=\frac{qH}{(T_w-T_{\text{in}})k_f}=\frac{1}{\theta}, \quad (5)$$

where q is the heat flux, H is the height of porous channel, k_f is the thermal conductivity of the fluid, and T_w and T_{in} are the upper wall temperature and the inlet fluid temperature. It can be seen

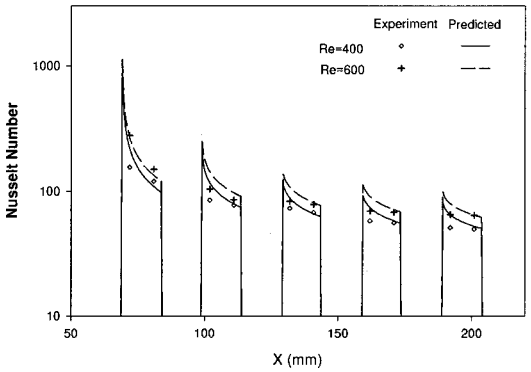

Fig. 3 The variation of local Nusselt number on the upper channel wall for different Reynolds numbers. The heat flux $q=10$ W/cm^2

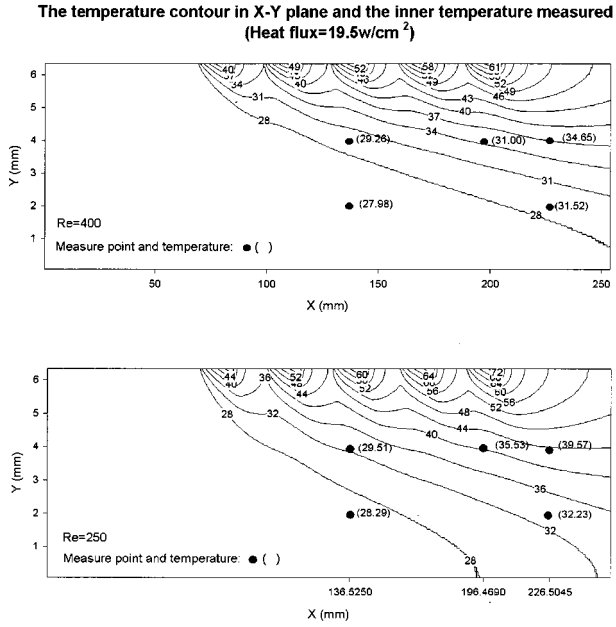

Fig. 4 The temperature contour in the vertical plane predicted by the analytical model and the temperature measured inside the porous channel

that a large Nusselt number occurs at the leading edge of each heater and then the Nusselt number declines along the channel wall. This is because the growth of the intermittent thermal boundary layer starts from the leading edge of each heater and stops in the adiabatic sections. It is confirmed, therefore, that the heat transfer is more significant at the leading edge of each heater. The experimental data agree with the predicted values very well. Figure 4 shows the temperature contour in the lateral plane of the channel, which was calculated by using Eqs. (1) and (2) for the temperature on X-Y plane. The dot points indicate the location of the inserted thermal couples and the measured values are given in the parenthesis. In general, the temperatures at the 5 thermocouples inside the channel are close to the predicted temperature fields, although the discrepancies are obviously there. Since the heads of the thermocouples are about 0.3 mm, they may give the water temperature in the porous matrix, so that the results show the discrepancies which are generally lower than the predicted values. It is also seen that the temperature distributions are sensitive to the Reynolds numbers; the higher Reynolds number, corresponding to a stronger forced convection, will result in a lower wall temperature profile.

Conclusions

The heat transfer in a porous channel with discrete heat sources on the upper wall was experimentally studied and the results were presented. The temperature distributions and the local Nusselt numbers were measured along the upper channel wall, as well as the temperatures inside the porous channel. The results were compared with the predictions from an analytical model and it was demonstrated that they agreed with each other in general. The experimental results confirmed that the heat transfer is more significant at leading edges of the strip heaters and at higher Reynolds numbers. The results presented in this work may be useful in further study on the heat transfer in low permeability porous channels with discrete heat sources.

Acknowledgment

This work was part of a project funded by National Science and Technology Board of Singapore.

References

[1] Mahalingam, M., and Berg, H., 1984, ''Thermal Trend in Component Level Packaging,'' Int. J. Hybrid Microelectron. **7**, pp. 1-9.
[2] Lage et al., 1995, ''Numerical Simulations of Low Permability Microporous Heat Sink for High-Heat-Flux Electronics,'' *Cooling and Thermal Design of Electronic Systems*, HTD-Vol. 319/EEP-Vol. 15, ASME 1995, pp. 85–92.
[3] Koh, J., and Colony, R., 1974, ''Analysis of Cooling Effectiveness for Porous Material in a Coolant Passage,'' ASME J. Heat Transfer, **96**, pp. 324–330.
[4] Hwang, G., and Chao, C., 1994, ''Heat Transfer Measurement and Analysis for Sintered Porous Channels,'' ASME J. Heat Transfer, **116**, pp. 456–464.
[5] Kaviany, M., 1985, ''Laminar Flow Through a Porous Channel Bounded by Isothermal Parallel Plate,'' Int. J. Heat Mass Transf., **28**, pp. 851–858.
[6] Vafai, K., and Kim, S. J., 1989, ''Forced Convection in a Channel Filled With a Porous Medium: an Exact Solution,'' ASME J. Heat Transfer, **111**, pp. 1103–1106.
[7] Hunt, M. L., and Tien, C. L., 1988, ''Effects of Thermal Dispersion on Forced Convection in Fibrous Media,'' Int. J. Heat Mass Transf., **31**, pp. 301–310.
[8] Kuo, S. M., and Tien, C. L., 1988, ''Heat Transfer Augmentation in a Foam-Material Filled Duct with Discrete Heat Sources,'' *Proc. Thermal Phenomena in Electronics Components Conference*, Los Angeles, CA, May 11–13, pp. 87–91.
[9] Rizk, T. A., and Kleinstreuer, C., 1991, ''Forced Convective Cooling of a Linear Array of Blocks in Open and Porous Matrix Channels,'' Heat Transfer Eng. **12**, pp. 4–47.
[10] Hadim, A., 1994, ''Forced Convection in a Porous Channel with Localized Heat Sources,'' ASME J. Heat transfer, **116**, pp. 465–474.
[11] Cheng, P., and Hsu, C., 1986, ''Applications of Van Driest's Mixing Length Theory to Transverse Thermal Dispersion in Forced Convective Flow Through a Packed Bed,'' Int. Commun. Heat Mass Transfer, **13**, pp. 613–635.
[12] Kuwahara, F., Nakayama, A., and Koyama, H., 1996, ''A Numerical Study of Thermal Dispersion in Porous Media,'' ASME J. Heat Transfer, **118**, pp. 756–761.
[13] JHT Editorial Board of ASME J. Heat Transfer, 1993, ''Journal of Heat Transfer Policy on Reporting Uncertainties in Experimental Measurements and Results,'' ASME J. Heat Transfer, **115**, pp. 5–6.
[14] Cui, C., Huang, X. Y., and Liu, C. Y., 2000, ''The Green's Function and Application for Heat Transfer in a Low Permeability Porous Channel,'' Int. J. of Electronic Packaging, in press.

A Quasi-Steady Analytical Solution to Freezing Planar Couette Flow With Viscous Dissipation

Carsie A. Hall, III
Assistant Professor, Assoc. Member ASME, Department of Mechanical Engineering, University of New Orleans, New Orleans, LA 70148
e-mail: cahall@uno.edu

Calvin Mackie
Assistant Professor, Assoc. Member ASME, Department of Mechanical Engineering, Tulane University, New Orleans, LA 70118
e-mail: cmackie@mailhost.tcs.tulane.edu

A quasi-steady analytical solution to freezing planar laminar Couette flow with viscous heating effects is presented. Closed-form expressions for the dimensionless freeze-front location, interface Nusselt number, and dimensionless power density (or dimensionless shear stress) are derived as a function of various dimensionless parameters. Several classical results are obtained in the appropriate asymptotic limits. [DOI: 10.1115/1.1351177]

Keywords: Analytical, Conduction, Heat Transfer, Phase Change, Solidification

Contributed by the Heat Transfer Division for publication in the JOURNAL OF HEAT TRANSFER. Manuscript received by the Heat Transfer Division December 17, 1999; revision received July 10, 2000. Associate Editor: B. Chung.

Introduction

Solidification and melting of materials under forced flow conditions has been the subject of many investigators [1] due to potential applications in manufacturing processes such as extrusion, freezing of water (and other liquids) in pipes, low-temperature viscometers, shear-plate squeeze film dampers in machine tools [2], and others. Such fluids exhibit Newtonian as well as non-Newtonian behavior [3]. However, fluid flows that exhibit Couette or Couette-like behavior such as purely shear-driven flows and near-wall turbulent flows in the presence of phase change (melting or freezing) have scarcely appeared in the literature. One particular application has been in crystal growth whereby researchers have investigated the effects of coupling of parallel shear flows to directional solidification [4]. While most of the studies on parallel shear flows with solid-liquid phase change have been experimental in nature, few have been treated theoretically. For example, Huang [5] studied analytically the incipient Couette flow problem and derived a closed-form solution for one-dimensional melting of the semi-infinite solid region by a hot moving wall. A combination of the similarity technique and Green's function was used in obtaining solutions for the melting of large Prandtl number fluids. The author noted that the shear stress within the melt layer decreased as a function of the square root of time as the melt layer thickens. However, the opposite effect is expected to occur with a solidifying Couette flow.

In this note, an analytical solution is presented for one-dimensional freezing of laminar Couette flow within a finite planar region with viscous dissipation in the low Stefan number limit. A closed-form expression for the instantaneous location of the solid-liquid interface is derived. In addition, expressions for the Nusselt number at the solid-liquid interface, dimensionless power density (or shear stress), and dimensionless solid-liquid interface re-melt or steady-state location are all derived as a function of pertinent dimensionless parameters. Several classical results are obtained in the appropriate asymptotic limits.

Problem Formulation

Consider the one-dimensional region of thickness L shown in Fig. 1. The motion of the liquid, assumed to be laminar, is shear-driven by a flat plate (on top) moving at constant speed V. The top flat plate is modeled as an adiabatic surface, and the liquid is considered an incompressible, Newtonian fluid. With the liquid initially at or above its fusion temperature (T_m) according to a prescribed distribution $T_l = T_l(y, t<0)$, the bottom surface is suddenly exposed to a fluid whose temperature (T_∞) is maintained below the liquid's fusion temperature. This induces the motion of a freeze front that propagates towards the top flat plate.

Upon introducing the following dimensionless parameters into the describing one-dimensional momentum and energy equations, including viscous dissipation,

$$Y=\frac{y}{L},\quad \Delta=\frac{\delta}{L},\quad U=\frac{u}{V},\quad \theta=\frac{T-T_\infty}{T_m-T_\infty},\quad \tau=\frac{t}{L^2/\alpha_s}$$

$$\mathrm{Br}=\frac{V^2 Pr}{c_l(T_m-T_\infty)}=\frac{\mu V^2}{k_l(T_m-T_\infty)},\quad \mathrm{Pr}=\frac{\mu c_l}{k_l},\quad \gamma=\frac{k_l}{k_s},$$

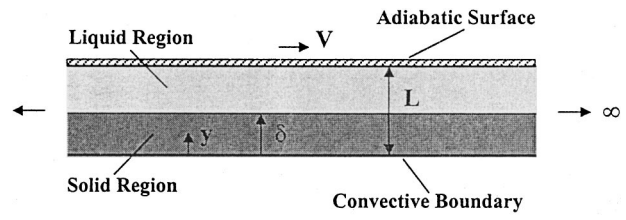

Fig. 1 Schematic model of planar Couette flow region undergoing solidification

$$\mathrm{Bi}=\frac{hL}{k_s},\quad \mathrm{Ste}=\frac{c_s(T_m-T_\infty)}{h_{sf}}, \tag{1}$$

where τ is the Fourier number, Br is the Brinkman number, Pr is the Prandtl number, Bi is the Biot number, and Ste is the Stefan number, the classical steady-state, linear Couette flow solution for the velocity distribution in the liquid region [6] is modified or can be derived as (assuming no-slip conditions at the solid-liquid interface)

$$U(Y,\tau)=\left[\frac{Y-\Delta(\tau)}{1-\Delta(\tau)}\right]. \tag{2}$$

Subsequently, the solution $U(Y,\tau)$ is used to determine the dimensionless temperature distribution in the liquid region via the dimensionless energy equation, i.e.,

$$\omega\frac{\partial\theta_l}{\partial\tau}=\frac{\partial^2\theta_l}{\partial Y^2}+\mathrm{Br}\left(\frac{\partial U}{\partial Y}\right)^2, \tag{3}$$

or, by using Eq. (2),

$$\omega\frac{\partial\theta_l}{\partial\tau}=\frac{\partial^2\theta_l}{\partial Y^2}+\frac{\mathrm{Br}}{(1-\Delta)^2}, \tag{4}$$

where $\omega=\alpha_s/\alpha_l$. Eq. (4) is subject to the initial condition

$$\theta_l(Y,\tau=0)=\mathrm{Br}\left[Y-\frac{Y^2}{2}\right]+1 \tag{5}$$

and boundary conditions

$$\left.\frac{\partial\theta_l}{\partial Y}\right|_{Y=1}=0 \tag{6a}$$

$$\theta_l(Y=\Delta^+,\tau)=1. \tag{6b}$$

Integrating the quasi-steady form of Eq. (4), subject to Eqs. (6*a*) and (6*b*), gives

$$\theta_l(Y,\tau)=\frac{\mathrm{Br}}{(1-\Delta)^2}\left[\frac{1}{2}(\Delta^2-Y^2)+(Y-\Delta)\right]+1. \tag{7}$$

The transient term in Eq. (4) is neglected due to the low value of the liquid-side Stefan number, which is explained as follows. First, it is observed that the maximum liquid temperature, $T_{\max}$, is at the adiabatic boundary ($Y=1$), which reduces Eq. (7) to

$$\theta_{l\,\max}=1+\frac{\mathrm{Br}}{2}, \tag{8}$$

where $\theta_{l\,\max}$ corresponds to θ_l evaluated at $T_{\max}$. Now, the liquid-side Stefan number is defined as

$$\mathrm{Ste}_l=\frac{c_l(T_{\max}-T_m)}{h_{sf}}. \tag{9}$$

Then, using the definition of the solid-side Stefan number [Eq. (1)], the ratio of liquid-to-solid-side Stefan number can be expressed as

$$\frac{\mathrm{Ste}_l}{\mathrm{Ste}_s}=\frac{c_l}{c_s}\left(\frac{T_{\max}-T_m}{T_m-T_\infty}\right)=\frac{c_l}{c_s}\left(\frac{T_{\max}-T_\infty}{T_m-T_\infty}-1\right)=\frac{c_l}{c_s}(\theta_{l\,\max}-1). \tag{10}$$

Using Eq. (8), this ratio reduces to

$$\frac{\mathrm{Ste}_l}{\mathrm{Ste}_s}=\frac{c_l}{c_s}\left(\frac{\mathrm{Br}}{2}\right). \tag{11}$$

In this study, the Brinkman number will be of order unity or several orders of magnitude less than unity while the liquid-to-solid specific heat ratio will remain of order unity. As a result, the liquid-side Stefan number will always be of the same order of magnitude or less than the solid-side Stefan number. In what follows, the solid-side Stefan number is assumed to be small but

non-vanishing, which also applies to the liquid-side Stefan number. Therefore, the sensible heat contributions on both the solid and liquid sides are neglected. Alexiades and Solomon [7] show that when the Stefan number is less than 0.1, the quasi-steady approximation gives excellent results.

The dimensionless one-dimensional temperature distribution in the solid region is described by the heat diffusion equation, expressed in dimensionless form as

$$\frac{\partial \theta_s}{\partial \tau} = \frac{\partial^2 \theta_s}{\partial Y^2} \tag{12}$$

subject to the initial condition

$$\theta_s(Y, \tau = 0) = \mathrm{Br}\left[Y - \frac{Y^2}{2} \right] + 1, \tag{13}$$

which cannot be satisfied under quasi-steady conditions. The corresponding boundary conditions are given by

$$\left.\frac{\partial \theta_s}{\partial Y}\right|_{Y=0} = \mathrm{Bi}\,\theta_s(Y=0,\tau), \tau > 0 \tag{14}$$

$$\theta_s(Y = \Delta^-, \tau) = 1, \tau > 0 \tag{15}$$

and the Stefan condition is given by [7]

$$\left.\frac{\partial \theta_s}{\partial Y}\right|_{Y=\Delta^-} - \gamma \left.\frac{\partial \theta_l}{\partial Y}\right|_{Y=\Delta^+} = \frac{1}{\mathrm{Ste}} \frac{d\Delta}{d\tau}. \tag{16}$$

In order to obtain an analytical solution to the present problem as formulated, solidification is assumed to progress in a quasi-steady manner, which is valid at low Stefan numbers. Therefore, the solution to the quasi-steady form of Eq. (12), subject to Eqs. (14) and (15), is

$$\theta_s(Y, \tau) = \frac{\mathrm{Bi}^{-1} + Y}{\mathrm{Bi}^{-1} + \Delta} \tag{17}$$

As a result, the Stefan condition becomes

$$\frac{1}{\mathrm{Bi}^{-1} + \Delta} - \frac{\gamma \mathrm{Br}}{1 - \Delta} = \frac{1}{\mathrm{Ste}} \frac{d\Delta}{d\tau}, \tag{18}$$

which is separated and cast in the following form:

$$\int_0^{\Delta} \frac{\mathrm{Bi}^{-1} + (1 - \mathrm{Bi}^{-1})\Delta' - \Delta'^2}{1 - \gamma \mathrm{Br} \mathrm{Bi}^{-1} - (1 + \gamma \mathrm{Br})\Delta'} d\Delta' = \mathrm{Ste} \int_0^{\tau} d\tau'. \tag{19}$$

Integration of Eq. (19) gives an analytical solution to the instantaneous freeze front location as a function of several dimensionless parameters, i.e.,

$$\left\{ \frac{\Phi^2}{\Psi^3} - \frac{\lambda}{\Psi^2} - \frac{1-\lambda}{\Psi} \right\} \ln\left[\frac{|\Phi - \Psi \Delta(\tau)|}{|\Phi|} \right] + \frac{1}{2\Psi} [\Delta(\tau)]^2 + \left(\frac{\Phi}{\Psi^2} - \frac{\lambda}{\Psi} \right) \Delta(\tau) = \mathrm{Ste} \cdot \tau \tag{20}$$

where

$$\Phi = 1 - \gamma \cdot \mathrm{Br} \cdot \mathrm{Bi}^{-1}, \quad \Psi = 1 + \gamma \cdot \mathrm{Br}, \quad \text{and} \quad \lambda = 1 - \mathrm{Bi}^{-1}. \tag{21}$$

Note that as the freeze front moves towards the top flat plate, the shear stress and, hence, the amount of viscous dissipation increases, which increases the liquid-side heat flux at the solid-liquid interface. Consequently, the solidification rate decreases and eventually reaches zero (steady state) when the liquid-side heat flux exactly balances the solid-side heat flux. If any additional energy is added to or is generated inside the liquid region (due to, for example, suddenly increasing the plate speed), re-melting of the solid will occur and the solid-liquid interface will begin to recede. The mathematical equivalent of this re-melt or steady-state condition can be expressed as

$$\frac{1}{\mathrm{Bi}^{-1} + \Delta_{ss}} - \frac{\gamma \mathrm{Br}}{1 - \Delta_{ss}} = 0 \Rightarrow \Delta_{ss} = \frac{1 - \gamma \mathrm{Br} \mathrm{Bi}^{-1}}{1 + \gamma \mathrm{Br}} = \frac{\Phi}{\Psi}. \tag{22}$$

Within the framework of the present model, there are some other quantities of interest, namely the Nusselt number at the freeze front, i.e.,

$$\mathrm{Nu} = \frac{hL}{k_l} = \frac{q'' L}{k_l (T_{\max} - T_m)} = (\theta_{l\,\max} - 1)^{-1} \left.\frac{\partial \theta_l}{\partial Y}\right|_{Y=\Delta^+} = \frac{2}{1 - \Delta(\tau)}, \tag{23}$$

and the power or power density required (which is a function of the shear stress) to maintain the plate in motion at constant speed, given by

$$P = V \int \tau_{y=L} dA = VA\mu \left.\frac{\partial u}{\partial y}\right|_{y=L} \Rightarrow p'' = \frac{P}{A} = V\mu \left.\frac{\partial u}{\partial y}\right|_{y=L} = \frac{\mu V^2}{L} \left.\frac{\partial U}{\partial Y}\right|_{Y=1} \Rightarrow \frac{p'}{\mu V^2/L} = \frac{1}{1 - \Delta(\tau)}. \tag{24}$$

Note that Eqs. (23) and (24) are related by

$$\frac{\mathrm{Nu}}{2} = \frac{p''}{\mu V^2/L} = \frac{1}{1 - \Delta(\tau)} \tag{25}$$

and when Eq. (22) is substituted into Eq. (25) to obtain steady-state values, the expression

$$\left(\frac{\mathrm{Nu}}{2}\right)_{ss} = \left(\frac{P''}{\mu V^2/L}\right)_{ss} = \frac{1 + (\gamma \mathrm{Br})^{-1}}{1 + \mathrm{Bi}^{-1}} \tag{26}$$

results.

Results and Discussion

Asymptotic Limits. The solution given by Eq. (20) reduces to a few classical solutions when certain asymptotic limits are approached. For example, as the Brinkman number approaches zero ($\mathrm{Br} \to 0$), in which the liquid medium is everywhere stationary, the parameters Φ and Ψ both approach unity ($\Phi \to 1$ and $\Psi \to 1$). As a result, the solution expressed by Eq. (20) reduces to

$$\Delta(\tau) = \left[\left(\frac{1}{\mathrm{Bi}} \right)^2 + 2 \cdot \mathrm{Ste} \cdot \tau \right]^{1/2} - \frac{1}{\mathrm{Bi}}, \tag{27}$$

which is the non-dimensional form of the quasi-steady solution found in Alexiades and Solomon [7]. Furthermore, if the Biot number approaches infinity ($\mathrm{Bi} \to \infty$), which is the isothermal limit, then Eq. (27) becomes

$$\Delta(\tau) = [2 \cdot \mathrm{Ste} \cdot \tau]^{1/2}. \tag{28}$$

Equation (28) equals the exact Neumann solution when the parameter in the transcendental equation of Neumann's solution is approximated by $(\mathrm{Ste}/2)^{1/2}$, which is valid in the limit of low Stefan numbers. Note that Eq. (28) can also be deduced from Eq. (20) since as $\mathrm{Bi} \to \infty$, the parameter $\lambda \to 1$ (still with $\mathrm{Br} \to 0$) and only the quadratic term on the left-hand side remains, and Eq. (28) is obtained directly. The solution given by Eq. (20) also reveals another asymptotic limit. As the freeze front location Δ approaches Φ/Ψ ($\Delta \to \Phi/\Psi$), which is the steady-state condition expressed by Eq. (22), the product $(\mathrm{Ste} \cdot \tau)$ approaches infinity ($\mathrm{Ste} \cdot \tau \to \infty$), which is consistent with the steady-state limit. This is mathematically justified since it can be shown that when Eq. (20) is multiplied by Ψ^3, where Ψ is always positive, the resulting quantity pre-multiplying the logarithmic term is always negative, i.e.,

$$\Omega = \Phi^2 - \lambda\Psi - (1 - \lambda)\Psi^2 = -\gamma \mathrm{Br}[1 + 3\mathrm{Bi}^{-1} + \gamma \mathrm{Br} \mathrm{Bi}^{-1}] + (\gamma \mathrm{Br} \mathrm{Bi}^{-1})^2 < 0. \tag{29}$$

The parameter Ω is always negative because the quantity $(\gamma \mathrm{BrBi}^{-1})$ is required to be less than unity $(\gamma \mathrm{BrBi}^{-1}<1)$ for physically realistic results. This less than unity condition can also be expressed as

$$\gamma \mathrm{Br} < \mathrm{Bi}, \tag{30}$$

which is most evident in Eq. (22). Therefore, if $\gamma \mathrm{Br} > \mathrm{Bi}$, then $\Delta_{ss}<0$, which is physically unrealistic. Furthermore, the physical interpretation given to Eq. (30) is that the amount of viscous dissipation should always be smaller than the amount of convective heat removal.

Graphical Representation of Solutions. Shown in Fig. 2(*a*) is the temporal development of the solid-liquid interface location and solid-liquid interface Nusselt number (or power density), both normalized with respect to their steady-state values. Solutions are presented for Brinkman numbers of 0.01, 0.1, and 1. The liquid-to-solid thermal conductivity ratio is fixed at 0.8 and the Biot number is held at unity. The reader is cautioned not to interpret these results as direct comparisons since each unique Brinkman number yields a distinct steady-state freeze front location and Nusselt number. Nonetheless, some general trends can be observed. In the figure, the normalized freeze front location is shown to increase monotonically from 0 to 1 for all representative Brinkman numbers. It should also be noted that increasing the Brinkman number delays the time that it takes to reach steady-state conditions. This is due to the fact that increasing the Brinkman number increases the level of viscous dissipation, which increases the liquid-side heat flux at the freeze front. As a result, the effect of viscous heating in the liquid dominates the heat conduction in the solid, particularly at latter times, which slows down the solidification rate. In fact, the time that it takes to reach steady-state conditions is given by the Stefan number-Fourier number product $(\mathrm{Ste}\cdot\tau)$ of 1.72, 2.76, and 3.8 for Brinkman numbers of 0.01, 0.1, and 1, respectively. The corresponding steady-state freeze front locations, which occur when $\Delta/\Delta_{ss}\rightarrow 1$, for Brinkman numbers of 0.01, 0.1, and 1 are calculated to be 0.984, 0.852, and 0.111, respectively. The effect of heat transfer at the solid-liquid interface is quantified by the Nusselt number. It is observed that when the Brinkman number is small $(\mathrm{Br}=0.01)$, significant viscous heating effects are delayed until $\mathrm{Ste}\cdot\tau\approx 1.25$, before which the solid thickness is about 86 percent of its steady-state value. When $\mathrm{Ste}\cdot\tau>1.25$, the Nusselt number rises significantly, signifying enhanced viscous heating effects. In fact, the steady-state Nusselt number reaches approximately 0.63. For Brinkman numbers of 0.1 and 1, the increase in the Nusselt number is more gradual (with some changes in curvature for $\mathrm{Br}=0.1$), indicating increased viscous heating effects at earlier times as compared to the smaller Brinkman number. The steady-state Nusselt numbers are calculated to be 0.675 and 1.125, respectively, for Brinkman numbers of 0.1 and 1.

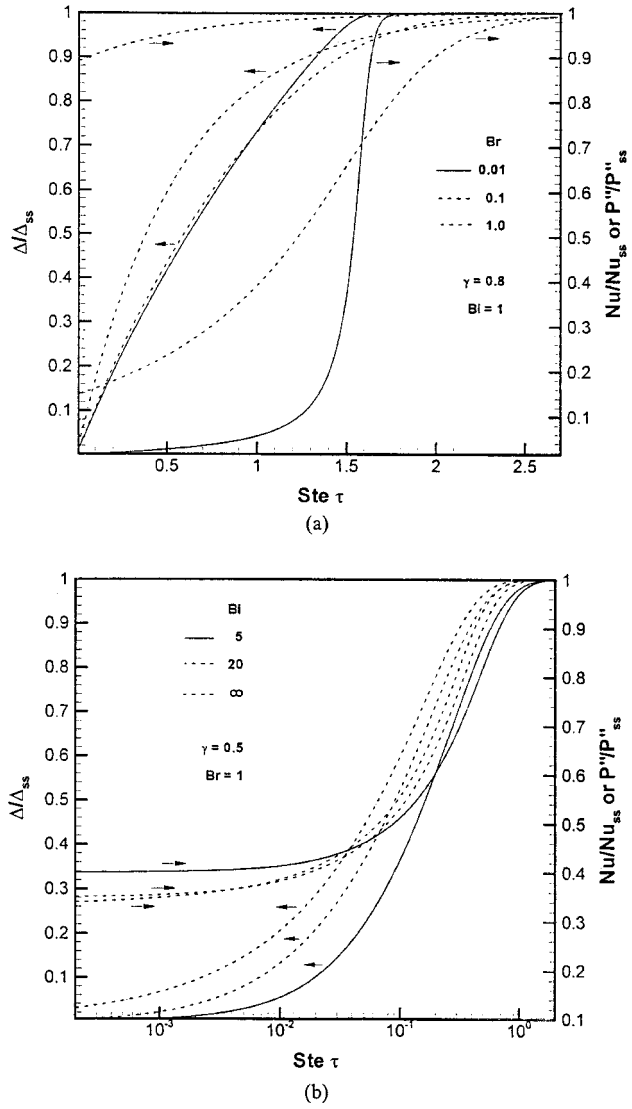

Fig. 2 Graphical representation of temporal variations in normalized freeze front location and interface Nusselt number (or dimensionless power density from Eq. (24)) for selected (*a*) Brinkman numbers and (*b*) Biot numbers

Figure 2(*b*) illustrates solutions for the instantaneous normalized freeze front location and Nusselt number (or power density) for Biot numbers of 5, 20, and ∞ (isothermal cooling). The liquid-to-solid thermal conductivity ratio is held at 0.5 and the Brinkman number is fixed at unity. In general, the effect of increasing the Biot number is to increase the solid thickness. However, at the same time, increasing the solid thickness decreases the thickness of the remaining liquid region, which increases the amount of viscous heating. This is evident in the figure, particularly at latter times $(\mathrm{Ste}\cdot\tau>10^{-2})$, by the significant increases in the Nusselt number for all representative Biot numbers. Therefore, at earlier times $(\mathrm{Ste}\cdot\tau<10^{-2})$, heat transfer on the liquid-side of the freeze front is not significantly affected by the growing solid layer. Note that when the product $(\gamma \mathrm{Br})$ is much smaller than the Biot number, the steady-state freeze front location is not greatly affected by changes in the Biot number. In this case, the lowest representative Biot number $(\mathrm{Bi}=5)$ is an order of magnitude higher than the product $(\gamma \mathrm{Br}=0.5)$, and the steady-state freeze front location changes from 0.6 to 0.65 to 0.66667 when the Biot number is increased from 5 to 20 to ∞. Correspondingly, the steady-state Nusselt number at the freeze front is calculated to be 2.5, 2.86, and 3, respectively, for Biot numbers of 5, 20, and ∞. Furthermore, the time to reach steady-state conditions, as indicated by $\mathrm{Ste}\cdot\tau$, is determined to be 1.8, 1.26, and 1.23 for Biot numbers of 5, 20, and ∞, respectively.

Conclusions

An analytical solution was presented for one-dimensional freezing of laminar Couette flow within a finite planar region (with viscous heating effects) in the limit low Stefan numbers (less than 0.1). Closed-form expressions for the instantaneous location of the freeze front, Nusselt number at the freeze front, dimensionless power density (or shear stress), and dimensionless solid-liquid interface re-melt or steady-state location were derived as a function of liquid-to-solid thermal conductivity ratio, Brinkman number, Biot number, and Stefan number. The analytical solution demonstrated that some classical results could be obtained in the appropriate asymptotic limits. The results also illustrated that the

product of liquid-to-solid thermal conductivity ratio and Brinkman number must always be less than the Biot number in order to obtain physically realistic results.

References

[1] Cheung, F. B., and Epstein, M., 1984, ''Solidification and Melting in Fluid Flow,'' in *Advances in Transport Processes*, A. Mujumdar and R. A. Mashelkar, eds., Vol. **3**, Wiley, New York, pp. 35–117.

[2] Slocum, A. H., 1992, *Precision Machine Design*, Prentice-Hall, Englewood Cliffs, NJ.

[3] Luelf, W. C., and Burmeister, L. C., 1996, ''Viscous Dissipation Effect on Pressure Gradient for Laminar Flow of a Non-Newtonian Liquid Through a Duct of Subfreezing Wall Temperature,'' ASME J. Heat Transfer, **118**, pp. 973–976.

[4] Huang, T., Liu, S., Yang, Y., Lu, D., and Zhou, Y., 1993, ''Coupling of Couette Flow and Crystal Morphologies in Directional Freezing,'' J. Cryst. Growth, **128**, pp. 167–172.

[5] Huang, S. C., 1984, ''Melting of Semi-Infinite Region with Viscous Heating,'' Int. J. Heat Mass Transf., **27**, pp. 1337–1343.

[6] Bird, R. B., Stewart, W. E., and Lightfoot, E. N., 1960, *Transport Phenomena*, Wiley, New York.

[7] Alexiades, V., and Solomon, A. D., 1993, *Mathematical Modeling of Melting and Freezing Processes*, Hemisphere, Washington, D.C.